BANGLADESH NETWORK OFFICE FOR URBAN SAFETY

BNUS ANNUAL REPORT-2022

BANGLADESH NETWORK OFFICE FOR URBAN SAFETY

BUET, DHAKA, BANGLADESH

Edited By:

Mehedi Ahmed Ansary

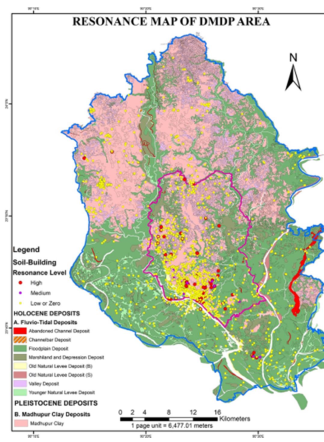

April 2023

CONTENTS

BANGLADESH NETWORK
OFFICE FOR URBAN SAFETY

PART-I

SEISMIC PERFORMANCE ANALYSIS OF SPUN PRECAST CONCRETE PILE IN RECLAIMED SOIL

BANGLADESH NETWORK OFFICE FOR URBAN SAFETY (BNUS), BUET, DHAKA

Prepared By: **Kh. Afia Farzana Haque**

Mehedi Ahmed Ansary

CHAPTER 1
INTRODUCTION

1.1 General

Increased demand for high-rise buildings for the ever-growing urban population made engineers build structures in poor ground condition. In this case, heavy loads coming from structures near the ground drive the engineers to adopt a deep foundation. Pile foundations can be classified into two categories: displacement piles and replacement piles. The displacement pile is installed by pushing into the ground which causes soil displacement around the pile. In replacement piles, the soil is replaced with subsequent placement of pile material. A Prestressed spun concrete pile is a displacement pile driven into an end bearing layer. It is newly introduced in Bangladesh for its better-quality control technique and quiet pilling operation. A precast prestressed spun pile can provide high bearing capacity from large shaft resistance and toe bearing.

The main reason for the pile foundation is to limit the settlement and control damage of the structure due to the soft layer underground. If the loose sand under the structure is saturated, it tends to behave like a liquid during earthquake shaking and tries to flow laterally. This makes the foundation vulnerable to extensive damage as the soil losses shear strength due to pore water pressure generation. The extensive damage caused by liquefaction of both superstructure and foundation is observed during past earthquakes namely Niigata earthquake in Japan 1964, 1995 Kobe Earthquake. Bangladesh and north Indian states are seismically active regions in the world. In the last 200 years, it has experienced numerous large magnitude of earthquakes. Though Dhaka did not encounter large to moderate magnitude earthquakes in the past but researchers pointed out four vulnerable points as a source of an earthquake that makes Dhaka a risky city among 20 unsafe cities in the world. Recently a mild tremor of 3.4 magnitudes was felt in Sylhet, Bangladesh. An earthquake of 4.5 magnitudes was felt in 2001 with a focal depth of 10 km near Dhaka. With the increased population, Dhaka city is going through rapid urbanization. As a result, many lowland areas are now being used and filled up with loose sandy dredged soil which is susceptible to liquefaction during seismic action.

Most piles are designed considering the axial load coming from the structure but during seismic events, it can suffer from substantial lateral pressure and large settlement in liquefiable soil. Previous studies showed that a pile can sustain axial load during the earthquake but it fails in lateral load, so it is mandatory to design a pile in the seismic region considering both axial and lateral load to overcome unwanted sudden damage of foundation and superstructure.

Numerical analysis is a reliable way to determine the seismic performance of a pile for a particular subsoil condition. By considering both geological properties and structural loading conditions, numerical investigation can evaluate the pile-soil response during seismic wave propagation. Researchers use finite element modeling to determine the factors affecting pile behavior in seismically vulnerable areas where piles can encounter possible failure due to weak soil during the liquefaction phenomenon.

For simulating pile-soil behavior, PLAXIS 3D finite element software is used in this thesis. Emphasis is given on soil modeling with earthquake loading and its effect on the pile. Different constitutive models are incorporated in PLAXIS such as Mohr-Coulomb (MC) model, the elastic-plastic non-linear stress-dependent stiffness Hardening Soil (HS) model, UBC3D-PLM, etc. In this study, the Hardening soil model is used for soil modeling for analysis of static and earthquake loading conditions. UBC3D-PLM model is used to capture the liquefaction probability during earthquake in loose sandy soil. The pile is modeled as an embedded beam row element. The function of embedded beam row is widely acknowledged by researchers in simulating dynamic pile response.

In this investigation, a static SPC pile load test has been conducted, and also SPT test has been also carried out in the study site. After the field tests, a numerical model is validated with the pile load test data and pile is simulated under static loading. A detailed numerical investigation has been conducted to observe the SPC pile response in earthquake loading in liquefiable soil situated in Jolshiri reclaimed land.

1.2 Background of the Study

Researchers have found much evidence of pile damages during earthquakes due to inertia forces of superstructures and piles lateral displacement. Spun Prestressed Concrete (SPC) pile has become a convenient choice for engineers in cohesionless liquefiable soil for building structures because of its low construction cost, high bearing capacity, and good reliability. The pile foundation is designed to sustain vertical and lateral load but sufficient lateral resistance needs to be considered for resisting structural damage of piles during an earthquake. The SPC piles are widely used abroad and many researchers have conducted experimental and numerical investigations to see the SPC pile capacity under axial and lateral load. The present study intends to investigate the seismic performance of SPC pile foundation in a reclaimed area of Dhaka susceptible to earthquake-induced liquefaction using three-dimensional numerical modeling.

Spun Prestressed Concrete (SPC) pile is a reliable alternative to conventional driven or bored pile due to its high ultimate load capacity and skin friction (Akiyama et al., 2012). Under dynamic loading prestressed pile showed larger peak displacement for saturated soil rather than unsaturated soil but prestressed pile can resist the damage well (Huang et al., 2017; Huang and Yu, 2017). A pile can be yielded before the complete liquefaction took place in the reclaimed layer (Uzuoka et al., 2007). The static load test can accurately measure the ultimate bearing capacity of prestressed high strength concrete pile compared to SPT blow count, CPT method (Wei et al., 2020). Numerical investigations are also done by researchers to observe pile performance in different soil characteristics (Kyi and Yangon; Lozovyi and Zahoruiko, 2014; Mohey Mohamed et al., 2020; Shafiqu and Sa'ur, 2017). Belinchón et al. (2016) have carried out a numerical investigation to model the negative skin friction of hollow prestressed pile driven into soft soil. The increased reinforcement ratio, pile depth, and prestressing level can move the plastic hinge location of the pile at a deeper depth and improve soil-pile interaction (Huang et al., 2020). Yang et al. (2018) have observed that the increase in reinforcement ratio of prestressed tendons and concrete infilling can improve ductility and bearing capacity of the piles.

Though SPC is widely used worldwide for its high strength capacity but in the context of Bangladesh SPC pile is newly introduced for reclaimed areas. Again, there is gap in literature to study SPC pile in loose soil susceptible to liquefaction during seismic excitation. Very few researchers addressed the problem of pile behavior in weak liquefiable soil. So, it is imperative to understand the pile behavior both in terms of vertical loading and lateral loading condition in subsoil conditions like reclaimed areas where the soil is highly susceptible to liquefaction phenomenon. The accurate way to measure the bearing capacity of pile foundation is to conduct in situ static pile load test. In the study area, this test is conducted to know the ultimate pile vertical load-bearing capacity. Pile foundation analysis is a three-dimensional problem. This study uses 3D finite element software to validate the vertical bearing capacity with field load test data and simulate the seismic behavior of the SPC pile under earthquake loading.

1.3 Objectives of the Study

The following are the main objectives of the research:

(i) To investigate the soil characteristics of the study site by conducting field and laboratory tests.

(ii) To develop a 3D finite element numerical model of SPC pile of at the site soil condition and compare it with the static pile load test data.

(iii) To observe SPC pile performance numerically under seismic excitation and conduct the parametric study.

1.4 Scope of the Study

Firstly, to know the soil characteristics of the soil Standard Penetration Test (SPT) has been done and soil samples has been collected to the laboratory for determining soil index and shear strength properties. A static pile load has also been performed to estimate pile capacity in Jolshiri Abashon area.

Secondly, a numerical finite element modeling has been done in PLAXIS 3D using Hardening soil model and embedded beam row to simulate static pile load test behavior. The developed model has been validated with the results of the static pile load test. A parametric study has also been done to observe the influence of mesh size, pile length and diameter on pile response.

Thirdly, the numerical model has been subjected to earthquake ground motion to observe the pile dynamic response using proper boundary condition. Liquefaction behavior of pile and soil has been simulated using UBC3D-PLM model during earthquake excitation.

Figure 1.1 shows the flowchart of the work procedure used to conduct the study.

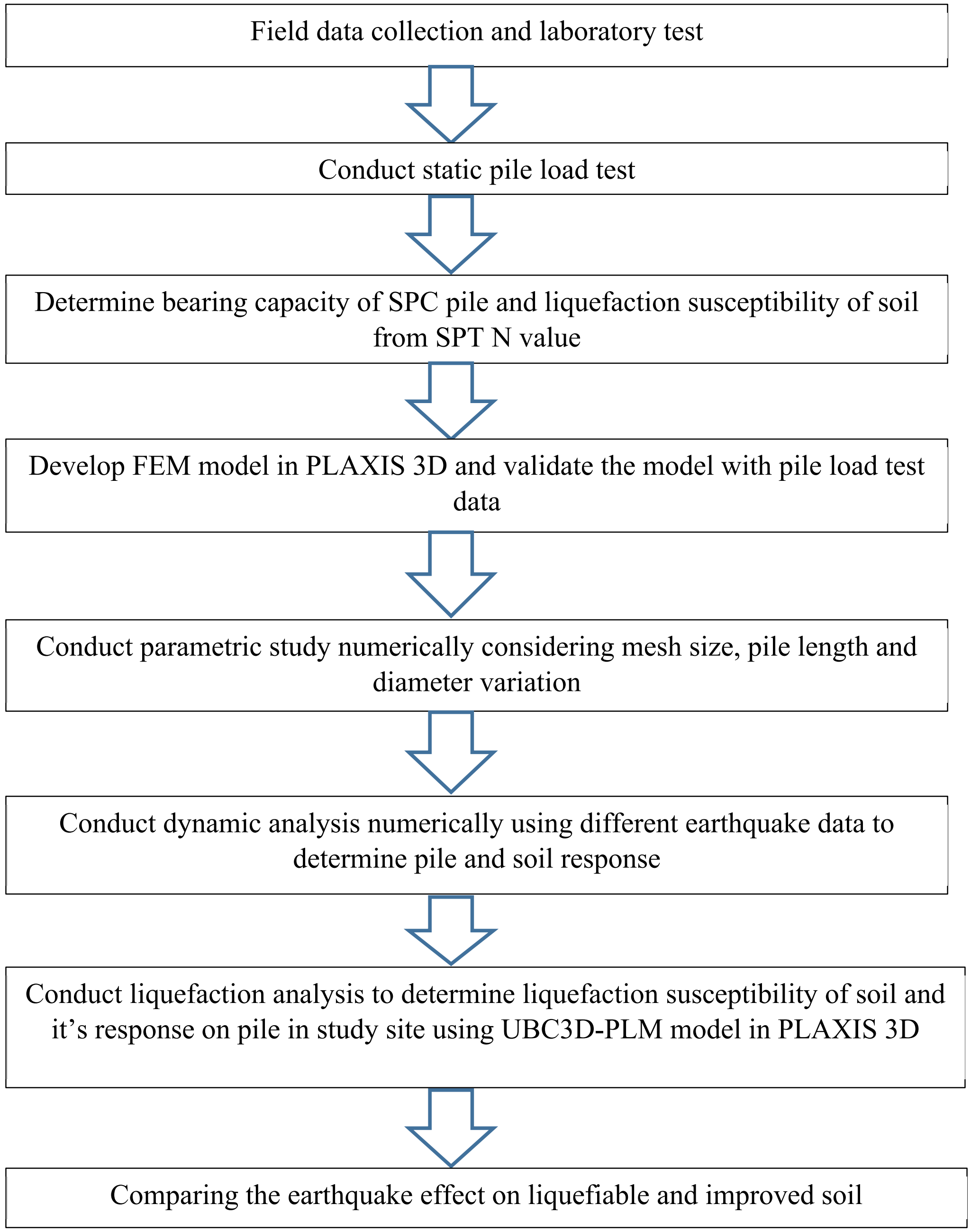

Figure 1.1: Flowchart of the study

CHAPTER 3

FIELD DATA COLLECTION AND BEARING CAPACITY ANALYSIS

3.1 Introduction

In this present study, the Jolshiri Abashon project area has been selected which is a reclaimed land located at the center of the eastern side of the DMDP area, Dhaka, Bangladesh. Jolshiri Abashon is 1.3 km from the south side of Purbachal's new town and it is surrounded by the Balu River on the west and the Shitalakkhya River on the east. Figure 3.1 shows the site location.

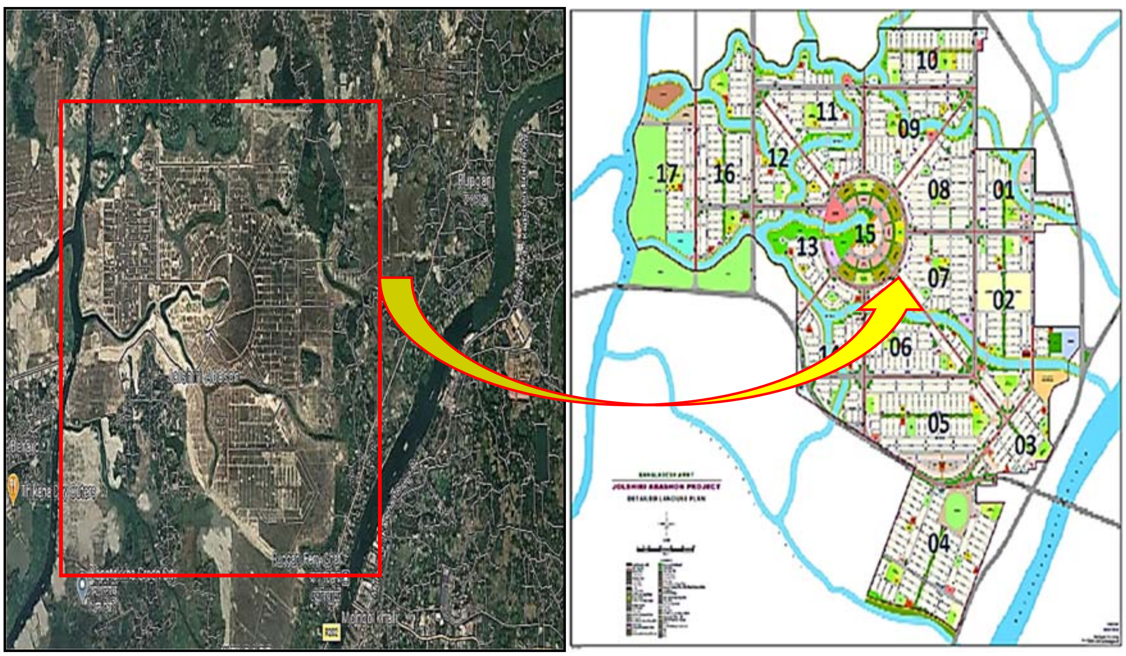

Figure 3.1: Jolshiri Abashon area

Primarily, at this site the subsoil investigation has been carried out and required soil properties are determined in the laboratory. A pile load test has also been conducted on a SPC pile in Jolshiri area for determining in-situ vertical bearing capacity. The results are verified with different existing empirical methods to estimate the bearing capacity.

3.2 Geometry of SPC Pile

Hollow prestressed precast reinforced concrete piles are termed as spun prestressed concrete (SPC) pile. SPC pile's geometry is commonly used in electric poles and they can be fabricated at the same factory. The concept of using spun pile as the foundation of soft soil particularly in the coastal zone has gained popularity for the last two decades mainly due to its easier installation, low cost, higher bearing capacity and easier insurance of material quality before pile casting. The hollow circular geometry of the SPC pile used in this study is shown in Figure 3.2 (a), the fabricated SPC pile and the long section of the pile with reinforcement are shown in Figure 3.2 (b), and Figure 3.2 (c), respectively. The SPC piles are fabricated through a special arrangement of caging, prestressing followed by the procedure of concrete pouring, rotating, steam curing etc. The aggregate size is usually 12mm and downgrade and ordinary portland cements (OPC) are used in the construction of SPC piles. PCC cements are also used in some construction. Relatively, high strength concrete (a concrete strength 50 MPa and above) and high strength strands (a nominal strength of 1860 MPa) are used for SPC pile casting. A prestress of 50 MPa is used in these piles to enhance the bending capacity that can ensure the piles to sustain lifting and handling stress. The basic features of the used SPC piles in this study are presented in Table 3.1.

Generally, the bearing capacity of the SPC pile is governed by the structural capacity of the pile. The length of the pile is designed based on the ability to penetrate through the soil. Subsequently, the lateral capacity of the pile is also designed as per the requirement of the site condition. The cross-sectional area of the SPC piles are low therefore shear reinforcement plays a key role against shear forces generated from seismic excitation. The allowable vertical capacity of SPC piles may be given by the API guideline as shown in equation 3.1 (Piling.2019).

$$\mathrm{P_a} = \mathrm{A_g}\left(0.33\ \mathrm{f'_c} - 0.27\mathrm{f_{pc}}\right) \tag{3.1}$$

Where

P_a, the allowable service level axial load bearing capacity of SPC pile

A_g, gross cross-sectional area of pile

f'_c, compressive strength of concrete at 28 days

f_{pc} = effective prestress in the pile

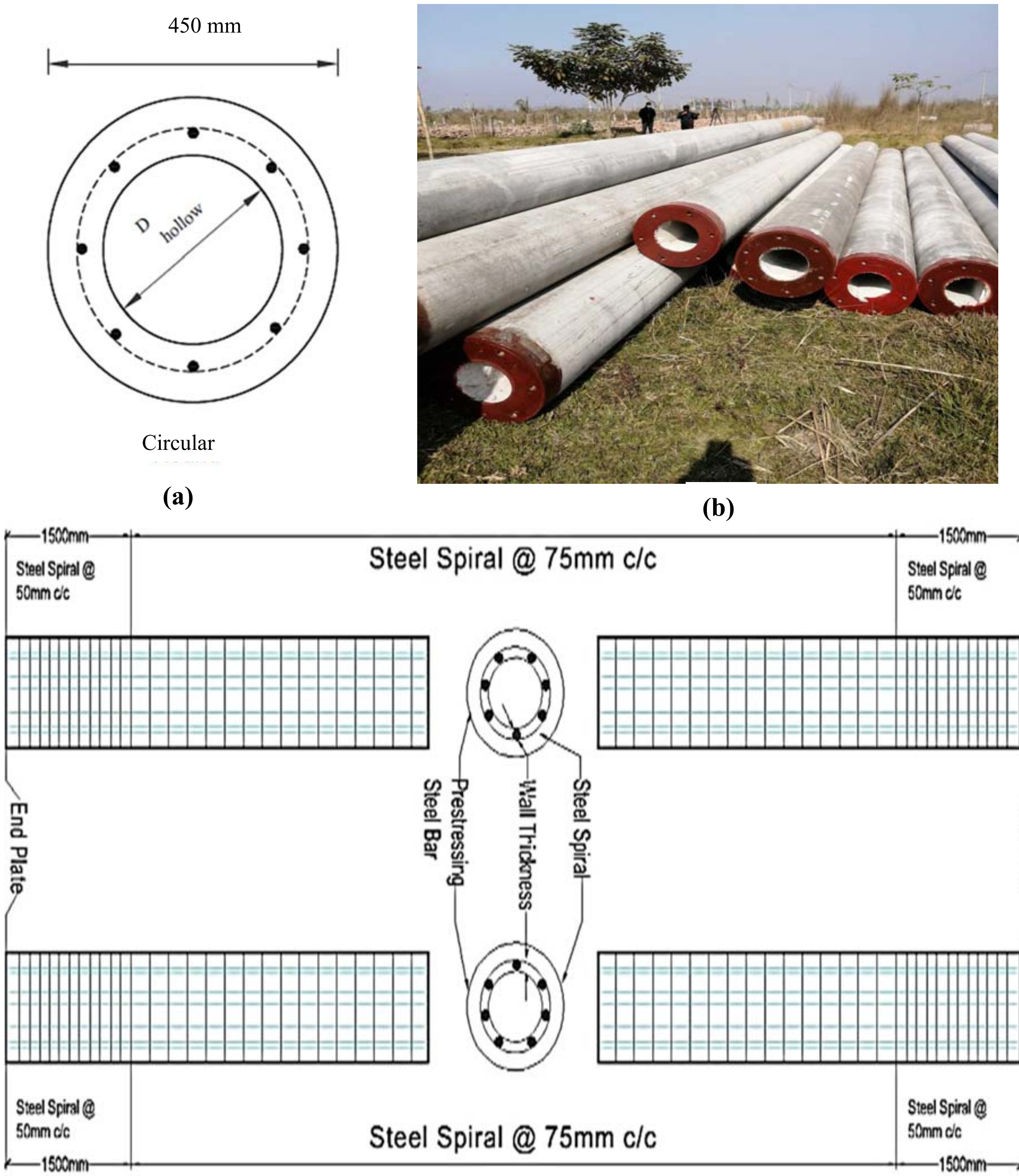

(c)

Figure 3.2: Geomtery of SPC pile: (a) Circular hollow cross section; (b) SPC pile ready for transportation; (c) Long section of SPC piles showing the spiral reinforcement details.

Table 3.1: Properties of SPC pile used in this study

SI	Description	Properties (Unit)
1.	Diameter	450 mm
2.	Length	12 m / 9 m / 6 m
3.	Cement used	OPC/PCC
4.	Concrete Mix Ratio FM of Sand Max Agg Size	1:1.25:2.5 2.5 FM (4-8) mm and (12 to 16) mm
5.	Wall Thickness	110 mm
6.	Material Spec: Concrete Strength Strands: 9mm dia 4mm MS wire ultimate load	7 Nos (pre-stressed) 50 MPa 1860 MPa 440 MPa
7.	4mm MS wire @50mm c/c 4mm MS wire @75C/C	At top and bottom 1.5 m At the middle
8.	Design Compressive Load (12m)	2500 kN
9.	Bending Strength	180 kN-m

3.3 Laboratory Test Results

To obtain the soil stratification of the selected site, subsoil investigation has been carried out. Three boreholes have been conducted within a residential building site. Each boring is associated with a Standard Penetration Test (SPT) and collection of disturbed and undisturbed samples from different depths of the boreholes. Figure 3.3 (a, b) shows the schematic diagram of borehole location for Standard Penetration Test (SPT). Figure 3.4 also shows the different soil stratum which are obtained from the subsoil investigation. In Figure 3.5, three boreholes are presented with respect to SPT blow count at different depths. As can be seen from the Figure, the top layer of the soil (up to 4.5 m depth) is consisting of very loose sand with an SPT value below 11. All three boreholes confirmed that there is a 33 m thick soft clayey sandy silt.

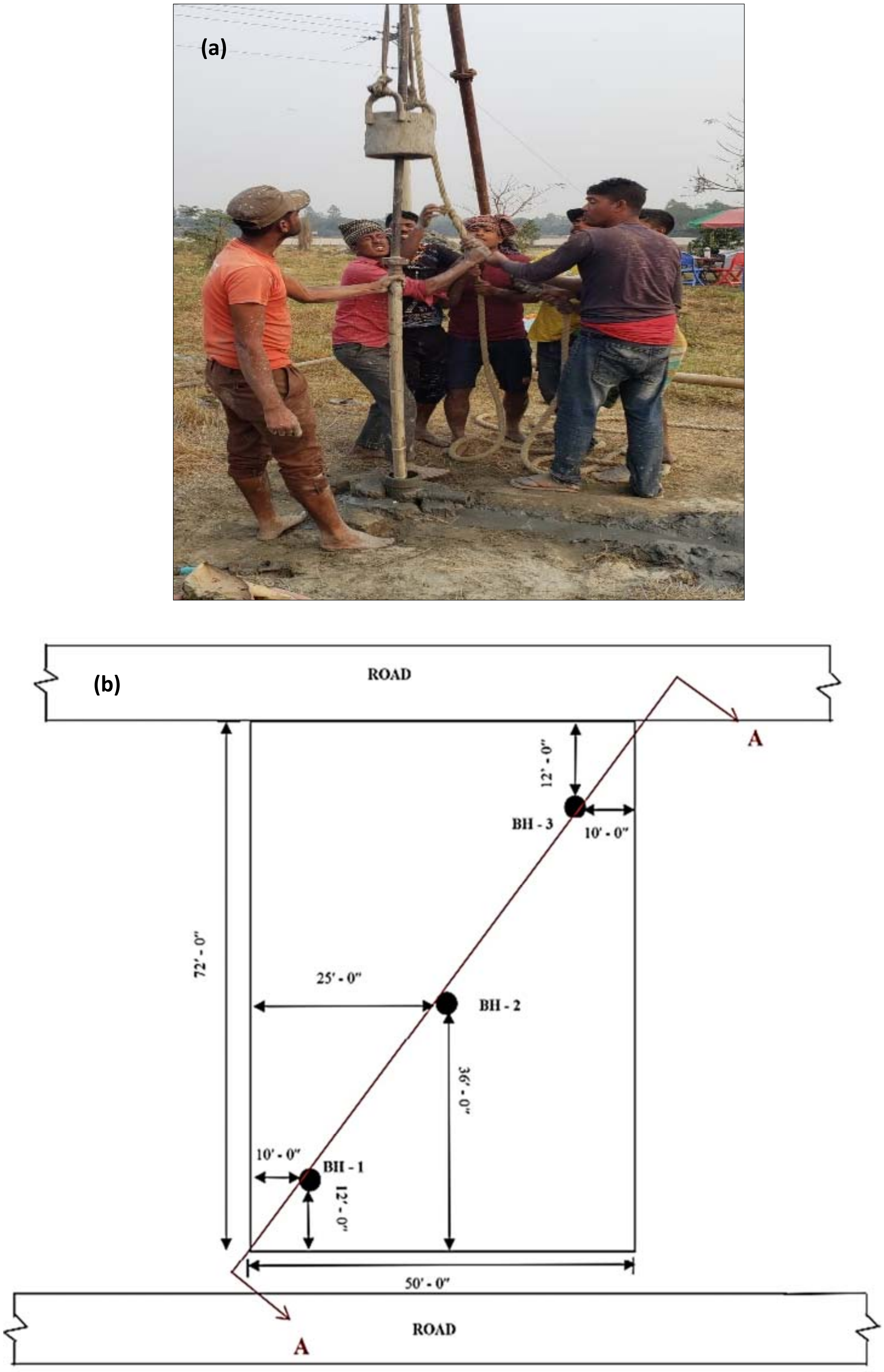

Figure 3.3: a) Standard Penetration Test (SPT) b) Borehole Location

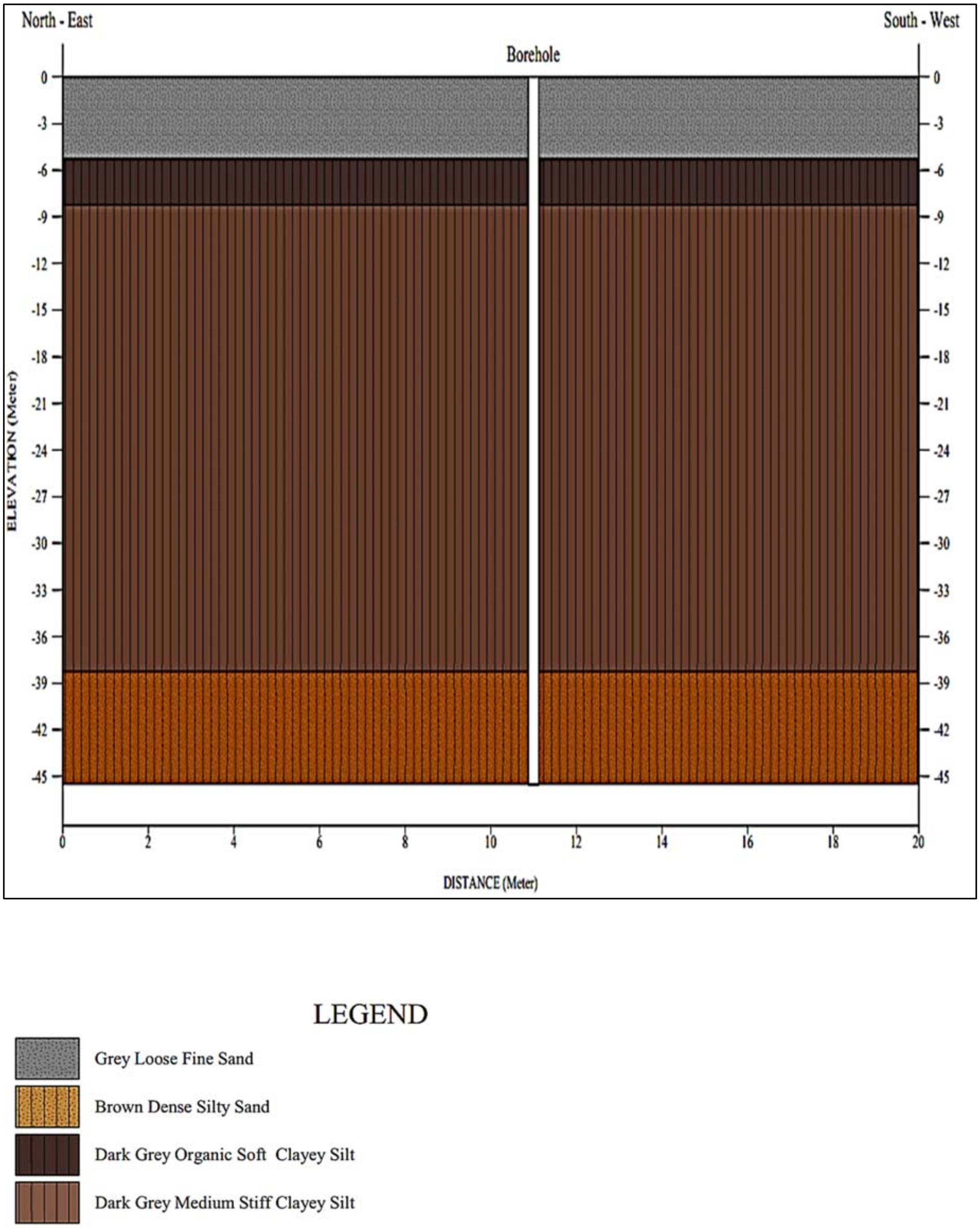

Figure 3.4: Borehole cross-sections

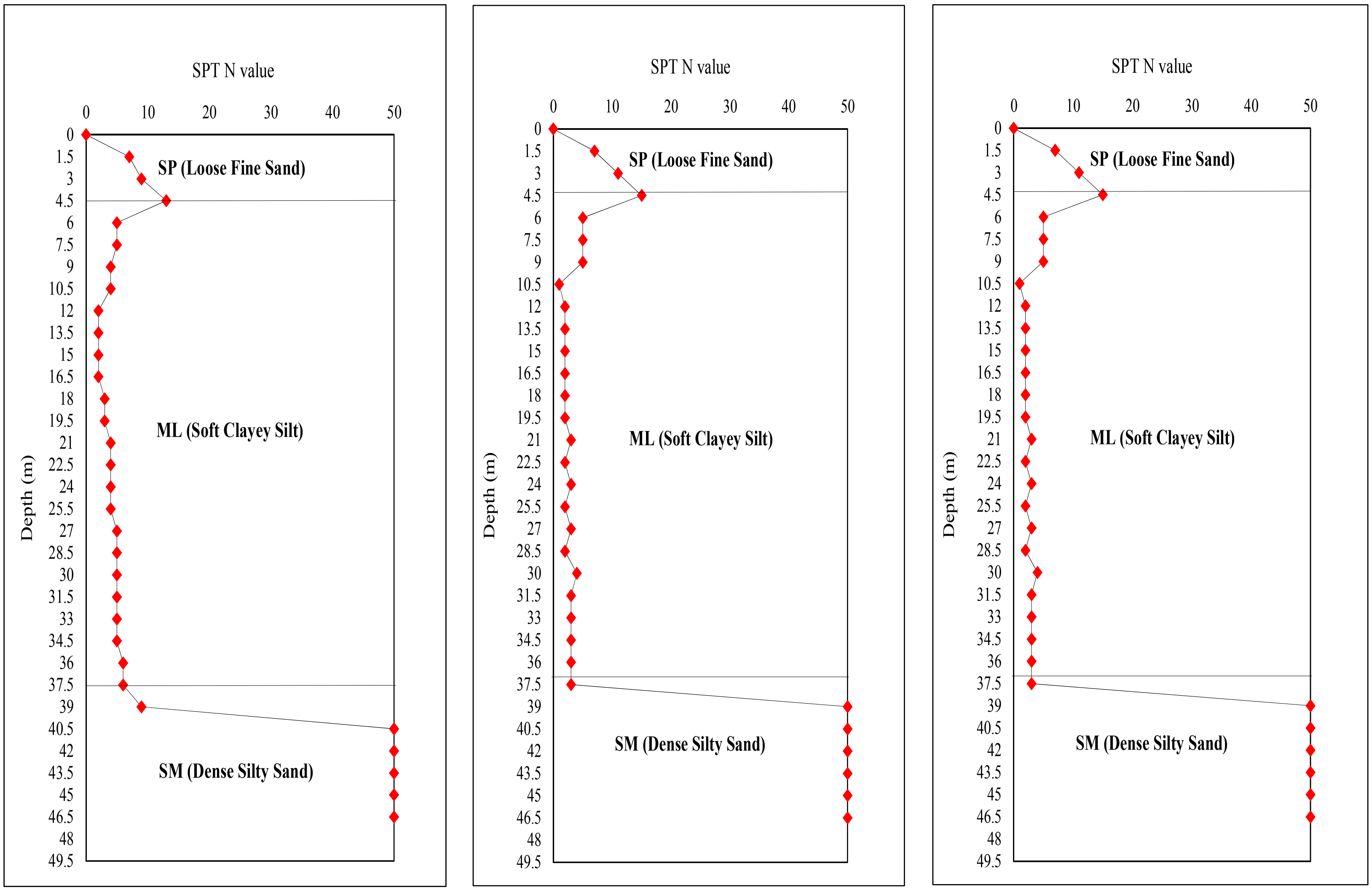

Figure 3.5: SPT N values for three boreholes

The first layer shows loose sandy soil, the second layer is soft clayey silt, third layer is dense silty sand layer. A hard stratum is found once the depth of penetration exceeds 37.5 m. The soil classifications are done with the data found from laboratory test results such as grain size analysis, CD triaxial test, Atterberg limit, moisture content, direct shear test, organic content test, unit weight, consolidation test, unconfined compressive strength test etc. Disturbed and undisturbed test samples have been collected from the study site at different depths. The laboratory tests are performed to identify the soil index and strength properties. The Laboratory tests are conducted by following the provisions of the standard code of practices such as BNBC, AASHTO and ASTM as shown in Figure 3.6. The soil layers are classified on the basis of laboratory test results according to the Unified Soil Classification System (USCS) for three boreholes. In absence of test results for any depth of a borehole, standard correlation with SPT-N values is followed based on soil characterization presented in this study.

3.3.1 Grain Size Analysis

Sieve Grain Size Analysis is done to determine the particles' size ranging from 0.075 mm to 100 mm. Particles smaller than 0.075 mm is distributed using the Hydrometer Method. The particle-size distribution curve is used to calculate the coefficient of uniformity and the coefficient of curvature. Based on the lab test results, grain size distribution curve is presented on Figure 3.7. The D_{50} mean for loose and medium sand are 0.1850 mm and 0.3038 mm, while the fine fraction < 0.075 mm are 11% and 9%, respectively. For clayey silt the D_{50} mean is 0.0125 mm and fine contents is 95%. In dense sand, D_{50} mean is 0.255 mm and fine contents are between 44% and 25%. The SPT, soil classification, basic strength and index properties are presented in Table-3.2. The tables show that the soil strata containing ML is highly plastic with a LL of 32-38% and PI of 6-12%. Nearly 90-95% of the particle is passing #200. When the depth exceeds 37.5 m, dense silty sand is found with a SPT value of 50 and above. From 7.5 m to 37.5 m a layer of dark gray soft clayey silt layer exists which is not suitable for supporting end bearing resistance of pile foundation. Beyond 37.5 m brown dense silty sand continues which is capable of withstanding deep foundation's end bearing. Based on the geotechnical parameters, it is decided that the toe of the SPC piles will rest at this layer.

Figure 3.6: Laboratory test (a) Disturbed soil sample (b) Undisturbed soil sample (c) Specific gravity test (d) Direct shear test (e) Atterberg limit test (f) Triaxial test.

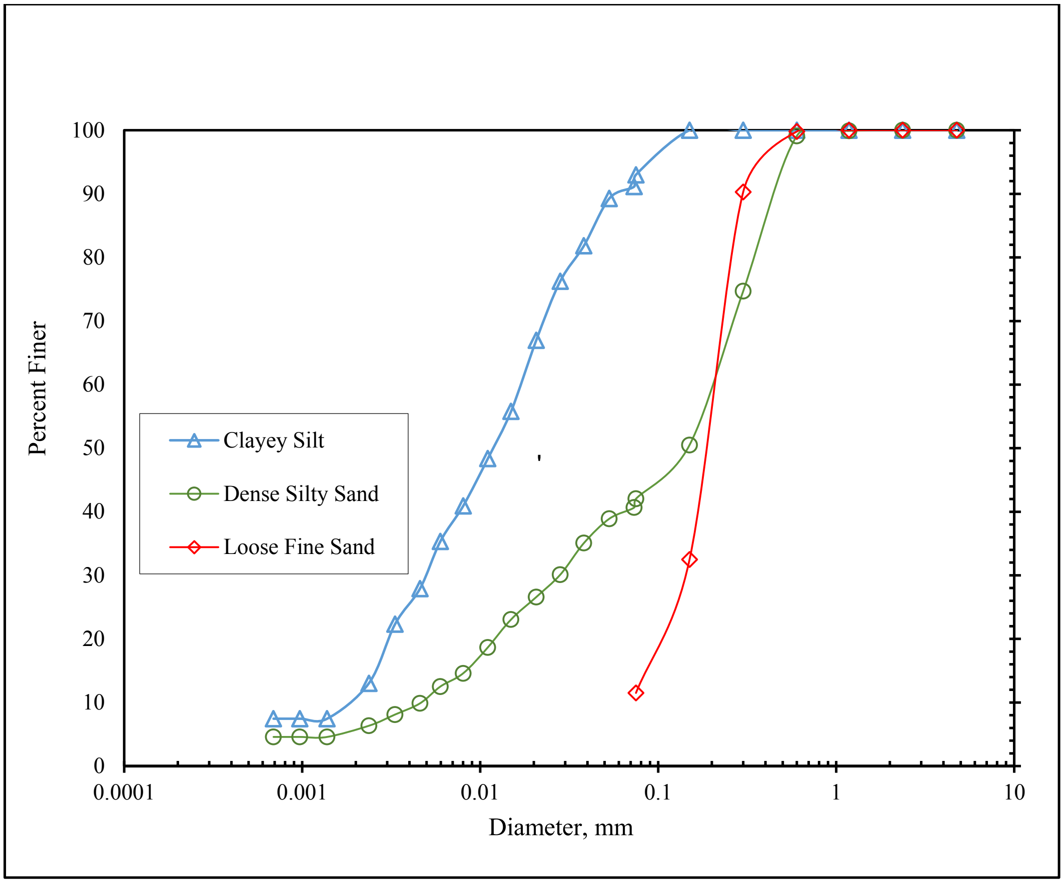

Figure 3.7: Particle size distribution curve

3.3.2 Atterberg Limit Test

Atterberg limit tests has been conducted with the soil samples collected from different depts to estimate the liquid limit, plastic limit and plasticity index of soil. Thus the soil is classified at depth 16 m using Casagrande Plasticity Chart as shown in Figure 3.8. At depth 21 m, 16 m and 30 m the Atterberg limit test has been done and it is found that the LL is between 36-37%, PI ranges from 6-9 %. The soil at this layer is classified as Clayey silt soil.

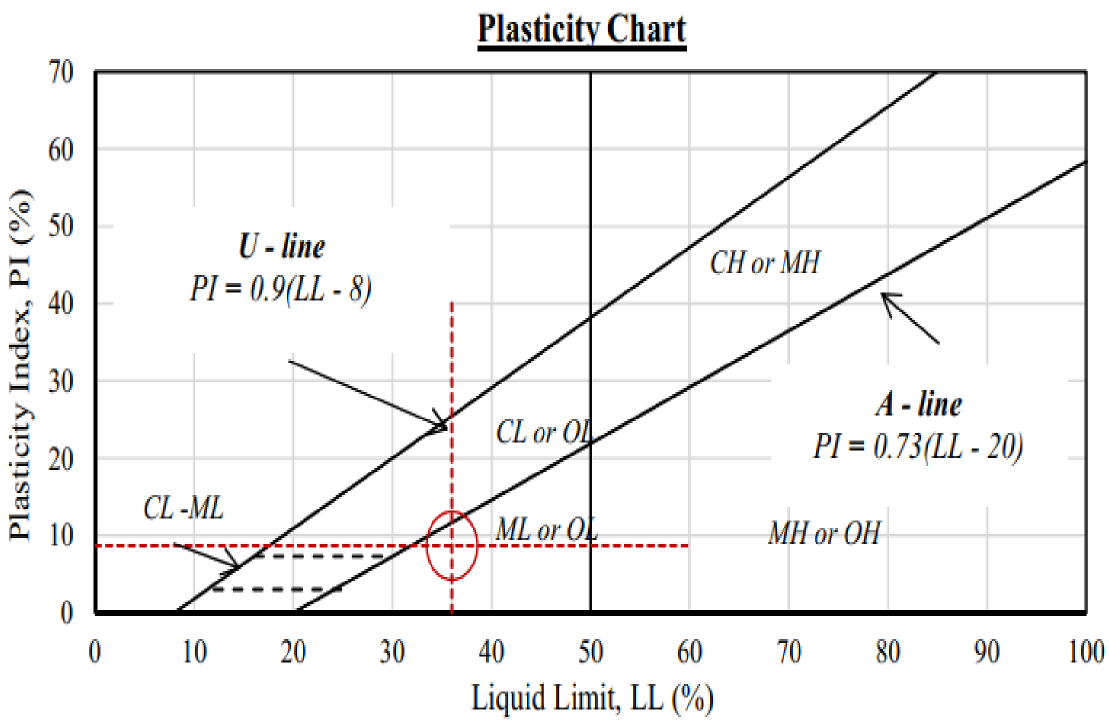

Figure 3.8: Casagrande Plasticity Chart

3.3.3 Unconfined Compression Test

The unconfined compression test is also called unconfined compressive strength test. It is done under uniaxial compression condition to determine undrained shear strength of saturated soil C_u. In this study unconfined compression test has been done at a depth of 8.7 m. The C_u value ranges from 20-35 kPa for different borelogs, see Figure 3.9 (a). The shear failure of soil samples are shown in Figure 3.9 (b).

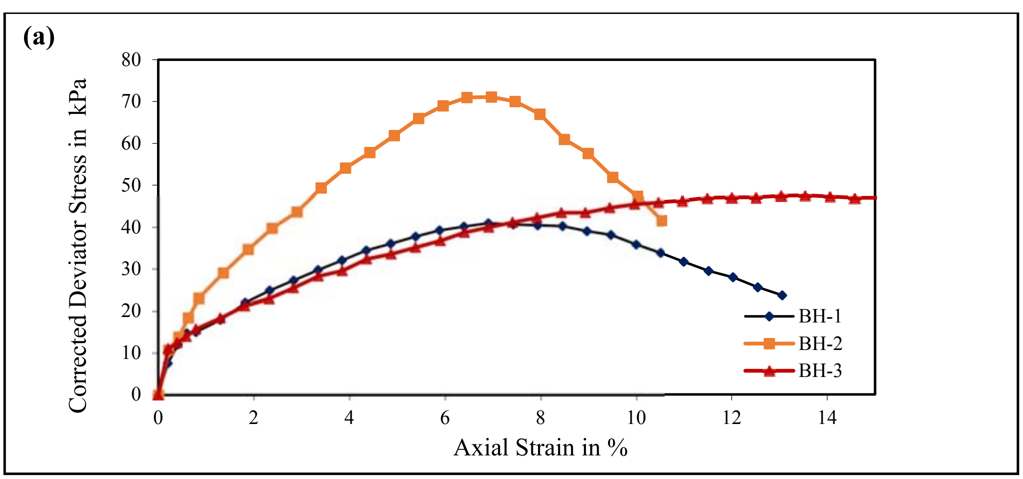

(b)

Figure 3.9: (a) Relationship between axial strain and stress and (b) brittle failure mode

3.3.4 Consolidated Drained Direct Shear Test

To determine the shear strength of soil materials, direct shear test has been done at different depth 37 m, 39 m and 40 m. It is conducted for cohensionless soil to determine internal angle of friction. The internal angle of friction value varies between 25- 32^{o} for different depth. In Figure 3.10 the stages of direct shear test has been shown and at depth 40 m the phi value is found to be 32^{o}.

(a)

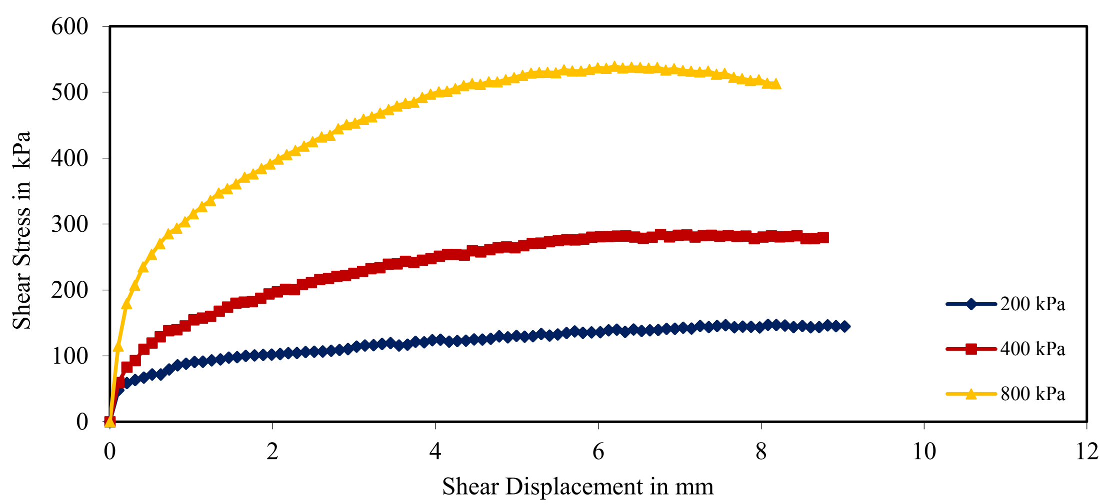

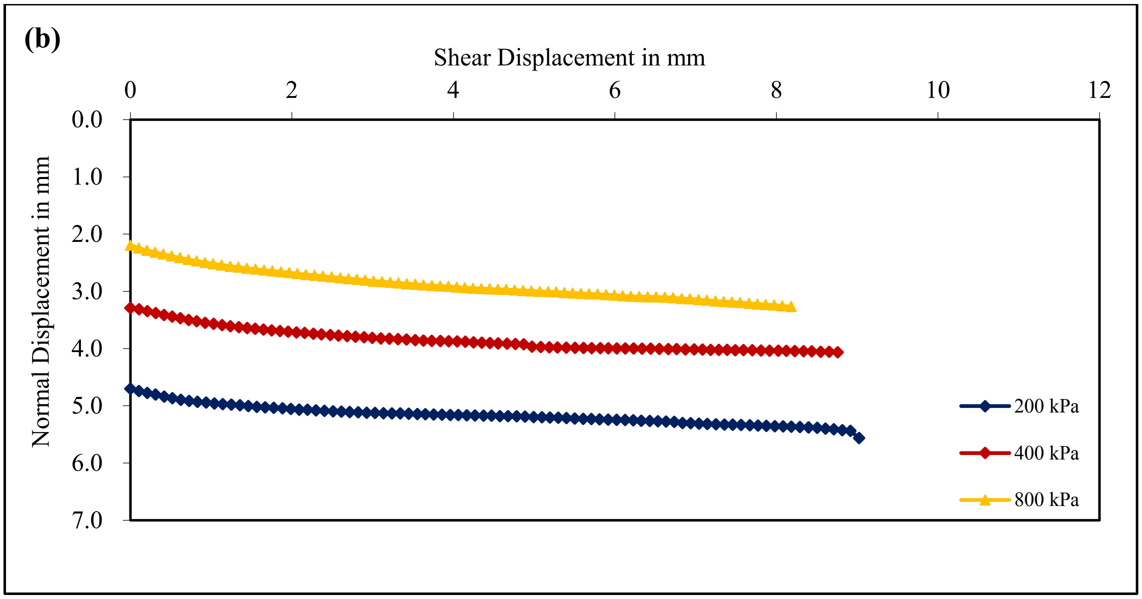

(c)

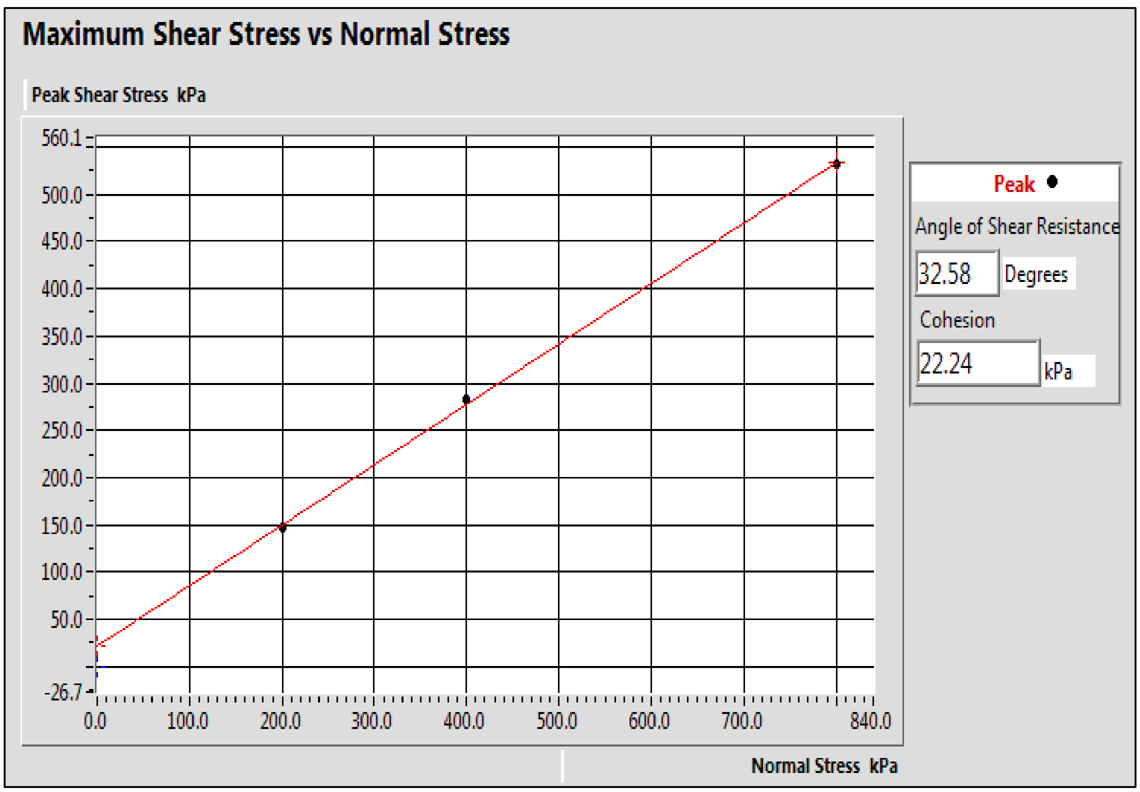

Figure 3.10: Direct shear test, relationship between (a) maximum shear stress and normal stress (b) deformation and root time (c) shear stress and horizontal displacement (d) vertical and horizontal displacement

3.3.5 Consolidated Drained Triaxial CompressionTest

To determine the soil shear strength parameter in drained condition Consolidated Drained (CD) triaxial compression test is an effective way. The CD test has been done at a depth of 11.7 m. The mohr circles obtained from the test is shown in Figure 3.11 (a). From the stress and strain relationship in Figure 3.11 (b) is used to determine stiffness parameters of soil. Figure 3.11 (c) Explains the change of volumetric strain with axial strain. Figure 3.11 (d) shows the shear failure modes of soil samples.

(a)

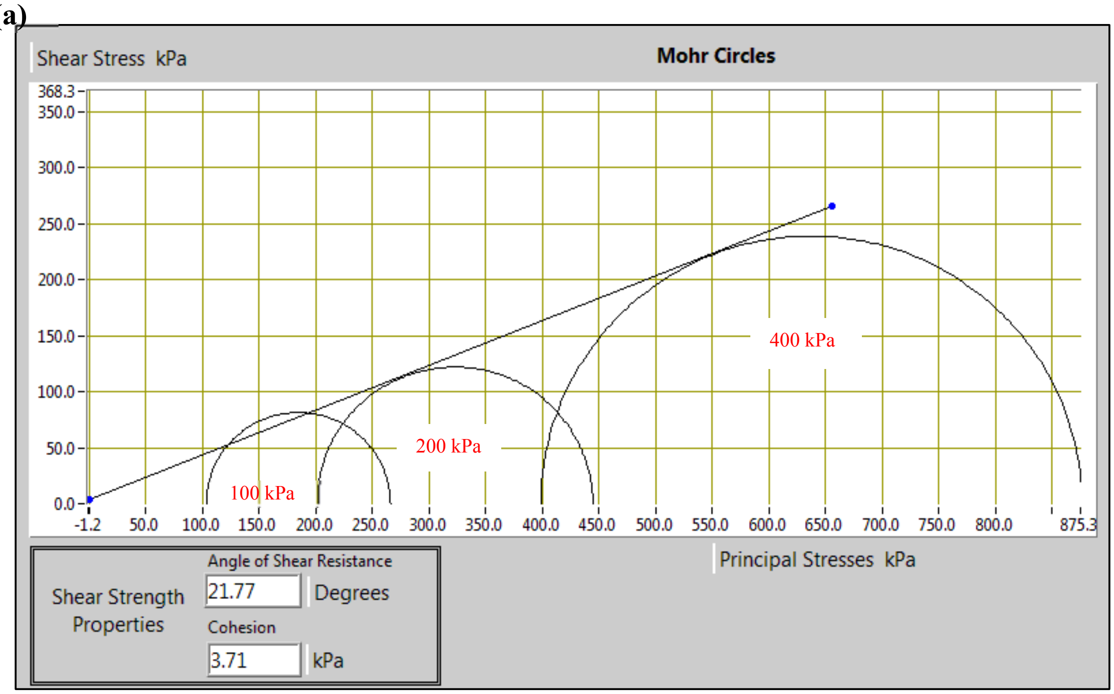

(b)

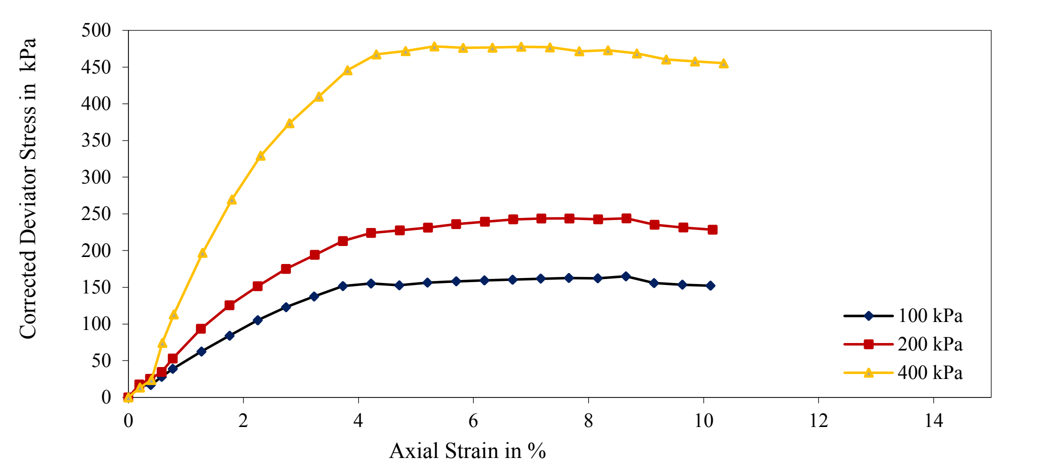

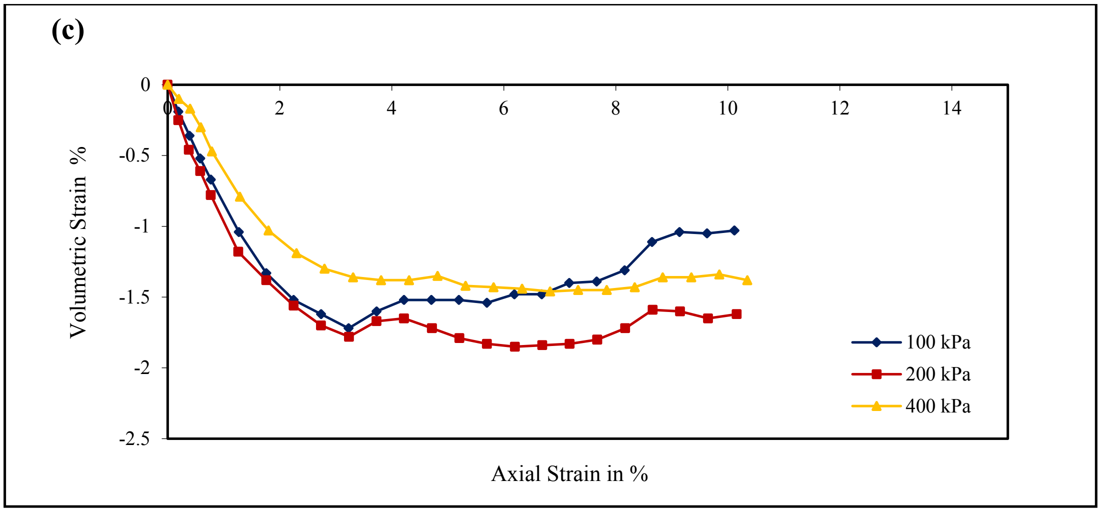

(d)

Figure 3.11: Relationship between (a) Shear stress and principal stress (b) Deviator stress and axial strain (c) Volumetric strain and axial strain and (d) shear failure modes of soil samples

3.3.6 One-Dimensional Compression Test

One dimensional consolidation test has been done at a depth of 10 m with undisturbed soil sample to determine the initial void ratio, compression index. From void ratio to applied pressure graph as shown in Figure 3.12, the void ration is 0.87 and compression index is 0.261 and swelling index is 0.058 with a preconsolidation pressure of 100 kPa.

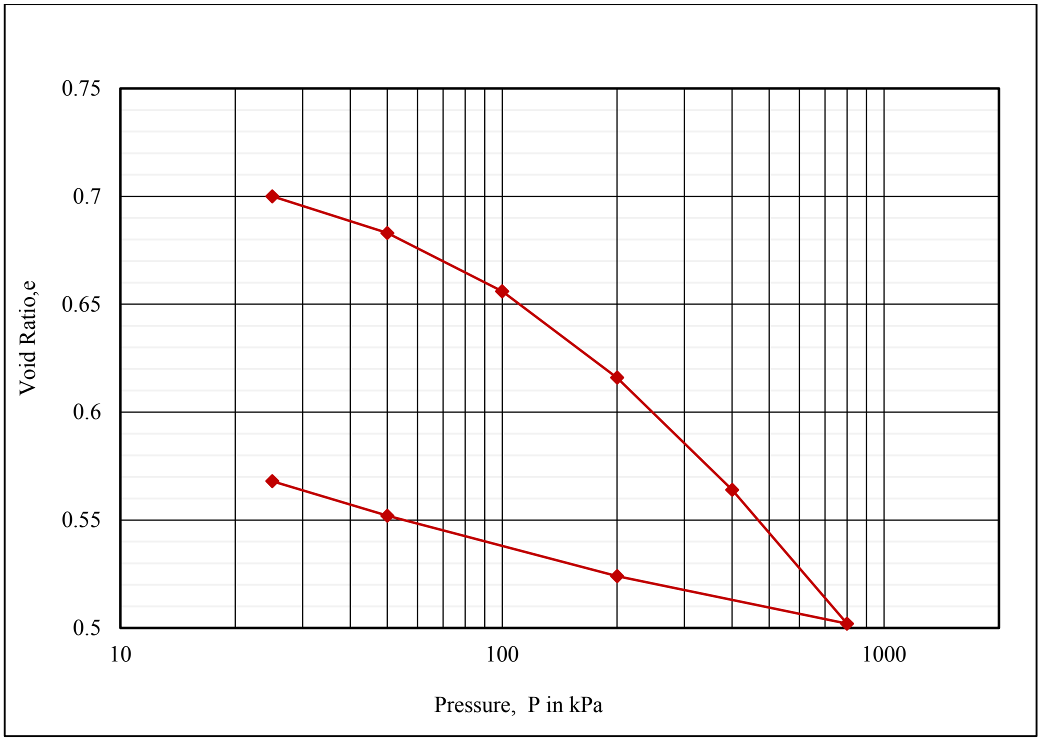

Figure 3.12: Relationship between void ratio and applied pressure

Table 3.2: SPT and Subsoil Classification

Result Summary			
Depth	**SPT range**	**USCS**	**Basic soil properties**
0 to 4.5	0 to 11	SP	γ =14 kN/m^3, γ_{sat} =15 kN/m^3,Gs=2.61,w_n=41.7% , Fines (#200 passing) = 11.0% , φ= 26.0°
4.5 to 37.5	1 to 4	ML	γ =16 kN/m^3, γ_{sat} =17.5 kN/m^3, LL = 32-38%, PI = 6 -12%, Fines (#200 passing) = 90-95%, w_n = 35 %, C_u = 20-24 kPa.
>37.5	30 to 50	SM	γ =18 kN/m^3, γ_{sat} =20 kN/m^3 , G_s=2.67, w_n=13-15%, Fines (#200 passing) = 25-44%, φ = 33.0°

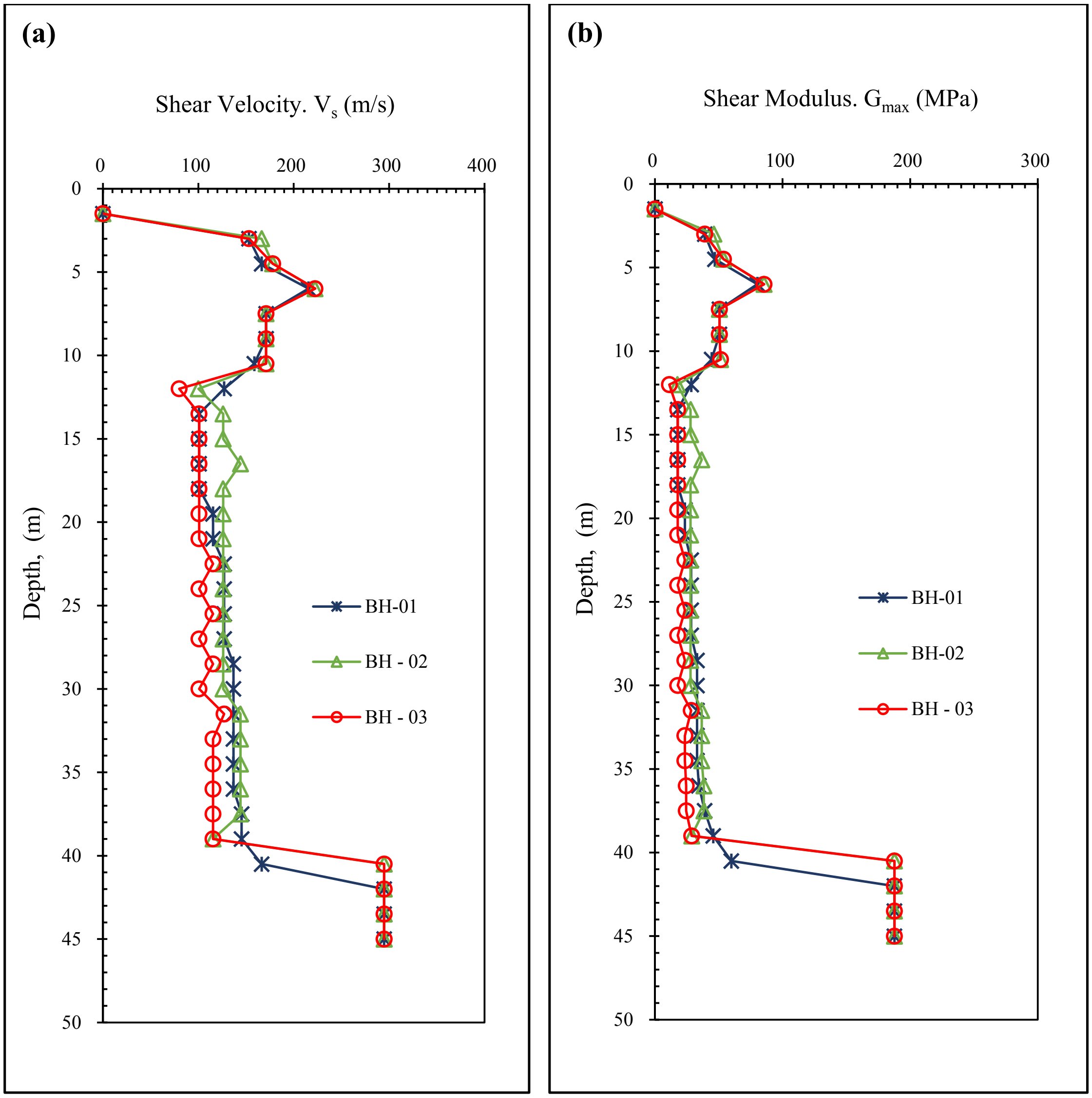

Figure 3.13: a) Depth vs Shear wave Velocity b) Depth vs Shear Modulus, G_{max}

The dynamic soil properties like Shear-Wave Velocity (V_s) and Small Strain Shear Modulus (G_{max}) are correlated from field SPT N values as described in chapter two. In this study, equation suggested by JRA (1980) has been used for calculating of shear wave velocity and shear modulus from SPT N values and presented in Figure 3.13 (a) and (b) respectively. The Figure shows that both the shear wave velocity and shear modulus of the soil increase as the depth of penetration increases though there are some fluctuations.

The minimum shear wave velocity is observed in a layer of 12-37.5 m deep which is 100-130 m/s. The maximum wave velocity is observed to be 300 m/s at a depth 40 m and above. As can be seen from Figure 3.13 (b) that the minimum shear modulus is 18 MPa at a depth of 12 to 37.5 m and the maximum value of the G is 200 MPa which is observed at depth 40 m and above.

3.4 Field Test

The SPC pile is installed in the site by push piling method. Then a static pile load test has been conducted on the installed SPC pile to determine the in-situ pile bearing capacity.

3.4.1 Pile Load Test

A single circular hollow SPC pile of 450 mm diameter and 110 mm wall thickness is driven through the soil stratum where it has been rested on a dense sand layer at an embedment depth of 42.5 m. To obtain a stable foundation, the pile is penetrated through the soft layers to dense sand layer. The pile is inserted by push piling method with maximum load of 4067 kN. Later on the static pile load test on spun pile is performed according to ASTM D-1143 (ASTM.1994).

The incremental compressive load is applied as 10% of design load until 250 ton design load is reached. The pile is loaded till failure by applying 428 ton load. The applied load is maintained in each case for 1 hr and the load is removed in decrements equal to the loading increments, a 20 min in between gap is provided for decrements. After removing each maximum applied load, reapply the load to each preceding load level in increments equal to 50 % of the design load, allowing 20 min between increments. Applied the additional loads after the design load is reached and maintained till failure occurs. After the maximum required test load has been applied, hold and removed the test load when the pile is failed under maximum load. Site photographs showing push-in test is presented in Figure 3.14 and in Figure 3.15 the pile load setup is shown.

Figure 3.14: Push-in test in study area

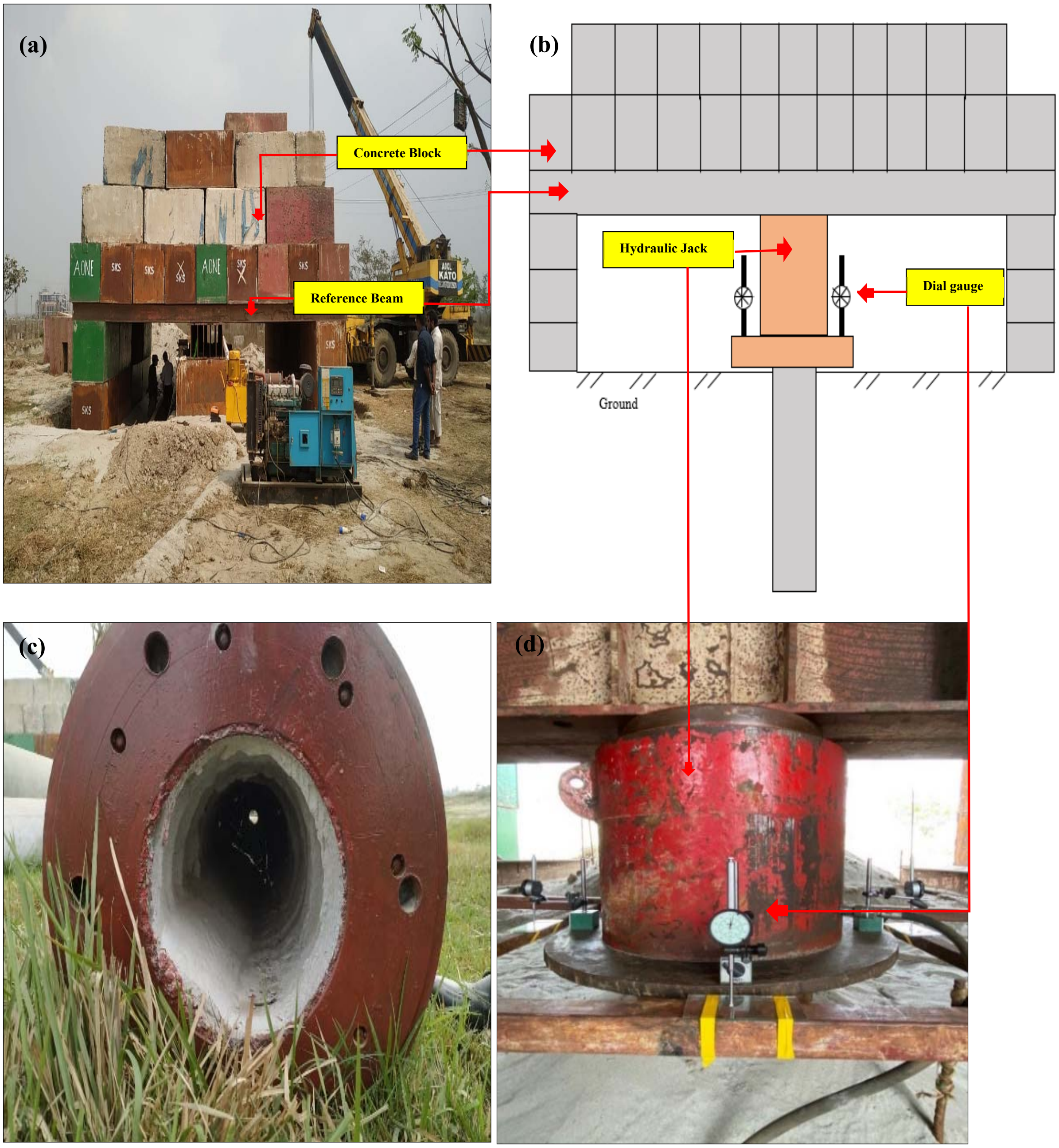

Figure 3.15: a) Performing static load test b) Schematic diagram of static load test c) spun pile for driving in soil d) Hydraulic jack and dial gauge setup during the test

3.5 Liquefaction Analysis in Jolshiri Site

After determining different soil parameters from field and laboratory test of disturbed and undisturbed samples, the liquefaction analysis has been done after (Seed et al.,1983). The soil parameters like SPT N values, fine contents, unit weight, groundwater table, D_{50} results have been obtained and used for the liquefaction analysis.

The reclaimed areas are expanding at a faster rate due to industrialization and facilitate the inhabitants. To provide a safe structure, a geotechnical engineer needs to do the liquefaction analysis. In Jolshiri site, the liquefaction analysis is done for identical boreholes from SPT N values and data acquired from soil investigation reports. The cyclic stress ratio is determined using borehole information, total and effective overburden pressure. The SPT test is done at each 1.5 m interval and ended up to 45 metres.

The SPT N values are used to estimate the cyclic resistance ratio. According to Bangladesh National Building Code (BNBC) 2020 the maximum considered earthquake (MCE) for Bangladesh corresponds to 2% probability of exceedance for 50 years of return period. Recent researches and historical data shows that Bangladesh is prone to experience a magnitude of 7.0 or greater earthquake near future. There are four zone coefficient in BNBC-2020 and Dhaka lies in zone-II. So for Dhaka city maximum peak ground acceleration (PGA) at the ground surface and magnitude of earthquake is considered to be 0.20 g and 7.5.

At different depths, the factor of safety against liquefaction is calculated. Figure 3.16 shows the liquefaction assessment curve for three boreholes analysed by the mentioned method above. The curve is shown for different magnitude of earthquake 7.5, 6.5, 6, 5.5 and 5. The three borehole are identical and first layer is loose sandy type of soil. Up-to depth 4.5 metre the factor of safety values lies less than one which indicates strong liquefaction probability at upper layer. The result has also showed compatibility with existing literature for loose sandy or silty soil layers liquefaction analysis.

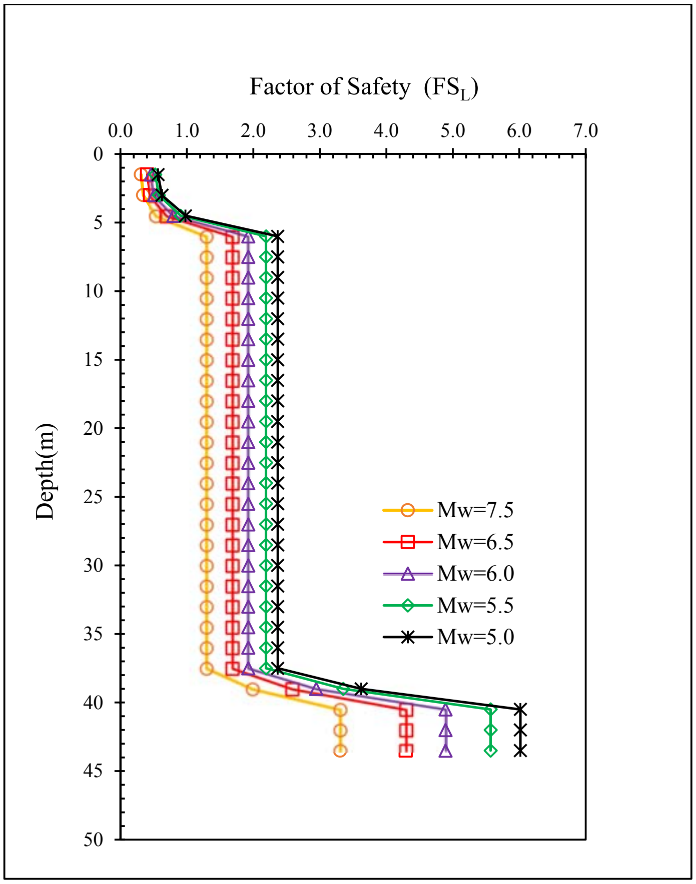

Figure 3.16: Comparison of liquefaction assessment

3.6 Bearing Capacity Analysis of SPC pile

After collecting the SPT values and data from laboratory test results, the bearing capacity for the test site is evaluated by analytical procedure as described in chapter two. In Figure 3.17 (a) and (b) the bearing capacity with and without considering liquefaction is shown with respect to borehole depth. From Figure 3.18 (a), it is observed that in liquefiable soil the skin friction of pile is reduced considerably for borehole one, two and three around 9.41 %, 8.71 % and 10.15 % respectively. The ultimate bearing capacity is also affected by liquefiable soil characteristics as shown in Figure 3.18 (b). The ultimate pile capacity decreases 3.97% for borehole one and 3.80 %, 4.50% for borehole two and three respectively. So the liquefaction potentiality of any vulnerable site should be taken into consideration to evaluate the actual bearing capacity for designing a safe foundation system.

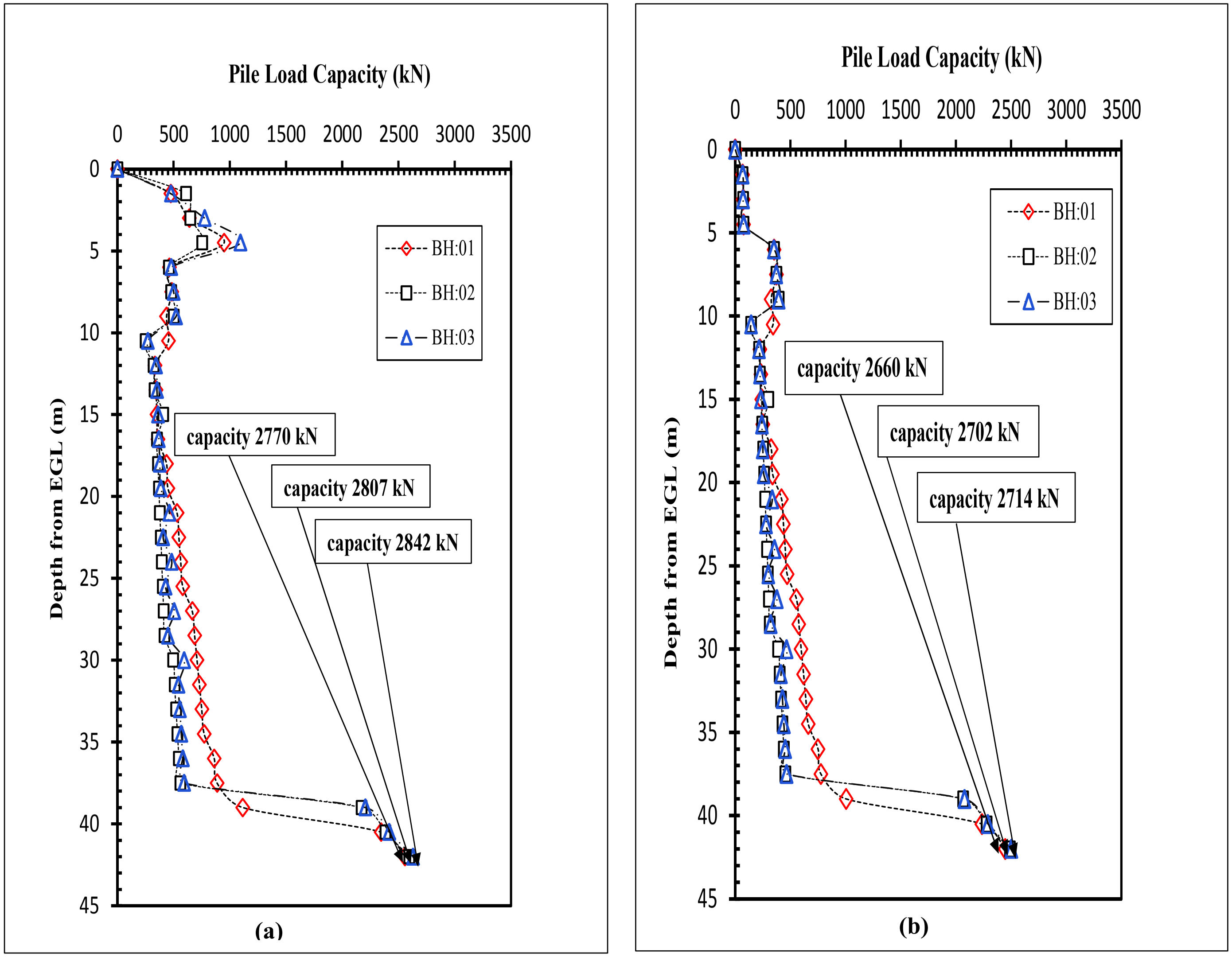

Figure 3.17: (a) Bearing capacity without considering liquefaction by analytical method.
(b) Bearing capacity considering liquefaction by analytical method

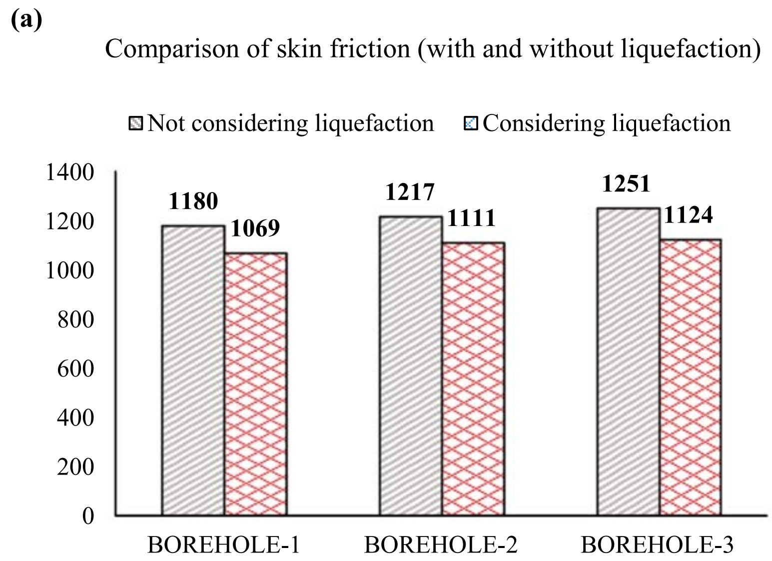

Figure 3.18: (a) Comparison of skin friction considering with and without liquefaction

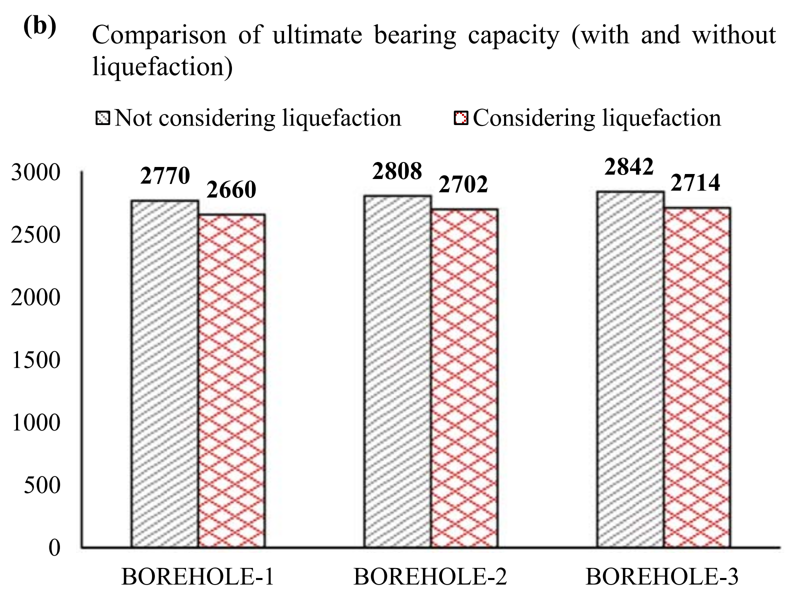

Figure 3.18: (b) comparison of bearing capacity considering with and without liquefaction.

After completion of pile load test, the result has been prepared from the field data. Load-settlement curve of tested SPC pile (450mm dia) is shown in Figure 3.20 . Final result of static load test is presented by following Bangladesh National Building Code (BNBC).

However, for simplicity and as widely adopted practice in Bangladesh, load correponding to a settlement of 12 mm is considered as design criteria in this study as shown in Figure 3.19. The allowable load from the load-settlement curve is 150 ton corresponding to 12 mm settlement for 450 mm diameter pile with a design load of 250 ton and maximum applied failure load 427.88 ton. Davission offset method is another widely accepted method for load capacity interpretation from pile load test. In this method the ultimate capacity is estimated to be 3790 kN concerning 43.13 mm settlement as shown in Figure 3.20. The shape of curvature method is widely used practice to determine the ultimate bearing capacity from field test data. The tangent from the initial part of the loading curve and the ending part of loading part intersect at a point and that point is considered as the ultimate loading capacity of the pile. Figure 3.21 shows the bearing capacity 3463 kN and settlement is 24.60 mm in shape of curvature method.

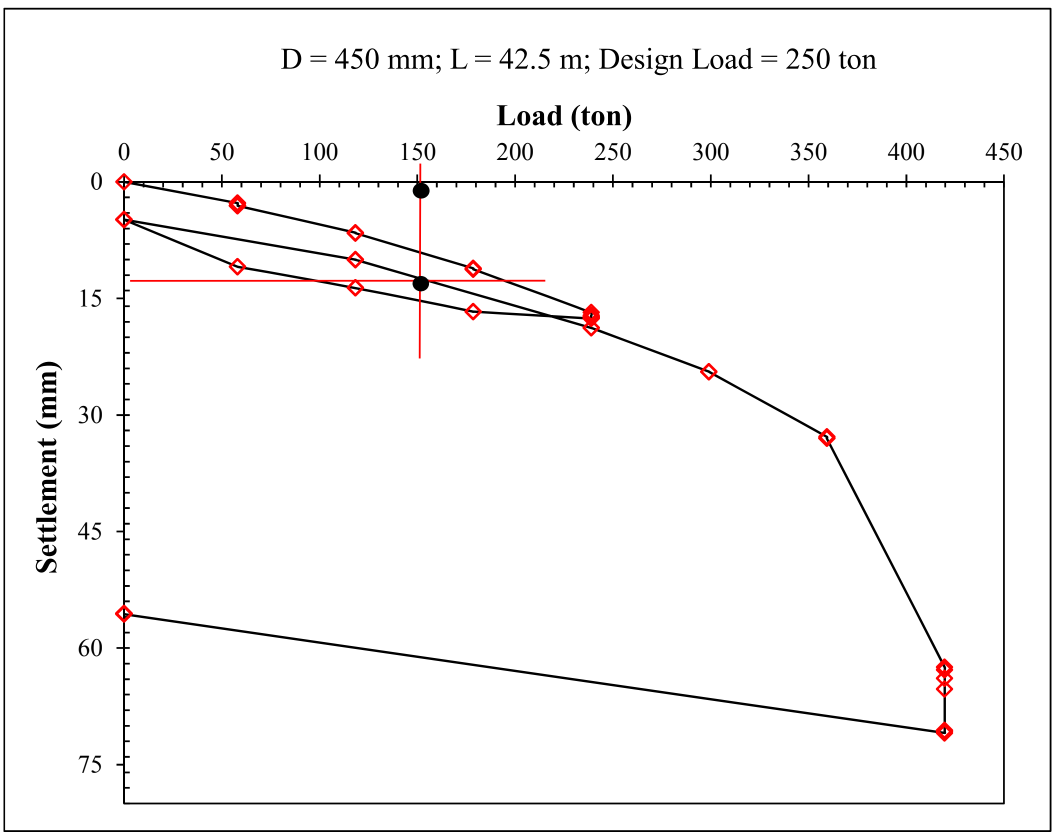

Figure 3.19: Load vs Settlement plot of conducted load tests

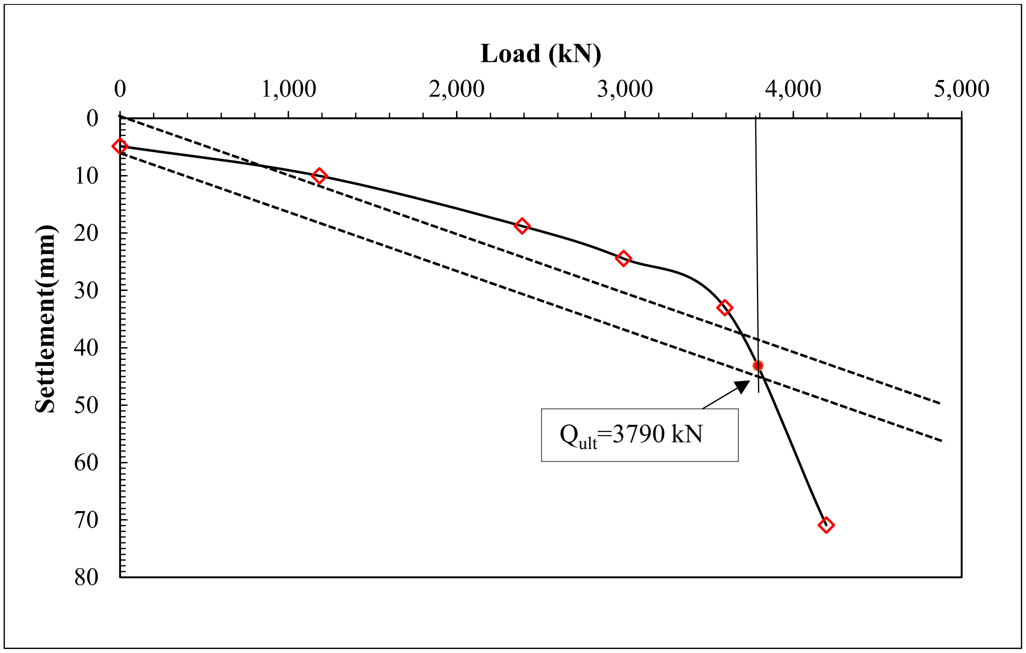

Figure 3.20: Load-Settlement curve derived from pile load test by Davisson offset method

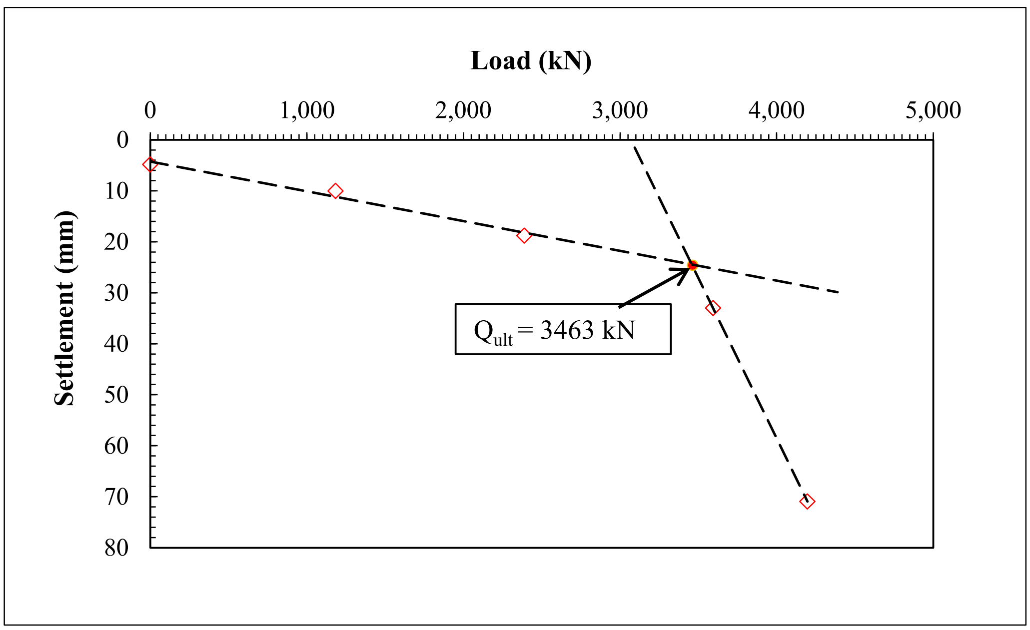

Figure 3.21: Load-Settlement curve derived from pile load test by Shape of curvature method

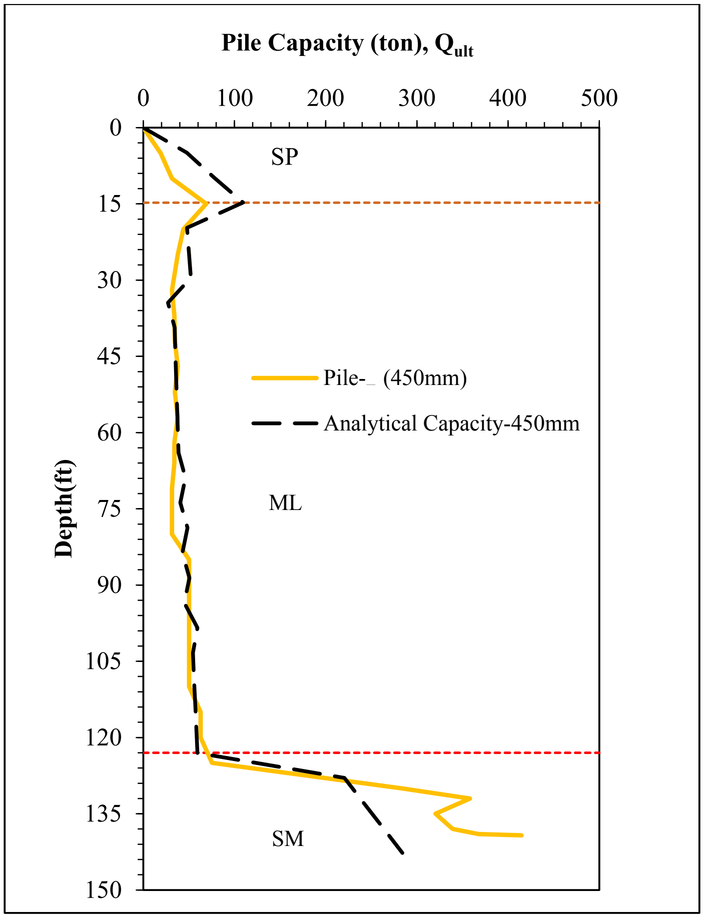

Figure 3.22: Comparison of pile bearing capacity determined from Push-in test and analytical method

Analytical bearing capacities of SPC piles are verified through field push-in test at selected site of Jolshiri Abason. Push-in test has been conducted for 450 mm diameter SPC piles with a progressive load at the rate of 1.52 m (5 ft) length. Figure 3.15 shows comparison between analytical capacities and push-in values. Site photographs showing push-in test is presented in Figure 3.14. From Figure 3.22, it is observed that beyond 37.5 m ultimate capacities of 450mm diameter piles yield greater than 100 ton. However, in practice after 37.5 m further driving in to the layer of hard soil (SPT>50) will depend on pile's structural capacity and requirements on pile tip stability.

3.7 Summary

This chapter deals with the field test data acuired in invetigation site. The bearing capacity determined from both analystical and in-situ pile load test is obtained in this part. From the analysis it can be summarized that:

1. For determining different soil strength parameters, conducting field and laboratory test is the only viable way. With this aim at the very outset, sub soil investigation is performed in the study area and soil samples both disturbed and undisturbed are collected for laboratory tests.

2. The soil boring data obtained from the site is important to classify the soil. From soil investigation it is found that the top 4.5 m is filled with loose sand with a shear wave velocity less than 180 m/s and SPT value less than 15. This layer is susceptable to liquefaction in saturated condition under seismic event.

3. The liquefaction analysis is done to observe the liquefaction susceptibility of the top layer of soil using Seed and Idrris method. It is obtained that the CRR/CSR ratio is less than 1. So in this type of soil SPC pile is installed to increase the bearing capacity and reduce probable pile failure during earthquake.

4. The pile is installed by Push-in method in the site with an ulmimate load capacity of 414 ton for 450 mm diameter SPC pile. After that, in situ static pile load test is performed in the site. The design load for the pile is 250 ton and the pile is tested to failure with 427.88 ton load. The ultimate pile bearing capacity is also determined in this chapter by analytical method with and without considering liquefaction phenomenon.

5. The allowable bearing capacity of pile is determined from load-settlement curve obtained from field load test data according to BNBC 2020. This curve is used further to validate the FEM model for numerical investigation. Finally the Push-in test method result is compared with the analytical at the pile tip.

CHAPTER 4

NUMERICAL MODELING

4.1 Introduction

To evaluate the bearing capacity of pile under static loading condition, the in situ pile load test is the most reliable and accurate method. In this investigation, the study area is filled with loose silty sand type soil which is susceptable to liquefaction if earthquake occurs, so the chance of pile failure during earthquake event is more likely to happen. Though the pile can sustain axial load under design condition but the possibilities of failure under seismic excitation in liquefiable soil should be taken into consideration. The performance of SPC pile is evaluated numerically considering both axial and earthquake loading condition.

In this segment, the results of numerical investigation is presented for SPC pile installed into the study location. The FEM model is calibrated with the field pile load test data. The result of embedded pile deformation is shown using HS soil model. The model parameters are determined from field test results. Also the different stress distribution in soil during earthquake and liquefaction are discussed here. At the end, a comparison is made between axially loaded pile with the earthquake loading.

4.2 FEM Model in PLAXIS 3D

In this section, modeling assumptions for numerical analysis is described. Soil is modeled by 10 noded element. Drained analysis has been adopted for Hardening Soil (HS) model. Groundwater table is taken at the GL. The soil parameters are determined from SPT N value correlations and laboratory test results. A 42.5 m SPC pile is modeled using embedded beam element with a outer diameter of 450 mm and wall thickness of 110 mm. Each soil layer thickness is taken from the borelog profile collected from the study site and presented in chapter three.

4.3 Derivation of Soil Stiffness Parameters

In Jolshiri study area, both field and laboratory tests are performed to determine different soil index and strength properties which can act as input parameters for soil modeling in plaxis.

4.3.1 Field and Laboratory Tests Performed for Determination of Soil Parameters

Standard penetration test has been conducted in Jolshiri site up-to 45 m depth. SPT N values are recorded at every 1.5 m depth. Both disturbed and undistrubed samples are collected for testing in laboratory. The test procedure is done according to ASTM D 1586. To determine soil index and shear strength properties and to know the actual soil condition in site, performing laboratory test is a must. In this investigation different laboratory tests such as specific gravity test, grain size analysis, Atterberg limit test, CD triaxial test, consolidation test, direct shear test, unconfined compression test etc are carried out.

4.4 Modeling Parameters

In this section the input parameters in PLAXIS 3D for both soil and structural element are presented.

4.4.1 Soil Modeling Parameters

Hardening Soil (HS) model is advanced model in predicting and simulating behavior of soft soil as well as stiff soil. In hardening soil model yield surface is not fixed in principle stress space but as a result of plastic straining yield surface can develop. This will change the soil stiffness after loading and unloading. After applying primary deviatoric loading, soil shows decreasing stiffness and irreversible plastic strain develops. For HS model the basic idea is to develop hyperbolic relationship between vertical strain and deviatoric stress. It also controls stress dependency level. The parameters requires for HS model are shown in Figure 4.1. HS model uses the theory of plasticity than elasticity theory. In this model the input parameters are; m the stress dependent stiffness according to power law, plastic straining due to primary deviatoric loading E_{50}^{ref}, plastic straining due to primary compression E_{oed}^{ref}, elastic unloading E_{ur}^{ref} and c, φ, ψ are the failure according to the Mohr-Coulomb failure criterion parameters. The stiffness parameters are determined from triaxial test and consolidation test. In PLAXIS K_{0nc} is automatically recommended based on Jacky's formula. ν_{ur} and R_{int} are also recommended values from PLAXIS. The required estimated parameters for HS model is presented in Table 4.1.

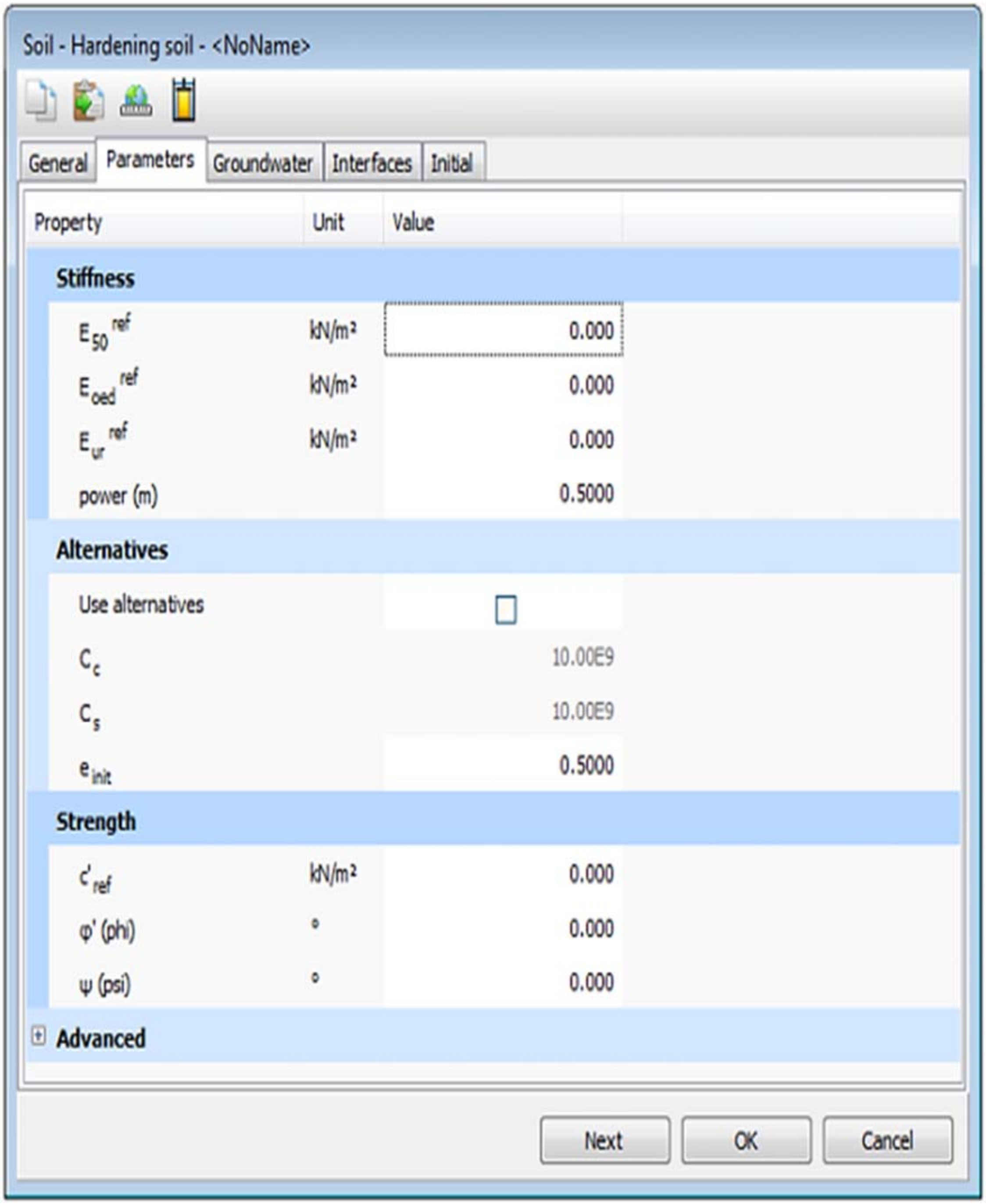

Figure 4.1: Parameters for HS model

Table 4.1: Material properties for the soil layers

Parameters	Unit	Loose sand	Clayey silt	Silty sand
Unsturated unit weight (γ_{unsat})	kN/m^3	16	16	18
Sturated unit weight (γ_{sat})	kN/m^3	17	17.5	20
Secant stiffness modulus (E_{50}^{ref})	kN/m^2	10000	15000	38000
Oedometer modulus (E_{oed}^{ref})	kN/m^2	10000	15000	38000
Unloading/reloading stiffness (E_{ur}^{ref})	kN/m^2	30000	45000	114000
Poisson's ratio, ν		0.3	0.3	0.3
Cohesion, c		0	15	0
Angle of friction, φ		23	25	36
Dilation Angle, Ψ		0	0	0
Unloading/reloading poisson's ratio, ν_{ur}		0.2	0.3	0.25
Power for stress-level dependency of stiffness, m		0.5	0.5	0.5
K_0 value for normally consolidated factor, $K_{0\,nc}$		0.531	0.577	0.412
Interface factor, R_{int}		0.7	0.9	0.9

4.4.2 Embedded Pile Modeling Parameters

The finite element modeling is done in PLAXIS 3D and validiated with the static pile load test conducted on site. The soil is modeled using HS model parameters and SPC pile is modeled as embedded beam element in PLAXIS. The SPC pile is loaded under different axial load during pile load test and reached to the ultimate load capacity. In PLAXIS the bearing capacity of pile is the input parameter for embedded pile rather than the result of finite element calculation. The embedded pile input parameters are determined from pile load test. As embedded pile is considered as beam element so the parameters are presented in terms of Young modulus E and the unit weight γ of pile material. For modeling different geometric properties of pile, predefined shapes (masive circular pile, circular tube, square pile) with pile diameter and wall thickess are provided. The properties of pile soil interaction is defined by skin resistance and base resistance. In Table-4.2 the required properties of embedded pile are given.

Table 4.2: Required parameters of the embedded pile

Parameters	Name	Value	Unit
Predefined beam type	Circular tube	-	-
Diameter	Diameter	0.450	m
Wall thickness	Thickness	0.110	m
Young's modulus	E	$32.88*10^6$	kN/m^2
Unit weight	γ	24	kN/m^3
Skin resistance	Type	Linear	-
Skin resistance at the beginning of the embedded beam	$T_{top,start,max}$	20	kN/m
Skin resistance at the end of the embedded beam	$T_{bot,end,,max}$	100	kN/m
Base resistance	F_{max}	1600	kN

4.5 Numerical Modeling

The FEM model is developed for both axial and earthquake loading condition using same parameters stated in Table 4.1 and 4.2. The soil profiles are modeled by consulting the borelog collected from site to the depth of borelog up-to 45 m. Each layer has different characteristics according to several tests performed. At first a borehole is located at (0,0,0) point. For model perimeter 20 m in x direction and 20 meter in y direction are taken as model width. The model depth is taken as 45 m in z direction as shown Figure 4.2. The water table is assumed at the existing ground level. The pile is located at the middle of the soil perimeter as shown in Figure 4.3 (a). In this stage axial load is provided as a ponit load at the top of the pile. After completing the soil and structural modeling, the finite elemnt meshing is done. Figure 4.3 (b) shows the connectivity plot of the model after meshing stage. The stage construction phases of PLAXIS for axially loaded pile are given below in Table 4.3. In Table 4.4 the break down of loading and unloading stages are given.

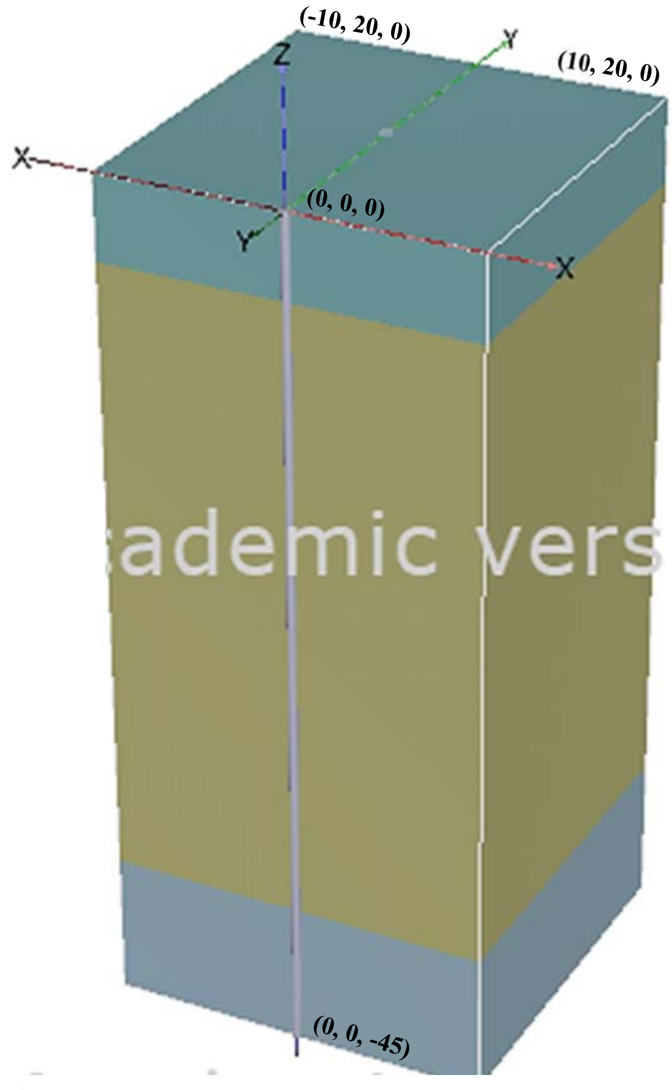

Figure 4.2: FEM model developed in PLAXIS 3D

Table 4.3: Stage construction phases for compressive loading

Phase	Analysis type	Elements	Activated
Initial	K_0	Soil volume	√
		Embedded pile element	x
		Point load	x
Pile construction	Plastic	Soil volume	√
		Embedded pile element	√
		Point load	x
Loading stage	Plastic	Soil volume	√
		Embedded pile element	√
		Point load	√
		Deformation in z direction	√
Unloading stage	Plastic	Soil volume	√
		Embedded pile element	√
		Point load (design load in reverse order)	√
		Deformation in z direction	√

Table 4.4: Stage construction phases for increamental loading and unloading stages

Phase	Analysis type	Increamental loading and unloading stages
Loading stage	Plastic	L = 0
		L = 590 kN
		L = 1202 kN
		L = 1815 kN
		L = 2490 kN
Unloading stage	Plastic	UL = 1815 kN
		UL = 1202 kN
		UL = 590 kN
		UL = 0

Figure 4.3: (a) Axially loaded embedded pile and (b) connectivity plot

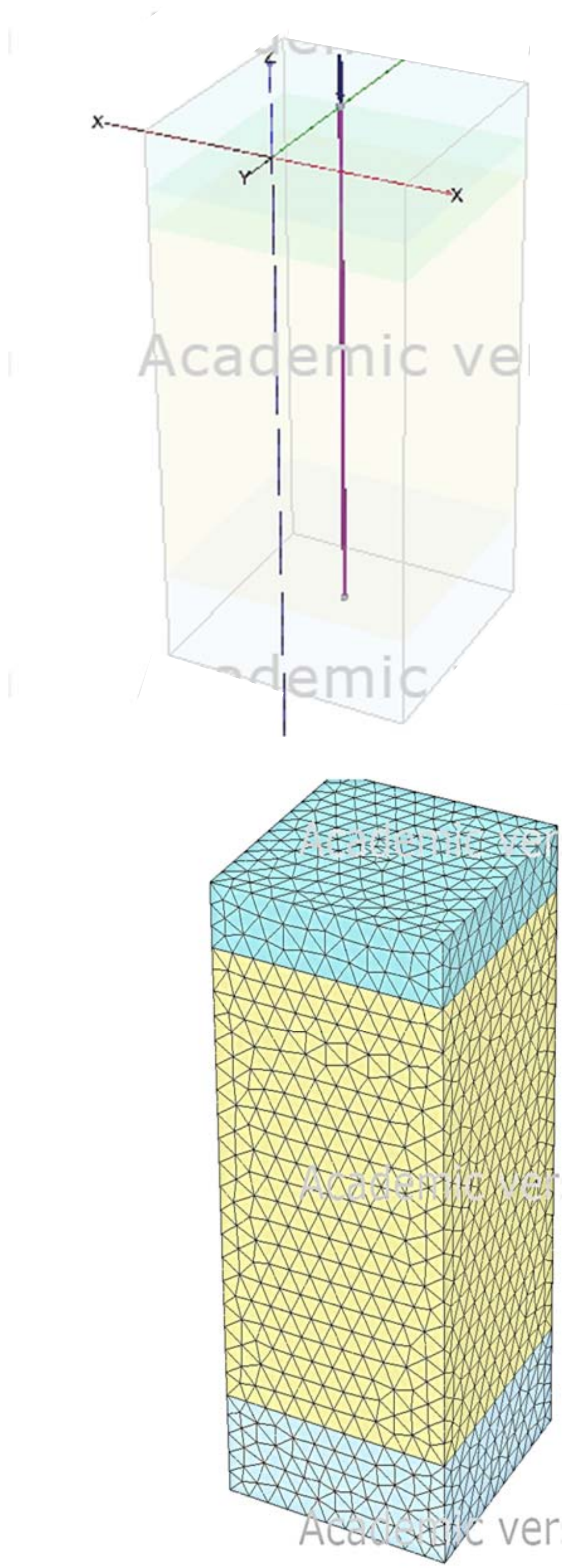

Figure 4.3: (a) Axially loaded embedded pile and (b) connectivity plot

4.5.1 Validation with Field Pile Load Test Data

The pile load test is simulated in PLAXIS 3D and the maximum settlement from the analysis is 18.47 mm which is very close to the maximum settlement of field test 17.60 mm as shown in Figure 4.4. The simulated result shows good agreement with the field pile load test results under static loading condition. Therefore, this calibrated model can be used for further analysis.

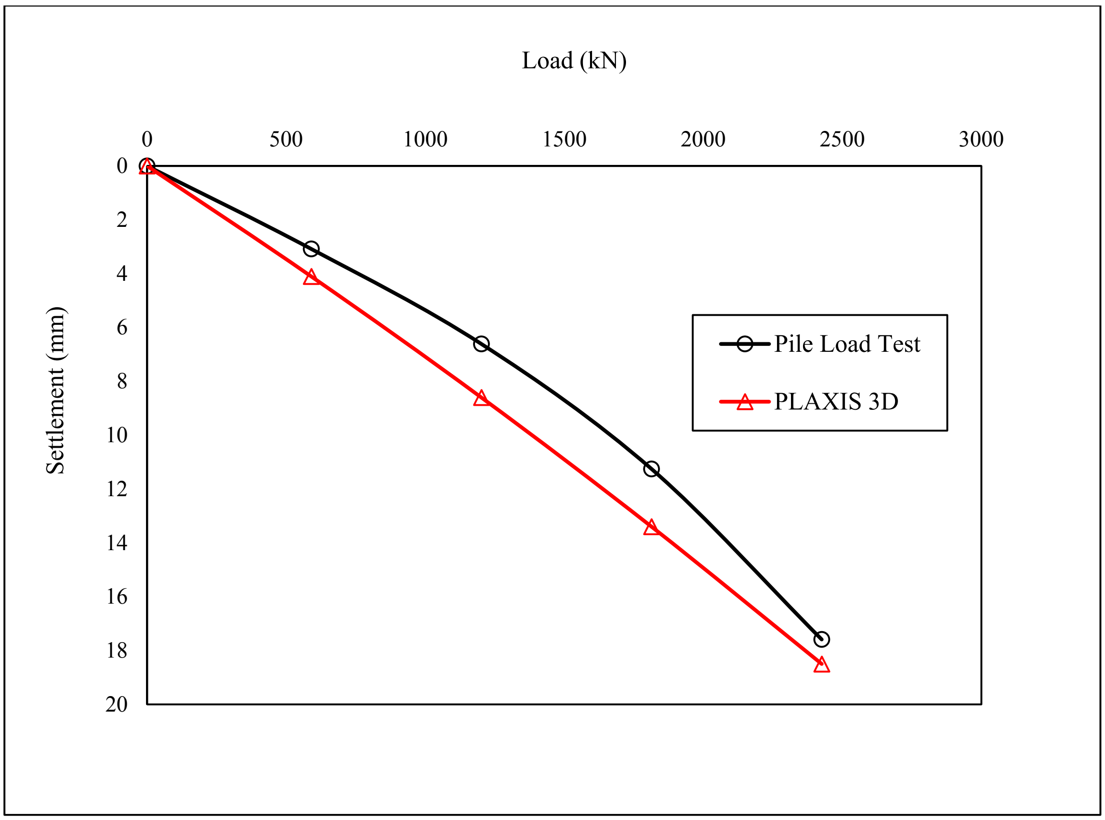

Figure 4.4: Comparison of PLAXIS 3D obtained results with field measured result

4.5.2 Pile Deflection under Axial Loading

After completing the numerical model, the pile is analysed under different incremental loading condition similar to the field condition as shown in Table 4.4. At different loading stages pile exhibits displacement in both lateral and vertical direction. In PLAXIS displacement are shown in three direction i.e. U_x, U_y, U_z as well as total displacement is also depicted in form of graph or contour plot. U_x, U_y displays displacement in lateral direction and U_z in vertical direction.

Figure 4.5 shows the axial load distribution along the pile length. The vertical load is applied at pile head at different stages and the result shows that with increasing depth the axial load decreases. Figure 4.6 shows the three dimentional view of displacement contour of pile in z direction around the pile from the modeling results from compression loading. The displacement field is concentrated around the pile with a pile head displacement of 18.47 mm. Figure 4.7 shows the top view of pile displacement. The pile shows tolerable displacement under design load 2500 kN.

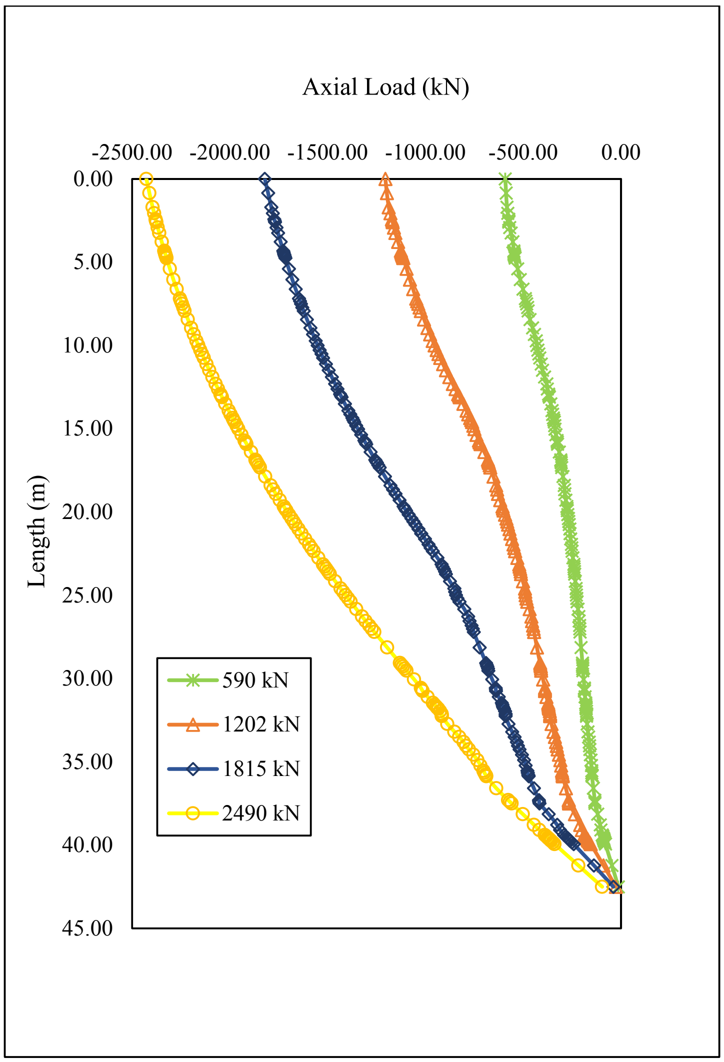

Figure 4.5: Relationship between pile depth and axial load

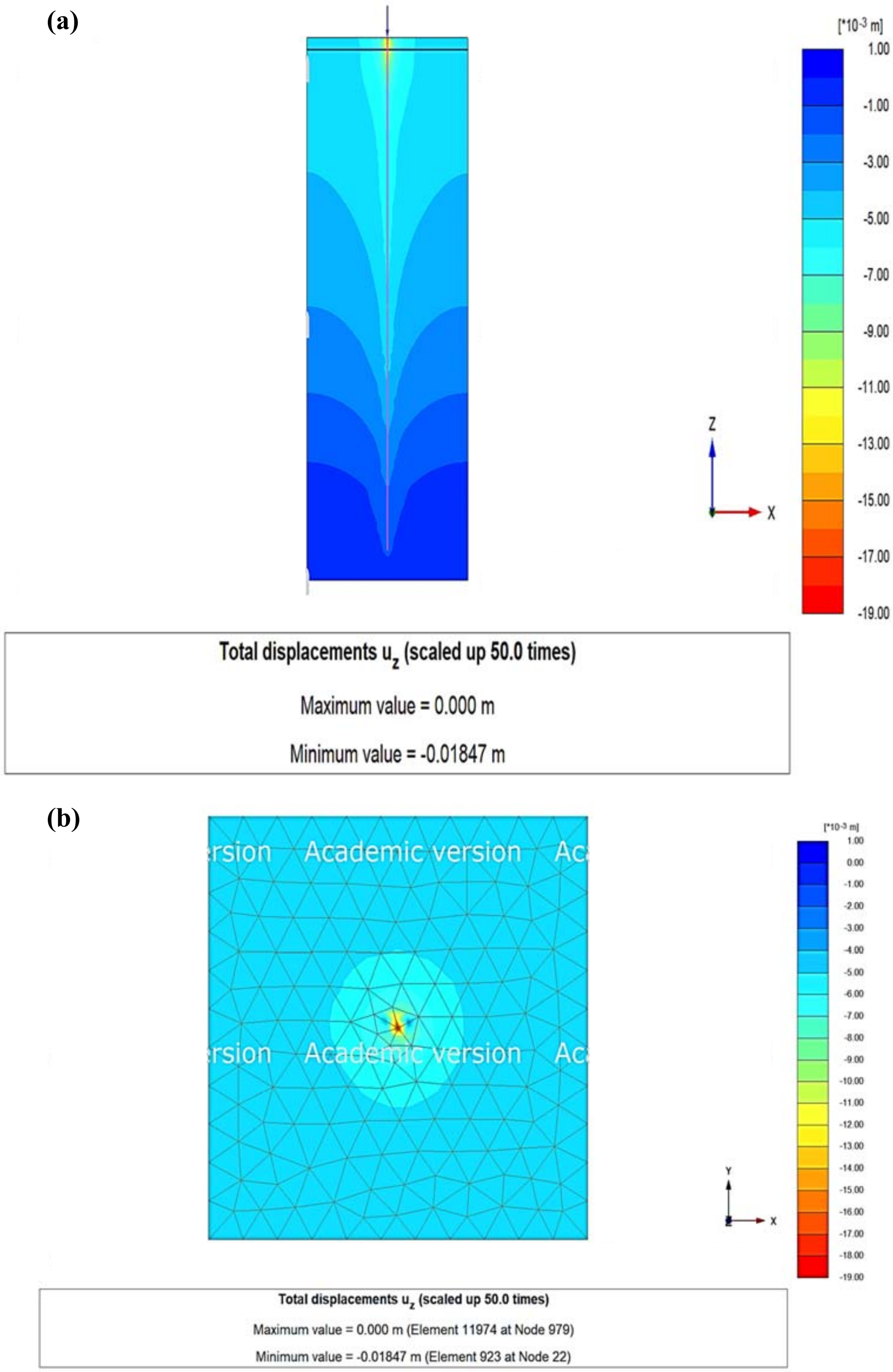

Figure 4.6: a) Displacement field around pile b) Top view of displacement contour

4.5.3 Stress Distribution

The Principle total stress in soil skeleton is shown in Figure 4.7 at 42.5 m depth. The maximum stress generated due to axial loading is 647 kN/m^2. The stress field is concentrated around the pile and it is represented as red color. The yellow field shows stress distribution in soil particles. The total strain contour at the top of the pile in z direction is presented in Figure 4.8 and the maximum strain is 0.016. The stress strain relationship of a particular point at bottom end is displayed in Figure 4.9. It seems that mostly the strain develops in soil element as the result of plastic strain.

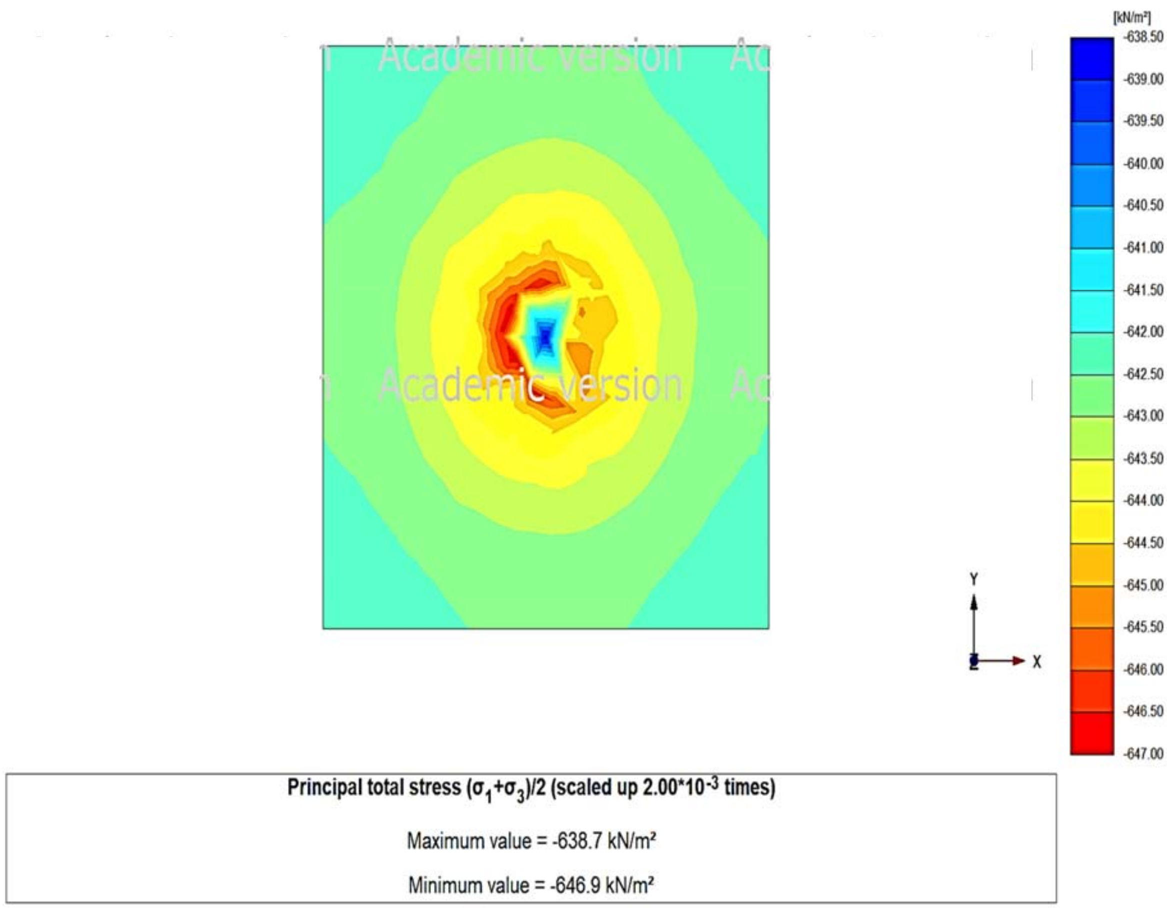

Figure 4.7: Total principle stress at surrounding soil at pile bottom

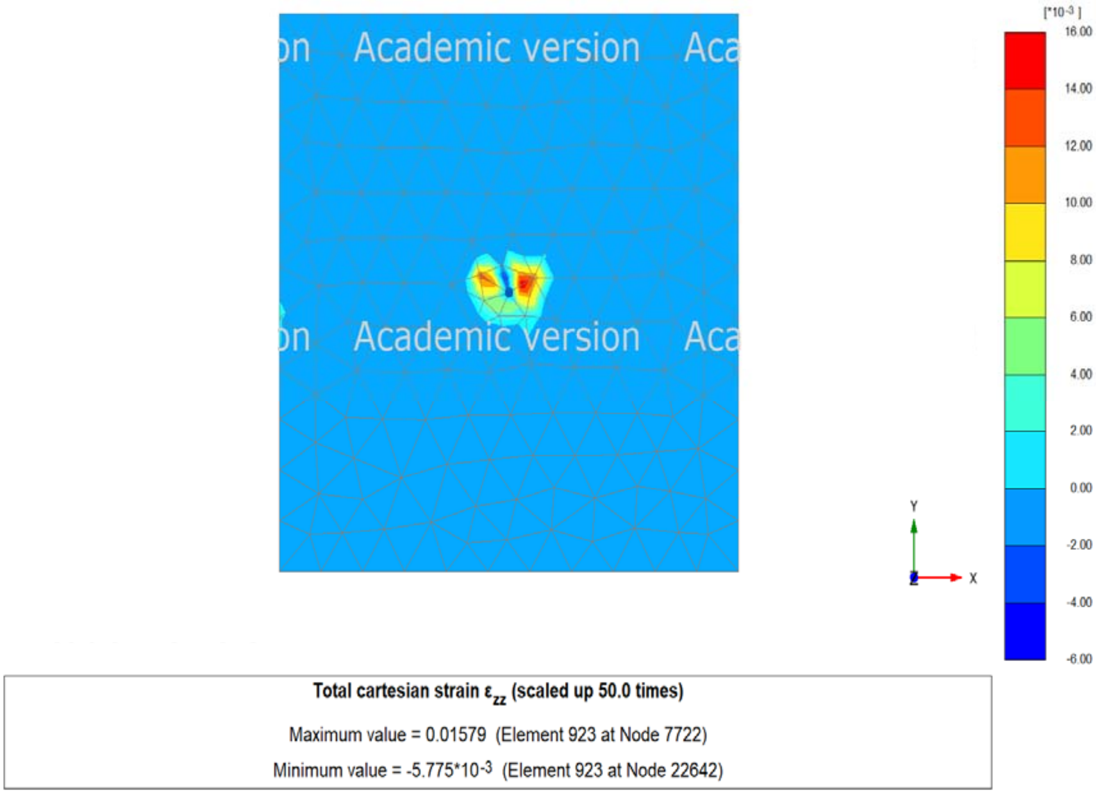

Figure 4.8: Total strain in z direction

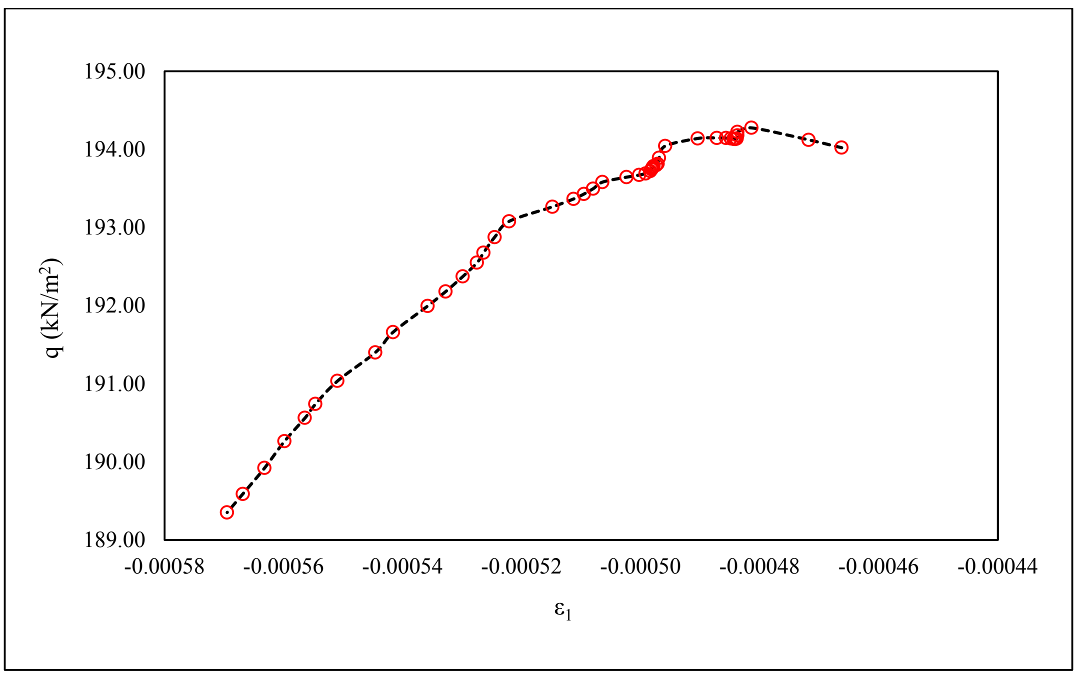

Figure 4.9: Stress-strain relationship

4.6 Parametric Study

The numerical model can be influenced by pile diameter, length and mesh size that can affect the pile response in soil body. The parameters can make differences in terms of accuracy and efficienecy of the computation. Influence of different pile diameter, length and mesh sizes is also investigated through parametic analysis.

4.6.1 Influence of Mesh Size

For performing finite element calculation, a fully defined geometry is divided into finite elements. This combinations of finite element is called mesh. Mesh coarseness is considered to have significant effect on calculated results. Fine meshing is important to get accurate result in any analysis but it takes longer time for calculation. The mesh generation process includes soil stratigraphy, structure, loads and boundary. The element distribution depending on relative element size factor (r_e), there are five global levels in PLAXIS as as shown in Table 4.5.

Table 4.5: Element size factor with element distribution

Element Distribution	r_e
Very Coarse	2
Coarse	1.5
Medium	1.0
Fine	0.7
Very Fine	0.5

In this study, three mesh sizes have been used to see the sensitivity of mesh sizes on results obtained in the analysis. Figure 4.10 (a), (b) and (c) shows the fine, medium and coarse mesh connectivity plot respectively. For the current study fine mesh element has been used for both vertical and earthquake loading conditions. Figure 4.11 shows that the full loading stage is completed and M_{stage} value reaches to 1 which means all the out-of-balance forces are omitted during each stage calculation process. In the end, ultimate displacement is found to be very close for fine and medium mesh sizes on the top of the pile, 18.47 mm and 18.35 mm respectively at ultimate load. For coarse mesh the axial displacement is 17.54 mm as shown in Figure 4.12. Figure 4.13 diplays the moment generated under different meshing condition. It is evident from these above plotted graph that effect of meshing variation on the ouput results is significant in case of moment generation. The deviation among the result are very close to each other in terms of displacement.

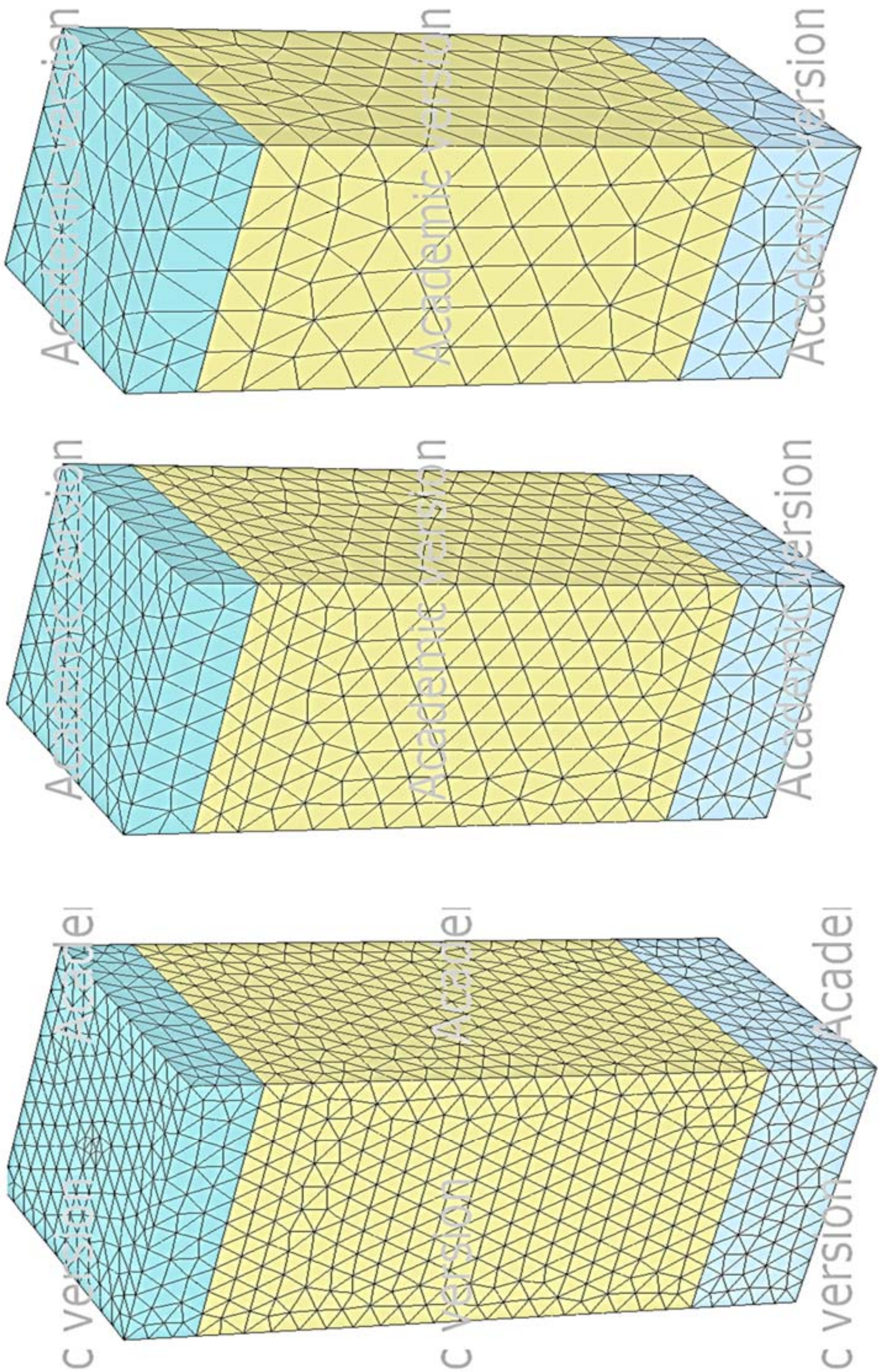

(a) Fine

(b) Medium

(c) Coarse

Figure 4.10: mesh element connectivity plot

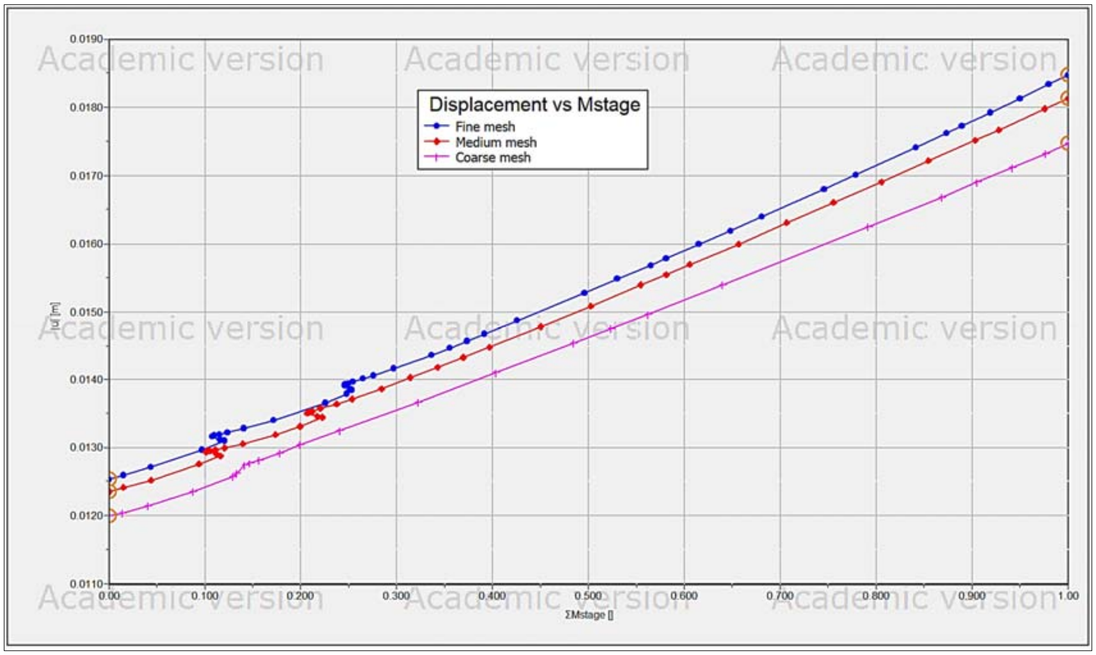

Figure 4.11: Total displacement of pile with respect to full loading stage for different mesh condition

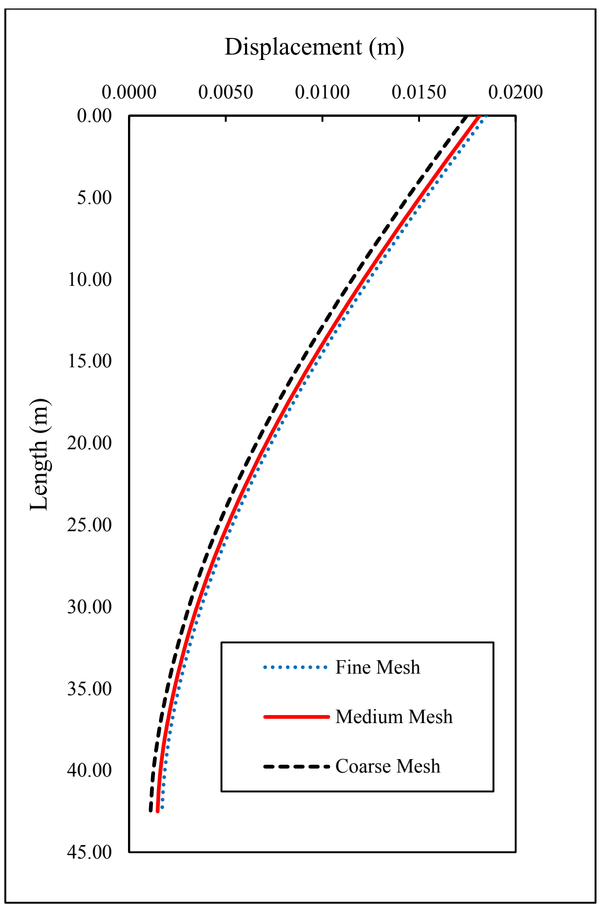

Figure 4.12: Distribution of displacement with pile depth for different mesh condition

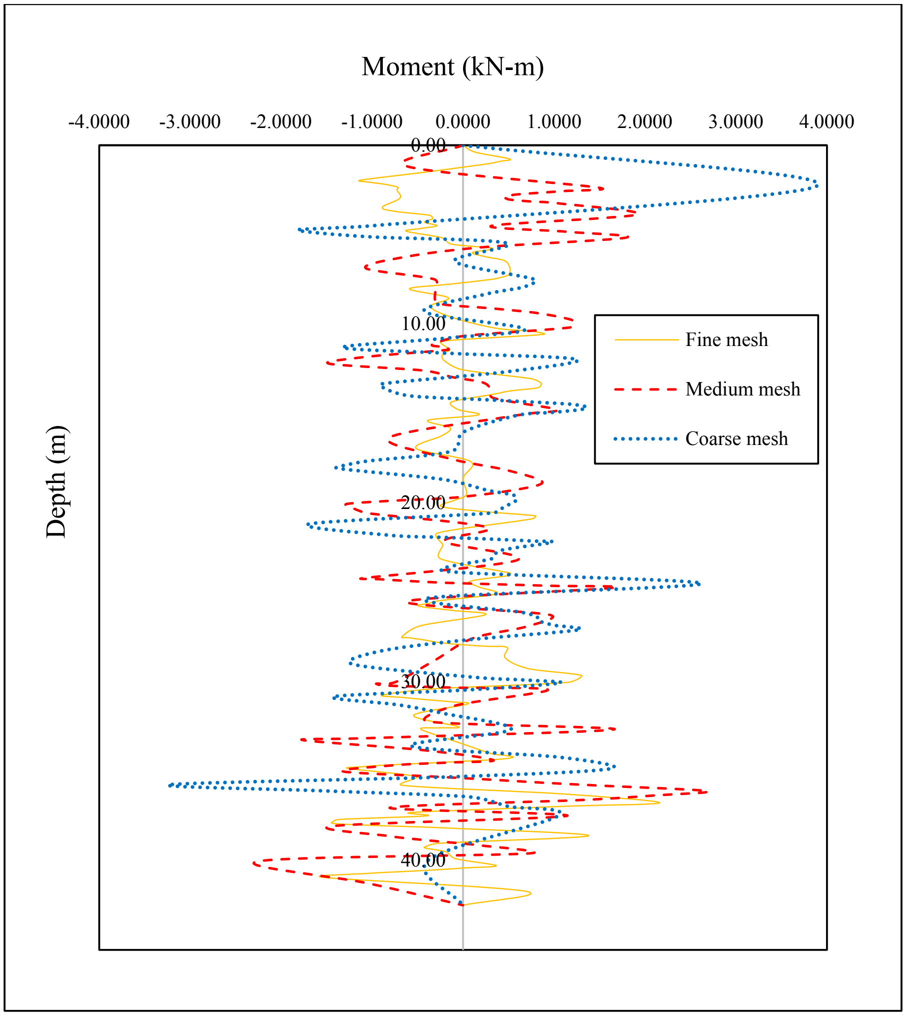

Figure 4.13: Comparison of moment for different mesh size

4.6.2 Effect of Pile Length

To achieve adequate bearing capacity, a pile tip needs to be placed in dense stratum of soil. In this study the different soil layers from borelog shows that up-to 37.5 m depth soil is clayey silt. After that the dense sand layer is found with SPT value 50. The required pile depth is 42.5 m for this area. To observe the effect of pile length on displacement, three pile depths 35 m, 42.5 m and 50 m are selected. By using pile length 35 m, pile shows higher displacement about 24.20 mm. But when pile lengths are 42.5 and 50 m, the pile shows almost similar displacement 18.47 mm and 18.56 mm respectively which are lower than the displacement related to 35 m pile length as shown in Figure 4.14. It can be seen that increase in pile length can reduce pile displacement significantly.

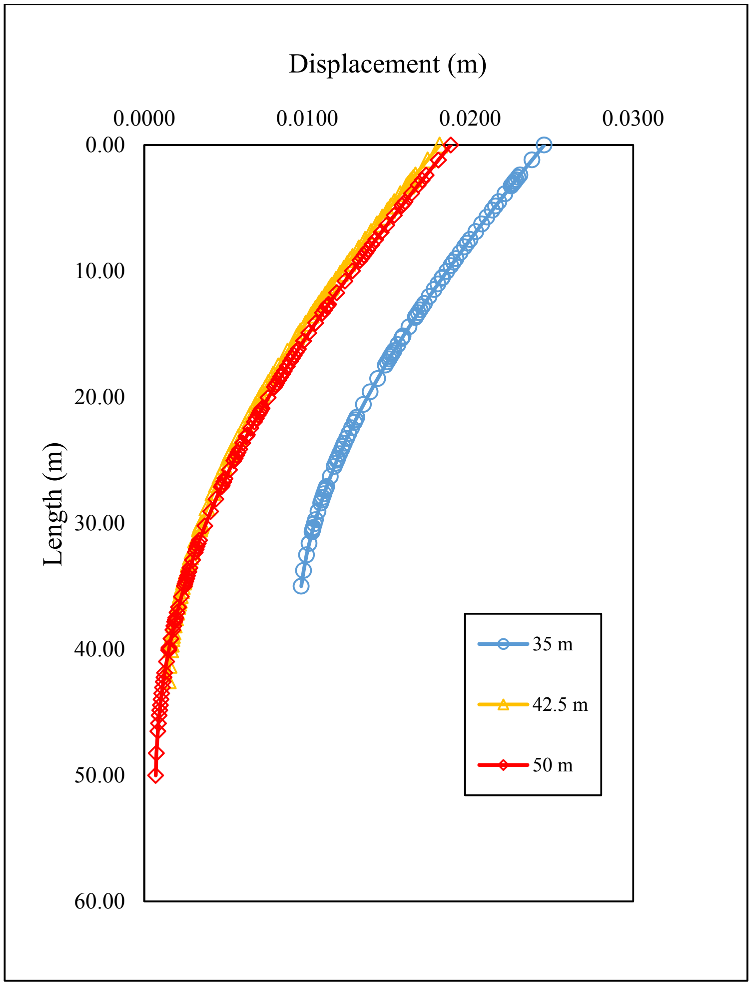

Figure 4.14: Distribution of displacement with pile depth for different pile length

4.6.3 Effect of Pile Diameter

Effect of pile diameter on axially loaded pile is investigated by considering three different pile diameters and same wall thickness in this analysis, i.e 400, 450 and 500 mm. Wall thickness of the hollow pile is assumed to be 110 mm in all cases. This variation shows that pile with larger diameter results in lower displacement of pile at the top whereas small diameter pile causes larger displacement, see Figure 4.15. The maximum displacement of pile occurs at the top in loose sandy soil. For D 400 and 450 mm the displacements are 24.02 and 18.47 mm. For D = 500 mm the displacement is 16.50 mm. That portrays that piles with larger diameters offers more resistance to the soil movements, resulting in a higher load carrying capacity of pile.

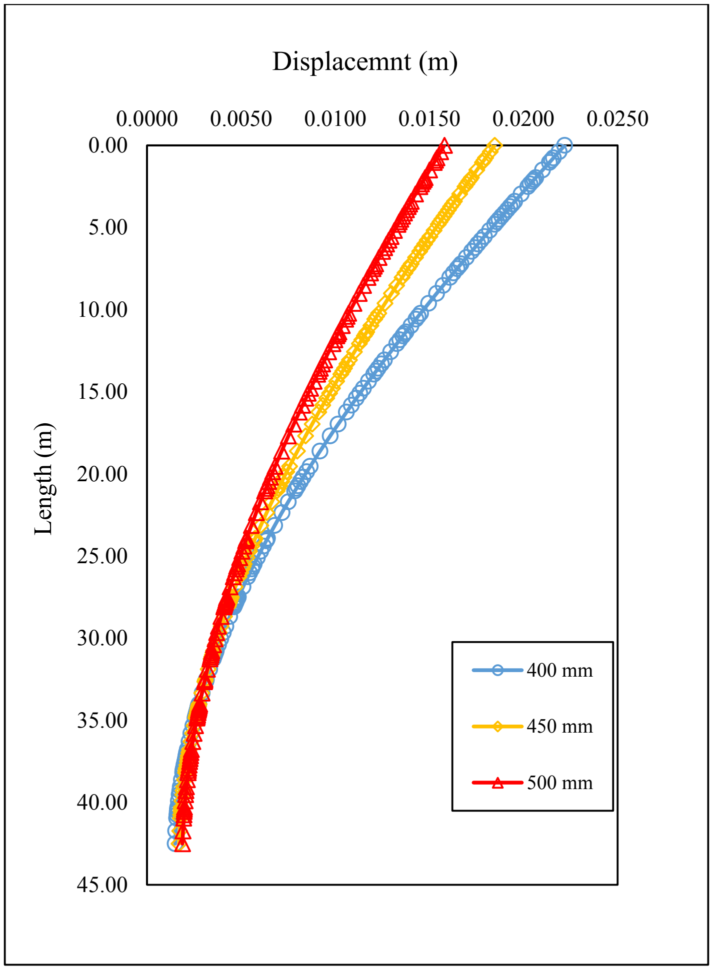

Figure 4.15: Distribution of displacement with pile depth for different pile diameter

4.7 Earthquake Analysis

For earthquake analysis, the free field site response has been carried out along a 1D linear elastic frequency domain. In this study, PLAXIS 3D finite element software is used to conduct this analysis. For the current study HS model is used for modeling soil element according to soil investigation done in the study site previously. The earthquake load is applied at the bottom of the FEM model as prescribed displacement. In dynamic loading condition, using HS model generates plastic strain with increased preconsolidation stress in soil. Under this condition damping is defined by Rayleigh damping. The stage construction phases in PLAXIS 3D for earthquake loading condition are given below in Table 4.6.

Table 4.6: Stage construction phases for earthquake analyis

Phase	Analysis type	Elements	Activated
Initial	K_0	Soil volume	√
		Embedded pile element	x
		Point load	x
Pile construction	Plastic	Soil volume	√
		Embedded pile element	√
		Point load	x
Loading stage	Plastic	Soil volume	√
		Embedded pile element	√
		Point load (design load)	√
		Deformation in z direction	√
Earthquake loading stage	Dynamic	Soil volume	√
		Embedded pile element	√
		Prescribed surface displacement (input earthquake loading)	√
		Deformation in x direction	√
		Boundary condition for dynamic	√

4.7.1 Dynamic Soil Behavior

Constitutive model presents in PLAXIS needs to be validated for seismic analysis before implementation. Every constitutive model can be used for modeling material behavior. But due to some limitations each model cannot simulate seismic behavior. During an earthquake, soil is subjected to cyclic shear loading showing a nonlinear disipative behavior. The total amount of damping is introduced through frequency dependent Rayleigh formula. Which is considered in HS model as previously discussed. Generally HS and hardening soil with small strain (HSSM) models are recognized for using in earthquake analysis. Here in this study, Hardening Soil model with the same soil properties have been used for seismic analysis as shown in Table-4.1 with assigning 5% Rayleigh damping as shown in Figure 4.16.

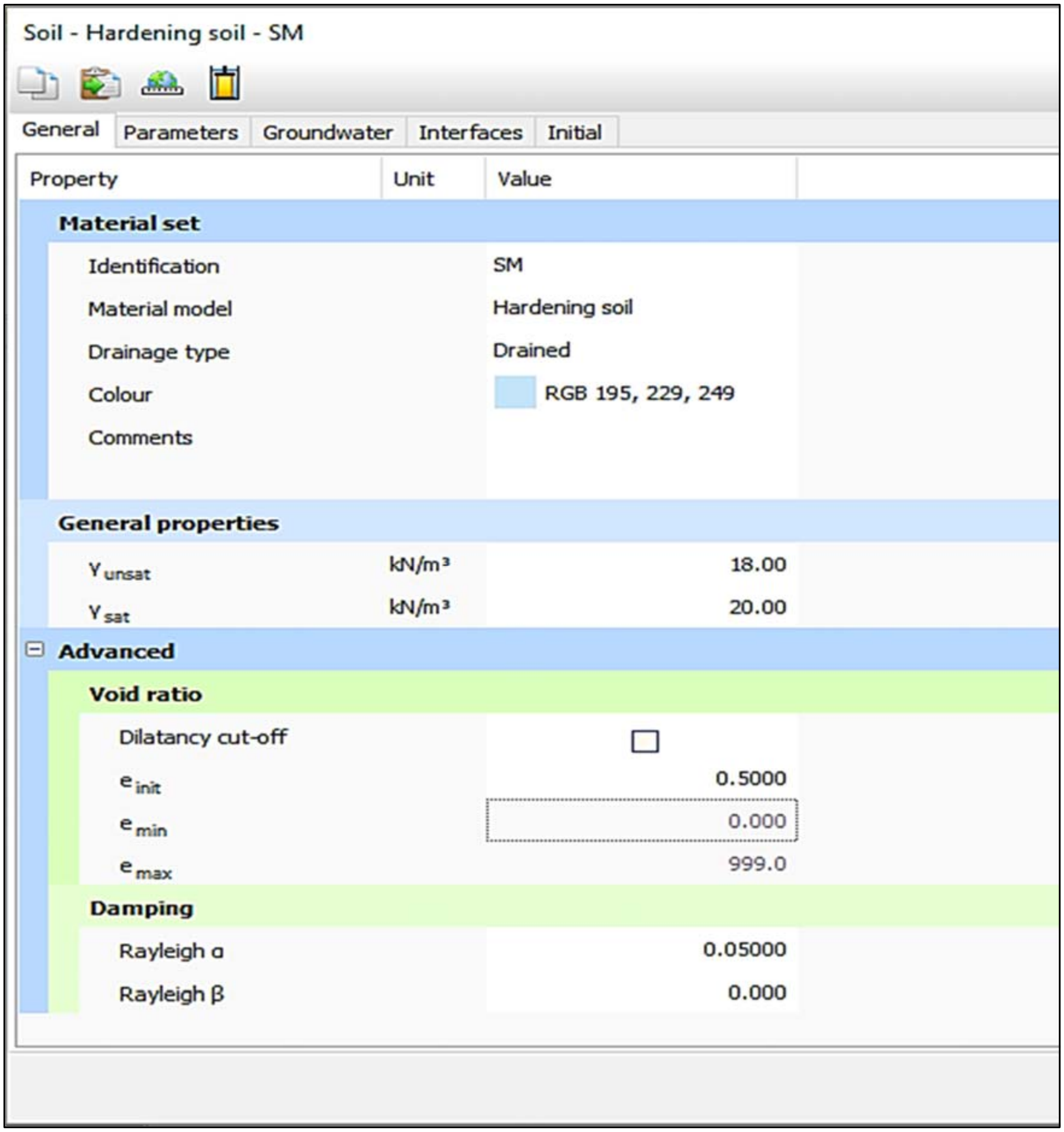

Figure 4.16: Assigned Rayleigh damping for soil

4.7.2 Boundary Condition

A proper boundary condition is important for analyzing pile accurately. The overall dimension of the model is same as the axially loaded pile model. Earthquake load is applied in the model as uniform prescribed displacement in x direction as shown in Figure 4.17. The deformation is free in X_{min} and X_{max} direction. In $Y_{min,max}$ and $Z_{min,max}$ direction the deformation is kept fixed. To introduce the soil strength reduction due to soil movement, an interface surface with strength reduction at the bottom surface is added. For input seismic motion the boundaries in x direction are kept free. The free field boundary condition for lateral deformation keeps the boundary free for motion to move at the sides and also absorbs the reflected secondary waves. In Y direction it is none as no absorbant boundary condition is applied. In Z_{min} compliant base is assigned and Z_{max} is none for unabsorbing bedrock. A Compliant base boundary for bottom boundary ensures the reflection of waves from above layers are absorbed and thus direct earthquake accelerogram can be applied directly.

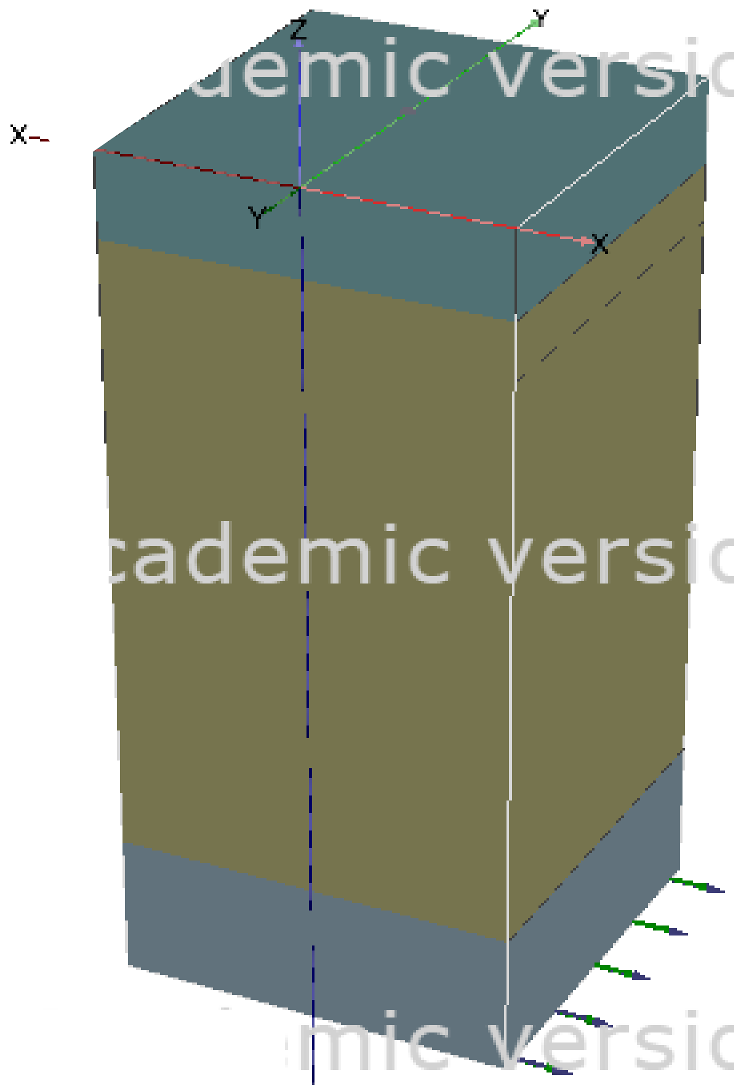

Figure 4.17: 3-D view of boundary condition

4.7.3 Earthquake Input Signal

In this analysis 1995 Kobe and 1989 Loma Prieta earthquake motions are used. These two motions have different charateristics. Kobe earthquake is a severe one with a magnitude M_w= 7.2 and PGA = 0.75 g. Loma Prieta has a magnitude M_w= 6.8 and PGA = 0.36 g. The acceleration time histories of 40 s duration are presented in Figure 4.18 a and b. These records are applied in the horizontal direction at all bottom node of the model. They are scaled into same acceleration 0.15 g for Dhaka zone. In order to reduce the calculation time only 5 s of Kobe earthquake and 5 s of Loma prieta earthquake are applied. Figure 4.19 shows the Kobe earthquake acceleration data input in PLAXIS 3D for earthquake analysis.

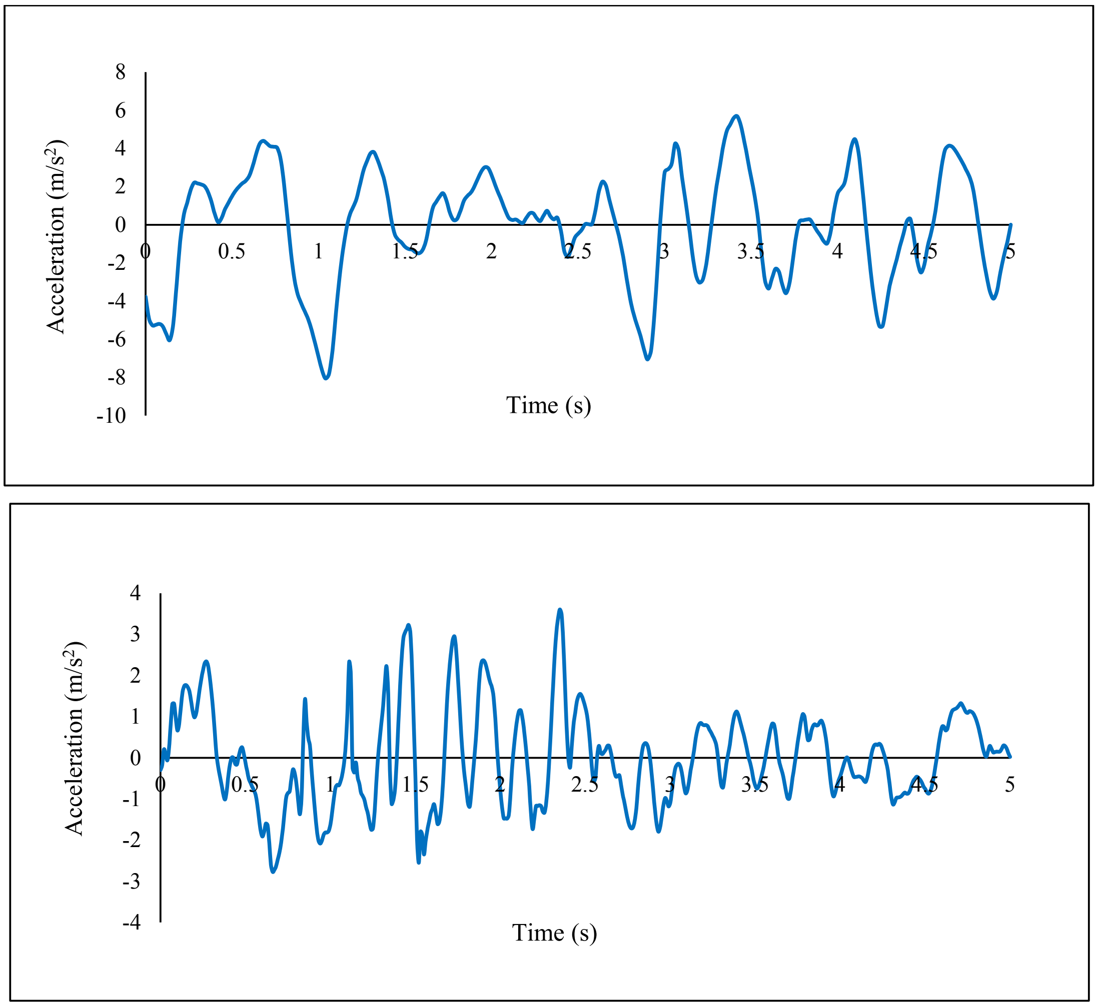

Figure 4.18: Original earthquake frequency (a) 1995 Kobe (b) 1989 Loma Prieta.

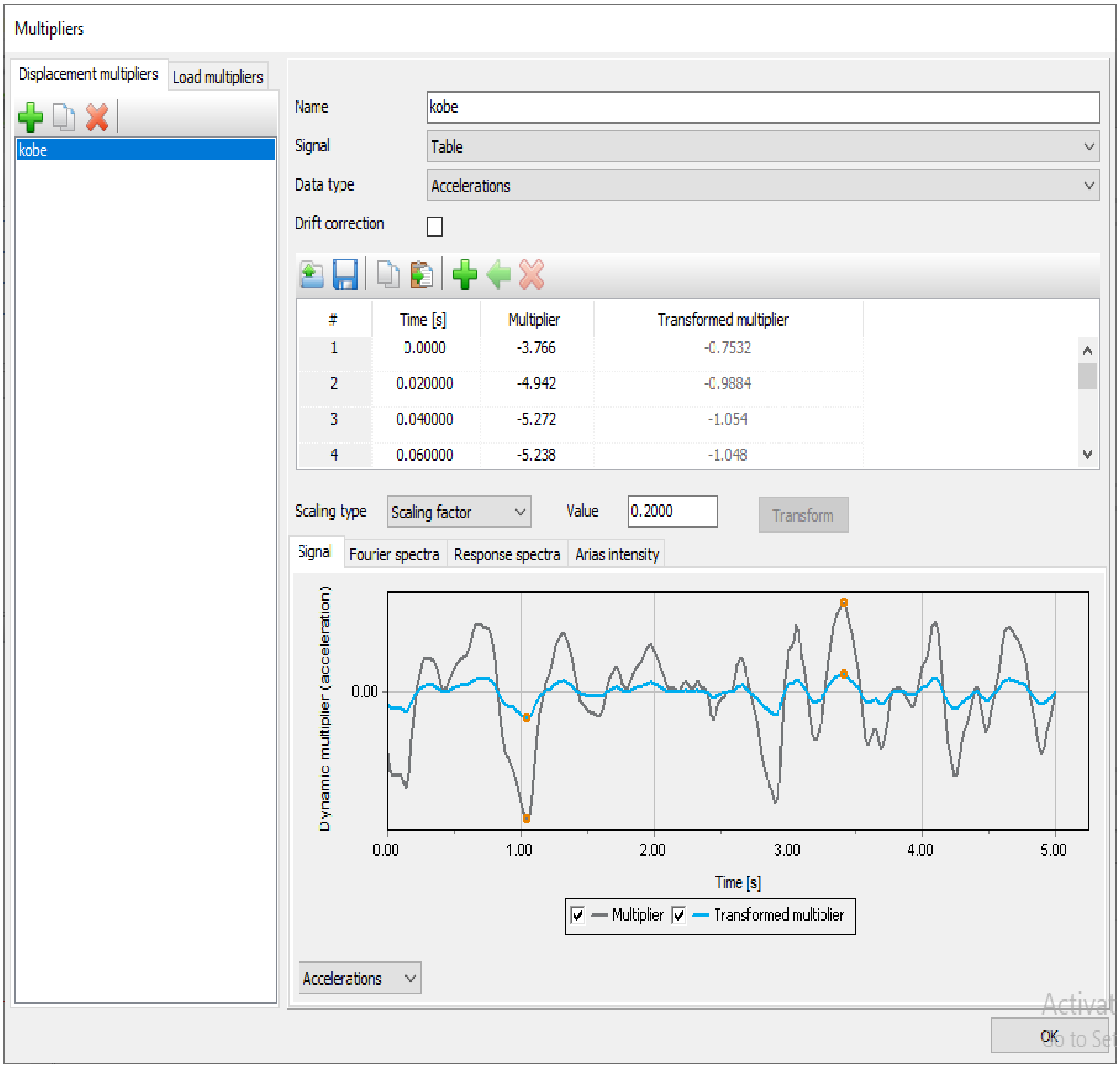

Figure 4.19: Kobe earthquake input signal

4.8 Pile Deformation under Earthquake Loading

The deformed shape of soil body after a seismic activity can be observed in Figure 4.20. It is seen that the top soil layer is displaced in x direction relating more than the other soil layers as the top layer is loose sandy soil. The vertical and lateral deformation of soil are illustrated in Figure 4.21 and 4.22. It is found that majority of the vertical deformation are concentrated at the boundaries but in case of lateral deformation, it is spread all over the soil body, see Figure 4.22 and 4.23.

Figure 4.20: Soil deformation due to earthquake loading (Kobe)

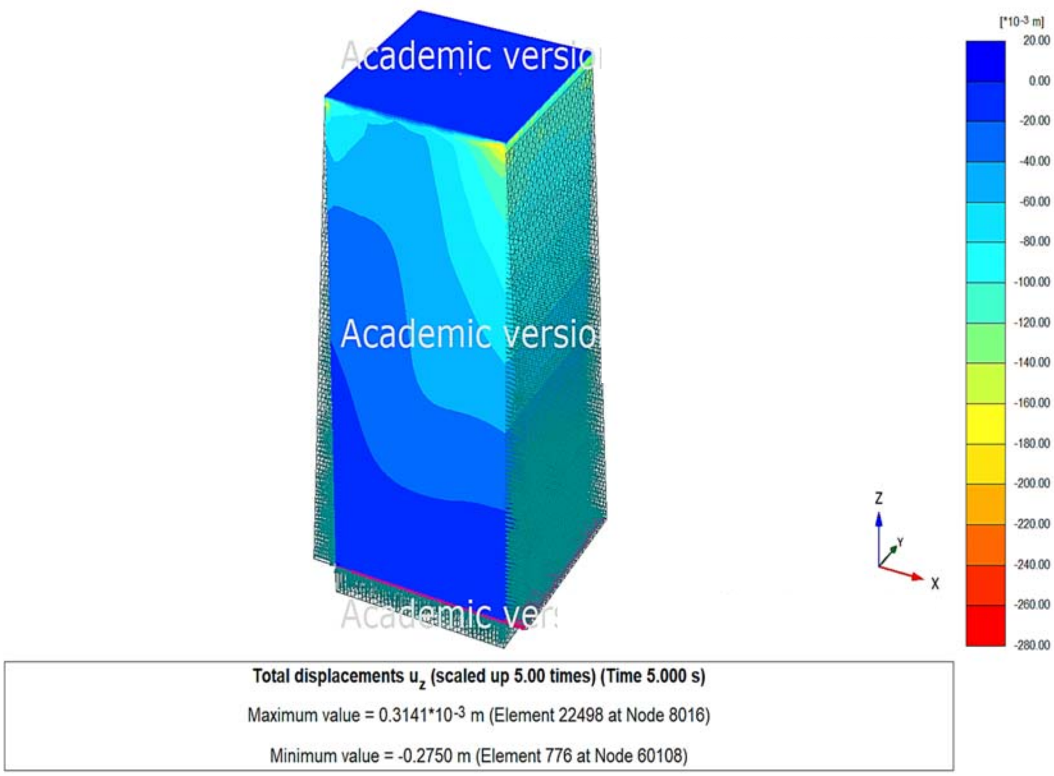

Figure 4.21: Vertical diplacement of soil under earthquake loading

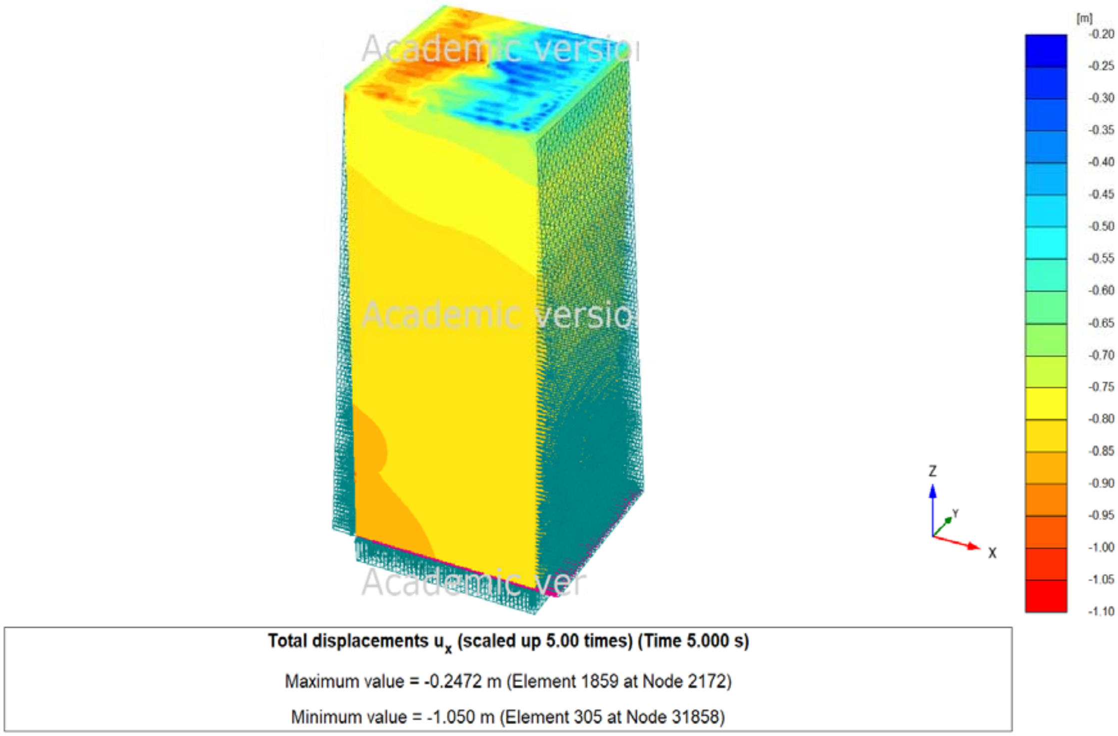

Figure 4.22: Lateral diplacement of soil under earthquake loading

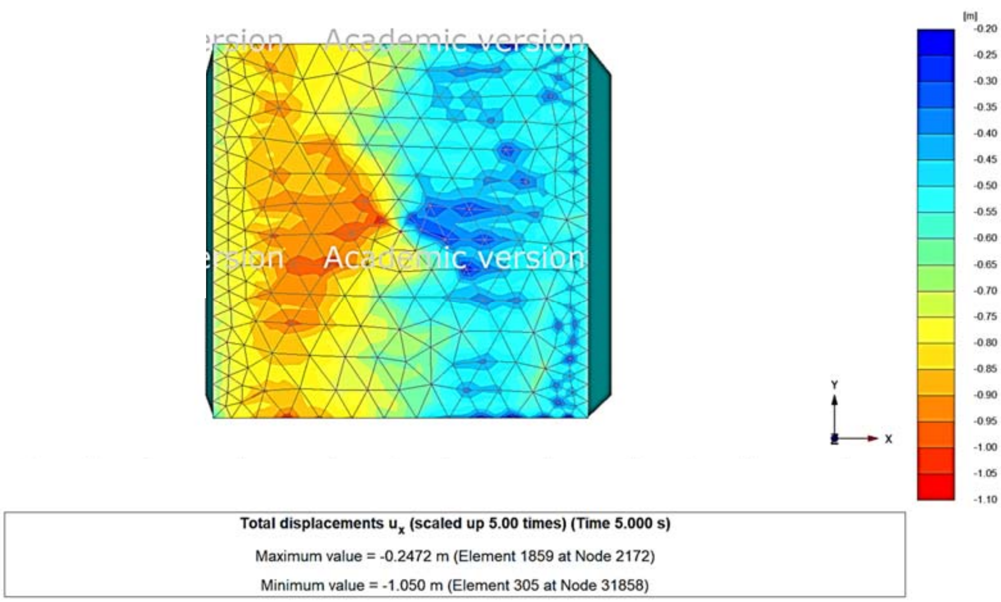

Figure 4.23: Top view of lateral diplacement of soil under earthquake loading

The displacement in pile occurred due to earthquake loading is compared with the displacement occurred only under axial loading over the length of pile. The displacement at the top of the pile is significantly increased for earthquake loading condition than the axial load. In case of Loma Prieta earthquake, the pile top displacement is increased by 8.5 times than axial load and for Kobe earthquake loading it is reported to be increased by 40 times as shown in Figure 4.24. This phenomenon explains that during seismic action a pile can experience excessive lateral deformation and tends to fail. But during axial loading condition the pile can sustain the load with a minimum settlement. So seismic assessement should be taken into account even the pile can sustain the compressive load.

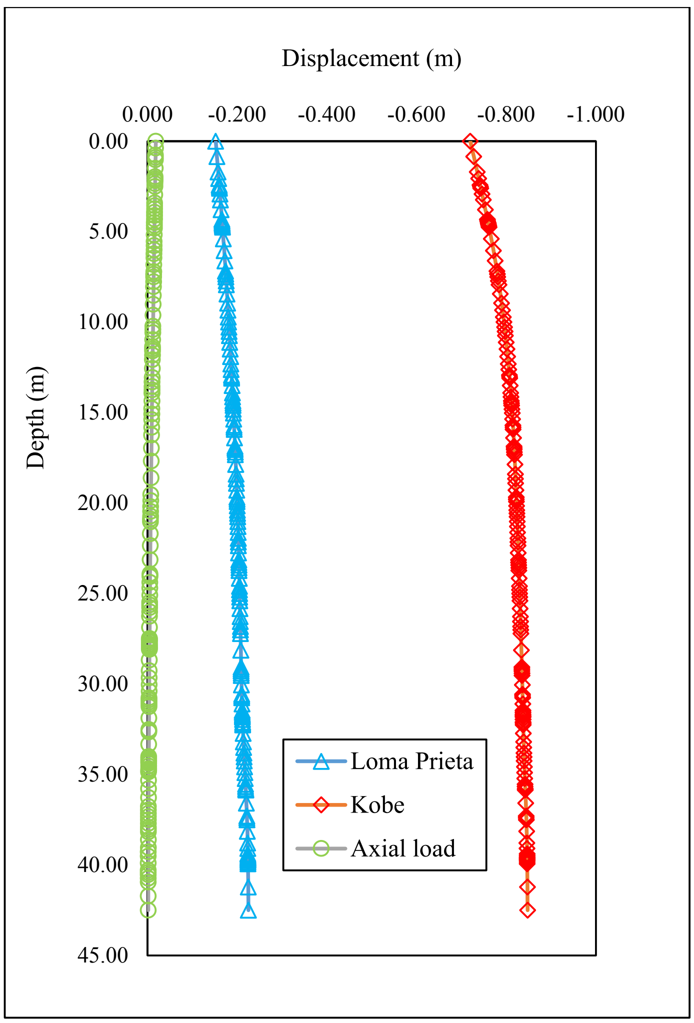

Figure 4.24: Displacement comparison of pile under both axial and earthquake loading

Earthquake load produces interal forces in the structure which causes stresses in foundation system and propagates to the soil. These spectrums describe the maximum response of foundation system for a specified earthquake ground motion and 5% of damping. The PSA value with respect to the natural period of vibration of structure allows to calculate the maximum shear stress at the base of the structure. In Figure 4.25 spectral acceleration for Kobe earthquake is compared at three different depth of soil body for damping ratio $\xi = 5\%$. At top layer of soil there is loose sand which is susceptable to liquefaction during earthquake. This liquefiable layer magnifies the response spectra as shown in Figure 4.25 with blue color. The red and cyan color spectral acceleration represents the mid and bottom layer respectively. The PSA for these two layers are relatively lower than the top layer as these layers have stiffer soil properties. The predominant period can be determined from PSA graph, which is 0.25 s. Figure 4.26 shows the magnitude of acceleration in x direction of Kobe earthquake at three different soil depth. It is evident that at the top layer the acceleration is amplified.

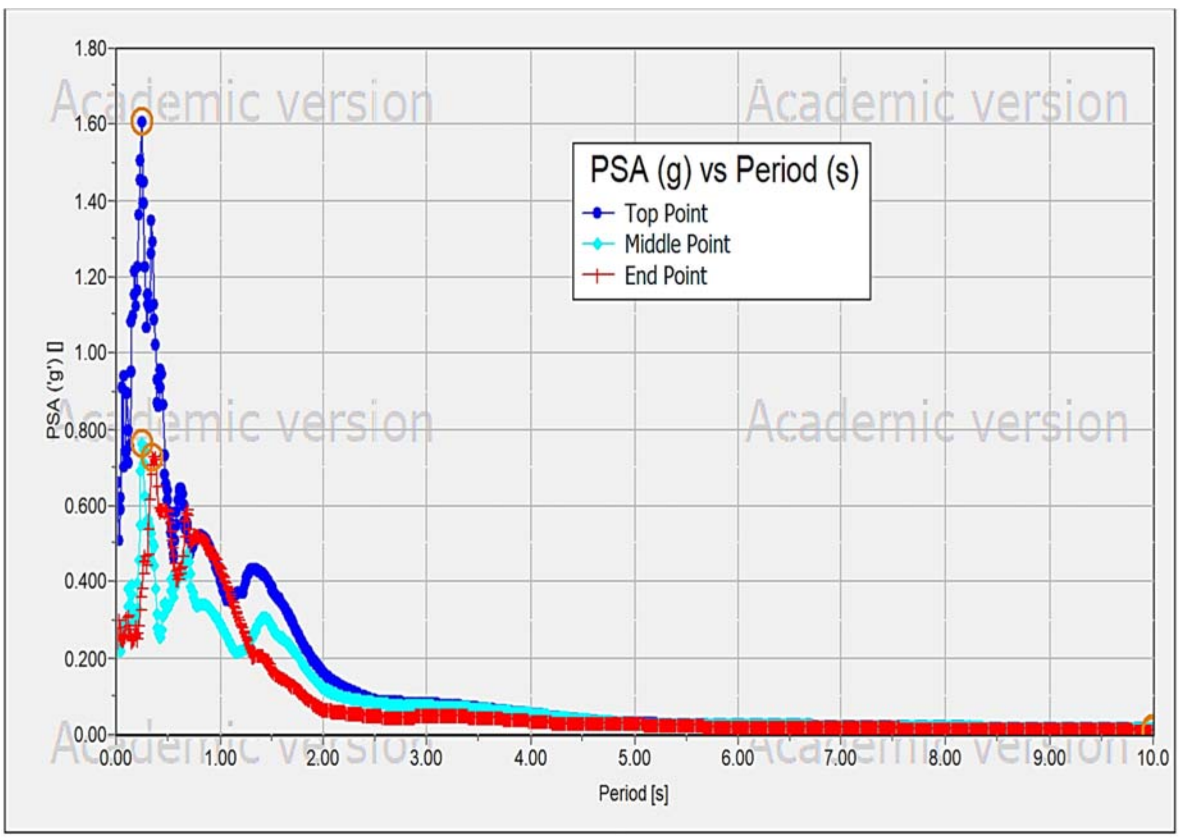

Figure 4.25: Acceleration response spectrum of analysed model for Kobe earthquake at different depth

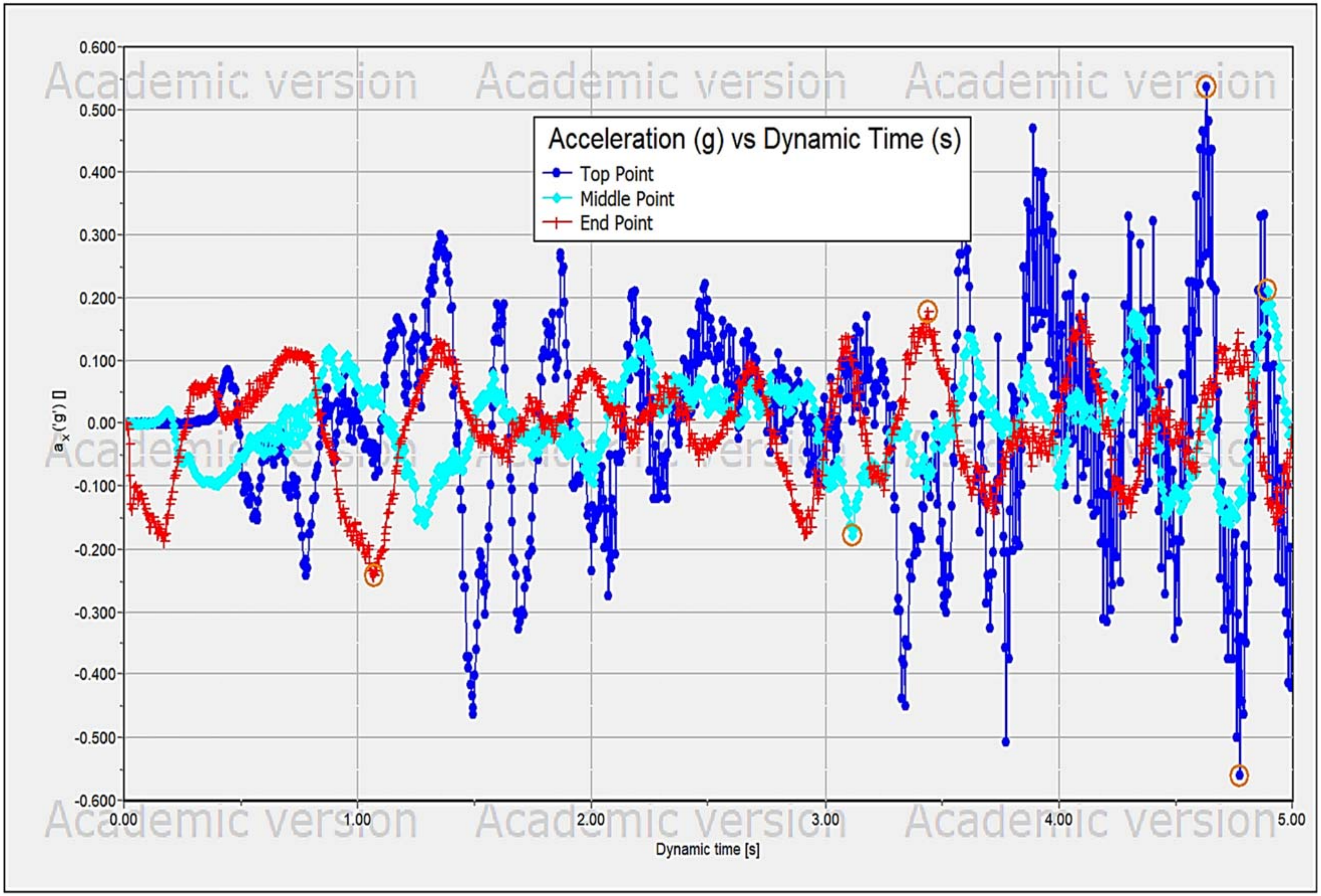

Figure 4.26: Earthquake acceleration at different depth of soil

The ratio of acceleration response at the top to the response at the bottom is reported in Figure 4.27. It shows that the top point is amplified to 131 ratio with respect to bottom point under given earthquake loading.

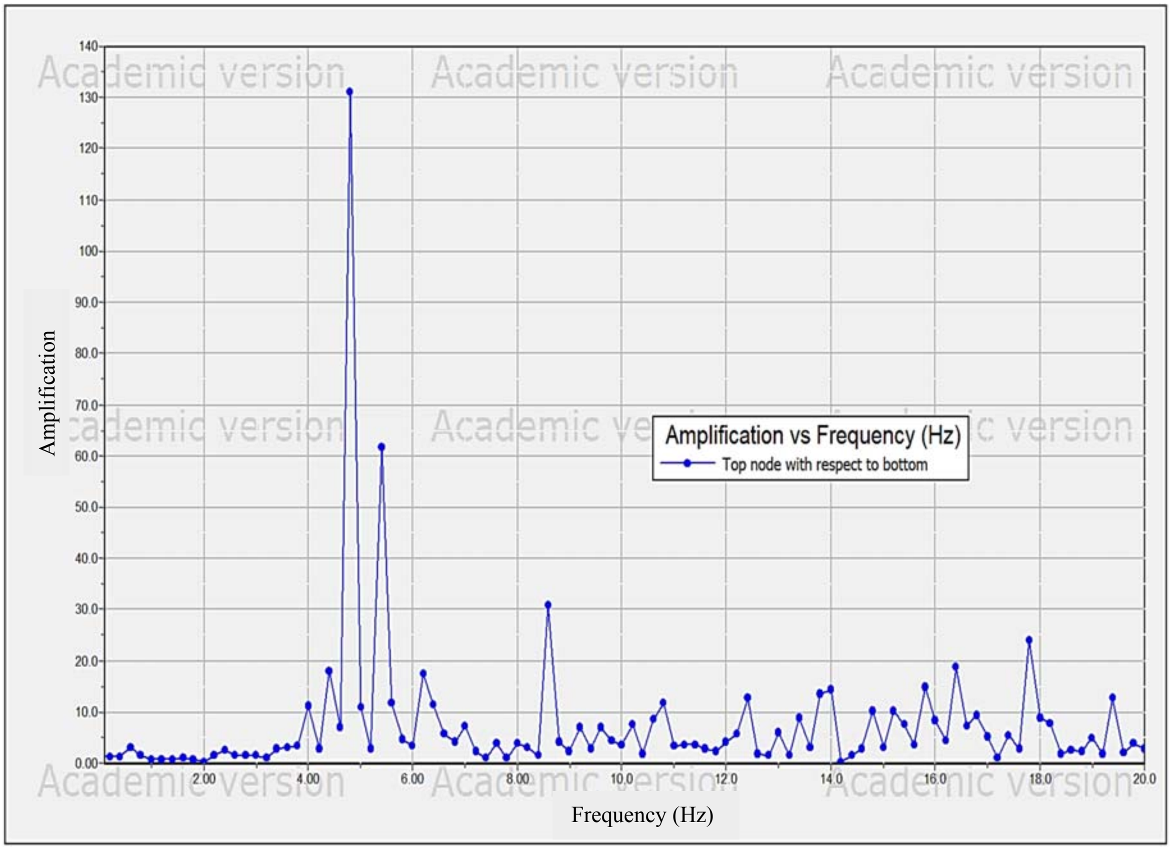

Figure 4.27: Amplification spectrum

The maximum strain develops at top and bottom stress point in soil element are shown in Figure 4.28 and 4.29 for Kobe and Loma Prieta earthquake. It is seen that at top the strain value of Kobe earthquake is 7.6 times greater than Loma Prieta whereas at bottom point it is 1.6 times higher with respect to Loma Prieta earthquake. It is clear that the seismic excitation causes large deformation at top level by magnifying the response spectrum. Large magnitude earthquake can develop higher strain in soil body.

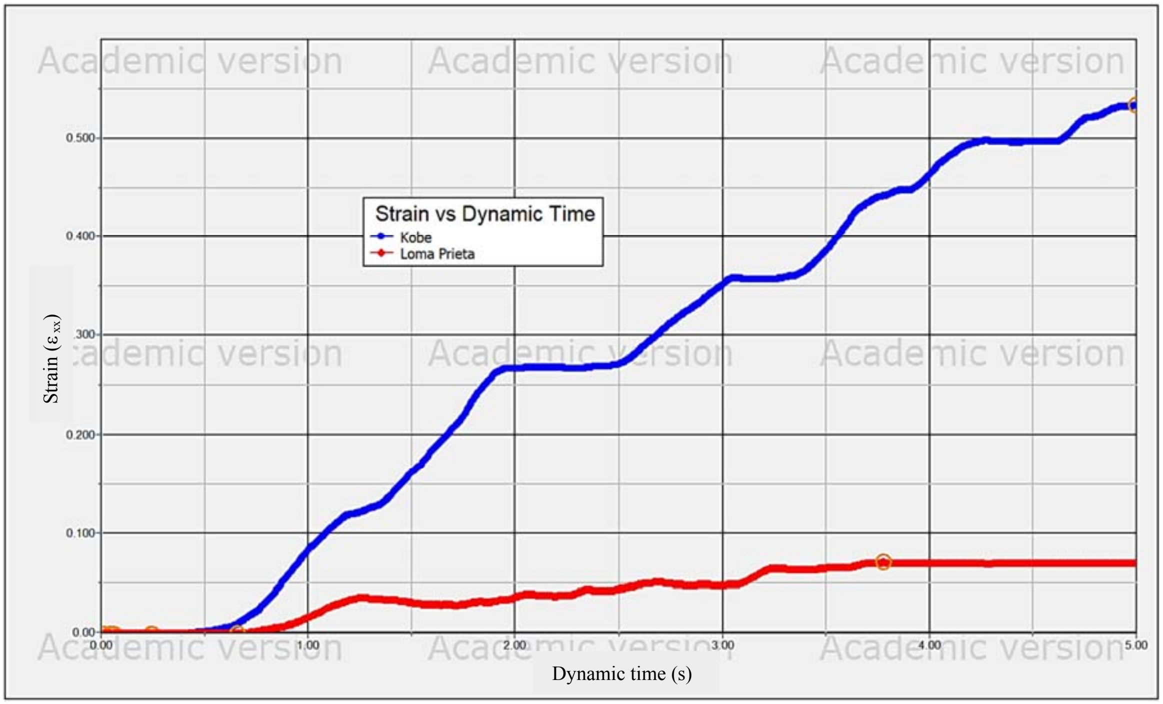

Figure 4.28: Maximum strain at top of soil profile for earthquake loading

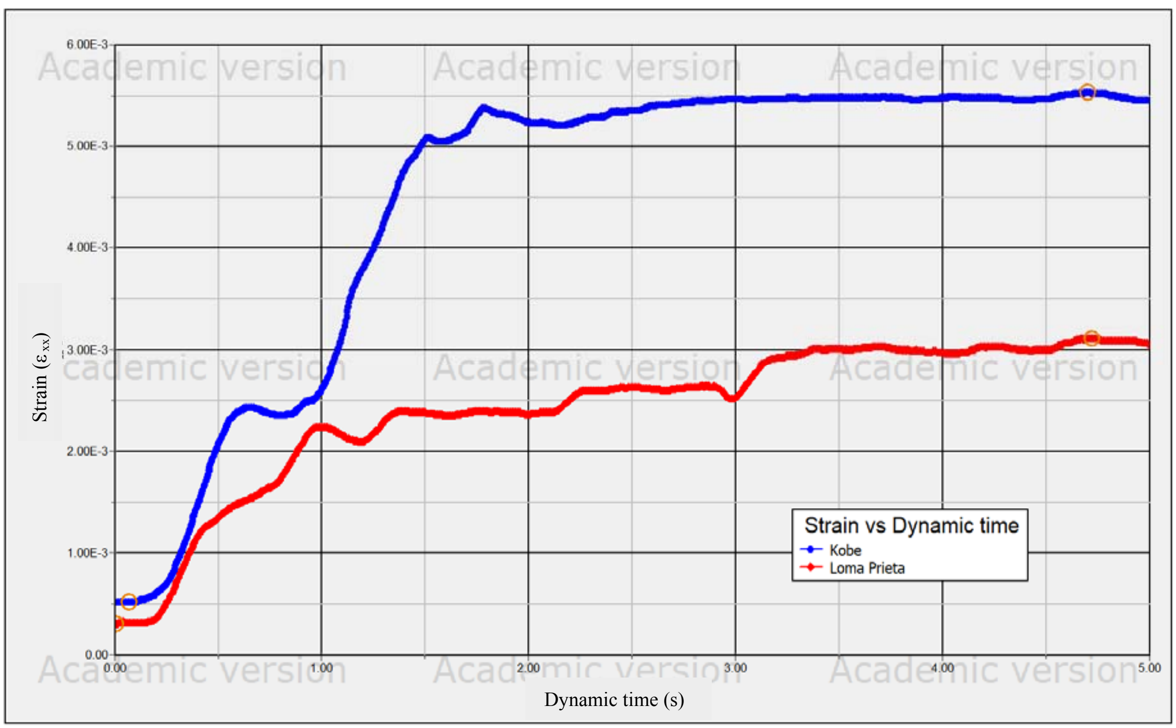

Figure 4.29: Maximum strain at bottom of soil profile for earthquake loading

Maximum shear stress τ_{max} in the soil at the bottom of the pile is shown in Figure 4.30. At maximum shear stress the Mohr's circle is expanded to touch coulomb failure envelop. The max value of shear stress is 146 kN/m^2. It is 7.2 % higher than the shear stress under axial loading, see Figure 4.31. Total stress increases about 8.5 % for seismic activity than only axial loading condition at the bottom of pile as shown in Figure 4.32.

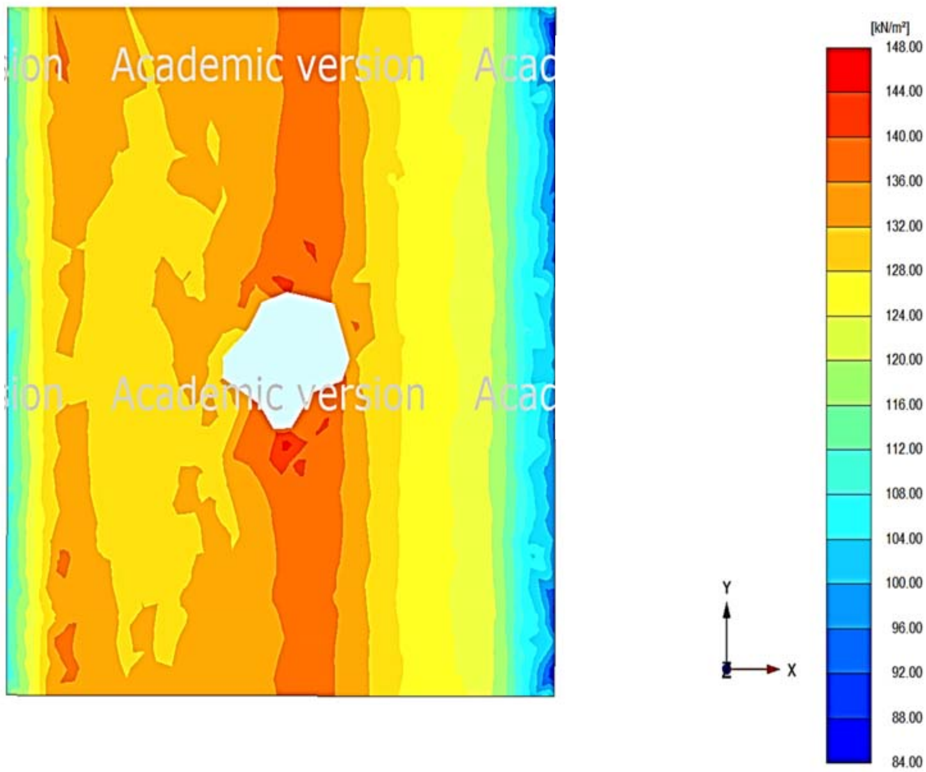

Shear stress τ_{max} (scaled up 0.0100 times) (Time 5.000 s)

Maximum value = 145.9 kN/m²

Minimum value = 84.71 kN/m²

Figure 4.30: Maximum shear stress under earthquake loading

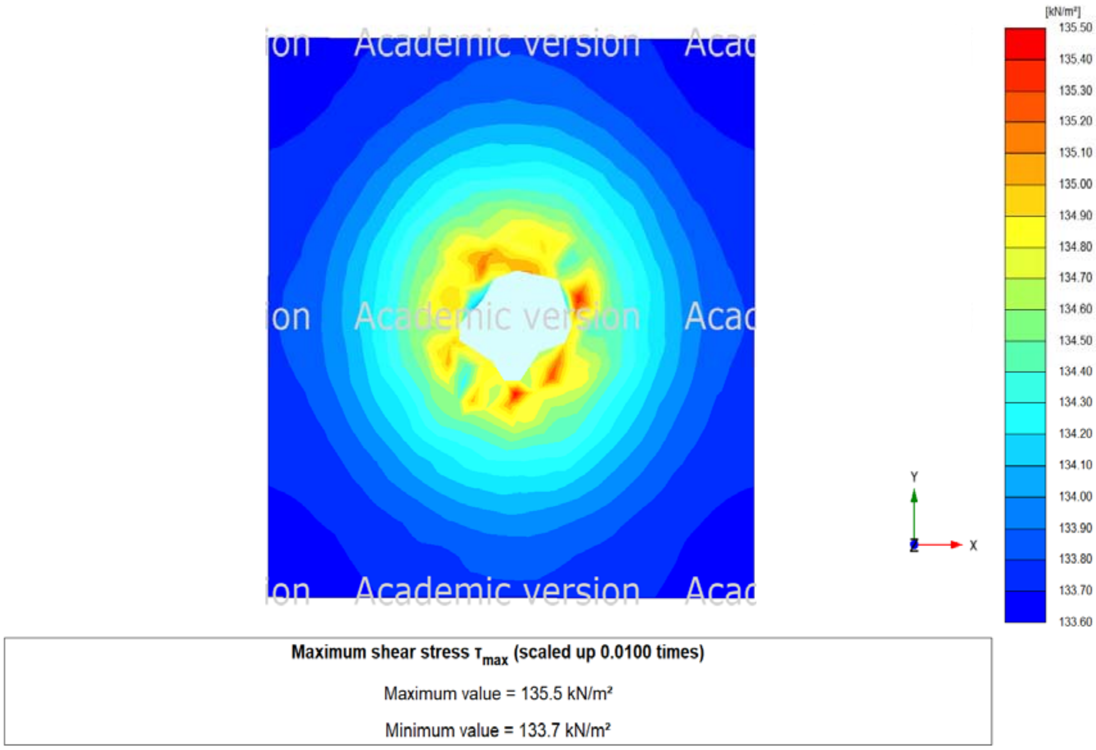

Figure 4.31: Maximum shear stress under maximum axial loading

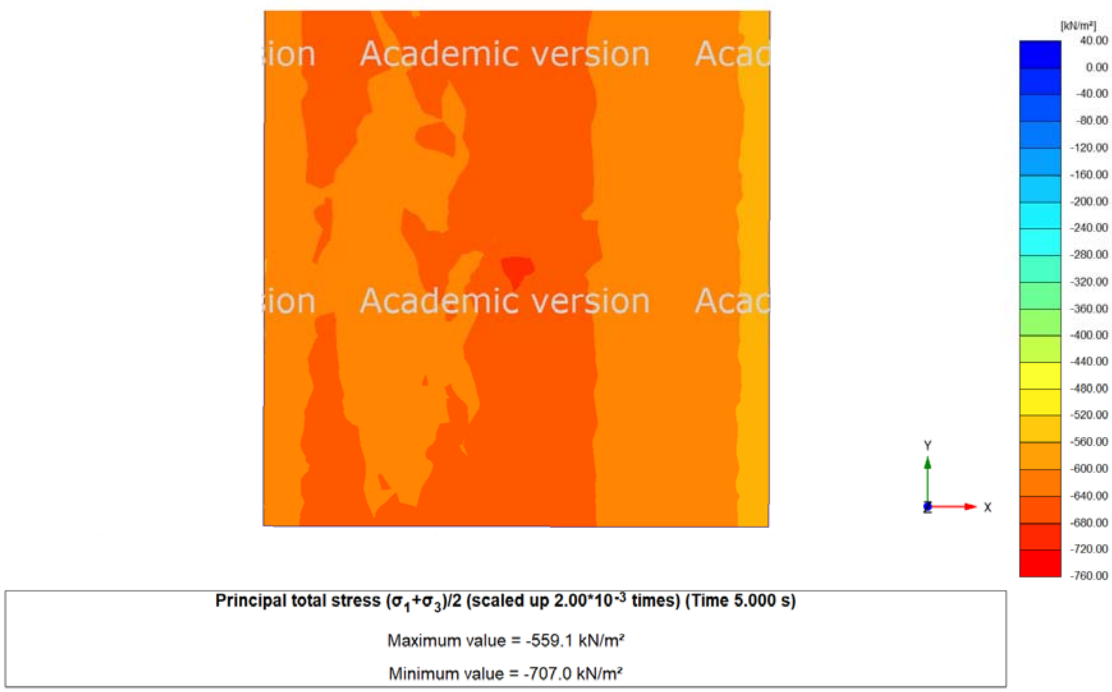

Figure 4.32: Principle total stress under earthquake loading

4.9 Liquefaction Analysis

During earthquake seismic wave propagation, it not only causes damage to structure but also initiate other phenomenon like landslides and soil liquefaction. So liquefaction should also be considered while performing site response analysis in loose cohesionless soil. To evaluate the liquefaction potentiality, the triggering factor for liquefaction is to be identified. The triggering factors depend on the earthquake magnitude, duration and peak ground acceleration. To understand the possibility of liquefaction in a specific site nonlinear dynamic analysis can be done. In PLAXIS 3D hardening soil model is not able to capture the liquefaction phenomenon. The UBC3D-PLM is a nonlinear elastic-plastic model that is capable of capturing seismic liquefaction behavior of sands and silty sands. The model can accumulate strain and pore pressure of sandy soil that can capture the onset of liquefaction. the Initialy UBC3DPLM implementation in PLAXIS was developed by Tsegaye (2010).

4.9.1 Liquefiable Sand Layer Parameters

The parameters for UBC3D-PLM can be determined from laboratory tests under cyclic loading but if it is not possible then data can be extracted from in-situ tests like SPT N value and CPT. There are some corelation proposed by Beaty and Byrne (1998) which can be used to determine required parameters from corrected SPT N value. The correlations are presented below:

$$K^e_G = 21.7 \text{ x } 20 \text{ x } ((N_1)_{60})^{0.333} \tag{4.1}$$

Here K^e_G is the elastic shear modulus

$$K^e_B = K^e_G \text{x } 0.7 \tag{4.2}$$

Here K^e_B is the elastic bulk modulus

$$K^p_G = K^e_G \text{x } ((N_1)_{60})^2 \text{ x } 0.003 + 100.0 \tag{4.3}$$

Where K^p_G is the plastic shear modulus

$$\varphi_{pi} = \varphi_{cv} + \frac{(N1)_{60}}{10} \tag{4.4}$$

$$\varphi_p = \varphi_{pi} + \max\left(0.0, \frac{(N1)_{60} - 15}{5}\right) \tag{4.5}$$

Where φ_{pi} and φ_{cv} are peak friction angle and constant volume friction angle

$$R_f = 1.1 \text{ x } ((N_1)_{60})^{-0.15} \quad (4.6)$$

R_f is the failure ratio

In this study, during earthquake analysis the liquefaction phenomenon is not considered and only HS model is used for soil modeling. In this segment earthquake analysis is done considering liquefaction phenomenon with undrained behavior in loose sandy type soil using UBC3D-PLM model. The liquefiable sand layers parameters are shown in Table 4.7

Table 4.7: Input parameters of liquefied sand layer of UBC3D-PLM model

Parameters	Symbol	Unit	Value applied in model
Unit weight	γ_{unsat}	kN/m^3	16
Saturated unit weight	γ_{sat}	kN/m^3	17
Poisson's ratio	ν	-	0.3
Constant volume friction angle	φ_{cv}	(°)	22
Peak friction angle	φ_p	(°)	23
Cohesion	c	kPa	0
Elastic shear modulus	K^e_G	-	1019.0
Elastic bulk modulus	K^e_B	-	713.0
Plastic shear modulus	K^p_G	-	617.0
Elastic shear modulus index	n_e	-	0.5
Elastic bulk modulus Index	m_e	-	0.5
Plastic shear modulus index	n_p	-	0.5
Failure ratio	R_f	-	0.74
Atmospheric pressure	P_A	-	100
Tension cut-off	σ_t	kPa	0.00
Densification factor	f_{dens}	-	0.45
Corrected SPT value	$(N_1)_{60}$	-	13.0
Post liquefaction Factor	f_{Epost}	-	0.20

Figure 4.33 shows the deformation in soil element at top layer due to liquefation. It is noted that UBC3D-PLM model can describe the liquefaction phenomenon in loose sandy soil which tends to liquefy at the moment of earthquake loading. There are some other state parameters that can confirm the liquefaction event using UBC3D-PLM model. In PLAXIS liquefaction can be explained by excess pore water pressure ratio r_u. It is the ratio between excess pore pressure and initial effective vertical stress at the depth.

$$r_u = 1 - \frac{\sigma'_v}{\sigma'_{v0}} \tag{4.7}$$

Here σ'_v is the vertical stress at the end of dynamic calculation and σ'_{v0} is the initial vertical effective stress earlier seismic activity. If r_u is equal to 1 then the layer is in complete liquefied state. If a layer has r_u value equal or greater than 0.7 then the layer will be defined as liquefied. In the analysis the maximum excess pore pressure ratio r_u is about 0.99 ~ 1 as shown in Figure-4.34 and 4.35 for both Kobe and Loma Prieta eartquake is equal to 1.

It is obtained that if a soil layer is loose sandy soil or silty soil it can liquefy during seismic event due to generation of excessive pore pressure. The maximum pore pressure generated during earthquake in the liquefied layer is 1178 kN/m^2 and 1048 kN/m^2 for Kobe and Loma Prieta earthquake as shown in Figure 4.36. It shows that larger the peak acceleration the larger the pore pressure generates. During liquefaction, the relative diplacement at pile head increases about 30 to 60 % for both Kobe and Loma Prieta earthquakes as shown in Figure 4.37. It is observed from the deformed shape of pile that the displacement profile puts the pile in bending. It can also be seen that the nonliquefiable layers of the soil begin to displace laterally with respect to the liquefiable layer.

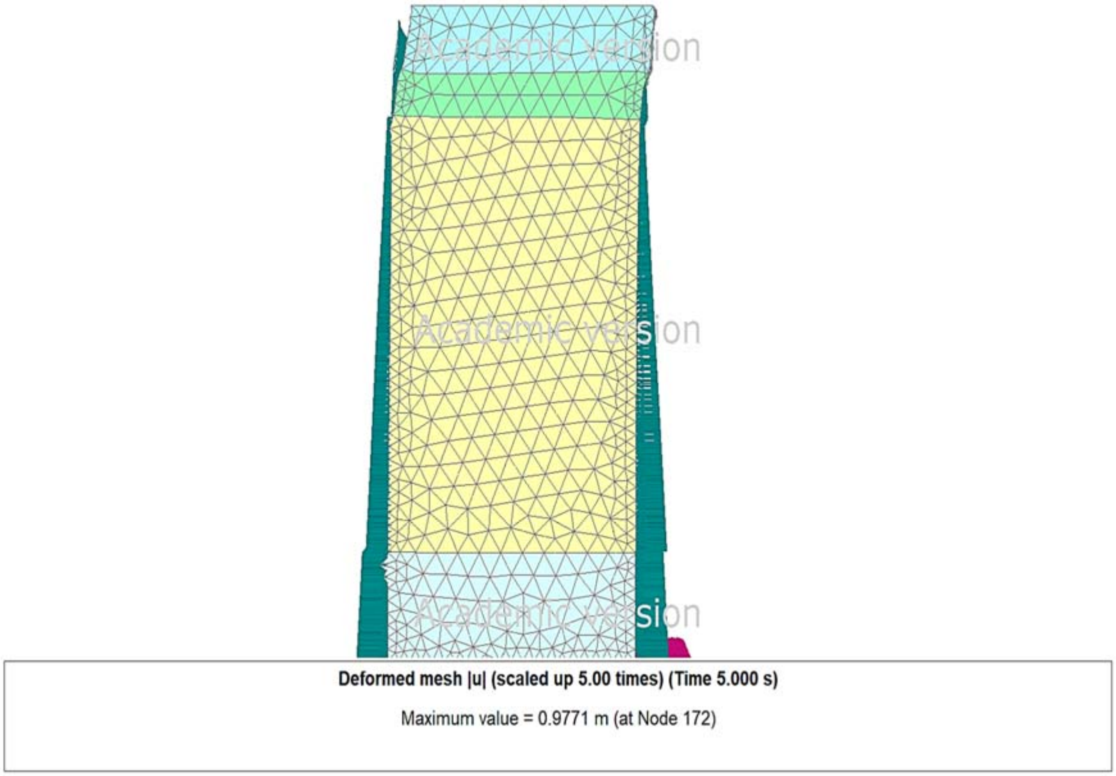

Figure 4.33: Deformation at the top soil layer due to liquefaction

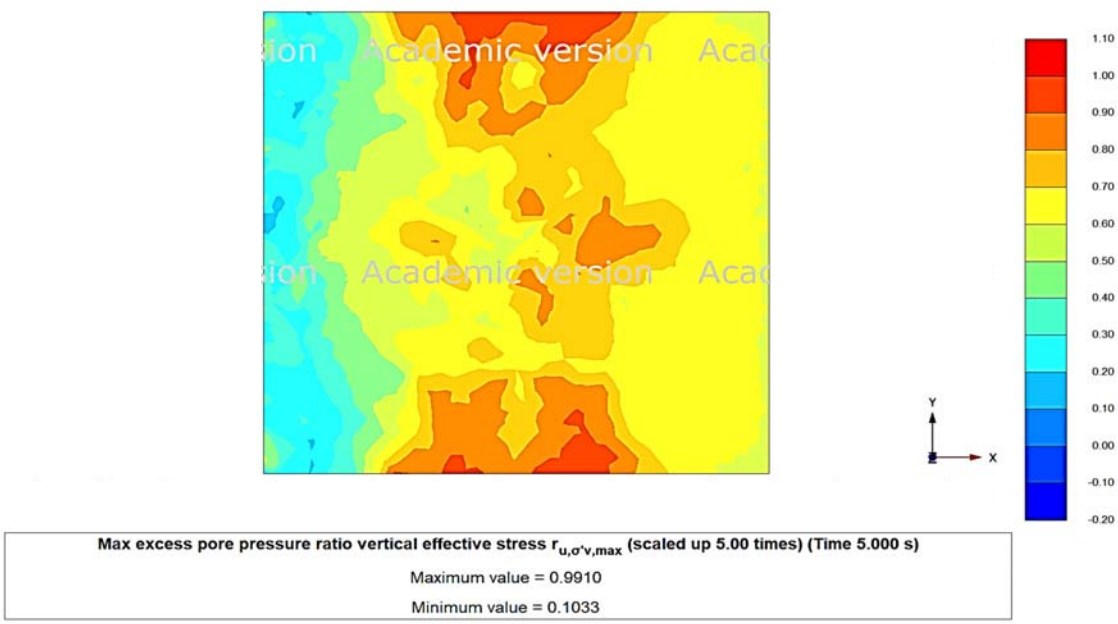

Figure 4.34: Maximum pore pressure ratio at top soil layer for Kobe earthquake

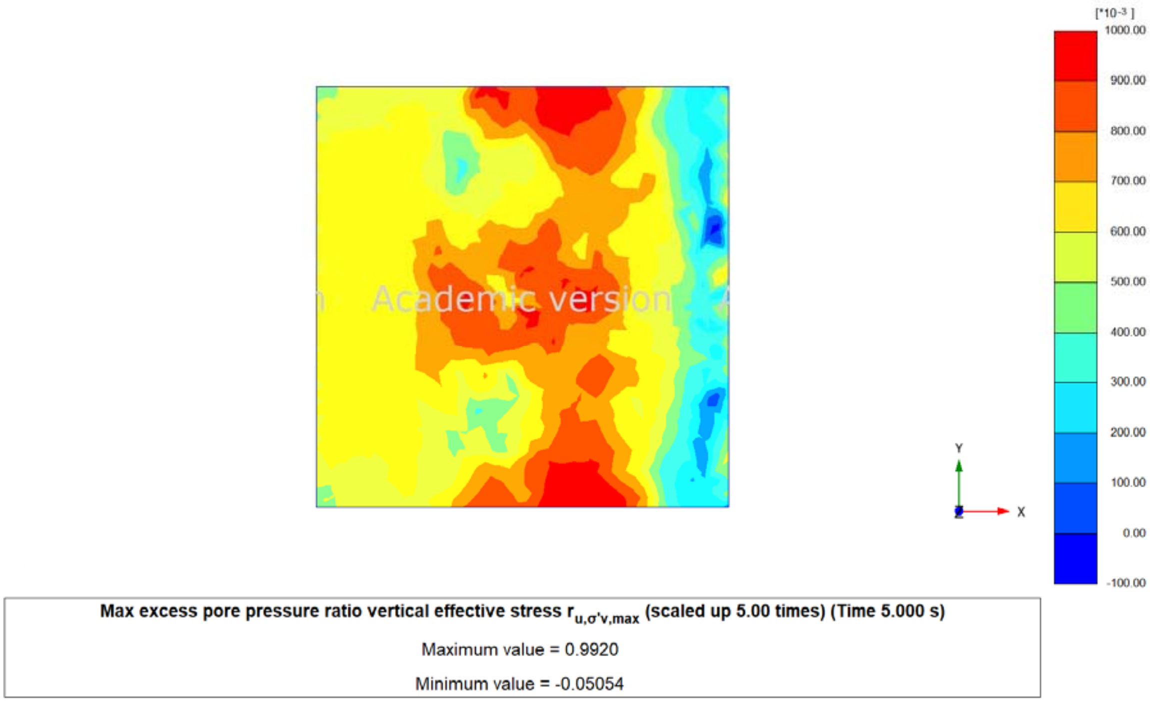

Figure 4.35: Maximum pore pressure ratio at top soil layer for Loma Prieta earthquake

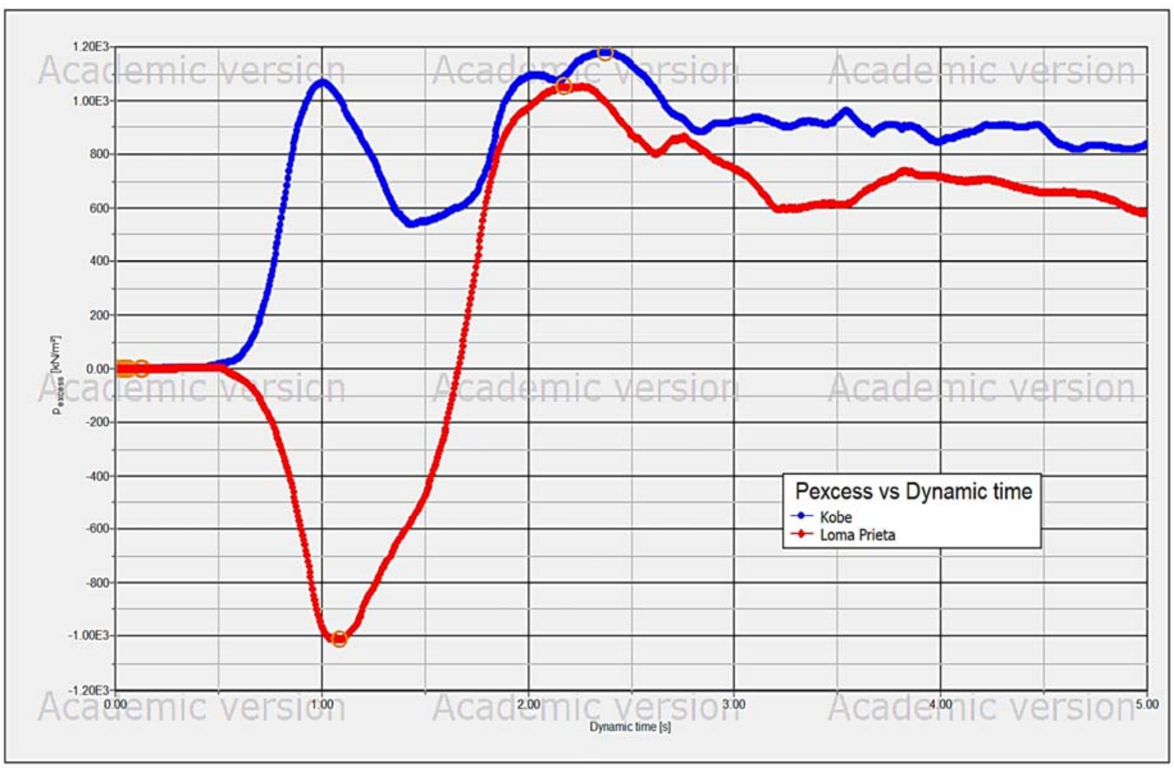

Figure 4.36: Maximum excess pore water pressure generated during Kobe and Loma Prieta earthquake

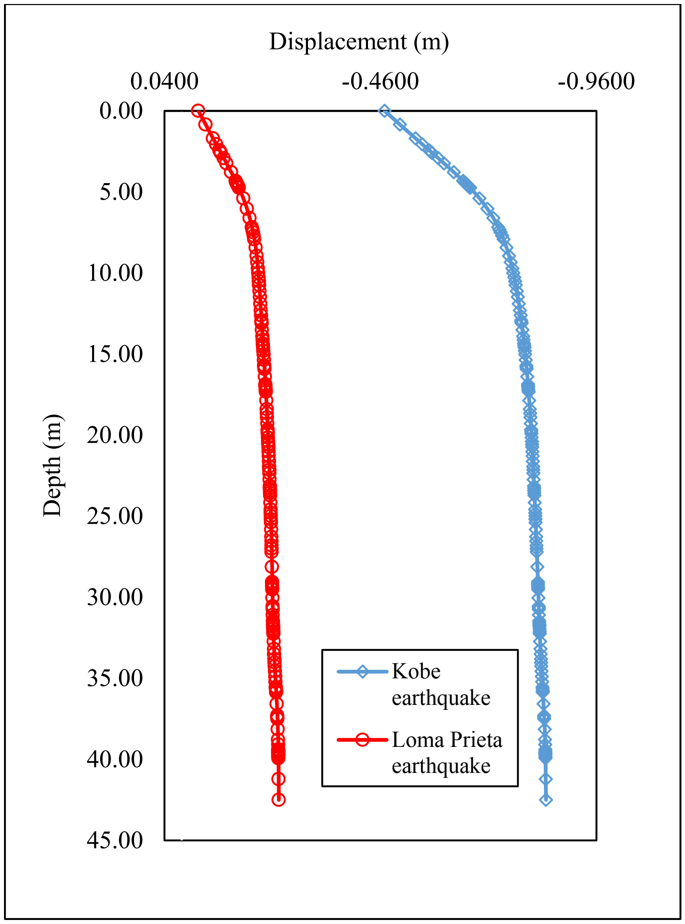

Figure 4.37: Displacement comparison of pile under earthquake loading

4.10 Soil Improvement Impact on Liquefiable Soil

The presence of liquefiable soil layer in any site can immensely influence the pile response both in deflection and bending moment especially when subjected to increased magnitude. During seismic action there is possibilties to develop large amount of moment that cannot be resisted by pile. If only earthquake is considered then the observed maximum moment is 42 kN-m and 10 kN-m for Kobe and Loma Prieta earthquake respectively, see Figure 4.38. From the sectional analysis it is found that the maximum moment carrying capacity of 450 mm dia SPC pile is 180 kN-m, see Table 3.1. In this study area as there is fill soil upto 5 m so while liquefaction event is taken into account, the maximum bending moment is found to be 478 kN-m for Kobe earthquake and 242 kN-m for Loma Prieta earthquake. It is 11 times and 26 times higher than the moment found without considering liquefaction, see Figure 4.39. The maximum bending moment is found at the interface of liquefiable and non-liquefiable soil layers which agrees with the existing literatures. However, location of maximum bending moment also depends on pile head condition. The bending moment demand for fixed head pile is greater than free headed pile.

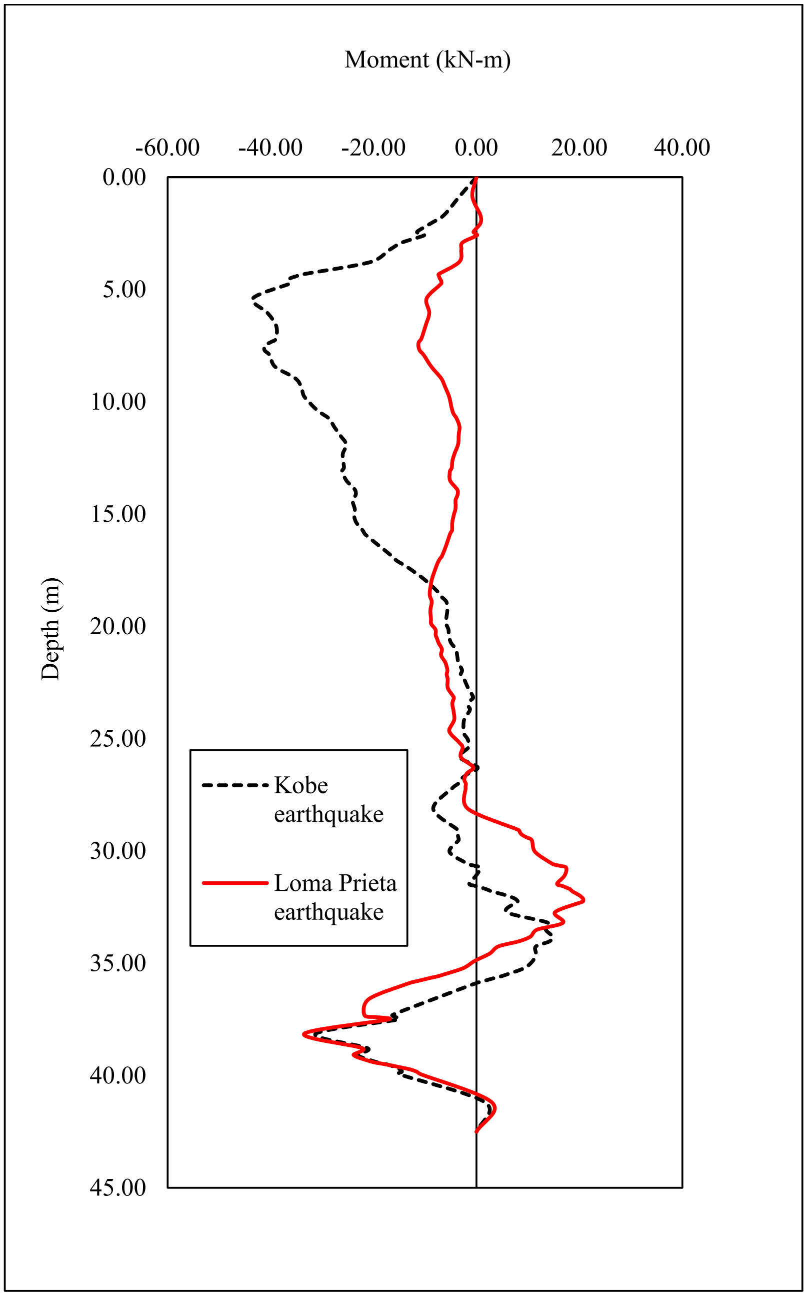

Figure 4.38: Comparison of moment developed under earthquake loading condition

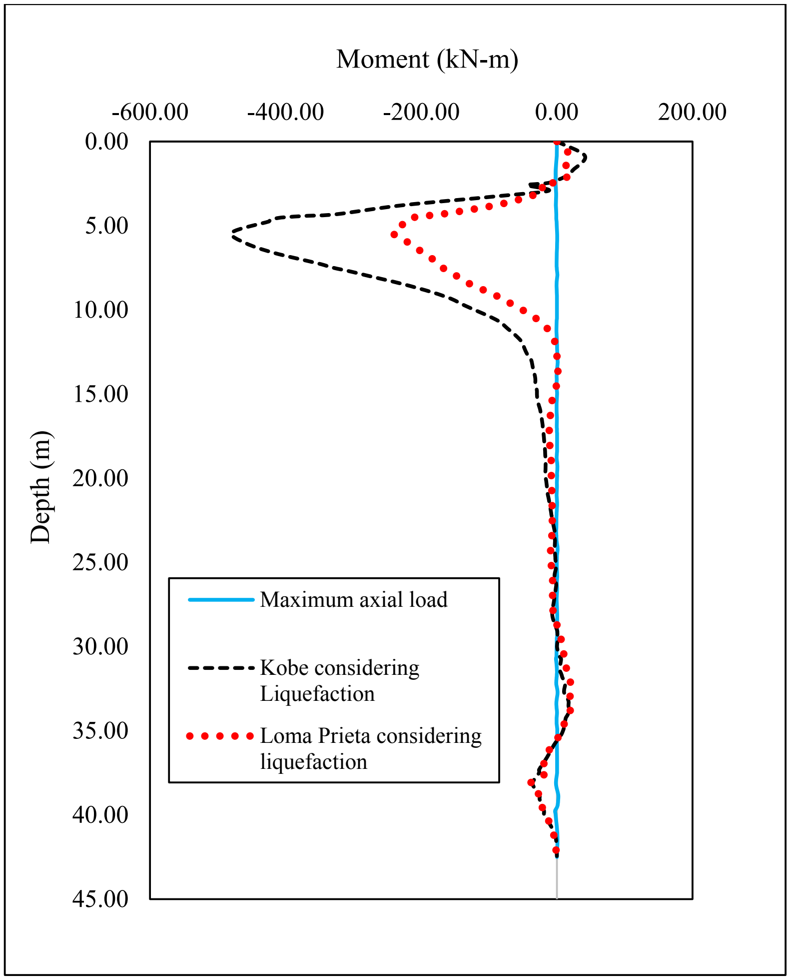

Figure 4.39: Comparison of moment developed both considering and without considering liquefaction

With generation of large force due to the lateral movement of the liquefiable and non-liquefiable layer has the potential to induce large bending moments in the piles leading to failure. Lateral load can cause pile failure due to change in flexural stiffness and capacity. So up-to a certain depth the soil needs to be improved so that the generated moment can be reduced. Soil in liquefied site showed larger stiffness degradation and piles showed larger bending moment than piles in non-liquefied site. In this study two cases are considered for soil improvement. Up-to depth 5 m and 15 m the soil is improved to see the moment capacity of pile. The soil improvement is simulated by increasing soil strength parameters used in UBC3D-PLM model and HS model. For soil improvement only up-to 5 m, the first loose sand layer is improved and analyzed using UBC3D-PLM model considering drained behavior. In case of 15 m soil improvement strength parameters of soil layer up-to 15 m is increased and analyzed with

UBC3D-PLM and HS model to observe the improved soil behavior. The improved soil parameters for first 5 m soil improvement is presented in Table 4.8. Keeping the first layer as the same properties given in Table 4.8, material properties of remaining 10 m soil is improved as shown in Table 4.9.

Table 4.8: Material properties for soil improvement up-to 5 m

Parameters	Symbol	Unit	Value applied in model
Unit weight	γ_{unsat}	kN/m^3	17
Saturated unit weight	γ_{sat}	kN/m^3	18
Poisson's ratio	ν	-	0.3
Constant volume friction angle	φ_{cv}	(°)	30
Peak friction angle	φ_p	(°)	33
Cohesion	c	kPa	0
Elastic shear modulus	K^e_G	-	1316.0
Elastic bulk modulus	K^e_B	-	921.0
Plastic shear modulus	K^p_G	-	3195.0
Elastic shear modulus index	n_e	-	0.5
Elastic bulk modulus Index	m_e	-	0.5
Plastic shear modulus index	n_p	-	0.5
Failure ratio	R_f	-	0.9
Atmospheric pressure	P_A	-	100
Tension cut-off	σ_t	kPa	0.00
Densification factor	f_{dens}	-	1.0
Corrected SPT value	$(N_1)_{60}$	-	28.0
Post liquefaction Factor	f_{Epost}	-	1.0

Table 4.9: Material properties for soil improvement up-to 15 m

Parameters	**Unit**	**Clayey silt (10 m)**
Unsturated unit weight (γ_{unsat})	kN/m^3	17
Sturated unit weight (γ_{sat})	kN/m^3	18.5
Secant stiffness modulus (E_{50}^{ref})	kN/m^2	20000
Oedometer modulus (E_{oed}^{ref})	kN/m^2	20000
Unloading/reloading stiffness (E_{ur}^{ref})	kN/m^2	60000
Poisson's ratio, ν		0.3
Cohesion, c		25
Angle of friction, φ		28
Dilation Angle, Ψ		0
Unloading/reloading poisson's ratio, ν_{ur}		0.3
Power for stress-level dependency of stiffness, m		0.5
K_0value for normally consolidated factor, $K_{0\ nc}$		0.577
Interface factor, R_{int}		0.9

Figure 4.40 and 4.41 shows that if the soil layer is improved only up to 5 m then moment in pile is reduced to a certain limit 45 kN-m and 6 kN-m for Kobe and Loma Prieta earthquake respectively which is within the pile moment capacity but if up to 15 m soil can be improved then it comes to 20 kN-m and 3 kN-m. It is significantly smaller under earthquake loading.

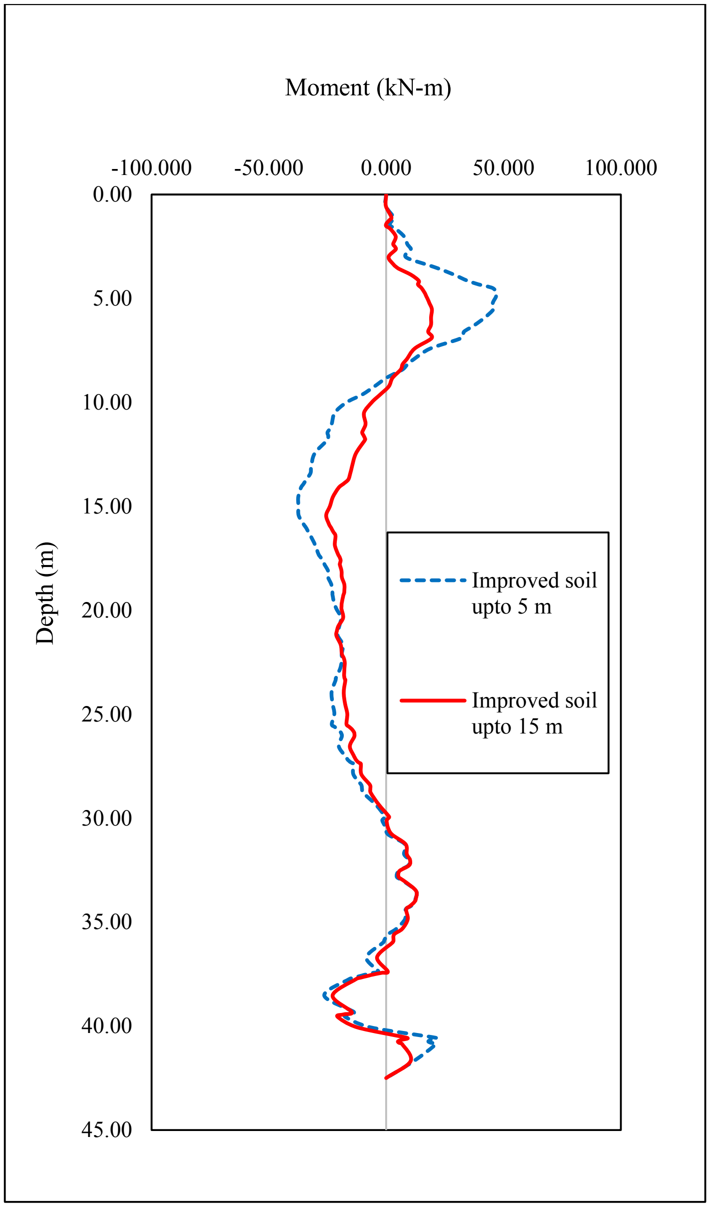

Figure 4.40: Comparison of moment reduction after soil improvement for Kobe earthquake

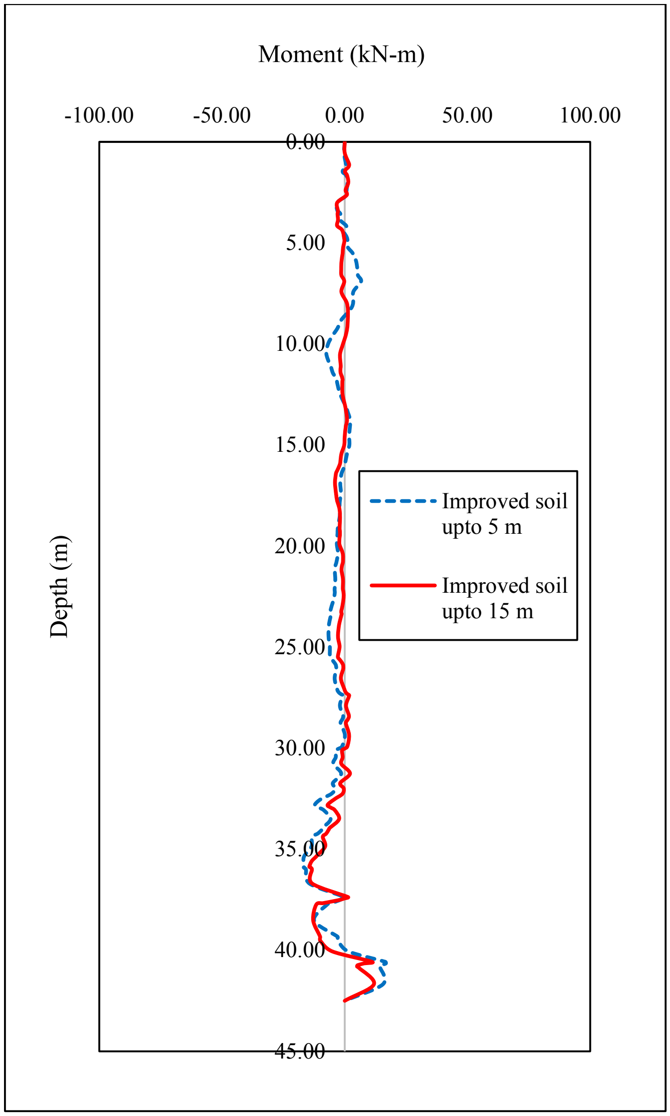

Figure 4.41: Comparison of moment reduction after soil improvement for Loma Prieta earthquake

In Figure 4.42, a comparison is made among moment generated during earthquake without considering liquefaction, considering liquefaction phenomenon and soil improvement. Due to soil improvement the moment in pile decreases to 96% and 100% at the interface of filled soil and clayey silt soil for Kobe and Loma Prieta earthquake respectively than the unimproved soil. Again, it can be observed that soil improvement up-to 15 m depth can reduce moment considerably than improved soil up-to 5 m depth. However, it can be concluded that soil improvement technique can enhance the pile flexural capacity under earthquake loading. Mostly spun pile damages occurs due to flexural failure. So soil improvement technique can minimize the chance of pile collapse and probability of liquefaction as well.

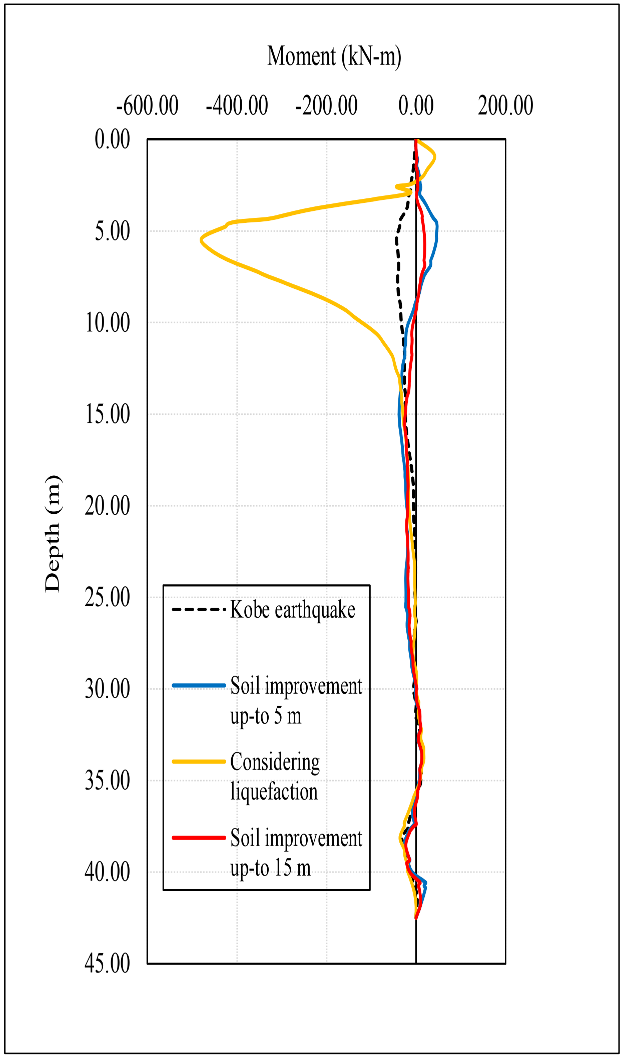

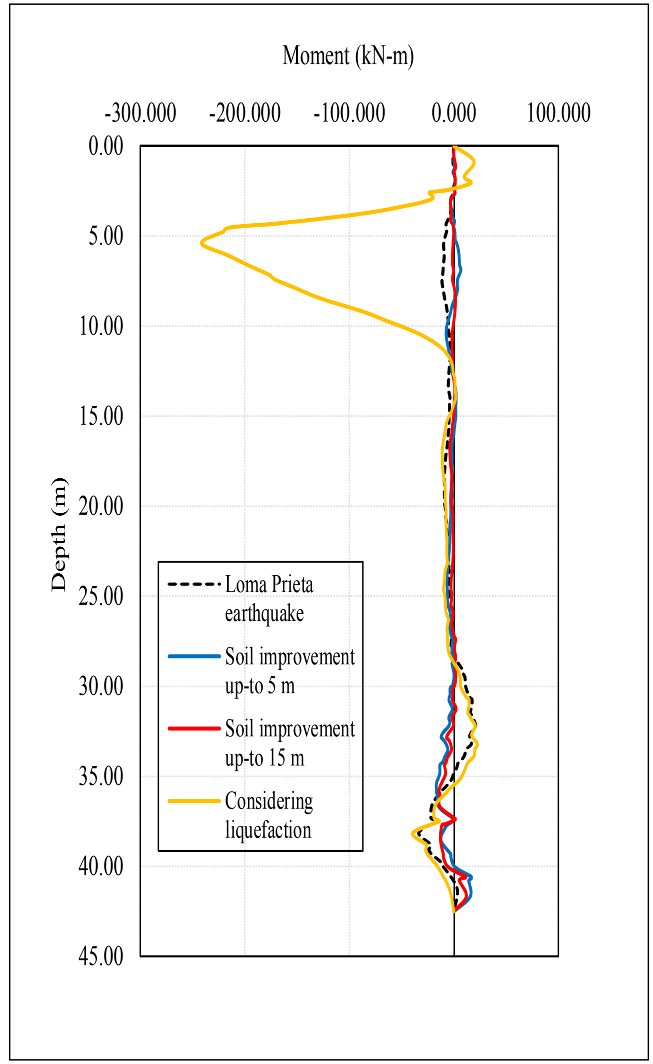

Figure 4.42: Comparison of moment considering liquefaction, withoutout liquefaction and soil improvement for (a) Kobe (b) Loma Prieta earthquake

4.11 Summary

This chapter explains the finite element modeling analysis of SPC pile under both axial and earthquake loading condition. The analysis can be summarized as follows:

1. For practical application and model validation a realistic soil constitutive soil model needs to be chosen which can simulate the nonlinear and stress dependent characteristics of soil. For FEM model HS model is chosen for simulate soil behavior. For structural component like pile embedded beam element is chosen. The input parameters are determined from laboratory test results and empirical correlations. The static pile load test result is validated with the FEM model using the soil and structural modeling parameters in PLAXIS 3D for Jolshiri site.

2. The parametric study is conducted to observe the influencing effect of pile diameter, length and mesh size of model on the simulated results under static loading condition.

3. The pile response under earthquake loading is simulated. The stage construction steps are presented for the analysis in PLAXIS 3D. Two seismic signal, Kobe and Loma Prieta are used as input earthquake loading to observe pile displacement, stress and strain distribution in soil body.

4. Liquefaction phenomenon has been simulated using UBC3D-PLM model in PLAXIS 3D during earthquake event. The top layer is susceptible to liquefaction effect due to excess pore water pressure generation. The maximum pore pressure ratio and pile displacement are determined for Kobe and Loma Prieta during liquefaction.

5. The large moment generation during liquefaction can lead the pile to collapse due to flexural failure. Liquefaction can trigger the pile to produce larger moment than the moment generated during seismic event without liquefaction occurrence. Soil improvement effect on the liquefiable layer is observed at the end of this chapter to reduce large moment generation and pile failure.

BANGLADESH NETWORK
OFFICE FOR URBAN SAFETY

PART-II

A NUMERICAL INVESTIGATION OF NEW AUSTRIAN TUNNELING METHOD AND TUNNEL BORING METHOD FOR TUNNEL CONSTRUCTION

BANGLADESH NETWORK OFFICE FOR URBAN SAFETY (BNUS), BUET, DHAKA

Prepared By: Johana Sharmin
Mehedi Ahmed Ansary

Chapter 1

INTRODUCTION

1.1 General

Tunnels can be defined as an important section of subterranean structures and underground passages constructed to mitigate the traffic hassle by ensuring the direct transportation of passengers or goods between two certain points through certain obstacles. Tunnels are analyzed according to their shapes, prevailing ground conditions, construction techniques, ground response, changes in pore pressure, plasticity, lining deformations, effects of existing structures, etc. Numerical procedures, such as finite element technique, can simulate construction sequence, model realistic soil behavior, handle complex ground and hydraulic conditions, deal with ground treatment, account for adjacent services and structures, deal with multiple tunnels, simulate intermediate and long-term conditions, etc. and produce realistic results.

When underground space or a large span tunnel is excavated, there is an inevitable chance of disturbing the in-situ stress field causing ground movements leading to surface settlement and potential damage to adjacent structures. Selection of an appropriate excavation method (depends on tunnel depth, tunnel shape, tunnel length, tunnel diameter, conditions of ground water present, use of tunnel, supporting logistics, and appropriate management of risks) for large span urban tunnel projects in soft ground is a key factor for successful completion of the project.

NATM (New Austrian Tunneling Method) is based on the concept that the ground around the tunnel acts as a load as well as a load-bearing element and the tunnel can stabilize itself by using the surrounding rock mass geological stress. It was developed soon after World War II and since then consistent improvements have been made by Mueller, Rabcewiz, Brunner and Pacher. It is now established as a well-recognized flexible technique due to its success in diverse conditions ranging from hard rock to soft rock, soft stable ground to weak, friable and unstable ground. Depending on the project conditions (e.g., shallow soft ground tunnel, deep rock tunnel) and the result of the geotechnical parameters, the requirements of the specific support are determined. The excavation cross section is divided into crown, bench and invert (for soft ground, invert arch is generally required to ensure stability) depending on environmental factors, surface settlements, ground conditions and logistical requirements and the tunnel is typically advanced by drill and blast following the sequential excavation method. The performance of this method is not found satisfactory in weak formations and shallow tunnels in the urban areas because (1) deformation to some extent is the requirement of the system to relieve or minimize he amount of stress, (2) the ratios of the horizontal to the vertical stress is not the requirement to keep the tunnel face stable, (3) vibration may cause damage to the existing buildings, and (4) need of installation of structural support around the tunnel excavation to re-establish the equilibrium.

TBM (Tunnel Boring Machine) is used for the excavation of tunnels with a cross section of circular or rectangular shape through the different types of rock and soil strata. Diameters of the excavated tunnel can be varied from 1m to almost 16m. TBMs have limitations of predetermined tunnel diameter and shape along the length of TBM drive. During the excavation process of tunnel, TBMs limit the surrounding ground disturbance and produce a smooth wall of tunnel. EPB (Earth Pressure Balance) tunneling machine is used to provide the support to the tunnel face by the excavated soil itself during the excavation process. EPB consists of several devices like cutting wheel for excavating soil, screw conveyor for removing soil from working compartment, pressure cells for monitoring the pressure in the working chamber, excavation chamber closed from tunnel face by pressure bulkhead, mixing vane for assisting to remould the soil. EPB machine is mostly used in the variable and poor ground conditions with low cohesion ground, high permeable ground, high water pressure ground, and clay with gravel, boulder and sand interfaces.

The construction of a tunnel usually leads to surface disturbance, particularly settlement (not important in greenfield sites). The available analytical and empirical solutions are not sufficient to include complex ground conditions and hence a comprehensive analytical solution couple with numerical modelling is necessary to model the effect of surface settlement due to soft ground tunneling. This research discusses different approaches in predicting the settlement and comparison with numerical analysis is also done to validate the solutions.

The objective of the MRT Line – 1 project is to mitigate the traffic congestion, improve environmental pollution, and contribute to economic and social development in Dhaka city by constructing mass rapid system. MRT Line 1 consists of two lines: one route connects Kamlapur in central Dhaka with the Dhaka International Airport (hereafter the Airport Line), and the other route branches off from the Airport line at Notun bazar station to the Purbachal area (hereafter the Purbachal Line) where large scale urban development is currently under way. The airport line will run entirely through an underground tunnel (14.765km) and the Purbachal line will become an elevated structure to its destination at depot in Rupganj (15.426km). This research presents a framework for selecting the appropriate tunneling method (NATM and TBM) with respect to induced ground surface settlements considering proposed underground tunnel alignment of MRT Line 1 based on PLAXIS 3D numerical analysis.

For simulating tunnel construction methods interaction with soil, PLAXIS 3D finite element software is used in this thesis. Different consecutive models are incorporated in PLAXIS such as simple linear elastic-perfect plastic Mohr-Coulomb (MC) model, the elastic-plastic non-linear stress-dependent stiffness Hardening Soil (HS) model, and isotropic work-hardening plasticity cap Modified Cam-Clay (MCC) model. The real behavior of the excavation process, 3D arching of soil, distribution of settlement, etc. can be precisely simulated in this software. In addition to evaluating the effects of the consecutive model on the soil behavior, empirical methods are used and all results are compared with each other eventually.

1.2 Background of the Study

The Strategic transport Plan (STP) (20-year long plan) has been addressed by Bangladesh Government with JICA (Japan International Corporation Agency) to fix the road congestion caused by crippled transportation system coupled with sluggish traffic conditions. Since 2009 till date, a plan for Mass rapid Transit (MRT) was conceptualized forming the implementing agency DMTCL (Dhaka Mass Transit Company Ltd.). According to the plan, there will be six MRT lines comprising of 61.172km long underground and 68.729km long elevated network system featured with 105 stations across Dhaka city to ease the traffic situation. MRT Line-1 is comprised of 31.241km long and is divided into two sections: Airport Route (19.872km long, total 14 stations) and Purbachal Route (11.369km, total 7 stations). In this thesis, underground portion is focused, where the route alignment is: Airport – Airport Terminal 3 – Khilkhet – Nadda – Natunbazar – North Badda – Badda – Hatirjheel East – Rampura – Malibagh – Rajarbagh – Kamlapur. (NKDOS Consortium Proposal, 2019)

1.2.1 General Topography and Geology of the Study Area: Dhaka is situated between latitudes 23º42’N and 23º54’N and longitudes 90º20’E and 90º28’E. The city is bounded by the Buriganga River to the south, Turag to the west, Balu to the east, and Tongi Khal to the north. The Dhaka city area does not show any surface folding, however a large number of faults and lineaments have N-S, E-W, NE-SW, NW-SE trends recognized from air photo interpretation and the nature of the stream courses. Dhaka city and its surroundings are shown to be situated in the seismic zone 2 (medium risk zone). The studied area falls into Madhupur Tripura Tract physiographic division of Bengal basin. The soil carried out up to maximum to the Holocene and Pleistocene age sediments in geological time scale in this area. The study area is mostly consisted of clayey soil than the sandy soils. The upper soil layer comprises of grayish to brownish stiff to medium stiff clayey soil and brownish medium dense soil of Basabo Silty Clay formation and hard clayey soil or brownish very dense sand below this, can be of from Madhupur Clay and Sand formation. (ProSoil Survey, 2019)

1.2.2 Parameters Affecting Settlements in Tunnel: To have knowledge about the effects of the parameters of influence zone of ground settlement, it may be helpful to carry out the measurement and give a better solution in the form of numerical modeling. Ground surface settlement behind a reinforced wall takes place due to the unbalanced pressures resulting removal of soil mass inside tunnel excavation. Based upon several case history reviews, the factors that effecting the settlement in tunneling can be grouped into three major categories, such as, geometric parameters (tunnel diameter, tunnel depth, depth of tunnel axis from ground level, the distance from tunnel face excavation and face stability of shield-driven tunnels), geological conditions (geology at tunnel invert and crown, groundwater level, etc.), and shield operation parameters (penetration rate, face pressure, pitching angle, percent of tail void grouting and amount of excavated material per ring). In this thesis, we emphasized the effects of tunnel geometry parameters (tunnel depth, tunnel diameter, influence zone) to the settlements. (Loganathan and Poulos, 1998)

1.2.3 Importance of The Research: In comparison, NATM and TBM are essentially equivalent from the viewpoint of construction operation. The final choice is determined by the local geological conditions for the project and the length of the tunnel. Though International Consultants team has already proposed the Shield tunnel by TBM-EPB as the tunnel construction method for Line 1 project, I want to shed light on some factors of NATM in urban areas. Also, I want to compare the displacement effects between both techniques and from this perception I want to establish the fact if NATM is also viable like TBM for our Dhaka city or not.

1.2.4 Reliability of FEM as Method for Numerical Analysis: In a real tunnel, the different facets are clearly coupled and the problem is complex, involving pore pressure changes, plasticity, lining deformations and existing structures. Numerical procedures, such as the finite element technique, lend themselves to the analysis of such complex problems (Potts, 2001). The finite element method can:

i. Simulate construction sequence.

ii. Deal with complex ground conditions.

iii. Model realistic soil behavior.

iv. Handle complex hydraulic conditions.

v. Deal with ground treatment (e.g., compensation grouting).

vi. Account for adjacent services and structures.

vii. Simulate intermediate and long-term conditions.

viii. Deal with multiple tunnels.

1.2.5 Choosing 3D Numerical Analysis over 2D Analysis: The complex interrelation between the interconnected elements makes for a highly complex mathematical problem. The analysis is performed by solving the equation matrix that models, the mesh made up of the limited number of elements. That is, a system of equations is set up which relates unknown quantities to known quantities via a global stiffness matrix. For instance, the relationship of nodal forces to displacements is analyzed this way throughout the finite element mesh. Highly complex underground conditions and tunnel characteristics can be analyzed in 3D. The capability of the 3D analysis includes the simulation of complex constitutive laws, non-homogeneities, and the impact of advance and time dependent characteristics of the construction methods. As tunnel excavation is clearly a three-dimensional problem, considering the third dimension should intuitively lead to more accurate predictions (Tatiya, 2005).

1.3 Objectives of the Study

The main goals of the research:

i. To conduct numerical analysis of proposed tunnel in NATM method to obtain ground movement and deformation.

ii. To conduct numerical analysis of proposed tunnel in TBM method to obtain ground movement and deformation.

iii. Comparison between two methods based on the results (comparative parameter: displacements for three types of models) of numerical analysis and establish a portfolio for the suitable method.

1.4 Methodology and Flow Chart of the Study

The field data collection are prior arrangements for determining site conditions (ground water level, soil type, visual soil parameters, etc.) mobilizing the soil samples to laboratory for further testing. Through conducting laboratory tests according to the codes, soil properties (geotechnical) can be determined which can be used as parameters for FEM analysis. FEM analysis needs to follow some definite steps to acquire approximately accurate results which are described later in this section. Literatures of previous researchers are needed to be verified and numerical analysis with PLAXIS 3D have been used for the establishment of the papers. Also, PLAXIS 3D is used to develop models varying different types and different parameters for the NATM and TBM methods. The methodology of the study can be described in the Figure 1.1:

Field data Collection: The investigation consisted of soil boring and sampling for observation from secondary sources.

↓

Determination of Geotechnical Parameters: Laboratory tests were conducted on the soil samples to classify soil and to detemine mechanical properties. These data are collected from secondary data source.

↓

Development of FEM Model using Plaxis 3D: For accurate modeling of tunnel, constitutive soil model, tunnel lining, shield element, support face pressure should be considered. Simplified cylindrical geometry is considered and lining is modeled by elastic constitutive model.

↓

Validation of Model with Empirical Formula: For validation of TBM methods, two literatures have been verified and comparison of numerical analysis with empirical formula provided by different researchers have been emphasized.

↓

Conduct Numerical Analysis by Varying Geometry Parameters: Numerical analysis was done for three different models: MC, MCC and HS as well as varying depths of 30m,32m and 35m and diameters of 5m, 6m and 7m for TBM. For NATM, three different models were prepared for 35m depth and 7m diameter.

↓

Conclusions and Recommendations: Perspectives of NATM and TBM for Metro Rail Line-1 has been focused and by comparing two methods numerically and empirically, a conclusive remarks about functionality of both tunnels in Dhaka city is made.

Figure 1.1: Overall Methodology Flow Chart of the Research

Development of FEM model analysis consists of following steps:

Step 1: Define the Objectives for Model Analysis: If the objective is to decide which is proposed to explain the behavior of a system, then a crude model may be constructed, provided that it allows the mechanisms to occur. Complicating features should be omitted if they are likely to have little influence on the response of the model.

Step 2: Create a Conceptual Picture of the Physical System: It is important to have a conceptual picture of the problem to provide an initial estimate of the expected behavior under the imposed conditions. The considerations which will dictate the gross characteristics of the numerical model are: anticipation of stability or instability of the system, linear or non-linear response, large or small expected movements, effect of well-defined discontinuities, influence of groundwater interaction, geometric symmetry of the structure, etc.

Step 3: Construct and Run Simple Idealized Models: When idealizing a physical system for numerical analysis, it is more effective to construct and run simple test models first before creating the detailed model. The results from the simple models help to guide the plan for data collection by identifying which parameters have the most influence on the analysis.

Step 4: Assemble Problem-Specified Data: The types of data required for analysis of a model include: details of the geometry, locations of geologic structure, material behavior, initial conditions, and external loadings. Since typically, there are large uncertainties associated with specific conditions, a reasonable range of parameters must be selected for this investigation.

Step 5: Prepare a Series of Detailed Model Runs: The numerical analysis involves a series of computer simulations that include the different mechanisms under investigation. It can be difficult to obtain information to arrive at a useful conclusion if model run times are excessive. The state of the models is saved at several intermediate stages so that the entire run does not have to be repeated for each parameter variation.

Step 6: Perform the Model Calculations: At any time during a sequence of runs, it is possible to interrupt or pause the calculation, view the results, and then continue the model.

Step 7: Present Results for Interpretation: The final stage of problem solving is the presentation of the results for a clear interpretation of the analysis.

Chapter 3

MODEL VALIDATION

2.11 Introduction

This chapter emphasizes on the validation of two metro rail lines of Iran and Delhi with PLAXIS 3D. For Mashhad Metro Line 2, each section of the ground was modeled by two constitutive models, namely MCC and Mohr-Coulomb (MC). Numerical modeling was originally performed by FLAC3D software. Afterwards, the results of two types of numerical analyses and empirical data were compared with each other. Based on the transverse and longitudinal sections settlement, the MCC model showed high capabilities of predicting the surface settlement in comparison to the MC model. And also, the deviated values are less for both of the models for O'Reily & New relationships. Originally, a 2D numerical model has been developed using finite element software OptumG2 to replicate the Delhi Metro Phase 3 tunnel project. An elastoplastic model of the tunnel at a standard depth of 18 m has been analyzed. After comparing results of two types of numerical analyses and empirical data of Peck & Schmidt formula, the vertical surface settlement shows relatively closer values for both PLAXIS 3D and OptumG2.

2.12 General Information about Line 2 Metro of Mashhad

Mashhad Metro Line 2 is the second metro line that is being developed to facilitate passengers' transport in Mashhad, Iran. This metro line is situated beneath the street level in a tunnel running in a Northeast-Southwest direction, as seen in Figure 3.1. In total, this line includes 12 stations. Furthermore, Metro Line 2 is connected to Mashhad Metro Lines 1 and 3 as well as the national railway line in Iran. The total length of Line 2 is about 14.3 km. A part of the tunnel running from Station A2 through L2 and going further to the TBM exit shaft is going to be constructed with mechanized tunneling methods, such as the Tunnel Boring Machine or TBM. The TBM excavates the ground in front of the cutter head while pushing itself forward. The tunnel is built up inside the TBM from concrete segments. Figure 3.2 shows the section of ground stratifications and tunnel's location along with water level position.

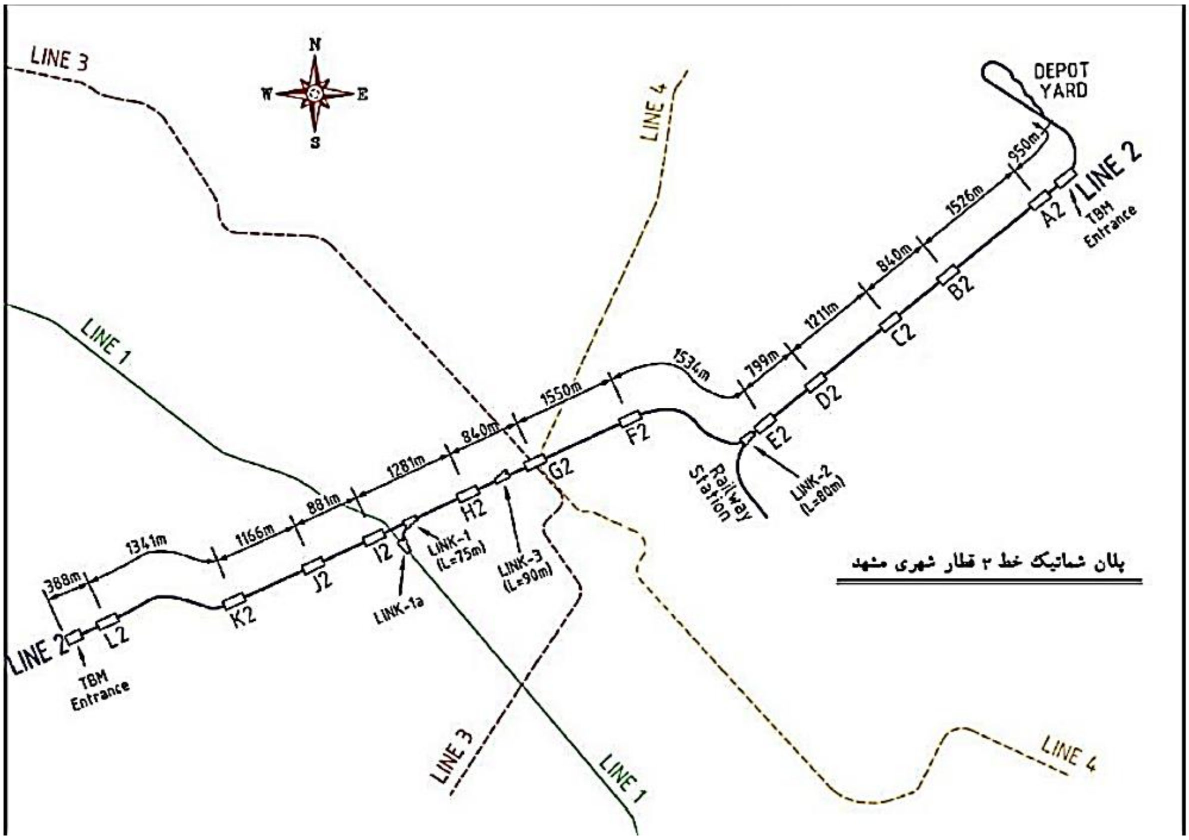

Figure 3.1: Plan of Line 2 Metro of Mashhad (Eslami et al., 2020)

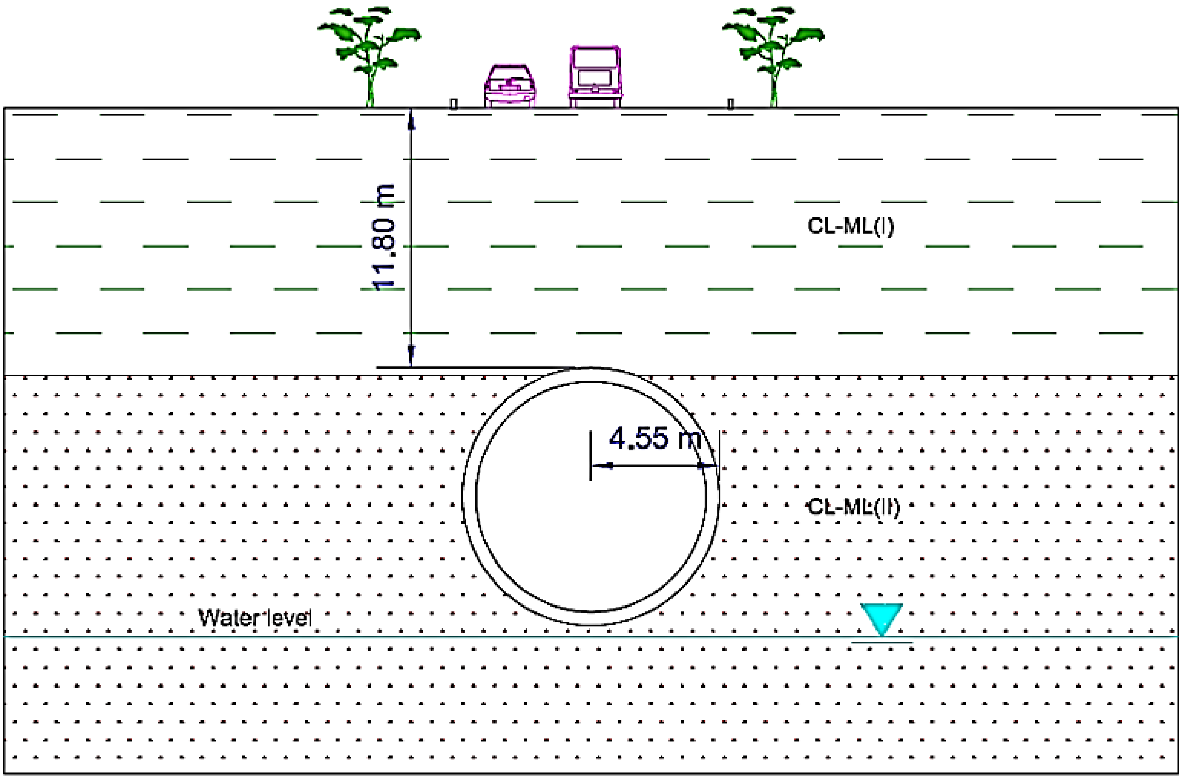

Figure 3.2: Section of ground line 2 Metro of Mashhad (Eslami et al., 2020)

3.2.1 Soil Condition

The detailed geotechnical investigations were performed by the excavation of 61 boreholes (a total length of 2,487.7 m) and 16 test pits (a total length of 296.95 m). These investigations mainly included some field tests and surveys, laboratory tests, and desk studies. The field tests included a plate loading test (PLT), in-situ shear test, pressure meter test, standard penetration test (SPT), Lufran permeability test, and in-situ density test. The laboratory tests comprised the direct shear test, triaxial test, particle size analysis, Atterberg limits test, consolidation, permeability, and the Los Angeles Abrasion test. The desk studies included the collection of the existing data such as previous reports, in-situ test results, and data processing and analyzing. The geological section of the project is illustrated in Figure 3.3. The soil sample for testing is considered from DH-09 Borehole.

The characteristics of Mashad's soil are illustrated in Table 3.1.

i. Medium clay-silt (CL-ML l): The uppermost layer is the soft clay soil by low plasticity and low moisture percentage. The average thickness is about 10 m in most areas.

ii. Medium clay-silt (CL-ML ll): The low layer is the soft clay soil by high plasticity and high moisture percentage. This layer can be found at depths of 10-35 m.

Table 3.1: Characteristics Profile of Mashhad's Soil

Layer No.	Notation	Depth	Dry Density	Moisture Content	Cohesion	Friction Angle	Undrained Cohesion	Undrained Friction Angle
		(m)	(kN/m^3)	(%)	kPa	deg	kPa	deg
I (A)	CL-ML I	0 ~ 10	17.00	17.00	10	25	10	25
I (B)	CL-ML II	10 ~ 35	17.50	18.00	30	23	12	20

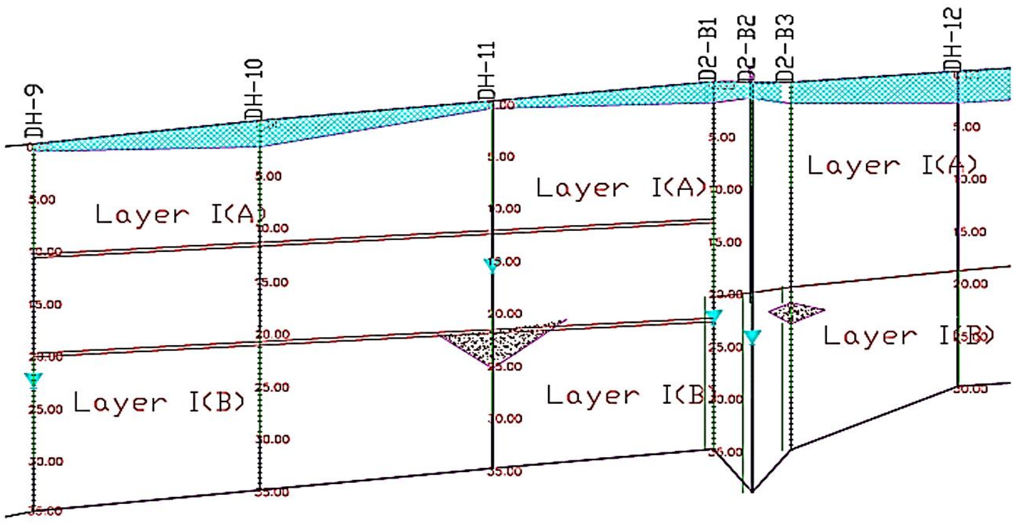

Figure 3.3: Geological Section of Mashhad Metro Line 2 (12+500km) (Eslami et al., 2020)

The calculation of the MCC parameter was performed based on the elasticity rule:

$$G = \frac{E}{2(1+\vartheta)} \tag{3.1}$$

$$K = \frac{E}{3(1-2\vartheta)} \tag{3.2}$$

$$\kappa = C_s.\,ln\,10 \tag{3.3}$$

$$\lambda = C_c.\,ln\,10 \tag{3.4}$$

$$\vartheta_0 = 1 + \vartheta \tag{3.5}$$

Table 3.2: Soil characteristics and the respective parameters for MCC Model

Parameter	**Description**	**Values for Soil Layer**	
		I (A)	II (A)
E (MPa)	Young Modulus	100	120
G (MPa)	Shear Modulus	40	48
ρ (kN/m^3)	Density	19.85	20.65
M	Frictional Constant	0.983	0.898
K	Slope of Swelling line	0.0345	0.044
υ	Poisson ratio	0.27	0.27

3.2.2 Numerical Modeling

For accurate modeling of a tunnel in soft ground by FEM methods, some of key parameters that affect the surface settlement such as constitutive soil model, tunnel lining, over excavation, and shield element should be considered. In this study, the result of field tests, in situ measurements, and laboratory data is utilized to describe two different constitutive models. Since there is a complicated correlation between the target parameter (surface settlement) and other factors, the input parameters of constitutive models should be considered accurately.

To obtain a rational result, all main elements of mechanized excavation should be modeled such as: TBM's shield, concrete tunnel lining, support face pressure, tail void grouting, and over excavation. Therefore, FLAC3D (Version 3.0) code, a commercial software package based on the generalized finite difference method, was used to develop the numerical simulation. The standard dimensions followed for the numerical modeling is displayed in Figure 3.4 in FLAC3D.

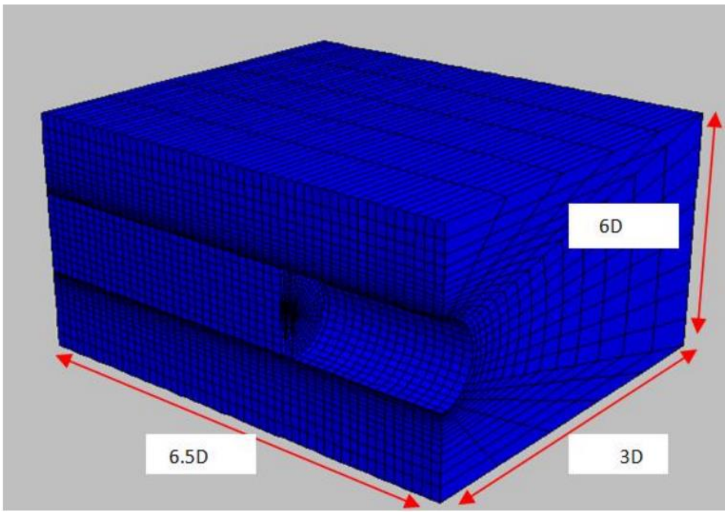

Figure 3.4: Dimension of the 3D Simulation in FLAC3D (Eslami et al., 2020)

For validation purpose, PLAXIS 3D software is used to compare the result with the literature's numerical and empirical results. The shield of TBM was modeled using a plate element and a simplified cylindrical geometry is considered. The segmental lining and shield elements are modeled by the elastic constitutive model. The effect of virtual boundary on the results were neglected because the model has a longitudinal dimension (y direction) of 6.5D, an extension under the tunnel axis (z direction) of 3D, and a transverse extension of 4D, where D is the tunnel diameter. As the underground water table in this project is lower than the project line, all analyses have been performed in drain condition. The tunnel length of 15m (1/1000th of actual length), radius of 4.55m and depth of 14m have been considered for simplified modelling.

The order of excavation integrated into the models is as follows:

Step 1: Excavation of tunnel (about 1.5m)

Step 2: Application of face pressure by the TBM on the new excavation face of the tunnel

Step 3: Excavation of the tunnel by driving the EPB machine

Step 4: Generation of both the gap filling and segment elements performed after excavation of the tunnel

Step 5: Removing the previous face pressure on the tunnel face.

Step 6: Repeating the steps 1 to 5 until the TBM reaches its destination

3.2.3 Distribution of Surface Settlements in Transverse Section

The semi-empirical relation of Peck was obtained in following equations, showing the shape of transverse settlement:

$$S = S_{max} e^{(-\frac{y^2}{2i^2})} = \frac{V_L}{i\sqrt{2\pi}} e^{(-\frac{y^2}{2i^2})} \quad (3.6)$$

$$V_S = \int_{-\infty}^{+\infty} S_{max}\, e^{(-\frac{y^2}{2i^2})} = \sqrt{2\pi} i S_{max} \quad (3.7)$$

$$V_L = \frac{V_S}{V_0} * 100 \quad (3.8)$$

Here,

S = vertical surface settlement at y location (m)

y = distance of the considered point from the tunnel axis (m)

Vs = volume of settlement per meter of tunnel advancement (m^3/m)

i = trough width parameter (i = kZ_0, where k is a dimensional constant depending on soil type and Z_0 is the depth of the tunnel axis below surface

V_L = volume of settlement per unit length expressed as a percentage of the total excavated volume of the tunnel

V_0 = volume required to construct the tunnel

In Figure 3.5, three-dimensional view of a tunnel is shown where the tunneling direction is considered along X-axis and settlement trough is considered to be deformed along vertically downward Z-axis. The distance between ground surface and center of the tunnel is considered Z_0. The inflection point where the sagging stops and hogging starts is considered the horizontal distance, i, from center point (maximum settlement), which is clearly shown in the A-A cross sectional view.

O'Reily & New showed that point of inflection (trough width parameter) i had a linear relation with depth of tunnel and they suggested equations:

$$i = 0.43Z_0 + 1.1 \text{ (For cohesive soil)} \tag{3.9}$$

$$i = 0.28Z_0 - 0.1 \text{ (For granular soil)} \tag{3.10}$$

A summary of all relations suggested by different researchers is presented in Table 3.3. The behavior of the surface settlement in transverse section follows the Gaussian distribution and based on this assumption, a Gaussian curve is fitted to the data monitoring outputs. As a result, the Gaussian distribution is analyzed for obtaining trough width parameter, i, which is about 7.41m and this value is very close to the O'Reily & New relation whose deviated value was about 3.91% (less deviation of all). In our numerical analyses, the deviated value for this relationship is also less than others. The deviated percentages are approximately 1.66% and 4.81% for MC and MCC models consecutively. The transverse profile of the surface settlement was compared with the numerical results obtained from the MCC model and the MC model. It can be clearly seen that results of the MCC model have the best fit to the data points. According to the literature, the MC model substantially differs from data monitoring outputs, thus the elasto-plastic model (e.g., the MCC model) is considered to be suitable for this type of soils. In the literature, comparing the maximum settlements of numerical analyses and Peck formula, about 9.6% and 41% deviations were found for MC and MCC models respectively. In our comparative analyses of Plaxis, the values are 11.11% and 44.4% for MC and MCC models respectively.

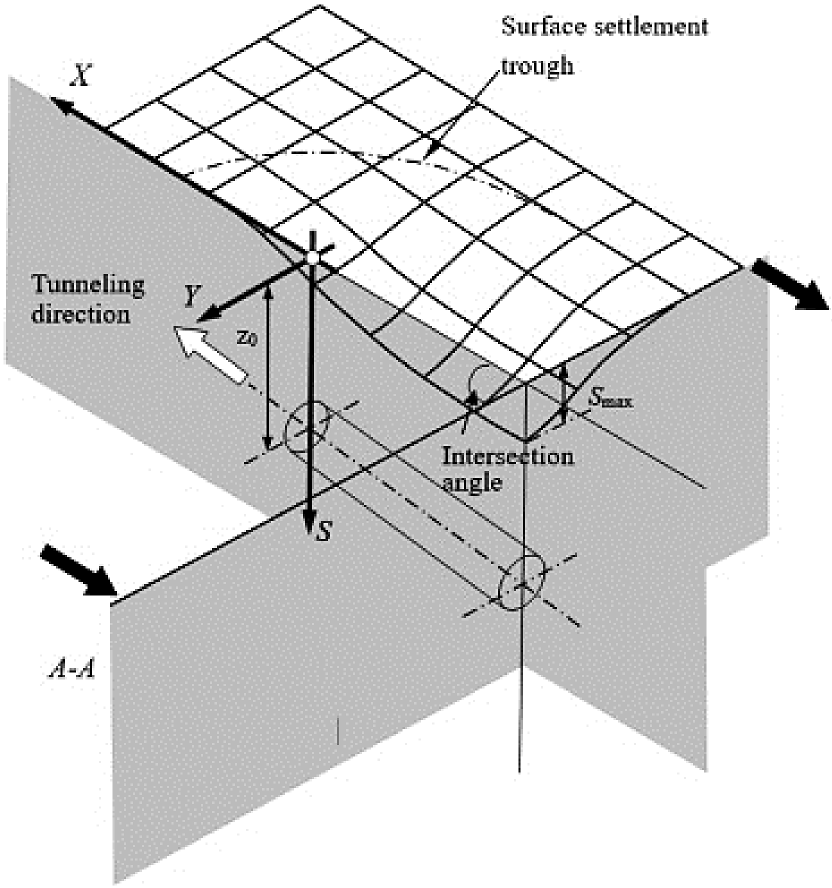

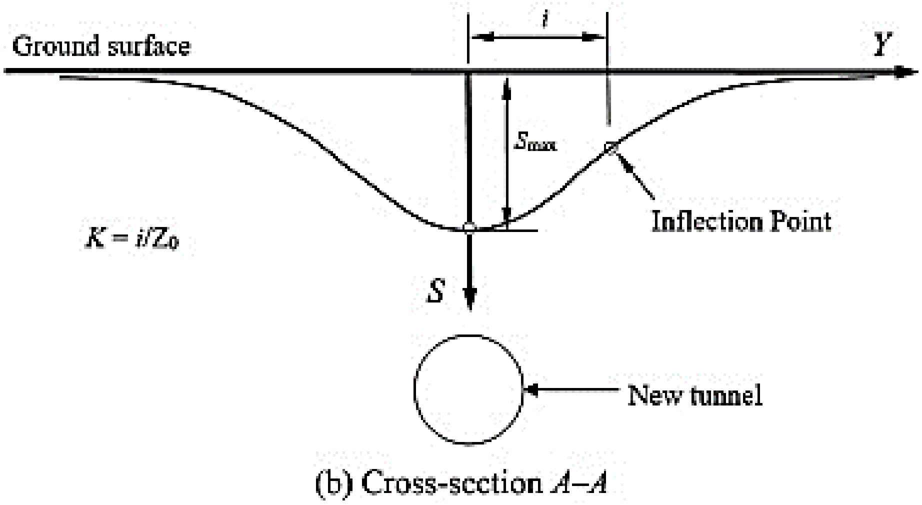

Figure 3.5: Distribution of Surface Settlement Trough (a) Three-dimensional view (b) Cross Sectional view (Transverse Section) (Lu et al., 2019)

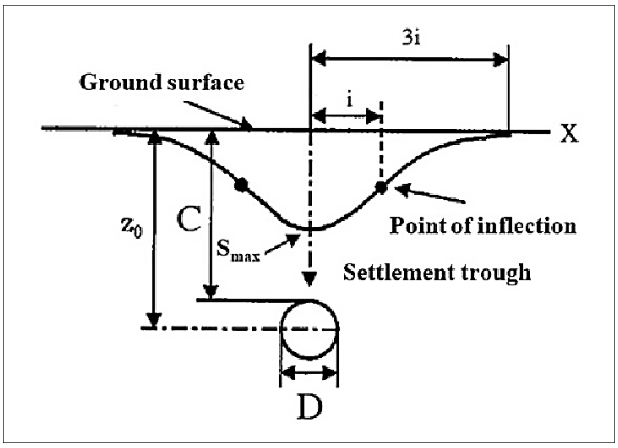

Figure 3.6: Relevant parameters for relations (Eslami et al., 2020)

Table 3.3: Empirical Relations based on different researchers

Researchers	**Empirical Relations**
Peck, 1969	$\frac{i}{R} = (\frac{Z_0}{2R})^n \ (n = 0.8 - 1)$
Clough & Schmidt, 1981	$\frac{i}{R} = (\frac{Z_0}{2R})^n \ (n = 0.8)$
Atkinson & Potts, 1977	$i = 0.25\ (1.5Z_0 + 0.5R)$
O'Reily & New, 1982	$i = 0.43Z_0 + 1.1$
Mair & Taylor, 1999	$i = (0.4 - 0.5)Z_0 + 1.1$
Attewell & Farmer, 1974	$\frac{i}{R} = (\frac{Z_0}{2R})$

To predict the surface settlement, the MCC model is proposed in soft clay with a low over consolidation ratio or normal consolidation similar to the soil in this site. In other words, where the shear modulus is independent of the shear strain, the surface settlement has a wide and shallow profile. Since the over consolidation clay exhibits non-linear stress strain behavior at the small strain prior to crossing the plastic yielding, it is very important to consider the behavior of these kinds of soils under small strain condition. Nevertheless, the shear modulus in the MC model is constant and the shear strain doesn't change with shear stress; this is probably the main reason for the difference between the results. Based on the results of Bolton for the prediction of surface settlement, strain non-linearity within the elastic domain must be implemented. The MCC model has a relatively precise prediction of the surface displacement in clay, either by normal consolidation or low OCR value.

In Table 3.4, the results are shown after calculating the distance of inflexion point from center based on different researchers' empirical formulas for both MC and MCC models of TBM method. And after analyzing, the deviated percentage from PLAXIS and literature is marked in O'Reily & New relationship as it shows the lowest deviated percentages (%) among all. Also, the maximum transverse settlement and settlement at inflection point do not vary a lot from literature's perspective. Therefore, for measuring the distance, i, O'Reily & New formula can be reliable to use which is validated in this chapter.

From the comparative analysis of Mashhad Metro Line 2, it can be seen that O' Reily & New empirical relation shows closest values (3.91%, 1.66% and 4.81% deviation with FLAC 3D, MC model in PLAXIS 3D and MCC model in PLAXIS 3D respectively).

Table 3.4: Calculation of inflexion point distance from center based on different researchers for MC and MCC Models (TBM method) and Comparison with Numerical Analysis (for literature and PLAXIS both)

Model Type	Researchers	Tunnel depth	Tunnel Radius	Distance to Point of Inflexion, i	Value from PLAXIS	Deviated Value	Value from Literature	Deviated Value	Difference in inflexion point	Max Settlement from PLAXIS	Max Settlement from literature	Settlement at inflexion (Plaxis)	Settlement at inflexion (Literature)
		m	m	m	m	%	m	%		mm	mm	mm	mm
MC	Peck	14	4.55	6.42	7.24	3.31	7.41	5.53	0.17	-8.0	-7.0	-5.0	-4.0
	Clough & Schmidt	14	4.55	6.42	7.24	11.32	7.41	13.33	0.17	-8.0	-7.0	-5.0	-4.0
	Atkinson & Potts	14	4.55	5.82	7.24	19.64	7.41	21.47	0.17	-8.0	-7.0	-5.0	-4.0
	O' Reily & New	14	4.55	7.12	7.24	1.66	7.41	3.91	0.17	-8.0	-7.0	-5.0	-4.0

Model Type	Researchers	Tunnel depth	Tunnel Radius	Distance to Point of Inflexion, i	Value from PLAXIS	Deviated Value	Value from Literature	Deviated Value	Difference in inflexion point	Max Settlement from PLAXIS	Max Settlement from literature	Settlement at inflexion (Plaxis)	Settlement at inflexion (Literature)
	Mair & Taylor	14	4.55	5.60	7.24	3.31	7.41	5.53	0.17	-8.0	-7.0	-5.0	-4.0
	Attewell & Farmer	14	4.55	7.00	7.24	3.31	7.41	5.53	0.17	-8.0	-7.0	-5.0	-4.0
MCC	Peck	14	4.55	6.42	7.48	6.42	7.41	5.53	0.17	-5.0	-4.0	-4.0	-3.0
	Clough & Schmidt	14	4.55	6.42	7.48	14.14	7.41	13.33	0.17	-5.0	-4.0	-4.0	-3.0
	Atkinson & Potts	14	4.55	5.82	7.48	22.21	7.41	21.47	0.17	-5.0	-4.0	-4.0	-3.0
	O' Reily & New	14	4.55	7.12	7.48	4.81	7.41	3.91	0.17	-5.0	-4.0	-4.0	-3.0
	Mair & Taylor	14	4.55	5.60	7.48	25.13	7.41	5.53	0.17	-5.0	-4.0	-4.0	-3.0
	Attewell & Farmer	14	4.55	7.00	7.48	6.42	7.41	5.53	0.17	-5.0	-4.0	-4.0	-3.0

In Figure 3.7, the transverse settlement profile from PLAXIS, FLAC3D and Peck's empirical formula is plotted in graphical form, where it can be seen that every curve follows the Gaussian distribution curve. Curves for MC (PLAXIS and FLAC3D both) tends to show similar pattern as the Peck's curve and settlement values are larger in MC than MCC models. The center of the tunnel is depicted as 0 in X-axis of the graph. Different findings of distance of inflection point from center from PLAXIS values and empirical relations established by various researchers is shown in Figure 3.8, where it can be indicated that the O'Reily & New formula gives comparatively closer value of numerical findings among all. The distribution of total displacement in PLAXIS 3D for MC and MCC model are represented in Figure 3.9 and Figure 3.10 respectively.

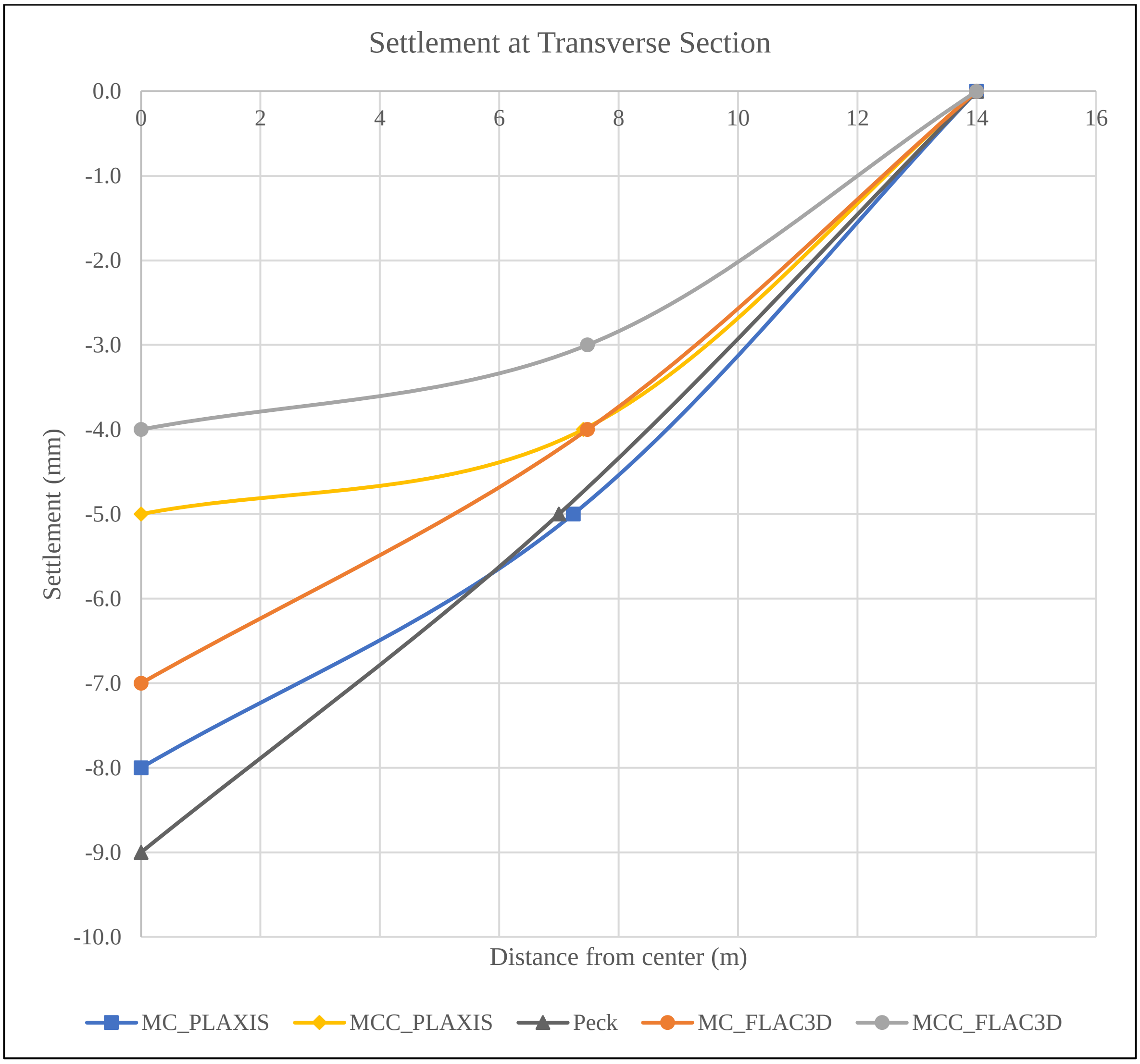

Figure 3.7: Comparison of Settlement at Transverse Section between PLAXIS 3D, FLAC 3D and Peck's Formula

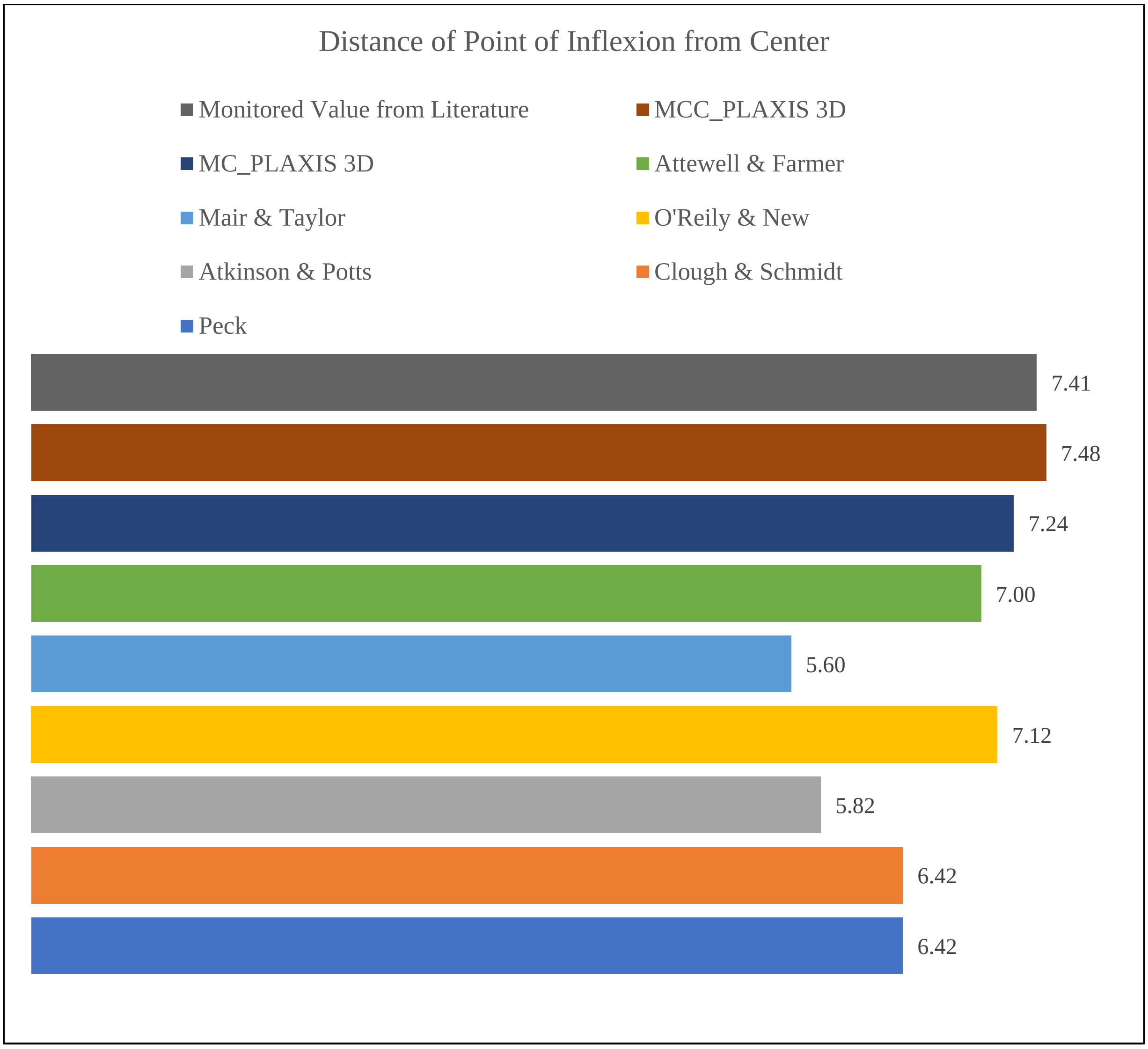

Figure 3.8: Comparison between Different Findings of Distance of Point of Inflexion from Center

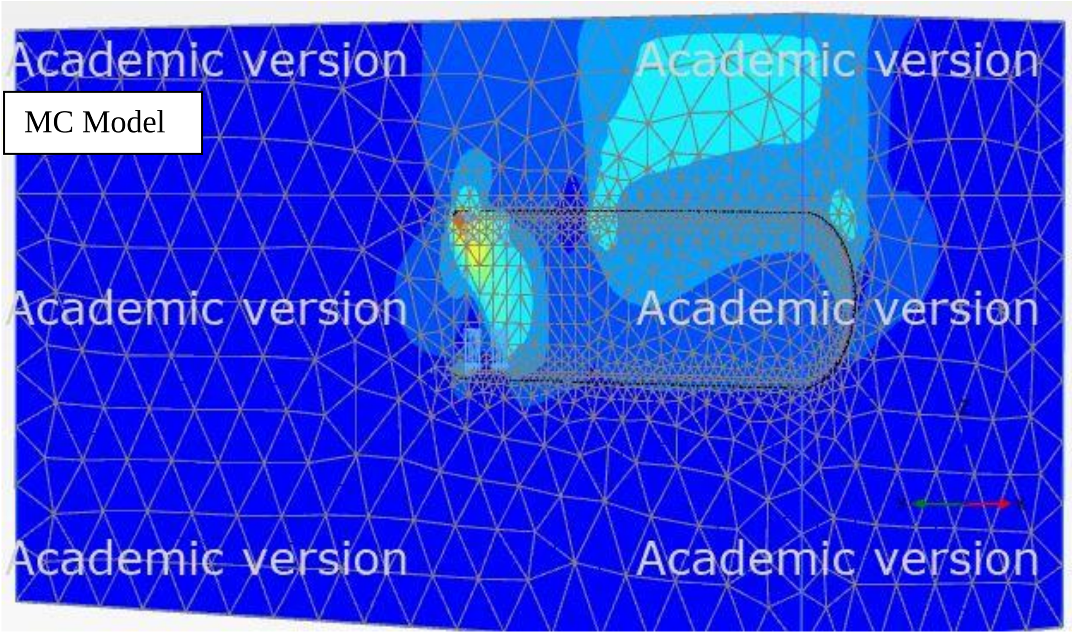

Figure 3.9: Representation of Distribution of Total Displacement of Mashhad Metro in PLAXIS 3D (MC Model)

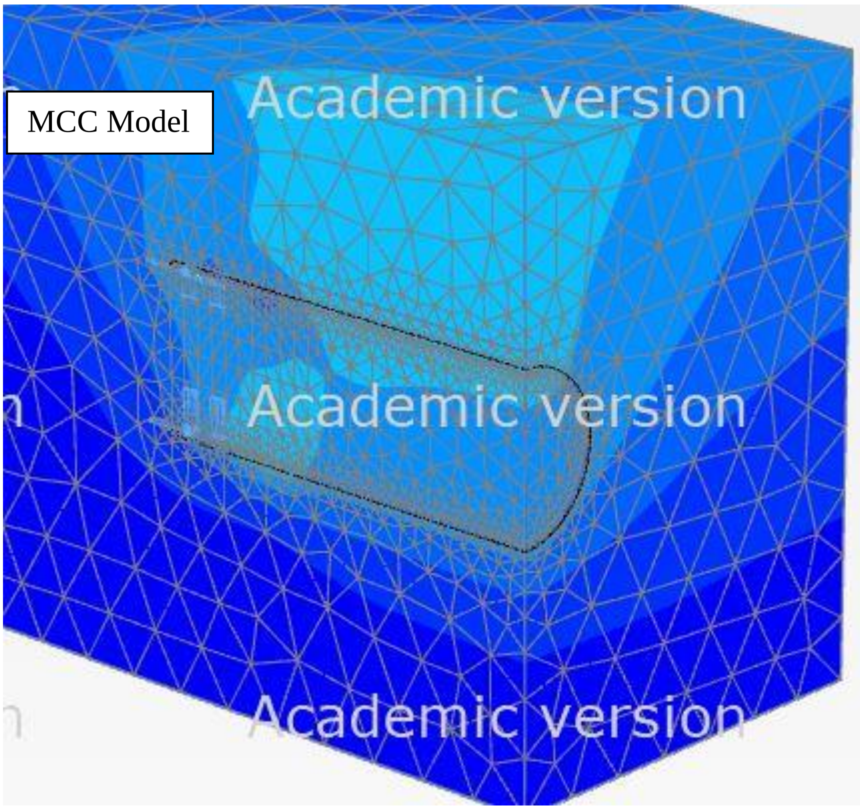

Figure 3.10: Representation of Distribution of Total Displacement of Mashhad Metro in PLAXIS 3D (MCC Model)

3.3 General Information about Delhi Metro Phase 3, India

In Delhi Metro Phase-3, a record of 30 TBMs was used to bore about 80km of underground tunnels in total (combining the length of both way tunnels). The total length of the underground corridor in this phase is about 54km. The new tunnels passed below existing operational elevated viaducts, an operational tunnel of DMRC, the rocky Aravalli ranges, heritage monuments, and densely populated areas. The tunnel passed underneath the old dilapidated buildings, which were undergoing reconstruction or repairs. The Figure 3.11 represents the proposed plan of Delhi Metro Phase 3.

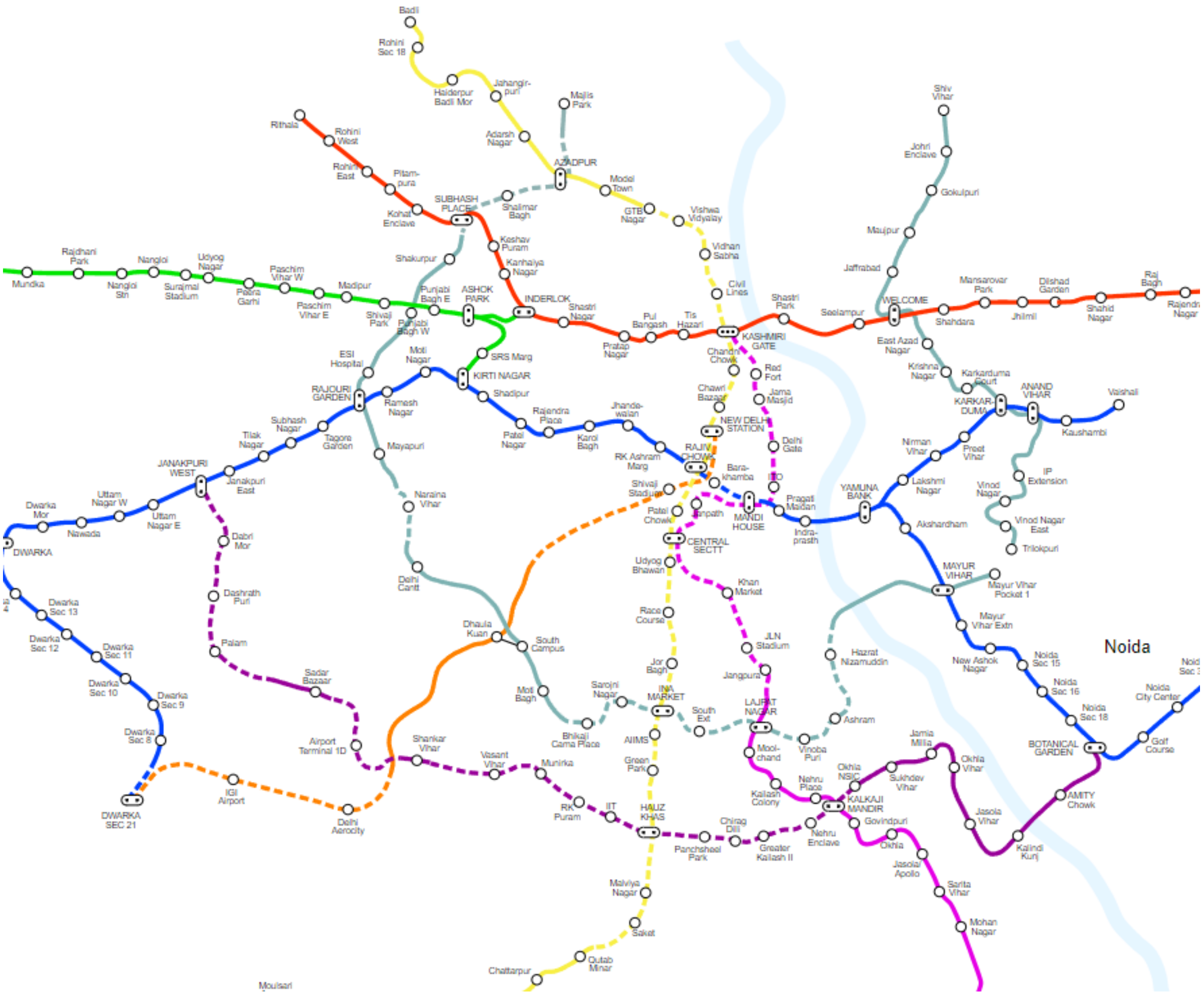

Figure 3.11: Proposed Plan of Delhi Metro Phase 3 Line (Dotted Lines are Underground portions) (Naqvi et al., 2021)

3.1.1 Soil Condition and Parameters

The soil used in this analysis was Delhi silty sand. The properties of soil and concrete tunnel lining are given in Table 3.5 and Table 3.6.

Field data shows that the cohesionless of soil of Delhi has horizontal stratification with the variation in Young's modulus at various depths. To replicate the field condition, the Young's modulus of soil is linearly varied from top to bottom, with 7.5 MPa at top and 50 MPa at the bottom. In Figure 3.12, the variation in Young's modulus with depth is shown for clear view. The location of tunnel and tunnel specification is defined in Figure 3.13.

Table 3.5: Soil and Concrete Lining Properties found from Soil Test Data

Delhi Silty Sand		
Bulk Density	kN/m^3	18
Saturated Density	kN/m^3	20
Poisson's Ratio		0.25
Friction Angle		35
Dilatation Angle		5
Concrete Lining		
Density	kN/m^3	25
Young's Modulus	kPa	3.16 X 10^7
Poisson's Ratio		0.15
Sectional Area	cm^2/m	2500
Plastic Section Modulus	cm^3/m	15625
Moment of Inertia	cm^4/m	130208.33
Yield Strength	MPa	30
Weight	kg/m/m	625

Table 3.6: Young's Modulus of Delhi Silty Sand at Various depths

Depth (m)	Young's Modulus (kPa)
0 ~ 10	7500
10 ~ 20	15000
20 ~ 35	30000
35 ~ 50	40000
50 ~ 60	50000

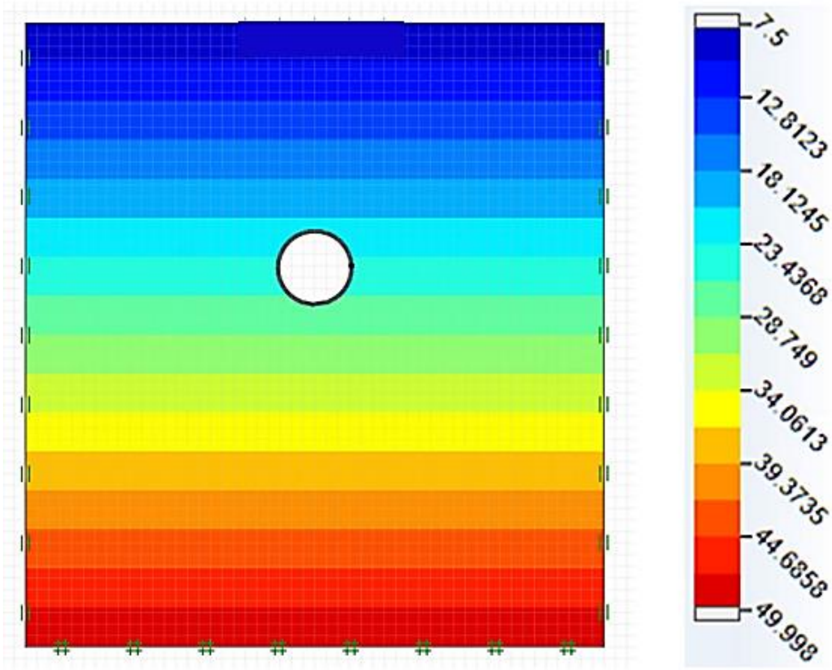

Figure 3.12: Representation of Young's Modulus of Delhi Silty Sand at Various depths (Naqvi et al., 2021)

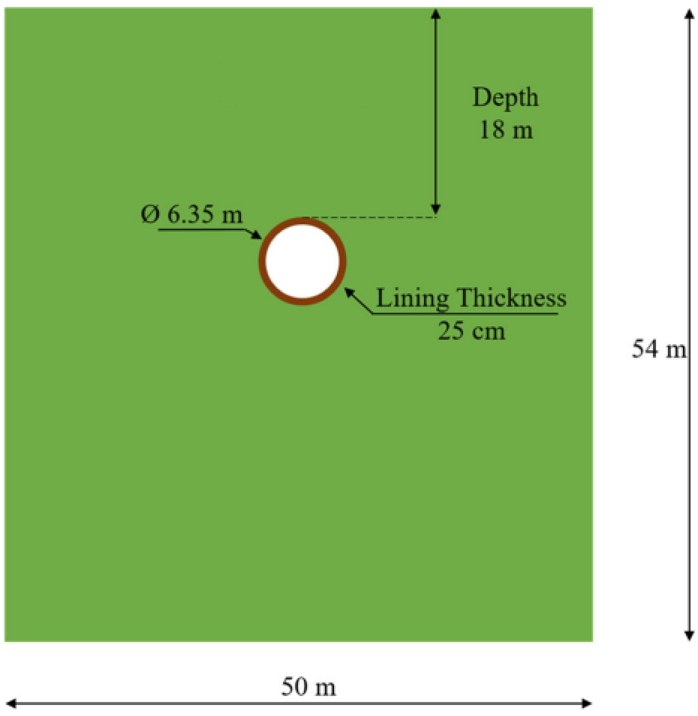

Figure 3.13: Schematic Representation of Model Parameters (Naqvi et al., 2021)

3.1.2 Numerical Modelling

2D plain strain model has been a model using commercially available finite element software Optum G2. The elastoplastic model of soil was modelled using the Mohr-Coulomb criterion. The dimensions of the soil model are considered as 50 m width and 54 m height. The range of depth of tunnel found in the Delhi Metro Phase 3 project is 12–30 m. Depth 18m was chosen for simplification of modeling. The excavated diameter of the tunnel is kept 6.35 m. In order to avoid the boundary effect in numerical analysis, the outer boundary was placed at a distance of 3 diameters away from the center of the tunnel. The thickness of the concrete lining used for the modelling was kept 25 cm. Tunnel length of 54m (1/1000th of actual length) and radius of 3.175m have been considered.

3.1.3 Stages of Analysis

The analysis was performed in below mentioned stages to simulate the real field conditions as follows:

Stage 1: A Greenfield condition having soil modelled similarly to field conditions. The analysis performed in this stage, known as initial stress analysis.

Stage 2: A second stage where the tunnel is excavated. The tunnel perimeter is here fully supported.

Stage 3: The lining was inserted in the third stage, and all supports around the tunnel perimeter were removed and were replaced by a plate to model the lining. The elastoplastic analysis was then carried out.

For the validation of the present numerical analysis, the surface settlement has been calculated through established empirical formulas and compared with the numerical results of OptumG2 in literature and of PLAXIS 3D in this research. A closed-form solution had been proposed by Peck and Schmidt (1969) to calculate the surface settlement in soil due to an underground opening.

$$S_v = \frac{V_s}{\sqrt{2\pi} K Z_0} e^{-\frac{y^2}{2K^2 {Z_0}^2}} \tag{3.11}$$

Where Vs is the volume of the settlement trough per meter of tunnel advance (m^3/m), defined as a percentage volume loss of the unit volume V of the tunnel, and was taken as 0.35% for low plastic silty soil, K is trough width parameter and was taken as 0.5 for ML soil, y is the lateral distance from the tunnel centerline (m), and Z_0 is the depth of the neutral axis from the surface. Vertical settlement profile of ground from the center of model (point above crown) to the lateral boundary was plotted using the above two formula and numerical results obtained from Optum G2 and PLAXIS 3D. The variation or deviation percentage between numerical analysis and peck formula was considered approximately 13% in literature whereas in our computation after numerical analysis, the deviations are approximately 15%. This comparison of settlement values of Peck's empirical formula, OptumG2 and PLAXIS 3D numerical analyses for MC model type are shown in Table 3.7 and Figure 3.14. In Figure 3.15, Figure 3.16, and Figure 3.17, the meshing condition in Optum G2, the meshing condition in PLAXIS 3D and distribution of vertical surface settlement in PLAXIS 3D are shown.

It can be seen from the validation result of PLAXIS 3D, Optum G2 and Peck formula, the difference percentage between Optum G2 and Peck's formula is 12.69% whereas the difference percentage between PLAXIS 3D and Peck's formula is 14.93% and the difference percentage between PLAXIS 3D and Optum G2 is 4.81%.

Table 3.7: Calculation of Vertical Surface Settlement based on Peck & Schmidt Formula and Comparison with Numerical Analysis Data

Model Type	**Tunnel Depth, Z_0**	**Radius, R**	**Vertical Surface Settlement (from Peck formula)**	**Vertical Surface Settlement (from Optum G2)**	**Vertical Surface Settlement (from PLAXIS)**	**Difference between Optum G2 and Empirical Formula**	**Difference between PLAXIS and Empirical Formula**	**Difference between PLAXIS and Optum G2**
	(m)	(m)	(mm)	(mm)	(mm)	(%)	(%)	(%)
MC	18	3.175	34.10	29.70	31.20	12.69	14.93	4.81

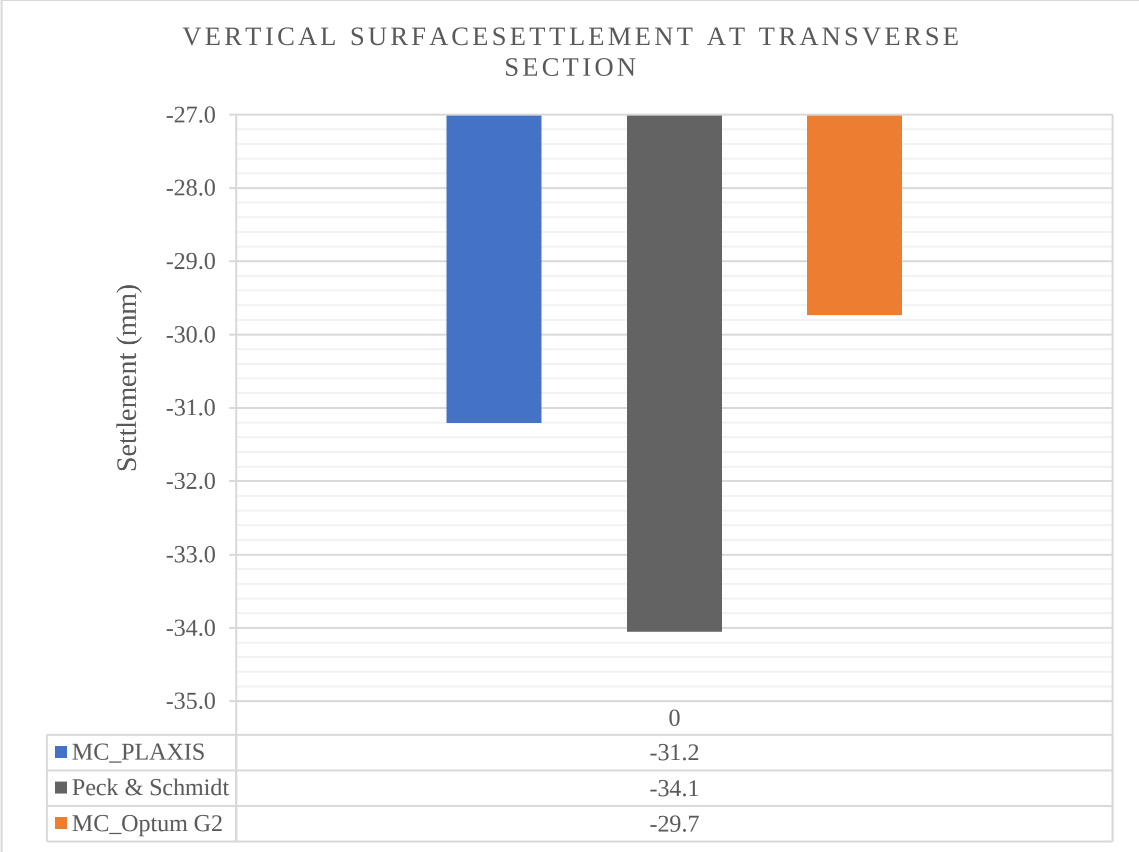

Figure 3.14: Comparison of Vertical Surface Settlement between PLAXIS 3D, Optum G2 and Peck & Schmidt Formula

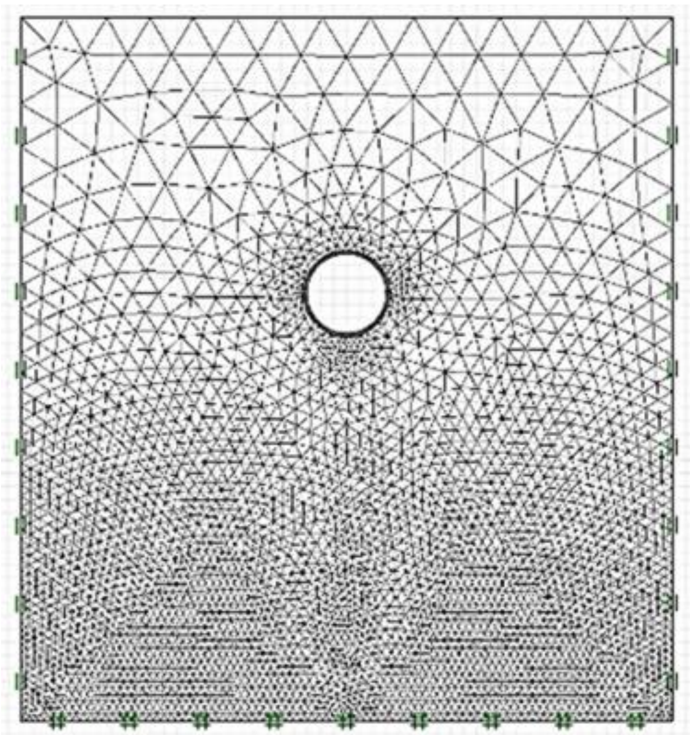

Figure 3.15: Meshing Condition in Optum G2

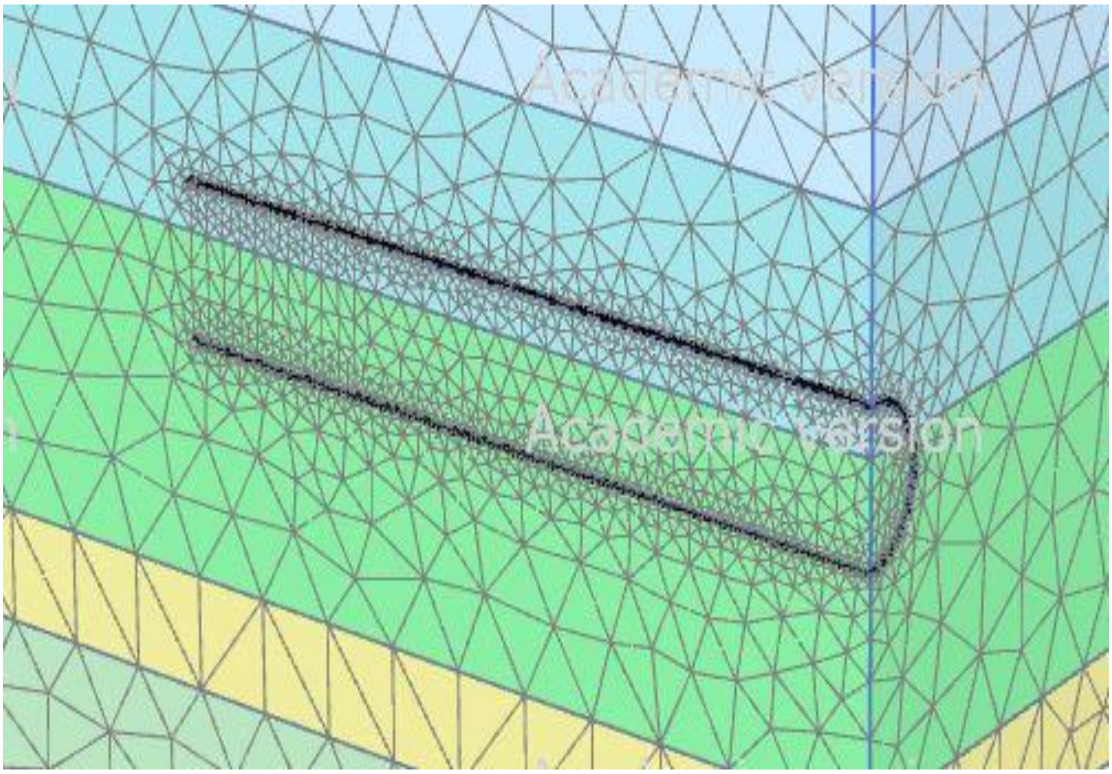

Figure 3.16: Meshing Condition in PLAXIS 3D

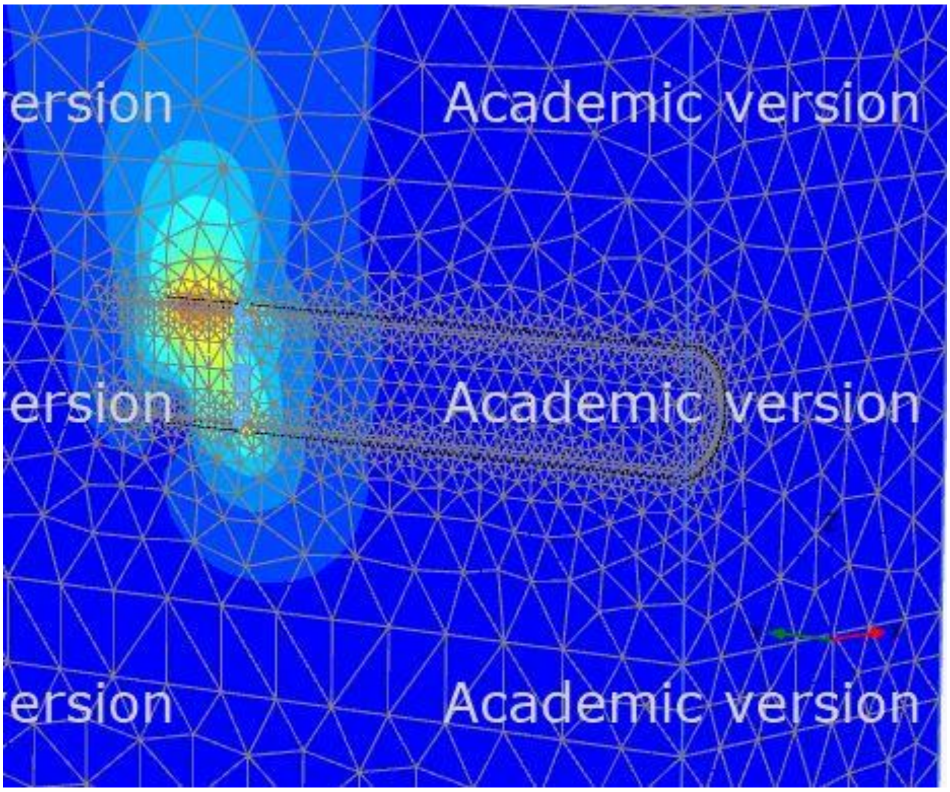

Figure 3.17: Distribution of Vertical Surface Settlement in PLAXIS 3D

3.4 Summary

i. The detailed geotechnical investigation report of Mashhad Metro Line 2 has been implied in PLAXIS 3D to validate the researcher's result with the numerical result. The researchers used FLAC 3D for numerical analysis and compared the result with empirical relations.

ii. From the empirical relations suggested by the researchers, it can be seen that O'Reily and New relations show better error value than others. Also, in our numerical analyses with PLAXIS 3D, the error values for this relationship are 1.66% and 4.81% for MC and MCC models respectively which are comparatively less than other relationships.

iii. Comparing the FLAC 3D result and Peck formula for maximum settlement, 9.6% and 41% error were found for MC and MCC models respectively, whereas comparing PLAXIS 3D and Peck formula for maximum settlement, 11.11% and 44.4% were found for MC and MCC models respectively which is approximately close to the literature.

iv. From the comparative analysis of Mashhad Metro Line 2, it can be seen that O' Reily & New empirical relation shows closest values (3.91%, 1.66% and 4.81% deviation with FLAC 3D, MC model in PLAXIS 3D and MCC model in PLAXIS 3D respectively).

v. The detailed geotechnical investigation report of Delhi Metro Phase 3 has been implied in PLAXIS 3D to validate the researcher's result with the numerical result. The researchers used Optum G2 for numerical analysis and compared the result with empirical relations.

vi. The variation percentage between numerical analysis of Optum G2 and Peck's formula was approximately 13% whereas in PLAXIS 3D and Peck's formula was approximately 15% which is approximately close.

vii. It can be seen from the validation result of PLAXIS 3D, Optum G2 and Peck formula, the difference percentage between Optum G2 and Peck's formula is 12.69% whereas the difference percentage between PLAXIS 3D and Peck's formula is 14.93% and the difference percentage between PLAXIS 3D and Optum G2 is 4.81%.

Chapter 4

NUMERICAL MODELING AND ANALYSIS

3.2 Introduction

In this chapter, the outline of proposed MRT line 1 project, the detailed route of underground part, and geology and soil condition of the selected study area are described with appropriate maps. The field study investigation including physical and laboratory tests of soil samples are done in accordance with the ASTM standards which are also discussed and a longitudinal soil profile for the study area is created with the help of the field study data. The different test results of the field study investigation are mentioned in this chapter and in Appendix which are collected from secondary sources. FEM analysis (numerical modelling) is done by PLAXIS 3D for both NATM and TBM methods for different types of models (MC, MCC and HS) are described in details in this chapter.

3.3 Context of Underground Part of Dhaka Mass Rapid Transit Line 1

The length of the MRT line 1 will be 28.2 km with 19 stations and one depot in Purbachal area. As per the plan, the MRT line 1 consists of two lines, one being the route that connects Kamalapur with the Hazrat Shahajalal International Airport (hereafter the "Airport Line"). The line will be runs through underground tunnel, starts at the Kamlapur station of Bangladesh National Rail (BR), travels westward under the Outer Circular Road, northward under the Rampura DIT Road and Pragati Sharani Road, crosses the Kuril flyover, and proceeds under the New Airport Road to its destination at Dhaka International Airport. Out of total 28.2 km, the airport line will be 14.8 km underground line comprising total 12 underground stations. Construction of the underground running section shall be done by Tunnel Boring Machine (TBM) and stations will be constructed either by Cut and Cover method. The outer diameter of the tunnel is 7m and standard length of station is 250m. The metro tunnels will range from 20m to 50m below the ground in different locations with average depth of 35 meter (NKDOS Consortium Proposal, 2019). The Figure 4.1 represents the alignment map of MRT Line 1 where green line, red line, green labels and red labels are represented as underground section, elevated section, underground stations, and elevated stations respectively. The Table 4.1 specifies the underground stations' names, station types and tier type or connectivity locations with other stations.

Table 4.1: List of Underground Stations in MRT Line 1

SL. No.	Underground Stations	Station Type	Special Consideration
1	Kamlapur	Standard	
2	Rajarbagh	Narrow/Deep	Two-tier Station
3	Malibagh	Narrow/Deep	Two-tier Station
4	Rampura	Standard	
5	Hatirjheel East	Standard	Connectivity with Line 5 South Station
6	Badda	Standard	
7	North Badda	Standard	
8	Natun Bazar	Wide Station	Connectivity with Line 5 North Station and proper protection for existing DWASA pipe line
9	Nadda	Double/Deep	Two-tier Station
10	Khilkhet	Standard	
11	Airport Terminal - 3	Standard	Connectivity with New Airport Terminal 3
12	Airport	Standard	Connectivity with BR Station and Extension Line 1

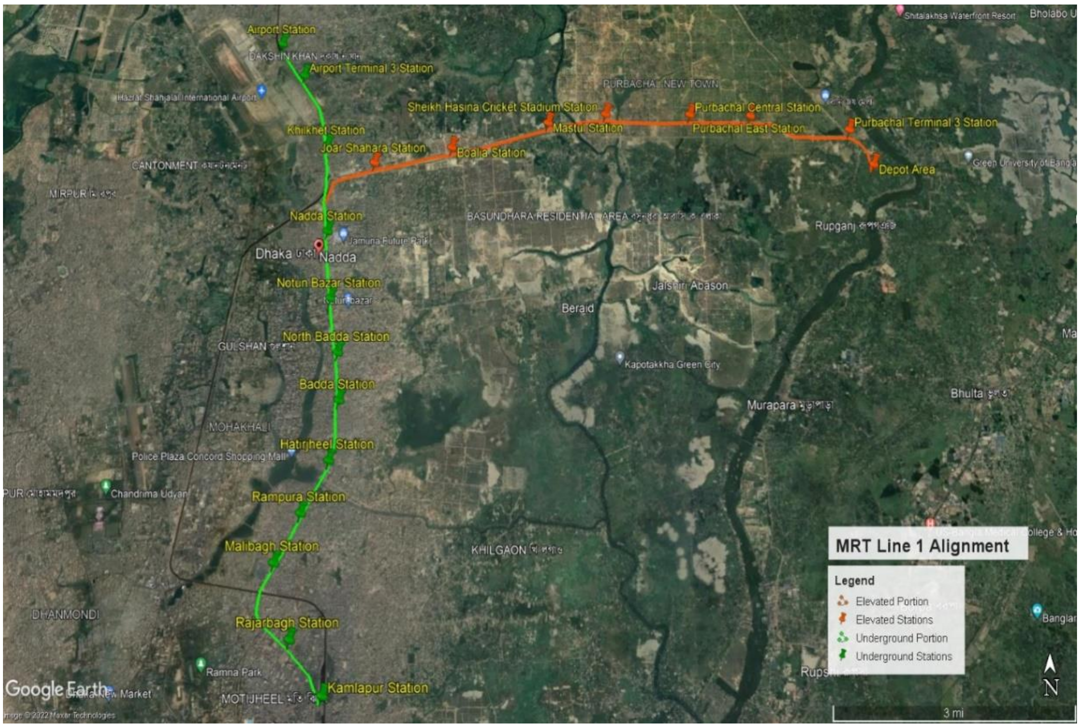

Figure 4.1: Map showing the MRT Line 1 Alignment with Stations Location (NKDOS Consortium Proposal, 2019)

3.3.1 Geology and Soils

Dhaka lies in the extreme south of the Madhupur Tract, which is situated in the central-eastern part of Bangladesh. The planning area is covered mainly by the Pleistocene Madhupur Clay, a yellowish brown to the highly oxidized reddish brown silty clay; and by Holocene sediments to the south, west and east made up of alluvial silt and clay and marshy clay and peat. The moisture content and liquid limit results obtained for the Madhupur clay show that it is normally consolidated to slightly over-consolidated, perhaps due to groundwater pumping. The clay has intermediate to high plasticity, and is overlain by the Dupi Tila formation of medium to coarse sand. The incised channels and depressions within the city are floored by recent alluvial flood plain deposits. The project location in geology of Bangladesh map is shown in the Figure 4.2.

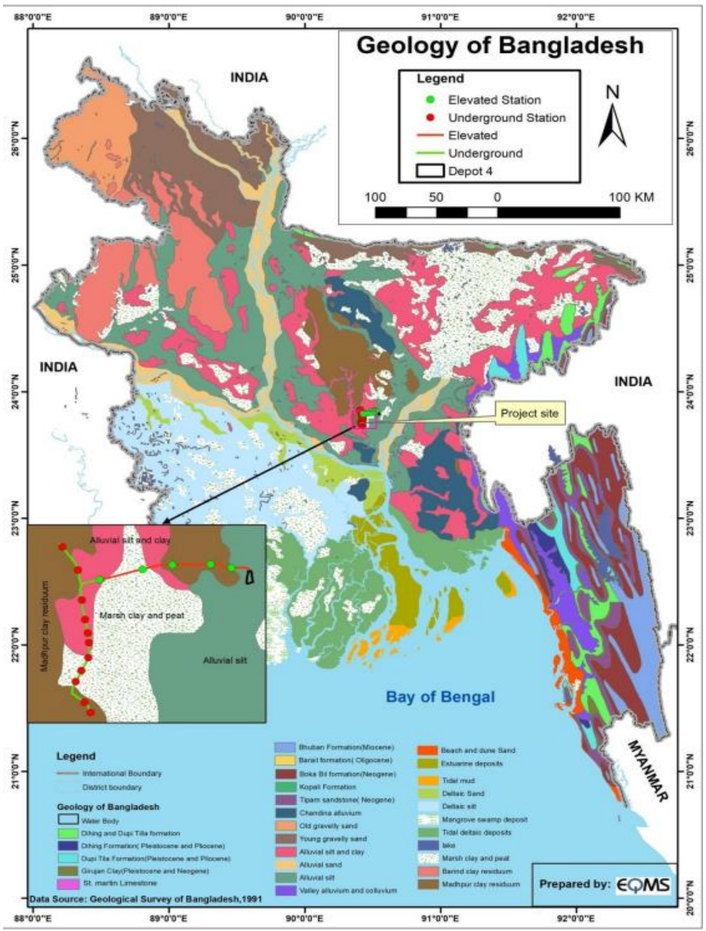

Figure 4.2: MRT Line 1 Location in Geology of Bangladesh Map (NKDOS Consortium Proposal, 2019)

According to the soil maps of Bangladesh (Figure 4.3), the project site falls under the shallow red-brown terrace soil and deep red-brown terrace soil. The shallow red-brown soils are imperfectly to moderately well drained. The topsoil of deep red-brown terrace soils usually is 8-10 cm thick and has a brown to yellow brown color, loam to clay loam texture and rusty stains along root channels. The subsoil usually is 60-120 cm thick.

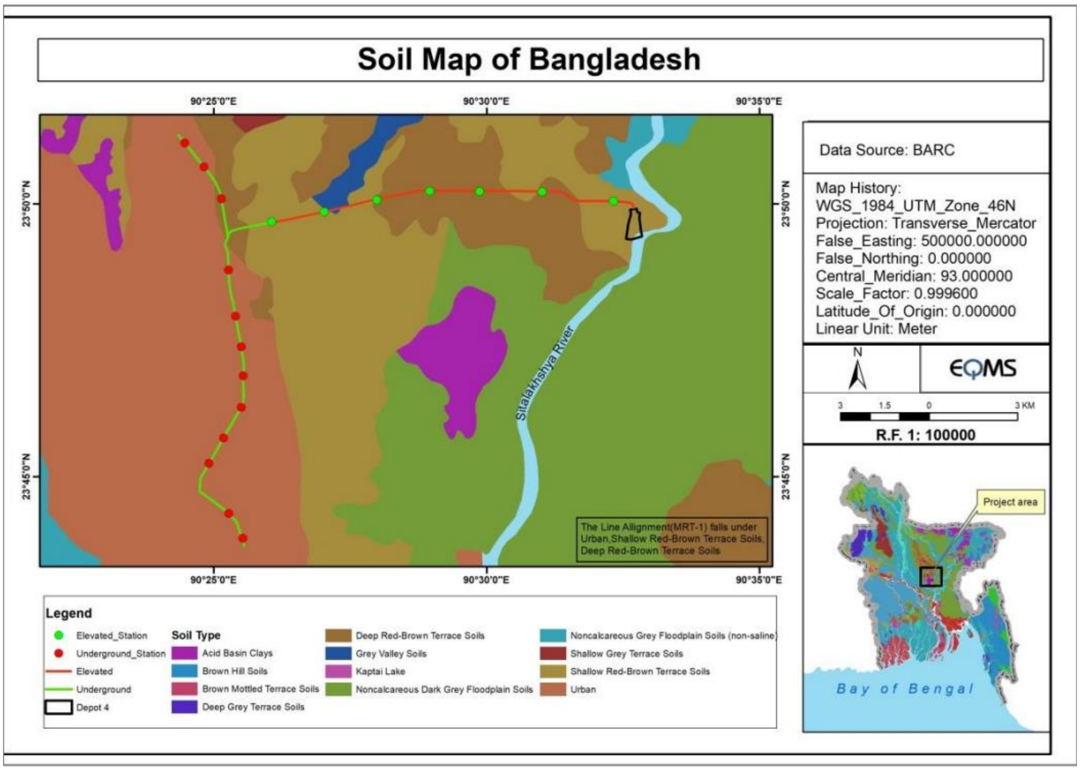

Figure 4.3: MRT Line 1 Location of Soils of Bangladesh Map (NKDOS Consortium Proposal, 2019)

Dhaka city falls in seismic zone II of the seismic zoning map of Bangladesh which means the city is at moderate risk (basic seismic coefficient is 0.5 g). Neotectonic movement in and around the city has been reported widely. The Madhupur Tract as a whole is a structural high in which the Dhaka-Tongi block is the most uplifted part. The boundaries of the tract to the west, south and east are characterized by step faulting. The high land area which varies up to 100ft shows low relief. The high lands are composed of Pleistocene Madhupur Clay and Sand formation where the low lands are recent floodplain deposits. The studied area is mostly consisted of clayey soil than the sandy soils. There are some sandy soils interbedded between these clay layers. The upper part comprises grayish to brownish stiff to medium stiff clayey soil and brownish medium dense soil of Basabo silty clay formation and lower brownish very dense sand and hard clayey soil below it can be of from Madhupur clay and sand formation. The degree of concentration and thickness of clayey soil is also influenced by the neo-tectonics of this region, which causes undulation of ground surface. The surface elevation of the area Dhaka are ranges between 1 and 14m and most of the built-up areas located at the elevations of 6-8m (Follow Figure 4.4). The drainage system will be hampered due to construction activities like as infilling, construction of the depot, construction yards and haul routes. A major impact during construction stage is due to suspended solids entrained in runoff that can bring soil surfaces and clog drainage system. Underground tunnel construction may impact on ground water quality and depth of the underground water level. Potential impacts on groundwater are insignificant. In Dhaka City, Ground Water extraction started from a depth of 100m and in some extreme condition the well goes up to 300 meters to reach the main aquifer.

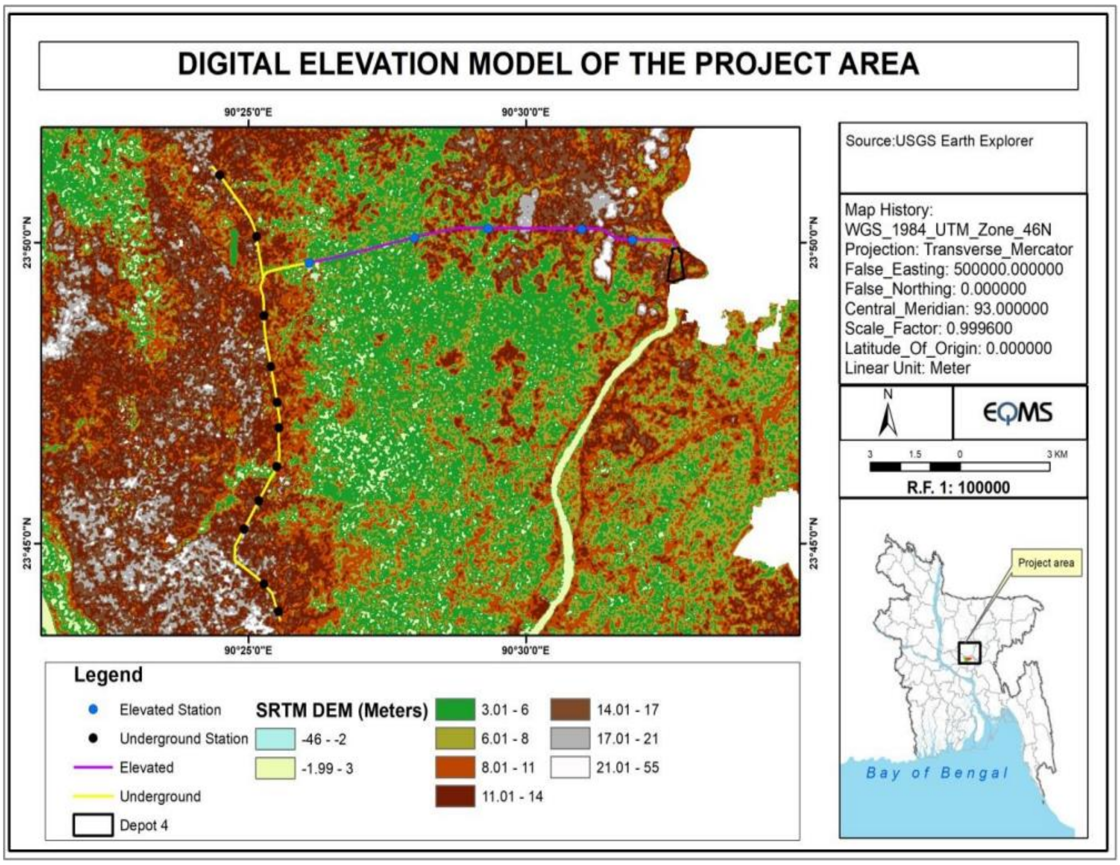

Figure 4.4: Elevation Map of the Project Area (NKDOS Consortium Proposal, 2019)

3.3.2 Field Investigation of the Study Area

The objectives of the geotechnical survey are to obtain physical and mechanical properties of soil and soil design parameters through field and laboratory tests. In field, in-situ tests, such as standard penetration tests and pressure meter tests were conducted and index and mechanical properties tests such as compression, consolidation tests etc. were conducted in the laboratory. The investigation program was consisted of soil boring and sampling at desired intervals for subsequent observation and laboratory testing (ProSoil Geotechnical Survey, 2019). The soil report and physical and mechanical properties of soil are collected from secondary data sources.

The selected borehole's location (BH-24) is marked in the route map in Figure 4.5 and Table 4.2. The portion of longitudinal soil profile (geotechnical) of the Airport route and soil stratification of BH-24 is presented in Figure 4.6. The physical description of soil strata with SPT values and depth range are mentioned in Table 4.3.

Figure 4.5: Location of Selected Borehole (BH-24) for Investigation (NKDOS Consortium Proposal, 2019)

Table 4.2: Identification of Borehole 24

Borehole No.	24
Location	Under Kuril Flyover (In front of Walton Showroom)
Coordinates	23.82075N, 90.42077E
RL	+8.313m

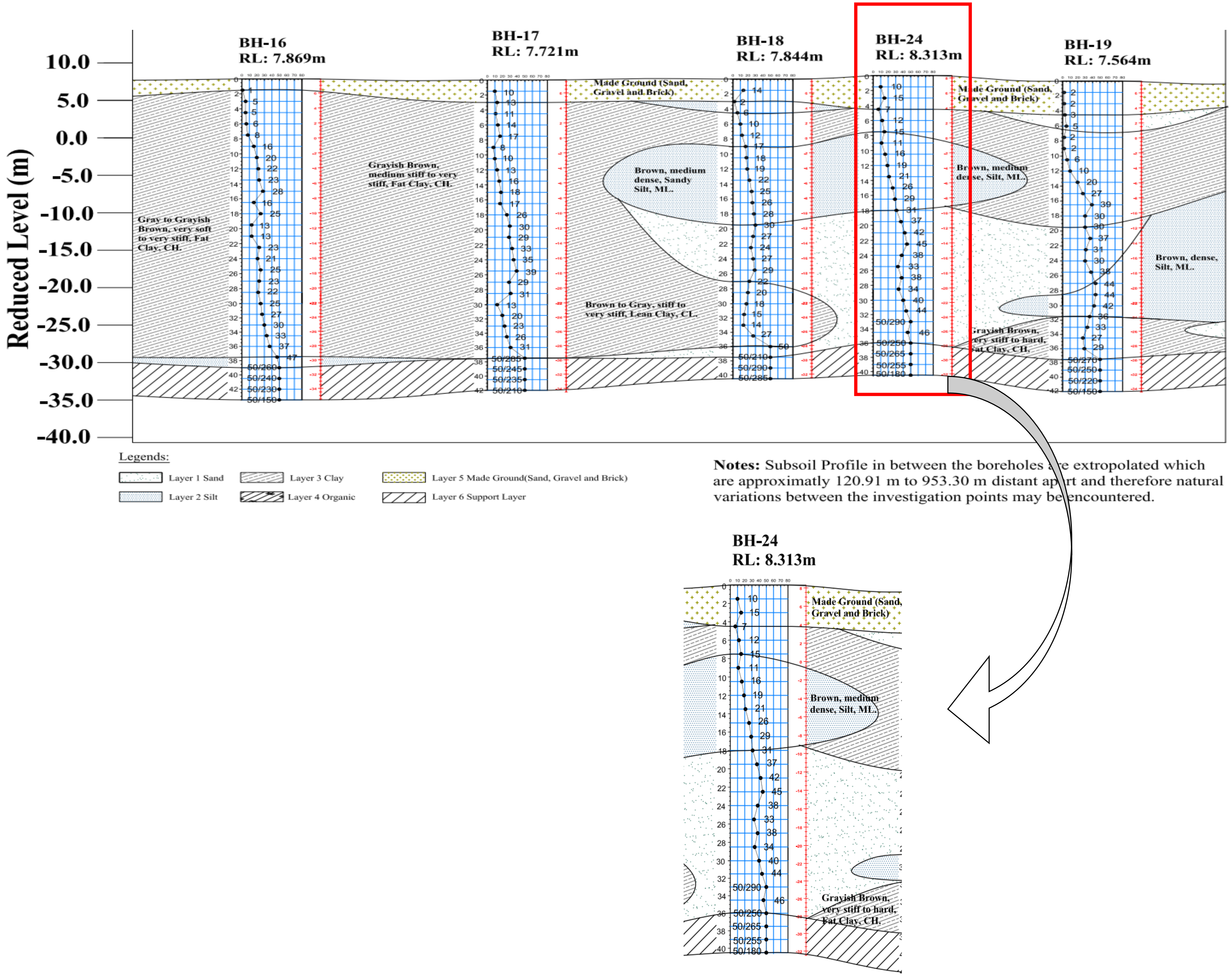

Figure 4.6: Subsoil Stratification of BH-24

Table 4.3: Description of Soil Layers from SPT Test Result (BH-24)

SL. No.	Soil Layer Notation	Description	Soil Consistency and Relative Density	Soil Color	Depth Range (m)	SPT Range
1	SF	Made Ground		Gray, Gray to Reddish Gray, Reddish Gray	0 – 4.5	10-15
2	AC3	Lean Clay	Medium Stiff	Gray, Reddish Gray, Gray to Yellowish Gray, Brown	4.5 – 5.0	7
3	AC4	Fat Clay	Stiff	Brown, Gray, Gray to Yellowish Gray, Grayish Brown to Gray, Gray to Brown, Grayish Brown	5.0-6.0	12
4	AC4	Lean Clay	Stiff	Brown, Gray, Gray to Yellowish Gray, Grayish Brown to Gray, Gray to Brown, Grayish Brown	6.0-7.5	15
5	AS3	Sandy Silt	Medium Dense	Gray, Yellowish Gray, Yellowish Gray to Brown, Brown	7.5 – 9.0	11
6	AS3	Silt		Gray, Yellowish Gray, Yellowish Gray to Brown, Brown	9.0-12.0	16
7	AC5	Lean Clay	Very Stiff	Yellowish Gray, Yellowish Gray to Reddish Brown, Brown to Gray, Gray, Gray to Reddish Gray, Reddish Brown, Brown, Dark Gray, Reddish Gray, Gray to Yellowish Gray, Red, Grayish Brown, Black, Gray to Brown, Brown to Brownish Gray, Brownish Gray to Brown	12.0 – 13.5	19 – 21
8	AS3	Silt		Gray, Yellowish Gray, Yellowish Gray to Brown, Brown	13.5 – 16.5	21-29
9	AS3	Sandy Silt	Medium Dense	Gray, Yellowish Gray, Yellowish Gray to Brown, Brown	16.5 – 18	31

SL. No.	Soil Layer Notation	Description	Soil Consistency and Relative Density	Soil Color	Depth Range (m)	SPT Range
10	AS4	Silty Sand	Dense	Gray, Yellowish Gray, Brown, Gray to Brown, Brown to Grayish Brown, Yellowish Gray to Brown, Gray, Reddish Gray, Brownish Gray to Gray	18 – 21	37
11	AS4	Sandy Silt	Dense	Gray, Yellowish Gray, Brown, Gray to Brown, Brown to Grayish Brown, Yellowish Gray to Brown, Gray, Reddish Gray, Brownish Gray to Gray	21 – 22.5	42 – 45
12	AS5	Silty Sand	Very Dense	Gray, Brown, Gray to Brown, Yellowish Brown, Yellowish Gray, Reddish Gray, Brown to Grayish Brown, Red, Grayish Brown to Brown, Brownish Gray to Gray	22.5 – 41	38 – 50

Unconfined compression test results, UU triaxial test results for determining undrained shear strength, secant modulus, angle of friction, and cohesion are included in this chapter and summary test result sheet collected from secondary source is mentioned in Appendix A. As the soil was found unsaturated, the angle of friction was found deviated from zero.

Loading Rate (mm/min)	Unconfined Compressive Strength qu (kPa)	Undrained Shear Strength Cu (kPa)	% Strain at qu max	Secant Modulus E_{50} (kPa)
2	106.00	53.00	15.00	3.53

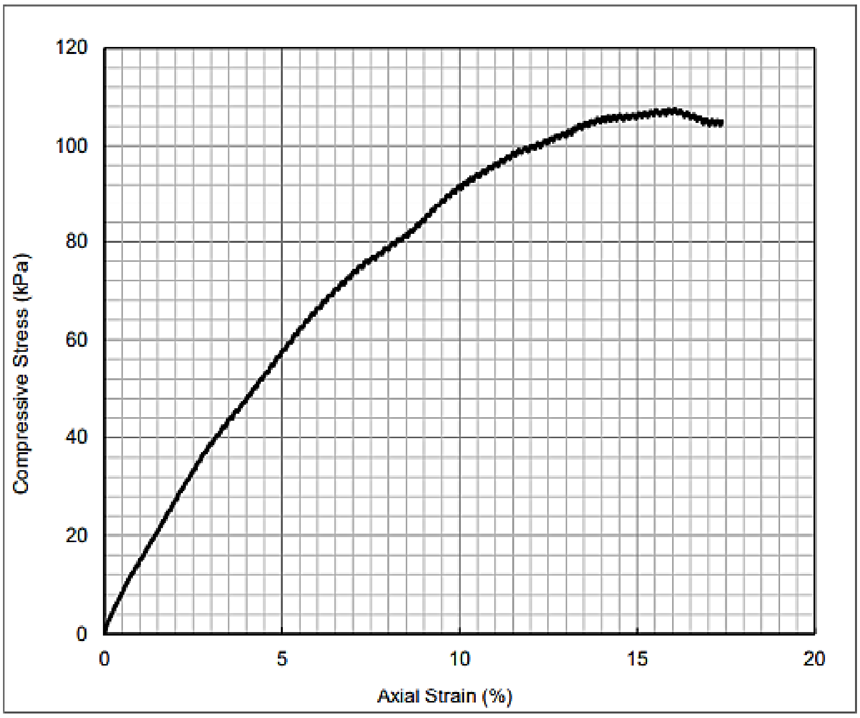

ASTM D-2166

Figure 4.7: Unconfined Compression Test Result (Depth 5.0-6.0m) – Soil Type: Fat Clay

Shear Strength Properties	
Angle of Friction , Φ	Cohesion, C (kPa)
5.1	48.0

Specimen ID	Initial Moisture Content (%)	Final Moisture Content (%)	Avg Initial Diameter (mm)	Avg Initial Height (mm)	Initial Bulk Density (gm/cm³)	Initial Dry Density (gm/cm³)	Deviator Stress (KPa)	Minor Principal Stress (δ_3') (kPa)	Major Principal Stress (δ_1') (kPa)
A	26.00	25.09	37.13	76.27	1.67	1.33	115	50	165
B	25.26	24.46	37.77	76.73	1.83	1.46	126	100	226

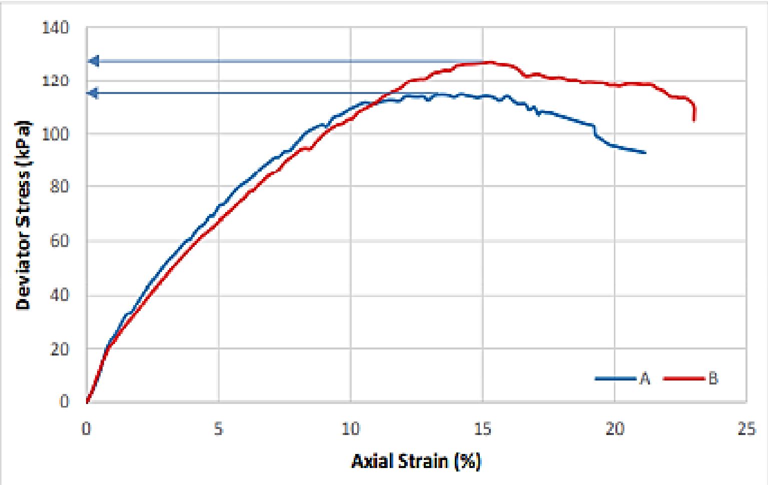

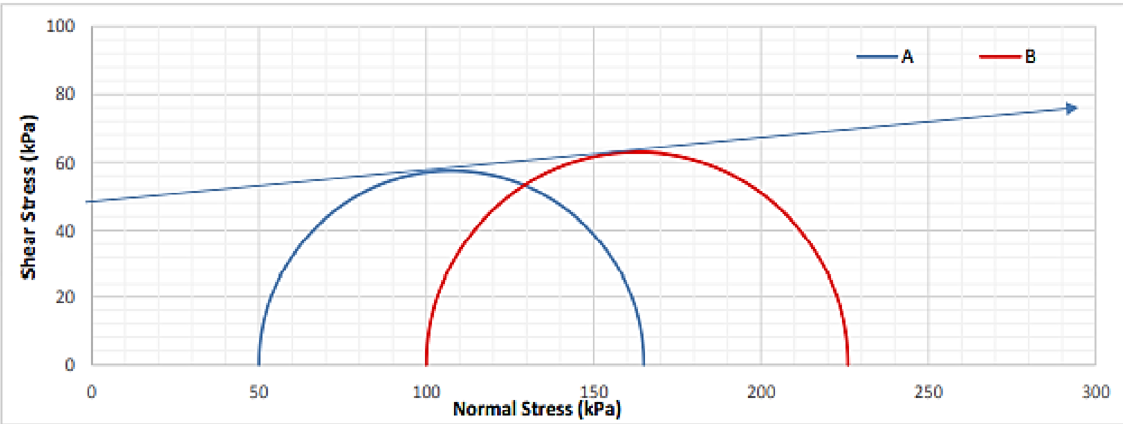

ASTM: D 2850-95

Figure 4.8: UU Triaxial Test Result (Depth 5.0-6.0m)

3.4 Numerical Modeling

To evaluate the settlement or displacement of tunnel under static condition, the numerical modelling in PLAXIS 3D can simulate the significant results which is difficult to conduct in laboratory or field or empirical conditions. In this investigation, the study area is filled with clayey type soil and sandy silt type soil in between. Therefore, there is a minimal chance of having liquefaction effect in seismic condition in this area. The FEM model is calibrated with the field and laboratory tests data. The result of TBM and NATM tunnels are shown using MC, MCC and HS soil models. The effect of varying tunnel depths and diameters is shown for TBM methods. At the end a comparison is made between NATM and TBM method in respect to settlement for three different models. Assumptions used in the estimations are as follows:

i. Cross-section of the tunnel is almost circular.
ii. Undulation in existing ground level is ignored.
iii. Tunnel is considered to move along a straight line.
iv. Tunnel is deep enough (35m from EGL) for avoiding the effect of adjacent structures and foundations.
v. Tunnel passes through clayey soil formation.
vi. Tunneling method is both NATM and TBM.
vii. Estimations are valid for completed primary support
viii. Long term consolidation settlement is ignored.
ix. Static and Dynamic loading effects are ignored.

3D model is chosen because for 2D FE models, it is not so easy to estimate pre-relaxation factors (sometimes called stress reduction factors), which is fraction of load effecting on tunnels, and purely based on practical experience. With the 3D model, estimation of pre-relaxation factor is no longer required when excavation stages can be modelled not only in cross-section but also in the longitudinal section, e.g., excavation of the bench and invert can be modelled in the actual distance behind the excavation of the top heading.

Limitations:

i. Existing ground surface abruption and ground water level effect (flow water condition) is not considered.

ii. Due to considering one borehole data, the soil properties and division of layers are kept equal all along the assumed length.

iii. Diameter (7m) is considered according to the feasibility report of MRT line 1 Project. Though for TBM analysis, variations in diameter (up to 5m) have been considered.

3.5 FEM Model in PLAXIS 3D (TBM Method)

The lining of a shield tunnel is often constructed using prefabricated concrete ring segments, which are bolted together within the TBM to form the tunnel lining. During the erection of the tunnel lining the TBM remains stationary. Once a tunnel lining ring has been fully erected, excavation is resumed, until enough soil has been excavated to erect the next lining ring. As a result, the construction process can be divided into construction stages with a length of a tunnel ring, often about 1.5m long. In each of these stages, the same steps are repeated over and over again. In order to model this, a geometry consisting of slices each 1.5m long was used. The calculation consists of a number of plastic phases, each of which models the same parts of the excavation process; the support pressure at the tunnel face needed to prevent active failure at the face, the excavation of soil and pore water within the TBM, the installation of the tunnel lining and the grouting of the gap between the soil and the newly installed lining. This tunnel advancement process is illustrated in Figure 4.9. In each phase the input for the calculation phase is identical, except for its location, which will be shifted by 1.5m each phase.

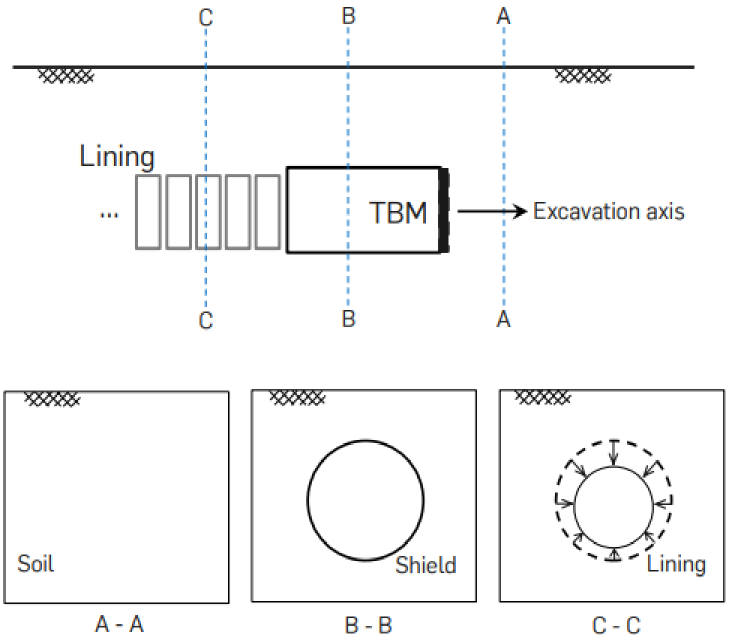

Figure 4.9: Schematic illustration of tunneling simulation process (Bentley, 2018)

3.5.1 Geometry

In the model, only one symmetric half is included. The model is 25m wide, it extends 60m in the y-direction and it is 41m deep. These dimensions are sufficient to allow for any possible collapse mechanism to develop and to avoid any influence from the model boundaries. The subsoil consists of 11 layers. The soil layers with depth and soil conditions with parameters for all models are given below. The tunnel excavation is carried out by a tunnel boring machine (TBM) which is 10m long and 7m diameter with 0.25m concrete lining. The TBM was considered to be advanced 25m into soil. Subsequent phases will model an advancement by 1.5m each. The locations of tunnels considered in simulation are 30m, 32m, and 35m depth from ground surface (Figure 4.10).

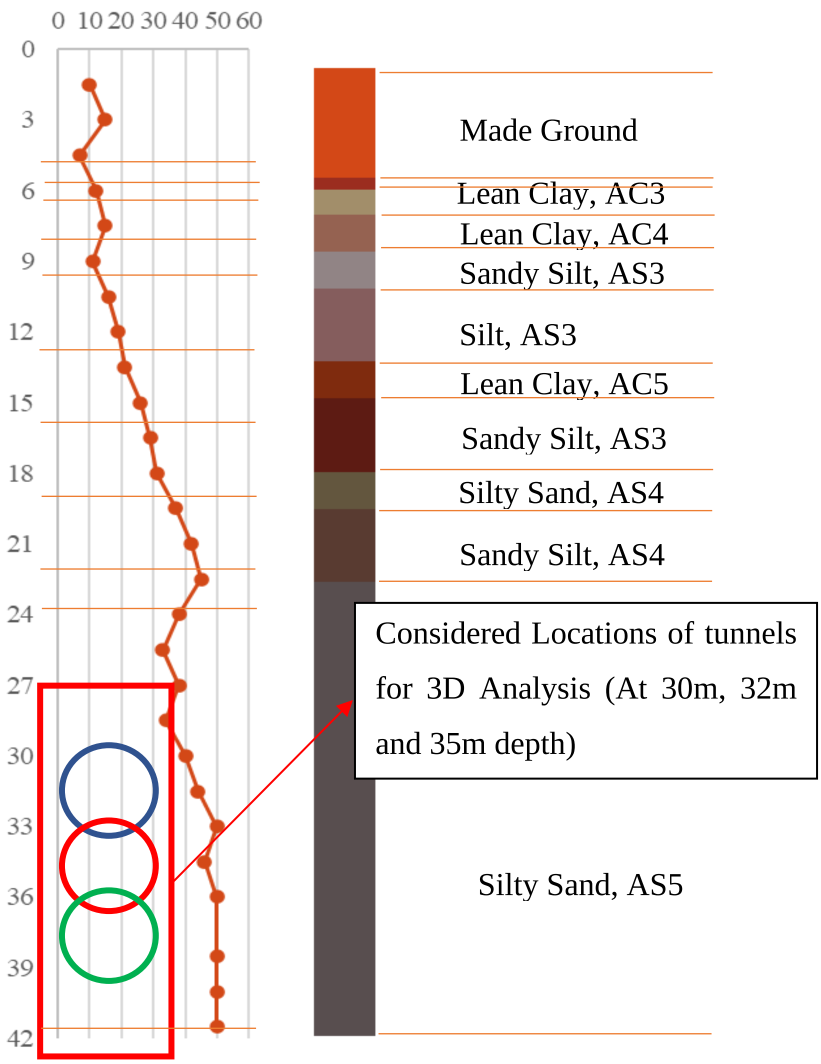

Figure 4.10: Locations of TBM machines in Soil (NKDOS Consortium Proposal, 2019)

3.5.2 Definition of Structural Elements

A soil structure interaction has to be added on the outside of the tunnel due to the slight cone shape of the TBM. Typically, the cross-sectional area at the tail of the TBM is about 0.5% smaller than the front of the TBM. The reduction of the diameter is realized over the first 7.5m length of the diameter while the last 1.5m to the tail has the constant diameter. So, in modeling, uniform and incremental contraction has been considered according to the advancement of the TBM. The surface load representing the grout pressure is constant during the building process. In the specifications of the tunnel boring process, it is given that the grout pressure should be -100kN/m^2 at the top of the tunnel and should increase with -20kN/m^2/length. The tunnel face pressure is a bentonite pressure (Bentonite slurry) or an earth pressure (Earth Pressure balance) that increases linearly with depth.

For the initial position of the TBM and the successive four positions when simulating the advancement of the TBM, a tunnel face pressure was defined. In order to simplify the definition of the phases in Staged construction mode, the sequencing of the tunnel was defined. The soil in front of the TBM will be excavated, a support pressure will be applied to the tunnel face, the TBM shield will be activated, and the conicity of the shield will be modelled, at the back of the TBM the pressure due to the backfill grouting will be modelled as well as the forces of the hydraulic jacks driving the TBM exert on the already installed lining, and a new lining ring will be installed. In the mesh mode, medium mesh was used to generate. Since water levels will remain constant the flow conditions mode was skipped. The excavation of the soil and the construction of the tunnel lining was modelled in the staged construction mode. The first phase differs from the following phases, as in this phase the tunnel is activated for the first time. In the Table 4.4, parameters are defined for HS, MC and MCC model types for TBM construction method. The soil parameters depicted are:

i. Dry and Wet Density, Initial Void Ratio, Cohesion (c_{ref}), Internal Friction (ϕ)
ii. Secant Modulus at 50% strength (E_{50}^{ref}), Modulus for Oedometer conditions (E_{oed}^{ref}), Unload-Reload Modulus (E_{ur}^{ref})
iii. Cam Clay isotropic compression index (λ), Cam Clay isotropic swelling index (κ), Tangent of the critical state line (M)
iv. Young’s Modulus (E’), Poisson’s Ratio (υ)

3.6 FEM Model in PLAXIS 3D (NATM Method)

NATM is characterized by the fact that a tunnel is excavated in different parts (crown, bench, and invert), where subsequent parts are executed at a certain distance (lag) behind the previous part. After each excavation part the tunnel contour is secured by means of a temporary lining of sprayed concrete. A final lining can be installed later if the long-term soil conditions require such. As per the real tunnel excavation, in the modelling excavation of three parts were included. The model is basic and medium in order to restrict the computation time and memory consumption.

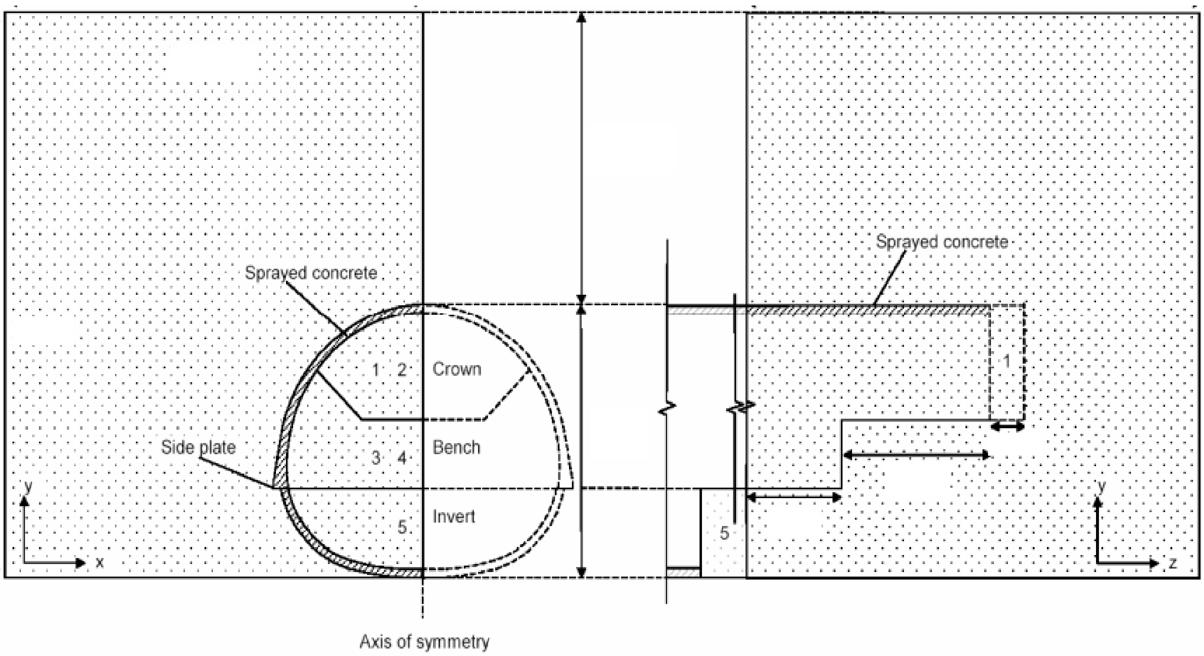

Figure 4.11: Basic NATM method assuming for Numerical Modelling (Sinha, 1989)

4.5.1 Geometry

The top of the tunnel is 35m below the ground surface considered. The full tunnel has the height of 7m and a width of 10m. The crown was excavated in a section of 1.0m length. After the excavation the surrounding soil was secured with sprayed concrete. The excavation of the bench is always some meters behind the heading. A length of 9m behind the bench excavation was included in the model to create the starting situation. The invert is much further behind and it is of almost 5m behind the benching. For reasons of symmetry, only half of the geometry is modelled, whereas symmetry conditions were adopted at the center plane. The model is extended 25m sideways (in y direction) from the center plane, 60m in x direction and -40m in z direction.

4.5.2 Definition of Structural Elements

The mesh is generated automatically (usually medium) and some refinements was applied by PLAXIS in order to get smaller mesh sizes in the tunnel vicinity where the stresses and deformations are concentrated. The mesh for the 3D model consists of the default 10-node tetrahedron elements. For plates used to simulate tunnel linings, 6-node plate elements are applied which are compatible with the 6-node face of a soil element. Moreover 12-node interface elements are used to simulate soil-structure interaction behavior. In the staged construction, the advancement of top heading, bench and invert excavations are assumed to 2m. Although this value is a little bit higher than the common practice, shorter advancements, i.e., shorter slice lengths, result in excessive run times and memory consumption. The tunnel length is taken as 19m which is suitable for displaying deformations and stresses due to surface excavation and construction along the tunnel of actual length of MRT Line-1.

The excavation process was divided in two different stages for each advance: the first stage simulates the excavation and the second stage the application of the concrete lining. It was assumed that the soil and initial ground support deforms to equilibrium after each 1 m advance before the primary sprayed lining is applied, furthermore no time effects were taken into account for the PLAXIS plastic calculations. The hosting media is assumed to be consisting of 11 layers of soil. It is assumed that no water table is encountered in the problem domain. All the analyses are performed by considering the drained condition. The tunnel is modelled with three different types of models (MC, MCC and HS), where modulus of elasticity (initial, unloading/reloading, oedometer, etc.) are chosen satisfactorily and according to the soil test results. The elasticity modulus of the soil is stress dependent and the loading history has a great influence on the soil non-linear behavior. Interfaces were applied only to the negative side of the tunnel lining, meaning only in the contact places with the soil mass, and not on the inside of the tunnel, where the soil volume is excavated. The shotcrete is modeled as a linear elastic material. The main parameter for the linear elastic materials in PLAXIS 3D tunnel is the Young’s modulus. The modulus for shotcrete has been evaluated by using the empirical formula suggested by American Concrete Institute which relates the Young’s modulus with the compression strength of the concrete:

$$E = 4900\sigma^{0.5} \tag{4.1}$$

Where σ is the 28-day compression strength of the concrete.

The final lining of the tunnels is actually not the main load carrying components in short term. They are designed for the long term since the shotcrete is degraded in time and it loses its load carrying capacity. The final lining is assumed to be reinforced concrete. After the K0 procedure, which is the initial phase, the phases of excavation and primary lining installation are modelled in a sequence as it would happen in site. The main idea behind the staged excavation modelling is to simulate the real construction procedure and thus take the arching effect and the effects of the sequential construction to the 3D model into account. After each of the excavation phase, a so-called nil step is used to regenerate equilibrium for the next calculation which reduces the instability of the model. Plastic calculations are executed in order to calculate the unfactored deformations and pressures to allow a fair comparison. The analyses have been made for excavation depth 35m and diameter 7m.

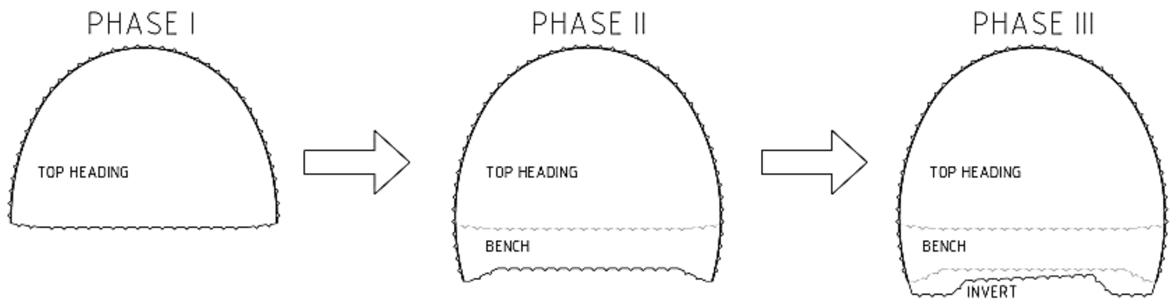

Figure 4.12: Phases of construction used for PLAXIS 3D modelling (Sinha, 1989)

The soil layers for different depths are specified along with soil condition parameters in Table 4.4. In the Table, parameters are defined for HS, MC and MCC model types for NATM and TBM construction method. The soil parameters depicted are: Dry and Wet Density, Initial Void Ratio, Cohesion (c_{ref}), Internal Friction (ϕ), Secant Modulus at 50% strength (E_{50}^{ref}), Modulus for Oedometer conditions (E_{oed}^{ref}), Unload-Reload Modulus (E_{ur}^{ref}), Cam Clay isotropic compression index (λ), Cam Clay isotropic swelling index (κ), Tangent of the critical state line (M), Young's Modulus (E'), Poisson's Ratio (υ).

In Table 4.5, the stage construction phases followed for numerical modelling in NATM and TBM construction methods are emphasized. And in Figure 4.13 and Figure 4.14, the deformation patterns in PLAXIS 3D for NATM method and TBM method (depth 35m and diameter 7m) for HS, MC and MCC models are depicted. The depth variation and diameter variation has been considered also in calculation which is not shown in this report.

Table 4.4: Soil Layers with Depth Range and Soil Condition Parameters using in NATM and TBM Methods

General Information								HS Model			MCC Model			MC Model	
SL. No.	Description	Depth Range (m)	Dry Density (kN/m^3)	Wet Density (kN/m^3)	Initial Void Ratio	c_{ref}	ϕ (deg)	E_{50}^{ref} (kN/m^2)	E_{oed}^{ref} (kN/m^2)	E_{ur}^{ref} (kN/m^2)	λ	κ	M	E’	υ
1	Lean Clay	4.5 – 5.0	17.50	21.04	0.60	48	10	$282.4*10^3$	$272.2*10^3$	$1.05*10^6$	0.40	0.10	0.90	$282.4*10^3$	0.20
2	Fat Clay	5.0-6.0	17.10	20.72	0.57	48	20	$282.4*10^3$	$222*10^3$	$1.01*10^6$	0.78	0.17	0.80	$282.4*10^3$	0.20
3	Lean Clay	6.0-7.5	17.50	21.04	0.60	48	10	$282.4*10^3$	$272.2*10^3$	$1.05*10^6$	0.41	0.10	0.90	$282.4*10^3$	0.20
4	Sandy Silt	7.5 – 9.0	18.70	21.71	0.44	30	25	$282.4*10^3$	$228.7*10^3$	$1.05*10^6$				$282.4*10^3$	0.20
5	Silt	9.0-12.0	18.67	21.76	0.45	30	27	$282.4*10^3$	$223*10^3$	$1.05*10^6$				$282.4*10^3$	0.20
6	Lean Clay	12.0 – 13.5	17.50	21.04	0.60	48	10	$282.4*10^3$	$272.2*10^3$	$1.05*10^6$	0.41	0.10	0.90	$282.4*10^3$	0.20
7	Silt	13.5 – 16.5	18.67	21.76	0.45	30	27	$282.4*10^3$	$223*10^3$	$1.05*10^6$				$282.4*10^3$	0.20
8	Sandy Silt	16.5 – 18	18.70	21.71	0.44	30	25	$282.4*10^3$	$225.7*10^3$	$1.05*10^6$				$282.4*10^3$	0.20
9	Silty Sand	18 – 21	17.85	20.22	0.32	30	30	$282.4*10^3$	$224.7*10^3$	$1.05*10^6$				$282.4*10^3$	0.20
10	Sandy Silt	21 – 22.5	18.70	21.71	0.44	30	25	$282.4*10^3$	$225.7*10^3$	$1.05*10^6$				$282.4*10^3$	0.20
11	Silty Sand	22.5 – 41	17.85	20.22	0.32	30	30	$282.4*10^3$	$224.7*10^3$	$1.059*10^6$				$282.4*10^3$	0.20
	Concrete		24		0.50				$31.11*10^6$					$28.0*10^6$	0.20

Table 4.5: Stage Construction Phases for both NATM and TBM

Method	Phase	Calculation Type	Action Taken
NATM	Initial	K0 procedure	
	Phase 1	Plastic	Crown excavation, bench excavation, invert excavation, Lining installed in the excavated portions
	Phase 2	Plastic	Crown excavation
	Phase 3	Plastic	Crown excavation
	Phase 4	Plastic	Bench excavation, lining installed in previous crown excavation
	Phase 5	Plastic	Bench excavation, lining installed in previous bench excavation
	Phase 6	Plastic	Invert excavation, lining installed in previous bench excavation
	Phase 7	Plastic	Crown excavation, lining installed in previous invert excavation
	Phase 8	Plastic	Crown excavation, lining installed in previous crown excavation
	Phase 9	Plastic	Bench excavation, lining installed in previous crown excavation
	Phase 10	Plastic	Bench excavation, lining installed in previous bench excavation
	Phase 11	Plastic	Invert excavation, lining installed in previous bench excavation
	Phase 12	Plastic	Invert excavation, lining installed in invert excavation
TBM	Initial	K0 procedure	
	Phase 1	Plastic	Excavation for TBM launching
	Phase 2	Plastic	Concrete Lining installation for the excavated portion, excavation stepping ahead, activation of negative interface, contract pressure, surface load
	Phase 3	Plastic	Excavation stepping ahead and concrete lining installation for previous excavation, activation of negative interface, contract pressure, surface load
	Phase 4	Plastic	Excavation stopped and concrete lining installation for previous excavation, activation of negative interface, contract pressure, surface load

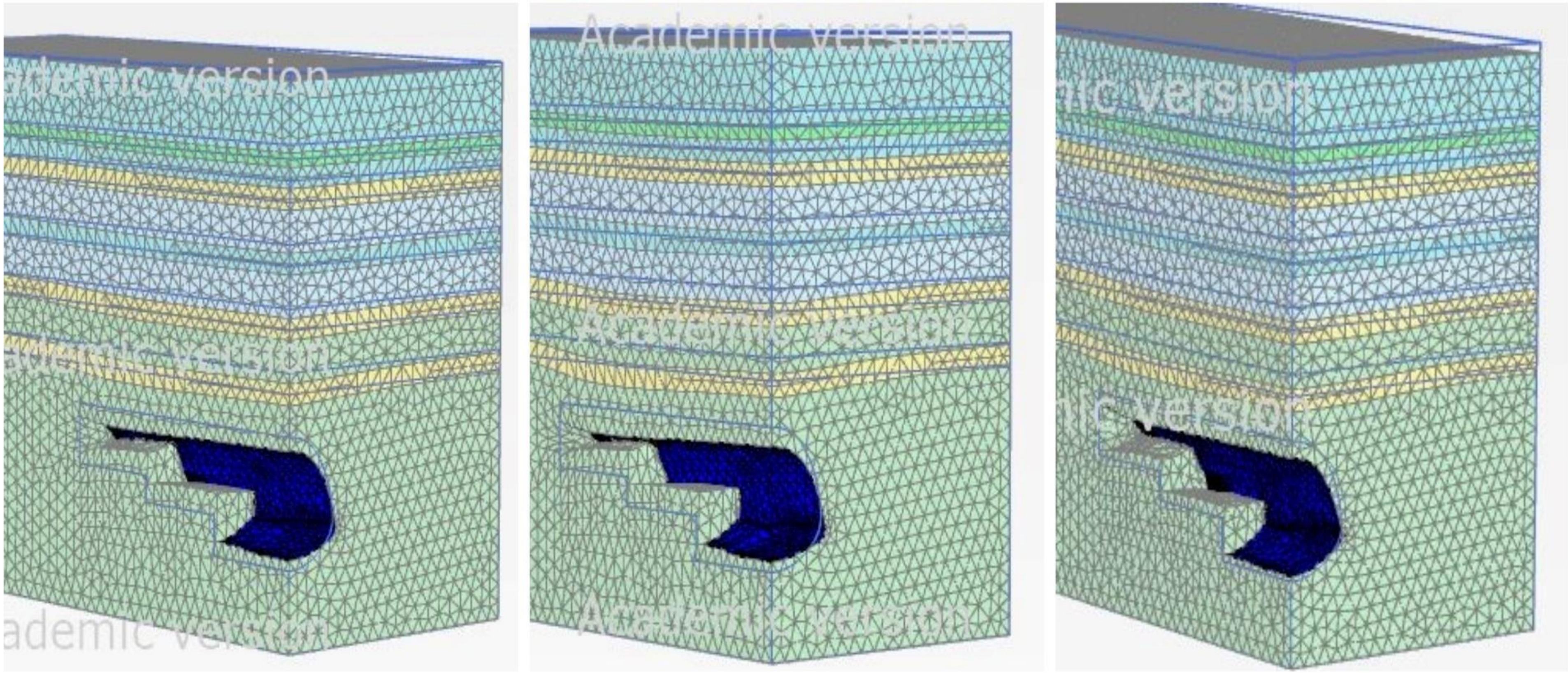

Figure 4.13: NATM Method (MC, MCC, HS model): Depth 35m and Diameter 7m

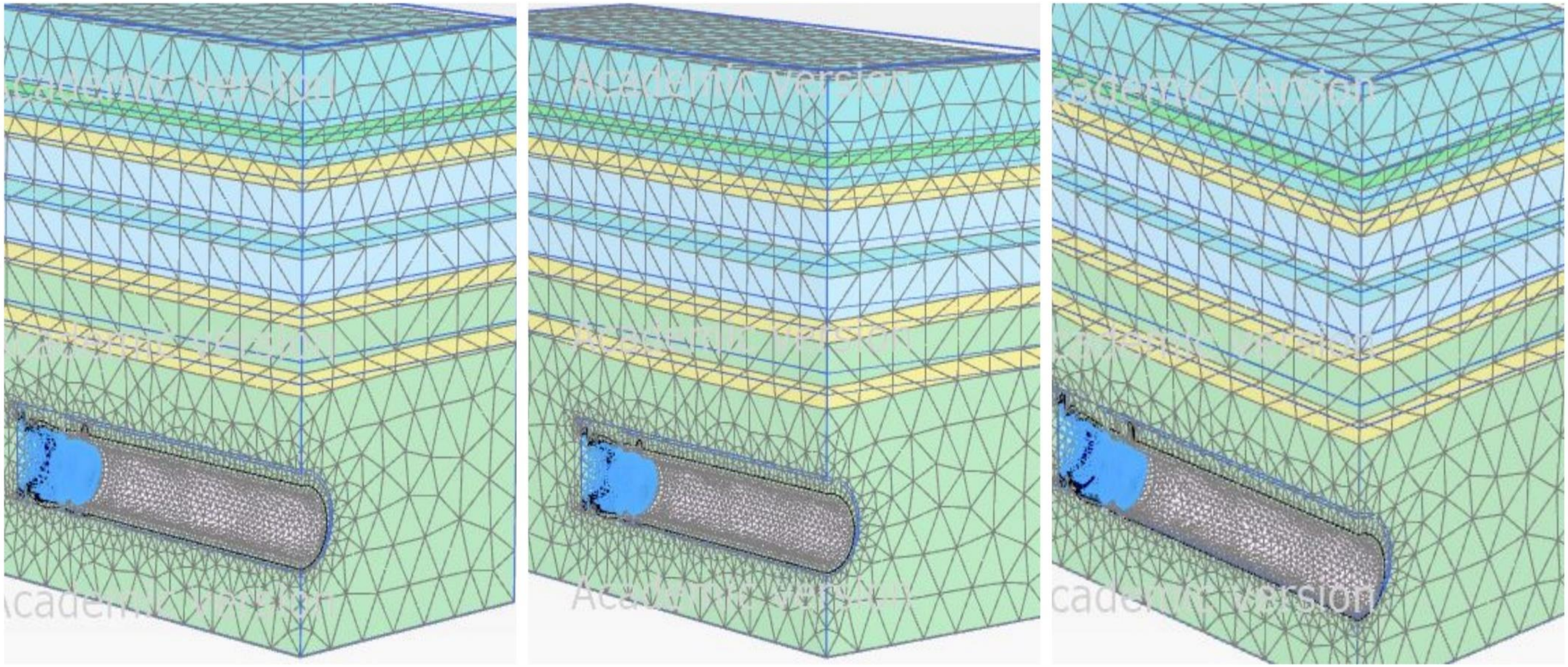

Figure 4.14: TBM Method (MC, MCC, HS model): Depth 35m and Diameter 7m

3.6 Effect of Meshing in Maximum Settlements for NATM and TBM Methods

FEA is the process of dividing geometry into smaller pieces (elements), applying loads and boundary conditions to those elements, and then solving the matrix equations assembled from the mesh. Theoretically, the more elements used in the model, the closer the results get to the actual behavior (as modeled), but it may take more computational time. It is found in Yaning Li and Tomasz Wierzbicki's research that the stress and strain fields have high gradients in the localization zone and the continuing application of the classical stress-strain relation in the localization zone is the cause for mesh size effects in Finite Element simulations. The smaller elements in a finer mesh can more accurately capture stress gradients across the element.

When the geometry model is fully defined the geometry has to be divided into the finite elements to perform finite element calculations. Very fine meshes should be avoided since this will lead to excessive calculation times. The basic soil elements of the 3D finite element mesh are the 10-node tetrahedral elements. The mesh generator in PLAXIS 3D requires a global meshing parameter that represents the target element size, l_e, which is based on the relevant element size factor (r_e). The values of this parameter for the element distributions predefined in the program are: very coarse = 2.0, coarse = 1.5, medium = 1.0, fine = 0.7, and very fine = 0.5. The exact number of elements depend on the shape of the geometry and optional local reinforcement settings. By default, the element distribution is set to Medium (1.0) but for this research, this value has been changed to coarse (1.5) and fine (0.7) also for comparing the analysis results for tunnel depth = 35.0m and diameter =7.0m for both NATM and TBM models.

From Figure 4.15 to Figure 4.20, different pattern of meshes (coarse, medium and fine) and effects in deformation for HS models of NATM and TBM construction methods are shown. Also, different patterns of meshes have been considered for MC and MCC models like this. And the element number, node number, and maximum settlement values for different mesh patterns are shown in Table 4.6 and Figure 4.21 with proper description.

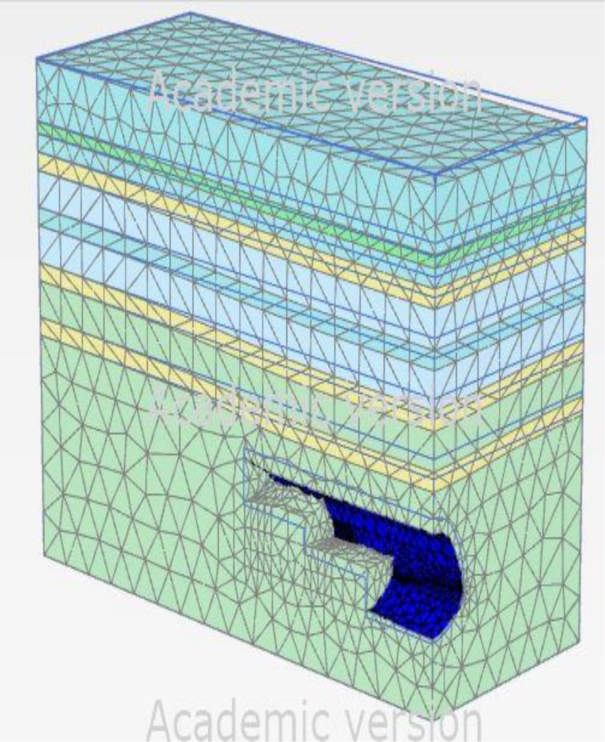

Figure 4.15: NATM method (HS Model): coarse mesh

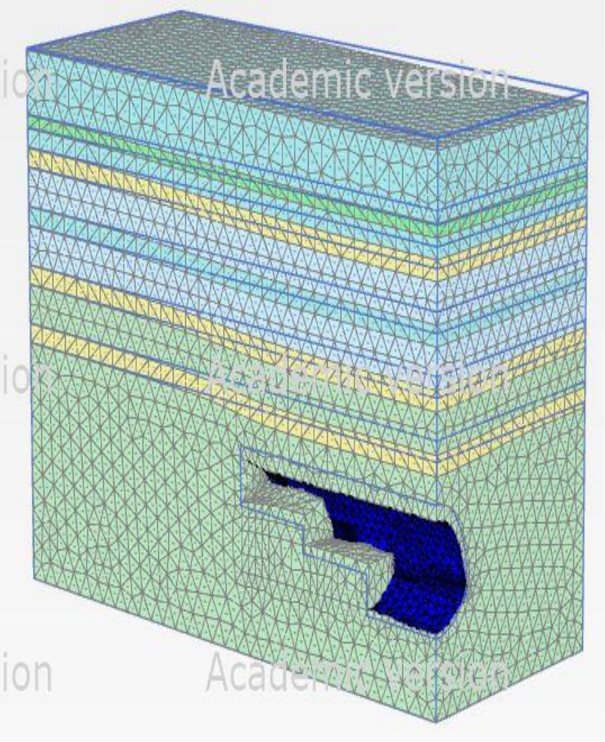

Figure 4.16: NATM method (HS Model): medium mesh

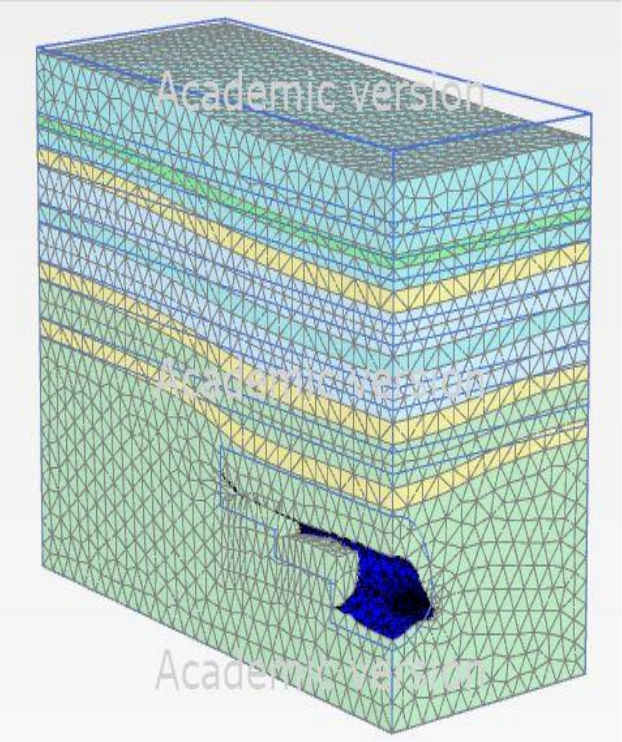

Figure 4.17: NATM method (HS Model): fine mesh

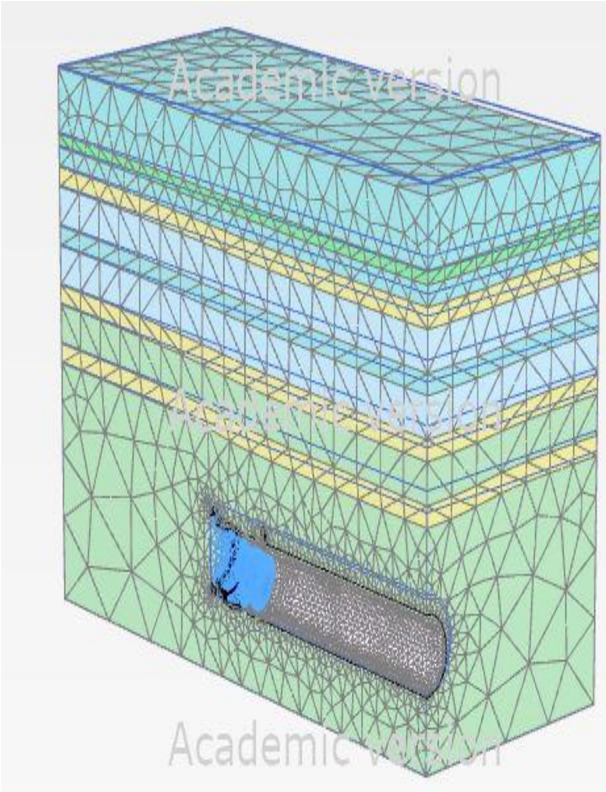

Figure 4.18: TBM method (HS Model): coarse mesh

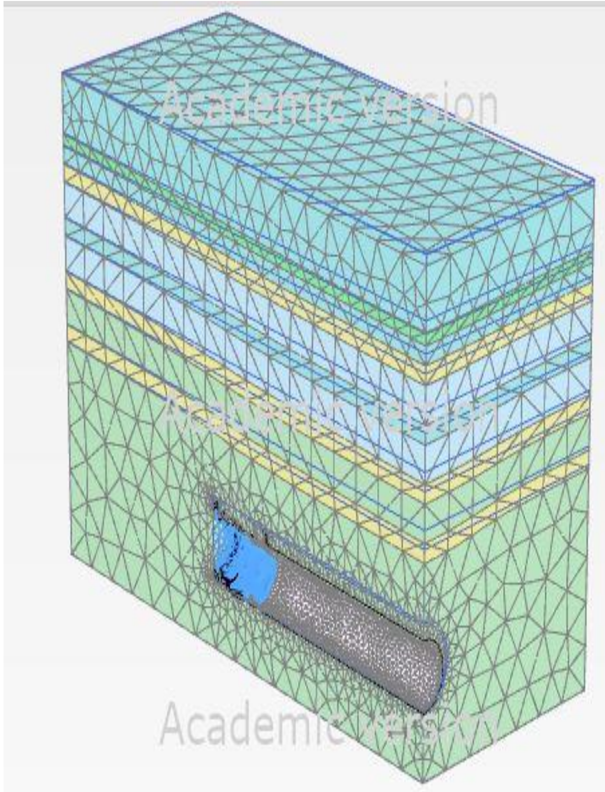

Figure 4.19: TBM method (HS Model): medium mesh

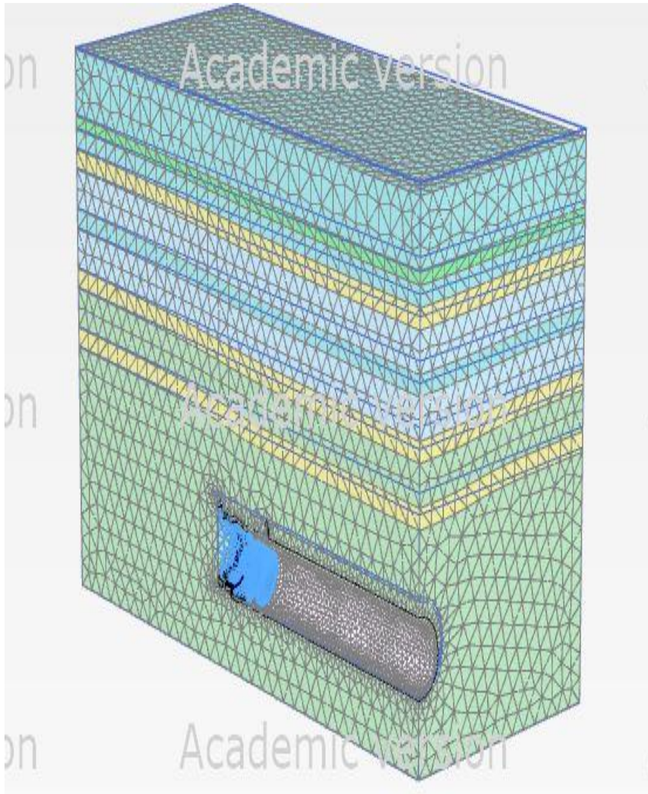

Figure 4.20: TBM method (HS Model): fine mesh

Table 4.6: Comparison of Settlement Values for Different Types of Mesh Sizes in NATM and TBM Methods

Method Type	Model Name	Meshing Type	Element No	Node No	Maximum Settlement (mm)
NATM	**HS**	Coarse	16987	24881	-23.72
		Medium	19246	28495	-20.98
		Fine	60145	87801	-19.22
	MCC	Coarse	16987	24881	-26.52
		Medium	19246	28495	-22.51
		Fine	60145	87801	-20.75
	MC	Coarse	16987	24881	-27.56
		Medium	19246	28495	-26.42
		Fine	60145	87801	-23.42
TBM	**HS**	Coarse	32439	51593	-19.53
		Medium	34047	54177	-18.54
		Fine	72882	110410	-18.46
	MCC	Coarse	32439	51593	-17.98
		Medium	34047	54177	-17.47
		Fine	72882	110410	-16.66
	MC	Coarse	32439	51593	-19.01
		Medium	34047	54177	-18.11
		Fine	72882	110410	-18.03

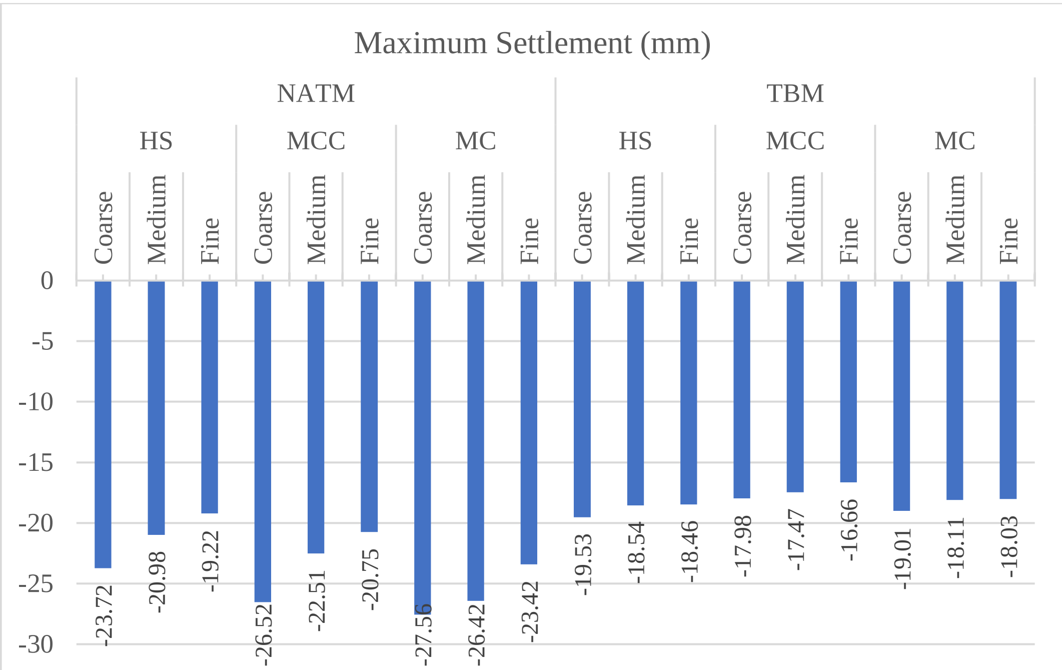

Figure 4.21: Effect on Maximum Settlement due to Refinements of Meshing for Different Models

It can be said from the above results that for the finer meshes, the settlement values are lower than the coarse and medium ones. It can be shown that the variation is more fluctuated for NATM models than TBM ones. For NATM models, the variation from medium mesh to coarse or fine mesh is about 10% whereas for TBM models, the variation value is almost 4% only. As the variation is considerable, medium mesh can be considered for models to save the running time.

3.7 Validation with Empirical Formulas for Inflexion Points and Maximum Settlement

Peck (1969) showed that a Gaussian distribution curve provided a reasonable fit to tunnel induced surface settlements. The value of inflexion point, i, is generally expressed as:

$$i = kZ_0 \tag{4.2}$$

Where Z_0 is the tunnel axis depth and K is a dimensionless empirical constant referred to as the trough width parameter. Values of K for Gaussian curves fitted to surface settlement data have been found to be close to 0.5 for tunnels in undrained clay, and typically range between 0.25 and 0.45 for tunnels in sands and gravels. Mair (1993) showed that subsurface settlement troughs in undrained clays can also be fitted well with a Gaussian curve, and that the value of i decreases approximately linearly with depth at a slope of -0.325.

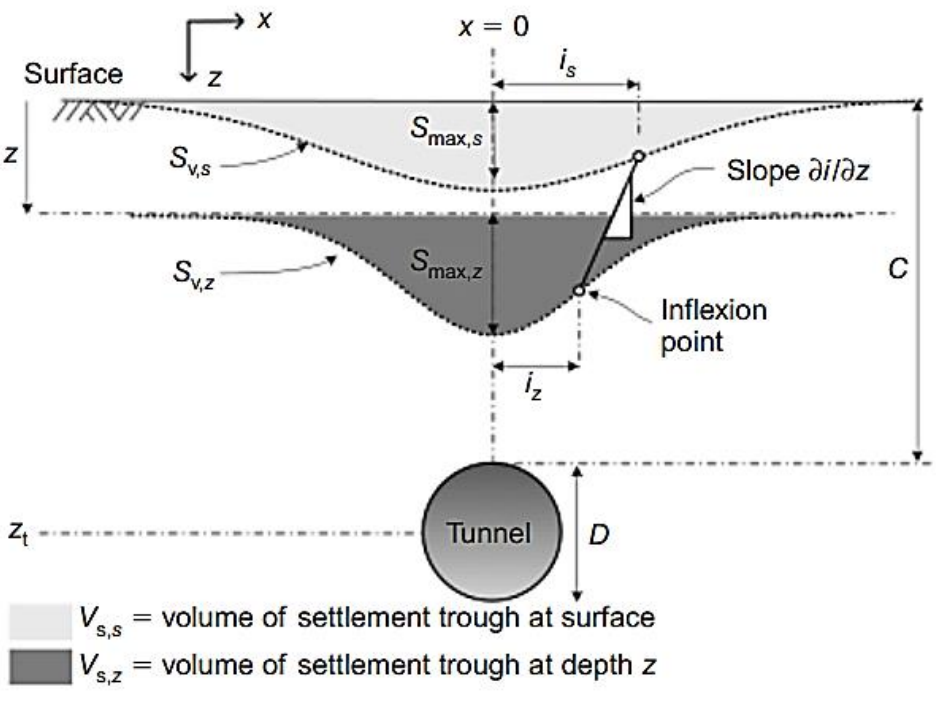

Figure 4.22: Greenfield Settlement Trough (Peck, 1969)

The tunnel excavation methods simulated in PLAXIS 3D and the settlement values from the analyses are validated with empirical formulas explained in different researches. These empirical formulas are applicable for TBM methods only. In numerical analyses, depth variations (30m, 32m and 35m) and diameter variations (5.0m, 6.0m, 7.0m) have been considered for TBM method to validate the analysis.

The empirical formula considered for validation are:

SL. No.	Researchers	Empirical Relations
1	Peck, 1969	$\frac{i}{R} = (\frac{Z_0}{2R})^n \ (n = 0.8 - 1)$
2	Clough & Schmidt, 1981	$\frac{i}{R} = (\frac{Z_0}{2R})^n \ (n = 0.8)$
3	Atkinson & Potts, 1977	$i = 0.25\ (1.5Z_0 + 0.5R)$
4	O'Reily & New, 1982	$i = 0.43Z_0 + 1.1$
5	Mair & Taylor, 1999	$i = (0.4 - 0.5)Z_0 + 1.1$

Following the empirical formulas, distance of inflexion point from center for different models at different diameters and depths are calculated and compared with PLAXIS value in Table 4.7. Also, maximum settlement values and settlement values at inflexion point are determined from PLAXIS models. From Figure 4.23 and Figure 4.25, comparison of distance of point of inflexions from centers calculated from different empirical formulas for different depths and diameters are emphasized in three graphs for MC, MCC, and HS models respectively. Transverse settlement trough pattern for the half tunnel segment for three types of models with variation of depths and radiuses are shown in Figure 4.26 and Figure 4.27 respectively. The pattern is then compared with the empirical standard Gaussian curve to validate the shape of the curve. Effect on maximum settlement at varying depths and radius are emphasized clearly in Figure 4.28 and Figure 4.29 respectively. Also, effect on distance of inflexion point from center at varying depths and radius are shown effectively by graphical representation in Figure 4.30 and Figure 4.31 respectively.

According to the empirical formula of different researchers, O'Reily & New relationship has the best behavior of surface settlement in transverse section which follows the Gaussian distribution. Based on this assumption, Gaussian curve is fitted to the data monitoring outputs.

As a result, the average deviated values between the numerical result for obtaining trough width parameter, i, and the empirical result of O'Reily & New are obtained as 5.38%, 3.84% and 6.39% for MC, MCC and HS models respectively. These deviations are very less than other empirical relations described in researches. This difference is due to the fact that other researchers used the probability function in the estimation of inflexion point location which may not necessarily fit with the present results.

The transverse profile of the surface settlement of numerical results obtained from the MC, MCC and HS models are compared with the empirical relationship's graphs. It can be clearly seen that results of the MCC model have the best fit to the data points. The MCC model is considered to be suitable for this type of clay-based soils. To predict the surface settlement, the MCC model is proposed in soft clay with a low over consolidation ratio or normal consolidation similar to the soil in this site. In other words, where the shear modulus is independent of the shear strain, the surface settlement has a wide and shallow profile. Since the over consolidation clay exhibits non-linear stress strain behavior at the small strain prior to crossing the plastic yielding, it is very important to consider the behavior of these kinds of soils under small strain condition. Nevertheless, the shear modulus in the MC model is constant and the shear strain doesn't change with shear stress; this is probably the main reason for the difference between the results. The semi empirical method does not yield a precise prediction of ground settlement and this approach must be used only to give a general overview to designers. The implementation of MCC model is suggested in clayey soils as it has a relatively precise prediction of the surface displacement in clayey soil (normally consolidated or low OCR value). At depth, or as volume loss is increased, the fit of the Gaussian curve becomes less good.

Tunnel diameter has significant effect on the magnitude of the ground settlement, as a smaller tunnel tends to cause lesser ground settlements than larger tunnel. Distance of inflexion point from center tends to be smaller for increasing tunnel diameter. The stress redistribution from overburden soil must be the reason for the possibility of influencing zone below the tunnel especially of smaller diameter. This effect reduces when the tunnel diameter increases. The self-weight of the tunnel and grains redistribution may increase the settlement in loose sand below the bottom of the tunnel when the tunnel diameter increases.

And for larger depth, maximum settlement decreases than smaller depth as well as distance of inflexion point from center decreases for increasing tunnel diameter. This variation in settlement due to the depth variation is because in elastic homogeneous medium, the upward movement of the soil is due to relief effect of the excavated soil above the tunnel but this movement decreases as depth increases. As the soil is remote from concentration of loading, the settlement value is larger in lesser depth and smaller in greater depth.

It can be concluded after analyzing the results that the total settlement decreases with an increase in depth of the tunnel (almost 11% decrement for every 5m increment of depth) and increases with an increase in diameter (almost 20% increment for every 1m increment of diameter). Increasing the TBM depth results to increase around 4% in distance of inflexion point from center whereas increasing in radius results to decrease around 5% in inflexion point distance from center of the tunnel.

Table 4.7: Calculation of distance of Inflexion Point from center and Settlement values (maximum and at inflexion point) for different models, diameters and depths

	Empirical Formula Researchers	Depth, Z_0 (m)	Radius, R (m)	Distance of Inflexion Point (m)	Distance of Inflexion Point from PLAXIS (m)	Deviated value (%)	Maximum Settlement (mm)	Settlement at Inflexion Point (mm)
MC Model	Depth considered as 30.0m, Radius considered as 3.50m							
	Peck, 1969	30	3.50	8.73	16.57	70.44	-20.85	-6.00
	Clough & Schmidt, 1981	30	3.50	8.73	16.57	39.81	-20.85	-6.00
	Atkinson & Potts, 1977	30	3.50	11.69	16.57	19.40	-20.85	-6.00
	O'Reilly & New, 1982	30	3.50	14.00	16.57	3.45	-20.85	-6.00
	Mair & Taylor, 1999	30	3.50	12.00	16.57	17.24	-20.85	-6.00
	Depth considered as 32.0m, Radius considered as 3.50m							
	Peck, 1969	32	3.50	9.19	15.85	71.16	-19.53	-6.00
	Clough & Schmidt, 1981	32	3.50	9.19	15.85	42.02	-19.53	-6.00
	Atkinson & Potts, 1977	32	3.50	12.44	15.85	21.53	-19.53	-6.00
	O'Reilly & New, 1982	32	3.50	14.86	15.85	6.25	-19.53	-6.00
	Mair & Taylor, 1999	32	3.50	12.80	15.85	19.24	-19.53	-6.00
	Depth considered as 35.0m, Radius considered as 3.50m							
	Peck, 1969	35	3.50	9.87	14.50	69.82	-18.11	-6.00
	Clough & Schmidt, 1981	35	3.50	9.87	14.50	40.42	-18.11	-6.00
	Atkinson & Potts, 1977	35	3.50	13.56	14.50	18.15	-18.11	-6.00
	O'Reilly & New, 1982	35	3.50	16.15	14.50	2.53	-18.11	-6.00
	Mair & Taylor, 1999	35	3.50	14.00	14.50	15.51	-18.11	-6.00
	Depth considered as 35.0m, Radius considered as 3.00m							

	Empirical Formula Researchers	Depth, Z_0 (m)	Radius, R (m)	Distance of Inflexion Point (m)	Distance of Inflexion Point from PLAXIS (m)	Deviated value (%)	Maximum Settlement (mm)	Settlement at Inflexion Point (mm)
	Peck, 1969	35	3.00	9.87	16.99	65.67	-16.7	-5.00
	Clough & Schmidt, 1981	35	3.00	9.87	16.99	41.89	-16.7	-5.00
	Atkinson & Potts, 1977	35	3.00	13.50	16.99	20.54	-16.7	-5.00
	O'Reilly & New, 1982	35	3.00	16.15	16.99	4.94	-16.7	-5.00
	Mair & Taylor, 1999	35	3.00	14.00	16.99	17.60	-16.7	-5.00
	Depth considered as 35.0m, Radius considered as 2.50m							
	Peck, 1969	35	2.50	9.87	17.89	60.87	-14.27	-4.00
	Clough & Schmidt, 1981	35	2.50	9.87	17.89	44.82	-14.27	-4.00
	Atkinson & Potts, 1977	35	2.50	13.44	17.89	24.89	-14.27	-4.00
	O'Reilly & New, 1982	35	2.50	16.15	17.89	9.73	-14.27	-4.00
	Mair & Taylor, 1999	35	2.50	14.00	17.89	21.74	-14.27	-4.00
	Depth considered as 30.0m, Radius considered as 3.50m							
MCC Model	Peck, 1969	30	3.50	8.73	16.27	70.00	-19.66	-9.00
	Clough & Schmidt, 1981	30	3.50	8.73	16.27	38.90	-19.66	-9.00
	Atkinson & Potts, 1977	30	3.50	11.69	16.27	18.18	-19.66	-9.00
	O'Reilly & New, 1982	30	3.50	14.00	16.27	1.99	-19.66	-9.00
	Mair & Taylor, 1999	30	3.50	12.00	16.27	15.99	-19.66	-9.00
	Depth considered as 32.0m, Radius considered as 3.50m							
	Peck, 1969	32	3.50	9.19	15.19	69.91	-18.93	-8.00
	Clough & Schmidt, 1981	32	3.50	9.19	15.19	39.51	-18.93	-8.00
	Atkinson & Potts, 1977	32	3.50	12.44	15.19	18.13	-18.93	-8.00
	O'Reilly & New, 1982	32	3.50	14.86	15.19	2.18	-18.93	-8.00
	Mair & Taylor, 1999	32	3.50	12.80	15.19	15.74	-18.93	-8.00
	Depth considered as 35.0m, Radius considered as 3.50m							
	Peck, 1969	35	3.50	9.87	14.28	69.27	-17.47	-8.00
	Clough & Schmidt, 1981	35	3.50	9.87	14.28	39.32	-17.47	-8.00
	Atkinson & Potts, 1977	35	3.50	13.56	14.28	16.64	-17.47	-8.00
	O'Reilly & New, 1982	35	3.50	16.15	14.28	0.74	-17.47	-8.00
	Mair & Taylor, 1999	35	3.50	14.00	14.28	13.95	-17.47	-8.00
	Depth considered as 35.0m, Radius considered as 3.00m							
	Peck, 1969	35	3.00	9.87	17.01	65.71	-16.25	-7.00

	Empirical Formula Researchers	Depth, Z_0 (m)	Radius, R (m)	Distance of Inflexion Point (m)	Distance of Inflexion Point from PLAXIS (m)	Deviated value (%)	Maximum Settlement (mm)	Settlement at Inflexion Point (mm)
	Clough & Schmidt, 1981	35	3.00	9.87	17.01	41.96	-16.25	-7.00
	Atkinson & Potts, 1977	35	3.00	13.50	17.01	20.63	-16.25	-7.00
	O'Reilly & New, 1982	35	3.00	16.15	17.01	5.06	-16.25	-7.00
	Mair & Taylor, 1999	35	3.00	14.00	17.01	17.70	-16.25	-7.00
	Depth considered as 35.0m, Radius considered as 2.50m							
	Peck, 1969	35	2.50	9.87	17.79	60.65	-13.95	-6.00
	Clough & Schmidt, 1981	35	2.50	9.87	17.79	44.50	-13.95	-6.00
	Atkinson & Potts, 1977	35	2.50	13.44	17.79	24.47	-13.95	-6.00
	O'Reilly & New, 1982	35	2.50	16.15	17.79	9.22	-13.95	-6.00
	Mair & Taylor, 1999	35	2.50	14.00	17.79	21.30	-13.95	-6.00
HS Model	Depth considered as 30.0m, Radius considered as 3.50m							
	Peck, 1969	30	3.50	8.73	16.92	70.67	-19.57	-9.00
	Clough & Schmidt, 1981	30	3.50	8.73	16.92	40.27	-19.57	-9.00
	Atkinson & Potts, 1977	30	3.50	11.69	16.92	20.00	-19.57	-9.00
	O'Reilly & New, 1982	30	3.50	14.00	16.92	4.18	-19.57	-9.00
	Mair & Taylor, 1999	30	3.50	12.00	16.92	17.86	-19.57	-9.00
	Depth considered as 32.0m, Radius considered as 3.50m							
	Peck, 1969	32	3.50	9.19	15.61	70.72	-18.77	-9.00
	Clough & Schmidt, 1981	32	3.50	9.19	15.61	41.14	-18.77	-9.00
	Atkinson & Potts, 1977	32	3.50	12.44	15.61	20.34	-18.77	-9.00
	O'Reilly & New, 1982	32	3.50	14.86	15.61	4.82	-18.77	-9.00
	Mair & Taylor, 1999	32	3.50	12.80	15.61	18.02	-18.77	-9.00
	Depth considered as 35.0m, Radius considered as 3.50m							
	Peck, 1969	35	3.50	9.87	14.61	70.45	-18.54	-9.00
	Clough & Schmidt, 1981	35	3.50	9.87	14.61	41.65	-18.54	-9.00
	Atkinson & Potts, 1977	35	3.50	13.56	14.61	19.84	-18.54	-9.00
	O'Reilly & New, 1982	35	3.50	16.15	14.61	4.55	-18.54	-9.00
	Mair & Taylor, 1999	35	3.50	14.00	14.61	17.25	-18.54	-9.00
	Depth considered as 35.0m, Radius considered as 3.00m							
	Peck, 1969	35	3.00	9.87	17.44	66.55	-17.04	-10.00
	Clough & Schmidt, 1981	35	3.00	9.87	17.44	43.39	-17.04	-10.00

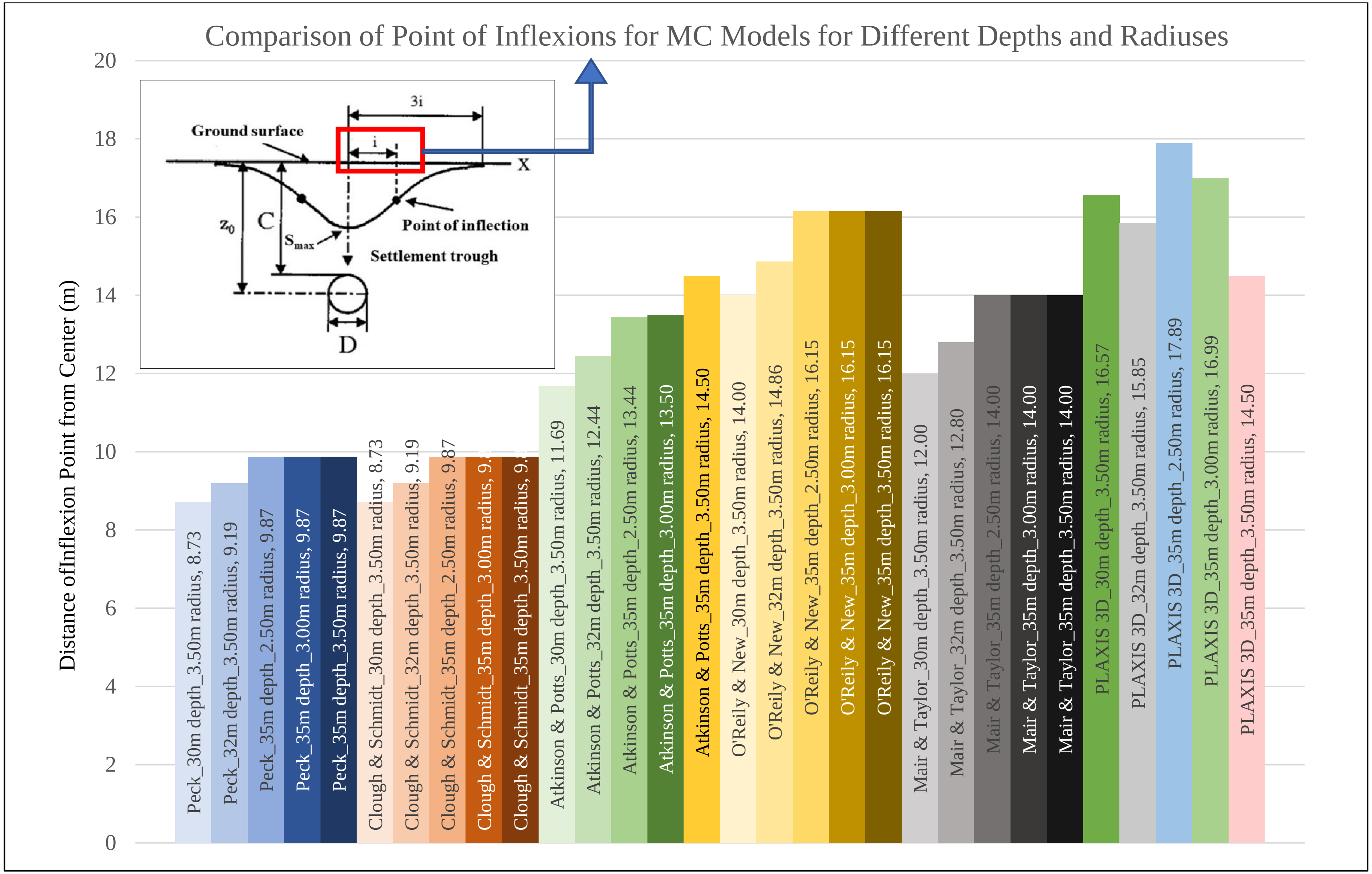

Figure 4.23: Comparison of Distance of Inflexion Points for MC Models for Different Depths (30m, 32m, 35m) and Different Radiuses (2.5m, 3m, 3.5m)

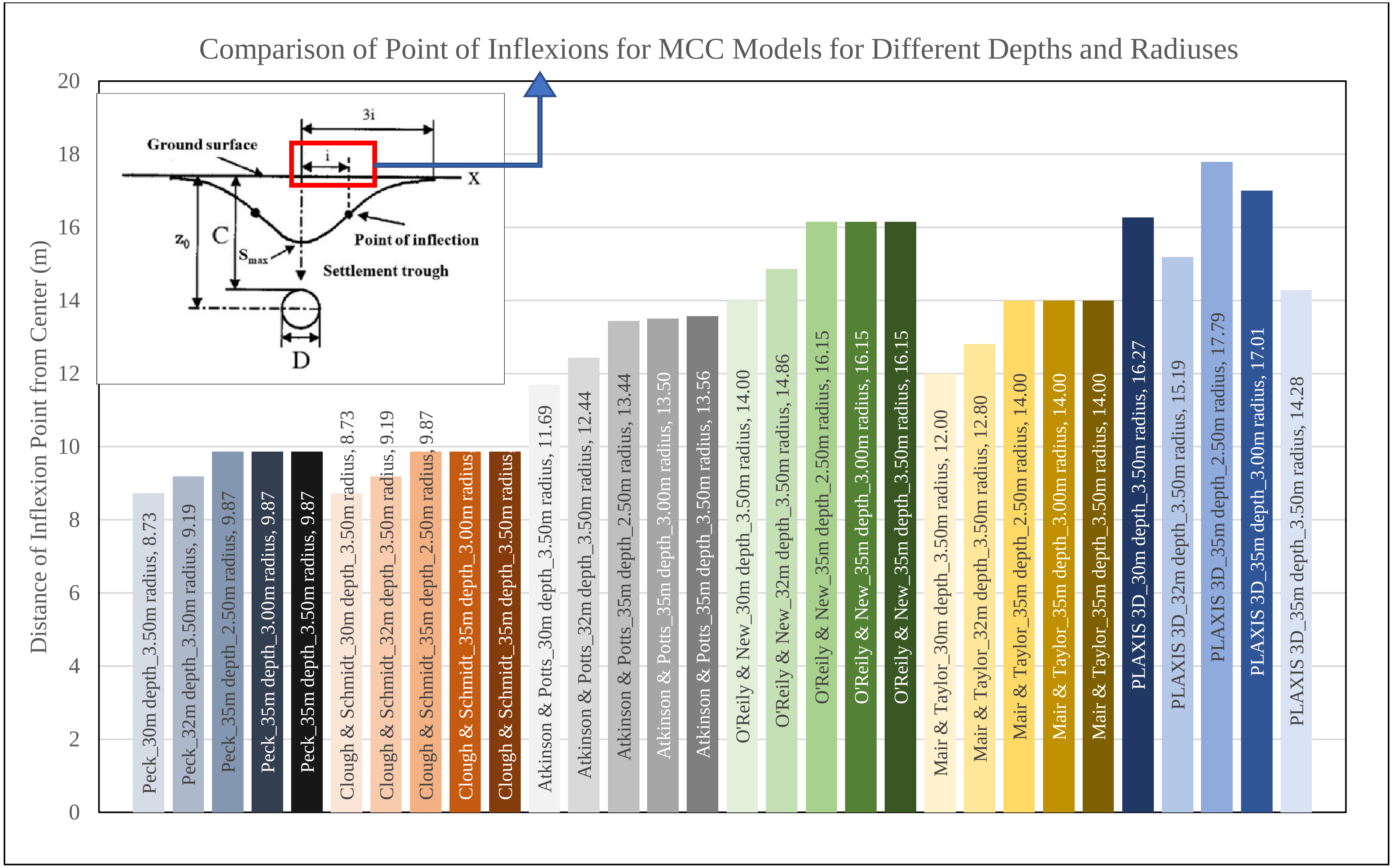

Figure 4.24: Comparison of Distance of Inflexion Points for MCC Models for Different Depths (30m, 32m, 35m) and Different Radiuses (2.5m, 3m, 3.5m)

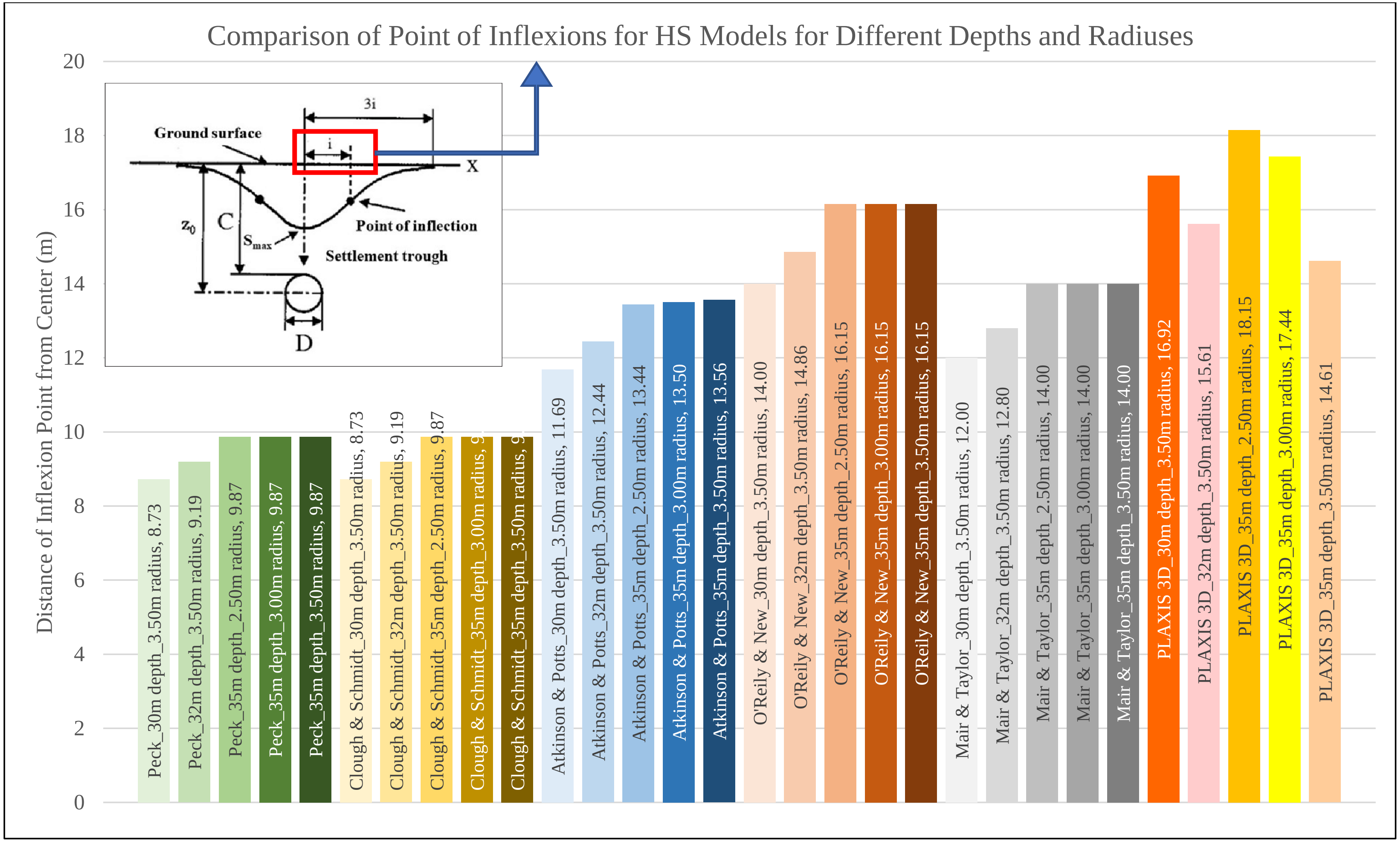

Figure 4.25: Comparison of Distance of Inflexion Points for HS Models for Different Depths (30m, 32m, 35m) and Different Radiuses (2.5m, 3m, 3.5m)

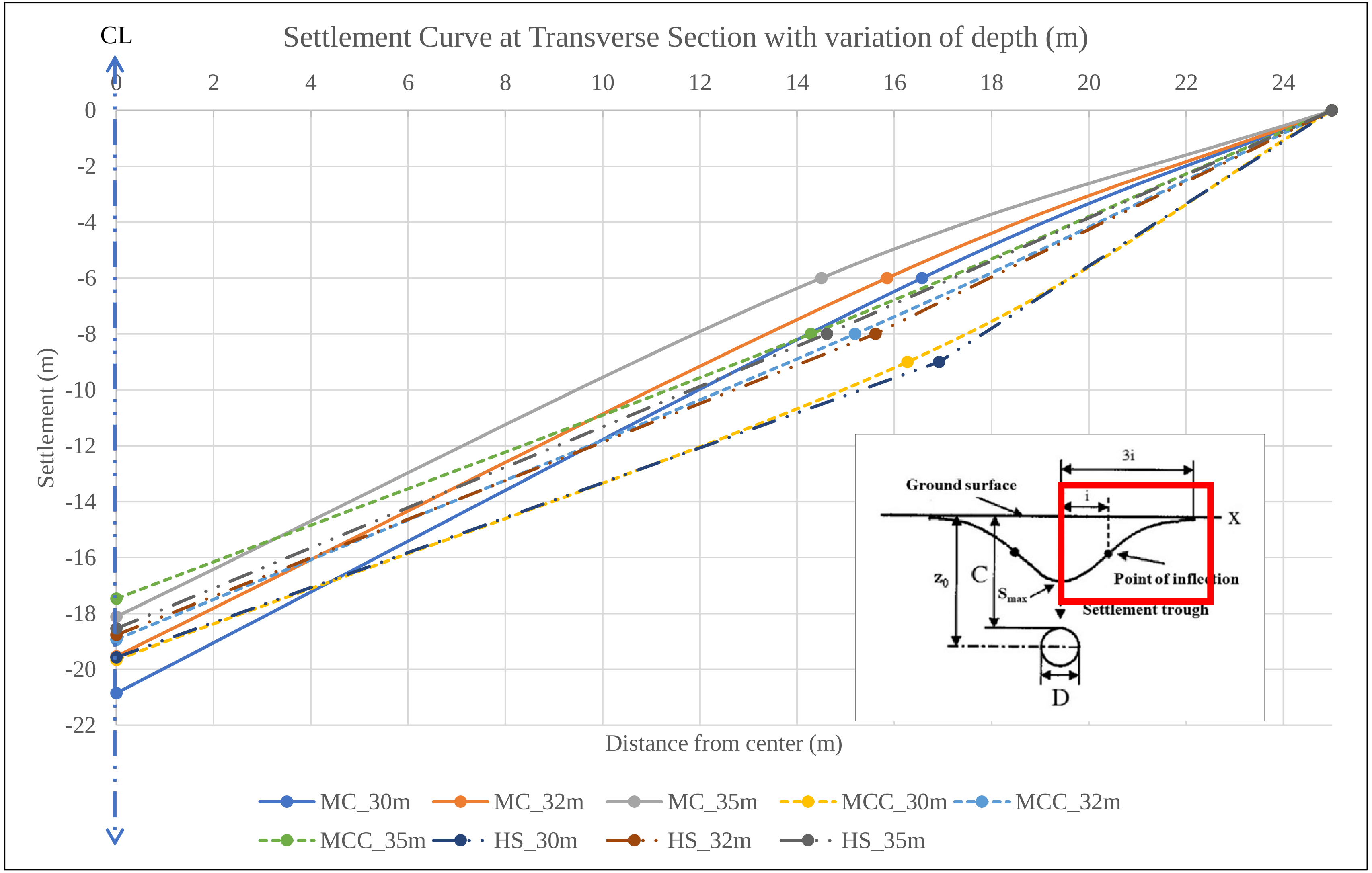

Figure 4.26: Transverse Settlement Trough Pattern with variation of depth (30m, 32m, 35m) for MC, MCC and HS Models

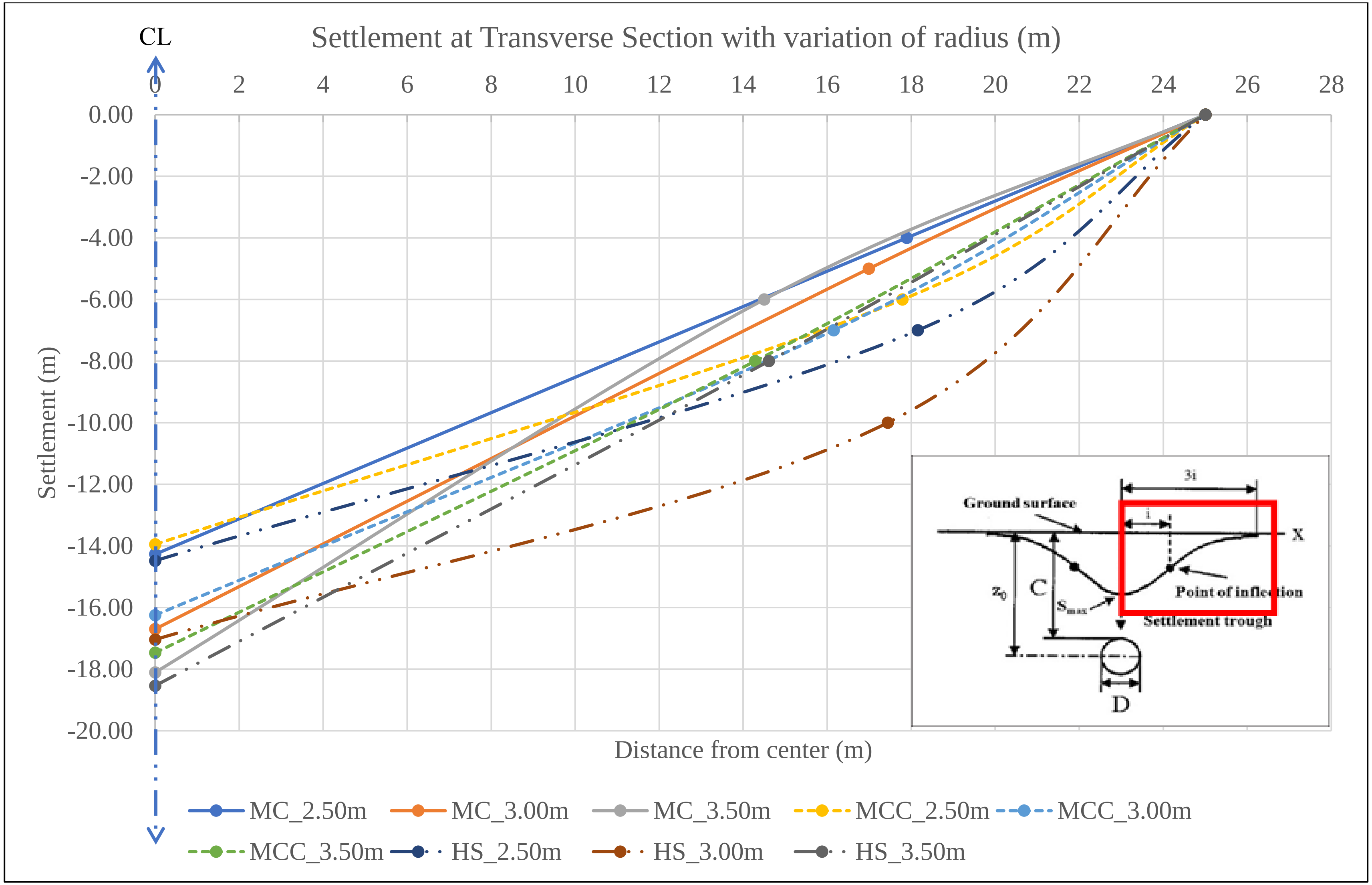

Figure 4.27: Transverse Settlement Trough Pattern with variation of radius (2.50m, 3.0m, 3.50m) for MC, MCC and HS Models

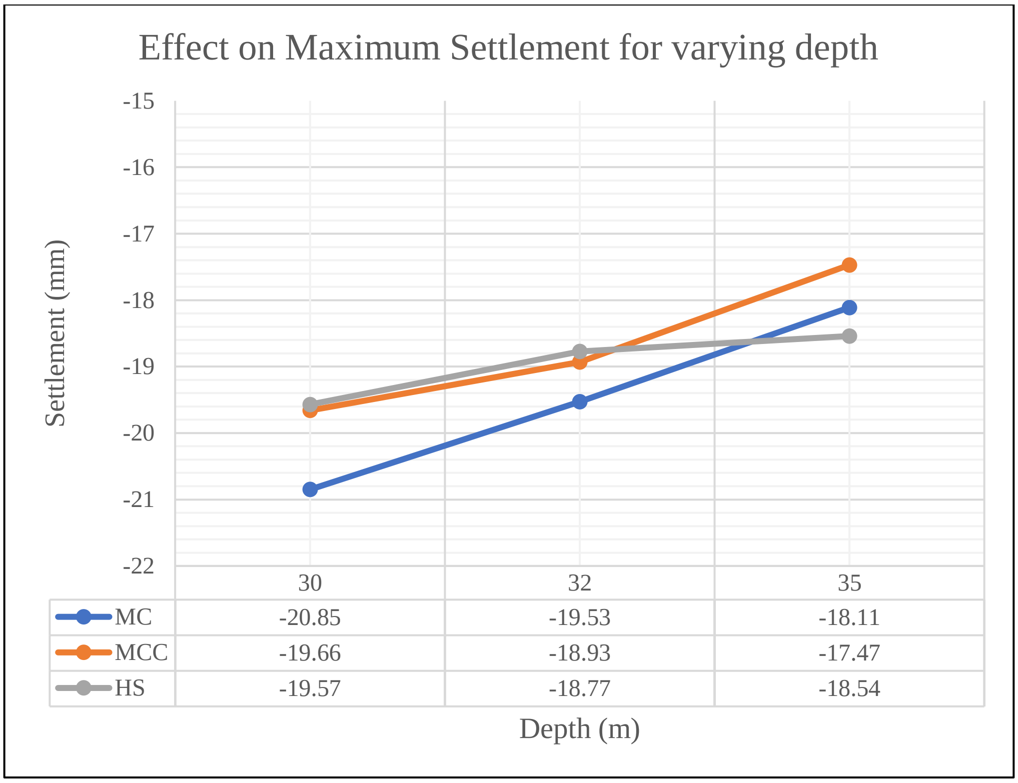

Figure 4.28: Effect on Maximum Settlement for increasing of depth (30m, 32m and 35m)

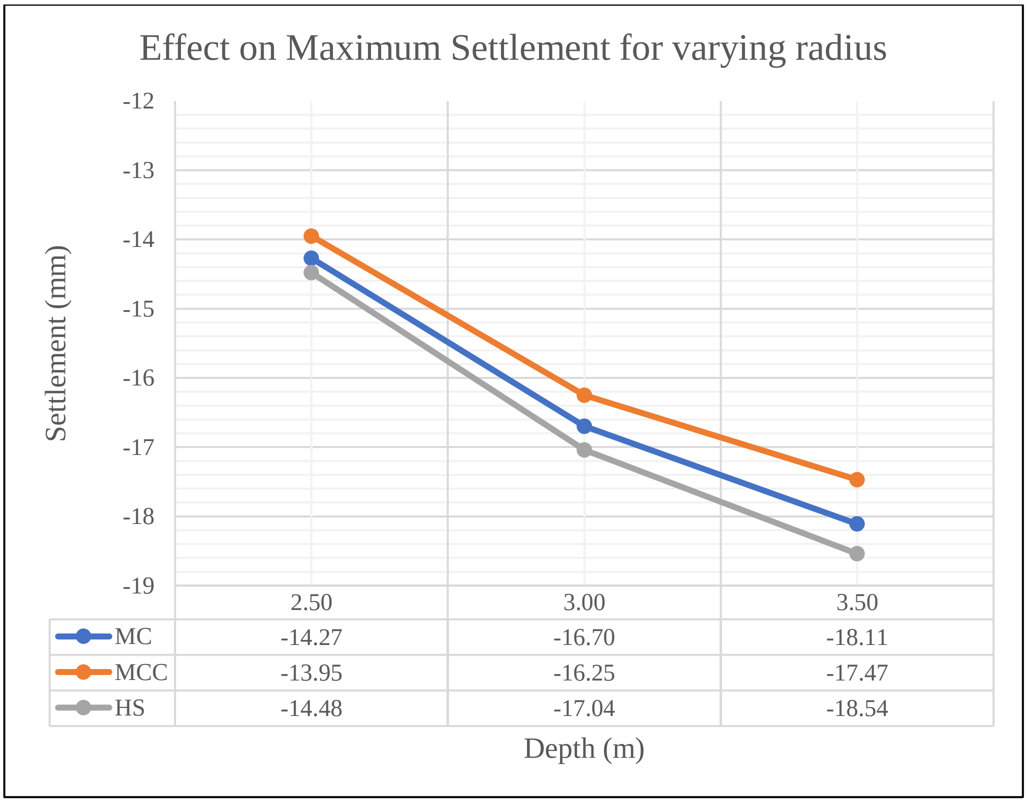

Figure 4.29: Effect on Maximum Settlement for increasing of radius (2.50m, 3.00m and 3.50m)

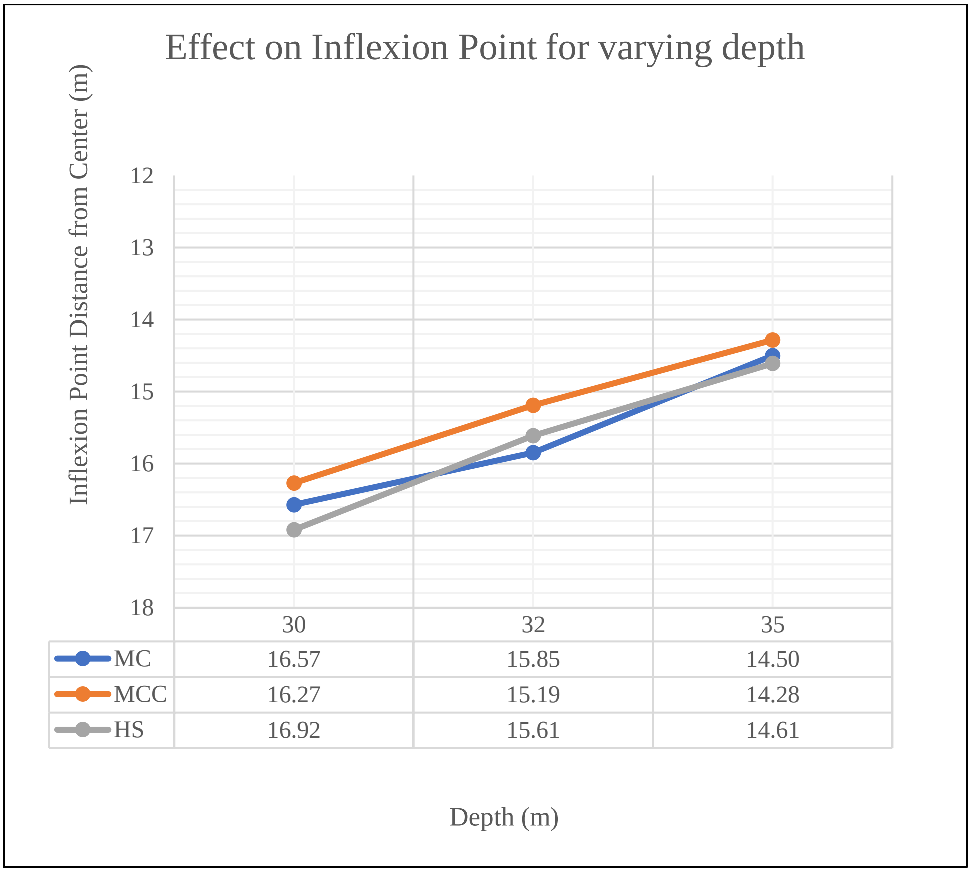

Figure 4.30: Effect on Inflexion Point for increasing of depth (30m, 32m and 35m)

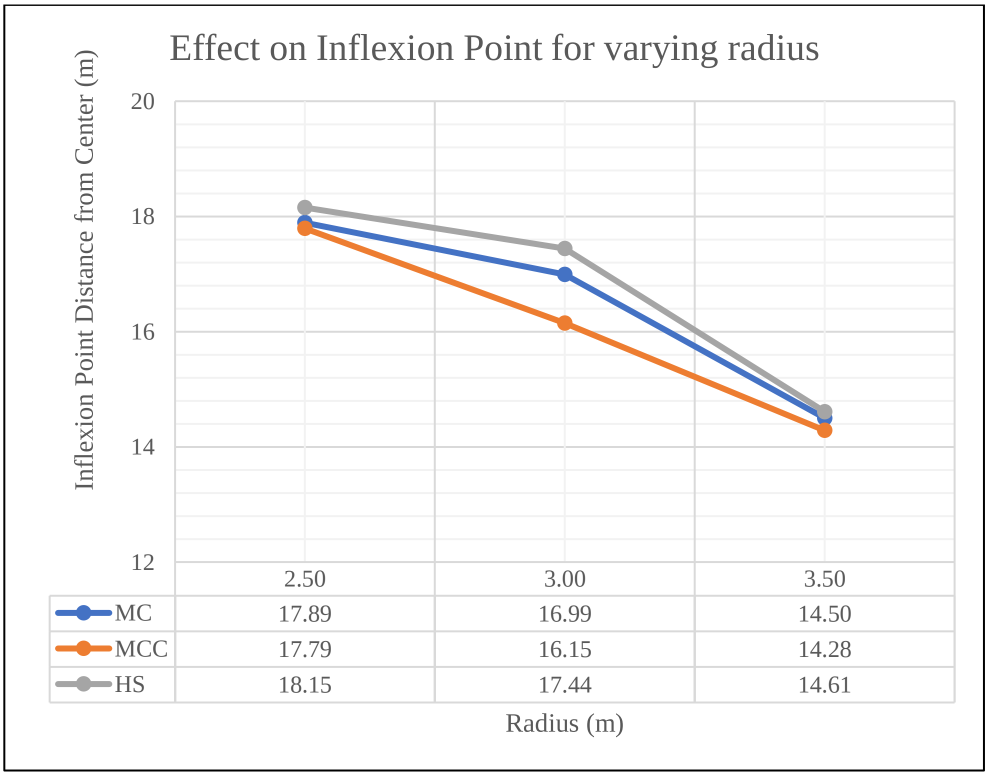

Figure 4.31: Effect on Inflexion Point for increasing of radius (2.50m, 3.00m and 3.50m)

3.8 Validation with Empirical Formulas for Vertical Settlement

For drained soils, such as sands and gravels, the volume of the soil is not constrained, and shearing causes contraction and dilation to occur. This causes the volume of the settlement trough, Vs, to vary with depth (Vs,s ≠ Vs,z), and means that an assessment of volume loss based on surface measurements will not provide an entirely accurate measurement of subsurface volume loss. In order to analyze trends in settlement trough shape, a curve must be fitted to settlement data. The use of a curve that gives a good fit to settlement data is important in order to perform an effective analysis of trough shape, and when evaluating the effect of tunnelling on nearby infrastructure or buildings. It has been reported that the Gaussian curve does not always provide a good fit to settlement trough data. Jacobsz (2004) used a slightly different version of the Gaussian curve that, like the Gaussian curve, has two degrees of freedom, represented by S_{max} and i. Celestino and Vorster used curves with one additional degree of freedom compared with the Gaussian curve, thus giving more flexibility to the shape of the curve.

Vertical settlement values derived from PLAXIS 3D and different empirical formula and also the deviation percentages for both NATM and TBM methods are shown in Table 4.8. In Figure 4.32, these values are depicted in graphical representation. Maximum settlements for NATM and TBM methods from PLAXIS 3D for different types of models are compared in Figure 4.33. Transverse settlement trough curves for both methods considering 35m depth and 7m diameter derived from PLAXIS 3D are shown in Figure 4.34. Longitudinal settlements and lateral settlements for both methods from PLAXIS 3D are emphasized in Figure 4.35 and Figure 4.36.

It can be evaluated from the result that the deviation percentages of vertical settlement from PLAXIS with Peck, Peck & Schmidt and Jacobsz formula are almost 10% and 34% for TBM and NATM respectively. Chow's formula shows much less values than other empirical formulas (Peck, Peck & Schmidt, and Jacobsz), which can indicate that this formula is not appropriate for clayey soil. Also, the Jacobsz formula (2004) shows a good agreement and approximately close value compared to the settlement values obtained from PLAXIS 3D (for NATM, the variation is about 2 ~ 16% and for TBM 3 ~ 10%.

From comparison of longitudinal and lateral settlement, it can be shown that NATM method shows more settlement (10 to 30% more) than TBM method as it includes blast technique which induce more ground surface variation than TBM machine advancement, especially in soft soil. In settlement at transverse sections for both NATM and TBM, MCC model shows the best fit curve in Gaussian distribution.

Table 4.8: Comparison of Settlements of PLAXIS with Empirical Formulas (for Depth 35m and Diameter 7m)

Method Type	Model Type	Maximum Settlement, Smax (mm)	Lateral Settlement, Ux (mm)	Longitudinal Settlement, Ux (mm)	Vertical Settlement, Uz (mm)	Inflexion Point from PLAXIS (m)	Uz according to Peck & Schmidt formula (mm)	Uz according to Peck formula (mm)	Uz according to Jacobsz formula (mm)	Uz according to Chow formula (mm)	U at Inflexion Point (mm)	Deviation of Uz value from Empirical formula to PLAXIS (%)
NATM	MC	-26.42	-5.818	-13.11	-12.31	9.85	-9.35	-16.01	-18.68	-1.94	-8.00	24.069
	HS	-20.98	-2.754	-11.24	-15.12	16.58	-12.50	-12.71	-14.83	-1.71	-9.00	17.343
	MCC	-22.51	-7.36	-10.34	-16.61	13.16	-10.58	-13.64	-15.91	-1.83	-11.00	36.280
TBM	MC	-18.11	-0.35	-8.67	-14.07	15.19	-12.49	-10.97	-12.80	-2.09	-6.00	11.218
	HS	-18.54	-0.85	-9.53	-13.53	16.92	-12.73	-11.24	-13.11	-2.09	-9.00	5.896
	MCC	-17.47	-0.62	-7.98	-13.99	18.15	-12.29	-10.59	-12.35	-2.09	-8.00	12.135

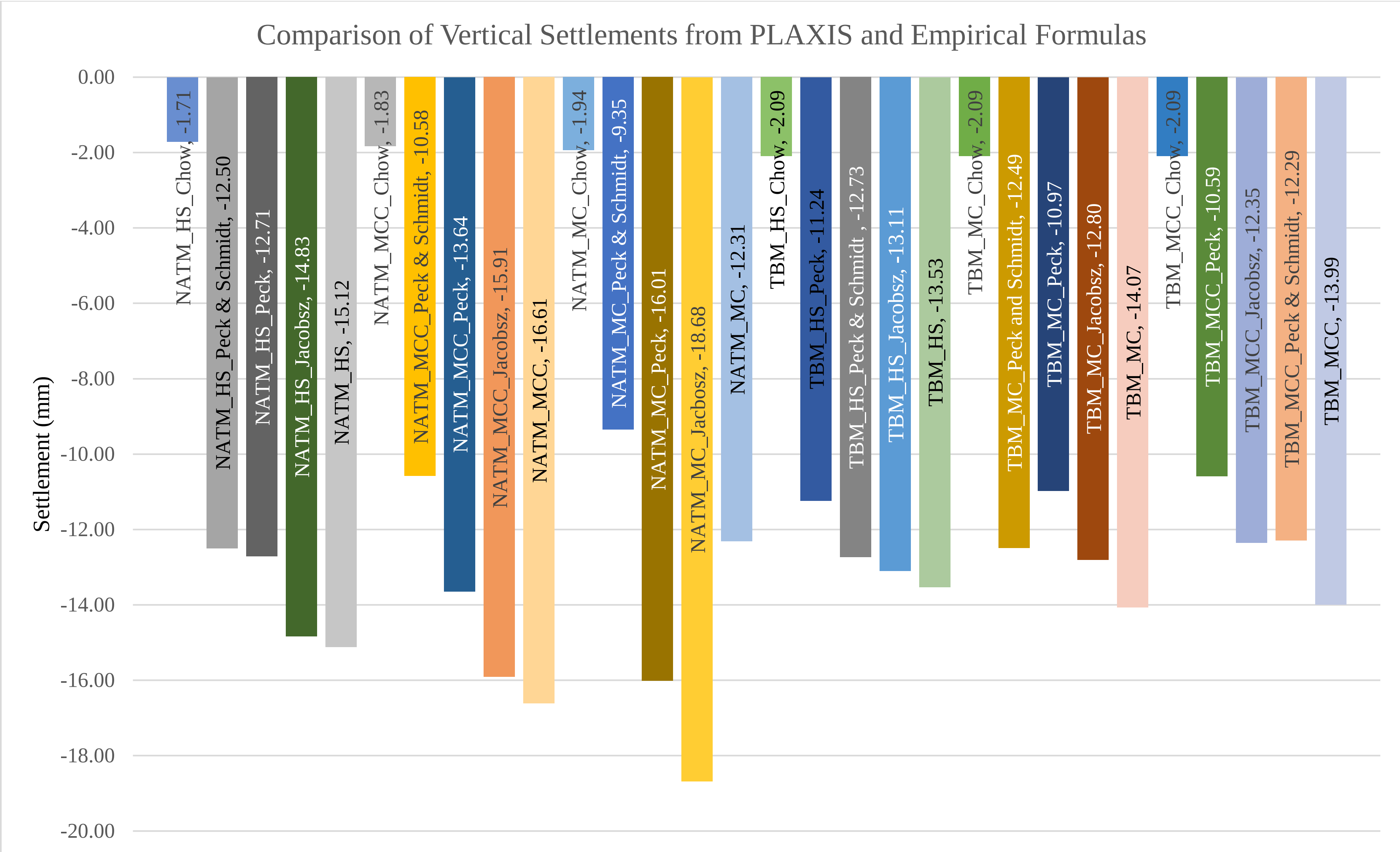

Figure 4.32: Comparison of Vertical Settlements of Different Empirical Formulas for both NATM and TBM methods (for different models)

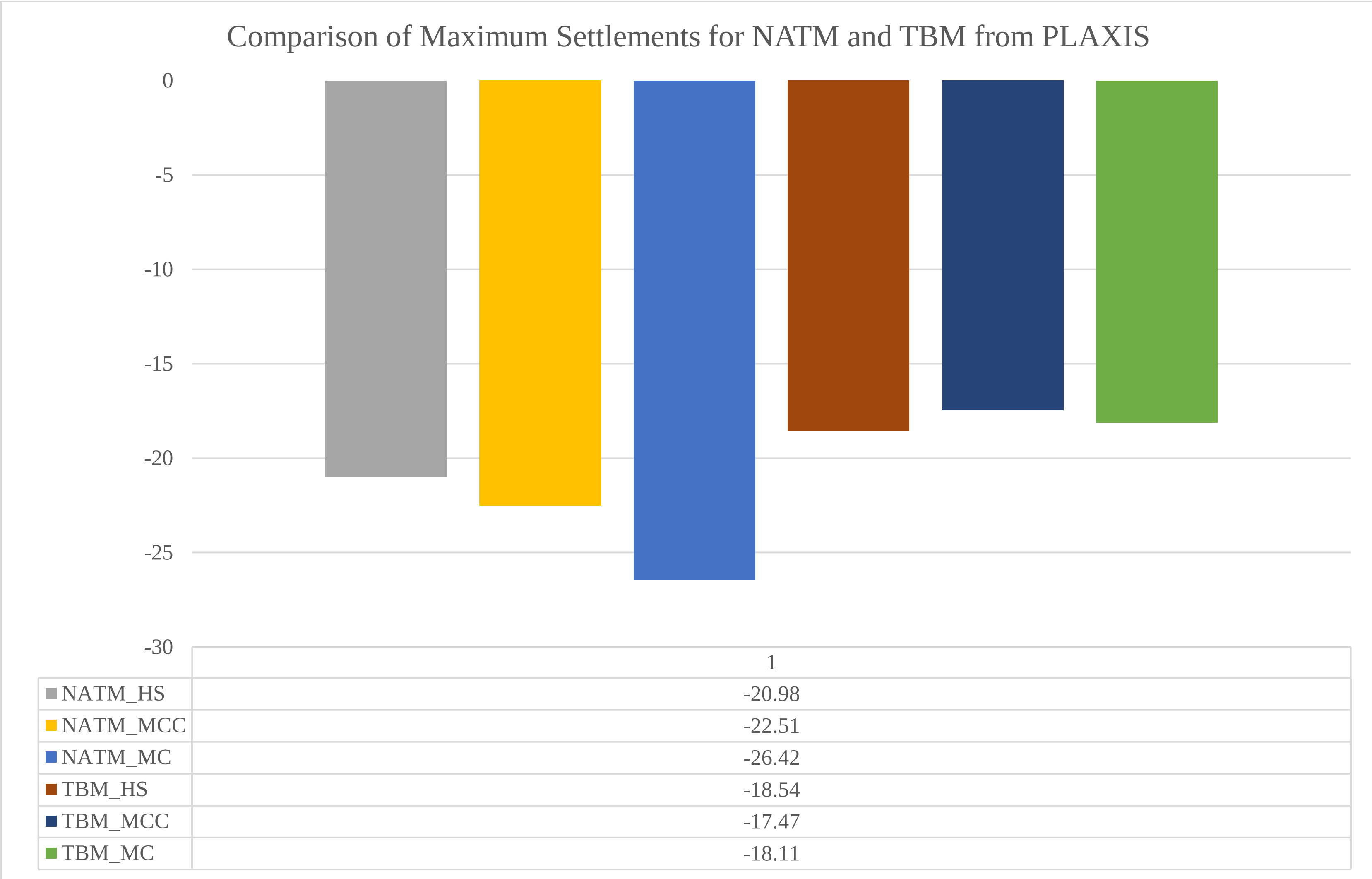

Figure 4.33: Comparison of Maximum Settlement for NATM and TBM Methods from PLAXIS (for different types of models)

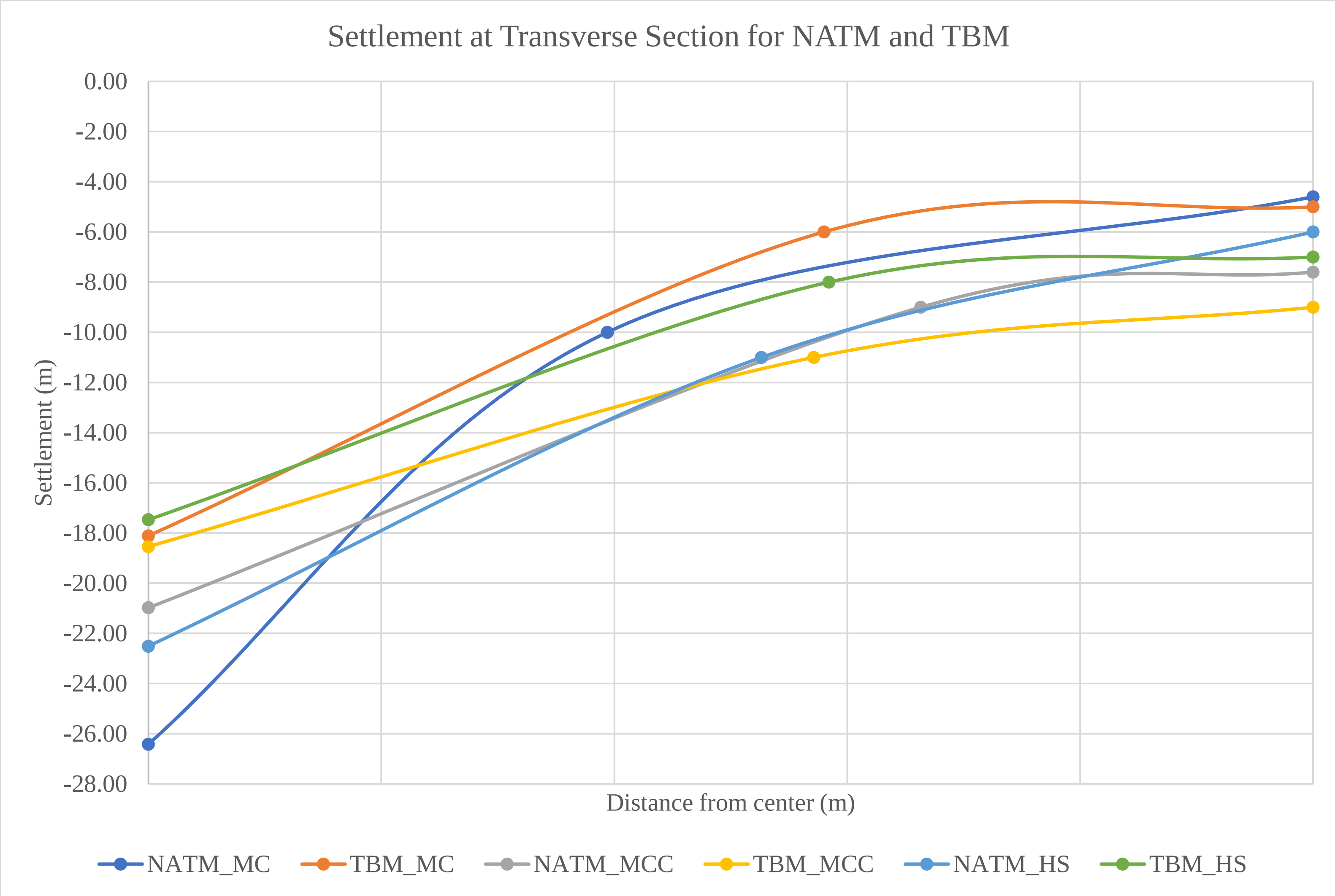

Figure 4.34: Settlement at Transverse Section for both NATM and TBM methods considering 35m depth and 3.50m radius (from PLAXIS)

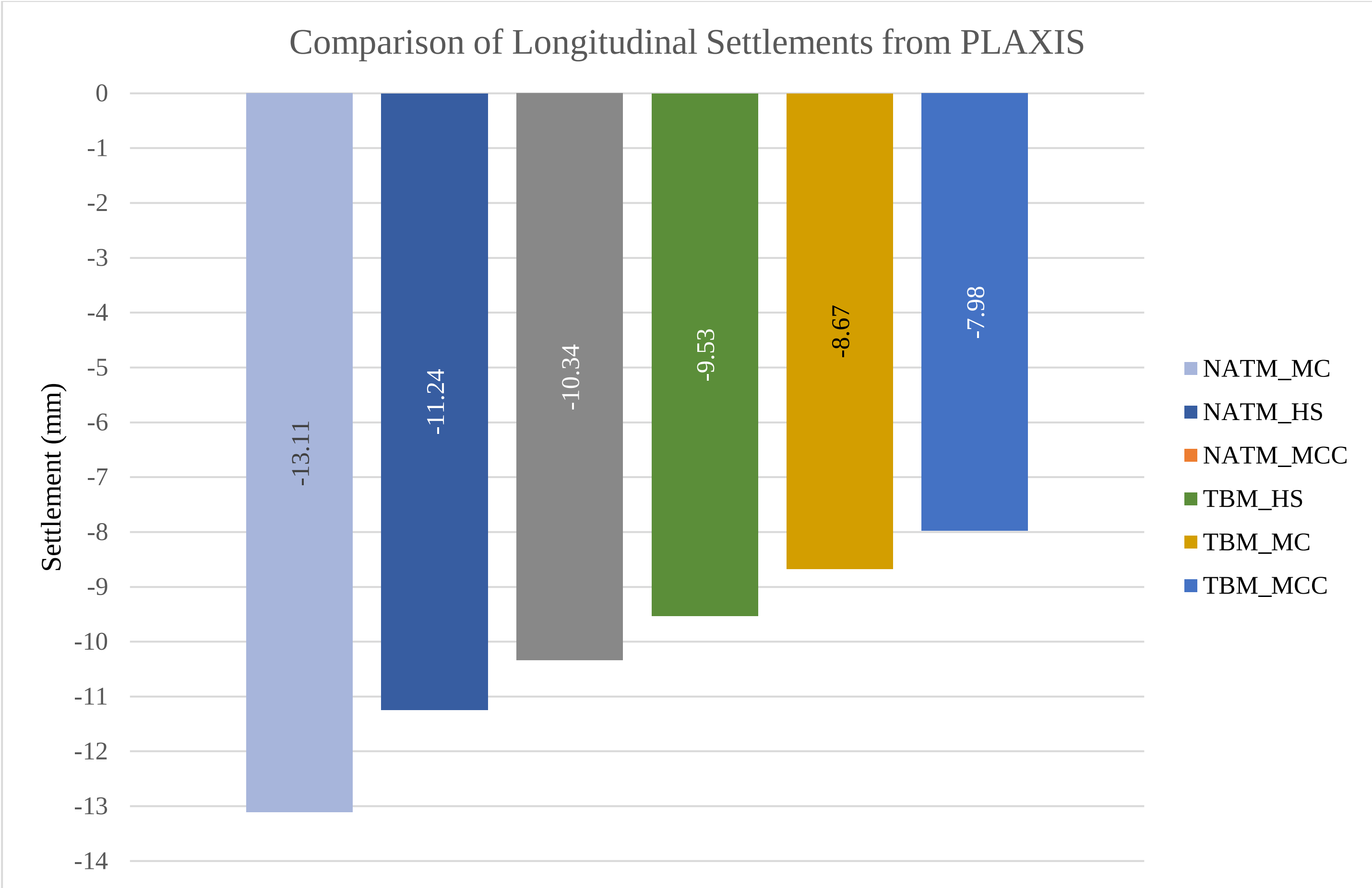

Figure 4.35: Longitudinal Settlements for both NATM and TBM methods considering 35m depth and 3.50m radius (from PLAXIS)

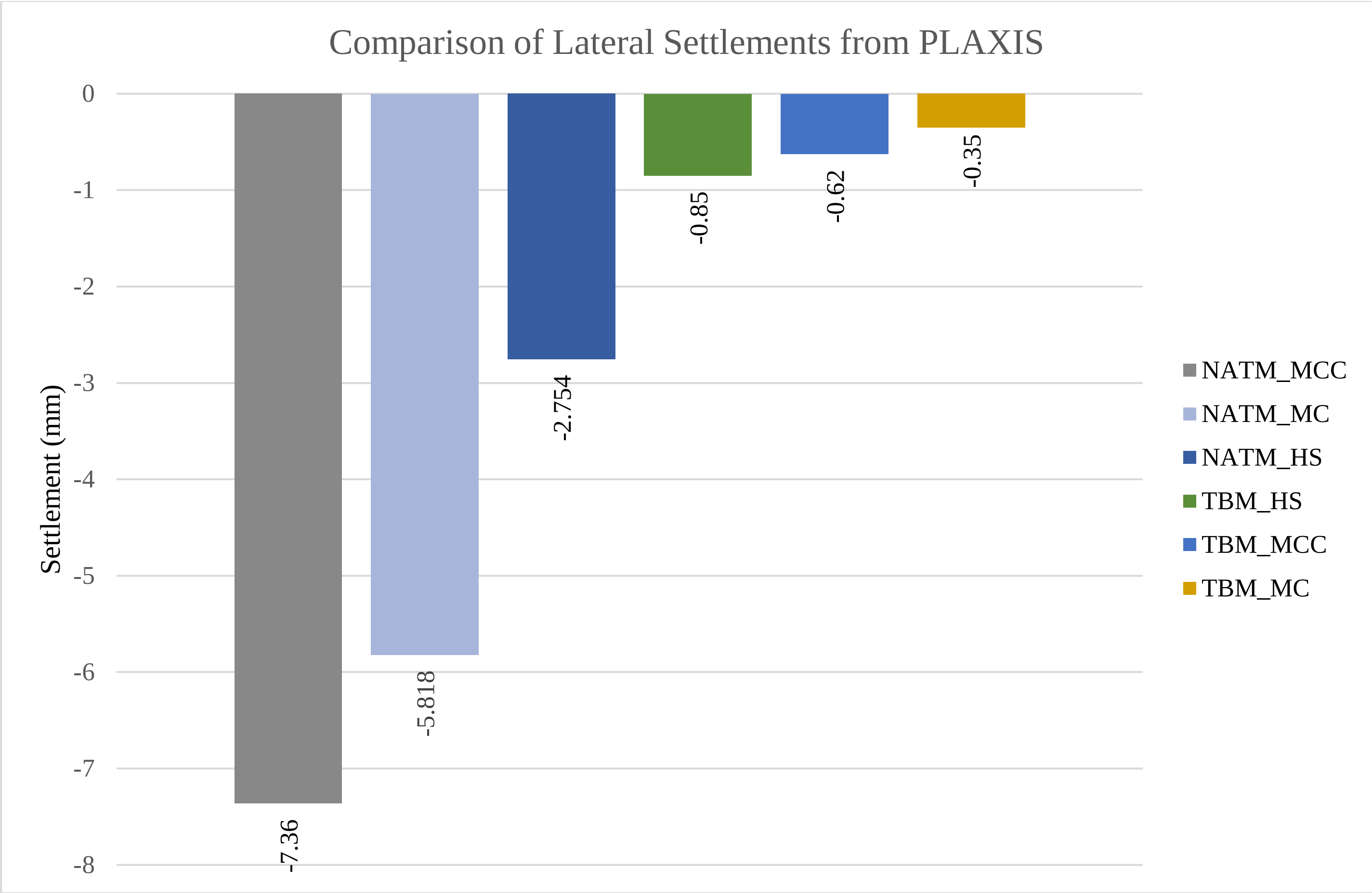

Figure 4.36: Lateral Settlements for both NATM and TBM methods considering 35m depth and 3.50m radius (from PLAXIS)

3.9 Summary

i. The mass rapid transit Line -1 is going to be established in underground and elevated portions. In this report, only underground section is focused whose length is approximately 14.8 km. The site area is basically from Pleistocene Madhupur clay and Holocene sediments with intermediate to high plastic clay and overlain by medium to coarse sand. The study area is in seismic zone II and it is mostly consisted of clayey soil than sandy soils. The borehole location is under Kuril flyover and all of the field investigation and laboratory tests collected from secondary sources. From the test results, subsoil stratifications are prepared.

ii. Numerical models are prepared in PLAXIS 3D for NATM and TBM methods for three different types of models (MC, MCC, and HS), where NATM models are done for depth 35m and 7m diameter, but TBM models are done for depth 30m, 32m, and 35m and for diameter of 5m, 6m, and 7m. Construction sequences for both methods are included in modelling.

iii. For practical application and model validation, realistic soil constitutive models need to be chosen which can simulate the nonlinear and stress dependent characteristics of soil. For FEM model, MC, MCC and HS model are chosen for simulating soil behavior with real time field and laboratory test data. The input parameters are determined from laboratory test results and empirical correlations. The empirical and analytical results are validated with the FEM model using the soil and structural parameters in PLAXIS 3D for MRT Line-1 tunnel alignment. Specific borehole data (BH-24, under the Kuril flyover) is chosen to simulate the soil structure interaction.

iv. The effect in maximum total displacements is computed for different types of mesh for different conditions of both NATM and TBM methods and for different models before starting the comparative analysis. For NATM models, the variation from medium mesh to coarse or fine mesh is about 10% whereas for TBM models, the variation value is almost 4% only. As the variation is considerable, medium mesh can be considered for models to save the running time.

v. From the comparison between the results of PLAXIS 3D and empirical formulas derived from different researchers for MRT Line 1, it can be said that the average deviated values between the numerical result for obtaining trough width parameter, i, and the empirical result of O’Reily & New are obtained as 5.38%, 3.84% and 6.39%

for MC, MCC and HS models respectively. These deviations are very less than other empirical relations described in researches.

vi. The transverse profile of the surface settlement of numerical results obtained from the MC, MCC and HS models are compared with the empirical relationship's graphs. It can be clearly seen that results of the MCC model have the best fit to the data points.

vii. After analyzing the relationship between settlement and depth or radius and also, between the location of inflexion point and depth or radius, it can be concluded to state that the total settlement decreases with an increase in depth of the tunnel (almost 11% decrement for every 5m increment of depth) and increases with an increase in diameter (almost 20% increment for every 1m increment of diameter). Increasing the TBM depth results to increase around 4% in distance of inflexion point from center whereas increasing in radius results to decrease around 5% in inflexion point distance from center of the tunnel.

viii. Comparing the vertical settlement found from PLAXIS 3D and various empirical formula given by different researchers, it can be said that the deviation percentages of vertical settlement from PLAXIS with Peck, Peck & Schmidt and Jacobsz formula are almost 10% and 34% for TBM and NATM respectively.

ix. The Jacobsz formula (2004) shows a good agreement and approximately close value compared to the settlement values obtained from PLAXIS 3D (for NATM, the variation is about 2 ~ 16% and for TBM 3 ~ 10%).

x. From comparison of longitudinal and lateral settlement found from PLAXIS 3D, it can be shown that NATM method shows more settlement (10 to 30% more) than TBM method. As the NATM method includes blast technique, it may induce more vibrating effect than TBM method which indicates this variation in settlement calculation.

xi. For Dhaka city, NKDOS consortium proposed TBM-EPB machine for MRT Line 1 tunnel construction. It can be said from this study that, for our city TBM should perform better than NATM method considering the settlement parameter and average soil condition.

BANGLADESH NETWORK
OFFICE FOR URBAN SAFETY

PART-III

NUMERICAL ANALYSES OF A MAT BELOW A NUCLEAR POWER REACTOR UNDER SEISMIC LOADING

BANGLADESH NETWORK OFFICE FOR URBAN SAFETY (BNUS), BUET, DHAKA

Prepared By: Md. Shariful Islam

Mehedi Ahmed Ansary

Chapter One

INTRODUCTION

1.1 General

Bangladesh is the largest delta island in the world, is formed predominantly by alluvial sediments. Development of heavy foundation like nuclear power reactor in this soils are challenging for the strain-sensitiveness and high seasonal ground water movement. There are various suitable modern technologies of soil improvement; such as pile foundation, the technology of jet grouting, the technology of deep vibration replacement and the technology of deep soil mix for the purposes of improving deformation properties of soils for heavy earth foundation. In case of pile foundation shaking-induced liquefaction and associated lateral spreading has caused extensive damage due to lack of efficient prediction for estimating seismic response of piles and soils in liquefied and laterally spreading ground.

Currently, Bangladesh Government is implementing country's first Nuclear Power Plant project in the history of Bangladesh, which is located in Rooppur, Pabna. Rooppur is located beside the Padma river. Nuclear Power Reactor is heat source of Nuclear Power Plant (NPP) in which the control of nuclear fission reaction has taken place and transformed enormous heat as thermal power from nuclear fuel. As of 2018, 451 nuclear power reactors are in operation and 55 reactors under construction in 33 countries as per International Atomic Energy Agency (IAEA). Among the 33 countries, Bangladesh is an embarked country in construction of Nuclear Power Reactors of VVER technology. Bangladesh has started the nuclear construction for two-reactor power unit 2x1200 MWe in Rooppur, Ishwardi, Pabna. Site location of Rooppur Nuclear Power Plant is shown in Figure-1.1.

Bangladesh is surrounded by regions of high seismicity like the Himalayan Arc and the Shillong plateau in the north, the Burmese Arc-Arakan Yonia anticlinoriurrt in the east and the complex Naga-Disang-Haflong thrust zones in the northeast. It is also the site of the major Dauki fault system along with numerous subsurface active faults and a flexure zone to be called as Hinge zone. These weak zones are believed to provide with the necessary planes for movements within the basin area. Bangladesh experienced several historical great earthquakes during last century and has been affected by small earthquakes occasionally. The epicenters of large earthquakes lying beyond the bonier of Bangladesh equally effect the country for its morphotectonic continuity. The movement in the Dauki fault system influences the present configuration of the Surma basin and plays a vital role in the seismicity of the northern region of Bangladesh. The seismicity of Bangladesh is deeply related with tectonic behavior in and around Bangladesh which is caused by the subduction of the Indian plate below the Tibet subplate in the north.

Figure 1.1: Site Location of Rooppur Nuclear Power Plant (Google Earth location map)

Heavy, durable and stable foundation is one of the key concerns in nuclear construction as it is directly related to plant safety. In connection of stable foundation subsurface investigation at a nuclear power plant site is important at stages of the site evaluation process. The purpose of this investigation is to provide information or basic data for decisions on the nature and suitability of the subsurface materials for constructing plant foundation. Bangladesh have already been faced four major earthquakes between 7-8.5 Mw. So, there is a threat for nuclear power plant in Bangladesh. The subsoil investigations, geotechnical, site specific seismic hazard assessment are the specific areas for major consideration for the selection of the site.

According to the seismic zoning map Bangladesh is divided in to zone-1, zone-2 and zone-3. Rooppur site is in zone-3 which is seismically quiet. No indication of surface faulting around RNPP has been realized. The peak ground acceleration (PGA) is estimated 0.18g for the return period of 2475 years which is much smaller than the designed basis PGA values of nuclear reactors. From the seismic hazard analysis and sub-soil investigation, any heavy structure like RNPP with the design basis PGA values above 0.2g-0.25g could withstand a 7.5-9.5 Mw earthquake and can damage the RNPP in future.

Nuclear power plant structures are designed to withstand the ground motion caused by most severe earthquake that is like to be experienced. From historical records of seismic event in the plant vicinity, the earthquake that would be expected to produce the largest ground motion at the Power Reactor site is predicted, which is called safe shutdown earthquake. In this earthquake power reactor can be tripped but the engineered safety features must be function properly to make plant safe. Furthermore, the plant must be capable of remaining in full operating condition should a specified “operating basis earthquake” be experienced. In developing the design necessary to meet these requirements, dynamic analysis based on expected ground acceleration spectra is applied to those components and structures (called class I). The proposed lay-out for construction of Rooppur Nuclear Power Plant has been shown in Figure-1.2.

Numerical analysis is a proven technique for visualization the geotechnical problems and the settlement of building or structures. Numerical analysis can deal both the geotechnical and structural aspect such as soil properties, structures and construction sequences of mat foundation placed on improved or unimproved soil. In this research, a mat foundation model of a nuclear reactor building is used for evaluating the status of unimproved and improved soil under static and dynamic (seismic) loading using Plaxis 3D software.

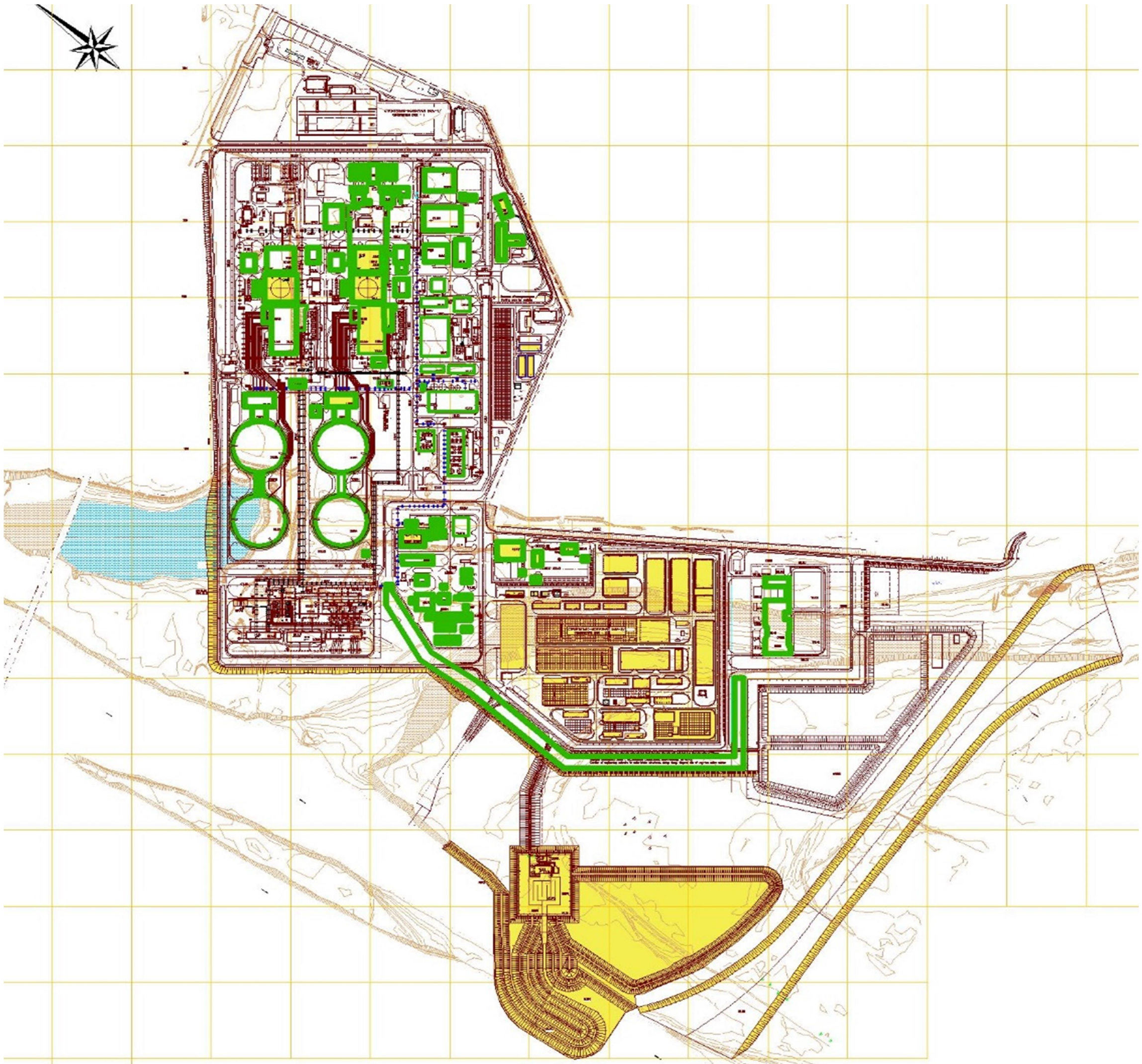

Figure 1.2: Lay-out of Rooppur Nuclear Power Plant (Rooppur NPP FCD Publication, 2017)

1.2 Objectives and possible outcomes

The objectives and possible outcomes of this research are mentioned below:

1. To conduct numerical analysis of a mat foundation on unimproved/natural soil of a nuclear power reactor under static and dynamic loads for getting the deformation results
2. To conduct numerical analysis of a mat foundation on improved soil of a nuclear power reactor under static and dynamic loads for getting the deformation results.
3. To compare results between unimproved and improvement soil.

produce relatively uniform block of modified soil, the establishment of secant soil-cement piles is implied. This method provides the reliable possibility of uniform block creation, significant soil deformation properties improvement and prevention of soil liquefaction over the depth of the improved soil interval.

Furthermore, the WSM technology implies the usage of drilling rods with the length up to 20 m. After reaching this length the additional operation is required – up building of drilling rods length with connection of them that can significantly affect the productivity. At the further design stages the technology is chosen for the maximal productivity, i.e. the making of the auxiliary construction pits if necessary. Between the buildings the movement joints are implied in order to prevent uncontrolled cracks formation due to various stress-strain states of improved soil blocks under different structures during construction and in the final state.

Chapter Three

DATA COLLECTION BEFORE AND AFTER GROUND IMPROVMENT

3.1 Introduction

In this chapter, the properties of the soil parameters of existing natural soil from field and laboratory tests are discussed. The first nuclear power plant (NPP) of Bangladesh is the Rooppur NPP which is under construction. For this research works all data were collected from Rooppur NPP site. The Data consists of angle of internal friction (φ), cohesion (c'), Young's Modulus (E), Density (γ), unit weight and Poisson's ratio ν, permeability coefficient (k), Secant Modulus of Elasticity, E_{50}^{ref}, Oedometer Modulus of Elasticity, E_{oed}^{ref}, Unloading/Reloading Modulus of Elasticity, Eur are collected and derived from empirical formulas.

3.2 Engineering-Geological Conditions of the Rooppur NPP Site

3.2.1 Geomorphological Characteristics

Geomorphology of the territory of Bangladesh is presented mainly with alluvial plains. Three main geomorphological types of relief are distinguished:

- Hills that occupy 12.5% of the territory of the country generally located in eastern and north-eastern parts of Bangladesh. Hills are composed of Neogene-Paleogene sandstones and mudstones;

- Uplands or so-called terraces comprising 8 % of the territory. These are Madhupur, Barind and Lalmay Highs composed of reddish and dark-brown clayey deposits of the Pleistocene age;

- Plains occupying 80 % of the territory: piedmont plains, alluvial plains and deltaic dales. Deposits are presented by disperse sandy and clayey soils.

The geomorphological scheme of Bangladesh is shown in Figure 3.1. The site is located on the east bank of the Ganges River (which is known as the Padma River in Bangladesh). The survey site is a plain locality, the ground absolute elevation varies from 13.96 m to 15.29 m from the sea level. The landscape is presented by chains of small hills, low lands and channels. The relief is locally irregular alongside the present and former river courses, comprising a rapidly alternating series of linear low ridges and depressions (Oxbow lake). Clayey soils prevail in depressions, loamy soils (in some places sandy) are present at ridge back.

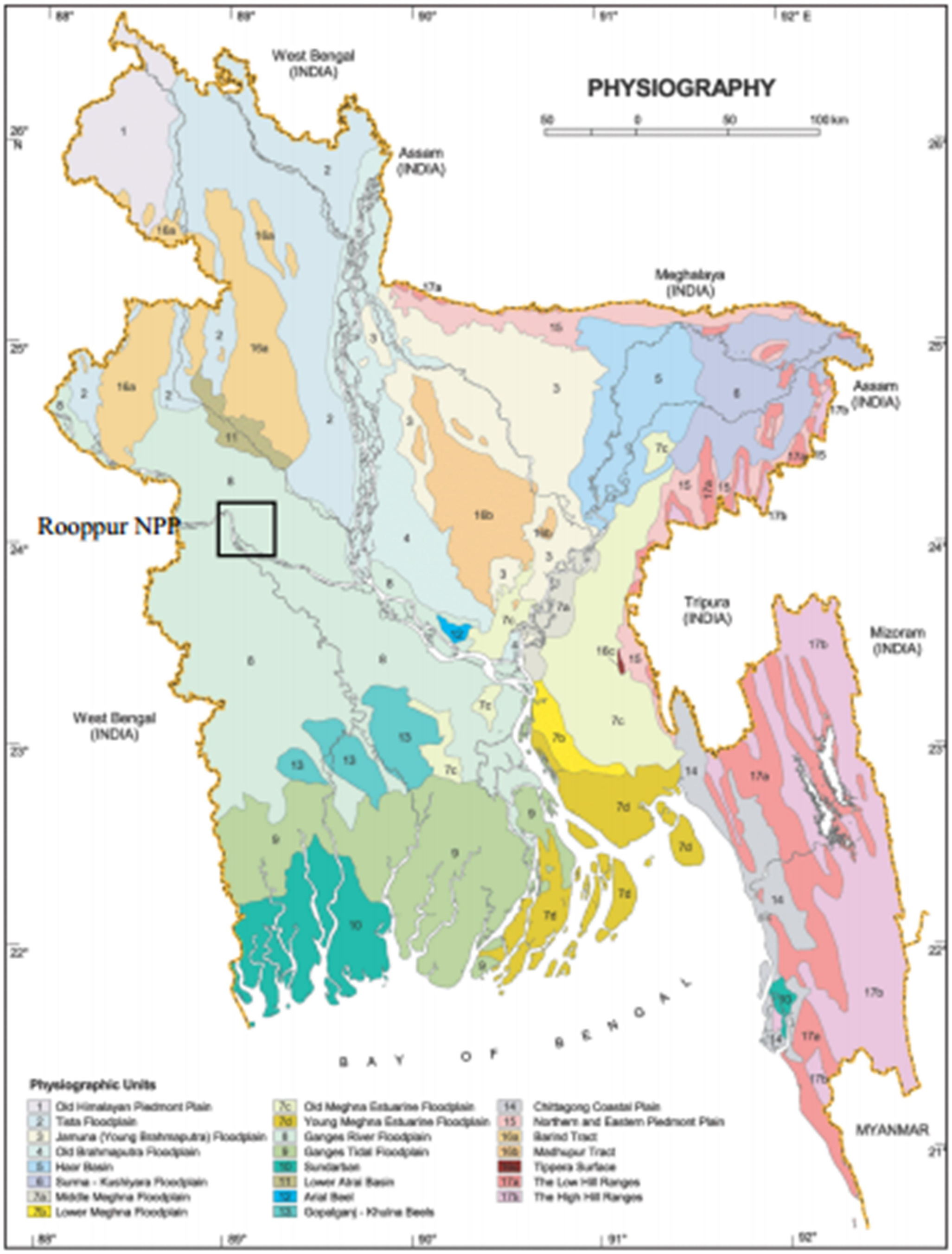

Figure 3.1: Geomorphological map of Bangladesh

3.2.2 Drilling and Digging Works

Drilling were be taken up to exactly define geological cross-section parameters. Field study of soil properties has been carried out to determine hydrogeological parameters of aquifiers and aeration zone, to perform geophysical survey, to take soil and water samples, to determine groundwater depth and to level. Drilling was carried out using cable-tool drilling method by GY-50, TBM-88 and DANDO BEOTEC 2 drilling tools. Soils samples were fully collected in course of drilling for laboratory tests, and hydrological observations were performed.

Soil samples were collected from every lithological difference at 2 m interval. On completion of drilling works boreholes were abandoned via backfilling and marks (benchmarks) with borehole No. indicated were installed on borehole drilling spot. In total 32 boreholes were drilled using cable-tool method (1152.5 running m). Location of boreholes is shown at the Map shown in Figure 3.2. Test excavations had dimensions of 2 x 2 m with depth of about 3.0 m, test pits were up to 0.6 m deep. In total 12 test excavations and 10 test pits were done at the NPP site.

3.2.3 Borehole Logs and Properties of Soil

Among boreholes, borehole no. 1, 5 and 26 are described in Figure- 3.3 to 3.5, which describe the soil profiles of total depth 30 m, 50 m and 106.5 m respectively. Other 5 soil profiles of Borehole Logs are shown in Appendix A.

Soil composition and conditions, strength and deformation properties were studied during field works (drilling, cone penetration tests, standard penetration tests, pressure meter (radioactive logging) and laboratory methods. Results of laboratory tests have been analyzed, soils were united into engineering geological layers with account of stratigraphy, genesis and textural and structural features.

Modern Man-made Soils (tQ_{IV}) are presented by fine loose in wash sands. As for grainsize distribution prevailing is fraction with diameter of particles of 0.25 to 0.1 mm (62.7 %). 15 soil samples were studied in the laboratory.

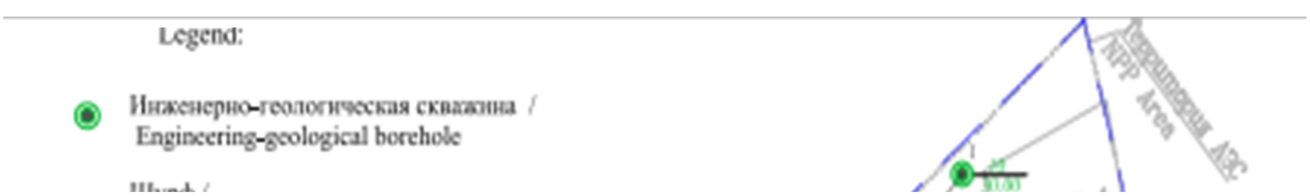

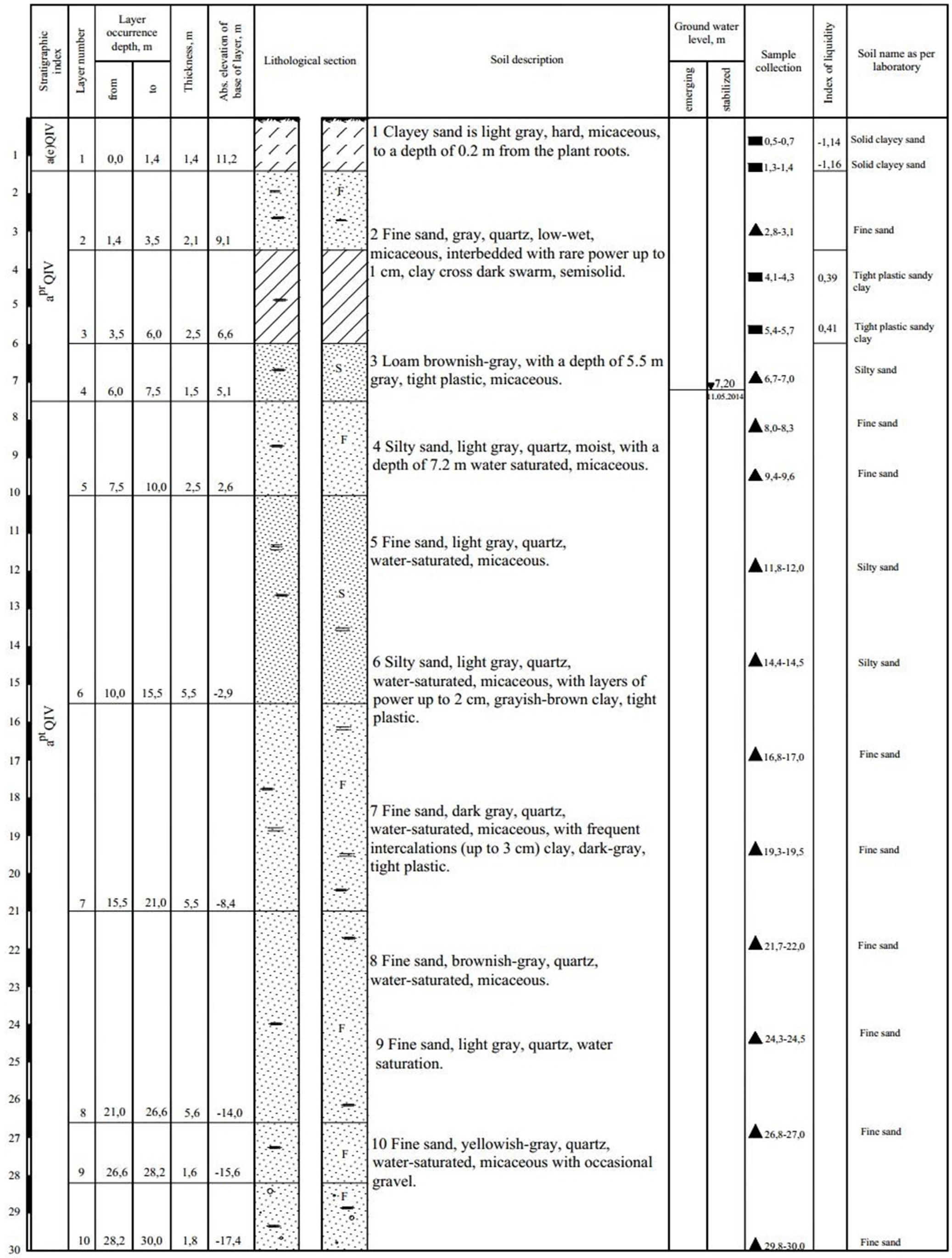

Figure 3.3: Borehole No. 1 (Absolute elevation of wellhead 12.6 and total depth 30 m)

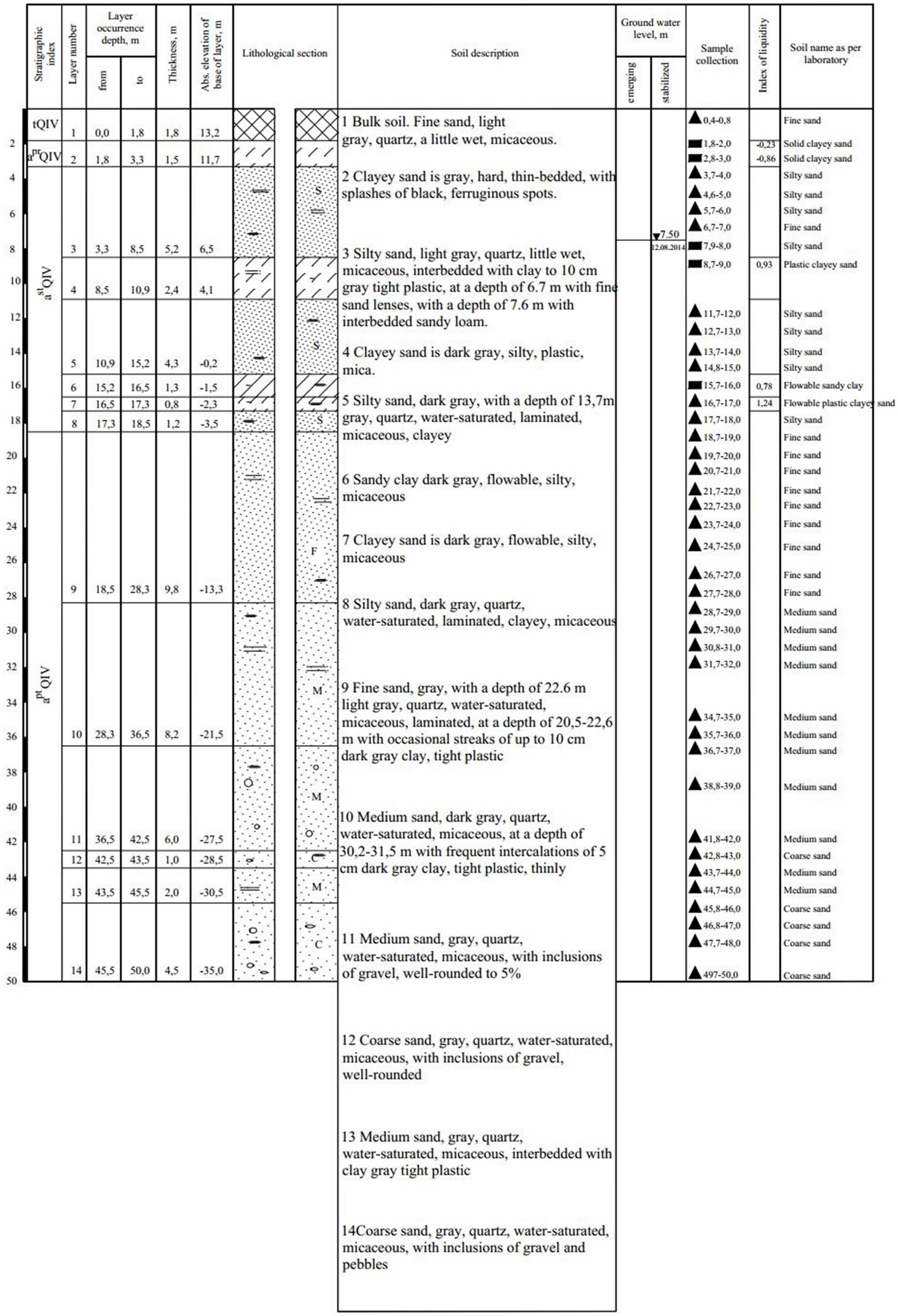

Figure 3.4: Borehole No. 5 (Absolute elevation of wellhead 15 and total depth 50 m)

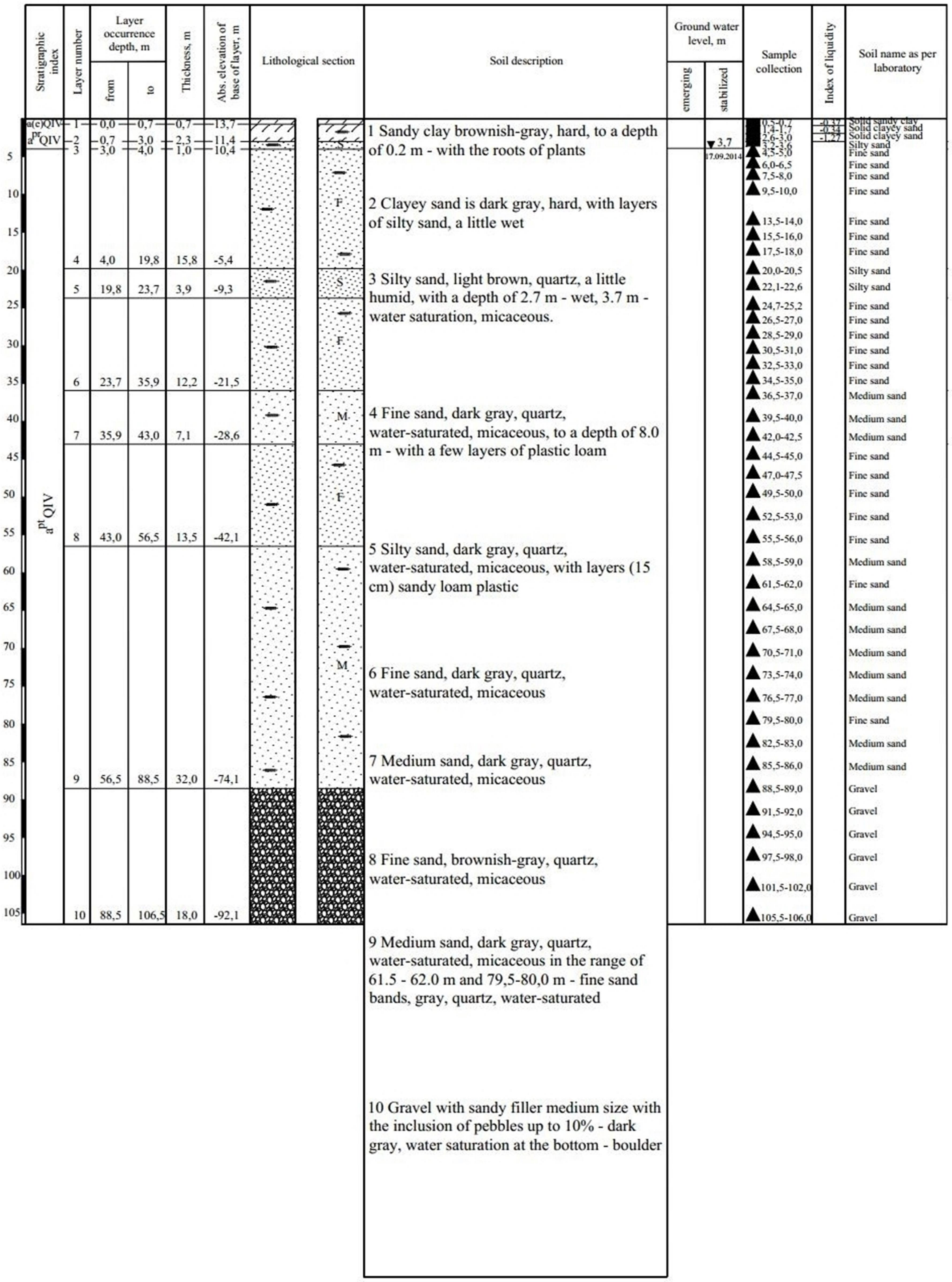

Figure 3.5: Borehole No. 26 (Absolute elevation of wellhead 14.4 and total depth 106.5 m)

Natural moisture content of soils is 0.054 to 0.93 u.f. (average value is W= 0.069 u.f.), density in-situ 1.4 to 1.7 g/cm^3 (average value is 1.59 g/cm3), density of soil particles is 2.66 t/m^3, porosity ratio is equal to e = 0.823 u.f., moisture content Sr =0.22. Density of soil in ultimate-loose and ultimate-compacted structure is in average 1.25 and 1.48 g/cm^3. Soil natural friction angle in air-dry state is 39^o, under water 31^o.

Facies of Flood Plain Eluviated Soils (a(e)QIV) comprises the upper part of the section down to depth of 0.2 to 2.0 m and is presented by light macropore loams and sandy loams, solid and semi-solid. 17 soil monoliths were studied in the laboratory. Natural moisture content of loams is 0.135 to 0.253 (average value is W= 0.209 u.f.), soil density ρ_H = 1.61 g/cm^3, density of dry soil is ρ_d = 1.33 g/cm^3. Average value of porosity ratio is above 1 and is equal to e = 1.022 u.f., liquidity index I_L= minus 0.30.

As for grain-size distribution in loams prevailing is fraction with diameter of particles of 0.05 to 0.01 mm. The content of such particles is average to 49, 4%. Content of clayey particles (less than 0.005 mm) is 11.7 %. According to grain-size distribution and plasticity index loam is light silty. Moreover, according to grain-size distribution and plasticity index unundoable loam is heavy silty. Physical properties of sandy loam were studied for 8 samples. As per results of performed tests natural moisture content of flood-plain sandy loams is W= 0.179 u.f., density in-situ 1.74 g/cm^3, density of dry soil is ρ_d = 1.48 g/cm^3, porosity ratio is equal to e = 0.823 u.f., density of soil particles – 2.68 to 2.69 g/cm^3 (average value is 2.68 g/cm^3). Plasticity index varies from 0.031 to 0.067 u.f., moisture content at the limit of liquidity is WL = 0.273 u.f., moisture content at the limit of plasticity WP = 0.224 u.f., liquidity index is less than zero.

As for grain-size distribution in sandy loams content of clayey particles (less than 0.005 mm) is in average 8.8 %, content of sandy particles is 45.9%, silty particles – 45.3%. Organic matter percentage in loams and sandy loams is 3.3 to 7.5 % respectively. Modern Quaternary Alluvial Deposits of the Flood Plain Facies (a^{pr}QIV) are presented by sandy soils and cohesive soils.

Loams are prevailing in cohesive soils of flood-plain alluvium, clays and sandy loams are much rarer. Loams are of semi-solid and low-plastic consistency. 28 soil monoliths were studied in the laboratory. Natural moisture content of semi-solid loams is 0.156 to 0.287 (average value is W= 0.247 u.f.), average soil density in-situ ρ_H = 1.74 g/cm^3, density of dry soil is ρ_d = 1.40 g/cm^3. Average value of porosity ratio is equal to e =

0.935 u.f., plasticity index IP= 0.093. Natural moisture content of low-plastic loams is in average WH= 0.297 u.f., average soil density in-situ ρ_H = 1.88 g/cm^3, density of dry soil is ρ_d = 1.45 g/cm^3. Average value of porosity ratio is equal to e = 0.863 u.f., plasticity index I_P= 0.092.

As for grain-size distribution in semi-solid and low-plastic loams content of clayey particles (less than 0.005 mm) is 16.4 to 15.7%, content of sandy particles is 29.5…31.7 %, silty particles 54.1 to 52.6%. According to grain-size distribution and plasticity index loam is light silty. Organic matter percentage by two determinations is 5.5 to 6.4% respectively. Sandy loams of flood-plain alluvium are solid (sometimes plastic). Physical properties of sandy loam were studied for 14 samples. As per results of performed tests natural moisture content of sandy loams is W= 0.262 u.f., density in-situ 1.77 g/cm^3, density of dry soil is ρ_d = 1.40 g/cm^3, density of soil particles 2.68 g/cm^3. Moisture content at the limit of liquidity is W_L = 0.340 u.f., moisture content at the limit of plasticity W_P = 0.285 u.f. Index of liquidity is I_L = 0.42.

As for grain-size distribution in sandy loams content of clayey particles (less than 0.005 mm) is in average 8.9 %, content of sandy particles is 42.3%, silty particles 48.8%. Organic matter percentage by single determination is 6.1%. Clays of flood plain alluvium are of limited distribution and thickness. Physical properties of clays were studied for 3 samples. As per results of performed tests natural moisture content of clays is W = 0.317 to 0.341 u.f. Moisture content at the limit of liquidity is, W_L = 0.43 to 0.452 u.f., moisture content at the limit of plasticity, W_P = 0.260 to 0.281 u.f., density of soils in-situ 1.87 to 1.95 g/cm^3. Average value of density is ρ = 1.91 t/m^3, porosity ratio is equal to e = 0.901 g/cm^3. Average value of soil liquidity index corresponds to low-plastic consistency, I_L= 0.34.

As for grain-size distribution in clays prevailing are silty fractions (55.6%). Weight content of clayey particles is 6.5 to 9.0 %. According to grain-size distribution and plasticity index clay is light silty. Sandy layer of modern alluvial deposits of the flood plain facies is presented by silty and fine loose sands (mostly silty sands).

As for grain-size distribution in fine sands prevailing is fraction of 0.25 to 0.1 mm diameter of grains (59 % in average). Organic matter percentage is 2.0 to 2.3%. Medium sands were studied in 120 samples. Natural moisture content is 0.223 u.f., density of soil particles is 2.65 t/m^3. Soil natural friction angle in air-dry state is 36^o, under water 32°. Density of sands in ultimate-loose and ultimate compacted conditions is in average 1.35 and 1.62 t/m^3. According to results of gamma-gamma density logging density of medium sands in situ is ρ = 1.96 g/cm^3. As for grain-size distribution in medium sands prevailing is fraction of 0.5 to 0.25 mm diameter (58.8 % in average). Organic matter content is 1.1 %.

Coarse sands have limited distribution in form of layers and lenses. Density of sands in ultimate-loose and ultimate compacted conditions is 1.44 and 1.69 g/cm^3. As per data of geophysical survey density of coarse sands in-situ is ρ = 2.05 t/m3. Soil natural friction angle in air-dry state is 37°, under water 33°. As for grain-size distribution in coarse sands prevailing is fraction of 0.25 to 0.1 mm diameter (52.6% in average). Content of particles with diameter of 2 to 1 mm varies from 0.0 to 25.1 % (average value is 0.9%). Content of fractions with diameter less than 0.1 mm is 4.9 %. Gravel soils contain 44.8% of pebble, 21.3% of gravel and almost no clayey material (less than 3 %).

3.3 Field Geotechnical Soil Survey

3.3.1 Pressuremeter Tests and Analysis of Results

Pressuremeter tests were done at the Rooppur NPP site within the area of the main structures. In total 43 tests in two 50-m deep boreholes (No 24a and 28a). 21 tests were done in borehole No 24a. 22 tests were done in borehole No 28a. Tests were be performed in every lithological difference uncovered starting from depth of 4.0 m to 50.0 m. Interval between tests was ~2.0 m.

Tests were conducted by stages (0.25 to 0.05 MPa) with a final load exceeding the total soil gravity load at the testing depth. It was required to keep ground pressure in the boreholes during test performance using dense clay drilling mud. All works were done in accordance with GOST 20276-99 named “Soils. Methods for Field Determination of Strength and Strain Characteristics”. Test results of first two pressuremeter tests of Borehole No. 28a have been shown in Figure 3.6 and 3.7. Other test results of pressuremeter tests are given in Appendix B. Results of pressuremeter tests are described in Table 3.1.

		Specification of measuring equipment		
Length of probe inner tube........	**52,0 cm**	Diameter of probe	**7,2 cm**	
Type of probe.....................	**Elastmeter-2**	Model.............................	**4180**	
		Results of test		
Initial pressure of linear range, Po			**0,080**	MPa
Final pressure of linear range, Pк			**0,202**	MPa
Pressure increment, P			**0,122**	MPa
Initial radius of borehole, Ro			**3,5699**	cm
Increment of borehole radius, R			**0,1146**	cm
Adjusting ratio, Kr			**1,35**	
Deformation modulus, E		Graph dR=f(p)	**5**	MPa

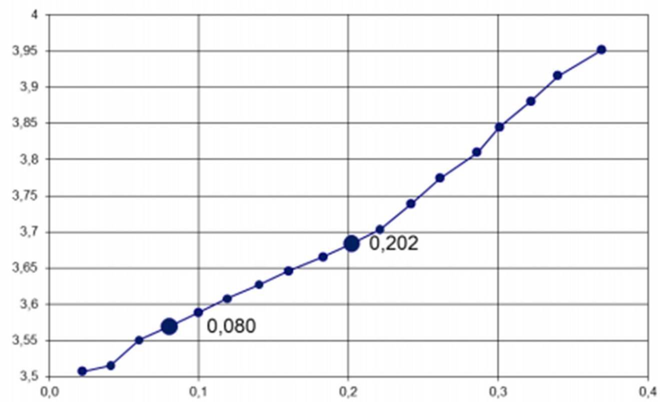

Figure 3.6: Pressuremeter Test No. 1 and Borehole No. 28a.

		Specification of measuring equipment		
Length of probe inner tube........	**52,0 cm**	Diameter of probe	**7,2 cm**	
Type of probe.....................	**Elastmeter-2**	Model.............................	**4180**	
		Results of test		
Initial pressure of linear range, Po			**0,127**	MPa
Final pressure of linear range, Pк			**0,343**	MPa
Pressure increment, P			**0,216**	MPa
Initial radius of borehole, Ro			**3,5522**	cm
Increment of borehole radius, R			**0,1523**	cm
Adjusting ratio, Kr			**1,3**	
Deformation modulus, E		Graph dR=f(p)	**7**	MPa

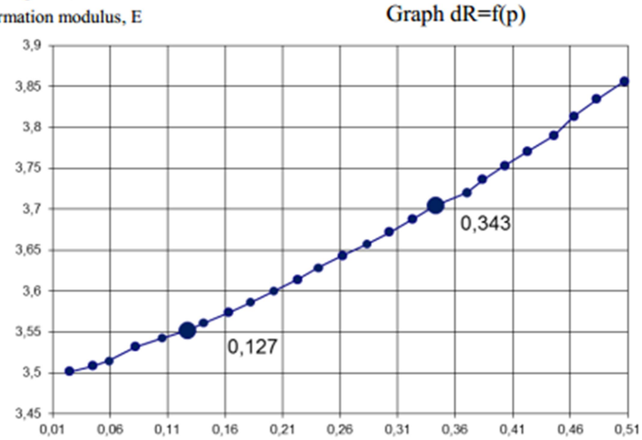

Figure 3.7: Pressuremeter Test No. 2 and Borehole No. 28a.

Table 3.1: Pressuremeter test Results

Borehole No.	Depth of testing	Name of Soil	Deformation modulus E, MPa	Normative value of deformation modulus E, MPa	
Deposits of flood plain facies ($a^{pr}Q_{IV}$)					
24a	4.0	Loam	10	7	7
28a	4.3	Loam	5		
28a	6.6	Silty sand	7	7	
Deposits of channel facies ($a^{pt}Q_{IV}$)					
24a	6.5	Silty sand	4	17	23
24a	8.5	Silty sand	11		
24a	10.5	Silty sand	13		
24a	15.0	Silty sand	18		
24a	18.0	Silty sand	13		
24a	20.0	Silty sand	17		
24a	22.0	Silty sand	20		
28a	8.6	Silty sand	15		
28a	10.6	Silty sand	18		
28a	12.6	Silty sand	21		
28a	14.6	Silty sand	18		
28a	16.6	Silty sand	22		
28a	18.6	Silty sand	19		
28a	20.6	Silty sand	21		
24a	13.0	Fine Sand	16	21	
24a	25.0	Fine Sand	16		
24a	27.5	Fine Sand	24		
24a	30.0	Fine Sand	26		
24a	32.0	Fine Sand	28		
28a	22.6	Fine Sand	20		
28a	25.5	Fine Sand	26		
28a	27.6	Fine Sand	17		
28a	30.0	Fine Sand	20		
28a	32.0	Fine Sand	23		
28a	34.0	Fine Sand	21		
24a	34.0	Medium Sand	29	32	
24a	36.0	Medium Sand	26		
24a	39.0	Medium Sand	28		
24a	40.8	Medium Sand	34		
24a	42.8	Medium Sand	33		
24a	44.8	Medium Sand	34		
24a	46.8	Medium Sand	39		
24a	49.5	Medium Sand	35		
24a	36.0	Medium Sand	26		
24a	38.0	Medium Sand	30		
24a	40.0	Medium Sand	27		
24a	42.8	Medium Sand	32		
24a	45.5	Medium Sand	33		
24a	47.0	Medium Sand	35		
24a	49.5	Medium Sand	36		

3.2 Standard Penetration Tests and Analysis of Results

Standard penetration tests at the Rooppur NPP site were done by following GOST 19912-2001 which refers to “Soils. Field Testing Methods for Cone and Standard Penetration Tests”. SPT method was applied to modern eluviated soils (a(e)Q_{IV}), modern alluvial deposits of flood plain facies ($a^{pr}Q_{IV}$), modern alluvial deposits of channel facies ($a^{pt}Q_{IV}$). SPT tests were executed at the studied site at 5 points. Depth of test penetration varies from 12.2 to 17.0 m. Total scope of SPT tests was 70.0 r.m. Recordings for every point were processed interval-wise (for every lithological difference).

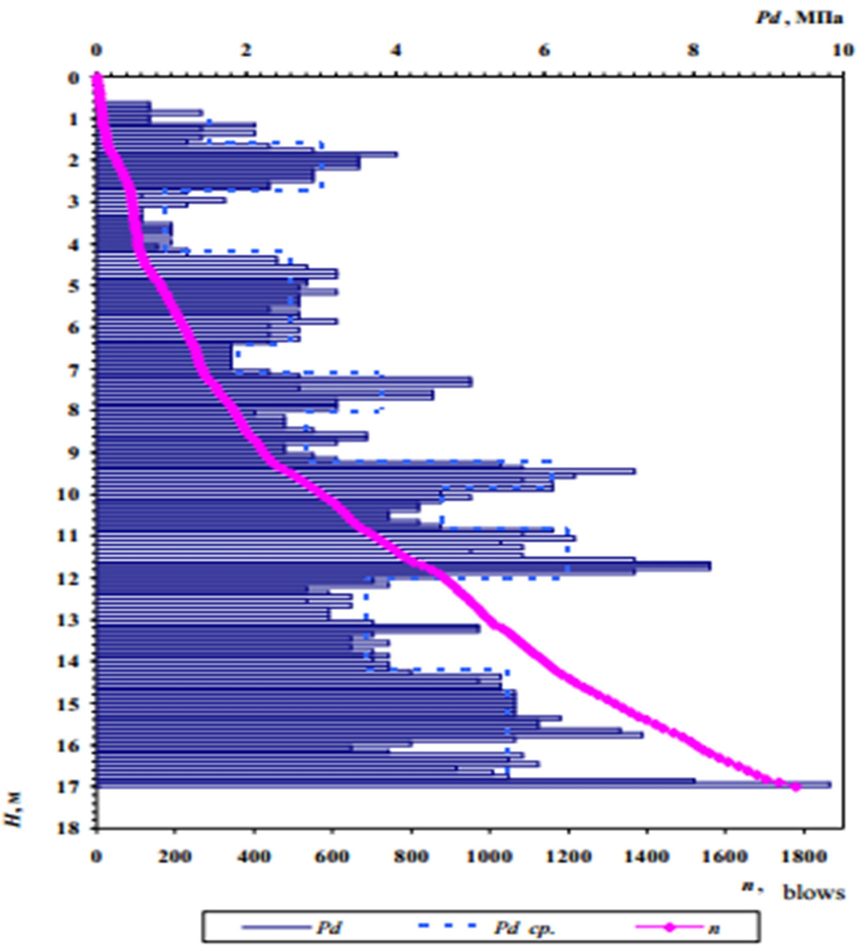

Figure 3.8: Changes of n (blows) and Pd (MPa) by immersion depth of probe H (m) (Results of soil test by dynamic sensing in point no. 2).

Recordings for every point were processed interval-wise (for every lithological difference). Boundaries of lithological differences were taken as per borehole data drilled in the close vicinity of the SPT point. Value of apparent dynamic resistance p_d was calculated for each stratigraphic lithological layer using formula

$P_d = A \,.\, K_1 . K_2 . n/h$

Where, A – specific energy of test, for used equipment is equal to 1120 N/cm;

K_1 – coefficient considering energy loss during hammer blows and elastic strain of rods (shall be determined using Table 4 from GOST 19912-2012“Soils. Field test methods by static and dynamic sounding”)

K_2 – coefficient considering energy loss due to friction of rods against soil (should be determined using GOST 19912-2012 “Soils. Field test methods by static and dynamic sounding”)

n – number of hummer blows per run;

h – probe penetration depth per one run, cm

As per results of SPT tests for eluviated soils and alluvial sands (below 1.0 m depth) using tables of SP 11-105-97 “Engineering and geological surveys for construction”, the following was calculated: density, normative values of angle of internal friction (φ) and deformation modulus (E) (specific cohesion is taken close to zero) and also liquefaction potential under dynamic loads. Location of SPT test is shown at the map of Figure-3.2. Soil resistance depth curves are given in Figure-3.8 for point no. 2. For other points of SPT test, graphs are presented in Appendix C.

Eluviated soils studied via SPT at the Rooppur NPP site are presented mainly by solid and semi-solid loams and solid sandy loams. Alluvial sandy deposits are presented by silty and fine sands (rarely medium sands) with various water saturation degree. Results of determination of relative dynamic resistance of sandy soils against probe penetration pd, normative values of deformation modulus and angle of internal friction are given in Table 3.2. As per results of standard penetration tests sandy soils have the following density:

- Silty sands ($a^{pr}Q_{IV}$) slightly wet and wet – medium density;
- Silty sands ($a^{pr}Q_{IV}$) water-saturated – medium density;
- Fine sands ($a^{pr}Q_{IV}$) slightly wet and wet – medium density;
- Fine sands ($a^{pr}Q_{IV}$) water-saturated – medium density;
- Silty sands ($a^{pt}Q_{IV}$) slightly wet and wet – medium density;
- Silty sands ($a^{pt}Q_{IV}$) water-saturated – medium density;
- Medium sands ($a^{pt}Q_{IV}$) water-saturated – medium density;

Table 3.2: Relative dynamic resistance for sandy soils against probe penetration pd, deformation modulus and angle of internal friction.

Name of the soil	Length of studied interval, m (No. of measurements)	Relative dynamic soil resistance p_d, MPa	Deformation modulus E, MPa	Angle of internal friction φ, degree
Silty sand ($a^{pr}Q_{IV}$), slightly wet and wet	12.8 (128)	$\frac{1.0…7.6}{2.7}$	17.0	27.5
Silty sand ($a^{pr}Q_{IV}$), water-saturated	3.2 (32)	$\frac{6.8…9.6}{3.7}$	-	-
Fine sand ($a^{pr}Q_{IV}$), slightly wet and wet	3.5 (35)	$\frac{1.6…6.2}{2.8}$	18.2	30.0
Fine sand ($a^{pr}Q_{IV}$), water-saturated	1.2 (12)	$\frac{4.0…5.2}{1.8}$	15.0	29.0
Silty sand ($a^{pt}Q_{IV}$), wet	0.7 (7)	$\frac{6.4…7.1}{1.9}$	15.0	27.0
Silty sand ($a^{pt}Q_{IV}$), water-saturated	19.0 (190)	$\frac{5.2…15.6}{4.8}$	-	-
Fine sand ($a^{pt}Q_{IV}$), water-saturated	7.5 (75)	$\frac{7.1…17.0}{5.0}$	26.3	32.5
Medium sand ($a^{pt}Q_{IV}$)	1.6 (16)	$\frac{8.9…10.5}{5.0}$	33.5	35.0
Note: value of relative dynamic resistance of soil (P_d) is given in decimal: in numerator – measurement interval, in denominator – average value.				

Assessment of sand liquefaction potential was done using average values of relative dynamic resistance p_d (Table 8 of SP 11-105-97). In the layer of Modern Quaternary alluvial deposits of the flood plain facies predominant are wet and water-saturated silty and fine sands. Liquefaction potential of Modern Quaternary alluvial deposits of the flood plain facies for slightly-wet, wet and water-saturated silty sands and slightly wet and wet fine sands is low, but for fine water-saturated sands liquefaction potential is rather high. In the layer of Modern Quaternary alluvial deposits of the channel facies ($a^{pt}Q_{IV}$) predominant are wet and water-saturated silty sands, water-saturated fine sands and medium sands. Liquefaction potential of Modern Quaternary alluvial deposits of the channel facies for slightly-wet and wet silty sands – is rather expectative, and for water-saturated silty, fine and medium sands – is almost equal to zero. Results of determination of liquefaction potential for sands under dynamic loads are given in Table 3.3.

Table 3.3: Liquefaction potential for sands under dynamic loads.

Stratigraphic index		Name of soils	Average value of p_d, MPa	Liquefaction potential for sands under dynamic loads
$a^{pr}Q_{IV}$		Silty sand, slightly wet and wet	2.7	Low
		Silty sand, water-saturated	3.7	Low
		Fine sand, wet	2.8	Low
		Fine sand, water-saturated	1.8	Possible
$a^{pt}Q_{IV}$		Silty sand, slightly wet and wet	1.9	Possible
		Silty sand, water-saturated	4.8	Almost Possible
		Fine sand, water-saturated	5.0	Almost Possible
		Medium sand	5.0	Almost Possible

At the Rooppur NPP site, clay soils are observed sandy loams and loams of various consistency. For clayey soils average values of relative dynamic soil resistance were determined as per SPT data. Results of standard penetration tests for clayey soils of the Rooppur NPP site are given in Table 3.4.

Table 3.4: Relative dynamic resistance for clayey soils against probe penetration pd and deformation modulus

Stratigraphic index	Name of soils	Length of studied interval, m (No of measurements)	Relative dynamic soil resistance pd, MPa	Deformation modulus E, MPa
$a(e)Q_{IV}$	Solid and semi-solid loam	1.3 (13)	$\frac{1.0\ldots1.7}{2.8}$	-
	Solid sandy loam	0.6 (6)	$\frac{1.0\ldots1.6}{1.5}$	-
$a^{pr}Q_{IV}$	Solid and semi-solid loam	1.3 (13)	$\frac{2.6\ldots4.2}{2.4}$	-
	Low-plastic and high plastic loam	5.1 (51)	$\frac{1.5\ldots4.2}{1.0}$	-
	Plastic sandy loam	1.4 (14)	$\frac{3.6\ldots5.0}{2.1}$	-

$a^{pt}Q_{IV}$	High-plastic loam	4.5 (45)	$\frac{6.2…11.7}{2.1}$	-

3.4 Geo-Physical Survey (Cross-Section of Soil Profile along Reactor Building)

Large-scale comprehensive engineering-geological and engineering-geotechnical survey was carried out for assessment and characterization of engineering-geological and engineering-geotechnical of the Rooppur NPP Site. The cross-sections of soil profile are presented through Figure 3.8 and 3.9 of reactor areas and characterization of engineering-geological and engineering-geotechnical comprising of the following laboratory works:

The selection of soil samples from the boreholes was performed every 1.0 - 2.0 m on average.

For sandy and coarse disturbed soils, the following properties were defined:

1. the natural moisture content by drying to constant weight;
2. the density of sand in loose and dense state;
3. density of soil particles with picnometric method;
4. angle of friction in air-dry condition and under water;
5. determination of granulometric composition by sieving;
6. determination of relative organic compound with the method of ignition loss;
7. strength properties using direct shear test for given values of density and moisture content;
8. deformation properties using triaxial compression test and uniaxial test for given density and moisture content.

The following properties were defined for the undisturbed sandy soil:

1. the natural moisture content by drying to constant weight;
2. density determination with cutting ring;
3. the density of sand in loose and dense state;
4. density of soil particles with picnometric method;

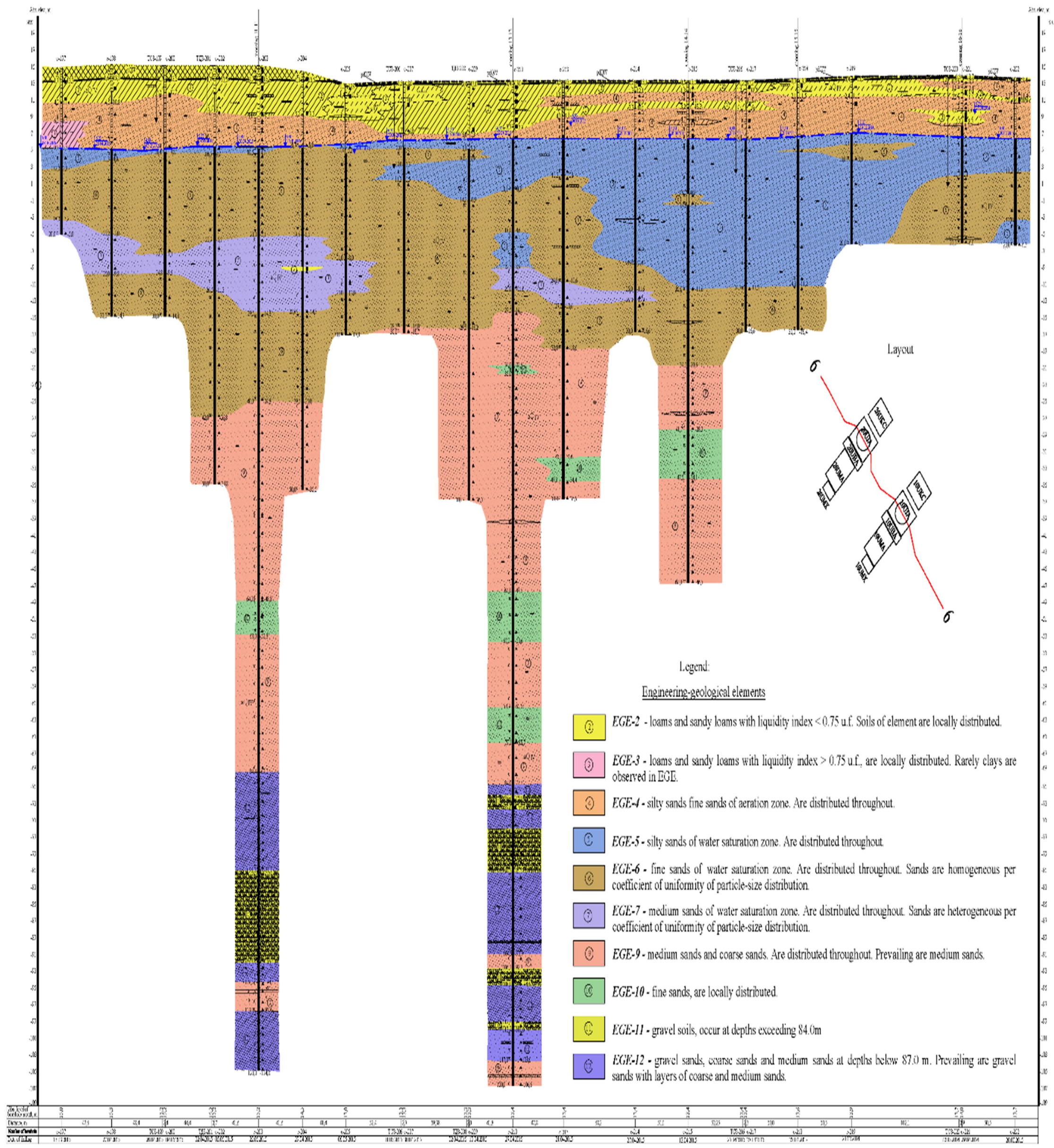

Figure 3.10: Section of engineering-geological borehole of Reactor Units

3.5 Physical-Mechanical Properties of Soils

Foundation soils of the RNPP site down to the studied depth of 120 m are combined in 12 engineering-geological elements (EGE) with consideration of genesis, lithological composition and physical-mechanical properties obtained during field and lab studies. EGE present main soil units for engineering-geological schematization of the soil mass.

The following EGE are differentiated in the foundation soil:

EGE-1 – clays with liquidity index < 0.75 u.f. Soils of element are locally distributed in form of lenses and interlayers.

EGE-2 – is presented by loams and sandy loams with liquidity index <0.75 u.f. Soils are locally distributed and occur mainly in upper part of the section in form of lenses and interlayers.

EGE-3 – is presented by loams and sandy loams with liquidity index ≥ 0.75 u.f. In some cases clays are observed in this EGE. Soils of the EGE are locally distributed in form of lenses and interlayers;

EGE-4 – is presented by silty and fine sands of the zone of GWL seasonal fluctuation. Soils of this EGE are distributed throughout;

EGE-5 – is presented by silty sands of water-saturation zone. Soils of this EGE are distributed throughout.

EGE-6 – is presented by fine sands of water-saturation zone. Soils of this EGE are distributed throughout;

EGE-7 – is presented by medium sands of water-saturation zone. Soils of this EGE are dis- tributed throughout.

EGE-8 – is presented by coarse sands of water-saturation zone. Soils are locally distributed in form of lenses and interlayers. Sandy soils that occur in water-saturation zone at depths below 27.5-45 m

EGE-9 – is presented by medium sands with lenses of coarse and gravel sands of water- saturation zone. Soils of this EGE are distributed throughout;

EGE-10 – is presented by fine sands with single interlayers of silty sands of water- saturation zone. Soils are locally distributed in form of lenses and interlayers.

EGE-11 – is presented by gravel soils of water-saturation zone. Soils of this EGE are dis- tributed throughout in the lower parts of geological section

EGE-12 – is presented by gravel sands with lenses and interlayers of coarse and medium sands of water-saturation zone. Soils of this EGE are distributed throughout in the lower parts of geological section.

3.6 Engineering and Geotechnical test Results. Summary Table of Physical-Mechanical Soil Properties

The collected samples from different engineering geological layers were subjective to laboratory studies and geophysical tests like pressuremeter and cone penetration were conducted to get deformation modulus, cohesion and angle of internal friction of respective soil layers. The outcomes of engineering and geotechnical test results are mentioned in Table 3.5.

Table 3.5: Engineering and Geotechnical Survey Results

EGE	Lithology	Physical-mechanical soil properties regarding to laboratory studies						Modulus of deformation pressuremeter tests results	Cone penetration tests			Soil density regarding to geophysical survey data
		Natural moisture content W. u.f.	Soil density ρd. g/cm3	Dry soil density ρd. g/cm3	Plasticity index Ip. u.f.	Liquidity index I L. u.f. .	Deformation modulus based on triaxial tests		Modulus of deformation	φ. °	C. kPa	
1	Clays with JL≤ 0.75	0.316	1.90	1.4	0.194	0.24	4					
2	Clay loams with JL<0.75	0.263		1.5	0.098	0.13	8	11	11	20	20	
	Sandy loams with JL< 0.75	0.210		1.5	0.056	-0.64	7	8	15	21	24	
	Clay loams and sandy loams with JL< 0.75 (joint processing)	0.243	1.81	1.5			7	11	12	20	21.5	1.45-1.86 / 1.73
3	Clay loams with JL≥ 0.75	0.352		1.4	0.106	0.91	8					
	Sandy loams with JL≥ 0.75	0.316		1.4	0.058	1.00	14		6	18	16	
	Clay loams and sandy loams with JL≥ 0.75	0.343	1.88	1.4			9		6	18	16	1.86-1.93 / 1.92
4	Dusty sand of aeration zone	0.101		1.4			5	9	22.7	31		
	Fine sand of aeration zone	0.071		1.4			5	10	24.2	32		
	Dusty and fine sands (joint processing)	0.097	1.56	1.4			5	9	22.9	32		1.51-1.87 / 1.71
5	Dusty sand of water saturation zone	0.244	1.85	1.5			16	15	24	31		1.80-1.94 / 1.92
6	Fine sand of water saturation zone	0.234	1.90	1.5			24	25	24	31		1.70-1.97 / 1.92
7	Mean coarseness sand of water saturation zone	0.202					28	33	28	33		1.86-1.95 / 1.92
8	Coarse sand of water saturation zone	0.216					37					1.93
9	Average coarse sand of water saturation zone	0.191		1.6			40	35				
	Coarse sand of water saturation zone	0.178					41					
	Medium and coarse sand of water saturation zone			1.6			40	35				1.92-1.97 / 1.94
10	Fine sand of water saturation zone	0.220					46	30				1.92-1.95 / 1.94
11	Gravel soil						142					1.92-1.96 / 1.94
12	Gravel sand with interlayers of medium and coarse sand						137					1.94

3.7 Improvement of Soil under Reactor Building

The ground improvement work was conducted by deep soil mixing technology under power reactor building and its surrounding facilities to enhanced soil deformation properties of the site soil. The ground improvement depth was 20 meters of having two meters diameter pile which overlapped each other's and formed a solid rock strata in that area. The average use of cement for improved soil was 278 kg/m^3

1. (b)

(c)

Figure 3.11: (a) works performed (b) piles top (c) digging pile for physical checking

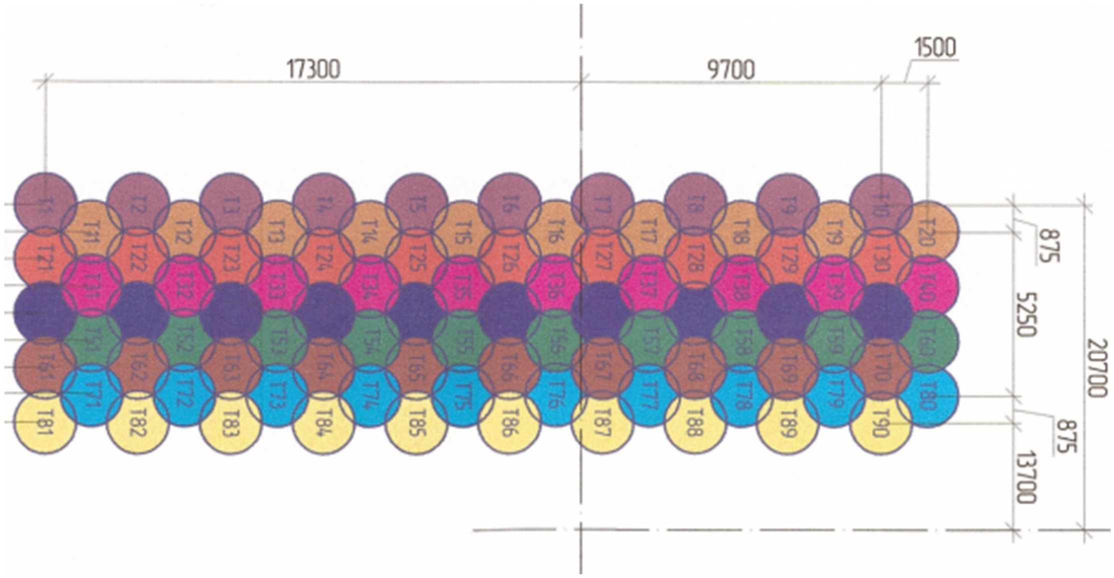

Figure 3.12: Plan view of cement grout piles

During performing soil stabilization works wet samples are collected and for hardening process water curing method is applied.

Figure 3.13: In situ wet grab samples collection during soil stabilization work

Figure 3.14: Wet grab samples are submerged in water for curing.

Coring is performed after 28 days of piles execution. The core samples are important to get actual information and engineering properties of soils as it collected from working platform.

Figure 3.15: Core samples are collected and transported to site laboratory.

3.8 Results of Stabilized Soil

Engineering properties of stabilized soil are found through following tests

3.8.1 Drilling Works

When recovering the core (49 boreholes), RQD index was determined, the average value of which for all the boreholes was 92%. Based on the RQD index obtained acc. to methodology of GOST 25100-2011, the quality of the rock soil is characterized as very good (> 90%).

3.8.2 Pressuremeter tests

Pressuremeter tests were performed in five piles (No 13, No 392, No 580, No 1760, No 2120) through the whole pile depth with interval of 3 m, achieving the maximal depth 19 m. Results of pressuremeter tests of stabilized soils are given in Table 3.6.

Table 3.6: Result of pressuremeter tests

No of pile	Depth of test, m	Deformation modulus E, MPa
For whole depth of the stabilized soil mass (down to 20 m)		
J13	4.0	890
J13	7.0	785
J13	10.0	851
J13	13.0	1145*
J13	16.0	1262*
J13	19.0	498
J392	3.0	615
J392	6.0	584
J392	9.0	772
J392	12.0	576
J392	15.0	510
J392	18.0	634

Table 3.7: Result of pressuremeter tests (continued..)

No of pile	Depth of test, m	Deformation modulus E, MPa
J580	6.0	416
J580	9.0	222
J580	12.0	398
J580	15.0	519
J580	18.0	431
J1760	19.0	804
J1760	16.0	1464*
J1760	13.0	684
J1760	10.0	1548*
J1760	7.0	300
J2120	4.0	655
J2120	7.0	591
J2120	10.0	695
J2120	16.0	501
J2120	19.0	525
Average value		**585**
Minimum value		222
Maximum value		890
No of determinations		23
J13	4.0	890
J13	7.0	785
J392	3.0	615
J392	6.0	584
J392	9.0	772
J580	6.0	416
J580	9.0	222
J1760	7.0	300
J2120	4.0	655
J2120	7.0	591
Average value		**583**
Minimum value		222
Maximum value		890
No of determinations		10
Note – Values marked with* were rejected and weren't included in calculation of average		

3.8.3 Plate-Bearing Tests

Six plate bearing tests were performed on heads of the piles No 413, No 524, No 896, No 1672, No 1744 and No 2354 after the cleaning of the site not earlier than 29 days after making of piles. Results of plate-beating tests are given in Table 3.7.

Table 3.8: Results of plate-beating tests

No of pile	Depth of test, m	Deformation modulus E, MPa
413	From surface of stabilized soil	448
524		402
896		452
1672		517
1744		484
2354		472
Average value		**462**
Minimum value		402
Maximum value		517
No of determinations		6
RMSD		38.739
Variation coefficient		0.1

3.8.4. Tri-axial Tests

Lab tests were performed on wet grab samples collected during stabilization works and core samples from piles of the age of 28-39 days. Results of lab tests for determination of values of physical-mechanical properties of stabilized soils and their statistical analysis in accordance with GOST 20522-2012. The results of tri-axial tests are in Appendix D.

3.8.5 Permeability test

Permeability test is also performed on samples taken from the depth from 7.3 to 17.9 m. The values of permeability were in the range from 5.58 x 10-6 to 2.93 x 10-5 m/s, average value 1.58 x 10-5 (or 1.36 m/day).

Table 3.9: Presents normative and design values of physical-mechanical properties of stabilized soils based on results of lab tests.

Name of soil	Water content W, %	Soil density ρ, g/cm³	Dry soil density ρ_d, g/cm³	Uniaxial compression strength (water-saturated), Rc, MPa	Angle of internal friction ϕ, degrees	Specific cohesion c, kPa	Deformation modulus, E, MPa
For whole depth of the stabilized soil mass (down to 20 m)							
soil-cement (core)	22.5	1.83/1.82*	1.50/1.49*	3.04/2.97*	51/49*	384/319*	666
soil-cement ("wet grab samples") age of samples is 28 days	-	-	-	3.05/2.98*	-	-	-
For stabilized soil mass (down to depth of 10 m)м							
soil-cement (core)	27.5	1.81/1.79*	1.42/1.40*	2.872.77*	53/-*	383/-*	676
Notes: 1 Values marked with * are design values at confidence level □ = 0.95 2 Rc values for "wet grab samples" were obtained for 28-day old samples							

3.8.6 Geophysical Survey

Engineering-geophysical studies as a part of engineering geological survey for quality control of the stabilized foundation soils of the Rooppur NPP buildings and structures solved the following tasks:

Determination of the propagation velocities of compressional (Vp) and shear (Vs) seismic waves and the study of their distribution in plan view and in depth of the stabilized foundation soil;

1. Assessment of homogeneity of the foundation according to seismic properties.
2. The set of geophysical studies included down hole and surface seismic methods:
3. Seismic logging;
4. Crosshole seismic survey on longitudinal P-waves;
5. Seismic profiling on compressional (P) and shear (S) waves.

Seismic logging (SL) in boreholes was performed to obtain data on the P- and S-wave velocities along borehole and to calculate dynamic moduli, Poisson ratio.

3.8.7 Seismic Properties of Stabilized Soil according to Seismic Logging Data

According to the data of seismic logging processing, all boreholes show an increase in the P- and S-wave velocities with depth. In the upper part of stabilized soil mass P-wave velocities are from 1920 to 2300 m/s, S-waves from 1020 to 1145 m/s. In the lower part P-wave velocities are from 2500 up to 2730 m/s, S-wave from 1320 to 1460 m/s.

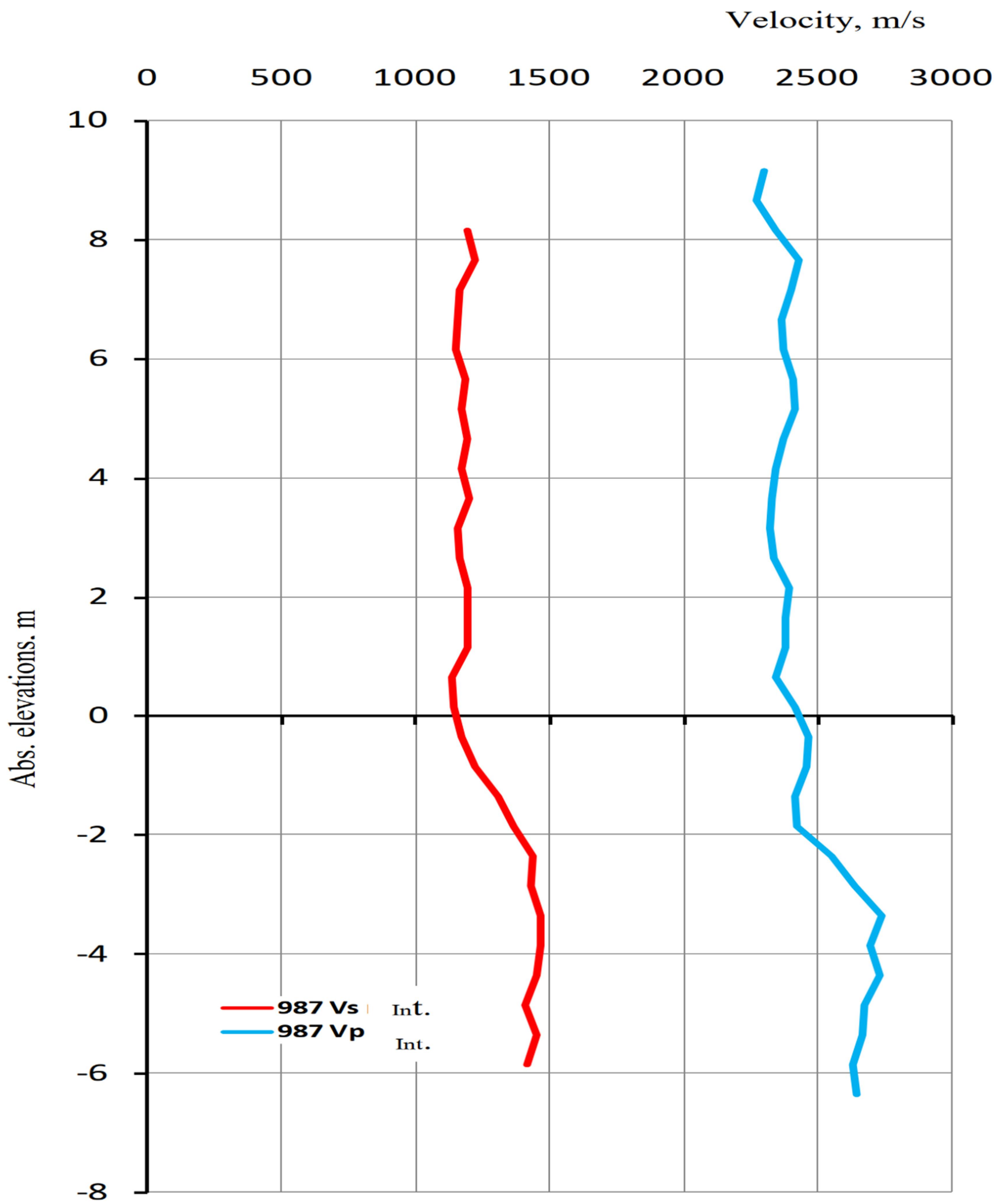

Figure 3.16: Charts of P- and S-wave interval velocities for borehole 987

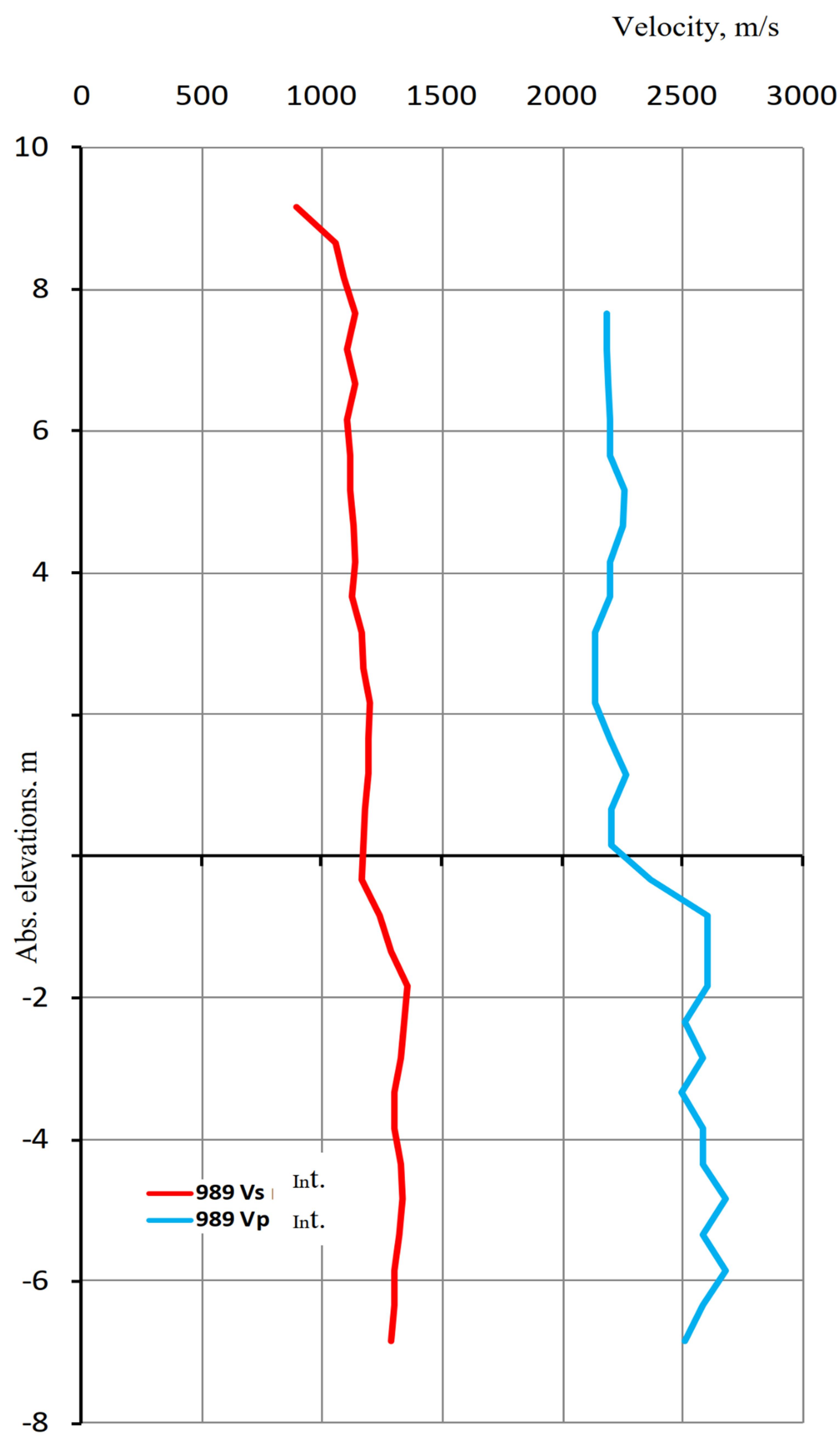

Figure 3.17: Charts of P- and S-wave interval velocities for borehole 989

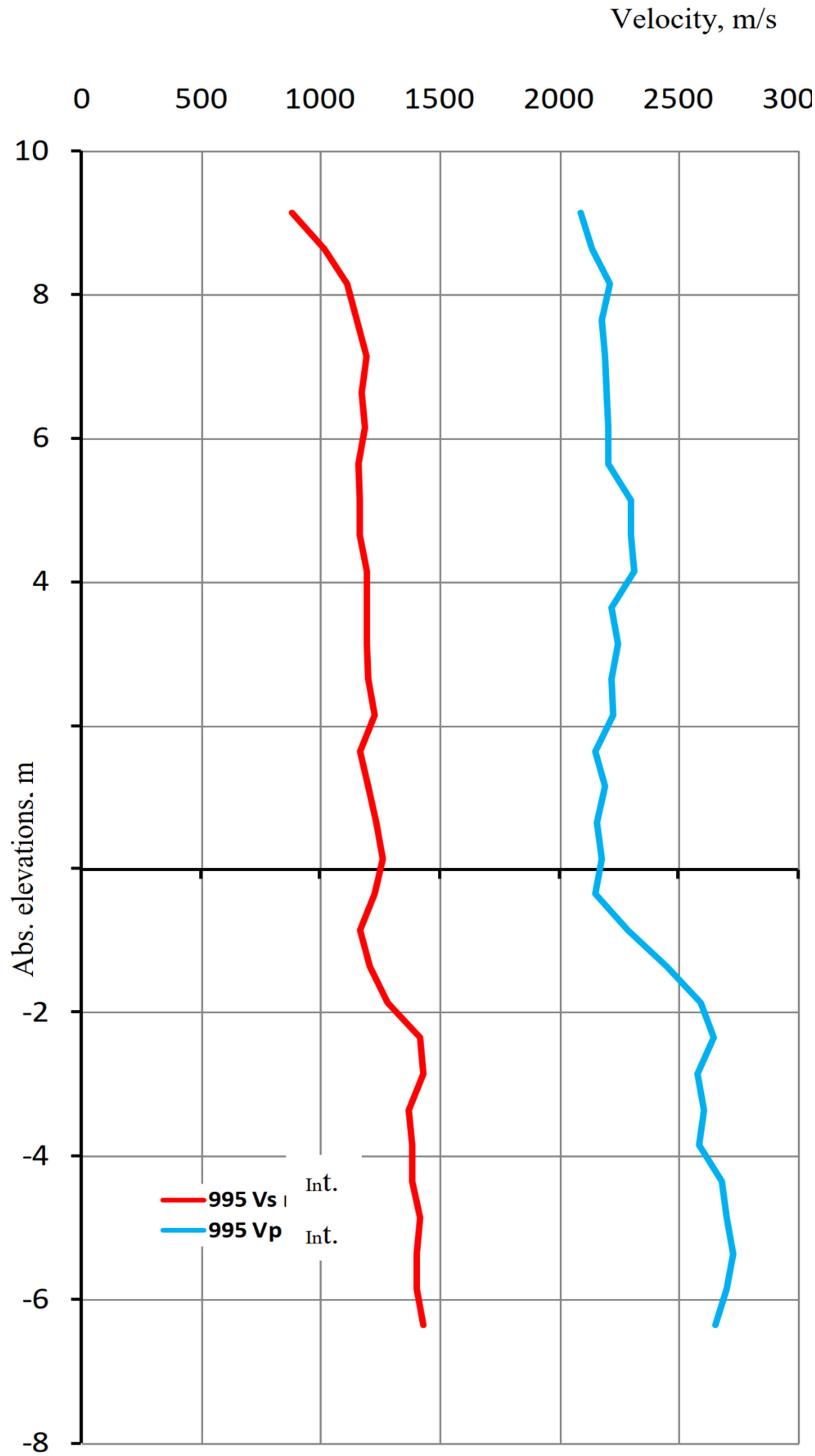

Figure 3.18: Charts of P- and S-wave interval velocities for borehole 995

3.9 Results Summery of Soil Samples

Based on the test results of soil samples of Rooppur NPP Site, the required engineering parameters are taken for developing Plaxis 3D software model of natural/unimproved and improved soil.

3.9.1 Input parameters of the Mohr Coulomb model and Hardening Soil model of unimproved soil.

Table 3.10: Parameters of Mohr-coulomb model of unimproved/natural soil

SL	Properties	Unit	Loam/ Layer thickness 1.8 m (-1.8 m)	Fine sand/layer thickess 13 m (-14.8 m)	Medium coarse sand/ layer thick 10 m (-24.8)	Coarse sand/ layer thickness 59.3 m (-84.1)	Gravel/ layer thickness 35.0 m (-119.1)
1	Unsaturated Unit Weight, γ_{unsat}	kN/m^3	14.5	15.0	15.3	16.3	16.3
2	Saturated Unit Weight, γ_{sat}	kN/m^3	18.2	18.5	18.9	19.4	19.4
3	Modulus of Elasticity, E	kN/m^2	9000	15000	25000	37000	137000
4	Poisson's ratio, ν		0.35	0.35	0.35	0.35	0.35
5	Cohesion, c'	kN/m^2	21.5	0	0	0	0
6	Angle of Friction, φ	Degree	19	29	29	36	39
7	Interface factor, Rint						
8	Dilation Angle, Ψ	Degree	0	0	0	0	0

Table 3.11: Parameters of HS Model of unimproved soil

SL	Properties	Unit	Loam/ Layer thickness 1.8 m (-1.8 m)	Fine sand/layer thickness 13 m (-14.8 m)	Medium coarse sand/ layer thick 10 m (-24.8)	Coarse sand/ layer thickness 59.3 m (-84.1)	Gravel/ layer thickness 35.0 m (-119.1)
1	Unsaturated Unit Weight, γ_{unsat}	kN/m ^{3}	14.5	15.0	15.3	16.3	16.3
2	Saturated Unit Weight, γ_{sat}	kN/m ^{3}	18.2	18.5	18.9	19.4	19.4
3	Secant Modulus of Elasticity, E_{50}^{ref}	kN/m^2	18000	30000	50000	74000	274000
4	Oedometer Modulus of Elasticity, E_{oed}^{ref}	kN/m^2	14400	24000	40000	59200	219200
5	Unloading/Reloading Modulus of Elasticity, E_{ur}^{ref}	kN/m^2	54000	90000	150000	222000	822000
6	Poisson's ratio, ν		0.35	0.35	0.35	0.35	0.35
7	Cohesion, c′	kN/m^2	21.5	0	0	0	0
8	Angle of Friction, φ	Degree	19	29	29	36	39
9	Dilation Angle, Ψ	Degree	0	0	0	0	0
10	Unloading Reloading Poisson's Ratio, ν_{ur}		0.2	0.2	0.2	0.2	0.2
11	Interface factor, Rint		0.7	0.7	0.7	0.7	0.7
12	K_0 value for normal consolidation (default K_0^{nc} = *1 - sin φ*) K_0^{nc}		0.674	0.515	0.412	0.412	0.37

SL	Properties	Unit	Loam/ Layer thickness 1.8 m (-1.8 m)	Fine sand/layer thickness 13 m (-14.8 m)	Medium coarse sand/ layer thick 10 m (-24.8)	Coarse sand/ layer thickness 59.3 m (-84.1)	Gravel/ layer thickness 35.0 m (-119.1)
13	Power for stress-level dependency of stiffness, m		0.5	0.5	0.5	0.5	0.5

3.9.2 Input parameters of the Mohr Coulomb model and Hardening Soil model of improved soil.

Summary of input parameters of Mohr Coulomb model and Hardening soil model of improved soil is given in Table 3.11 and Table 3.12.

Table 3.12: Parameters of Mohr-coulomb model of improved soil

SL	Properties	Unit	Soil-cement stabilized soils 20m (-20m)	Medium coarse sand/ layer thick 4.8 m (-24.8)	Coarse sand/ layer thickness 59.3 m (-84.1)	Gravel/ layer thickness 35.0 m (-119.1)
1	Unsaturated Unit Weight, γ_{unsat}	kN/m3	21.0	15.3	16.3	16.3
2	Saturated Unit Weight, γ_{sat}	kN/m3	22.0	18.9	19.4	19.4
3	Modulus of Elasticity, E	kN/m2	200000	25000	37000	137000
4	Poisson's ratio, ν		0.35	0.35	0.35	0.35
5	Cohesion, c'	kN/m2	0	0	0	0
6	Angle of Friction, φ	Degree	38.0	29.0	36.0	39.0
7	Interface factor, Rint					
8	Dilation Angle, Ψ	Degree	0	0	0	0

Table 3.13: Parameters of HS Model of improved soil

SL	Properties	Unit	Improved soil Layer thickness 20 m (-20 m)	Medium coarse sand/ layer thick 4.8 m (-24.8)	Coarse sand/ layer thickness 59.3 m (-84.1)	Gravel/ layer thickness 35.0 m (-119.1)
1	Unsaturated Unit Weight, γ_{unsat}	kN/m^3	14.71	15.3	16.3	16.3
2	Saturated Unit Weight, γ_{sat}	kN/m^3	18.63	18.9	19.4	19.4
3	Secant Modulus of Elasticity, E_{50}^{ref}	kN/m^2	83800	50000	74000	274000
4	Oedometer Modulus of Elasticity, E_{oed}^{ref}	kN/m^2	66000	40000	59200	219200
5	Unloading/Reloading Modulus of Elasticity, E_{ur}^{ref}	kN/m^2	251400	150000	222000	822000
6	Poisson's ratio, ν		0.35	0.35	0.35	0.35
7	Cohesion, c′	kN/m^2	176	0	0	0
8	Angle of Friction, φ	Degree	49	36	36	39
9	Dilation Angle, Ψ	Degree	0	0	0	0
10	Unloading Reloading Poisson's Ratio, ν_{ur}		0.2	0.2	0.2	0.2
11	Interface factor, Rint		0.7	0.7	0.7	0.7
12	K_0 value for normal consolidation (default $K_0^{nc} = 1 - \sin\varphi$) K_0^{nc}		0.245	0.412	0.412	0.37

SL	Properties	Unit	Improved soil Layer thickness 20 m (-20 m)	Medium coarse sand/ layer thick 4.8 m (-24.8)	Coarse sand/ layer thickness 59.3 m (-84.1)	Gravel/ layer thickness 35.0 m (-119.1)
13	Power for stress-level dependency of stiffness, m		0.5	0.5	0.5	0.5

Chapter Four

NUMERICAL MODELLING AND ANALYSIS

4.1 Introduction

The chapter is intended to present the numerical modeling and derivation of geotechnical parameters for numerical analysis using the finite element method PLAXIS 3D. Software PLAXIS is a package of calculation software using the Finite Element method, designed specifically for the analysis of deformations and the stability of geotechnical structures. The software allows to simulate incrementally the processes of construction and the excavation of soil, the application loads and calculate the consolidation, etc. This method gives a realistic assessment of the stresses and strains. The PLAXIS 3D has been chosen for the research study because it is mainly developed for foundation design and analysis and has popularity amongst practicing engineers, and over the years a wealth of knowledge and experience available for reference has been accumulated.

In the following sections, the original base design using the Harding Soil (HS) model together with the design assumptions and modeling approach using idealization of various structural components of the mat foundation is reported.

4.2 FEM Model in PLAXIS 3D Software

The software package PLAXIS 3D is designed for the performance of Finite Element stress-strain analysis considering the interaction of the foundation with the subsoil in 3D boundary conditions. The following steps are implemented utilizing the software: compilation of 3D design model of the foundation and subsoil below the building and structures, soil improvement by changing the physical and mechanical properties of soils under the buildings and structures, applying the loads from foundation to the subsoil, calculation of settlements of the foundations on the improved soil, calculation of deformations and stresses in the soil massive, calculation of tilting. Soils were modeled by 10-noded elements. The Drained Method was adopted for HS model. Groundwater is 6.5 meters below the existing ground surface at Rooppur site. The soil profile is modeled up to 119.1 m with varying layers.

4.2.1 Reactor Building geometry

The reactor building is the heart of a nuclear power plant, which produced enormous heat energy from a nuclear chain reaction. The building has two containments (inner and outer) to maintain radiological integrity and resist external thrust. The approx. size of the foundation is 73 m X 79 m. The thickness of mat foundation is 3.0 meters. The total height of the building from the foundation mat to above is about 72.0 meters. A nuclear reactor is a complex structure having different dimensional vibratory dynamic loads.

Following external loads are considered in Figure 4.1 including dead, live, and vibratory which come to the foundation mat as uniformly distributed load 491 kN/m^2. The mat's center of gravity and total building center of gravity is same.

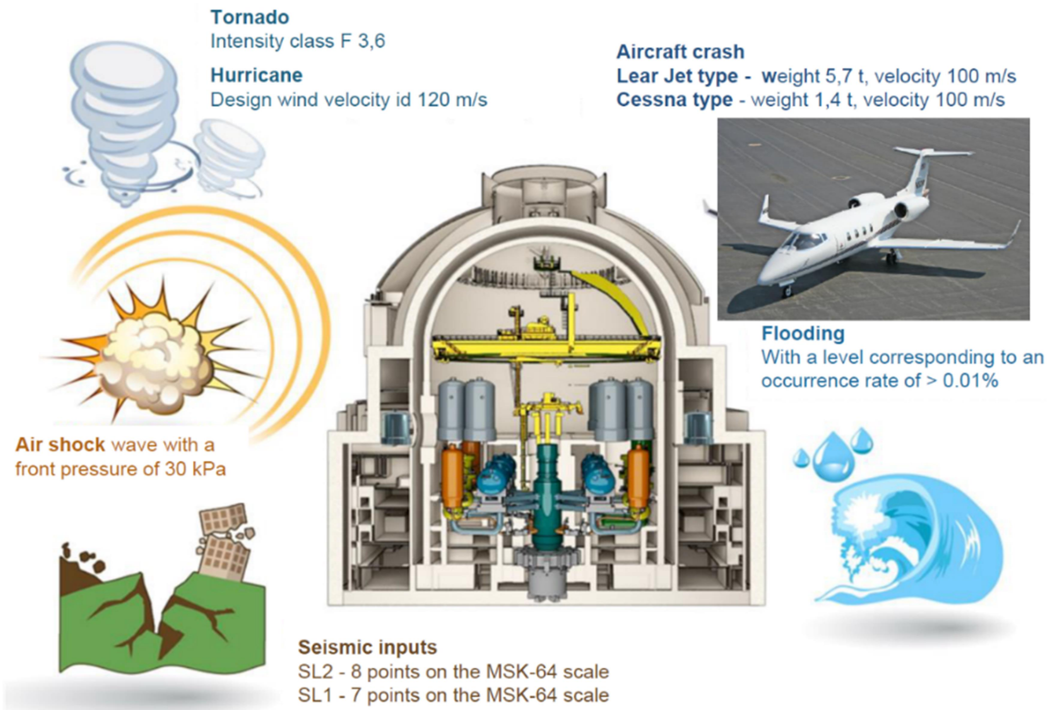

Figure 4.1: Cross-section of reactor building with all external loads

4.2.2 Soil Stratigraphy

a) Natural or Unimproved Soil

Considering the uniformity of soil properties in unimproved soil beneath reactor up to 120m the subsoil consists of five layers. The upper loam layer lies between the ground level (z=0) and z= -1.8 m. The under-laying 2nd layer is up to fine sandy layer lies to -14.8 m. The 3rd layer medium coarse sand up to -24.8, 4th layer coarse sand up to -84.1 m and 5th layer consists of gravels start from -84.1 to -119.1m. All other properties of soil geological layers are collected and recorded bellow in Table 4.1:

Table 4.1: Parameters of HS Model of unimproved soil

SL	Properties	Unit	Loam/ Layer thickness 1.8 m (-1.8 m)	Fine sand/layer thickness 13 m (-14.8 m)	Medium coarse sand/ layer thick 10 m (-24.8)	Coarse sand/ layer thickness 59.3 m (-84.1)	Gravel/ layer thickness 35.0 m (-119.1)
1	Unsaturated Unit Weight, γ_{unsat}	kN/m ^{3}	14.5	15.0	15.3	16.3	16.3

2	Saturated Unit Weight, γ_{sat}	kN/m ^{3}	18.2	18.5	18.9	19.4	19.4
3	Secant Modulus of Elasticity, E_{50}^{ref}	kN/m^2	18000	30000	50000	74000	274000
4	Oedometer Modulus of Elasticity, E_{oed}^{ref}	kN/m^2	14400	24000	40000	59200	219200
5	Unloading/Reloading Modulus of Elasticity, E_{ur}^{ref}	kN/m^2	54000	90000	150000	222000	822000
6	Poisson's ratio, ν		0.35	0.35	0.35	0.35	0.35
7	Cohesion, c′	kN/m^2	21.5	0	0	0	0
8	Angle of Friction, φ	Degree	19	29	29	36	39
9	Dilation Angle, Ψ	Degree	0	0	0	0	0
10	Unloading Reloading Poisson's Ratio, ν_{ur}		0.2	0.2	0.2	0.2	0.2
11	Interface factor, Rint		0.7	0.7	0.7	0.7	0.7
12	K_0 value for normal consolidation (default K_0^{nc} = *1 - sin φ*) K_0^{nc}		0.674	0.515	0.412	0.412	0.37
13	Power for stress-level dependency of stiffness, m		0.5	0.5	0.5	0.5	0.5

b) Improved Soil

The top layer of 20 m thickness is improved with cement slurry using DSM technology. The improved subsoil consists of four layers. The upper layer is improved and lies between the ground level (z=0) and z= -20.0 m. The under-laying 2nd layer is up to fine sandy layer lies to -24.8 m. The 3rd layer medium-coarse sand up to -84.1 and 4th layer consists of gravels starting from -84.1 to -119.1m. All properties of soil geological layers are recorded is below Table 4.2:

Table 4.2: Parameters of HS Model of improved soil

SL	Properties	Unit	Improved soil Layer	Medium coarse sand/	Coarse sand/ layer	Gravel/ layer thickne

			thickness 20 m (-20 m)	layer thick 4.8 m (-24.8)	thickness 59.3 m (-84.1)	ss 35.0 m (-119.1)
1	Unsaturated Unit Weight, γ_{unsat}	kN/m ^{3}	14.71	15.3	16.3	16.3
2	Saturated Unit Weight, γ_{sat}	kN/m ^{3}	18.63	18.9	19.4	19.4
3	Secant Modulus of Elasticity, E_{50}^{ref}	kN/m^2	83800	50000	74000	274000
4	Oedometer Modulus of Elasticity, E_{oed}^{ref}	kN/m^2	66000	40000	59200	219200
5	Unloading/Reloading Modulus of Elasticity, E_{ur}^{ref}	kN/m^2	251400	150000	222000	822000
6	Poisson's ratio, ν		0.35	0.35	0.35	0.35
7	Cohesion, c′	kN/m^2	176	0	0	0
8	Angle of Friction, φ	Deg	49	36	36	39
9	Dilation Angle, Ψ	Deg	0	0	0	0
10	Unloading Reloading Poisson's Ratio, νur		0.2	0.2	0.2	0.2
11	Interface factor, Rint		0.7	0.7	0.7	0.7
12	K_0 value for normal consolidation (default K_0^{nc} = *1 - sin φ*) K_0^{nc}		0.245	0.412	0.412	0.37
13	Power for stress-level dependency of stiffness, m		0.5	0.5	0.5	0.5

c) Structural properties of reactor foundation mat

The mat is reinforced cement concrete. The grade of concrete is B30W6, B30 is the compressive strength 30 MPa and W6 is water permeability category. Table 4.3 shows the other parameters required for analysis.

Table 4.3: Properties of foundation mat concrete

Parameter name	Symbols	Unit	Values
Thickness/depth	d	M	3.0
Density	γ	kN/m^3	25.0
Young's Modulus	E_1	kN/m^2	2.57 x10^7
Poisson's ratio	ν_{12}		0.2

4.2.3 Development of Plaxis 3D Model using unimproved and improved soil profile under Power Reactor.

The following four models are developed as per soil profiles and foundation mat mentioned in Table 4.1, 4.2 and Table 4.3 for numerical analysis using Plaxis 3D.

Table 4.4: Soil Models in improved and unimproved soil using Plaxis 3D

Designation	Model	Type of soil condition	Static loads On mat kN/m2	Applied earthquake	Earthquake load PGA
HS-US_Koba	Hardening Soil model	Unimproved	491	Kobe	0.33 g
HS-US_Loma	Hardening Soil model	Unimproved	491	Loma	0.33 g
HS-IS_Koba	Hardening Soil model	Improved	491	Kobe	0.33 g
HS-IS_Loma	Hardening Soil model	Improved	491	Loma	0.33 g

The soil model size in the plan views 300 meters x 300 meters and the size of mat foundation is 73 meters x79 meters. The elevation of the surface is considered at 13.4-meter from the mean sea level. The excavation depth is -1.0 meter. Earth's gravity is 9.8 m/s^2 and γ_{water} is 10 kN/m^3. The calculations are not taken into account the mutual influence of other surrounding buildings and structures.

Appropriate material properties and their parameters are assigned to the mat structures during modeling. For soil profile modeling, in situ soil properties are applied. Hardening Soil models (HS) are developed in Plaxis 3D for taking into account the difference in hardness elements during initial loading of soil and it's unloading with subsequent loading. Here, four models are developed. One, the mat is placed in natural (unimproved) soil and in another the mat is placed in improved soil.

The models are loaded with the same static and two different earthquake Kobe (1995) and Loma Prieta (1989) loads have been applied alternatively. These two motions have different characteristics. Kobe earthquake is a severe one with a magnitude Mw= 7.2 and PGA = 0.75 g. Loma Prieta has a magnitude Mw= 6.8 and PGA = 0.36 g. These records are applied in the horizontal direction at all bottom node of the model. They are scaled into same acceleration 0.33 g (Safe Shutdown Earthquake) for Rooppur NPP case. In order to reduce the calculation time only 5 s of Kobe earthquake and 5 s of Loma prieta earthquake are applied.

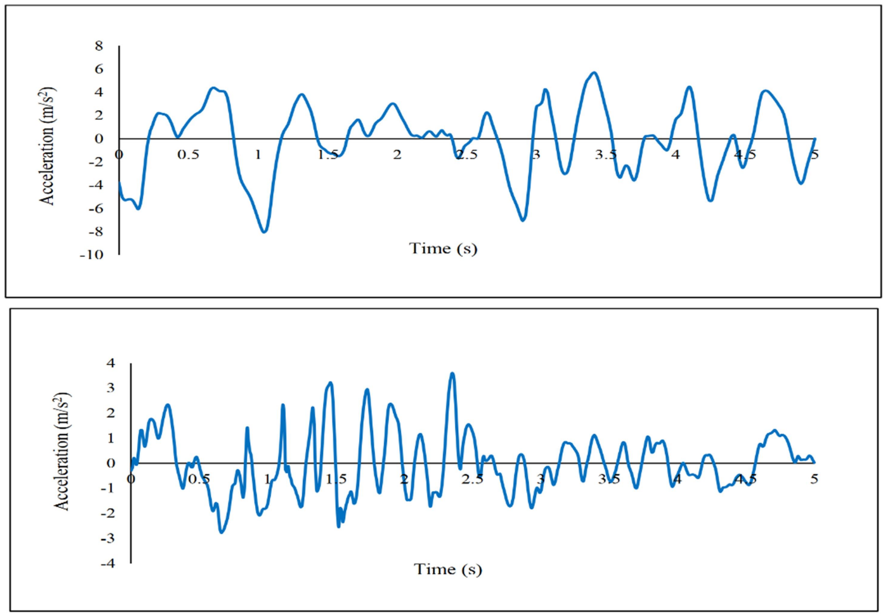

Figure 4.2: Original earthquake frequency (a) 1995 Kobe (b) 1989 Loma Prieta.

The design earthquake of Rooppur NPP is collected from Rooppur Project. The project is designed based on safety criteria of international regulations and safety guide of IAEA, the NPP structures and systems are required to be designed as follows:

i) Seismic Level, SL1- is called operating basis earthquake (OBE)/Design Earthquake. The OBE is reasonably expected to be experienced at the site during operating life of NPP. For Rooppur NPP, PGA 0.172g which is considered during analysis.

ii) Seismic Level, SL2- is called Safe Shutdown Earthquake (SSE). The SSE has a very low probability of being exceeded and a return period of the order of 10,000 years which is considered during analysis, for this PGA of 0.33 g.

4.3 Mesh Generation

Mesh generation is the practice of generating a mesh that approximates a geometric domain. Meshing is a collective term to denote the pre-processing phase of the Finite Element Analysis (FEA). For performing finite element calculation, a fully defined geometry is divided into finite elements. It is a tool that engineers use to complete their analysis of a particular design. The model is calculated using four types of meshing namely very course meshing, course meshing, medium meshing, and fine meshing. It is noticeable that the finer the meshing system, the more time has been required for the computation. The mesh generation process includes soil stratigraphy, structure, loads and boundary, the number of nodes generated for each type of meshing is shown in Table 4.5.

Table 4.5: Generated nodes for different type of meshing

Type of meshing	Soil elements	Number of nodes
Very course meshing	2343	4468
Course meshing	5814	9484
Medium meshing	12519	20491
Fine meshing	27366	40936
Very fine	64663	98127

For the current study medium mesh element has been used for both vertical and earthquake loading conditions. Following figures 4.3 to 4.7 shows the different meshing model.

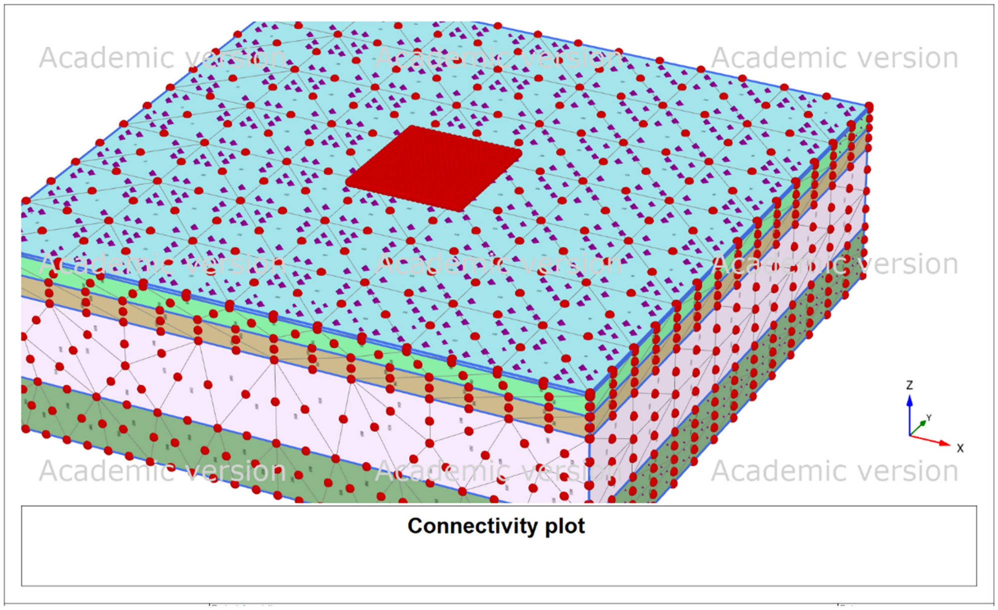

Figure 4.3: The model is meshed with Very Coarse meshing

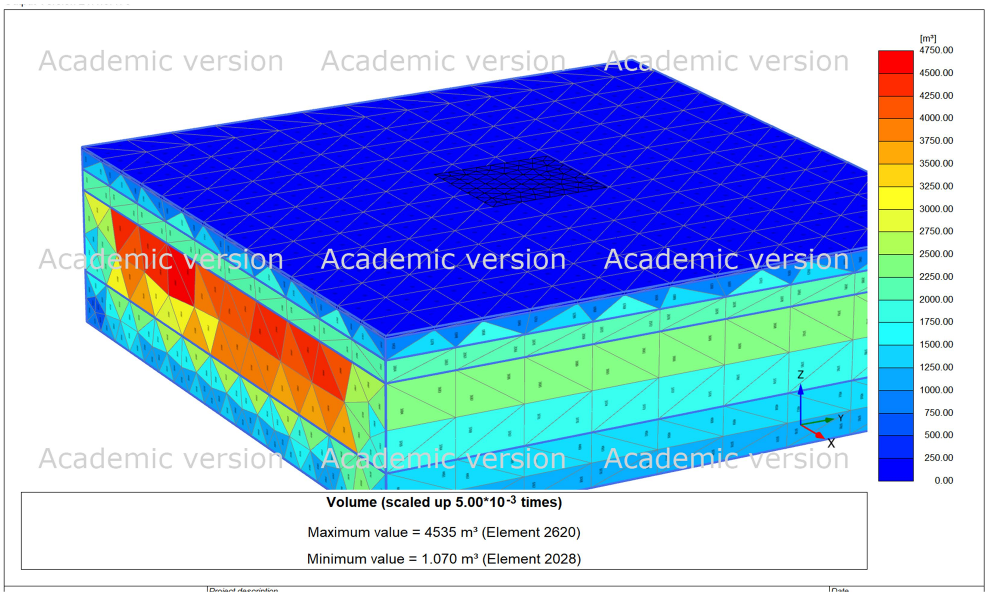

Figure 4.4: The model is meshed with Coarse meshing

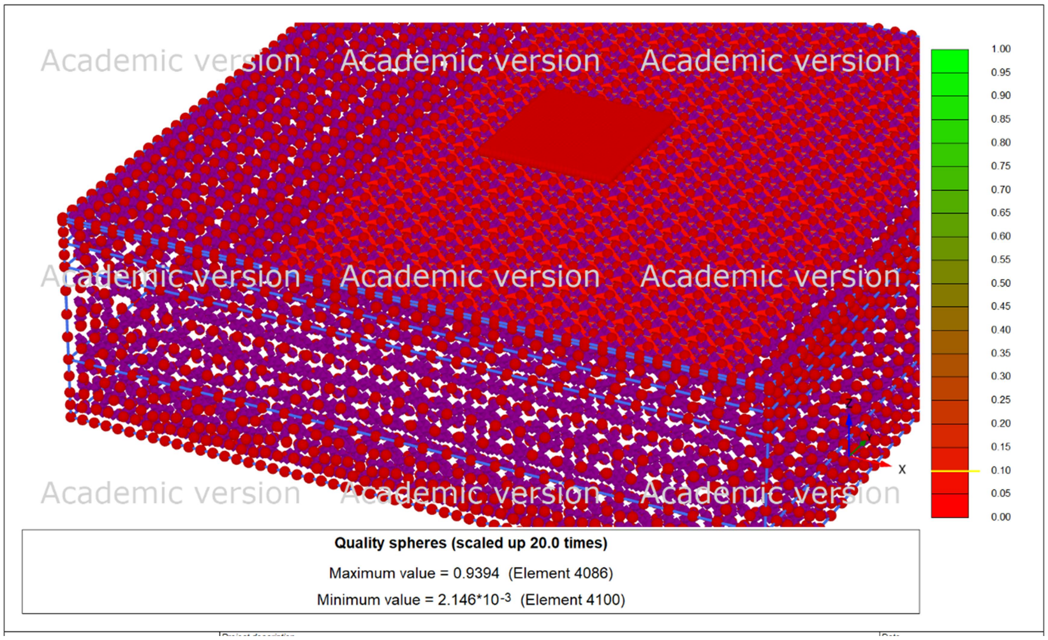

Figure 4.5: The model is meshed with medium meshing

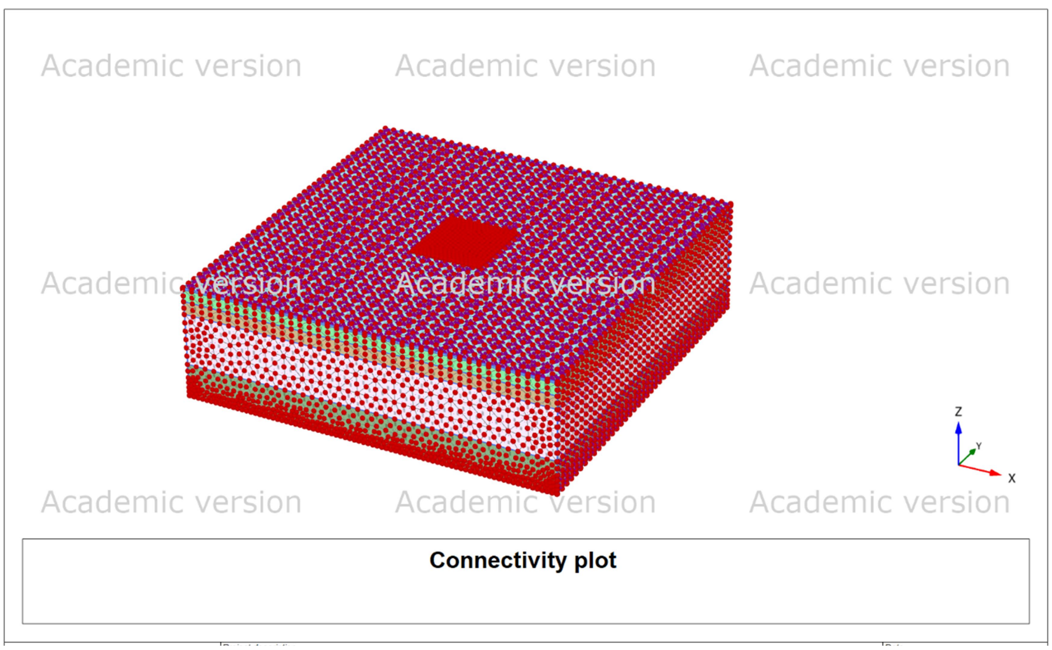

Figure 4.6: The model is meshed with fine meshing

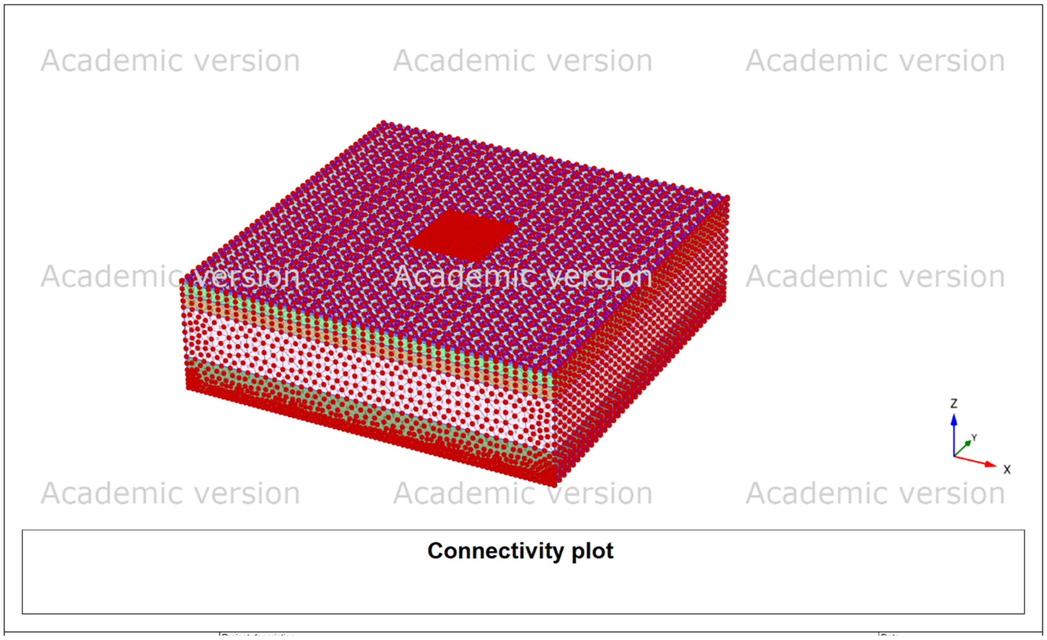

Figure 4.7: The model is meshed with Very fine meshing

4.4 Development of model and analysis

For the current study, HS model is used for modeling soil element according to soil investigation data available from Rooppur NPP which are listed in the above tables. The earthquake load is applied at the bottom of the FEM model as prescribed displacement in x-direction. In dynamic loading condition, using HS model generates plastic strain with increased preconsolidation stress in soil. Under this condition damping is defined by Rayleigh damping. The stage construction phases in PLAXIS 3D for earthquake loading condition are given below in Table 4.6.

The total amount of damping is introduced through frequency dependent Rayleigh formula. Here, Hardening Soil model with the same soil properties have been used for seismic analysis with assigning 5% Rayleigh damping. All the models medium meshing are used for getting results uniformity. The deviations of results between medium and fine meshes are less than 10%.

Table 4.6: Stage construction phases for calculation

Phase	Analysis type	Prime Elements	Activated
Initial	K_0	Soil volume	√
		Foundation mat	x
		loads	x
Excavation	Plastic	Soil volume	√
		Foundation mat	x
		loads	x
Foundation Mat stage	Plastic	Soil volume	√
		Foundation mat	√
		loads	x
Loading on Mat	Plastic	Soil volume	√
		Foundation mat	√
		Distributed load	√
		Dynamic loads	x
Earthquake loading stage	Dynamic	Soil volume	√
		Foundation mat	√
		Distributed load	x
		Dynamic loads	√

4.4.1 Model of Unimproved Soil with Kobe earthquake HS_US_Kobe

This Hardening Soil model is developed using natural/unimproved soil of Rooppur NPP site in accordance with Table 4.1 and 4.3. All static loads are applied on mat as distributed and Kobe earthquake load is applied considering design basis earthquake PGA (Peak Ground Acceleration) 0.172 g and SSE (safe shutdown earthquake) 0.33g. Since the maximum acceleration of Kobe was 0.75g, the scale is selected as (0.33g/0.75g) 0.44.

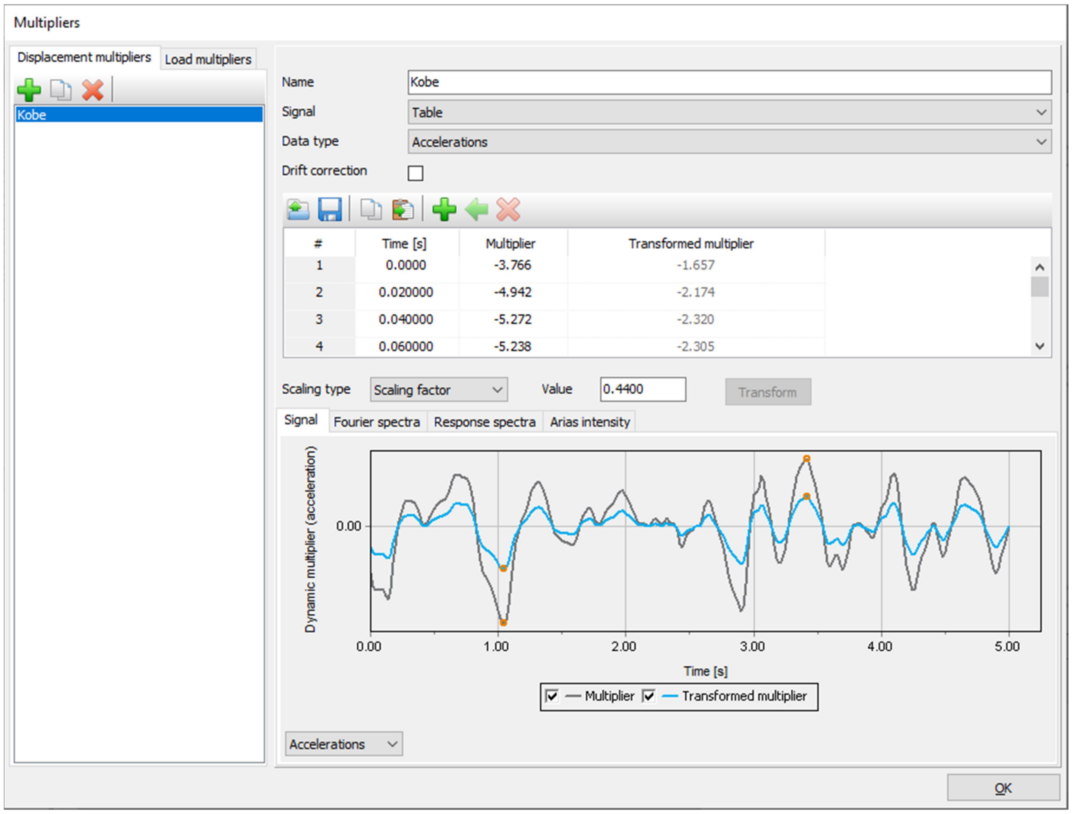

Figure 4.8: Applied earthquake Kobe using scaling factor for Rooppur NPP

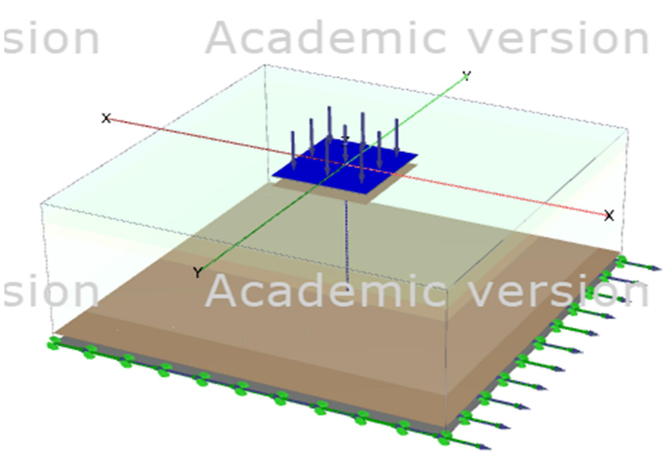

Figure 4.9: Model of Unimproved Soil with Kobe earthquake

The model is run for analyzing soil with the specified loads and earthquake and find impact on mat due to static and dynamic load. Following figures are shown the analysis results of displacements in different directions of mat is observed due to earthquake.

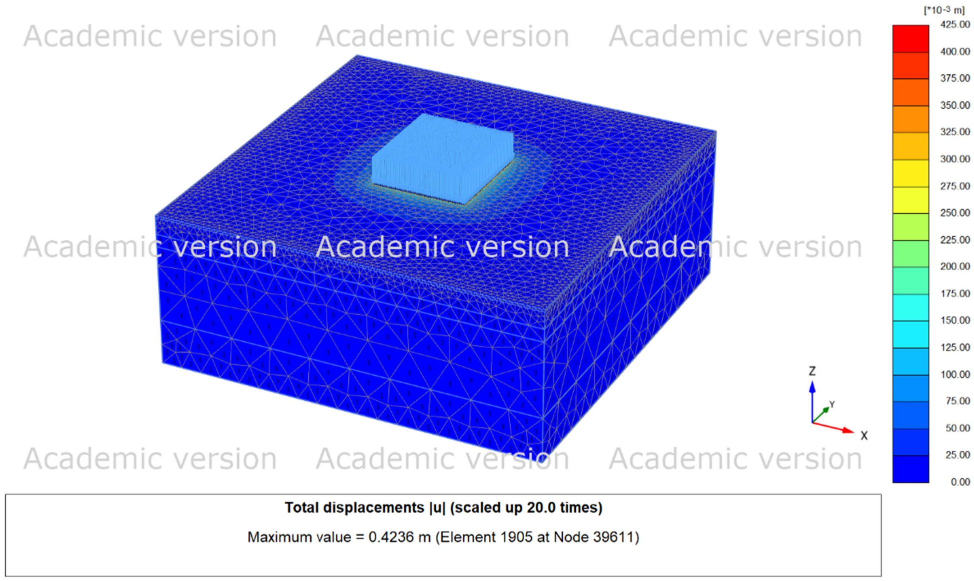

Figure 4.10: The total displacement due to Static load

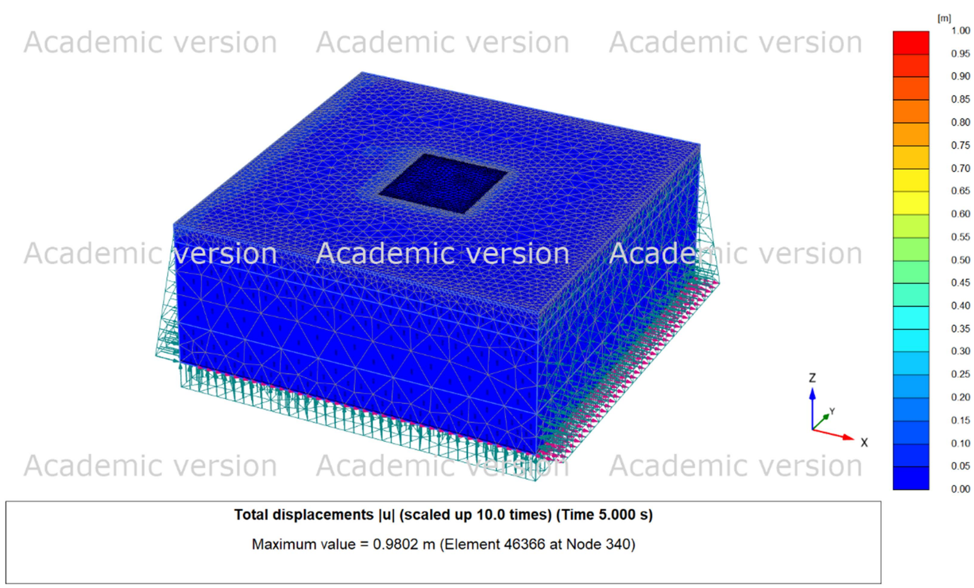

Figure 4.11: The total displacement due to earthquake

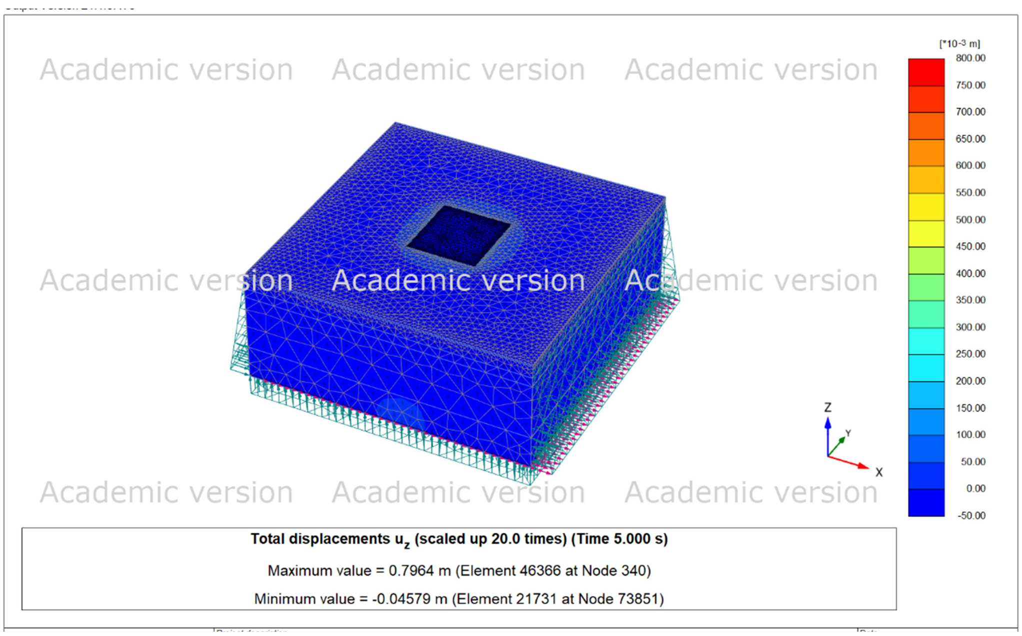

Figure 4.12: Tilting; Maximum and minimum displacements due to dynamic loading

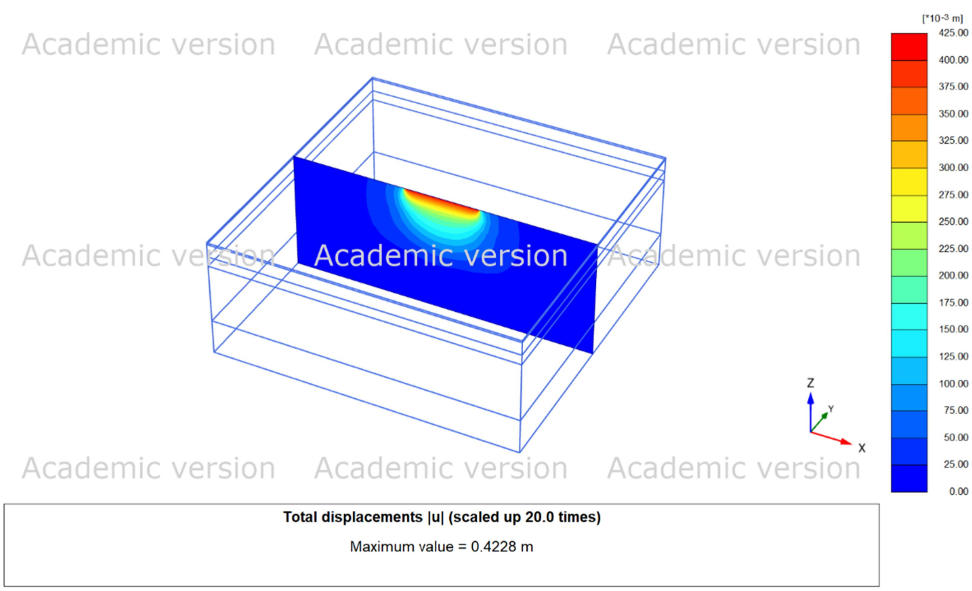

Figure 4.13: Cross-section of displacement due to static loading

The results of model analysis of settlement, tilting, forces and moments are tabulated in Table 4.7 and 4.8 respectively.

Table 4.7: Results of the deformation analysis of Reactor building on model HS_US_Kobe at operational stage

Model name	Max settlement due to Static load, cm	Displacement due to earthquake, cm		M Calculated related difference of settlementΔ s/L
		Max U_z	Mim U_z	
HS_U_Kobe	42.28	79.64	-4.57	0.0036

According to Russian code PiNAE-5.10-87 “Rules and Regulation in Nuclear Energy” regarding foundation for reactor compartment of NPP, the maximum allowable settlement of structural foundation of reactor building is $S_u \leq 30$ cm; and tilting is allowable ≤ 0.001. Considering seismic settlements, the tilting is i_u<0.003.

Table 4. 8: Forces on Reactor foundation mat of model HS_US_Kobe

	Force/moment	Maximum	minimum
1	Axial force, N	72.18×10^4 kN	-36.56×10^6 kN
2	Shear force, Q_{13}	46.98×10^4 kN	5332 kN
3	Shear force, Q_{23}	13.58×10^4 kN	-13.80×10^4 kN
4	Bending moment, M_2	68.19×10^7 kN-m	-57.19×10^6 kN-m
5	Bending moment, M_3	-26.08×10^7 kN-m	-54.52×10^7 kN-m

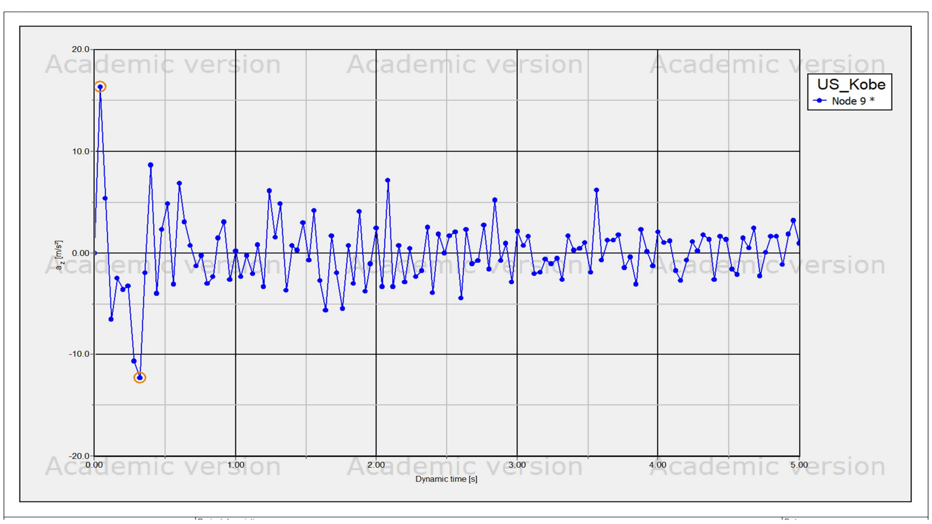

Figure 4.14: Dynamic time Vs Acceleration in unimproved soil of HS model

4.4.2 Model of improved Soil with Kobe earthquake HS_IS_Kobe

The model is developed considering improved soil of Rooppur NPP site and Kobe earthquake load. All static loads are applied on mat as distributed and Kobe earthquake load is applied considering design basis earthquake PGA (Peak Ground Acceleration) 0.172 g and SSE (safe shutdown earthquake) 0.33g.

Since the maximum acceleration of Kobe was 0.75g, the scale is selected as 0.33g /0.75g = 0.44

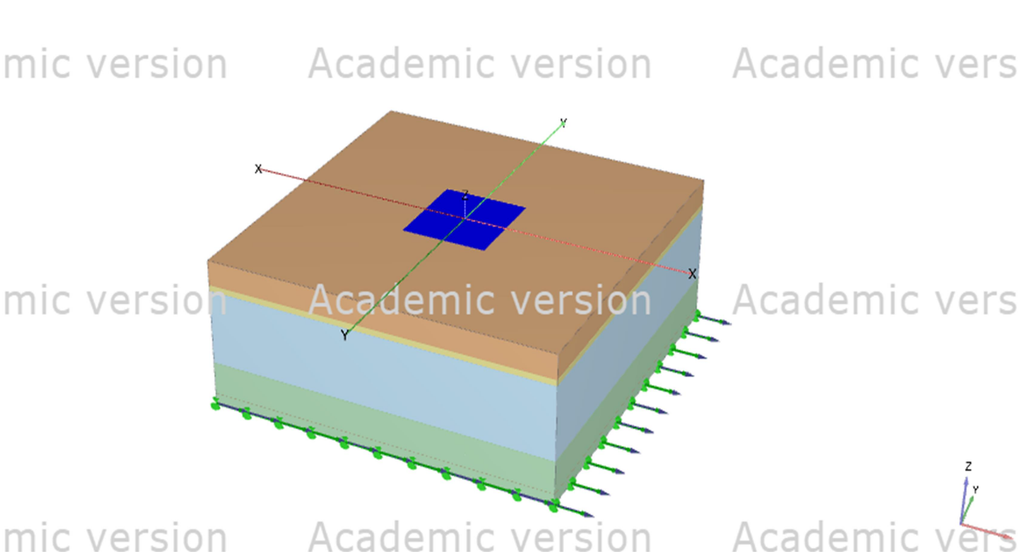

Figure 4.15: Prepared model using improved soil conditions

The model is run with the specified loads and earthquake and find impact on mat due to static and dynamic load. Following figures are shown the analysis results of displacements in different directions of mat is observed due to earthquake.

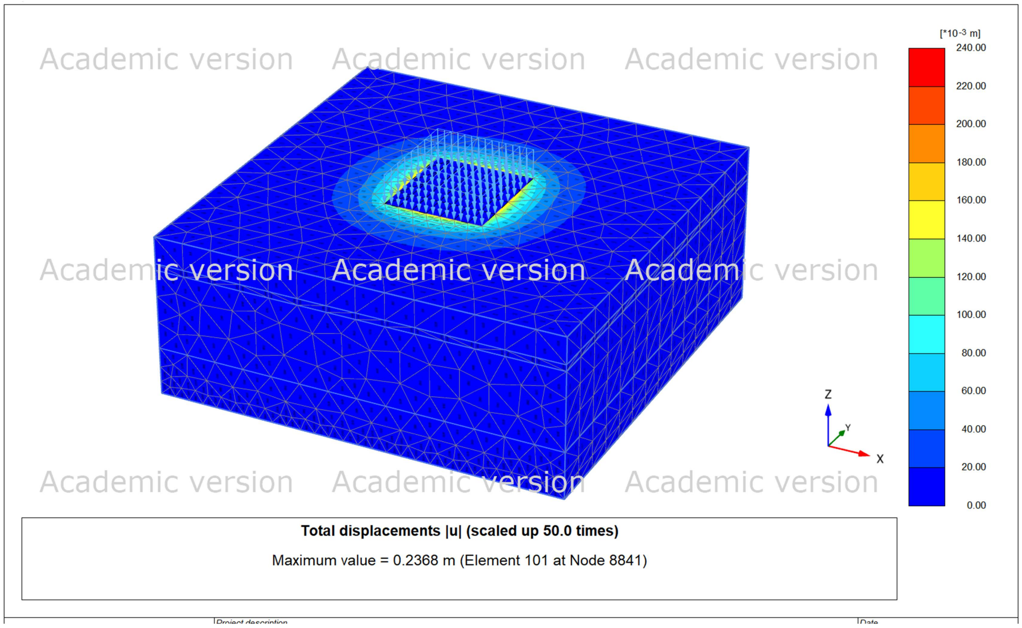

Figure 4.16: Maximum settlement due to static loading

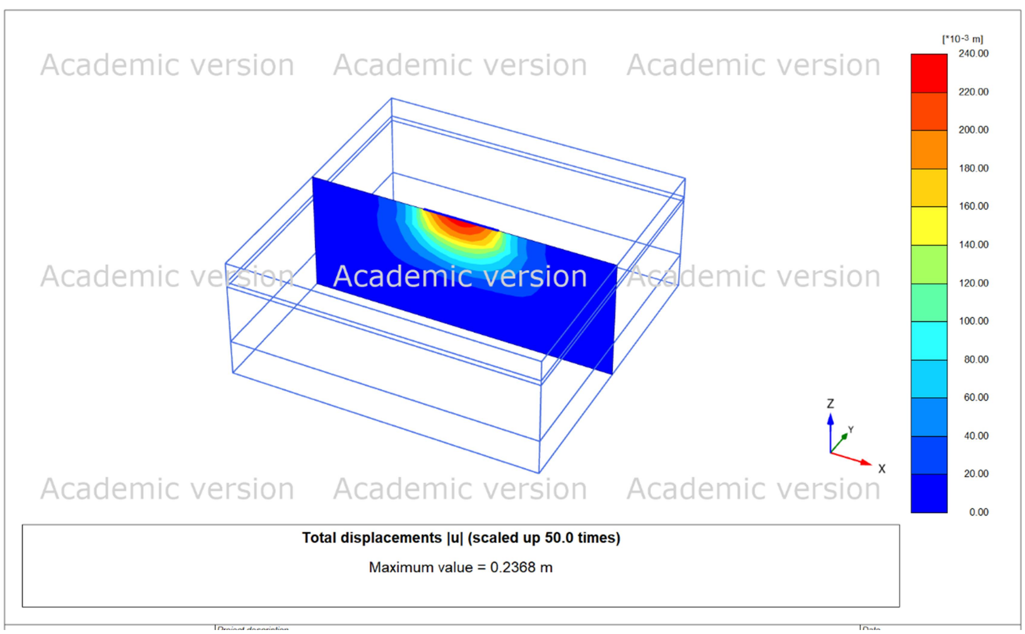

Figure 4.17: Cross-section of mat foundation under static loading

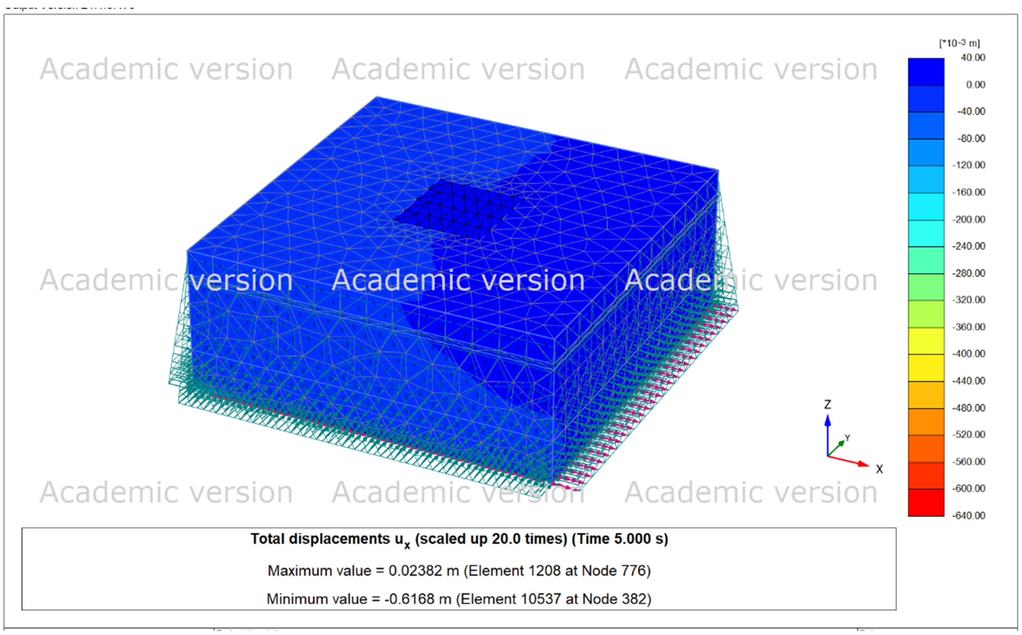

Figure 4.18: Maximum displacement in X-direction due to earthquake loading

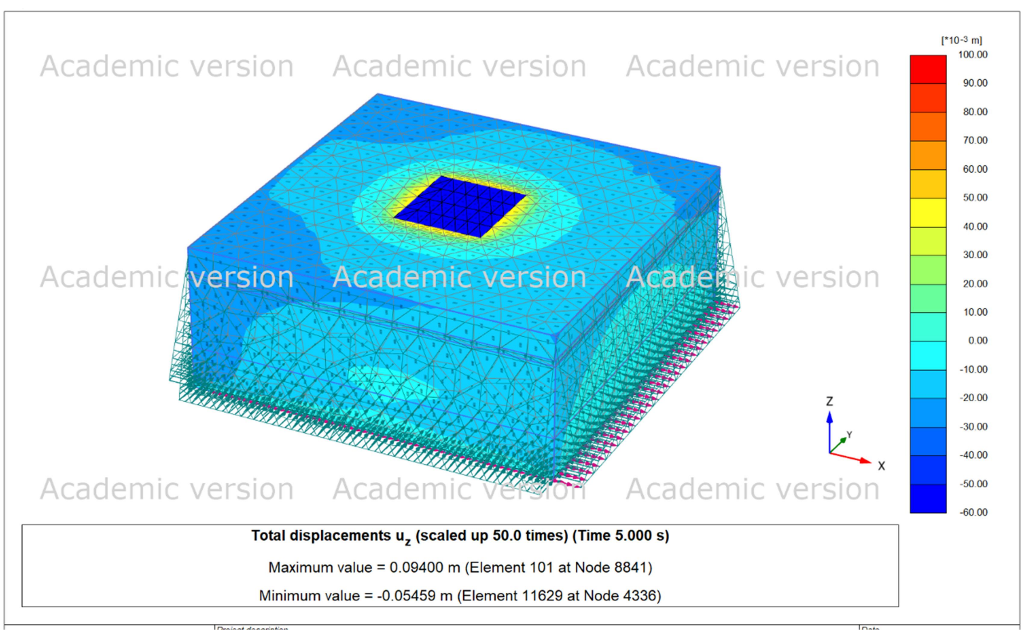

Figure 4.19: Maximum and minimum displacements due to dynamic loading

The results of model analysis of settlement, tilting, forces and moments are tabulated in Table 4.9 and 4.10 respectively.

Table 4.9: Results of the analysis of Reactor building on HS_IS_Kobe model

Model name	Max settlement due to Static load, cm	Displacement due to earthquake, cm		Calculated related difference of settlementΔ s/L
		Max U_z	Mim U_z	
HS_IS_Kobe	23.68	9.4	-5.45	0.00018

According to Russian code PiNAE-5.10-87 "Rules and Regulation in Nuclear Energy" regarding foundation for reactor compartment of NPP, the maximum allowable settlement of structural foundation of reactor building is $S_u \leq 30$ cm; where max ≤ 10 cm during operation life and tilting is allowable ≤ 0.001. Considering specific conditions and seismic settlements, the tilting is $i_u<0.003$.

Table 4.10: Forces/moments in foundation mat of HS_IS_Kobe

	Force/moment	Maximum	minimum
1	Axial force, N	-6.455×10^6 kN	-30.42×10^6 kN
2	Shear force, Q_{13}	62.78×10^3 kN	8300 kN
3	Shear force, Q_{23}	6.344×10^5 kN	-5.406×10^5 kN
4	Bending moment, M_2	36.76×10^7 kN-m	-14.33×10^8 kN-m
5	Bending moment, M_3	-12.63×10^7 kN-m	-57.73×10^7 kN-m

Being analyzed of two above models, the acceleration due to earthquake on improved soil is steady and less compare to unimproved soil which is reflected in graph Figure 4.20

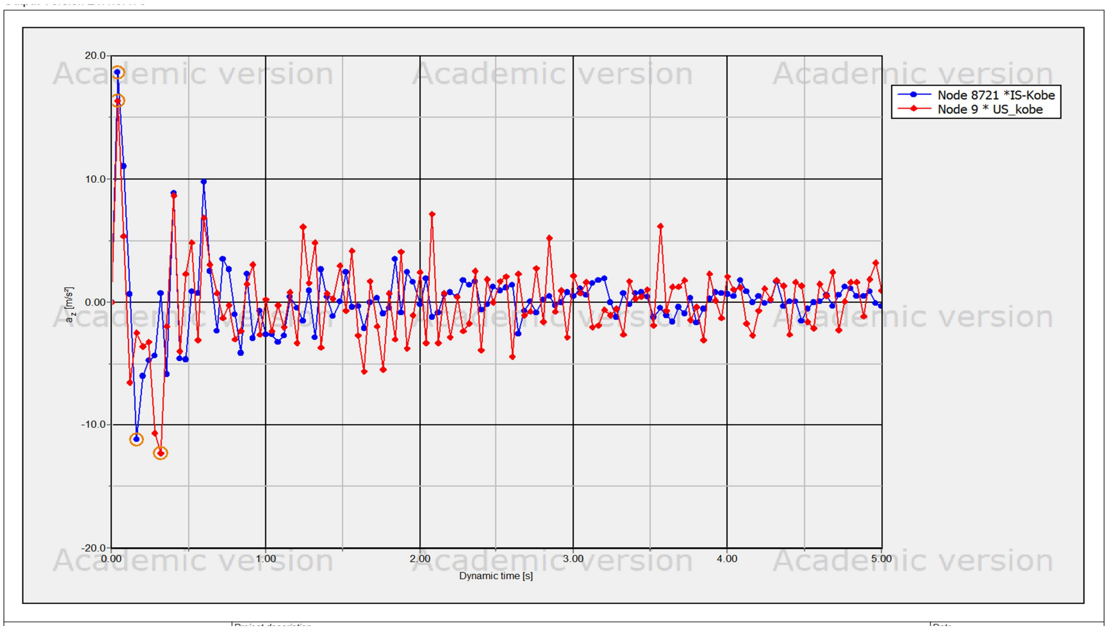

Figure 4.20: Acceleration Vs Dynamic time in improved and unimproved soil using Kobe earthquake

4.4.3 Model of Unimproved Soil with Kobe earthquake, HS_US_Loma

The model is developed using unimproved soil of Rooppur NPP site and Loma Prieta earthquake load. All static loads are applied on mat foundation as uniformly distributed and Loma earthquake load is applied considering design basis earthquake PGA (Peak Ground Acceleration) 0.172 g and SSE (safe shutdown earthquake) 0.33g. Since the maximum acceleration of Loma was 0.20 g, the scale is selected as (0.33g/0.20g) 1.65.

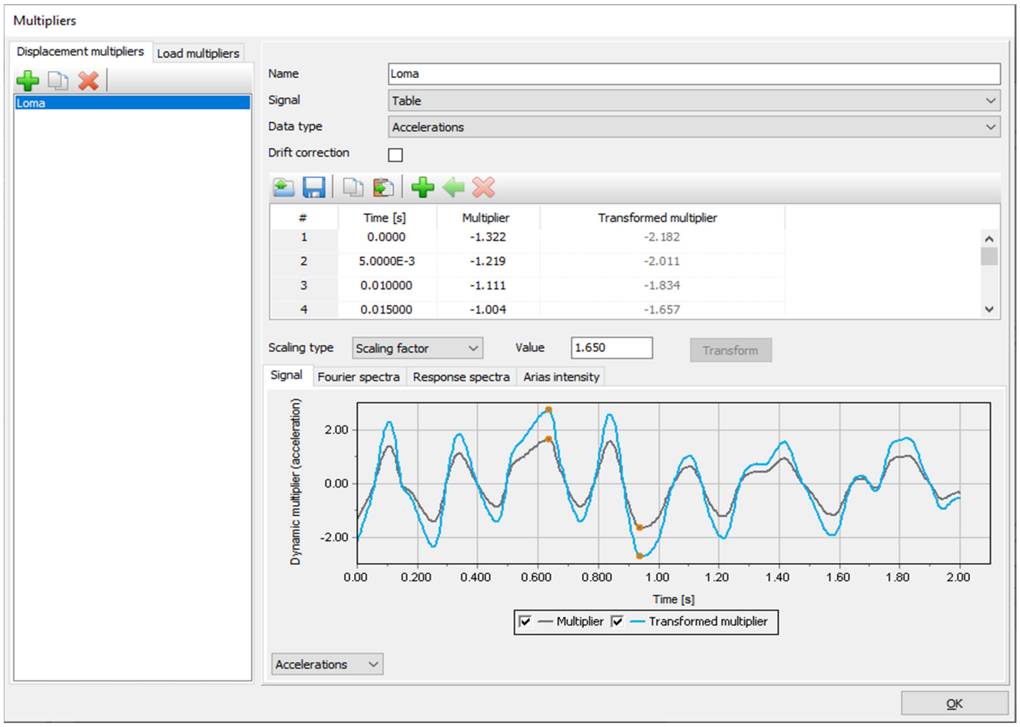

Figure 4.21: Loma earthquake loads is applied on HS_US_Loma model

The model is run with the specified loads and earthquake to find impact on mat due to static and dynamic load. Following figures are shown the analysis results of displacements in different directions of mat is observed due to static load and earthquake.

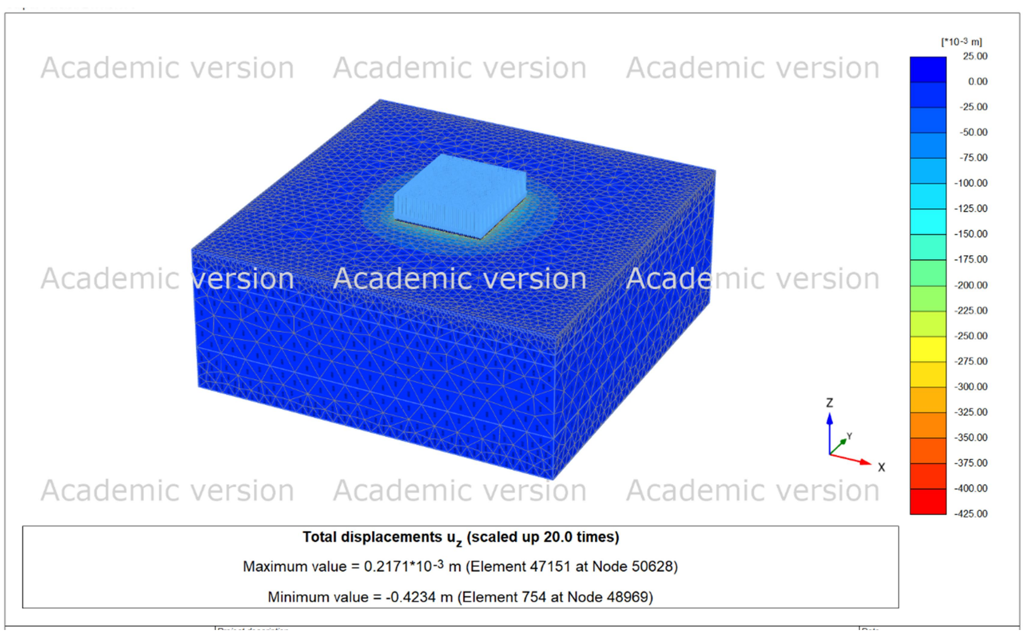

Figure 4.22: Max displacement in Z-direction due to static loads

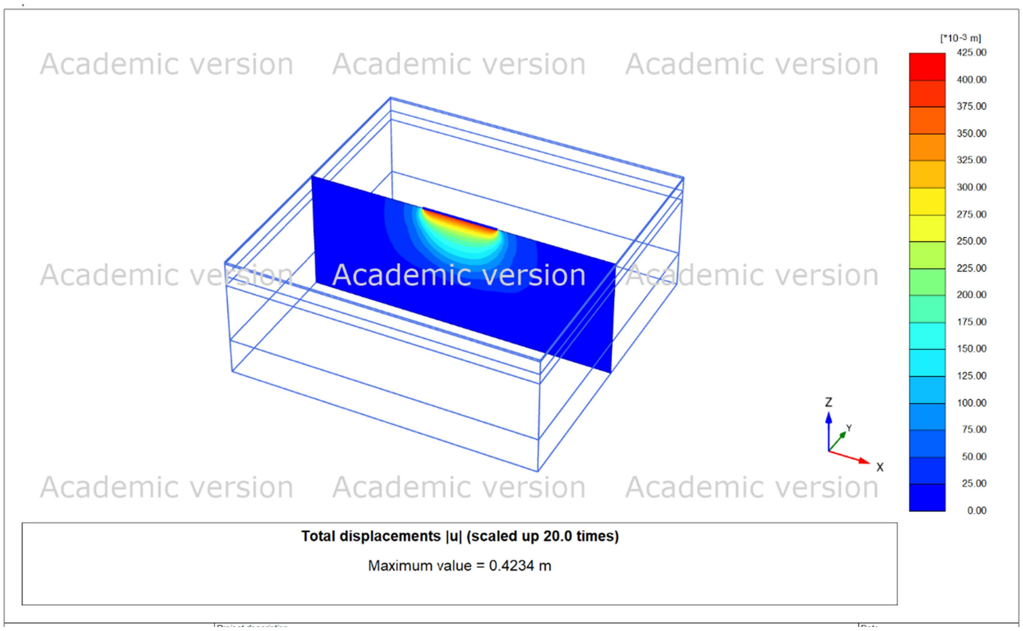

Figure 4.23: Cross-section of max displacement place due to static loads

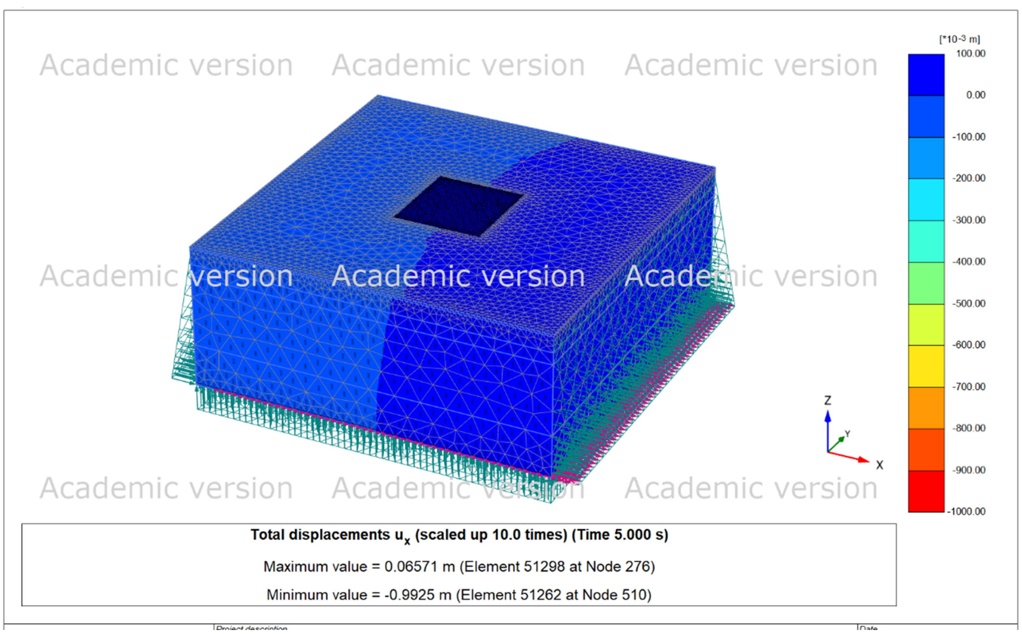

Figure 4.24: Max. displacements due to dynamic loading is revealed at X-direction

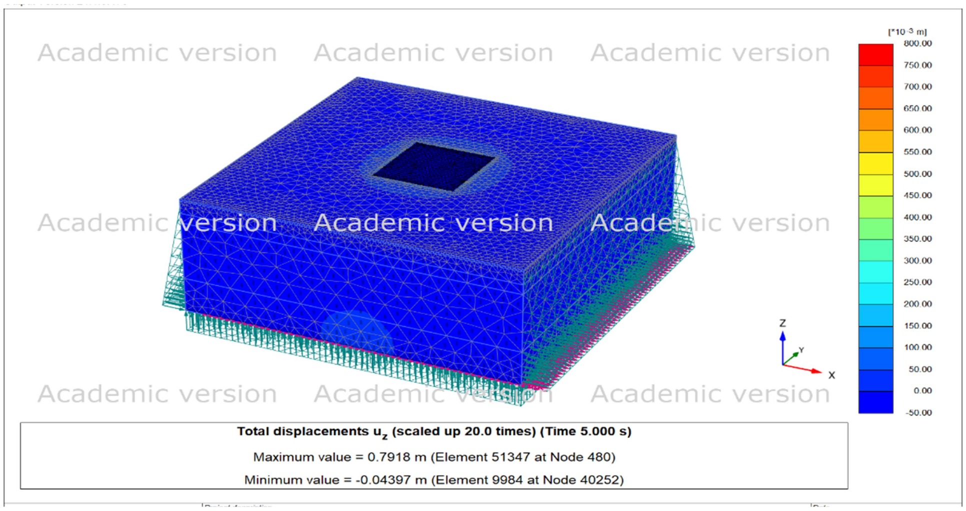

Figure 4.25: Displacements difference at Z-direction due to dynamic loading

The model analysis results of settlement, tilting, forces and moments are tabulated in Table 4.11 and 4.12 respectively.

Table 4.11: Results of the deformation analysis of Reactor building on model HS_US_Loma

Model name	Max settlement due to Static load, cm	Displacement due to earthquake, cm		Calculated related difference of settlement $\Delta s/L$
		Max U_z	Mim U_z	
HS_US_Loma	42.34	11.97	-18.84	0.002

According to Russian code PiNAE-5.10-87 "Rules and Regulation in Nuclear Energy" regarding foundation for reactor compartment of NPP, the maximum allowable settlement of structural foundation of reactor building is Su ≤ 30 cm and tilting is allowable ≤ 0.001.

Table 4.12: Forces/moments in foundation mat in model HS_US-Loma

	Force/moment	Maximum	minimum
1	Axial force, N	-2.501×10^6 kN	-37.12×10^6 kN
2	Shear force, Q_{13}	4.32×10^5 kN	-7.01×10^5 kN
3	Shear force, Q_{23}	20.30×10^3 kN	-11.71×10^3 kN
4	Bending moment, M_2	-51.19×10^6 kN-m	-77.73×10^7 kN-m
5	Bending moment, M_3	-33.58×10^6 kN-m	-15.04×10^8 kN-m

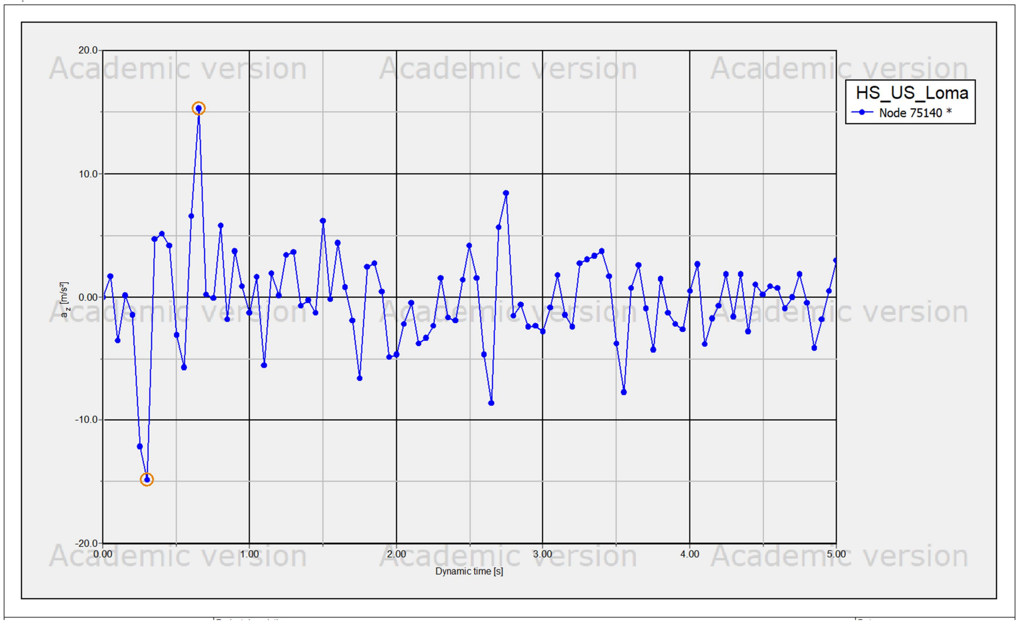

Figure 4.26: Acceleration Vs Dynamic time in unimproved soil in HS_US-Loma model

4.4.4 Model of Improved Soil with Kobe earthquake, HS_IS_Loma

The model is developed using improved soil of Rooppur NPP site and Loma Prieta earthquake load. All static loads are applied on mat foundation as distributed and Loma earthquake load is applied considering design basis earthquake PGA (Peak Ground Acceleration) 0.172 g and SSE (safe shutdown earthquake) 0.33g. Since the maximum acceleration of Loma was 0.20 g, the scale is selected as (0.33g/0.20g) 1.65. Following results are observed after analysis:

The model is run with the specified loads and earthquake to find impact on mat due to static and dynamic load. Following figures are shown the analysis results of displacements in different directions of mat is observed

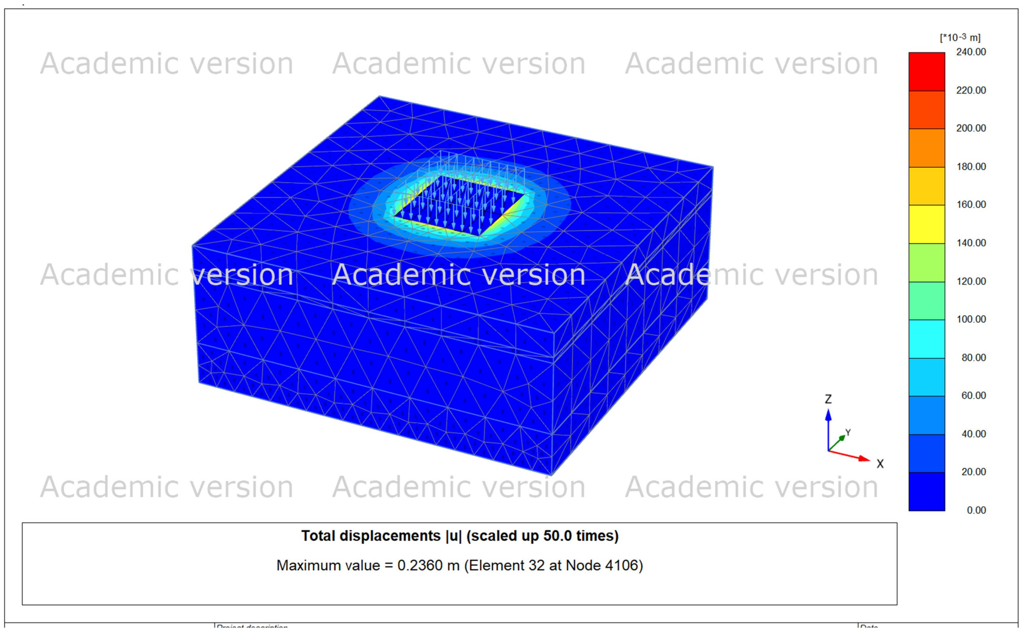

Figure 4.27: Maximum settlement in Z-direction due to static loading

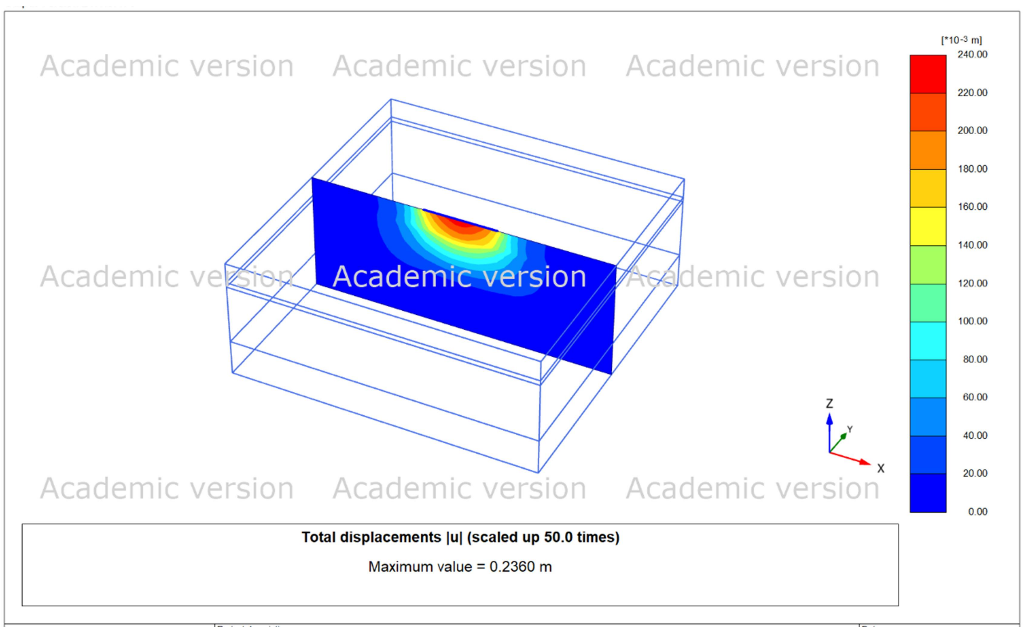

Figure 4.28: Cross-section of Maximum settlement in Z-direction due to static loading

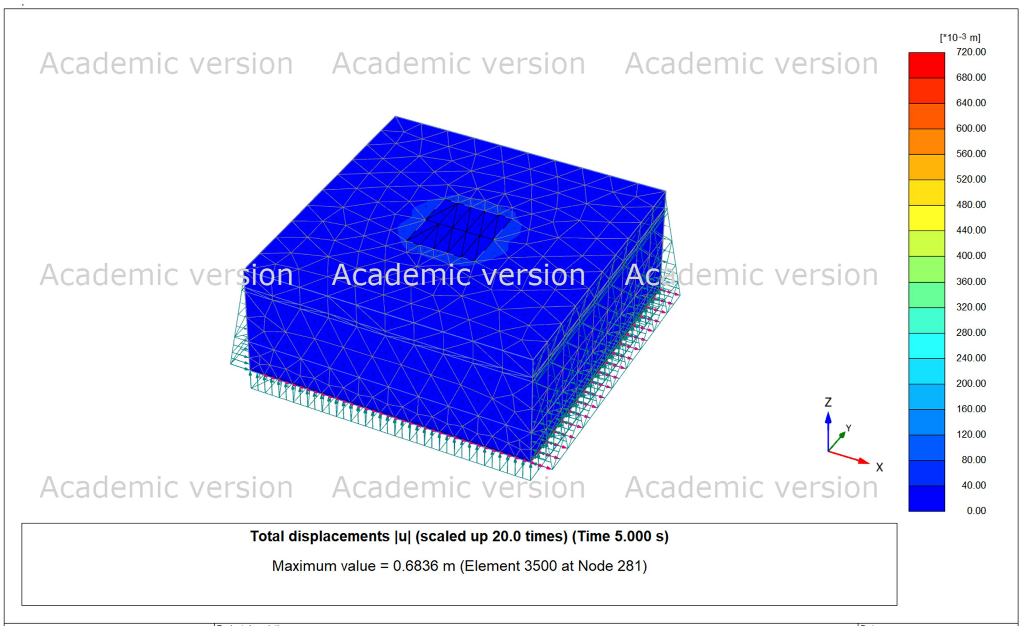

Figure 4.29: Maximum settlement due to earthquake loading

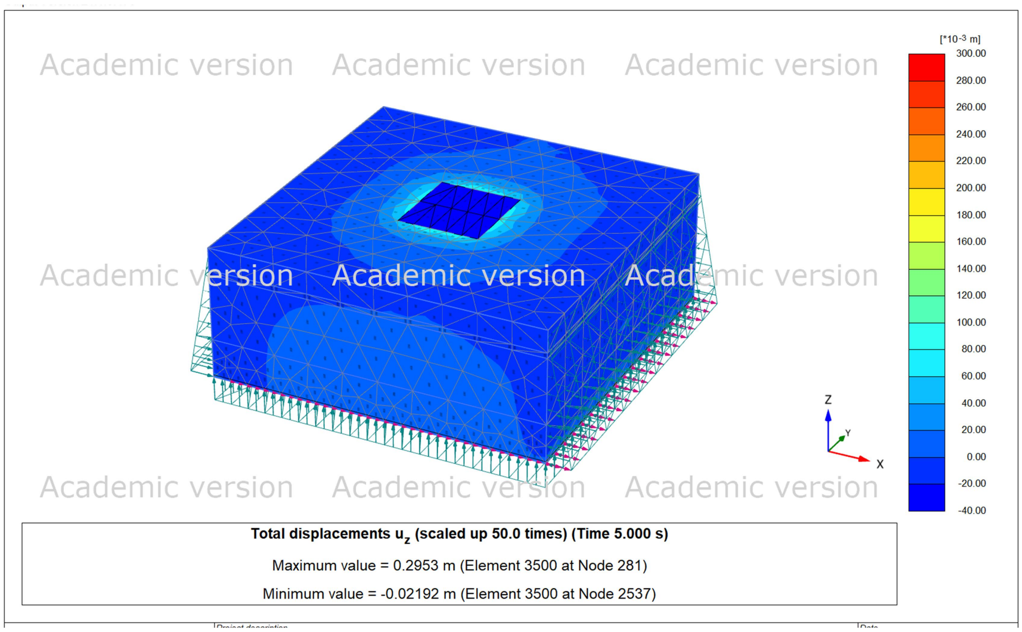

Figure 4.30: Displacements in X-direction due to seismic loading

The results of model analysis of settlement, tilting, forces and moments are tabulated in Table 4.13 and 4.14 respectively.

Table 4.13: Results of the deformation analysis of Reactor building on model HS_IS_Loma

Model name	Max settlement due to Static load, cm	Displacement due to earthquake		Calculated Relative difference of settlements, Δ s/L (Tilting)
		Max U_z cm	Mim U_z cm	
HS_IS_Loma	23.60	29.53	-2.19	0.0014

According to Russian code PiNAE-5.10-87 "Rules and Regulation in Nuclear Energy" regarding foundation for reactor compartment of NPP, the maximum allowable settlement of structural foundation of reactor building is S u ≤ 30 cm;

Table 4.14: Forces/moments in foundation mat in model HS_US-Loma

	Force/moment	Maximum	minimum
1	Axial force, N	-4.585×10^6 kN	-34.68×10^6 kN
2	Shear force, Q_{13}	3970 kN	-2.712×10^5 kN
3	Shear force, Q_{23}	20.29×10^4 kN	-1.573×10^6 kN
4	Bending moment, M_2	-91.45×10^6 kN-m	-19.17×10^8 kN-m
5	Bending moment, M_3	-14.19×10^7 kN-m	-84.35×10^7 kN-m

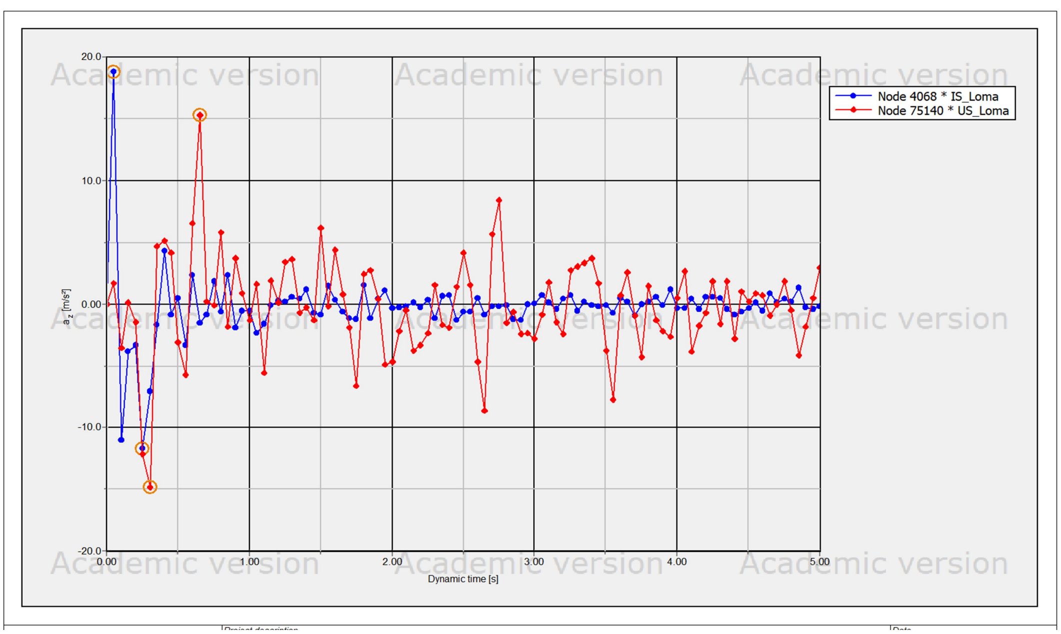

Figure 4.31: Acceleration Vs Dynamic time in improved and unimproved soil in Loma earthquake.

4.5 Result Summary

Upon application of Kobe and Loma earthquake loading on improved and unimproved soil conditions, four models have following summarized result on the Table 4.15:

Table 4.15: Displacement results summery of models in X and Z-direction of mat

SL	Model	displacement due to Static, cm				displacement due to earthquake, cm			
		X-direction		Z-direction		X-direction		Z-direction	
		Max.	Mim.	Max.	Mim.	Max.	Mim.	Max.	Mim.
1	HS-US-Kobe	10.82	-10.13	0.025	-42.36	6.53	-60.43	79.64	-4.57
2	HS-US-Loma	10.06	-10.19	0.021	-42.34	6.57	-99.25	79.18	-4.39
3	HS-IS-Kobe	3.31	-3.31	0.014	-23.68	2.38	-61.68	9.4	-5.45
4	HS-IS-Loma	3.16	-3.20	0.015	-23.60	6.33	-61.65	29.53	-2.19

The results show that the maximum settlement is 42.36 cm at Z-direction for static loadings and maximum displacement is found 145.80 cm at X-direction. Both values are found on unimproved soil model.

After improvement of soil using deep soil mixing technology same static and earthquake loadings are applied. The maximum settlement due to static loading is reduced to 23.68 cm at Z-direction and the maximum displacement is found 61.68 cm at X-direction.

Table 4.16: Tilting results of respective models

SL	Model	Settlement due to earthquake, cm				Calculated Relative difference of settlements, Δ s/L (Tilting)
		X-direction		Z-direction		
		Max.	Mim.	Max.	Mim.	
1	HS-US-Kobe	6.53	-60.43	79.64	-4.57	0.0036
2	HS-US-Loma	23.51	-145.8	11.97	-18.84	0.0025
3	HS-IS-Kobe	2.38	-61.68	9.4	-5.45	0.0018
4	HS-IS-Loma	6.33	61.65	29.53	-2.19	0.0014

After application of Kobe earthquake on unimproved soil, tiling is observed 0.0036 which is reduced to 0.0018 on improved soil. On the other hand, tilting is observed due

BANGLADESH NETWORK
OFFICE FOR URBAN SAFETY

PART-IV

NUMERICAL MODELING OF PILED RAFT FOUNDATION SYSTEM SUBJECTED TO SEISMIC LOADINGS

BANGLADESH NETWORK OFFICE FOR URBAN SAFETY (BNUS), BUET, DHAKA

Prepared By: Naim Parves

Mehedi Ahmed Ansary

Chapter 1
INTRODUCTION

1.1 General

Design of a safe and economical foundation system is an important task in tall building design. Deep foundations such as piled foundations are generally adopted to transfer heavy loads from superstructure to the bearing stratum. Providing adequate geotechnical capacity and limiting the deferential settlement are two important design considerations in the design of piled foundations. The foundation design becomes economical when both the criteria of bearing capacity and settlement are satisfied in an optimum way. A piled raft foundation is an advanced concept in which the total load coming from the superstructure is partly shared by the raft through bearing from soil and the remaining load is shared by piles through skin friction and end bearing. Consequently, piled raft system is generally adopted when pile foundations for tall buildings become uneconomical or unsatisfactory.

For situations in which a raft foundation is found to have an adequate factor of safety against failure but which is likely to settle excessively, a method is developed for determining the number of piles which need to be added to the raft to reduce the settlement to a tolerable amount. It is found from recent studies that the addition of relatively few long piles may be effective in reducing settlement even though the piles themselves may have reached their ultimate load. The design of the required number of piles on a settlement basis rather than on the more usual ultimate bearing capacity basis leads to a system which, although it contains considerably fewer piles, settles only slightly more and is quite adequate for bearing capacity purposes.

Firstly, the piles are constructed and then the raft is placed combining all the piles. Interaction of the pile, soil, and raft is the key factor considered in designing the piled raft foundation. The efficient use of the interaction leads to end up with the economical design. Due to the three-dimensional nature of the load transfer, piled raft foundations are regarded as very complex systems involving many interaction factors such as pile to-raft, raft-to-soil, and pile-to-soil. This study intended to present a detailed discussion on the analysis of piled raft system addressing the effect of different parameters for piled raft foundation system. PLAXIS-3D software has been used to generate Earthquake load and to analyze the results for different parametric study.

1.2 Background of The Study

Recently with the increasing in economic development, rapid industrialization and decreasing availability of land for construction in thickly populated cities like Dhaka, scope for extending construction in horizontal direction is becoming increasingly lesser resulting in construction of high-rise building with increasing number of floors. In the design of foundations for large buildings on deep deposit of soft or loose soils it is generally seen that raft foundation be chosen the foundation will have sufficient factor of safety against shear failure but corresponding settlement will be very high to permit. In such cases pile foundation are generally selected causing very large cost for such foundations. The settlements are successfully controlled in such foundations, however in the late, it has been recognized if few numbers of piles are installed at suitable locations below the raft foundation for such structures, the resultant settlement under such structure will be much smaller and will be within permissible limits compared to that below the raft without provision of piles. Use of raft in conjunction with some piles will be costlier than in case where only raft is used if possible but much less than the case when only piles are used.

As a result, in the past decades there has been increasing recognition to use some piles with raft to reduce the total and differential settlement of raft leading to considerable economy without compromising the safety and performance of the foundation structure system. Such a foundation system is called piled-raft. One of the most important buildings constructed with such system is for the foundation system of the world's tallest building the Burj Dubai. The adoption of piled-raft foundation for high rise buildings is also very common in European cities. Thus, it seems on the other countries, piled-raft foundation will be increasingly adopted as a most economic safe foundation system. A piled raft foundation has some advantages over the pile group in terms of the design and from a serviceability and economic point of view. They include the following: (i) a piled raft foundation will require fewer piles in comparison to a pile group to satisfy the same design requirements; this will lead to a more economical design; (ii) for a piled raft, the piles will provide sufficient stiffness to control the settlement and differential settlement at serviceability load; and the raft will provide additional capacity at ultimate load; (iii) in case any piles in the piled raft become defective, the raft allows re-distribution of the load from the damaged piles to the other piles (Poulos et al. 2011); (iv) a raft in the piled raft foundation can carry a higher percentage of the applied load and transmit to the soil (Clancy and Randolph, 1993); and (v) the pressure applied from the raft to the subsoil may increase the lateral stress between underlying piles and the soil, which can increase the pile bearing capacity accordingly compared to the piles in a pile group (Katzenbach et al. 1998).

In recent years, large number of mega projects were constructed using the piled raft foundation system concept in Dhaka city. Hence a noticeable attention has been drawn toward better understanding of the performance of piled raft foundation systems subjected to Seismic loading. An innovative application of the piled raft is its special adjustment to cases of foundations with large load eccentricities or very different loaded parts of buildings to avoid the need of complex settlement joints especially below ground water table. This research work has been studied on a piled raft supported structure in Dhaka city with various loaded portions. Due to application of earthquake load, eccentric load also acting on this selected structure. The study concentrates on the effect of engineering factors related to pile in raft foundation such as raft thickness, number of piles, pile layout and pile diameter on the behavior of the piled raft foundation; analysis is carried out by 3D finite element method via PLAXIS-3D Foundation software. Both the immediate and Consolidation settlement due to the variation of different parameters has been observed in this study.

1.3 Objective of The Study

The study will throw light on the effects of considering seismic effect on Piled-raft foundation system on the design parameters of a tall building for Dhaka soil conditions. The results are expected to give some guidelines for designing tall buildings/skyscrapers on piled raft foundations in Dhaka city. The main objectives of this research work are listed below.

1. Analyzing a selected structure in Dhaka using numerical model
2. Simulation of Earthquake load using PLAXIS-3D software
3. Parametric study of the developed piled-raft foundation system
4. Study the lateral deformation of pile under seismic loading

1.4 Organization of The Thesis

There are total six chapters which are chronologically developed on the basis of the research work towards its main objective. Brief descriptions of the five chapters are given below:

Chapter One deals with few general issues, background of the research, necessity of piled raft of foundation system in Dhaka city, research scheme and objective of the research. It also gives a brief overview of the other chapters.

Chapter Two is devoted to review past researches related to the theme of this thesis. Various analytical theories of pile raft foundations are discussed in this chapter. Overview of PLAXIS-3D software and a brief description of Hardening soil modeling in this software is also discussed in this chapter.

In Chapter Three, overall input parameters for the study like Site location, Subsoil parameters and Description selected structure of the thesis have been discussed.

Chapter Four represents the Numerical model development procedures. Soil and material model, embedded beam, details of different parametric study models and generation of earthquake effect in PLAXIS-3D have been discussed in this chapter.

Results obtained through the analysis and calculations are presented in Chapter Five with specific findings. Effects of different parametric study for both un-piled raft and piled raft have been discussed in this chapter. At the end of this chapter summary on findings are highlighted in the form of discussion.

Conclusive remarks on the parametric study of piled raft foundation system for Dhaka city are presented in Chapter six. This chapter also includes the scopes for future researches with specific recommendations.

Chapter 3
STUDY OF SUBSOIL INVESTIGATION DATA AND SELECTION OF SUITABLE STRUCTURE

3.1 Site Description

The selected site for this study is located in the center of Dhaka city. It is bounded by Kafrul, cantonment and Tejgaon industrial area thanas on the north, Kalabagan and Ramna thanas on the south, Tejgaon Industrial Area thana on the east, Sher-e-Bangla Nagar and Kafrul thanas on the west. The site is fairly level and elevations and the existing ground level vary from quarter to one and half-a meter above from existing site adjacent road level.

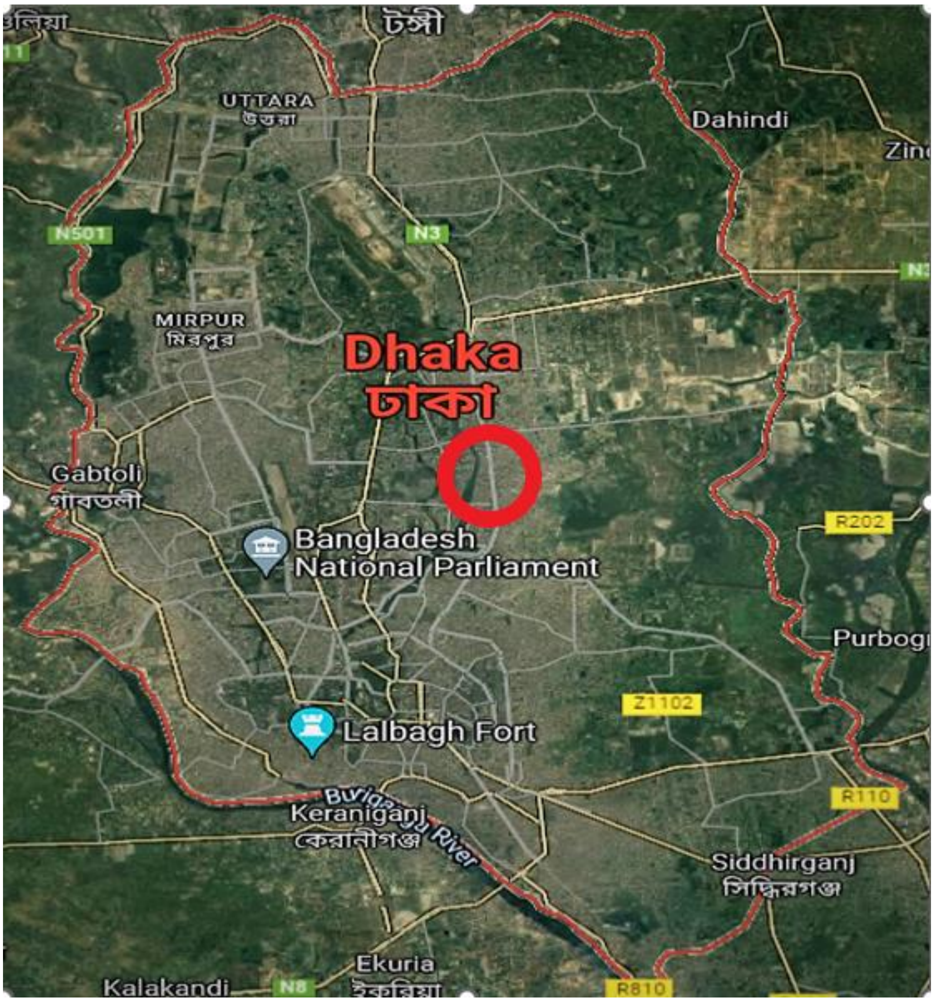

Figure 3.1: The selected site location (marked in red circle) for this study

3.2 Geological Condition of The Selected Site

At the beginning, field investigation and Standard penetration test is carried out to measure the SPT values up to 70.5m depth. Both disturbed and undisturbed samples are collected for further tests in laboratory. Based on the field investigation, visual classification of soil and Laboratory tests on the collected samples, it is found that the subsoil of the selected site represents the typical Dhaka soil. A summary of the subsoil strata description is as follows:

Table 3.1: General description of soil profile of the selected site

SL. No.	Depth (m)	Layer thickness (m)	SPT value	Average SPT value	Soil description
1	0-2	2	-	-	Fill
2	2-6	4	8-12	9	High Plastic Medium stiff to Stiff Clay
3	6-15	9	14-25	18	Medium dense Silty Sand
4	15-27	12	30-37	33	Medium dense to Dense Silty Sand
5	27-30	3	10-13	11	High Plastic Stiff Clay
6	30-70.5	40	50+	50+	Very dense poorly graded Sand with Silt

Details geotechnical description of the soil is described in later part of this chapter.

3.3 Ground water level of The Selected Site

With reference to the measured groundwater table during Soil investigation (SI) works, the groundwater table for the site was found to be varying between two stages of SI work due to the wash boring technique, therefore it was not possible to estimate the exact levels. Subsequently, a water standpipe had been installed at site and Table 3.2 below shows the ground waters tables reading between February 2019 and April 2019. Based on the information, the ground water table at this region are believed to be at a significant depth below EGL. However, the adopted ground water table respective to the onerous water table level could be adopted at 14m below ground level for the uplift design check and below the soffit of the slab for the pile raft design check. Again, the water level may rise above during rainy season. So, in this study we have assumed the ground water level at 14m below existing ground level.

Table 3.2: Ground water level measurement using standpipe method

SL. No.	Date of observation	Time of observation	Depth of water level below EGL
1	February 25, 2019	12:30 PM	Water was observed at a depth of 16.7 m
2	February 26, 2019	10:00 AM	Water was observed at a depth of 16.03 m
3	February 27, 2019	10:00 AM	No water was observed up to a depth of 18.3 m; mud was encountered at this level
4	February 28, 2019	10:00 AM	No water was observed up to a depth of 18.3 m; mud was encountered at this level
5	March 01, 2019	10:00 AM	No water was observed up to a depth of 18.3 m; mud was encountered at this level
6	March 02, 2019	10:00 AM	No water was observed up to a depth of 18.3 m; mud was encountered at this level
7	March 20, 2019	1:30 PM	No water was observed up to a depth of 18.3 m; mud was encountered at this level
8	April 15, 2019	10:00 AM	No water was observed up to a depth of 18.3 m; mud was encountered at this level

3.4 Subsoil Investigation Data

All the Subsoil investigation data used in this study was collected from reliable sources. Standard penetration test was done up to 70.5m depth to count the SPT values at 1.5m following ASTM D-1587 standard. The drilling work was done by rotary method. Later, the collected disturbed and undisturbed samples were transported to the laboratory with proper caution. Based on the Particle size distribution (as per ASTM D-6913 & ASTM D-7923) and Atterberg limit test (as per ASTM D-4318) results, the soil samples were classified by Unified Soil Classification System (USCS) as per ASTM D-2487. Unconfined Compression strength test was done on cohesive soil layers as per ASTM D-2166. One dimensional Consolidation test was also performed on cohesive soil layer as per ASTM D-2435. Details of field investigation and laboratory tests are mentioned in Appendix-1. Based on in situ and laboratory tests, the soil properties have been used while developing the numerical models in PLAXIS-3D for this study.

3.5 Seismic Information of The Site

The selected site is situated in the district of Dhaka, which falls into the seismic intensity zone with Z = 0.15 (Zone 2) and has a maximum PGA value of 0.15g. This zoning map is based on peak ground accelerations estimated by Hattori (1979) for a return period of 200 years. The study was initiated considering the PGA values as per BNBC 2006. However, while this study was in progress, the new Code BNBC-2020 get published. The intent of the seismic zoning map according to BNBC-2020 is to give an indication of the Maximum Considered Earthquake (MCE) motion at different parts of the country. In probabilistic terms, the MCE motion may be considered to correspond to having a 2% probability of exceedance within a period of 50 years. According to BNBC-2020, Dhaka district falls in the seismic intensity zone with Z=0.20 and a maximum PGA value of 0.20g. The design basis earthquake (DBE) ground motion is selected at a ground shaking level that is 2/3 of the maximum considered earthquake (MCE) ground motion. So, the design basis earthquake for the site becomes 0.133g.

Seismic down hole test is performed to directly measure the compressional (P) and shear (S) waves velocity profile of subsoil stratum of the selected site. P-wave travel time is calculated by the first arrival of either peak or trough in the seismogram. S wave travel time is calculated from the first cross of generated opposite phase shear waves in radial and transverse direction. First arrival time of P and S waves are plotted against depth and the time-depth curves for borehole as follows:

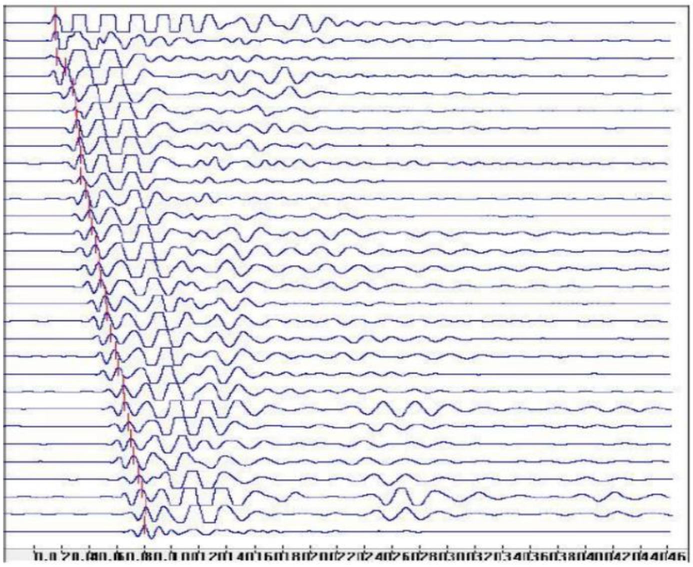

(a)

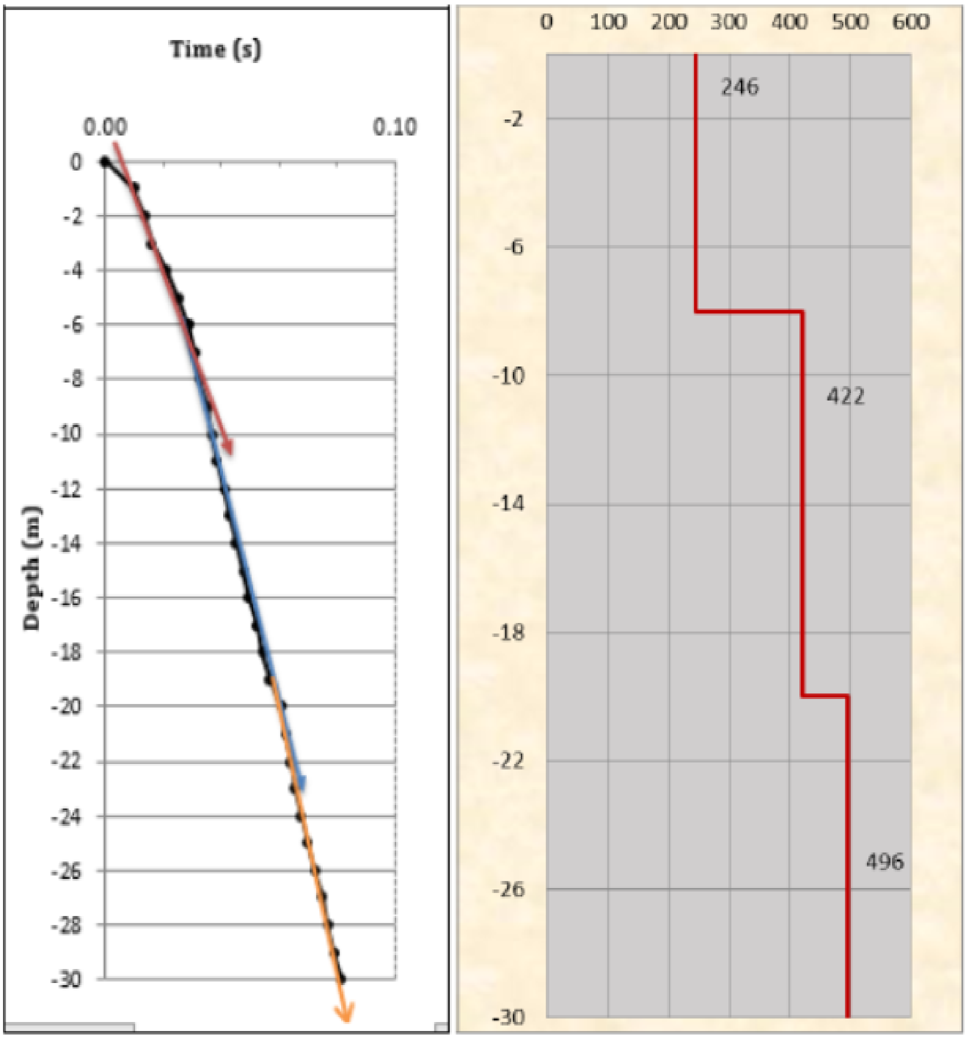

Figure 3.2: P-wave for upper 30m depth. (a) P-wave trace, (b) Corresponding time-distance curve with layer velocity at the selected site

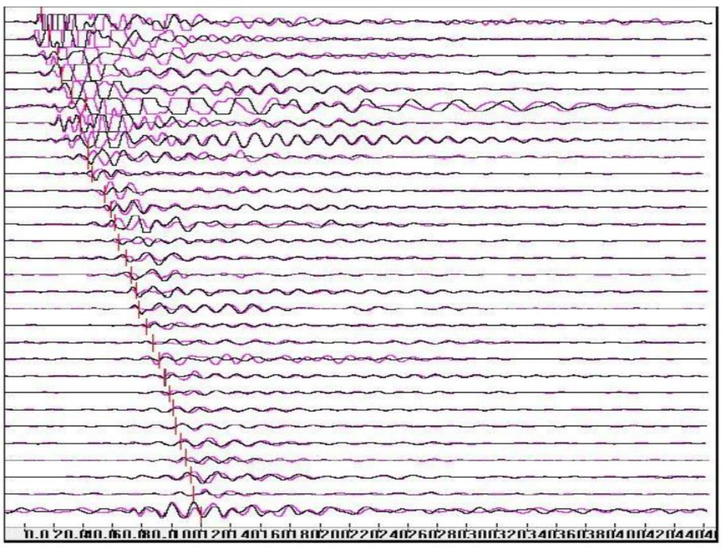

(a)

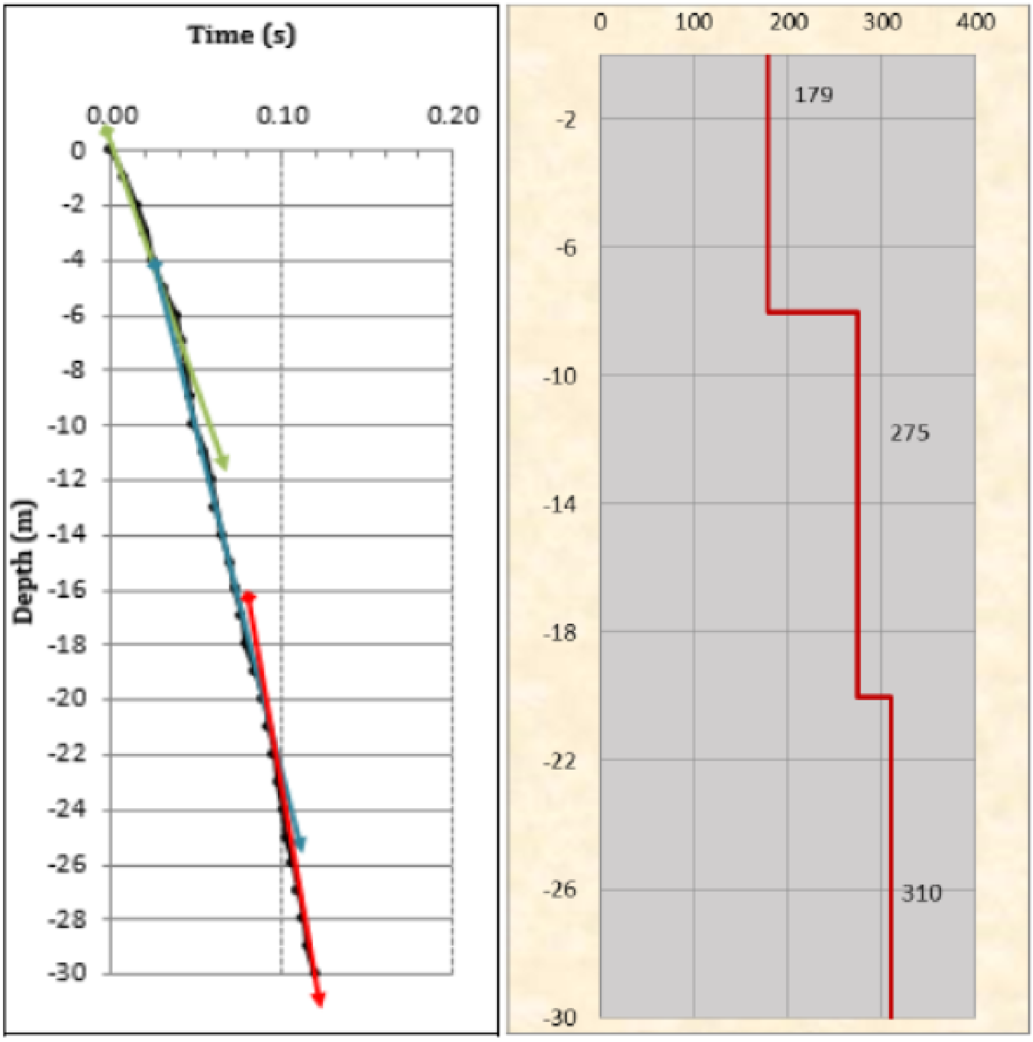

Figure 3.3: S-wave for upper 30m depth. (a) S-wave trace, (b)Corresponding time-distance curve with layer velocity at the selected site

As per BNBC-2020, Site should be classified as type SA, SB, SC, SD, SE, S1 and S2 based on the provisions of Table 6.2.13 of BNBC-2020 and based on the soil properties of upper 30 meters of the site profile. Site class could be determined by Shear wave velocity or Field (uncorrected) Standard Penetration Value or Undrained shear strength of cohesive layers.

According to BNBC-2020 Table 6.2.14, the soil that is deep deposits of dense or medium dense sand, gravel or stiff clay with thickness from several tens to many hundreds of meters should be classified as “SC”. For “SC” type soil, average shear wave velocity of upper 30m soil should be in between 180-360 m/sec and average SPT value for upper

30m soil should be in between 15-50. In this study, it is found that the site class is "SC" type soil by using both Shear wave velocity and SPT values.

Table 3.3: Down hole survey results showing S wave and AV_{s30} velocities

SL. no.	Shear Wave Velocity							
	Layer 1		Layer 1		Layer 1		Total depth investigated (m)	AV_{s30}
	S wave (m/s)	Thickness (m)	S wave (m/s)	Thickness (m)	S wave (m/s)	Thickness (m)		
1	179	8	275	12	310	Base not seen	30	293

Table 3.4: Down hole survey results showing P wave and AVp30 velocities

SL. no.	Shear Wave Velocity							
	Layer 1		Layer 1		Layer 1		Total depth investigated (m)	AV_{p30}
	S wave (m/s)	Thickness (m)	S wave (m/s)	Thickness (m)	S wave (m/s)	Thickness (m)		
1	246	8	422	12	496	Base not seen	30	443

Average shear wave velocity of upper 30 meters of the site profile is 293 m/s which satisfies the requirement of Site Class SC. Again, average field (uncorrected) Standard Penetration Value of upper 30 meters of the site profile is 15.96 which indicates the site class is SC.

3.6 General Description of The Selected Structure

The selected structure is an inverted L shaped 40 storied commercial building with approximate 155m height with five basements with the total area of 2716 square meter including the Podium area. Podium is 4 storied structure with a height of 14.55m. Central core shaft in the middle with dimensions 37.5m×28.5m. The foundation system is piled raft system. The reason behind selecting this structure is recently with the increasing in economic development, rapid industrialization and decreasing availability of land for construction in thickly populated cities like Dhaka, scope for extending construction in horizontal direction is becoming increasingly lesser resulting in construction of high-rise building with increasing number of floors. So, considering the current and future demand, this structure is selected. Overall summary of the structure is given in the following Table:

Table 3.5: General description of the selected structure

SL. No.	Name of feature	Description
1	Story	40
2	Approx. Length (m)	59.325
3	Approx. Width (m)	45.78
4	Area including Podium (sqm)	2716
5	Podium story	4
6	Podium height (m)	14.55
7	Core Length (m)	37.5
8	Core Width (m)	28.5
9	Core Area (sqm)	1068.75
10	Core height (m)	155
11	Clear floor to floor height (m)	4
12	Shape	Inverted L
13	Number of Basement	5
14	Basement floor to floor height (m)	3
15	Bottom of Basement below EGL (m)	18m
16	Foundation system	Both only Raft and Piled raft considered in this study
17	Raft thickness (m)	2.5, 3, 3.5
18	Pile diameter (m)	1, 1.2, 1.5
18	Pile number	58, 69, 82

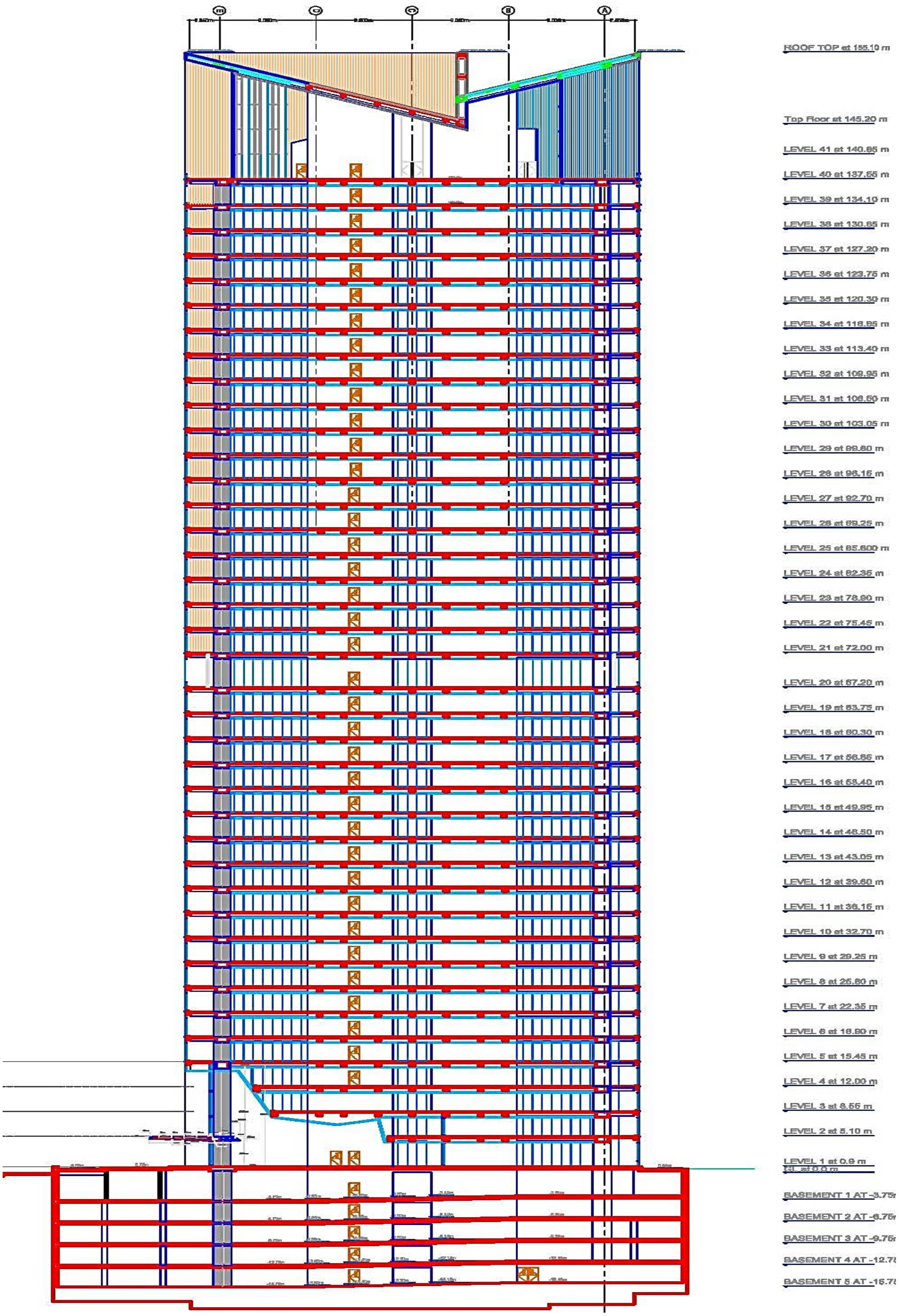

Figure 3.4: Front elevation of the structure

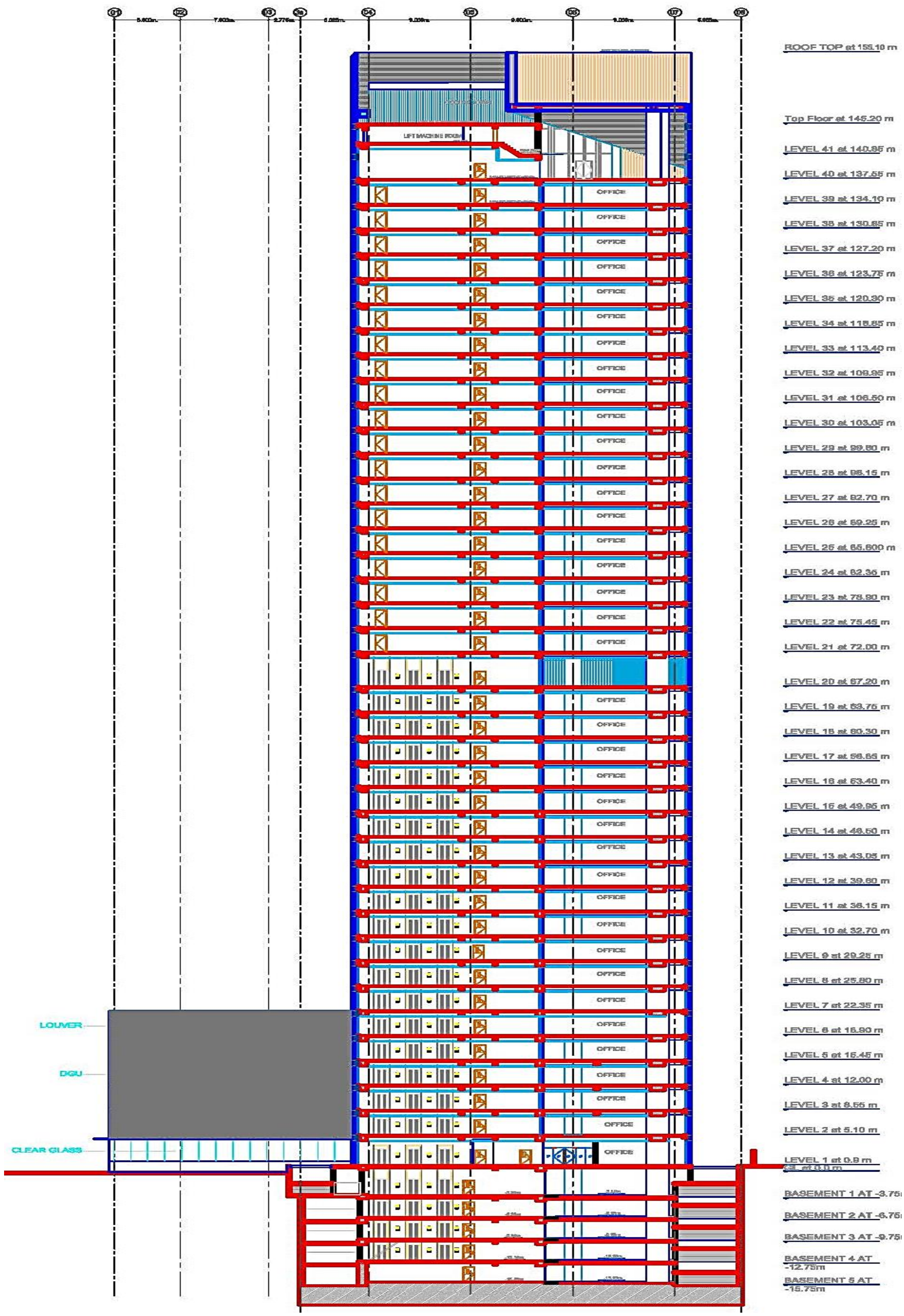

Figure 3.5: Side elevation of the structure

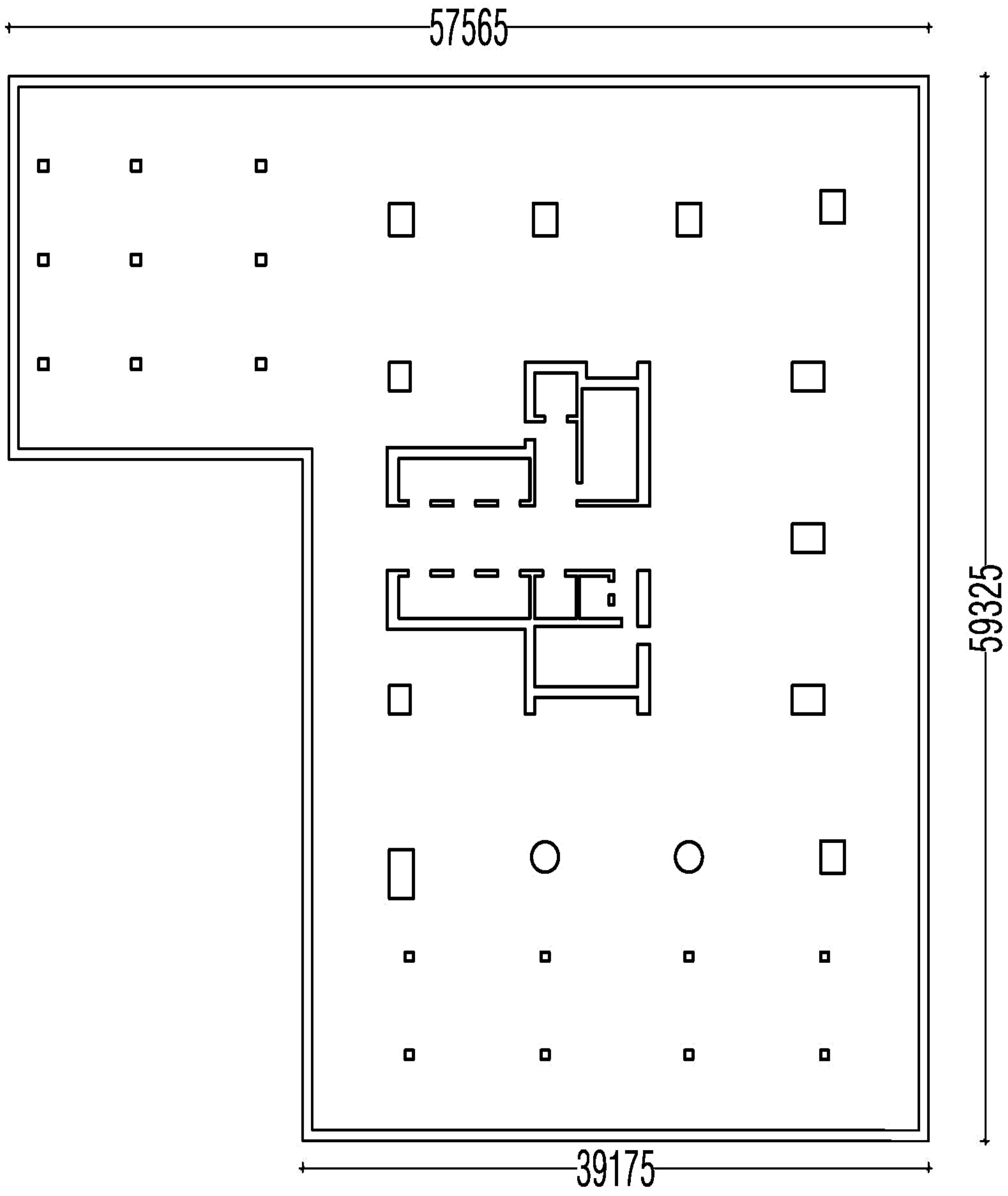

Figure 3.6: Column, Shear wall and Retaining wall layout plan

Foundation details have been discussed in chapter-4 as we have different Pile number, Pile diameter and mat thicknesses for parametric studies.

Chapter 4
NUMERICAL MODELING

4.1 Introduction

Identifying the important parameters which significantly affect the performance of piled-raft foundations can assist in optimizing the design of such foundations. Therefore, studying the effect of different design parameters on the behavior of piled-raft foundations was carried out. This study focused on the effect of some parameters on the load-settlement between the raft and piles of piled-raft foundations. The effect of the selected parameters on the load-settlement relationship will be investigated at small and large settlements. The tests in this study were carried out using the developed PLAXIS-3D model.

The software program consists of three basic components, namely Input, Calculation and Output. In the input program the boundary conditions, problem geometry with appropriate material properties are defined. In PLAXIS 3D, soil properties and material properties of structures are stored in material data sets. There are six different types of material sets grouped as data sets for soil and interfaces, beams, embedded beams, plates, geogrids anchors. All data sets are stored in the material database. From the database, the data sets can be assigned to the soil clusters or to the corresponding structural objects in the geometry model. The model includes an idealized soil profile, structural objects, construction stages and loading. Then the calculation phase starts which performs plastic, dynamic and consolidation analysis of the developed numerical model. As soon as the calculation phase is completed, the output can be checked where all the geotechnical and structural parameters of the numerical model can be thoroughly studied.

4.2 Development of the Numerical model in PLAXIS-3D

The finite element method based on software PLAXIS-3D is used for three-dimensional modelling of 40-storey building structure with five basements and having piled-raft foundation in layered soil field. An overall assessment of the both raft only and piled raft foundation system under actual loading conditions across the site was carried out by using PLAXIS-3D, which is a three-dimensional, finite-element-based geotechnical software. The overall numerical modelling in PLAXIS-3D has five steps as shown in the Figure 4.1. A brief discussion on each stage is given below:

Figure 4.1: Steps for numerical modelling in PLAXIS-3D

4.2.1 Soil

The subsoil was modelled using ten nodded tetrahedral elements that are available in the standard library of PLAXIS-3D. The subsoils primarily comprised typical Dhaka soil as discussed in Table 3.1 of chapter-3. The soil stratigraphy is defined in the soil mode using the Borehole feature of the program. When a new project is created, the soil contour defined in the Project properties window is displayed in the drawing area. There is an option "create boreholes" where all the information of boreholes can be provided. Boreholes are locations in the drawing area at which the information on the position of soil layers and the water table is given.

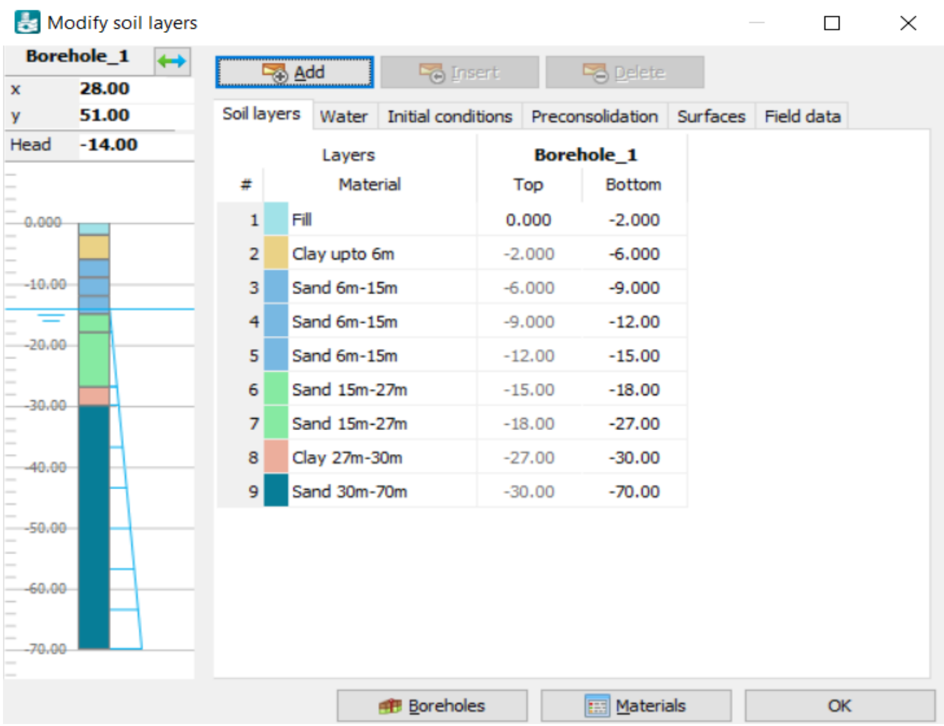

Figure 4.2: Defining the soil layers as per borelog mentioned in Appendix-1

If multiple boreholes are defined, PLAXIS 3D will automatically interpolate between boreholes, and derive the position of the soil layers from the borehole information. Each defined soil layer is used throughout the whole model contour. In other words, all soil layers appear in all boreholes. The top and the bottom boundaries of the layers may vary through boreholes, making it possible to define non-horizontal soil layers of non-uniform thickness as well as layers that locally have a zero thickness. To simlify the numerical model and to avoid long calculation time, only one borehole representing in PLAXIS-3D.

Ground water level has been considered at 14m below existing ground level. In order to avoid an undesirable boundary effect, the lateral dimensions of the soil model were set to be five times the width of the raft. The vertical extent of the soil model was set to be 10m below the pile tip. A mesh optimization study was carried out in order to determine the extent of the model boundaries, which helps in reducing computational effort. The soil model (500m long, 350m wide and 70 m deep) was created as shown in Figure 4.2.

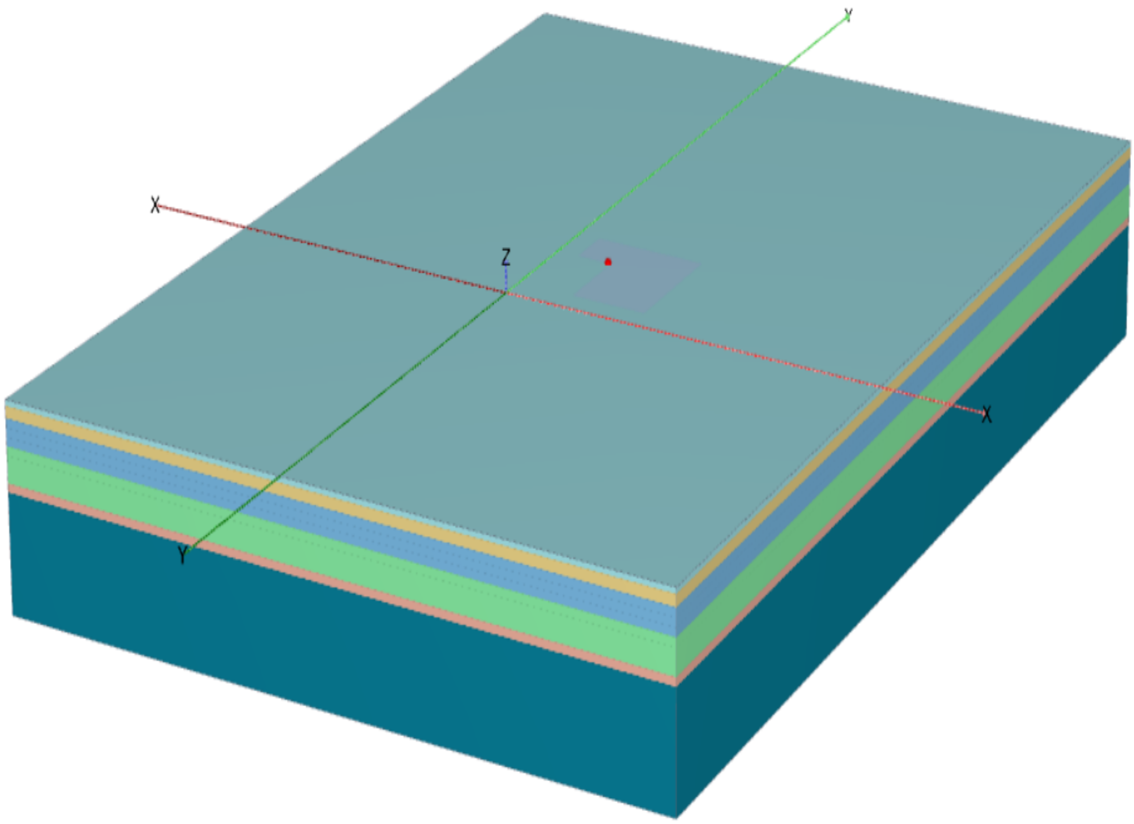

Figure 4.3: The volume of defined soil model in PLAXIS-3D

The soil was modelled using the Hardening soil constitutive model. This is an advanced model for the simulation of soil behavior. The Hardening Soil model is an elastoplastic type of hyperbolic model, formulated in the framework of shear hardening plasticity. Moreover, the model involves compression hardening to simulate irreversible compaction of soil under primary compression. This second-order model can be used to simulate the behavior of sands and gravel as well as softer types of soil such as clays and silts. Soil strength parameters (cohesion and angle of internal friction) and Modulus of Elasticity, E_{50}^{ref} values has been calculated from soil types and well-established correlations with SPT-values. Other parameters for performing the numerical model have been calculated the PLAXIS-3D based on the information given by the user. The soil properties for hardening soil model used in PLAXIS-3D are given in following Tables.

Table 4.1: Soil properties used in hardening soil model

Identification	**Fill**	**Clay upto 6m**	**Sand 6m-15m**	**Sand 15m-27m**	**Clay 27m-30m**	**Sand 30m-70m**
Layer thickness (m)	2	4	9	12	3	40
Soil Volume No.	Soil_1	Soil_2	Soil_3, Soil_7, Soil_8	Soil_4, Soil_9	Soil_5	Soil_6
Colour						
Drainage type	Drained	Undrained (B)	Drained	Drained	Undrained (B)	Drained
ϒ(unsat) (kN/m^3)	14	16	17	18	16	18
ϒ(sat) (kN/m3)	16	18	19	20	18	20

Contd. Table 4.1

Identification	Fill	Clay upto 6m	Sand 6m-15m	Sand 15m-27m	Clay 27m-30m	Sand 30m-70m
E_{50}^{ref} (kPa)	12000	8000	45000	85000	8000	130000
E_{oed}^{ref} (kPa)	12000	8000	45000	85000	8000	130000
E_{ur}^{ref} (kPa)	36000	24000	135000	255000	24000	390000
Power, m	1	1	0.5	0.5	1	0.5
c_{ref} (kPa)	1	50	1	1	70	1
Φ (deg)	30	0	32	36	0	38
R_f	0.9	0.9	0.9	0.9	0.9	0.9
R_{inter}	0.67	0.67	0.67	0.67	0.67	0.67

4.2.2 Structure

In this section, the structural component is modelled. This phase of numerical modeling consists of the following:

1. Material properties: All the structural member's properties are assigned in this phase of modeling. The interaction effect of pile and soil at the pile shaft is considered by means of Elasto-Plastic line-to-volume and point-to-volume interfaces as an embedded pile model. The embedded pile model consisting of beam elements with non-linear skin and tip interfaces. For defining the pile bearing the capacity, the option "Layer dependent" is chosen. The piles were modeled as "embedded elements." In this case, the piles do not have a "real" volume or a "real" interface. However, a virtual elastic zone is created by assigning an equivalent pile diameter within the material data set of the embedded pile. This virtual elastic zone disregards the plastic behavior of the

soil within the zone and approaches the actual volume pile behavior. On the other hand, due to the “virtual” volume and interface, evaluation of the effect of strength reduction factor (R_{inter}) cannot be realized. R_{inter} is taken as rigid (1.0) with the assumption that the interface does not have a reduced strength. There is no need for mesh refinement around piles as 3D mesh is not distorted by introducing embedded pile model. The basement floor slab, retaining wall and raft is discretized using 6-node triangular plate elements with linear elastic properties. Summary of the material properties is given in Table 4.2 and 4.3.

Table 4.2: Material properties of Plates
(Raft, basement floor slab and retaining wall) in PLAXIS-3D

Name of Structural Member	**Raft**	**Retaining wall**	**Basement slab**
Identification	Mat	R.wall	Basement floors
Material model	Elastic	Elastic	Elastic
Thickness (m)	1, 1.5, 2.5, 3, 3.5	0.6	0.3
ϒ (kN/m^3)	24	24	24
E (kPa)	29730000	29730000	29730000

Table 4.3: Material properties of Embedded beam or Pile in PLAXIS-3D

Name of Structural Member	**Pile**
Identification	P1
Material model	Elastic
Diameter (m)	1, 1.2, 1.5
ϒ (kN/m^3)	24
E (kPa)	24870000
Axial skin resistance	Layer dependent
Maximum base resistance (kN)	5000

2. Geometry: The geometry of raft, retaining wall and piles are assigned in this phase as per structural information mentioned in chapter-3. As mentioned, the shore protection and effect of excavation is not focused in this study.

3. Loads: Service loads like dead loads and live loads of superstructure has been created by creating a FEM model in ETABS-2017 software. Most of previous study and research on piled raft has been performed using uniformly distributed load over the raft. But to observe the actual and more accurate stress and settlement behavior of raft only or piled raft foundation, point load has been assigned in this study. The effect of eccentric load has been addressed due to point load application. Service loads from the superstructure has been given in Table 4.4.

Figure 4.4: Joint locations from structural FEM ETABS model

Table 4.4: Loads of Superstructure applied on raft in PLAXIS-3D

Joint location	Load combination	Loads (kN)
1	Dead + Live	39860
3	Dead + Live	52457
5	Dead + Live	13599
6	Dead + Live	15740
7	Dead + Live	29209
8	Dead + Live	1986
9	Dead + Live	7004
10	Dead + Live	6893
11	Dead + Live	20363
12	Dead + Live	5304
13	Dead + Live	4347
14	Dead + Live	9091
17	Dead + Live	5408
18	Dead + Live	2907
19	Dead + Live	18279
20	Dead + Live	3492
21	Dead + Live	22389
22	Dead + Live	22486
23	Dead + Live	37114
25	Dead + Live	404
26	Dead + Live	26846
29	Dead + Live	12683
31	Dead + Live	10635
33	Dead + Live	6428
35	Dead + Live	5900
39	Dead + Live	1505
41	Dead + Live	7538
45	Dead + Live	6468
54	Dead + Live	1539
55	Dead + Live	1666
56	Dead + Live	44771
71	Dead + Live	2416
72	Dead + Live	2348
73	Dead + Live	1919
81	Dead + Live	1668
82	Dead + Live	1859
83	Dead + Live	13678
85	Dead + Live	5502
86	Dead + Live	3380
88	Dead + Live	2352
89	Dead + Live	2625
91	Dead + Live	52040
94	Dead + Live	931

Contd. Table 4.4:

Joint location	Load combination	Loads (kN)
95	Dead + Live	4415
96	Dead + Live	17453
97	Dead + Live	1098
99	Dead + Live	1154
100	Dead + Live	7622
102	Dead + Live	6626
103	Dead + Live	2371
105	Dead + Live	6043
124	Dead + Live	5873
128	Dead + Live	3460
132	Dead + Live	5954
135	Dead + Live	6225
136	Dead + Live	4907
137	Dead + Live	3226
138	Dead + Live	3683
139	Dead + Live	3788
140	Dead + Live	3915
141	Dead + Live	3280
142	Dead + Live	3033
143	Dead + Live	3816
144	Dead + Live	3749
145	Dead + Live	2879
146	Dead + Live	2657
147	Dead + Live	2159
148	Dead + Live	2163
149	Dead + Live	2063
150	Dead + Live	2880
151	Dead + Live	2275
152	Dead + Live	3052
153	Dead + Live	2106
154	Dead + Live	1107
155	Dead + Live	1322
156	Dead + Live	1734
157	Dead + Live	2784
158	Dead + Live	2180
159	Dead + Live	2566
160	Dead + Live	3349
161	Dead + Live	3147
162	Dead + Live	2527
163	Dead + Live	2526
164	Dead + Live	2470
165	Dead + Live	1353
166	Dead + Live	770
167	Dead + Live	859

Contd. Table 4.4:

Joint location	Load combination	Loads (kN)
168	Dead + Live	2194
170	Dead + Live	5078
171	Dead + Live	2416
172	Dead + Live	2348
173	Dead + Live	1919
174	Dead + Live	3109
175	Dead + Live	2840
177	Dead + Live	2530
179	Dead + Live	3586
181	Dead + Live	2917
182	Dead + Live	1859
191	Dead + Live	4592
192	Dead + Live	1674
249	Dead + Live	49646
250	Dead + Live	50804
251	Dead + Live	53813
252	Dead + Live	45326
253	Dead + Live	49988
254	Dead + Live	50567
255	Dead + Live	1098
256	Dead + Live	27127
257	Dead + Live	1313
258	Dead + Live	443
259	Dead + Live	1537
260	Dead + Live	1564
261	Dead + Live	1693
262	Dead + Live	1698
264	Dead + Live	5449
265	Dead + Live	966
266	Dead + Live	964
267	Dead + Live	7526
268	Dead + Live	1088
269	Dead + Live	623
270	Dead + Live	768
271	Dead + Live	772

4. Interfaces: Interfaces are joint elements to be added to plates or geogrids to allow for a proper modelling of soil-structure interaction. Interfaces may be used to simulate, for example, the thin zone of intensely shearing material at the contact between a plate and the surrounding soil. Interfaces can be created next to plate or geogrid elements or between two soil volumes. When the geometric

entity (surface) is already available in the model it is advised to assign an interface to it without recreating the geometry in order to prevent the model from being unnecessarily large and unwieldy. Distinction is made between a positive interface (the side of the surface at the positive local z-direction) and a negative interface (the side of the surface at the negative local z-direction). The sign of an interface is only used to enable distinguishing interfaces at either side of a surface, but it does not affect its behavior. In the numerical model, negative interface has been used for raft and positive interface has been used for retaining wall.

4.2.3 Earthquake loads

Analysis: For earthquake analysis, the free field site response has been carried out along a 1D linear elastic frequency domain. In this study, PLAXIS-3D finite element software is used to conduct this analysis. For the current study HS model is used for modeling soil element according to soil investigation done in the study site previously. The earthquake load is applied at the bottom of the FEM model as prescribed displacement. In dynamic loading condition, using HS model generates plastic strain with increased pre-consolidation stress in soil.

Dynamic soil behavior: Constitutive model presents in PLAXIS needs to be validated for seismic analysis before implementation. Every constitutive model can be used for modeling material behavior. But due to some limitations each model cannot simulate seismic behavior. During an earthquake, soil is subjected to cyclic shear loading showing a nonlinear dissipative behavior. The total amount of damping is introduced through frequency dependent Rayleigh formula. Which is considered in HS model as previously discussed. Generally, HS and hardening soil with small strain (HSSM) models are recognized for using in earthquake analysis. Here in this study, Hardening Soil model with the same soil properties have been used for seismic analysis as shown in Table-4.1.

Boundary Condition: A proper boundary condition is important for analyzing pile accurately. Earthquake load is applied in the model as uniform prescribed displacement in x direction as shown in Figure 4.5. The deformation is free in Xmin and Xmax direction. In Ymin,max and Zmin,max direction the deformation is kept fixed. To introduce the soil strength reduction due to soil movement, an interface surface with strength reduction at the bottom surface (70m below existing ground level; bottom of the soil volume) is added as shown in Figure 4.6. For input seismic motion the boundaries in x direction are viscous. The viscous field boundary condition for lateral deformation keeps the boundary capable for motion to move at the sides and also absorbs the reflected secondary waves. In Y direction it is none as no absorbent boundary condition is applied. In Zmin none is assigned and Zmax is also none for unabsorbing bedrock. The dynamic analysis time interval is assigned 48 sec. A proper boundary for bottom boundary ensures the reflection of waves from above layers are absorbed and thus direct earthquake accelerogram can be applied directly.

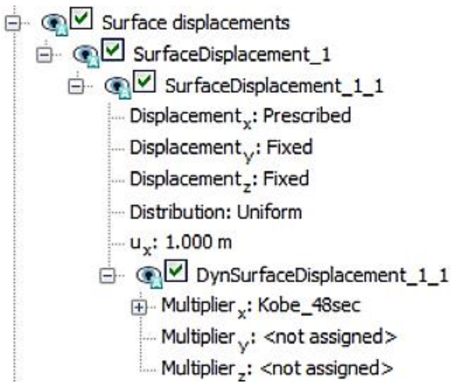

Figure 4.5: Boundary condition for earthquake load simulation

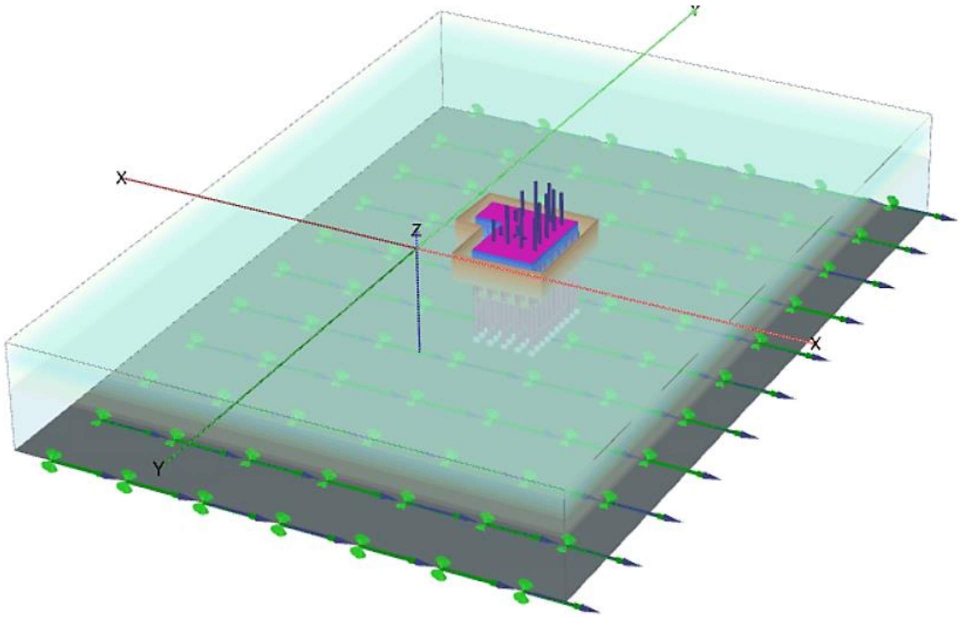

Figure 4.6: Prescribed displacement method for earthquake load simulation

Earthquake Input signal: In this analysis 1995 Kobe earthquake motion is used. Kobe earthquake is a severe earthquake with a magnitude Mw= 7.2 and PGA = 0.821g. The acceleration time histories of 48 second duration are presented in Figure 4.7. These records are applied in the horizontal X direction at all bottom (70m below EGL) node of the model. They are scaled to design basis earthquake value the site 0.133g for Dhaka zone. Figure 4.8 shows the Kobe earthquake acceleration data input in PLAXIS 3D for earthquake analysis.

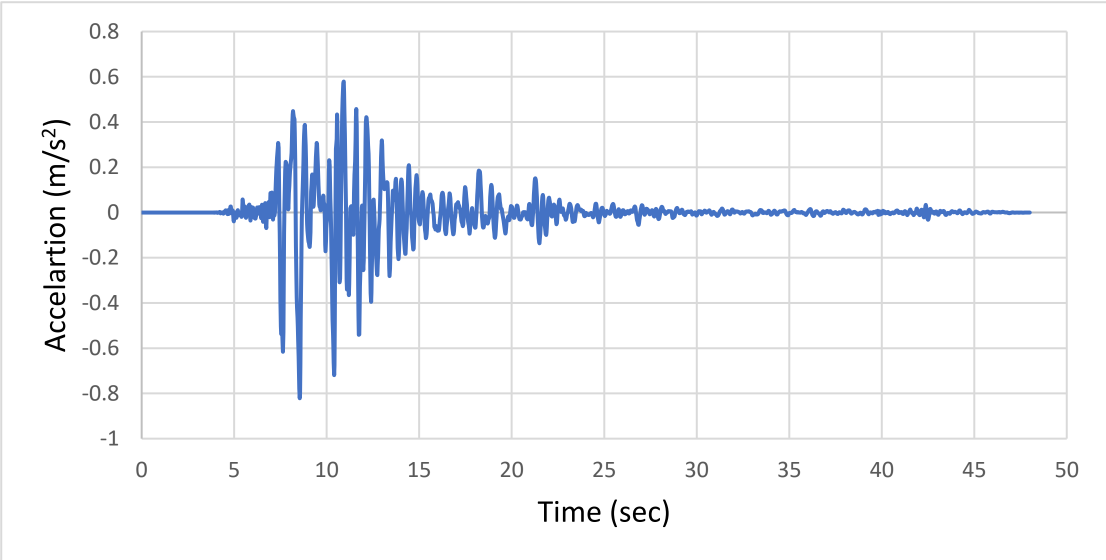

Figure 4.7: Original Kobe 1995 earthquake data

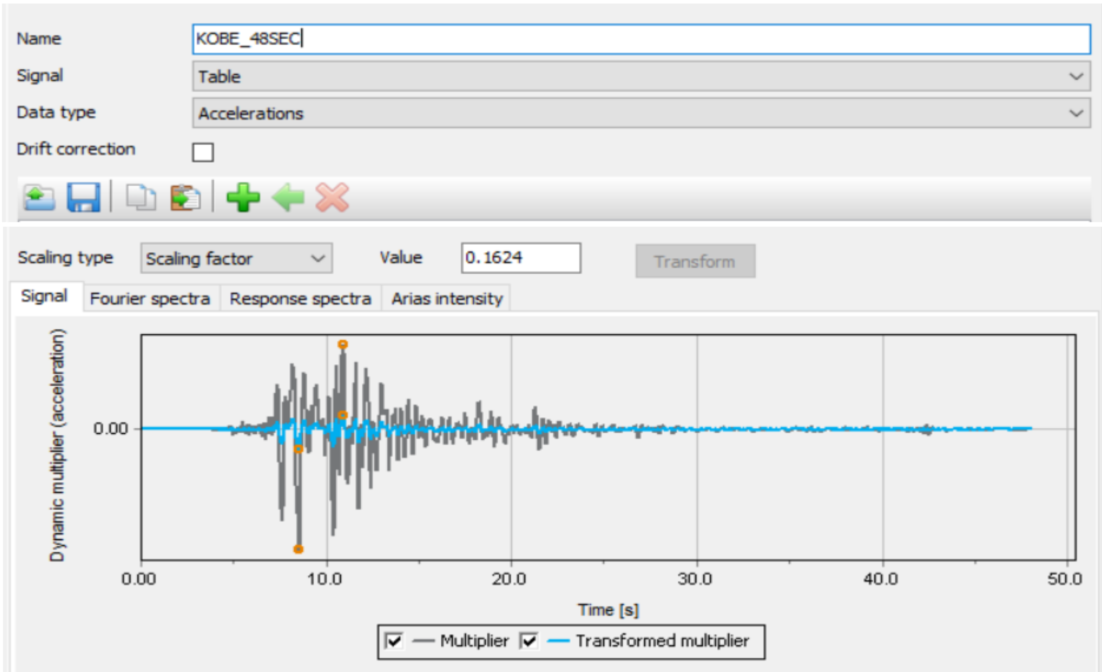

Figure 4.8: Kobe 1995 Earthquake input signal (both raw and scaled data)

4.2.4 Mesh

Generating a proper Finite Element mesh is an important intermediate step between the definitions of the geometry and the construction stages. In order to have a smooth and accurate calculation the finite element mesh has to fulfill several criteria. For the numerical stability of the calculation, the mesh should have a good quality, that is to say, the elements should be regular without being excessively long and thin. For the accuracy of the calculation, the elements should be small enough, especially in those areas where significant changes in stress or strain can be expected during the analysis. But that does not mean one should just generate an entire mesh of very small elements as this will lead to a very large calculation time. Therefore, proper care should be taken to find the right balance between accuracy and calculation time while supervising on the mesh quality.

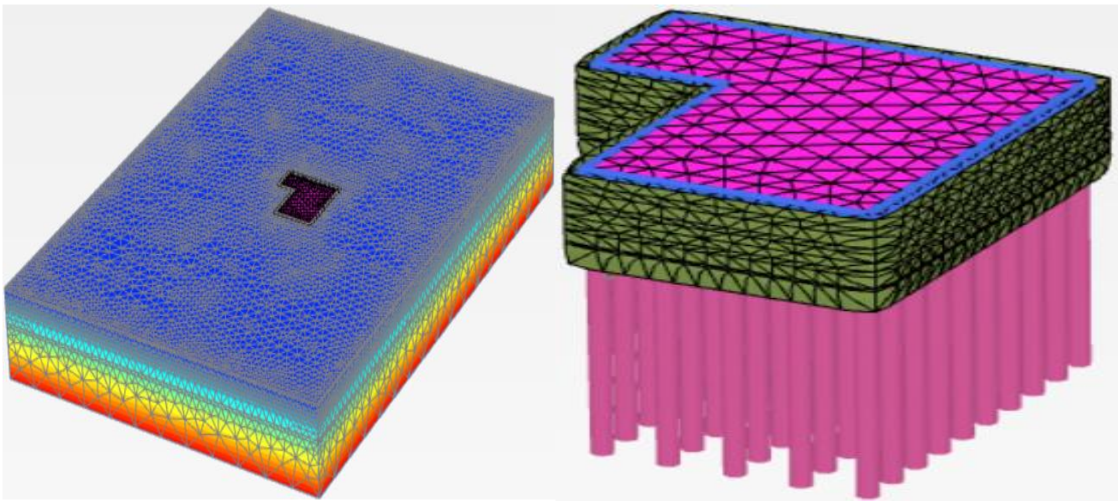

Figure 4.9: Mesh quality and quality spheres of numerical model

After assigning all the geometry parameters, meshing can be done. Mesh dimension should be appropriately defined, to prevent boundary conditions. Very fines mesh should be avoided in order to reduce the number of elements, thus reduce the memory consumption and calculation time. In this study, for raft only models, effect of different mesh size has been studied by applying very coarse, coarse and medium mesh. However, for piled raft models, only very course mesh was used to avoid longer computation time.

The mesh generator requires a global meshing parameter *le*, which represents the target element dimension. In PLAXIS 3D this parameter is calculated from the outer geometry dimensions (*xmin*, *xmax*, *ymin*, *ymax*, *zmin*, *zmax*) and the *Element distribution* selected in the Mesh options window. The target element dimension is calculated using the equation 4.1.

$$\mathrm{le} = \mathrm{re} \times 0.05 \times \sqrt{(\mathrm{xmax} - \mathrm{xmin})2 + (\mathrm{ymax} - \mathrm{ymin})2 + (\mathrm{zmax} - \mathrm{zmin})2} \tag{4.1}$$

where the Relative element size factor (re) is derived from the Element distribution. There are five global levels. By default, the Element distribution is set to Medium but the user may select one of the other levels to make the mesh globally finer or coarser. The predefined values of the parameter r_e (Element distribution) are:

Table 4.5: Relative element size factor for different mesh size

Element distribution	r_e
Very coarse	2
Coarse	1.5
Medium	1
Fine	0.7
Very fine	0.5

4.2.5 Staged Construction:

In PLAXIS 3D, only raft or piled raft foundation is provided as a staged construction process. In every calculation step, the material properties, geometry of the model, loading condition and the ground water level can be redefined. During the calculations in each construction step, a multiplier that controls the staged construction process denoted by ΣM stage is increased from zero to ultimate value 1. After staged construction the PLAXIS results were obtained. In this study total 4 construction stages were created. Stage construction details as follows:

Initial Phase: Firstly, in the initial stage, in-situ stress state or it is also called primary stress conditions is applied. In the step, only the own weight of the soil domain will be activated.

Phase_1: This phase starts after initial stage. As shore protection or excavation effect is not focused in this study so in this phase, retaining wall, raft, piles, interfaces all are activated. The soil excavation up to a depth of 18m below GL also done in this stage. This was modeled by deactivation of the soil element from ground surface up to 18m. The analysis type is Plastic.

Phase_2: This stage starts after Phase_1. In this stage, the loads from superstructure applied as point loads on the raft. The analysis type is Plastic in this phase.

Phase_3: This stage starts after Phase_2. This stage is devoted to application earthquake load and dynamic analysis of the numerical model. The analysis type is Dynamic in this phase. Total dynamic time interval is 48 seconds. Prescribed displacement is activated in this phase along with the necessary boundary condition modification discussed in 4.2.3.

Phase_4: This stage also starts after Phase_2. This final stage is created to calculated the consolidation settlement effect. Calculation type Consolidation is selected with 90% degree of consolidation in this stage of construction.

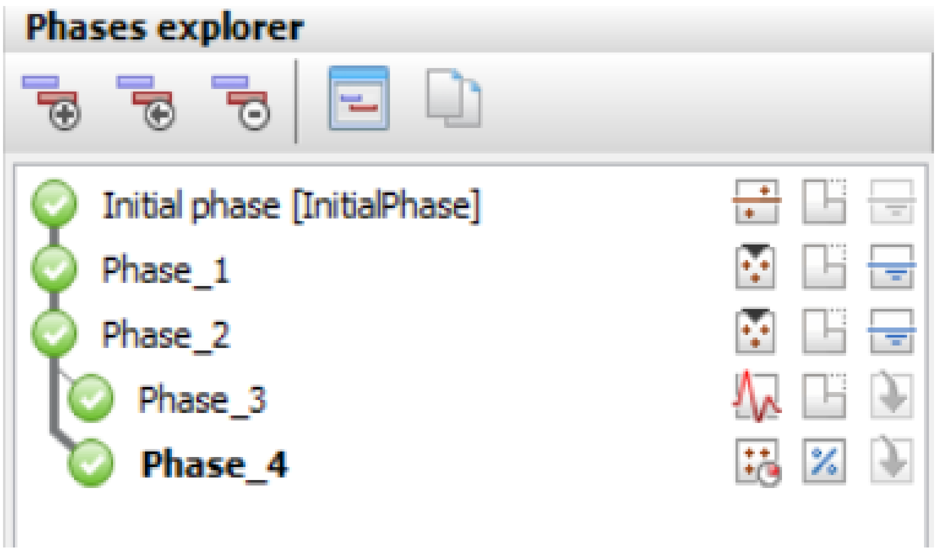

Figure 4.10: Different construction stages in PLAXIS-3D.

For better understanding of the stage construction, Table 4.6 can be followed.

Table 4.6: Summary of the stage construction

Phase	Analysis type	Elements	Activated
Initial phase	K_0	Soil volume	√
		Point loads	x
		Embedded beams	x
		Plates	x
		Interfaces	x
		Surface displacements	x
		Soil excavation	x
Phase_1 (Excavation up to dredging level, Raft, piles, retaining wall activation)	Plastic	Soil volume	√
		Point loads	x
		Embedded beams	√
		Plates	√
		Interfaces	√
		Surface displacements	x
		Soil excavation	√
Phase_2 (Gravity Load activation)	Plastic	Soil volume	√
		Point loads	√
		Embedded beams	√
		Plates	√
		Interfaces	√
		Surface displacements	x
		Soil excavation	√
Phase_3 (Earthquake Load activation)	Dynamic	Soil volume	√
		Point loads	√
		Embedded beams	√
		Plates	√
		Interfaces	√
		Surface displacements	√
		Soil excavation	√
Phase_4 (Consolidation analysis)	Consolidation	Soil volume	√
		Point loads	√
		Embedded beams	√
		Plates	√
		Interfaces	√
		Surface displacements	√
		Soil excavation	√

4.2.6 Calculation

In this study following calculation types are adopted in PLAXIS-3D

Initial stress generation: The first step in a PLAXIS 3D analysis is defining a calculation type of a phase in the Calculation type drop-down menu in the Phases window. The options available are K0 procedure and Gravity loading for the initial phase to generate the initial stress state of soil. Many analysis problems in geotechnical engineering require the specification of a set of initial stresses. The initial stresses in a soil body are influenced by the weight of the material and the history of its formation. This stress state is usually characterized by an initial vertical effective stress (σ'v,0). The initial horizontal effective stress σ'h,0 is related to the initial vertical effective stress by the coefficient of lateral earth pressure K_0 ($\sigma'h, 0 = K_0 \cdot \sigma'v, 0$).

Plastic calculation: A Plastic calculation is used to carry out an elastic-plastic deformation analysis in which it is not necessary to take the change of pore pressure with time into account. If the Updated mesh parameter has not been selected, the calculation is performed according to the small deformation theory. The stiffness matrix in a normal plastic calculation is based on the original undeformed geometry. This type of calculation is appropriate in most practical geotechnical applications.

Although a time interval can be specified, a plastic calculation does not take time effects into account, except when the Soft Soil Creep model is used. Considering the quick loading of saturated clay-type soils, a Plastic calculation may be used for the limiting case of fully undrained behavior using the Undrained (A), Undrained (B) or Undrained (C) option in the material data sets. On the other hand, performing a fully drained analysis can assess the settlements on the long term. This will give a reasonably accurate prediction of the final situation, although the precise loading history is not followed and the process of consolidation is not dealt with explicitly.

An elastic-plastic deformation analysis where undrained behavior (Undrained (A) or Undrained (B) is temporarily ignored can be defined by checking the “Ignore undrained behavior” (A, B) parameter. In this case the stiffness of water is not taken into account.

Note that “Ignore undrained behavior” does not affect materials of which the drainage type is set to Undrained (C).

In a Plastic calculation loading can be defined in the sense of changing the load combination, stress state, weight, strength or stiffness of elements, activated by changing the load and geometry configuration or pore pressure distribution by means of Staged construction. In this case, the total load level that is to be reached at the end of the calculation phase is defined by specifying a new geometry and load configuration, and/or pore pressure distribution, in the Staged construction mode.

The options for Pore pressure calculation type for a Plastic phase are:

1. Phreatic
2. Use pressures from previous phase
3. Steady state groundwater flow

Consolidation calculation: A Consolidation calculation is usually conducted when it is necessary to analyze the development and dissipation of excess pore pressures in a saturated clay-type soil as a function of time. PLAXIS- 3D allows for true elastic-plastic consolidation analysis. In general, consolidation analysis without additional loading is performed after an undrained plastic calculation. It is also possible to apply loads during a consolidation analysis. However, take care when a failure situation is approached, since the iteration process may not converge in such a situation. A consolidation analysis requires additional boundary conditions on excess pore pressures

In PLAXIS 3D, pore pressures are divided into steady-state pore pressures and excess pore pressures. Steady state pore pressures are generated according to the water conditions assigned to the soil layers for each phase, whereas excess pore pressures are calculated as a result of undrained soil behavior (Undrained (A) or Undrained (B)) or consolidation. A Consolidation calculation in PLAXIS 3D only affects the excess pore pressures. Rather than considering the drainage type settings Undrained (A) or Undrained (B), a Consolidation calculation considers the corresponding permeabilities as defined in the Groundwater tab of the material data set instead.

A Consolidation calculation does not affect Undrained (C) materials since such materials do not allow (excess) pore pressures to be generated.

In a Consolidation analysis, the following options are available:

1. Consolidation and simultaneous loading in the sense of changing the load combination, stress state, weight, strength or stiffness of elements, activated by changing the load and geometry configuration by means of Staged construction. It is necessary to specify a value for the Time interval parameter, which has in this case the meaning of the total consolidation period applied in the current calculation phase. The load is linearly increased to the specified level within the time interval. The applied first-time increment is based on the First-time step parameter in the Numerical control parameters subtree. The Staged construction option should also be selected if it is desired to allow for a certain consolidation period without additional loading.

2. Consolidation without additional loading, until all excess pore pressures have decreased below a certain minimum value, specified by the Minimum excess pore pressures parameter. By default, the Minimum excess pore pressures is set to 1 stress unit, but this value may be changed by the user. Please note that the Minimum excess pore pressures parameter is an absolute value, which applies to pressure as well as tensile stress. The input of a Time interval is not applicable in this case, since it cannot be determined beforehand how much time is needed to fulfill the minimum excess pore pressure requirement. The applied first-time increment is based on the First-time step parameter in the Numerical control parameters subtree.

3. Consolidation without additional loading, until a desired degree of consolidation, specified by the Degree of consolidation parameter, is reached. By default, Degree of consolidation parameter is set to 90.0 %, but this value may be changed by the user. The input of a Time interval is not applicable in this case, since it cannot be determined beforehand how much time is needed to fulfill the degree of consolidation requirement. The applied first-time increment

is based on the First-time step parameter in the Numerical control parameters subtree.

However, although the degree-of-consolidation is officially defined in terms of target settlement over final settlement, in PLAXIS-3D it is defined as the target minimum excess pore pressure over the maximum initial excess pore pressure p_{max}/p_{max}, initial.

Dynamic calculation: The Dynamic option should be selected when it is necessary to consider stress waves and vibrations in the soil. Dynamic loads can come in various types such as machine induced loads, impact loads, blast load, moving vehicle load or as earthquake loads. With PLAXIS 3D it is possible to perform a dynamic analysis for these types of loads after a series of plastic calculations. It is possible to apply dynamic loads through displacement multipliers or load multipliers. They can be defined as harmonic or as input table. The applied dynamic load is the product of the input value of the defined dynamic load and the corresponding dynamic load multiplier. Besides the activation of the dynamic load or dynamic prescribed displacement, special absorbent boundary conditions can be defined for a Dynamic calculation. A Dynamic time interval can be defined to specify the calculation duration and an automatic time stepping scheme takes care of the best combination of Max steps and Number of sub-steps, based on the estimated time steps.

Earthquake Analysis: This section provides an overview of the Geotechnical earthquake modelling and analysis capabilities of PLAXIS. A variety of nonlinear native and UDSM models for earthquake analysis are offered in PLAXIS. In general, all native models offered in PLAXIS can be used in combination with Dynamic analysis. However, the user is expected to know the limitations of each of the models being used. Here are some models which are often used in combination with Seismic analysis. HS-small and its UDSM version GHS can simulate strain dependency of stiffness and hysteretic damping. UBC3D-PLM (native) and PM4Sand (UDSM) are liquefaction models available in PLAXIS for which the parameters can be estimated from SPT or CPT data in the absence of lab tests. Processing and modification of input accelerograms are a key component of earthquake analysis. Options are available in the dynamic multiplier tab to scale the signal to the required PGA. Furthermore, the input accelerograms can be easily transformed and visualized as Fourier amplitude spectrum, Power spectrum, PSA as well as Arias Intensity. A drift correction to correct the displacement drift due to instrument noise or background noise can also be applied automatically during a dynamic calculation. Special boundary conditions are required for earthquake motion in order to minimize wave reflection at model boundaries. The compliant base boundary condition for the bottom boundary ensures that reflected waves from layers above are absorbed and allows direct application of an input (upward propagating) accelerogram. Free field boundary conditions for lateral boundaries impose free-field motion at the sides, additionally it absorbs the reflected secondary waves. Tied degrees of freedom connects the nodes on the same elevation at left and right boundaries, which can be used to simulate one-dimensional wave propagation.

Energy dissipation due to vibrational or cyclic loading can be defined through Damping. PLAXIS offers both hysteretic and viscous material damping, as well as numerical damping. Hysteretic damping is inherent to the HS-small model, whereas, Rayleigh damping is a numerical feature to simulate viscous material damping, which can be applied in each individual material data set. Numerical damping can be imposed by changing the default Newmark alpha and beta parameters. Dynamic calculations can be conducted as drained, undrained or as Dynamic with consolidation. Automatic time stepping scheme allows for a proper selection of the time step to accurately model wave propagation and reduce the numerical error due to integration of time history functions. The user can also control the number of steps using the semi-automatic or Manual option for accurate modelling.

Curves in Dynamic calculations explains output curves generation options for dynamic analysis. It is possible to transform the generated curves from the time domain to the frequency domain automatically using Fast Fourier Transform (FFT). From FFT, Power Spectrum and Fourier Amplitude Spectrum (FAS) can be plotted for each acceleration component. From output curves it is possible to produce PSA spectrum to determine the predominant period as well as Relative displacement response spectrum, Amplification factor that displays the magnification of the response at a point with respect to the given excitation, and Arias intensity to determine the strength of a ground motion. Furthermore, plots can be generated for extreme accelerations, velocities and displacements for dynamic phases.

It should be noted that steady-state pore pressures in a Dynamic calculation are always taken from the steady-state pore pressures generated in the parent phase. It is possible to calculate excess pore pressures in undrained soil layers in a dynamic analysis. However, the accuracy at which pore pressures are predicted depends on the capabilities of the soil models being used. A standard dynamic calculation may involve the generation of excess pore pressures, but not the dissipation of excess pore pressures. If the latter is required, a Dynamic with consolidation calculation should be performed. In a Dynamic calculation loading can be defined in the sense of applying a predefined combination of external loads as dynamic forces using dynamic multipliers activated in the Staged construction mode. Dynamic calculations can also deal with moving loads.

4.2.7 Output

The main output quantities of a finite element calculation are the displacements and the stresses. In addition, when a finite element model involves structural elements, the structural forces in these elements are calculated. An extensive range of facilities exists within the PLAXIS-3D Output program to display the results of a finite element analysis.

The main output features of PLAXIS-3D could be classified into four categories:

1. Connectivity plot

A Connectivity plot is a plot of the mesh in which the element connections are clearly visualized. It is the result of the meshing process. It is available only in the representation of spatial variation of the results. This plot is particularly of interest when interface elements are included in the mesh. Interface elements are composed of pairs of nodes in which the nodes in a pair have the same coordinates.

In the Connectivity plot however, the nodes in a pair are drawn with a certain distance in between so that it is made clear how nodes are connected to adjacent elements. This option is available from the Mesh menu. In the Connectivity plot it can, for example, be seen that when an interface is present between two soil elements, that the soil elements do not have common nodes and that the connection is formed by the interface. In a situation where interfaces are placed along both sides of a plate (Positive interface and Negative interface), the plate and the adjacent soil elements do not have nodes in common. The connection between the plate and the soil is formed by the interface. An example of Connectivity plot is given in Figure 4.11.

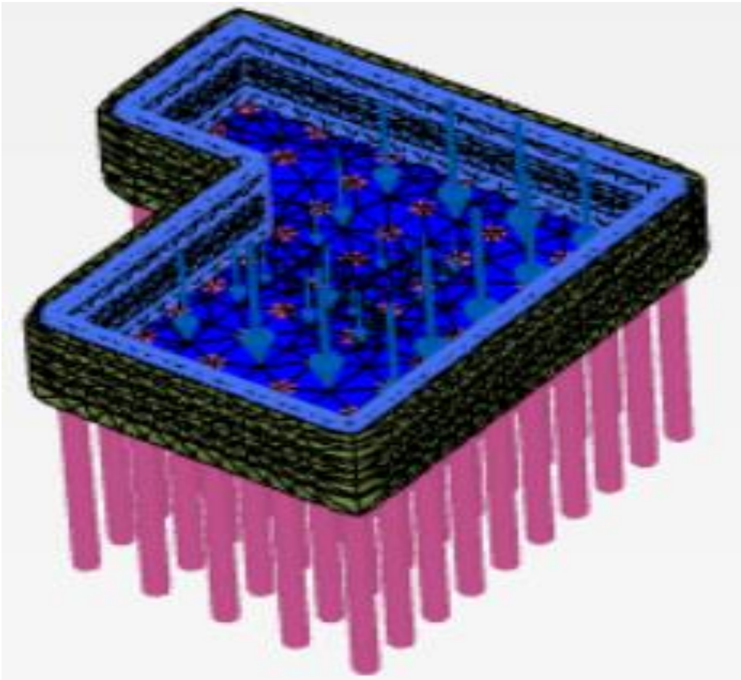

Figure 4.11: Typical connectivity plot in output interface (structure only view)

In the Connectivity plot it is possible to view soil clusters and structural chains that are excluded from the strength reduction procedure in a (enhanced) safety calculation, provided that the Hide items without strength reduction option in the View menu has been selected. These clusters and structures are indicated by a custom color; the default color is grey, but this can be changed in the settings of Modifying the display settings.

2. Deformations

The Deformations menu contains various options to visualize the displacements and strains in the finite element model. By default, the displayed quantities are scaled automatically by a factor (1, 2 or 5) $\cdot 10^n$ to give a diagram that may be read conveniently. The scale factor may be changed by clicking the Scale factor button in the toolbar or by selecting the Scale option from the View menu. The scale factor for strains refers to a reference value of strain that is drawn as a certain percentage of the geometry dimensions. To be able to compare plots of different calculation phases or different projects, the scale factors in the different plots must be made equal.

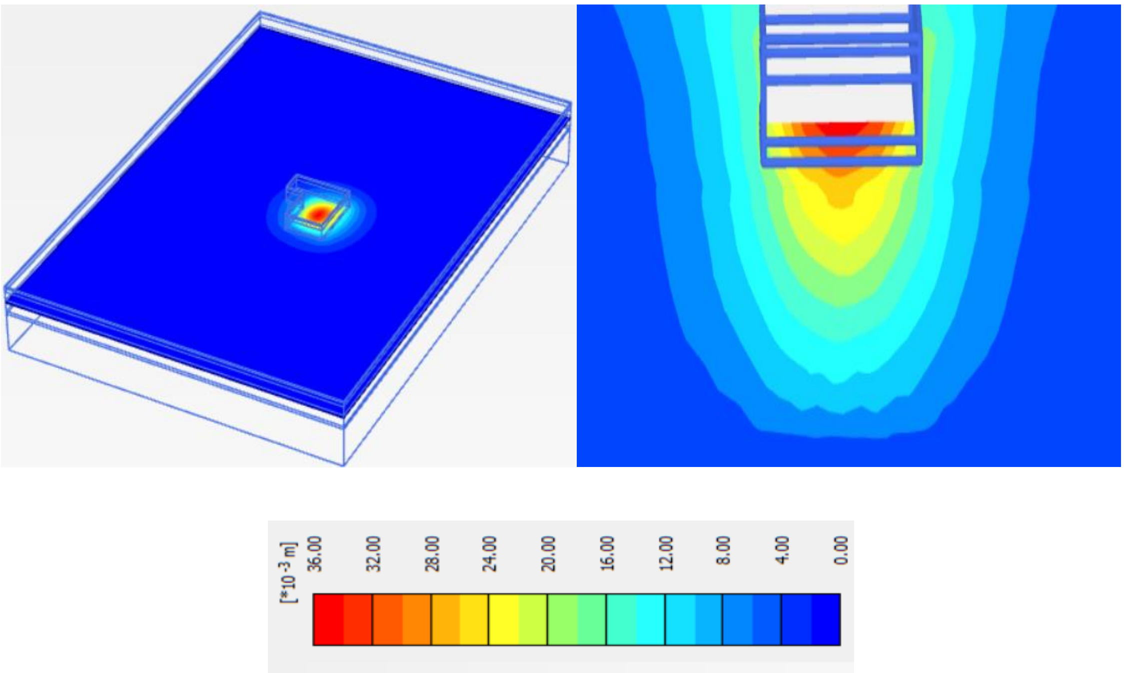

Figure 4.12: Typical deformation (plan and section) view in output interface

3. Stresses

Various options are available to visualize the stress state in the finite element model. The Stresses menu also contains options to display the results of groundwater flow and thermal flow calculations. Following parameters can be visualized in PLAXIS-3D output interface

1. Cartesian effective stresses
2. Cartesian total stresses
3. Principal effective stresses
4. Principal total stresses
5. Initial conditions
6. Pore pressures
7. Groundwater flow
8. Plastic points, etc.

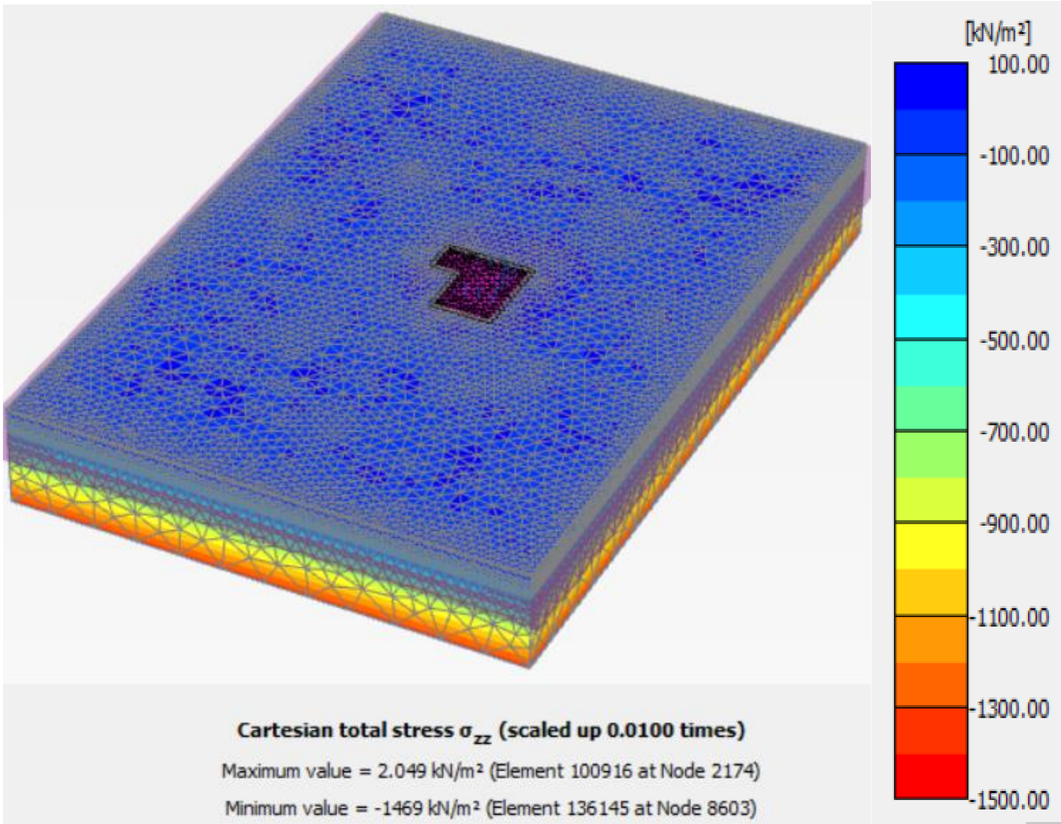

Figure 4.13: Typical cartesian total stress view in output interface

4. Structures and interfaces

By default, the structures active in the current phase are displayed in the model. Otherwise, these objects may be displayed in by switching the view on in the explorer. Output for structures and interfaces can be obtained by clicking the Select structures button and then double-clicking the desired object in the 3D model. As a result, a new form is opened on which the selected object appears. At the same time the menu changes to provide the particular type of output for the selected object.

All objects of the same type with the same local coordinate system are automatically selected. When multiple objects or multiple groups of objects of the same type need to be selected, the Shift key should be used while selecting the objects. The last object to be included in the plot should then be double clicked. When all objects of the same type are to be selected, select one of the objects while pressing Ctrl-A simultaneously. If it is desired to select one or more individual elements from a group, the Ctrl key should be used while selecting the desired element.

Another option of selecting structural elements in the output is by clicking the Drag a window to select structures button and drawing a rectangle in the model. As a results, the structures in the rectangle will be selected. Now for understanding the axial force, shear force and bending moment directions, the Structure axes option from the View menu may be used to display the beam's local system of axes (1,2,3). Figure 4.14 and 4.15 shows the local axis direction for beam or embedded beam structures. Local axis for plates is demonstrated in Figure 4.16-4.18.

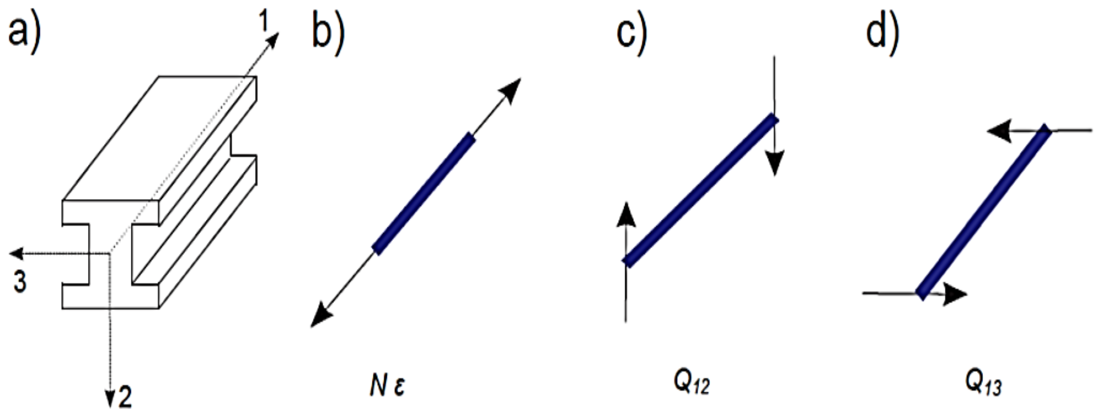

Figure 4.14: Forces in beam or embedded beam structure.

a) Local axes. b) Axial force N. c) Shear force Q_{12}. d) Shear force Q_{13}

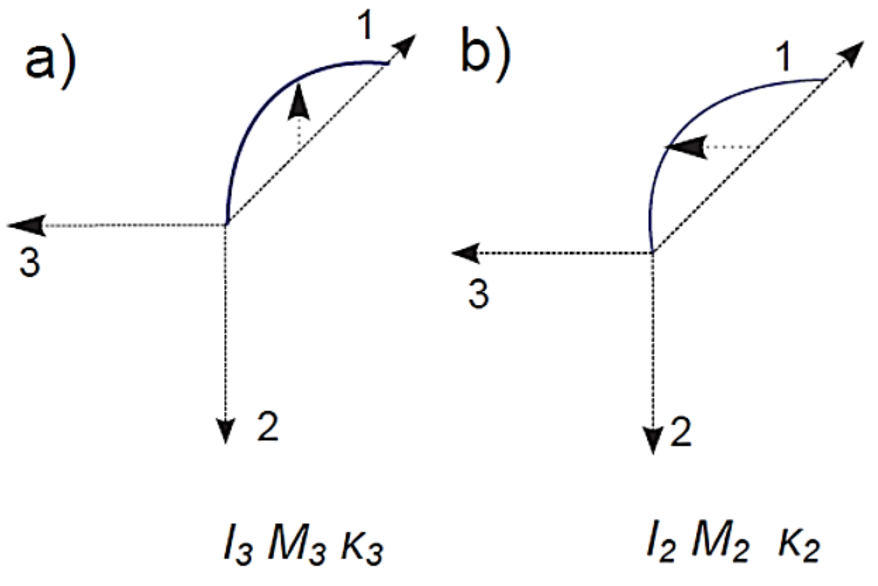

Figure 4.15: Positive bending moments in beams.

a) Bending Moment M3, b) Bending Moment M2

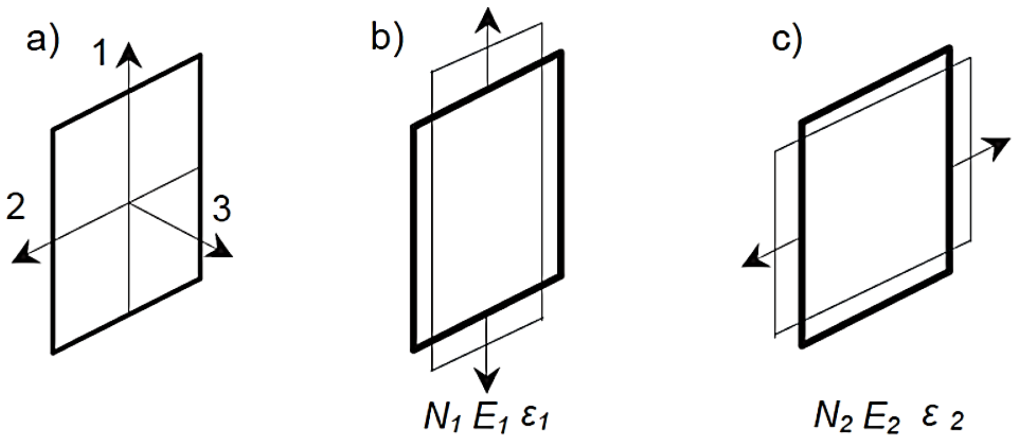

Figure 4.16: Positive axial forces in plates.

a) Local plate directions, b) Axial force N_1, c) Axial force N_2

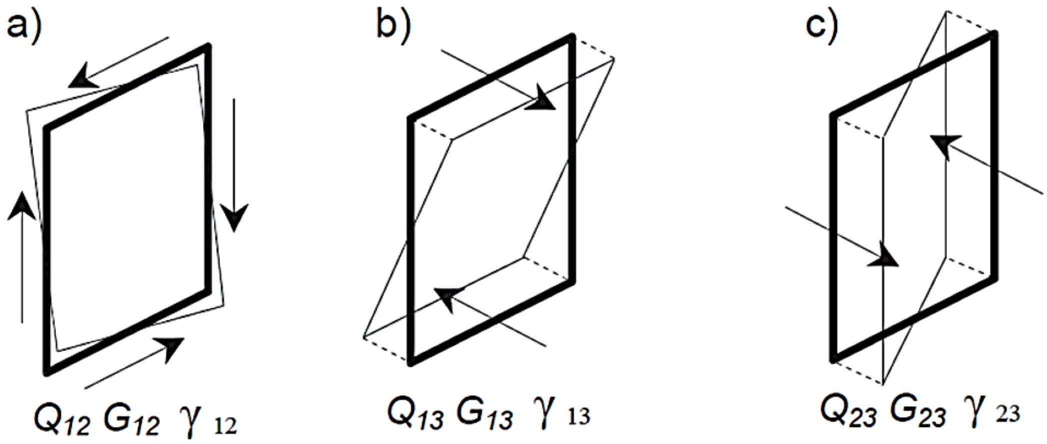

Figure 4.17: Positive shear forces in plates.

a) Shear force Q_{12}, b) Shear force Q_{13}, c) Shear force Q_{23}

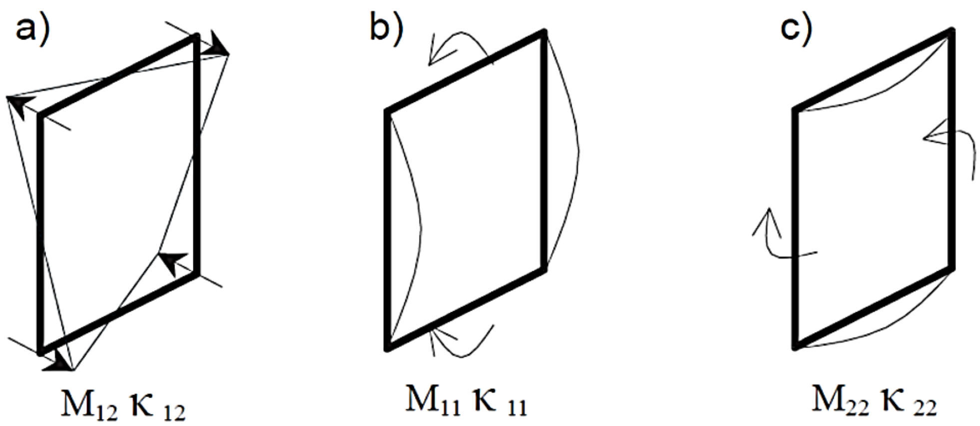

Figure 4.18: Positive bending moments in plates.

a) Torsion moment M12, b) M11, c) Bending moment M22

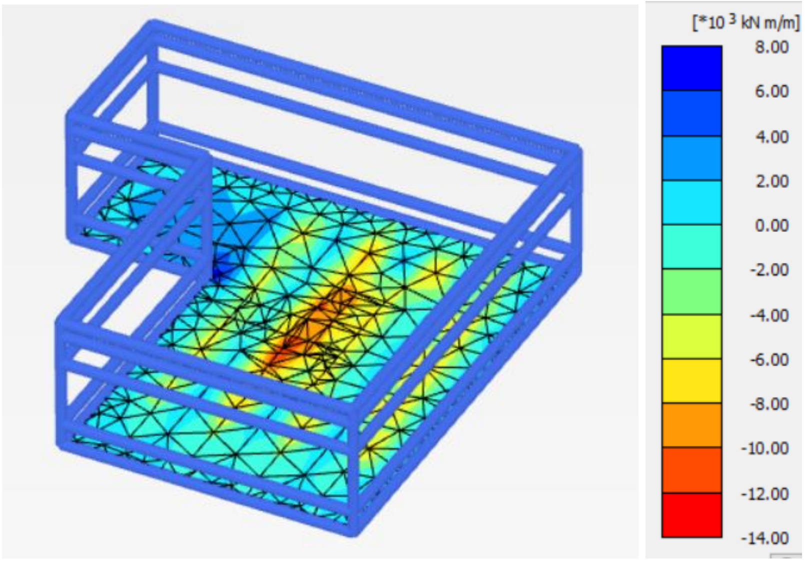

Figure 4.19: Typical bending moment M_{11} results view of raft in output interface

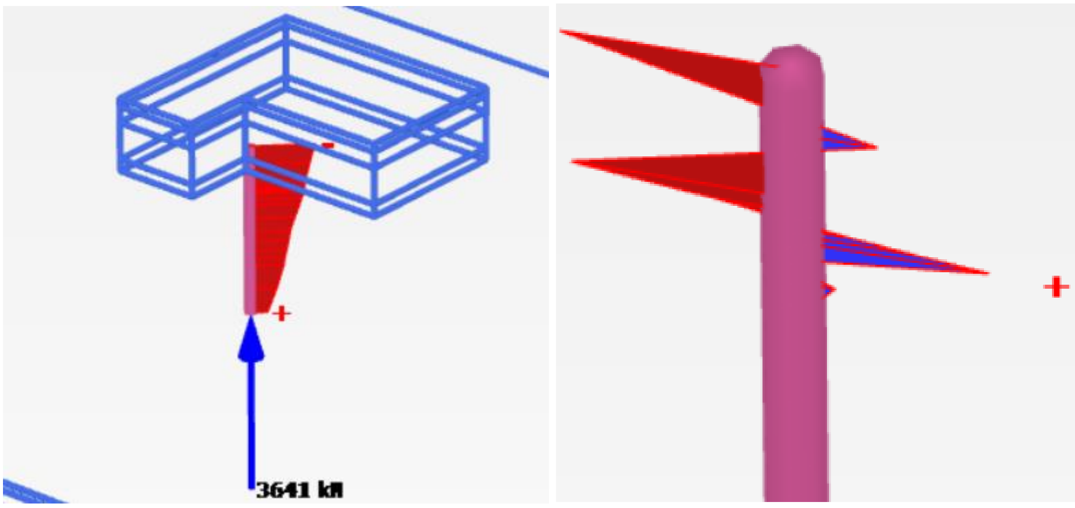

Figure 4.20: Typical axial force and bending moment diagram of embedded beam shown in PLAXIS output interface

4.3 Model Validation

Before starting the numerical modeling and parametric study of this research, the PLAXIS-3D software which has been used was calibrated and validated by remodeling some previous study examples. The objective of this validation is to make sure the PLAXIS-3D software is showing perfect results.

Validation model-1: A reputed journal on pile raft foundation named" Numerical modeling and parametric study of piled rafts foundations" authored by Ne'aimi and Hussain which was Published online on 6 March 2021 in Arabian Journal of Geosciences (2021) 14: 447. This study presents a series of 3D nonlinear analysis of un-piled and piled rafts by varying raft thickness and number, spacing and diameter of piles in the group. Using the same piled raft geometry, soil, material properties and constitutive modeling we found the settlement below is similar to the original studies performed by Ne'aimi and Hussain (2021). The summary of this validation modeling work is given in Table 4.7.

Table 4.7: Validation of Numerical modeling summary

Input for Validation							**Output**	
#SL	Type	Raft thickness (m)	Piles no.	Pile dia (m)	Pile to pile spacing (in terms of dia)	Pile length (m)	Original study Performed by Ne'aimi and Hussain (2021)	Performed in this study
1	Piled raft (10x10) sqm	1	9	0.5	5	18	173	173

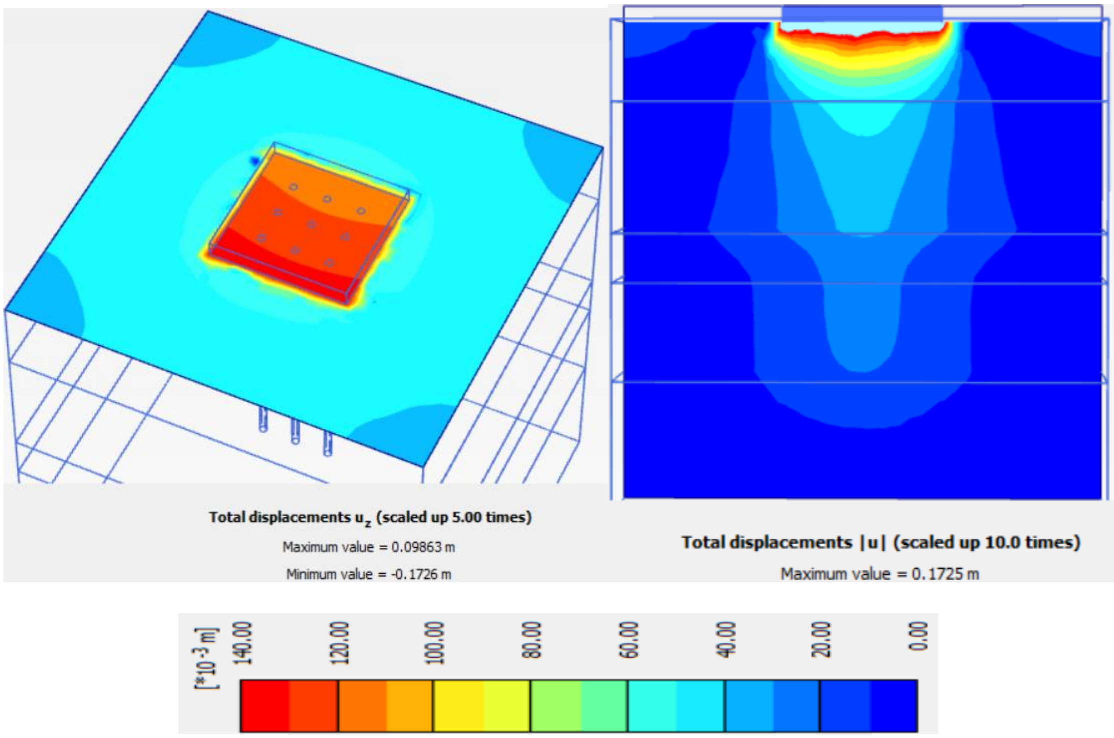

Figure 4.21: Output results showing Settlement values performed during this study

Validation model-2: Another reputed journal on pile raft foundation named "3D Numerical model for piled raft foundation" written by Sinha and Hanna which was published in International Journal of Geomechanics on 2016. The research presents the effect of pile length (5m, 10m and 15m) on granular soil for a piled raft foundation system. Later on, in 2019, Mali and Singh modelled the same for their PLAXIS-3D software validation. However, the same model once again modeled in this study to validate the PLAXIS software. Though in this study, the numerical model has been developed only for one type of pile length. The comparison of three studies is listed in Table 4.8.

Table 4.8: Comparison of Three studies for Validation of Numerical modeling software

Input for Validation								**Output**		
SL. No.	**Foundation Type**	**Raft thickness (m)**	**Number of Piles**	**Pile dia (m)**	**Pile to pile spacing (in terms of diameter)**	**Pile length (m)**	**Load (kPa)**	**Original study performed by Sinha and Hanna (2016)**	**Performed by Mali and Singh (2019)**	**Performed in this study**
1	Piled raft (24x24) sqm	2	16	1	6	5	0	0	0	0
							100	50	50	52
							200	100	100	106
							300	180	180	180
							400	300	290	294
							500	490	480	495

From the results, it is observed that the settlement obtained for different loading values found to be very close and almost similar. Figure 4.22 shows the output of numerical model discussed in above.

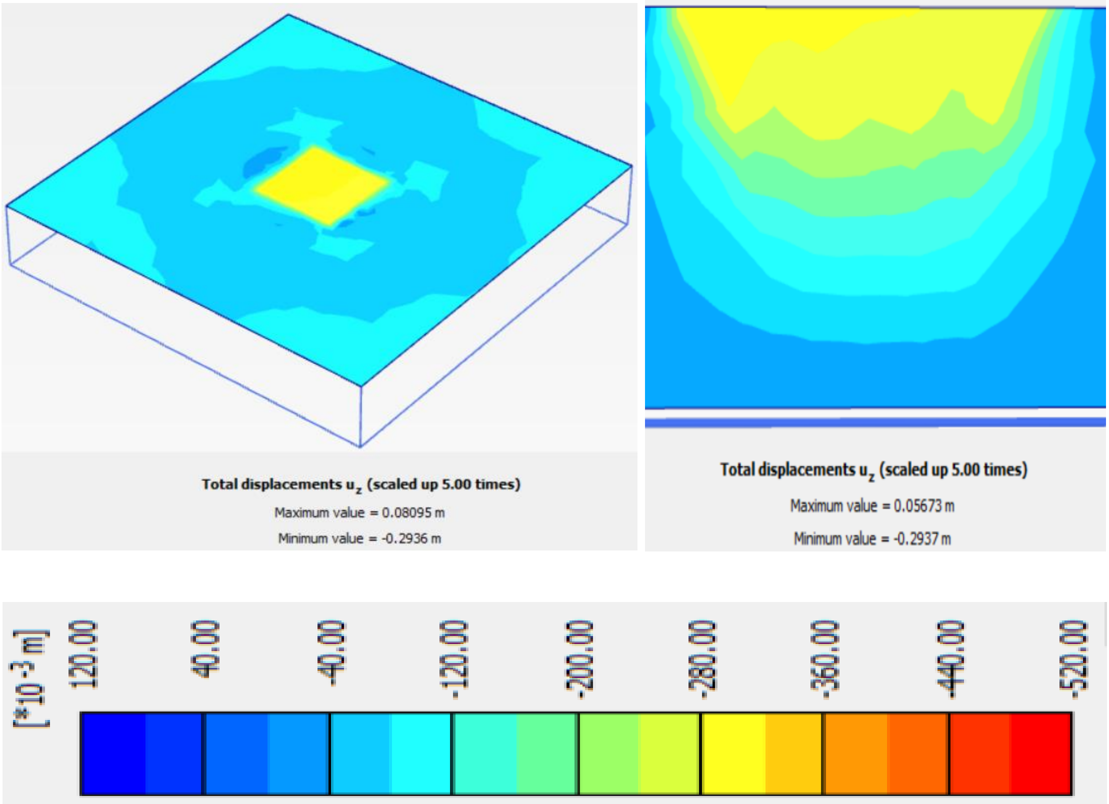

Figure 4.22: Output results showing Settlement values performed during this study

So, from two different model results validate the PLAXIS-3d software that has been used for this study.

4.5 Parametric Study

In this study, the effects of raft thickness, pile diameter, pile spacing, and number of piles on the displacement of footing system are investigated, and the results are accordingly compared with the un-piled raft cases. Again, the effect of mesh size was also taken in account for un-piled raft. In the parametric study, the immediate, earthquake induced and consolidation settlement of raft and pile, load-sharing, developed stress, pile reaction, bending moment, lateral deflection of piles and retaining wall, and shear force behavior of the large piled-raft foundation on selected soil profiles were studied.

In all the parametric study, only one parameter was varied at a time and standard values were selected for all other parameters. For both un-piled raft and piled raft foundation system, the length of piles, the soil and material properties were kept constant. A brief summary of the numerical models developed for parametric study are given in the Table 4.8 and 4.9.

4.5.1 Numerical models for Un-piled raft foundation system

In case of un-piled raft foundation, the raft is rested 18m below existing ground level. The length and width of the raft is mentioned in Figure 4.23. For this foundation system, the effect of mesh size and the effect of raft thickness was studied. Total eleven numerical models are developed to analyze the effect of mesh size and raft thickness for raft foundation. Un-piled foundation numerical models are named “UPR” in this study.

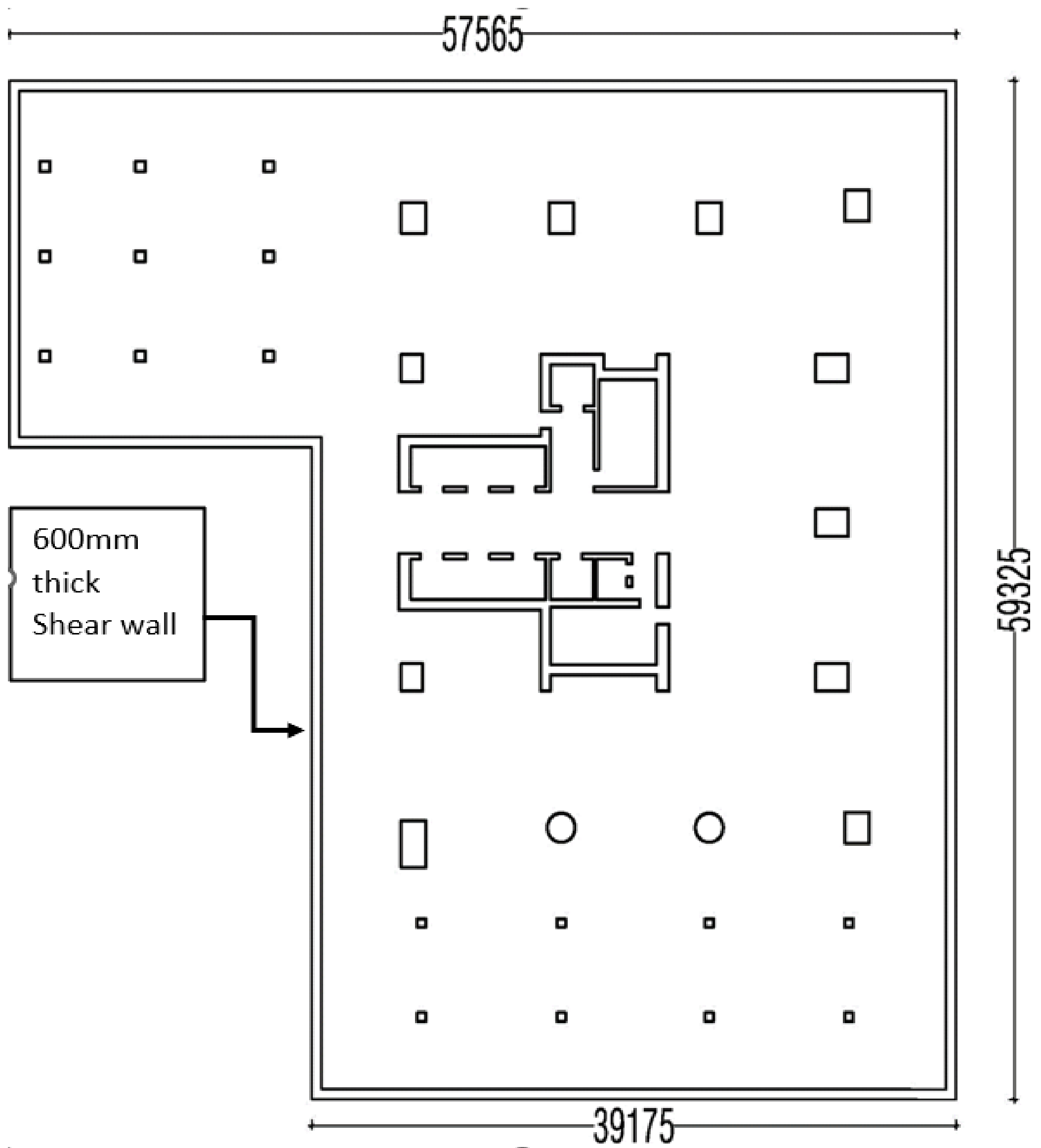

Figure 4.23: Un-piled raft foundation layout plan

For all the combinations mentioned in Table 4.9, the soil profile and depth of raft foundation (18m below EGL) was kept constant.

Table 4.9: Brief summary of un-piled raft

Name of Numerical model	Mesh size	Raft thickness (m)
UPR-1	Very Coarse	2.5
UPR-2	Coarse	2.5
UPR-3	Medium	2.5
UPR-4	Very Coarse	3
UPR-5	Coarse	3
UPR-6	Medium	3
UPR-7	Very Coarse	3.5
UPR-8	Coarse	3.5
UPR-9	Medium	3.5
UPR-10	Medium	1
UPR-11	Medium	1.5

4.5.2 Numerical models for Piled raft foundation system

For piled raft foundation system, the raft again rested 18m below existing ground level. In this case, the effect of pile numbers, pile diameter, pile to pile distance and the raft thickness were observed. In all combinations, the length of the piles, soil profile and depth of raft (18m below EGL) were kept constant. In all the piled raft numerical models, only one parameter was varied at a time and standard values were selected for all other parameters. Piled raft foundation are mentioned as “PR” in this study. At first, the piled raft was foundation system was evaluated using 58 nos. piles of different diameters (1m, 1.2m and 1.5m) with different raft thicknesses (2.5m, 3m and 3.5m). Then similarly the raft was studied for 69 nos. and 82 nos. piles with different pile diameters and raft thicknesses. In this study, total twenty numerical models are developed for the parametric study of piled raft foundation system using very coarse mesh size only. A brief summary of all piled raft foundation numerical models is given in Table 4.18.

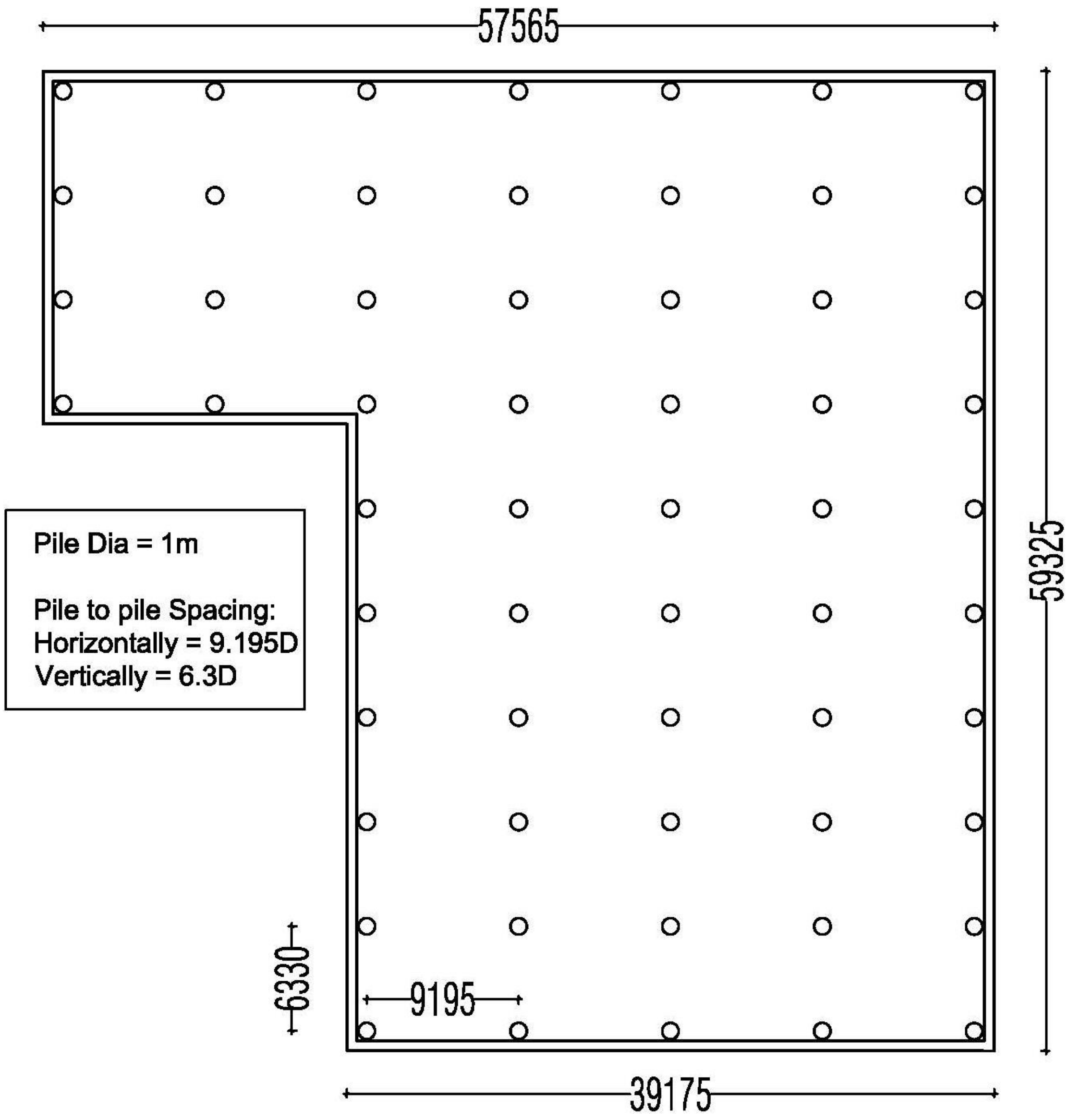

Figure 4.24: Piled raft layout plan for 58 nos. piles of 1m diameter.

Table 4.10: Brief summary of Piled-raft numerical model (for 58 nos. piles)

Name of Numerical model	Pile number	Pile diameter (m)	Raft thickness (m)
PR-1	58	1	2.5
PR-2	58	1	3
PR-3	58	1	3.5

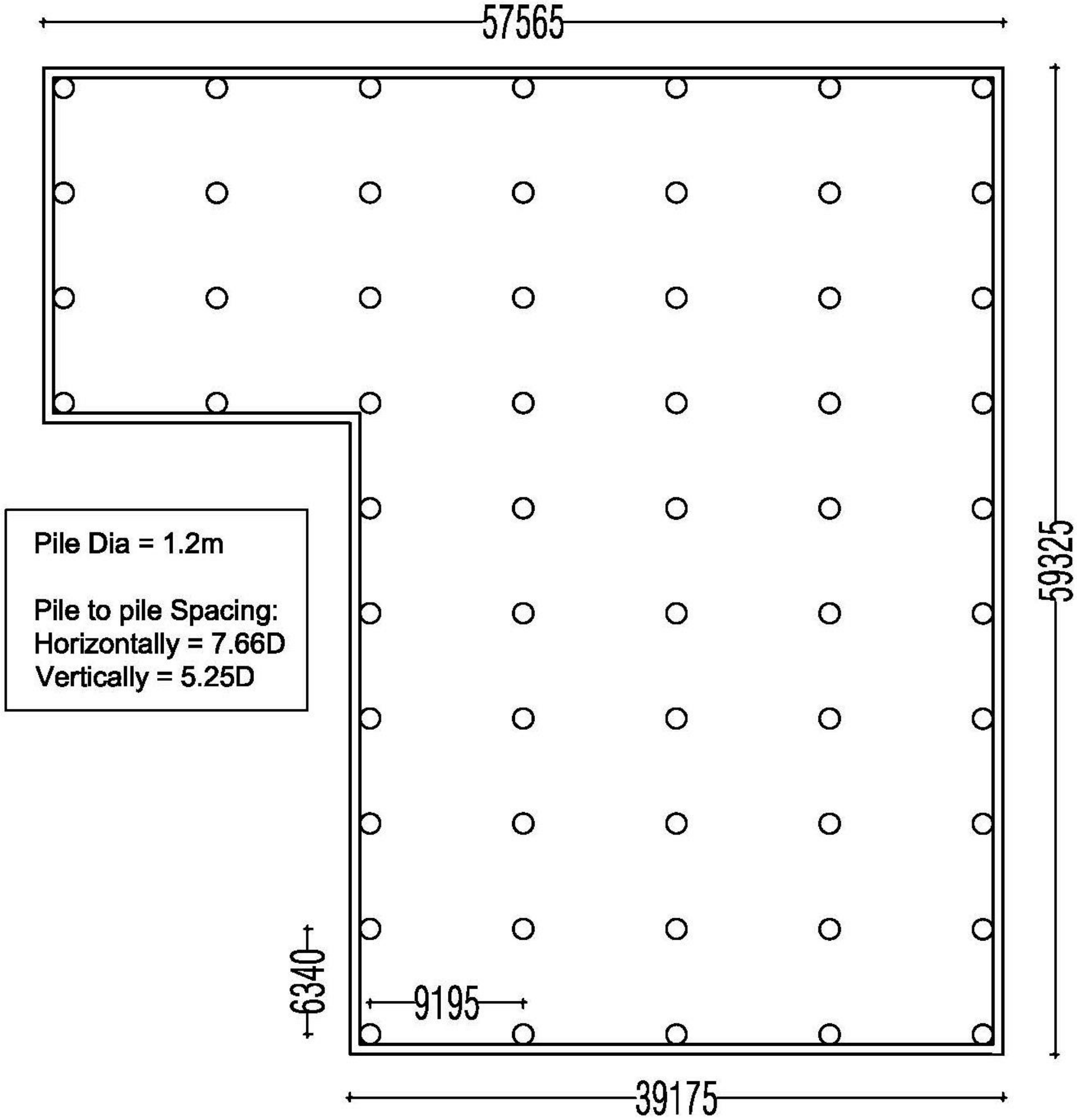

Figure 4.25: Piled raft layout plan for 58 nos. piles of 1.2m diameter.

Table 4.11: Brief summary of Piled-raft numerical model (for 58 nos. piles)

Name of Numerical model	Pile number	Pile diameter (m)	Raft thickness (m)
PR-4	58	1.2	2.5
PR-5	58	1.2	3
PR-6	58	1.2	3.5

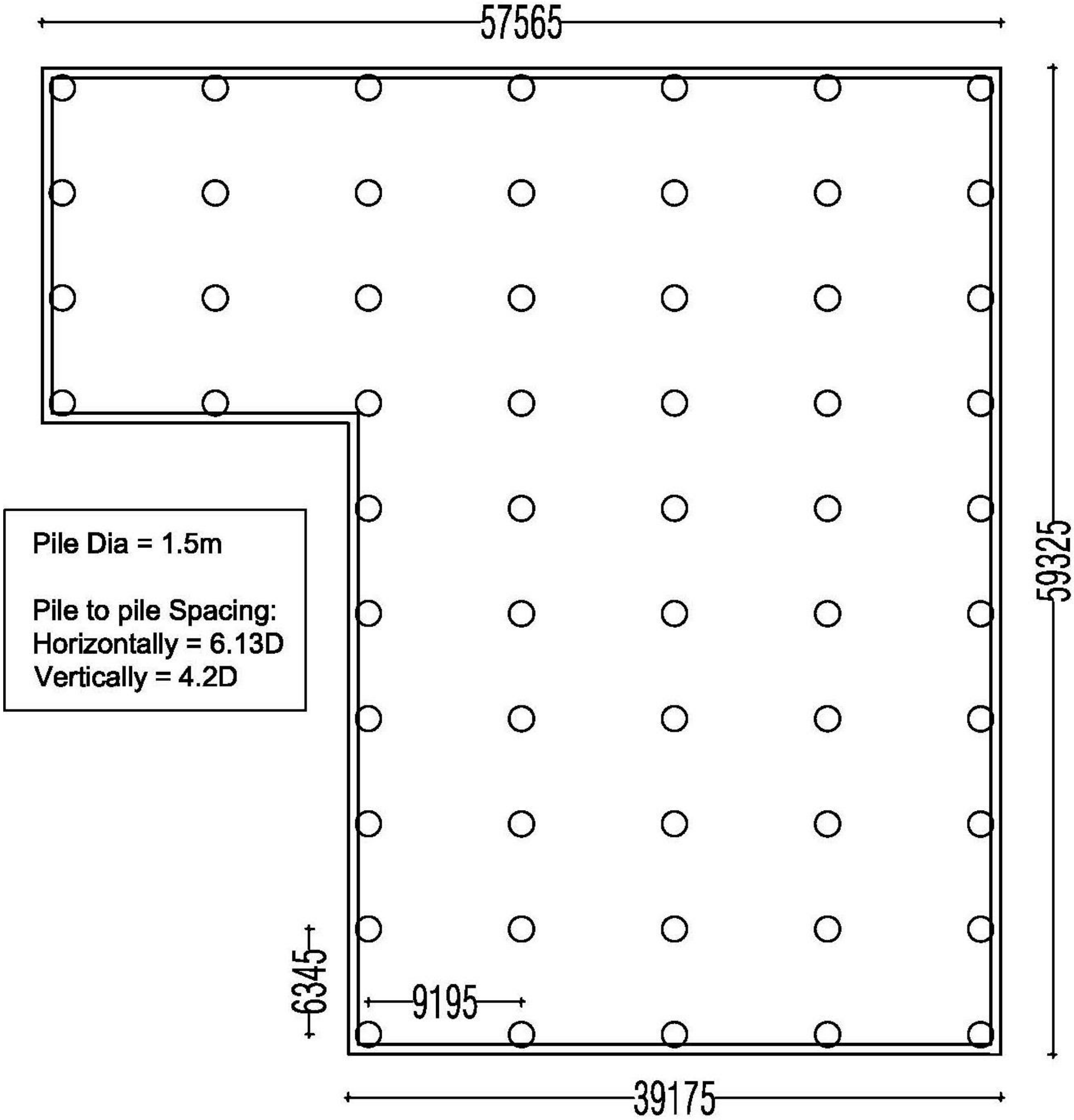

Figure 4.26: Piled raft layout plan for 58 nos. piles of 1.5m diameter.

Table 4.12: Brief summary of Piled-raft numerical model (for 58 nos. piles)

Name of Numerical model	Pile number	Pile diameter (m)	Raft thickness (m)
PR-7	58	1.5	2.5
PR-8	58	1.5	3
PR-9	58	1.5	3.5

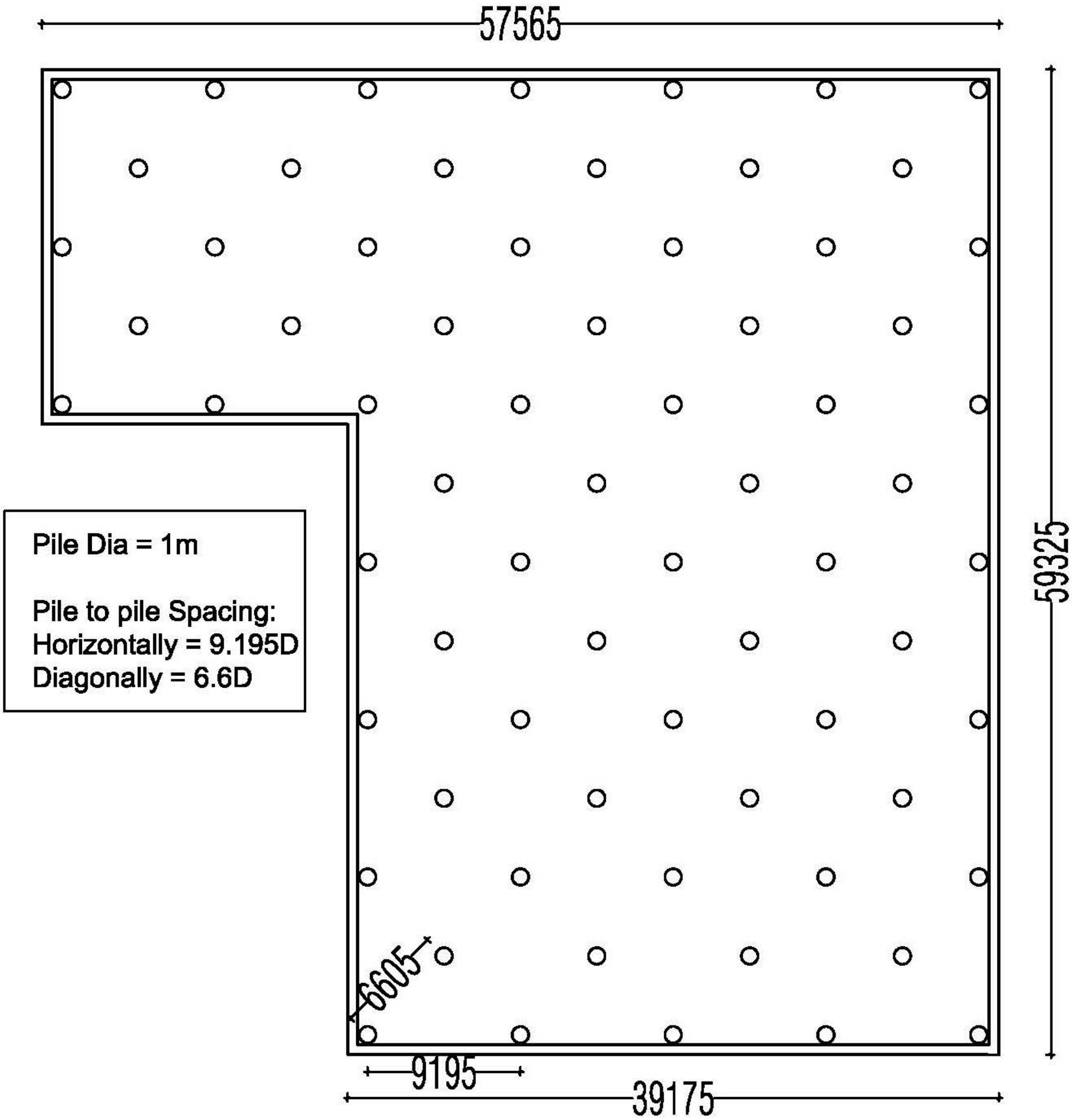

Figure 4.27: Piled raft layout plan for 69 nos. piles of 1m diameter.

Table 4.13: Brief summary of Piled-raft numerical model (for 69 nos. piles)

Name of Numerical model	Pile number	Pile diameter (m)	Raft thickness (m)
PR-10	69	1	2.5
PR-11	69	1	3
PR-12	69	1	3.5

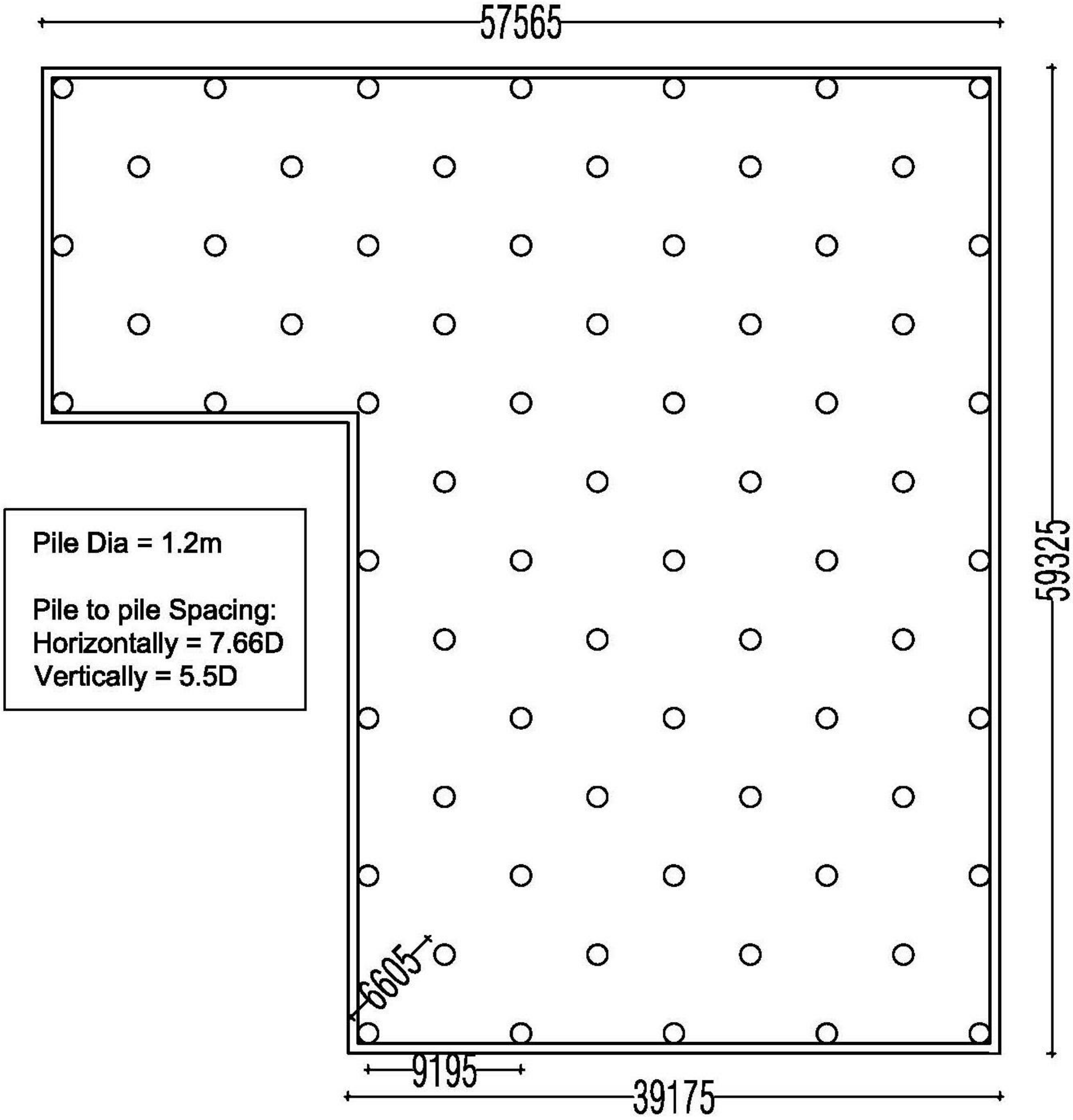

Figure 4.28: Piled raft layout plan for 69 nos. piles of 1.2m diameter.

Table 4.14: Brief summary of Piled-raft numerical model (for 69 nos. piles)

Name of Numerical model	Pile number	Pile diameter (m)	Raft thickness (m)
PR-13	69	1.2	2.5
PR-14	69	1.2	3
PR-15	69	1.2	3.5

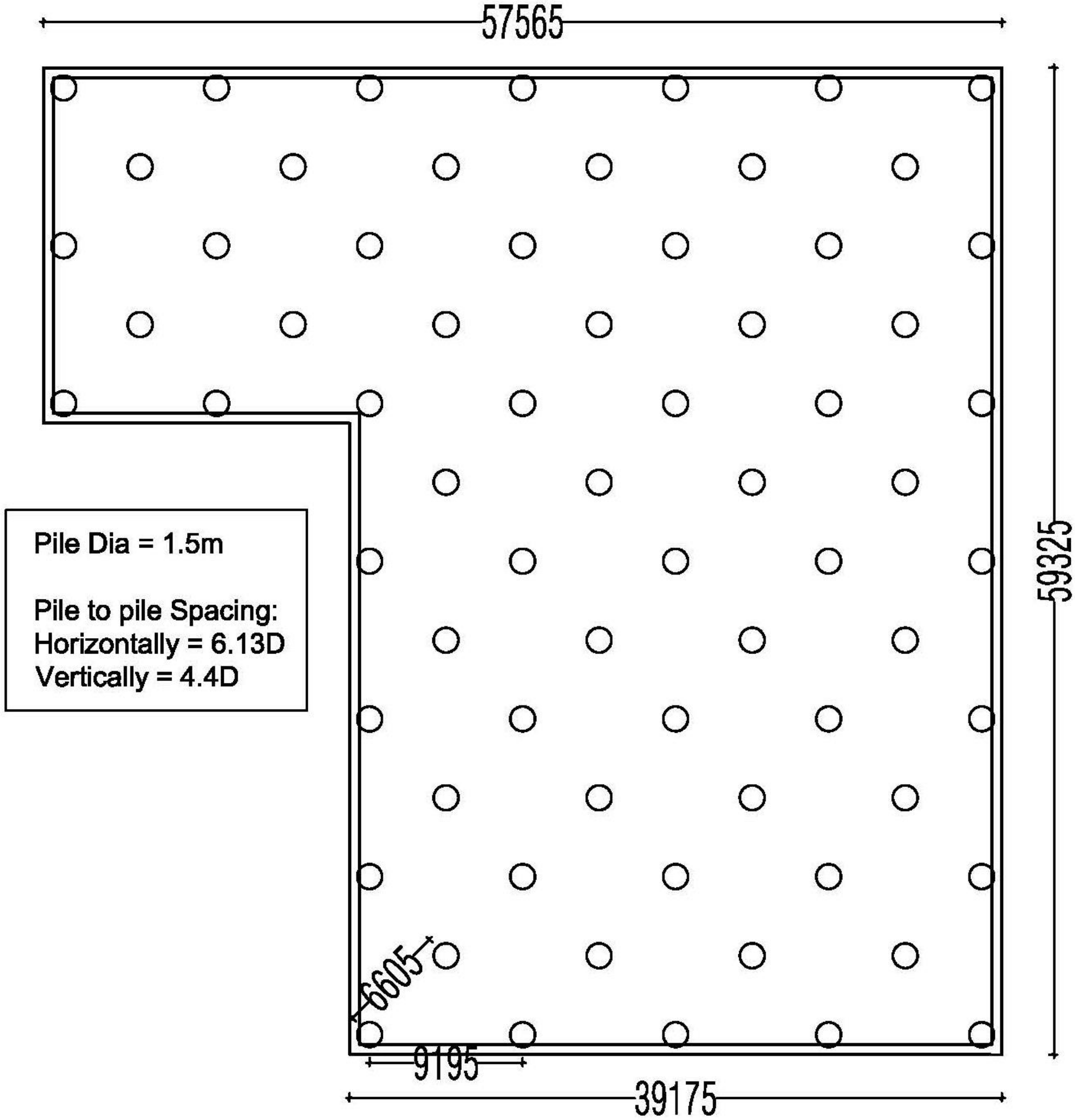

Figure 4.29: Piled raft layout plan for 69 nos. piles of 1.5m diameter.

Table 4.15: Brief summary of Piled-raft numerical model (for 69 nos. piles)

Name of Numerical model	Pile number	Pile diameter (m)	Raft thickness (m)
PR-16	69	1.5	2.5
PR-17	69	1.5	3
PR-18	69	1.5	3.5

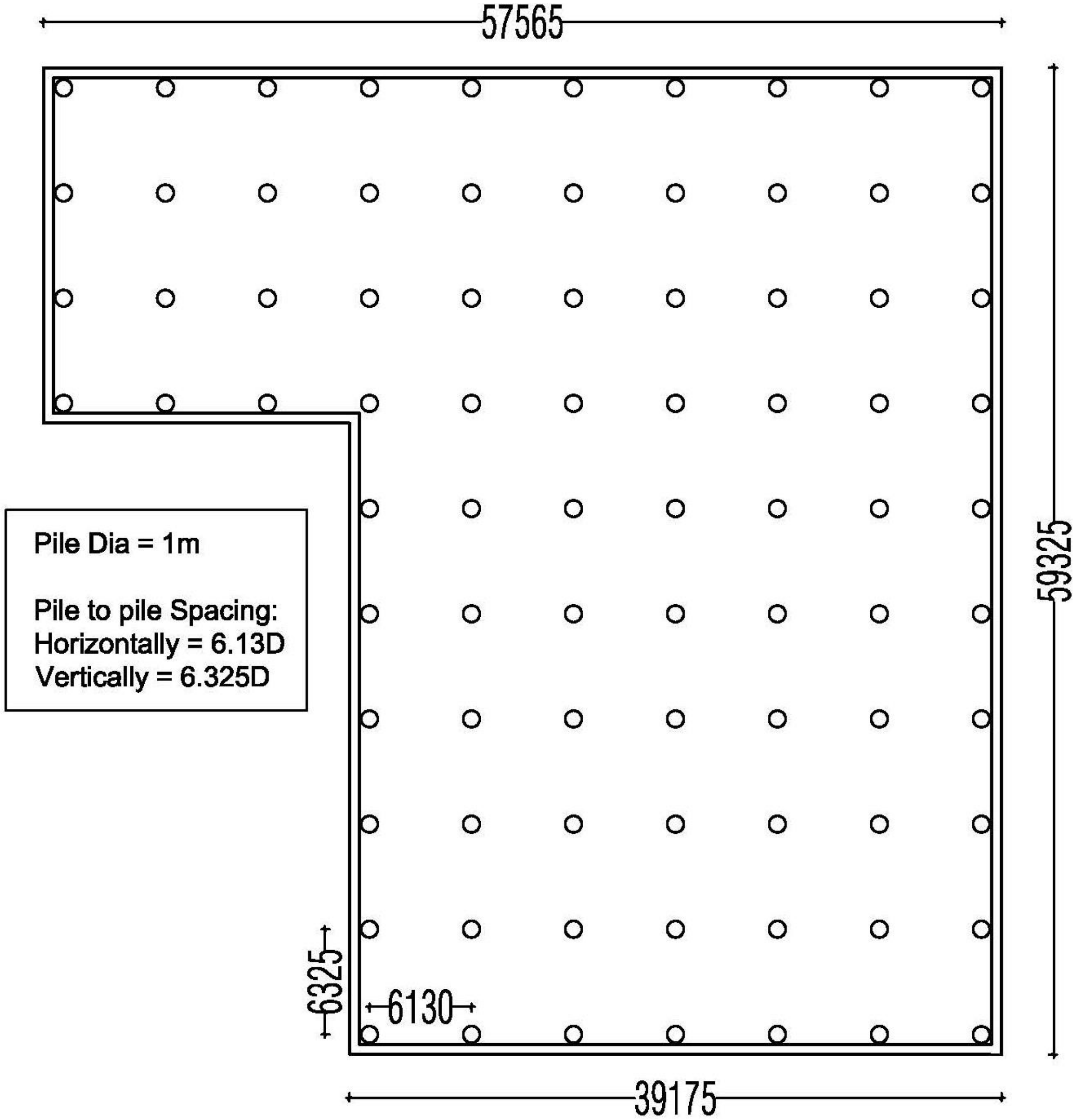

Figure 4.30: Piled raft layout plan for 82 nos. piles of 1m diameter.

Table 4.16: Brief summary of Piled-raft numerical model (for 82 nos. piles)

Name of Numerical model	Pile number	Pile diameter (m)	Raft thickness (m)
PR-19	82	1	2.5
PR-20	82	1	3
PR-21	82	1	3.5

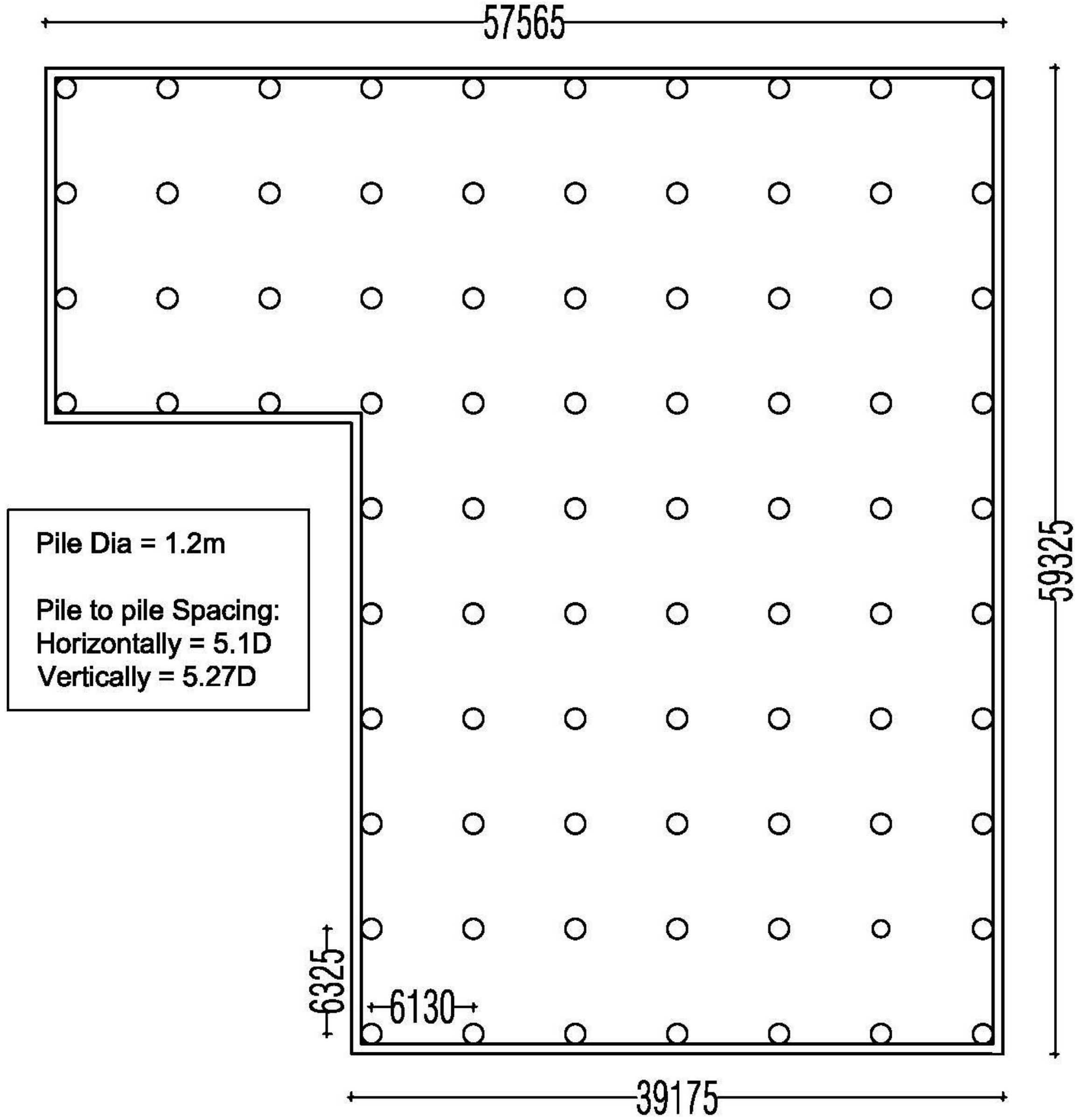

Figure 4.31: Piled raft layout plan for 82 nos. piles of 1.2m diameter.

Table 4.17: Brief summary of Piled-raft numerical model (for 82 nos. piles)

Name of Numerical model	Pile number	Pile diameter (m)	Raft thickness (m)
PR-22	82	1.2	2.5
PR-23	82	1.2	3
PR-24	82	1.2	3.5

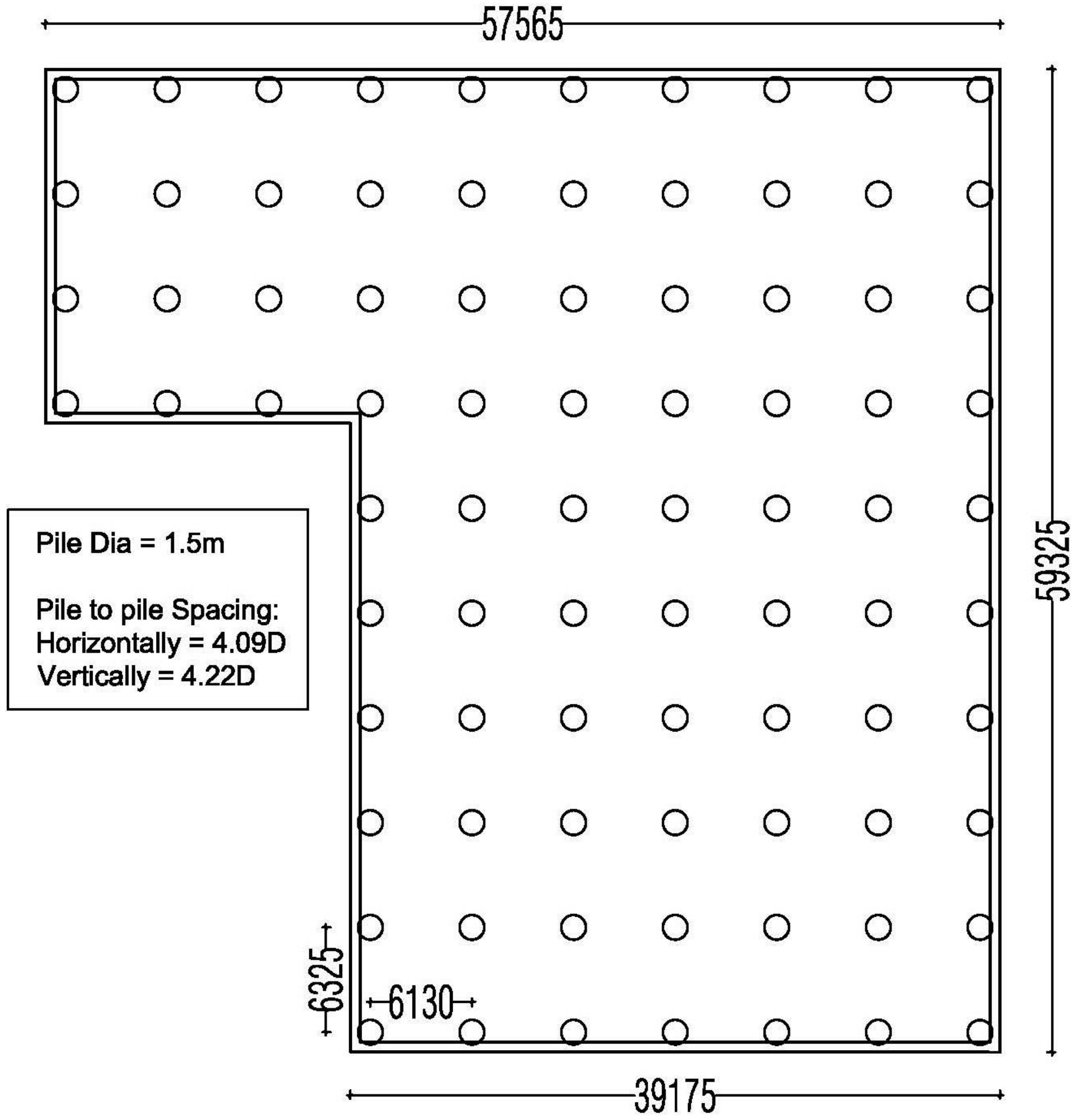

Figure 4.32: Piled raft layout plan for 82 nos. piles of 1m diameter.

Table 4.18: Brief summary of Piled-raft numerical model (for 82 nos. piles)

Name of Numerical model	Pile number	Pile diameter (m)	Raft thickness (m)
PR-25	82	1.5	2.5
PR-26	82	1.5	3
PR-27	82	1.5	3.5

Table 4.19: Brief summary of all Piled-raft numerical models

Name of Numerical model	Pile numbers	Pile diameter (m)	Raft thickness (m)
PR-1	58	1	2.5
PR-2	58	1	3
PR-3	58	1	3.5
PR-4	58	1.2	2.5
PR-5	58	1.2	3
PR-6	58	1.2	3.5
PR-7	58	1.5	2.5
PR-8	58	1.5	3
PR-9	58	1.5	3.5
PR-10	69	1	2.5
PR-11	69	1	3
PR-12	69	1	3.5
PR-13	69	1.2	2.5
PR-14	69	1.2	3
PR-15	69	1.2	3.5
PR-16	69	1.5	2.5
PR-17	69	1.5	3
PR-18	69	1.5	3.5
PR-19	82	1	2.5
PR-20	82	1	3
PR-21	82	1	3.5
PR-22	82	1.2	2.5
PR-23	82	1.2	3
PR-24	82	1.2	3.5
PR-25	82	1.5	2.5
PR-26	82	1.5	3
PR-27	82	1.5	3.5

Chapter 5
RESULTS AND DISCUSSION

5.1 Results of Un-piled Raft Foundation

In this part of the study and without considering the piles in the model, the effects of different thicknesses of rafts on its overall engineering performance are studied. Based on the results of the developed numerical models performed in PLAXIS-3D for un-piled raft foundation system, a detail parametric study has been executed. Effect of raft thickness and mesh size for an un-piled raft is discussed in this section.

5.1.1 Effect of mesh size

In this study, three mesh sizes have been used to see the sensitivity of mesh sizes on results obtained in the analysis. For the current study very coarse, coarse and medium mesh element has been used for both vertical and earthquake loading conditions. From the numerical analysis results of un-piled raft, it is found that the impact of the mesh sizes on different geotechnical and structural parameters are very insignificant. Figure 5.1 and 5.2 shows the total settlement values at raft center and raft corner respectively with different mesh sizes and mat thicknesses.

Figure 5.1: Effect of mesh size on total settlement values at raft center

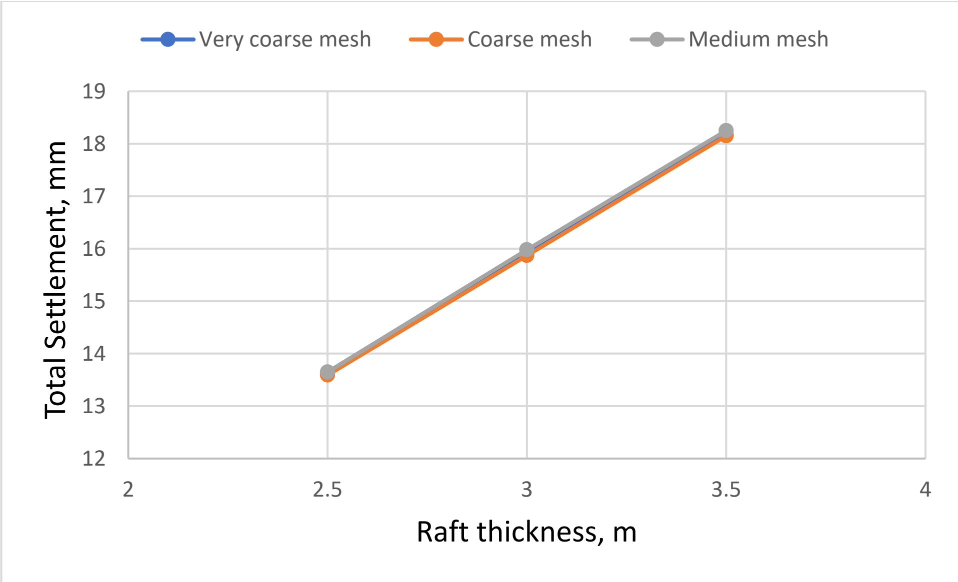

Figure 5.2: Effect of mesh size on total settlement values at raft center

Again, the effect of mesh size on developed stress beneath raft is also very negligible.

Figure 5.3: Effect of mesh size on maximum developed stress below raft

Effect of mesh size on bending moment of raft is also studied. Once again, the mesh size does not affect the bending moment value significantly.

Table 5.1 shows a brief summary of the mesh size effect on un-piled raft numerical models. Based on the numerical models on eleven different combinations of raft thickness and mesh size, we can conclude that the effect of mesh size can be ignored in the parametric study. So, from now onwards, all the un-piled raft parametric studies are shown for only medium mesh size. However, the results and outputs of all the studies for different mesh sizes are given Appendix-2.

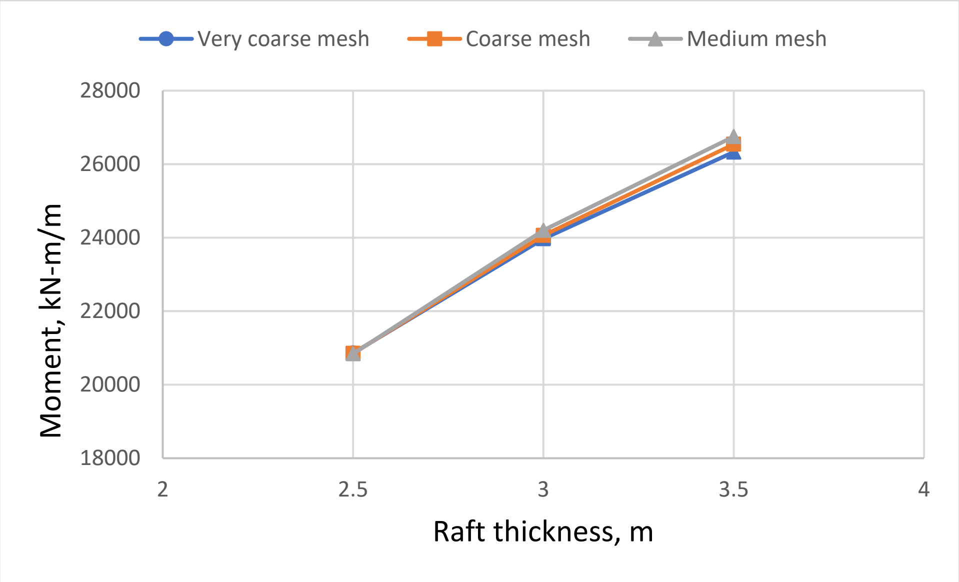

Figure 5.4: Effect of mesh size on bending moment values.

Table 5.1 Impact of different mesh size on un-piled numerical models

Foundation Combination	Raft thickness (m)	Mesh size	Total settlement at raft center (mm)	Total settlement at raft corner (mm)	Maximum developed stress below raft (kPA)	Bending moment of raft, M11 (kN-m/m)
UPR-1	2.5	Very coarse	118.69	13.62	364.29	20860
UPR-2		Coarse	119.31	13.59	366.72	20850
UPR-3		Medium	118.88	13.65	371.31	20840
UPR-4	3	Very coarse	109.19	15.9	345.55	23970
UPR-5		Coarse	109.26	15.87	346.74	24060
UPR-6		Medium	109.46	15.98	348.08	24200
UPR-7	3.5	Very coarse	104.57	18.17	343.13	26330
UPR-8		Coarse	104.3	18.15	338.01	26540
UPR-9		Medium	103.31	18.25	335.63	26750

5.1.2 Effect of raft thickness:

5.1.2.1 Settlement at raft center

Total settlement including immediate, consolidation and earthquake induced settlement occurred at the raft center is presented in Figure 5.5 for different raft thicknesses.

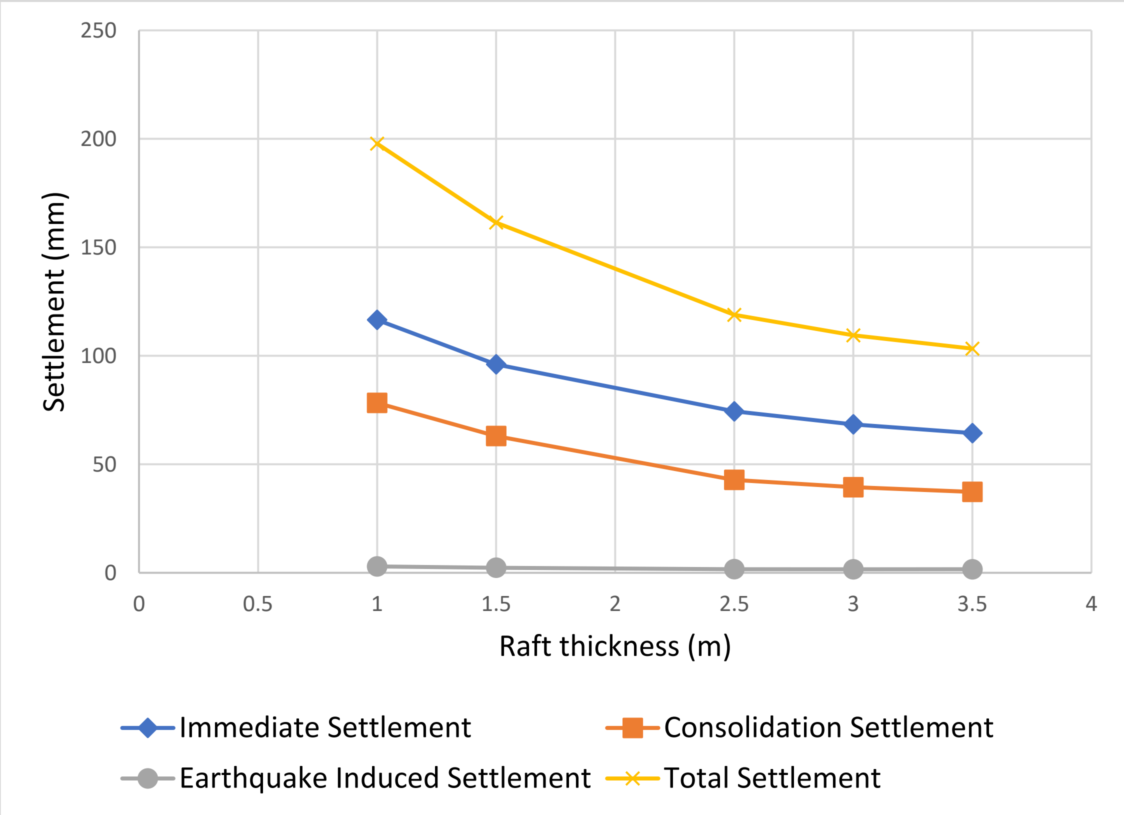

Figure 5.5: Effect of raft thickness on settlement values at raft center

From Figure 5.5 it is found that, the raft thickness plays a significant role. With the increase of raft thickness, all the settlement (Immediate, consolidation, earthquake induced and total settlement) decreases. Though due to increase in raft thickness the self-weight increases but the stiffness also increases due to higher thickness. It is easier for a rigid raft to distribute the stress throughout the raft preventing it from settling more locally in the center. Figure 5.5 also shows that the earthquake induced settlement is minor compared to immediate and consolidation settlement. The immediate settlement governs here as the soil beneath is raft is granular soil. The consolidation settlement happened here due to the soil layer of 27m to 30m.

5.1.2.2 Settlement at raft corner

Total settlement including immediate, consolidation and earthquake induced settlement occurred at the raft corner is also studied and presented in Figure 5.6 for different raft thicknesses.

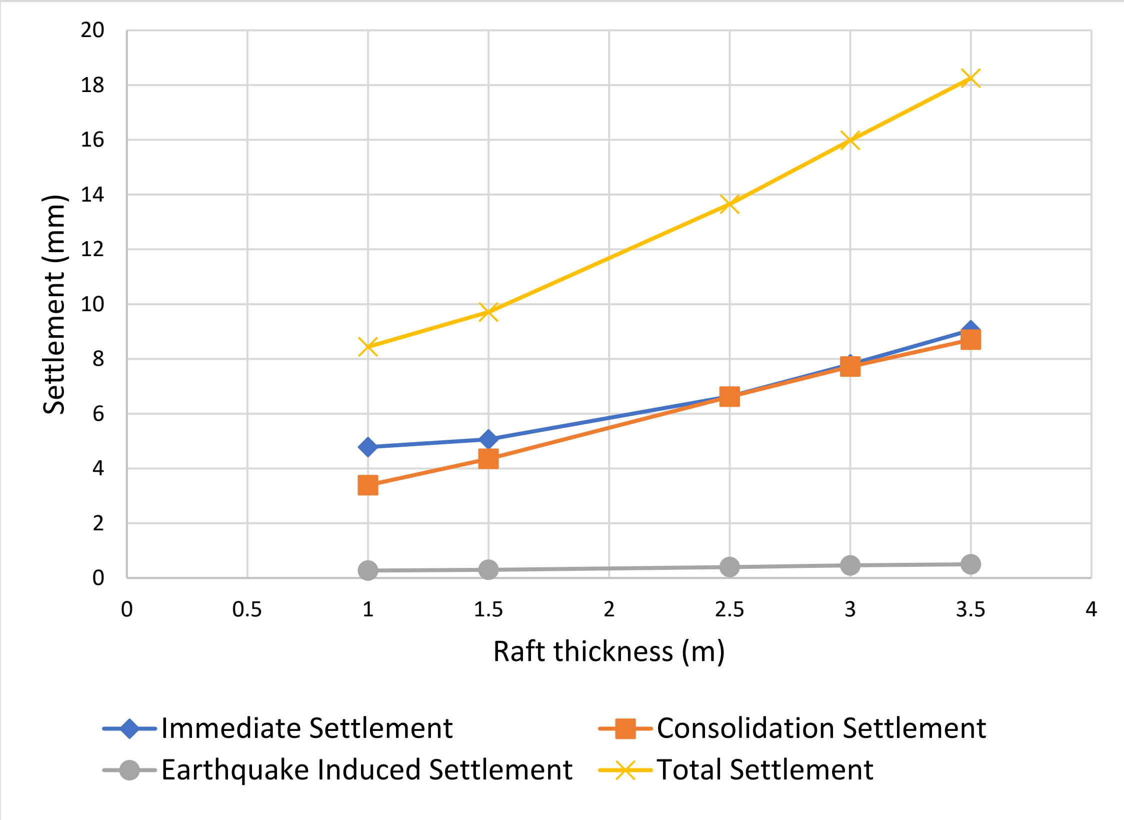

Figure 5.6: Effect of raft thickness on settlement values at raft corner

From Figure 5.6 it is observed that, the raft thickness has impact of settlement values at raft corner as well. With the increase of raft thickness, all the settlement (Immediate, consolidation, earthquake induced and total settlement) increases. The behavior is inverse for the settlement at the center of the raft. As the thickness represent the rigidity of a raft so, it is easier for a rigid raft to distribute the stress throughout the raft and even in the corners which prevents it from settling more locally in the center. Instead of settling locally, the raft tends settle uniformly. However, due to stress concertation at the center, the corner settlements are lower than center settlement values. Figure 5.6 also shows that the earthquake induced settlement is negligible compared to immediate and consolidation settlement.

5.1.2.3 Differential settlement

The relationship between the raft thickness and differential settlement is inversely proportional. Stiffness plays the vital roles as discussed earlier in section 5.1.2.1 and 5.1.2.2.

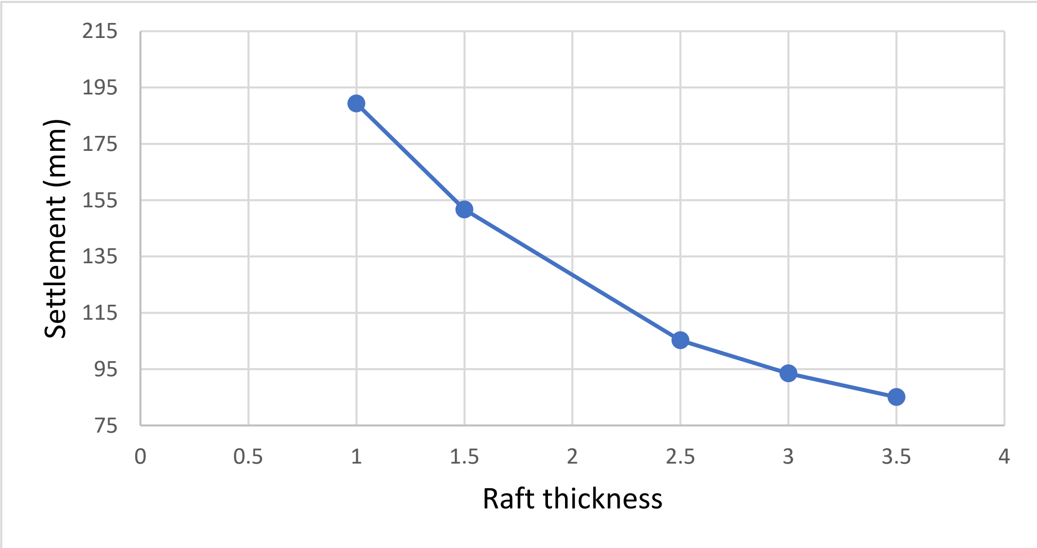

Figure 5.7: Effect of raft thickness on differential settlement values

5.1.2.3 Angular distortion

Angular distortion for different raft thicknesses is shown in Figure 5.8. With the increase in raft thickness, the angular distortion decreases.

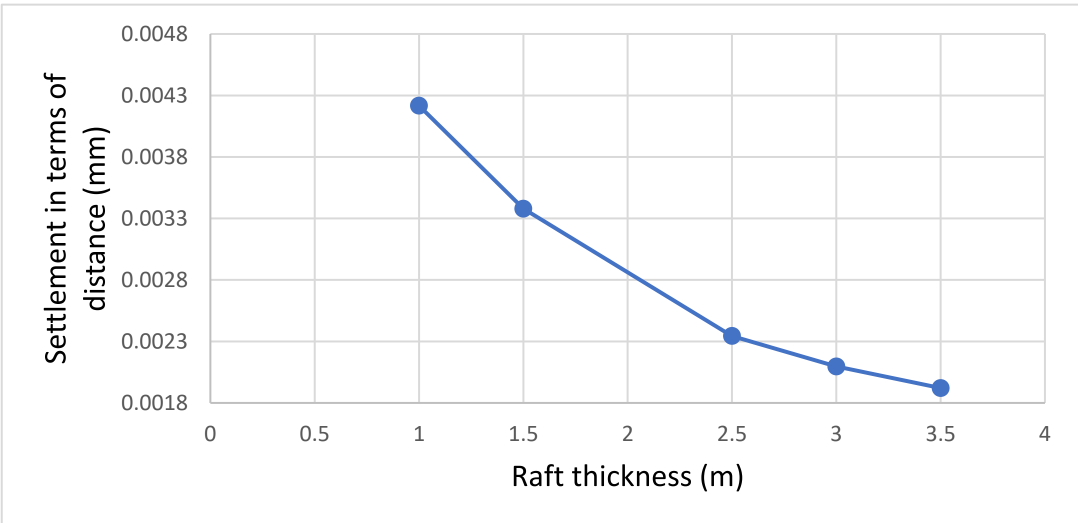

Figure 5.8: Effect of raft thickness on angular distortion

5.1.2.4 Maximum developed stress

Due to increase in raft thickness the self-weight increases but the stiffness also increases due to higher thickness. For increasing the stiffness of the raft, the stress is distributed throughout the raft preventing it from local stress concentration.

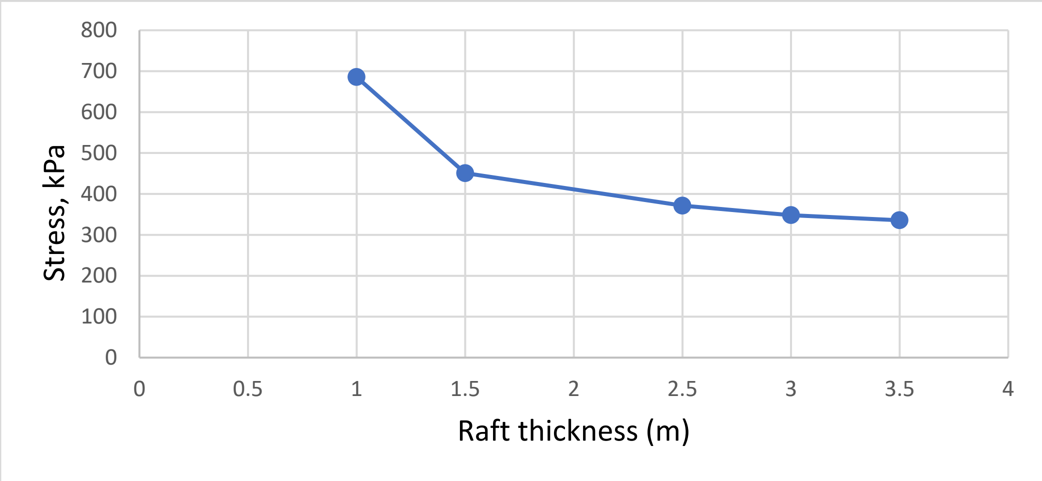

Figure 5.9: Effect of raft thickness on angular distortion

5.1.2.5 Maximum bending moment of raft, M11

The maximum bending moment values obtained from numerical model is shown in Figure 5.10. Figure 5.10 shows the relation between maximum bending moment, M11 and raft thickness. The bending moment, M11 increases with increase in raft thickness.

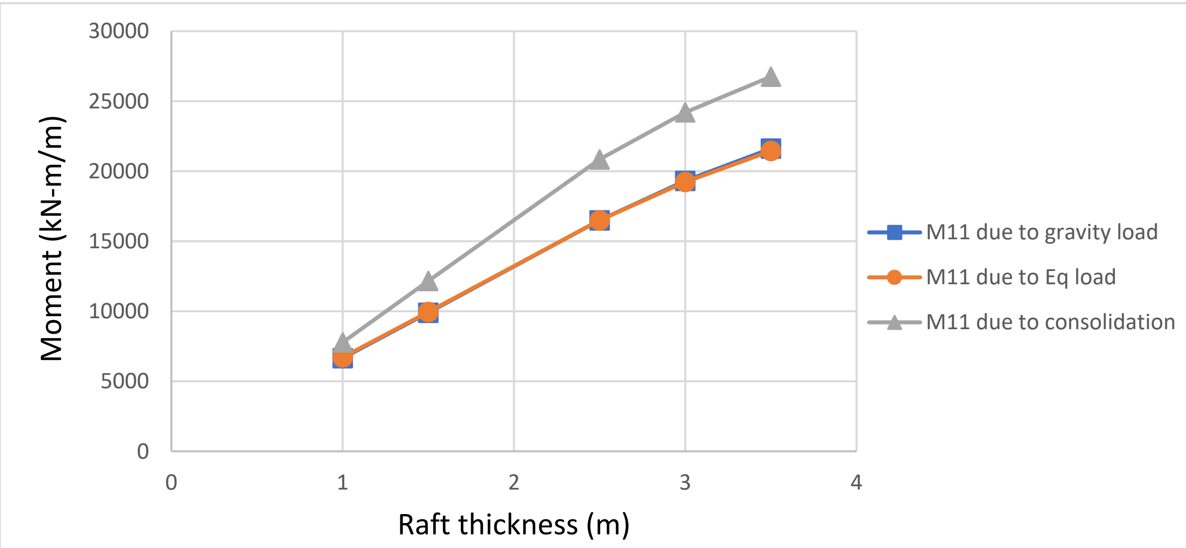

Figure 5.10: Effect of raft thickness on maximum bending moment, M11

5.1.2.6 Maximum bending moment of raft, M22

Figure 5.11 shows the relation between maximum bending moment, M22 and raft thickness. The bending moment, M22 also increases with increase in raft thickness.

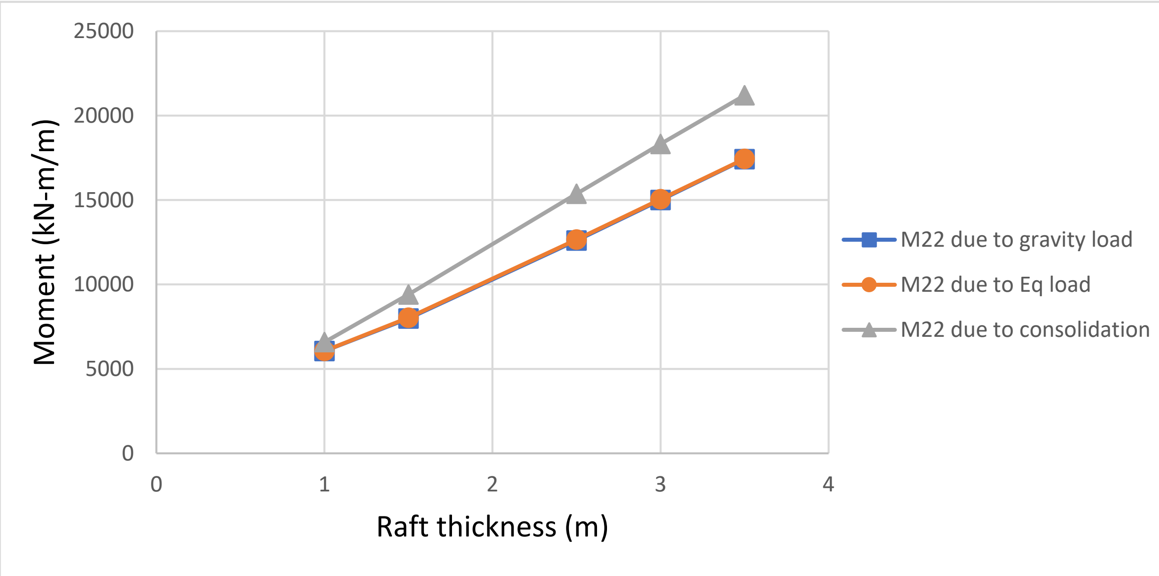

Figure 5.11: Effect of raft thickness on maximum bending moment, M22

5.1.2.7 Maximum torsional moment of raft, M12

Maximum torsional moment for different raft thicknesses is shown in Figure 5.12. Figure 5.12 shows the relation between maximum torsional moment, M12 and raft thickness. The torsional moment, M12 also increases with increase in raft thickness.

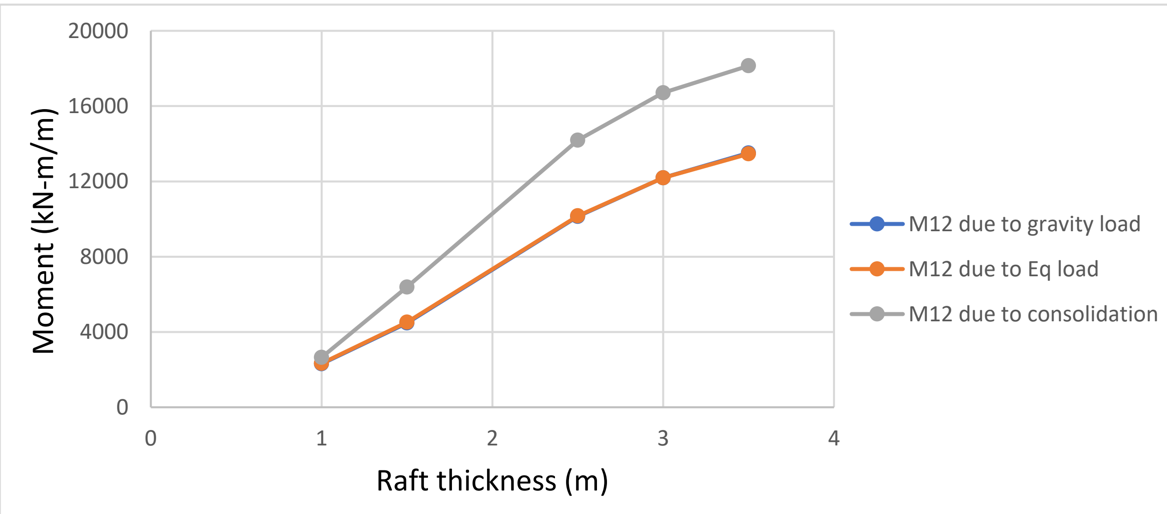

Figure 5.12: Effect of raft thickness on maximum torsional moment, M12

5.1.2.8 Maximum shear force of raft, Q12

Maximum Shear force, Q12 developed in numerical model for different raft thicknesses is shown in Figure 5.13. From the Figure, it is found that the shear force, Q12 increases with increase in raft thickness.

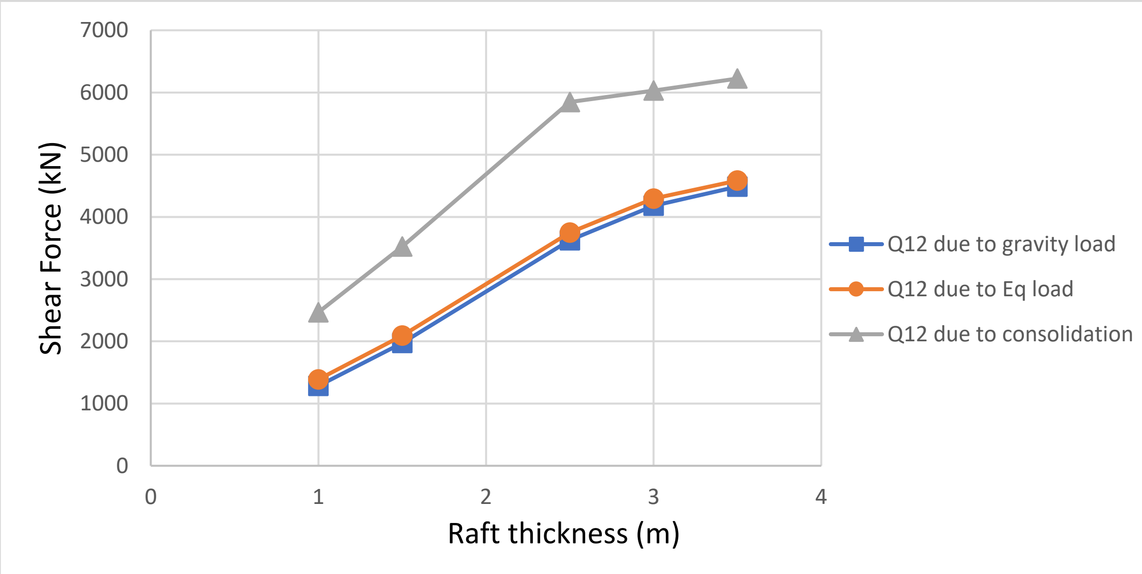

Figure 5.13: Effect of raft thickness on maximum shear force, Q12

5.1.2.9 Maximum shear force of raft, Q23

The maximum shear force, Q23 increases as the raft thickness increases up to 2.5m, after that it starts to decrease. Figure 5.14 shows the relationship between raft thickness and shear force Q23.

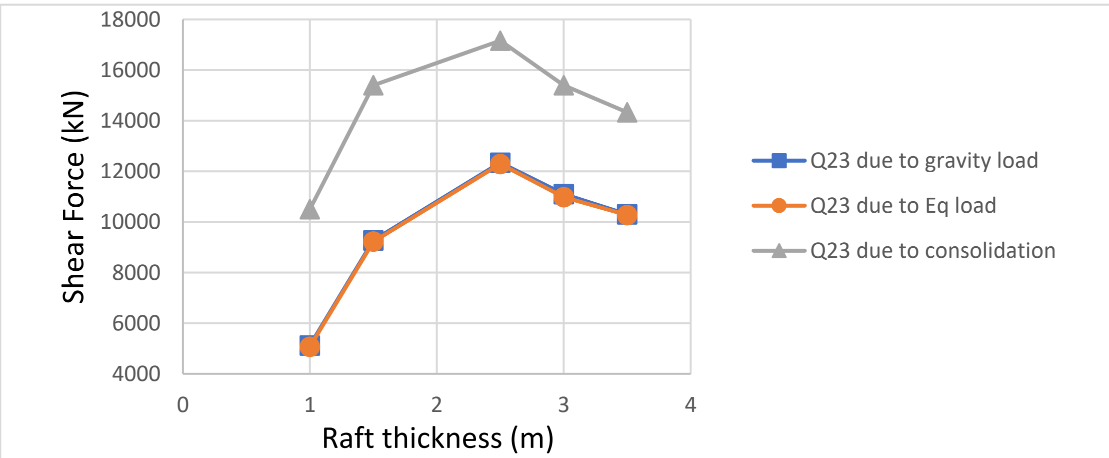

Figure 5.14: Effect of raft thickness on maximum shear force, Q23

5.1.2.10 Maximum shear force of raft, Q13

Relation between maximum shear force, Q13 and raft thickness is also similar as Q23. Figure 5.15 shows the relationship between raft thickness and shear force Q13.

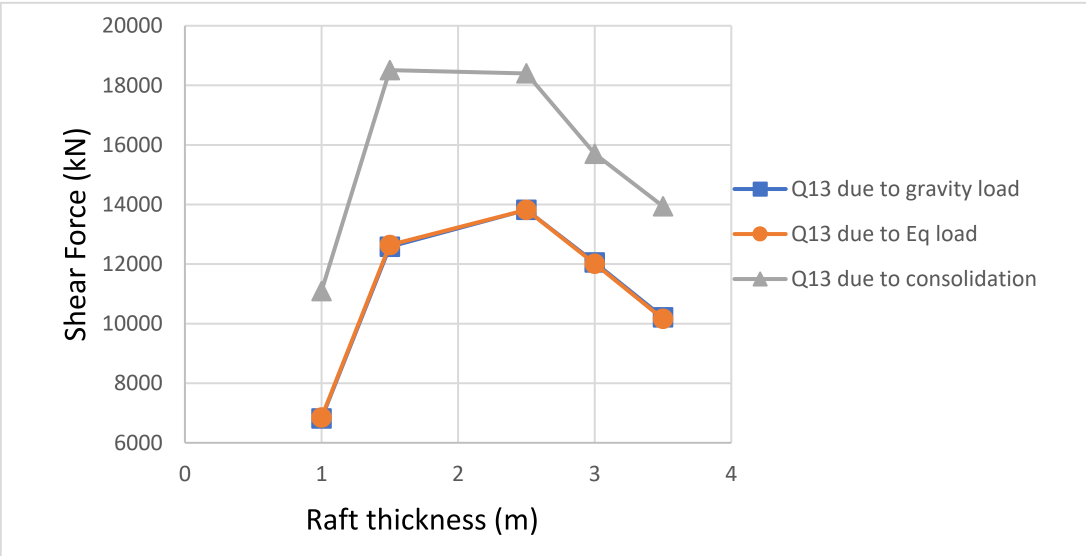

Figure 5.15: Effect of raft thickness on maximum shear force, Q13

5.1.2.11 Maximum bending moment of Retaining wall, M11

The maximum bending moment values of retaining wall for different raft thickness is shown in Figure 5.16. The retaining wall bending moment, M11 decreases with increase in raft thickness except for raft of 1.5m thickness.

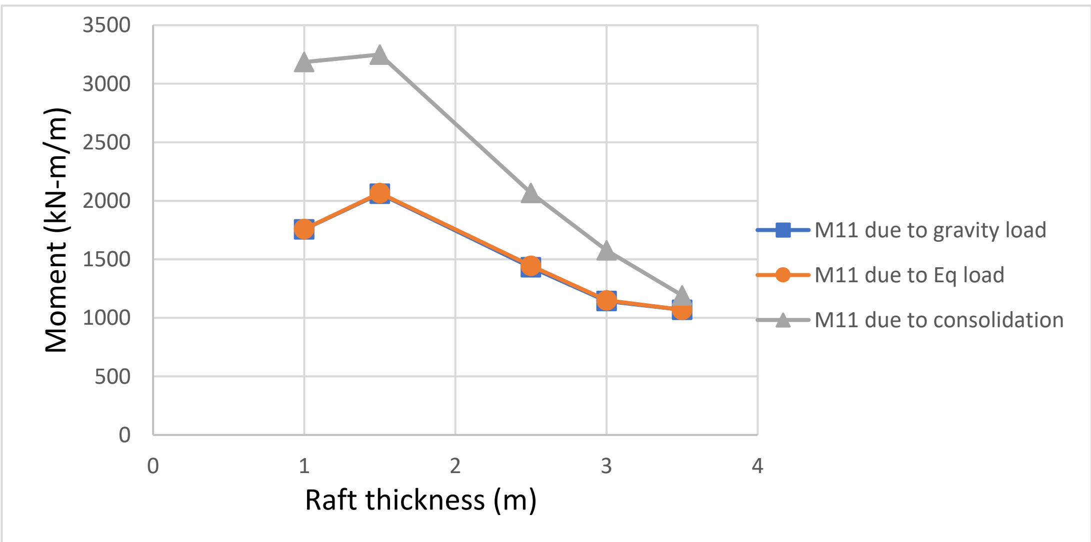

Figure 5.16: Effect of raft thickness on maximum bending moment, M11

5.1.2.12 Maximum bending moment of Retaining wall, M22

The maximum bending moment values of retaining wall for different raft thickness is shown in Figure 5.17. The value of M22 shows irregular behavior for changing raft thickness.

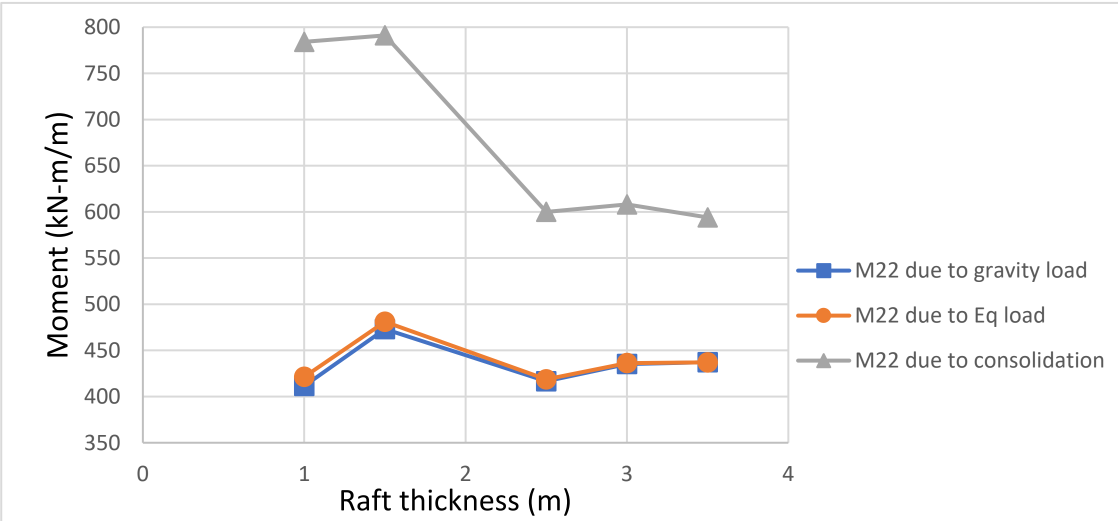

Figure 5.17: Effect of raft thickness on maximum bending moment, M22

5.1.2.13 Maximum torsional moment of Retaining wall, M12

The maximum torsional moment values of retaining wall for different raft thickness is shown in Figure 5.18. The retaining wall torsional moment, M12 decreases with increase in raft thickness.

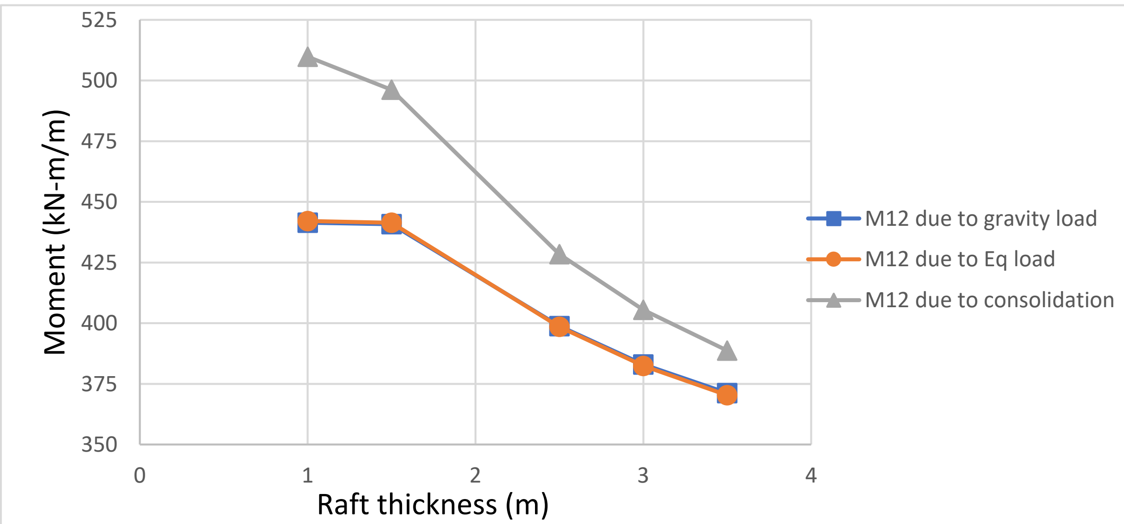

Figure 5.18: Effect of raft thickness on maximum torsional moment, M12

5.1.2.14 Maximum shear force of Retaining wall, Q12

Except for raft with 1.5m thickness, the retaining wall shear force, Q12 decreases with increase in raft thickness.

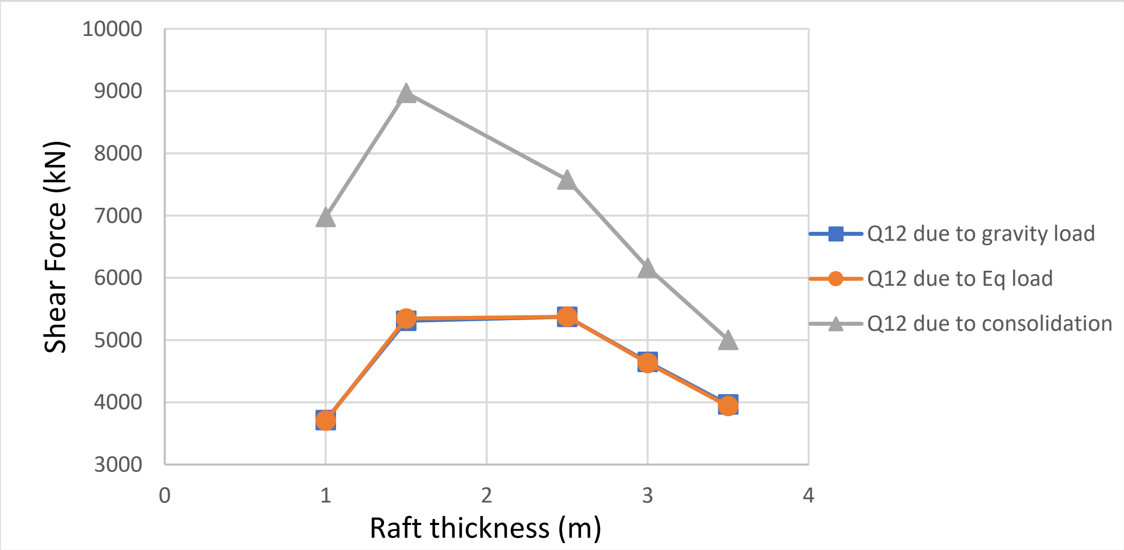

Figure 5.19: Effect of raft thickness on maximum shear force, Q12

5.1.2.15 Maximum shear force of Retaining wall, Q23

The maximum shear force values of retaining wall for different raft thickness is shown in Figure 5.20. The retaining wall shear force, Q23 decreases with increase in raft thickness up to 2.5m thickness, then it starts to increase after 2.5m thickness.

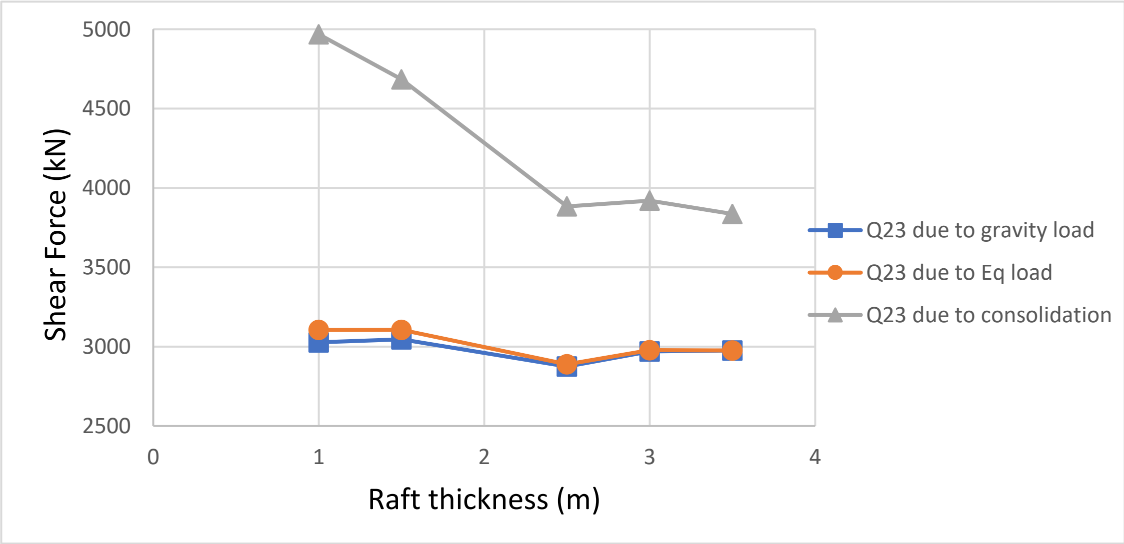

Figure 5.20: Effect of raft thickness on maximum shear force, Q23

5.1.2.16 Maximum shear force of Retaining wall, Q13

Except for consolidation settlement, the retaining wall shear force, Q13 increases with increase in raft thickness. The maximum shear force values of retaining wall for different raft thickness is shown in Figure 5.21.

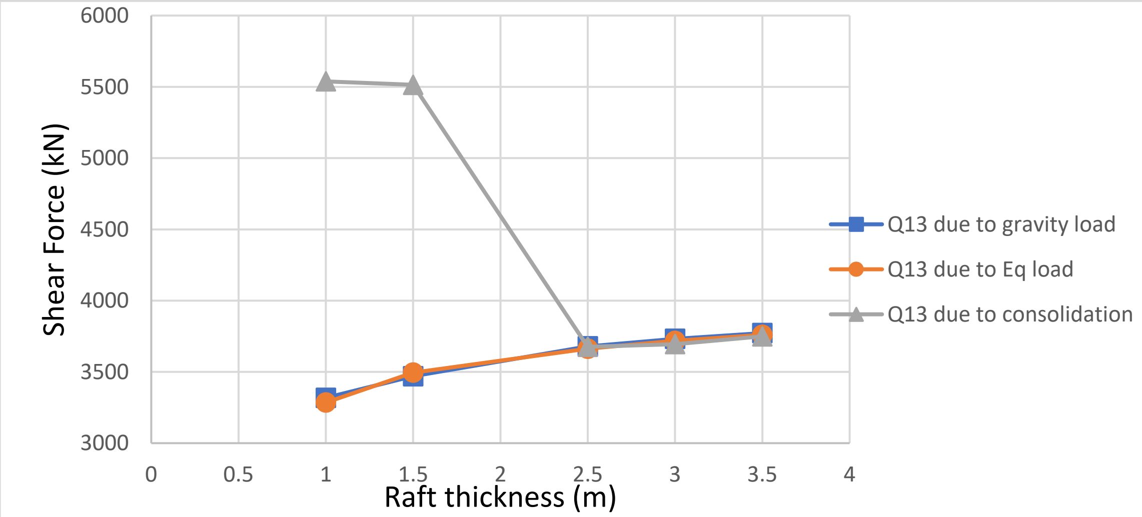

Figure 5.21: Effect of raft thickness on maximum shear force, Q13

5.1.2.17 Maximum normal force of Retaining wall, N1

The maximum normal force values of retaining wall for different raft thickness show irregular behavior. The maximum normal force values, N1 of retaining wall for different raft thickness is shown in Figure 5.22.

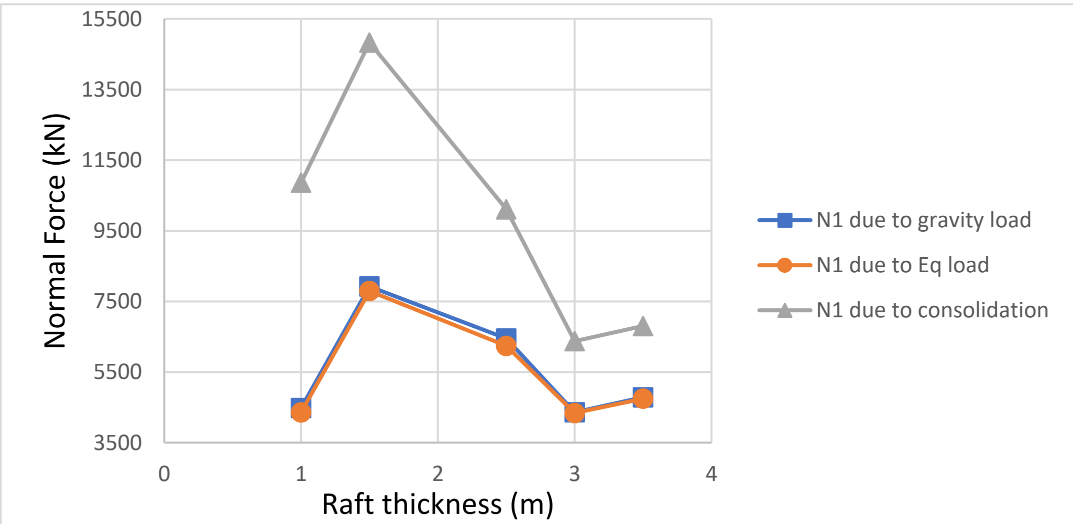

Figure 5.22: Effect of raft thickness on maximum normal force, N1

5.1.2.18 Maximum normal force of Retaining wall, N2

The maximum normal force values of retaining wall for different raft thickness is shown in Figure 5.23. The retaining wall normal force, N2 increases with increase in raft thickness up to 3m raft thickness but it starts to reduce after that.

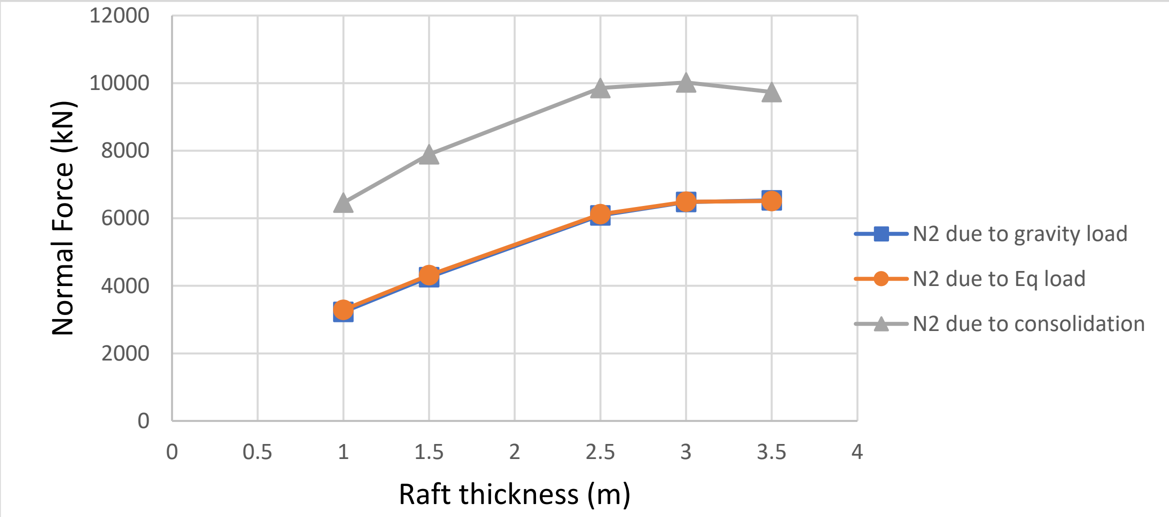

Figure 5.23: Effect of raft thickness on maximum normal force, N2

5.1.2.19 Horizontal deflection of Retaining wall (x-direction)

Figure 5.24 shows that the deflection (x-direction) increases with the increase in raft thickness up to 3m, but after that it remains almost same.

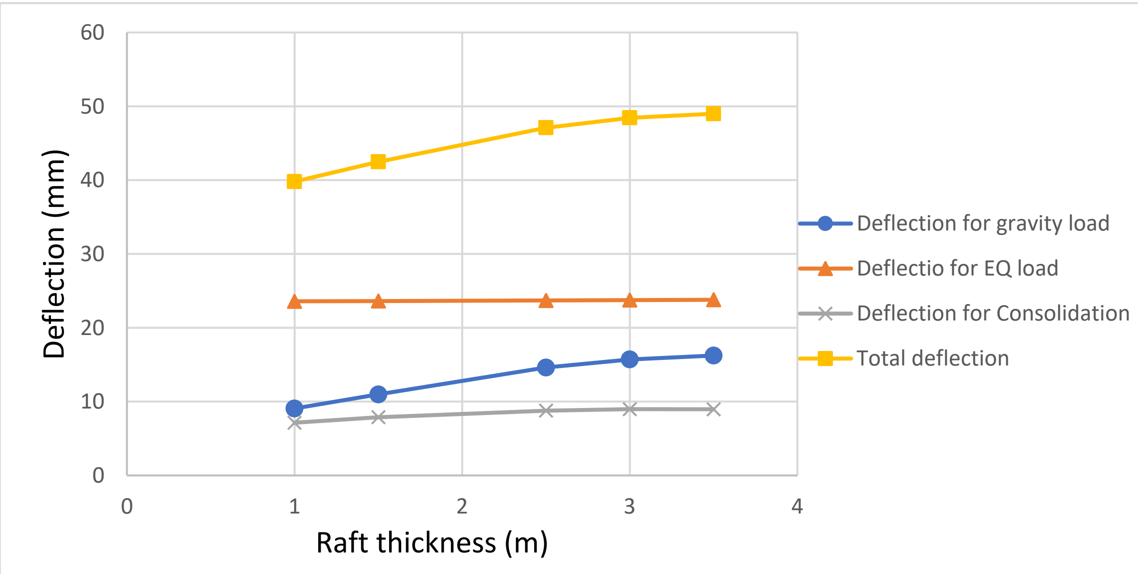

Figure 5.24: Effect of raft thickness on retaining wall horizontal deflection (x direction)

5.1.2.20 Horizontal deflection of Retaining wall (y-direction)

The maximum horizontal deflection at y direction for different raft thicknesses under gravity earthquake load has also been analyzed. The deflection after consolidation effect has also been taken into account. Figure 5.25 shows that the total deflection, deflection due to gravity and earthquake load increases with the increase in raft thickness. However, the deflection due to consolidation increases with the increase in raft thickness up to 3m, after 3m thickness the deflection due to consolidation starts to reduce. Again, the deflection on the y direction is less than the deflection of x direction because the earthquake load has been applied on the x direction by prescribed displacement method in PLAXIS-3D.

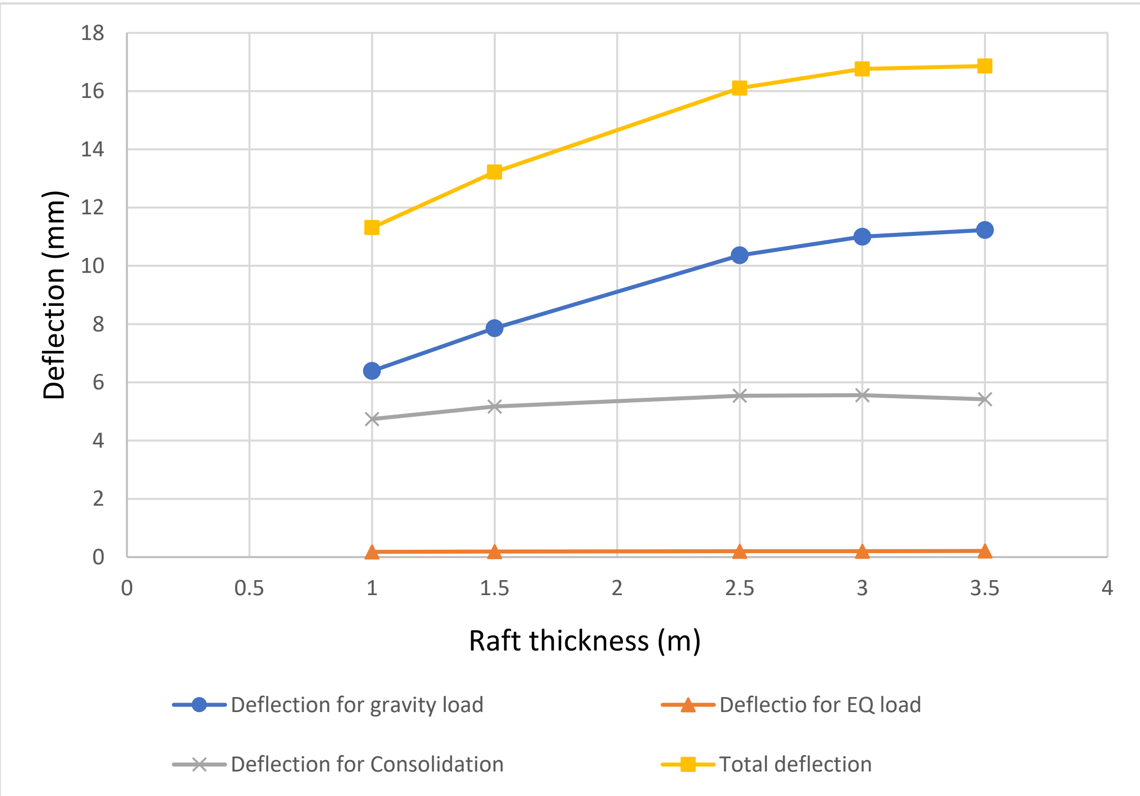

Figure 5.25: Effect of raft thickness on retaining wall horizontal deflection (y direction)

All the results and outputs of un-piled raft for different raft thickness are provided in Appendix-2.

5.2 Results of Piled Raft Foundation

Based on twenty-seven nos. finite element models developed in PLAXIS-3D software, the effect of raft thickness, pile diameter and pile number has been studied. Brief findings of the parametric studies on piled raft are mentioned in this section.

5.2.1 Effect of raft thickness:

5.2.1.1 Settlement at raft center

Total settlement including immediate, consolidation and earthquake induced settlement occurred at the raft center is presented in Figure 5.26 for different raft thicknesses.

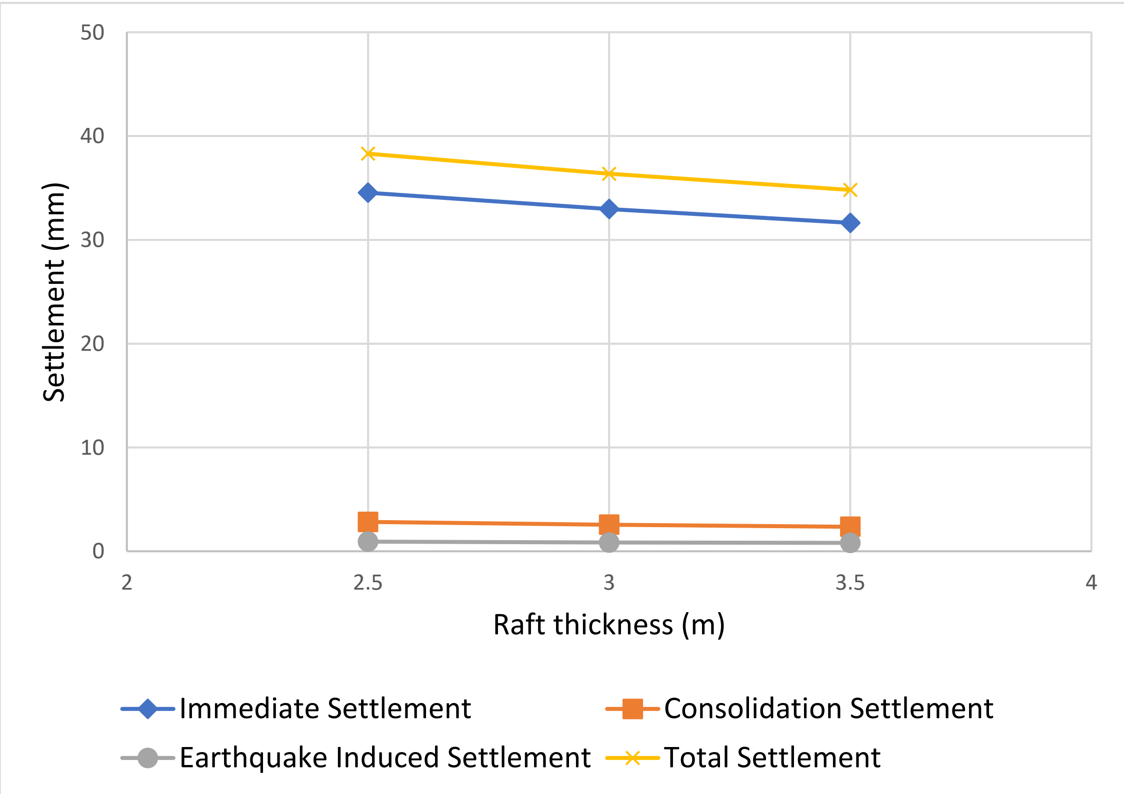

Figure 5.26: Effect of raft thickness on settlement values at raft center of Piled raft with 58 nos. 1m diameter piles

From Figure 5.26 it is found that, with the increase of raft thickness, all the settlement (Immediate, consolidation, earthquake induced and total settlement) decreases. As discussed earlier for un-piled raft foundation, it is easier for a rigid raft to distribute the stress throughout the raft preventing it from settling more locally in the center. Figure 5.26 also shows that the earthquake induced settlement and consolidation settlement is negligible compared to immediate. The immediate settlement governs here as the soil beneath is raft is granular soil. The consolidation settlement happened here due to the soil layer of 27m to 30m. As some percentages of the total load is transferred at 60m below through the piles, the consolidation settlement here is less than the un-piled rafts.

5.2.1.2 Settlement at raft corner

A thicker and stiffer raft can distribute stress at the rafter corners resulting in higher settlement at the rafter corner than a thinner raft. Figure 5.27 shows the effect of raft thickness on the settlement values at raft corners.

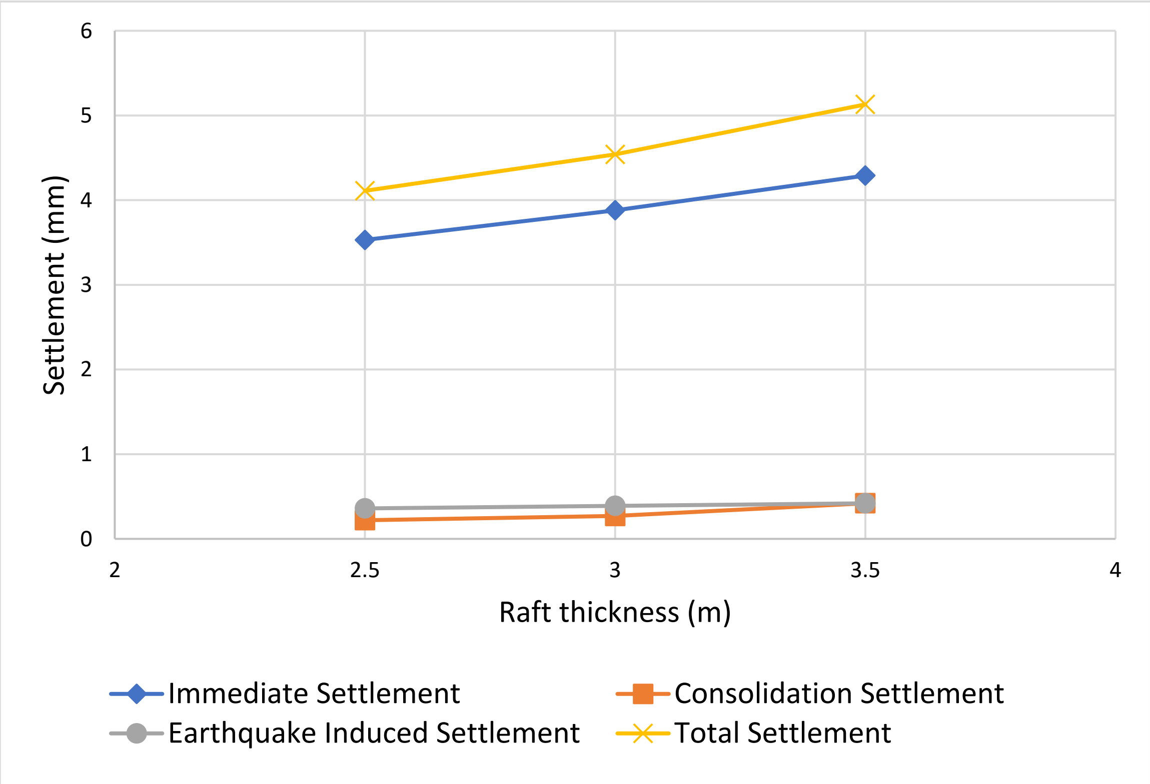

Figure 5.27: Effect of raft thickness on settlement values at raft corner of Piled raft with 58 nos. 1m diameter piles

From Figure 5.27, it is observed that the immediate settlement is again the governing settlement at the raft corner.

5.2.1.3 Differential settlement

Figure 5.28 indicates that the differential settlement of piled raft foundation decreases with the increase in raft thickness. As discussed, earlies in this section, increase in raft thickness results in increase in raft stiffness and rigidity. Rigidity of the raft helps to reduce the differential settlement by distributing the stress along the raft area.

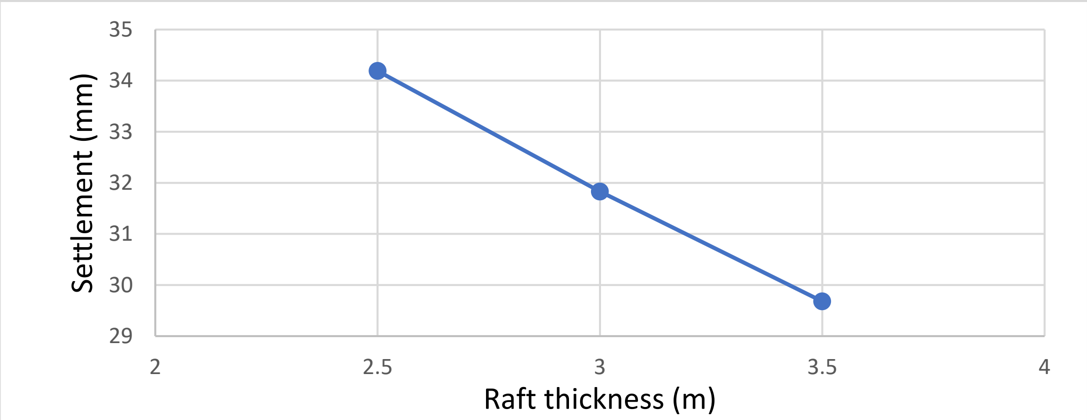

Figure 5.28: Effect of raft thickness on differential settlement of Piled raft with 58 nos. 1m diameter piles

5.2.1.4 Angular distortion

Angular distortion of piled raft foundation decreases with the increase in raft thickness for the same reason that reduces the differential settlement.

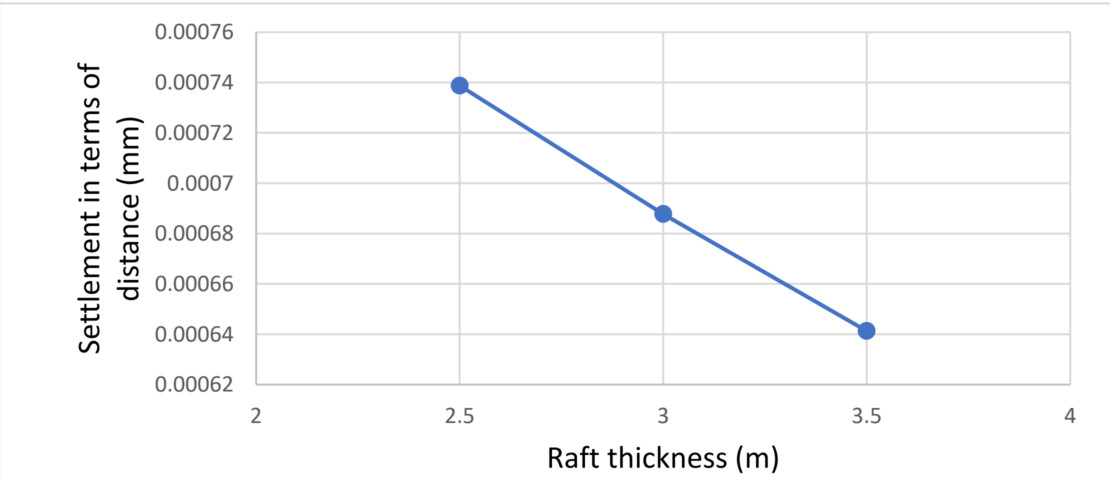

Figure 5.29: Effect of raft thickness on angular distortion of Piled raft with 58 nos. 1m diameter piles

5.2.1.5 Maximum developed stress at raft

The value of maximum stress developed at the raft decreases as the raft thickness increases. Due to increase in raft thickness the self-weight increases but the stiffness also increases due to higher thickness. For increasing the stiffness of the raft, the stress is distributed throughout the raft preventing it from local stress concentration.

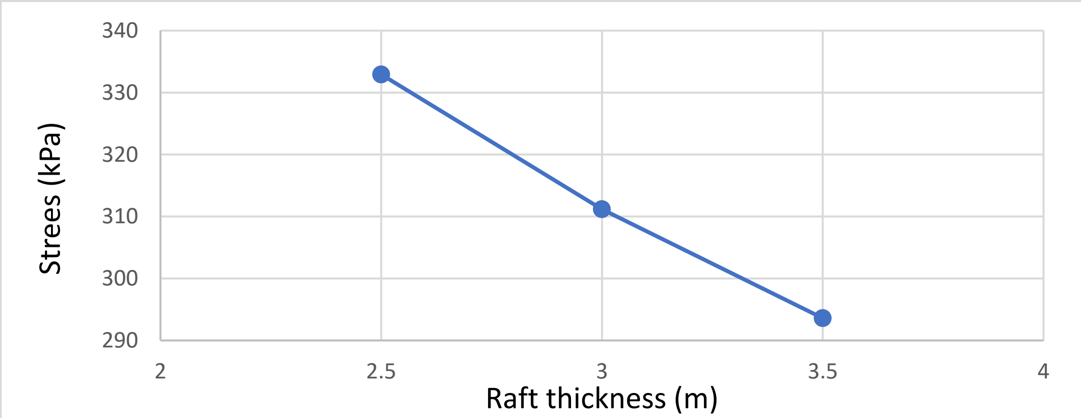

Figure 5.30: Effect of raft thickness on maximum developed stress of Piled raft with 58 nos. 1m diameter piles

5.2.1.6 Center pile reaction

The reaction of the center piles decreases with the increase in raft thickness for the same reason that reduces the maximum developed stress at raft center.

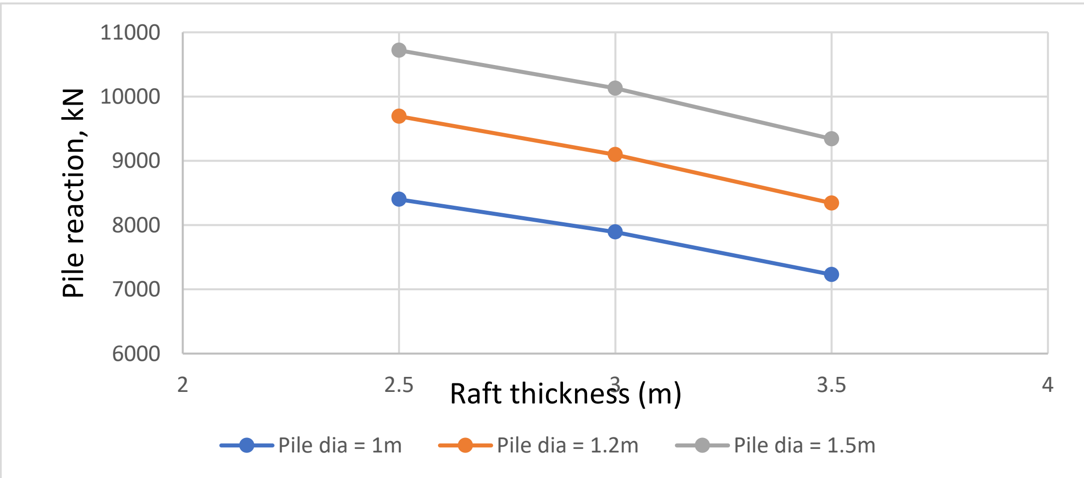

Figure 5.31: Effect of raft thickness on the center pile reaction of Piled raft with 58 nos. piles

5.2.1.7 Corner pile reaction

Figure 5.32 shows that the reaction of corner piles also decreases with the increase in raft thickness.

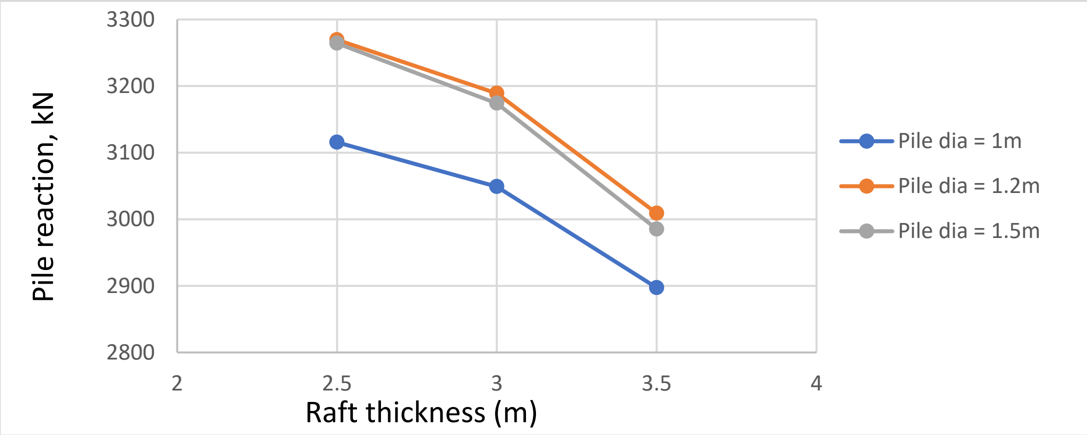

Figure 5.32: Effect of raft thickness on the corner pile reaction of Piled raft with 58 nos. piles

5.2.1.8 Settlement of piles

Figure 5.33 shows that the raft thickness does not significantly affect the settlement value of the center pile. Center piles are not likely to settle much (total settlement ranges between 7-9mm) as pile tips are rested at 60m below existing ground level where the soil is very dense sandy layer. However, the settlement value of the corner piles is too little to analyze and hence it is ignored in this study.

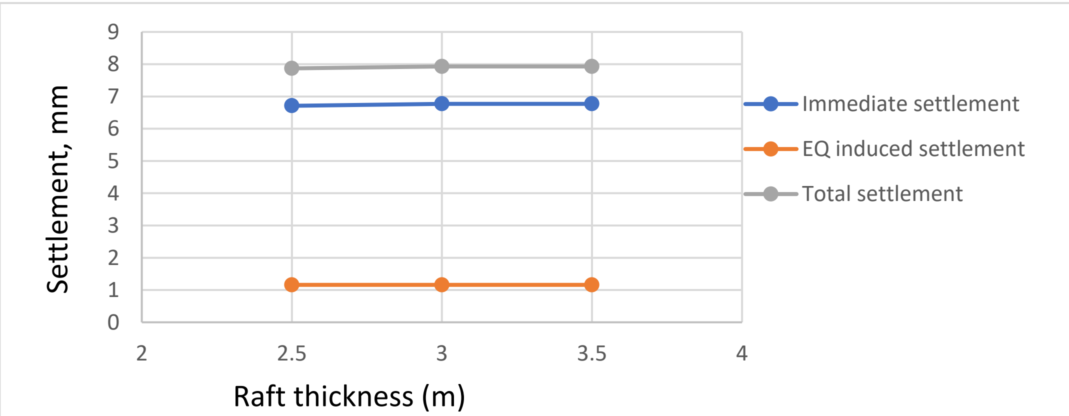

Figure 5.33: Effect of raft thickness on the center pile settlement of Piled raft with 58 nos. piles

5.2.1.9 Maximum bending moment of center piles

The maximum bending moment of center piles decreases as the raft thickness increases. Figure 5.34 shows the effect of raft thickness on the maximum bending moment values of center piles.

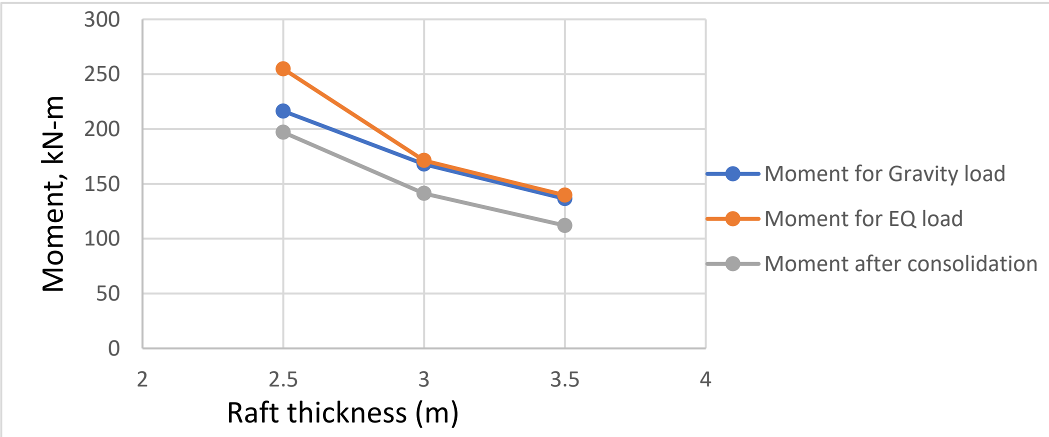

Figure 5.34: Effect of raft thickness on the center pile maximum bending moment of Piled raft with 58 nos. piles

5.2.1.10 Maximum bending moment of corner piles

Figure 5.35 shows the effect of raft thickness on the maximum bending moment values of corner piles. Maximum bending moment of corner piles increases with the increase in raft thickness.

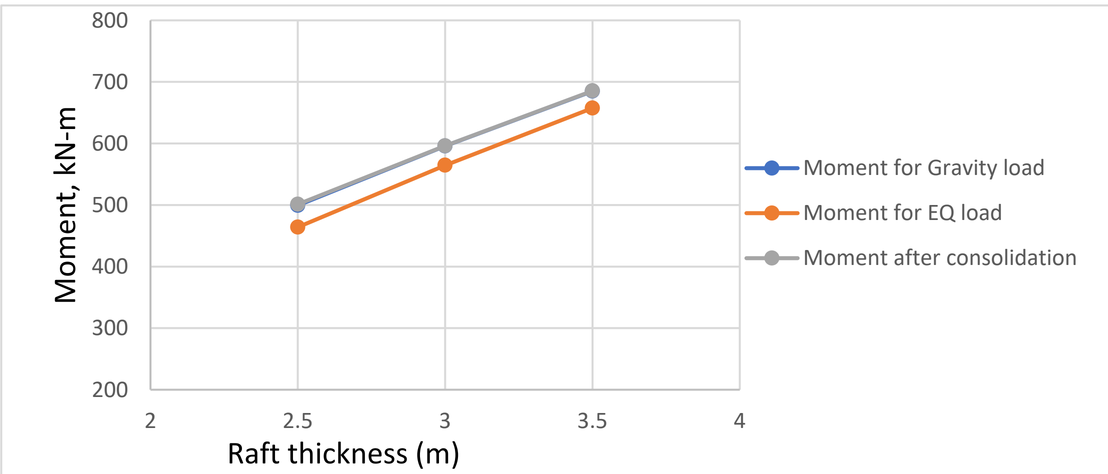

Figure 5.35: Effect of raft thickness on the corner pile maximum bending moment of Piled raft with 58 nos. piles

5.2.1.11 Maximum shear force of center piles

The maximum shear force of center piles decreases as the raft thickness increases. Figure 5.36 shows the effect of raft thickness on the maximum shear force values of center piles.

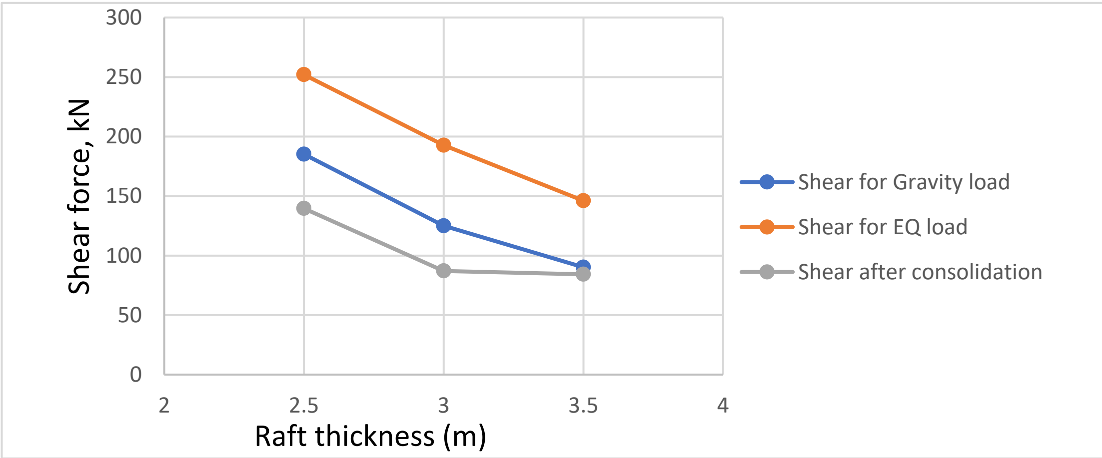

Figure 5.36: Effect of raft thickness on the center pile maximum shear force of Piled raft with 58 nos. piles

5.2.1.12 Maximum shear force of center piles

Figure 5.37 shows the effect of raft thickness on the maximum bending moment values of center piles. Maximum bending moment of corner piles increases with the increase in raft thickness.

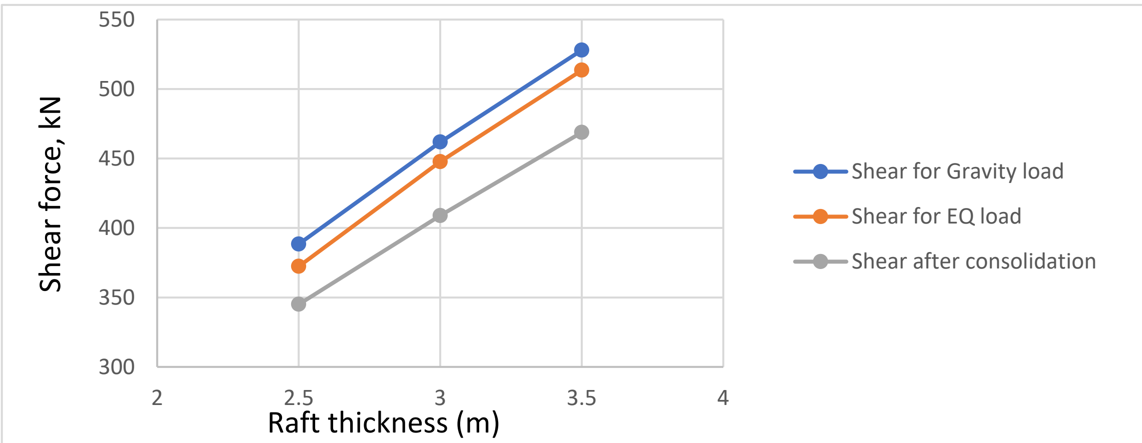

Figure 5.37: Effect of raft thickness on the corner pile maximum shear force of Piled raft with 58 nos. piles

5.2.1.13 Lateral deflection of center and corner piles (along x-direction)

Raft thickness does not affect the lateral deflection value of the piles below the rafts along x-direction. The deflection along the x-direction of both the center and corner piles remains in between 23.5-24mm for different raft thicknesses.

5.2.1.14 Maximum moments of raft

As moment is a function raft thickness so the maximum bending moment M11, M22 and the maximum torsional moment M12 all increase as the raft thickness increases.

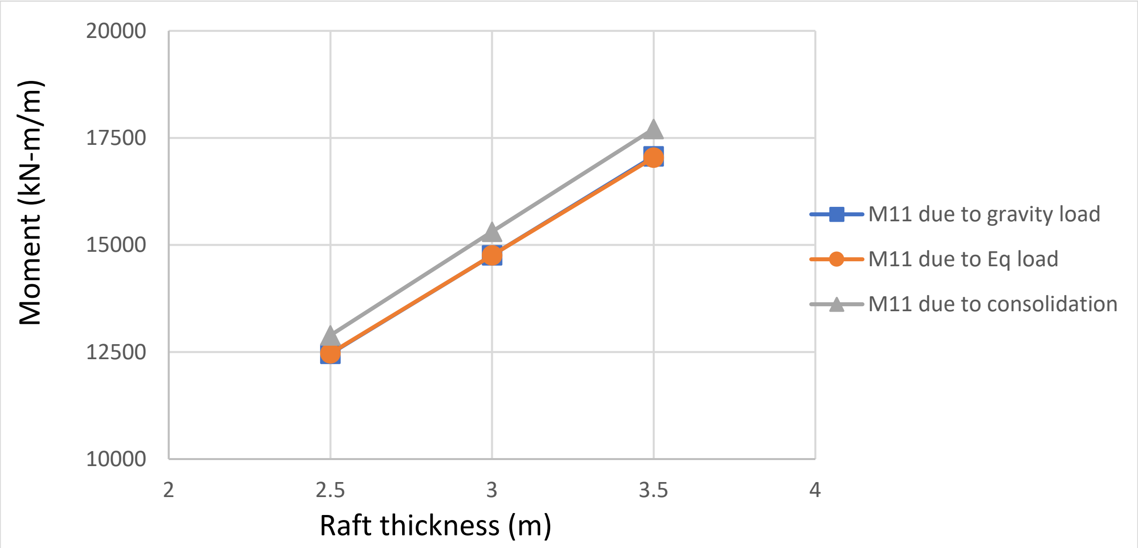

(a)

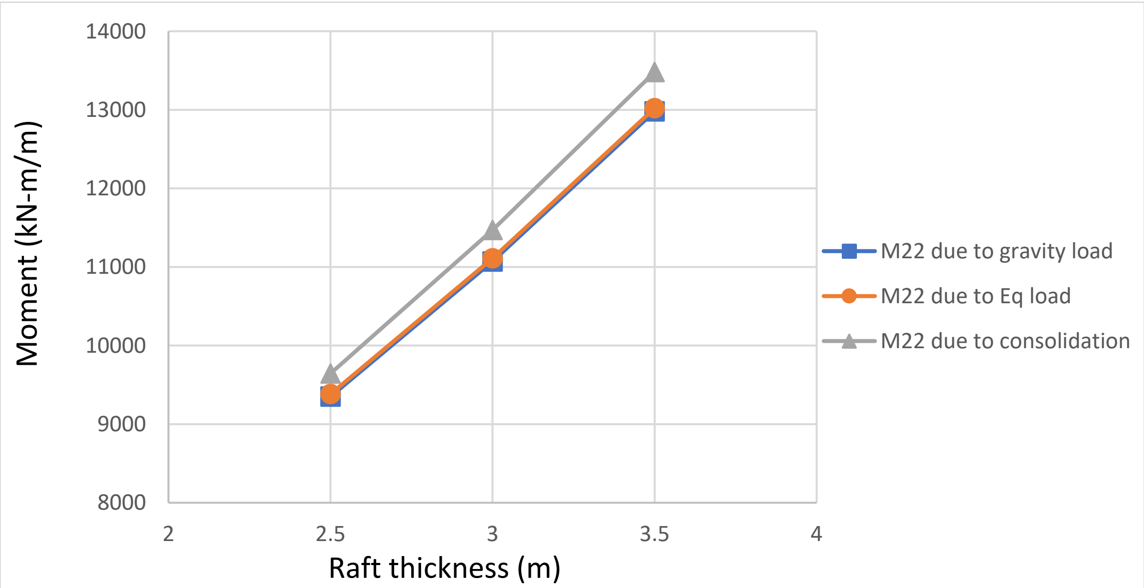

(b)

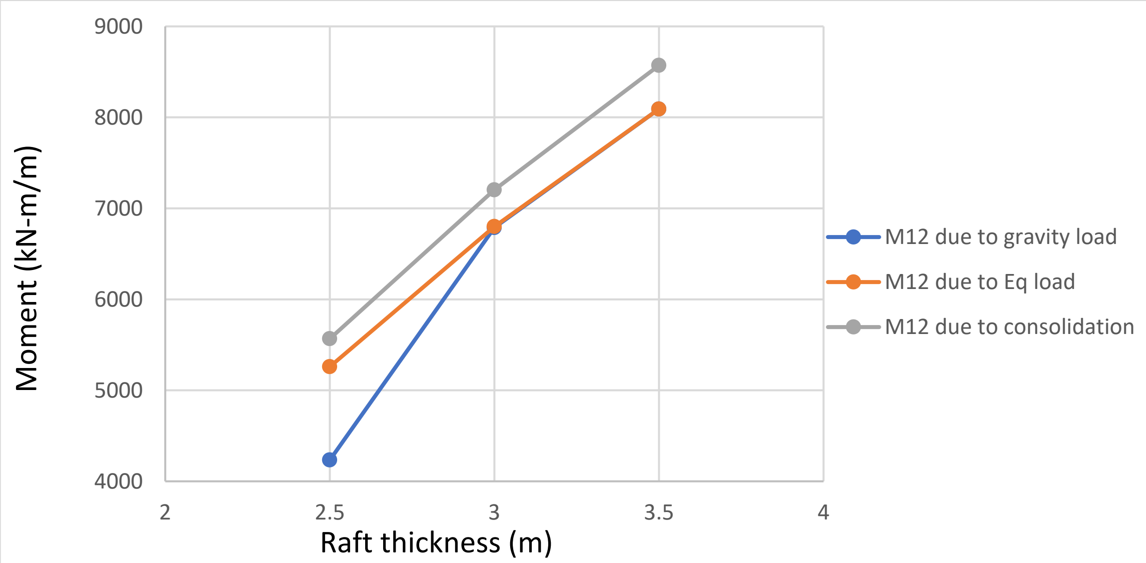

(c)

Figure 5.38: Effect of raft thickness on the raft maximum moments of the piled rafts with 58 nos. 1m diameter piles. (a) M11, (b) M22, (c)M12

5.2.1.15 Maximum shear forces of raft

The shear force Q12 of the raft increases with the increase in raft thickness. However, the shear force Q23 and Q13 decreases as the raft thickness increases. Figure 5.39 shows the relation between raft thickness and shear forces.

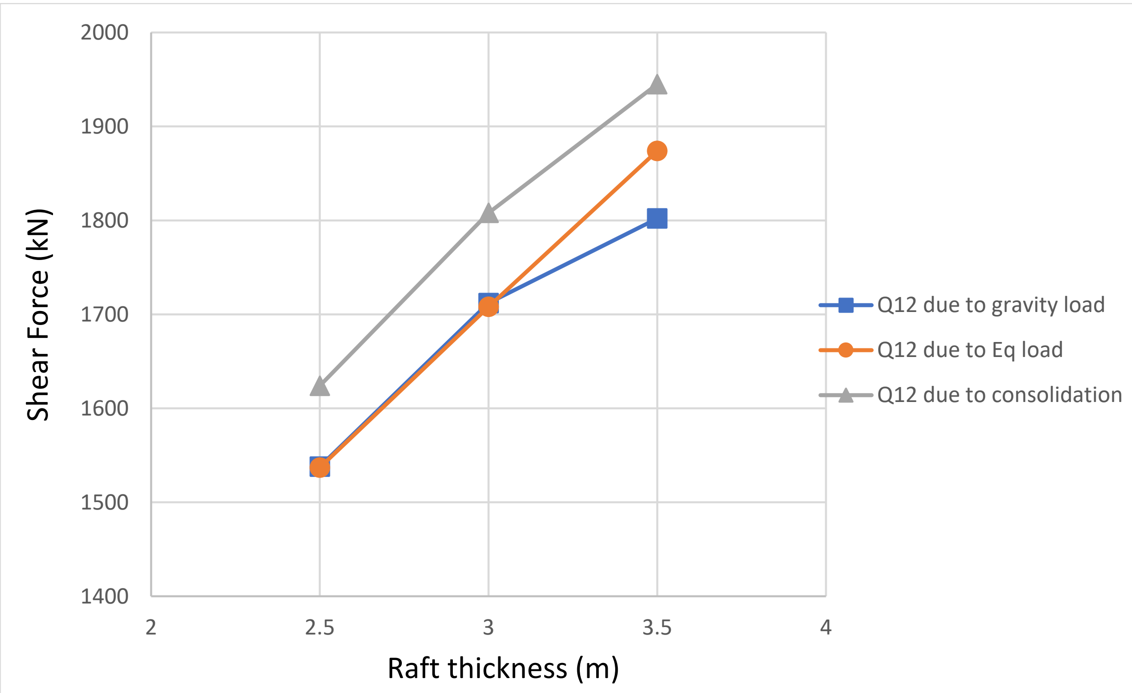

(a)

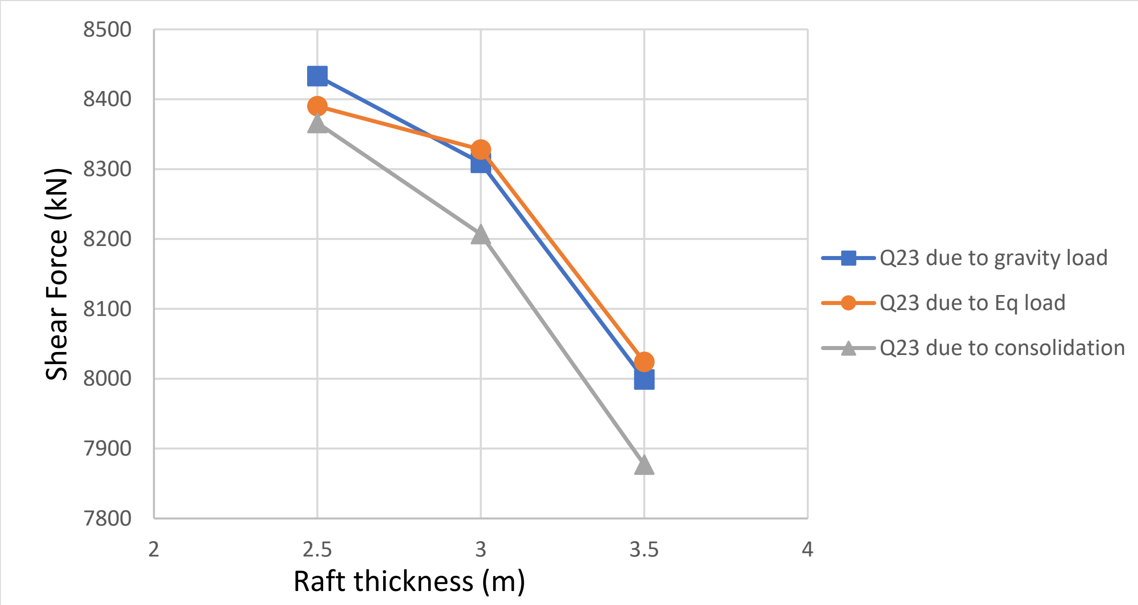

(b)

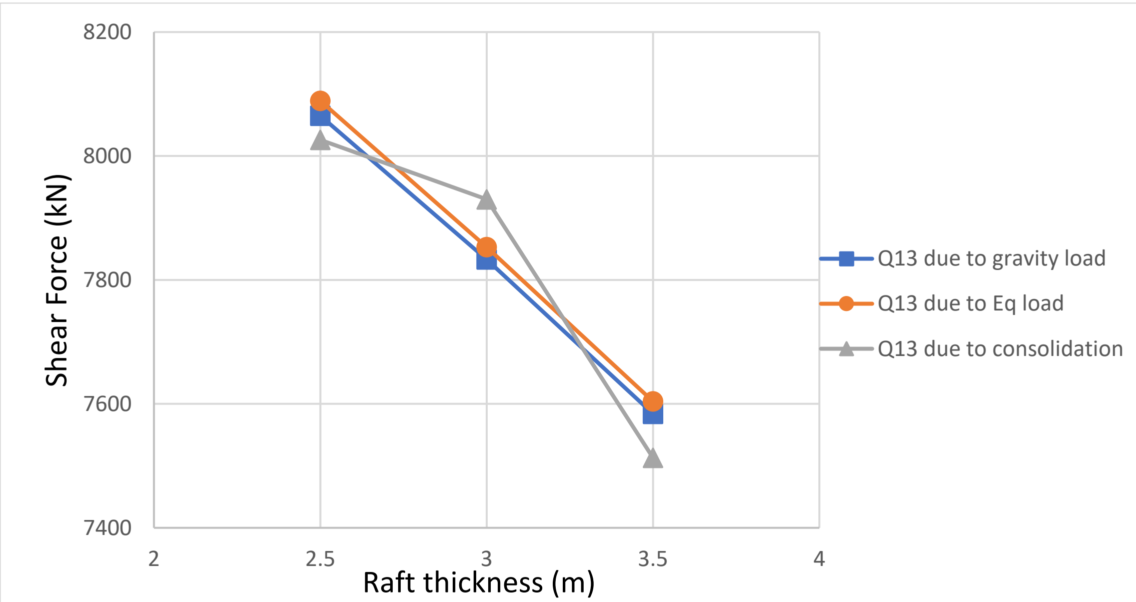

(c)

Figure 5.39: Effect of raft thickness on raft maximum shear forces of piled rafts with 58 nos. 1m diameter piles. (a) Q12, (b) Q23, (c) Q13

5.2.1.16 Maximum moments of retaining wall

The effect of raft thickness on the retaining wall maximum moments is very minor. Figure 5.40 shows that the maximum moments M11 and M12 of retaining wall slightly decreases as the raft thickness increases. However, the torsional moment M12 increases to some extent with the increase in raft thickness.

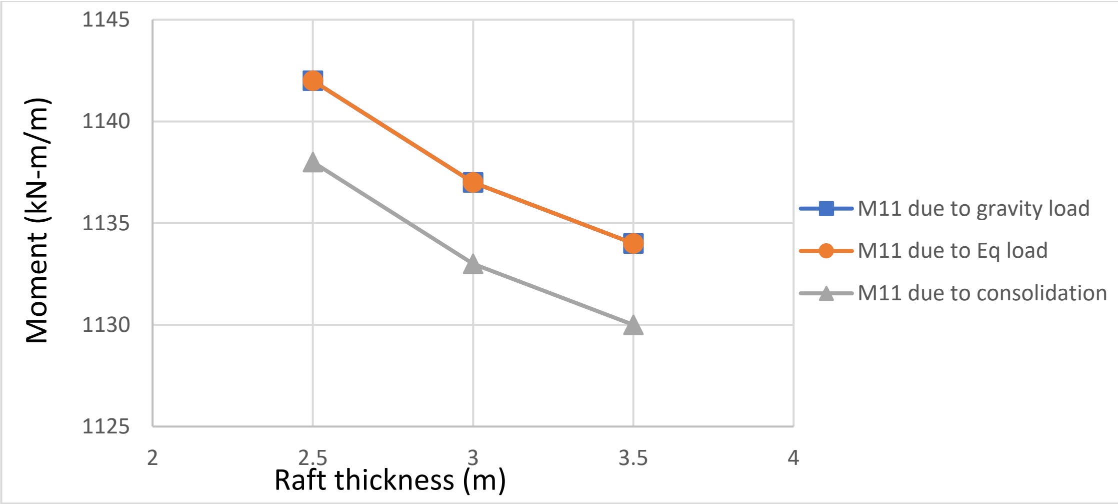

(a)

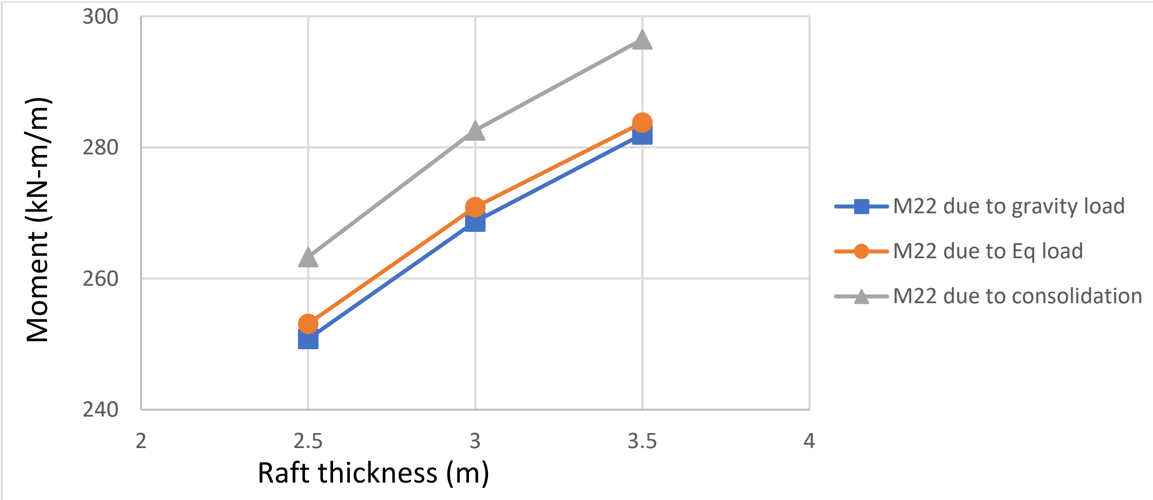

(b)

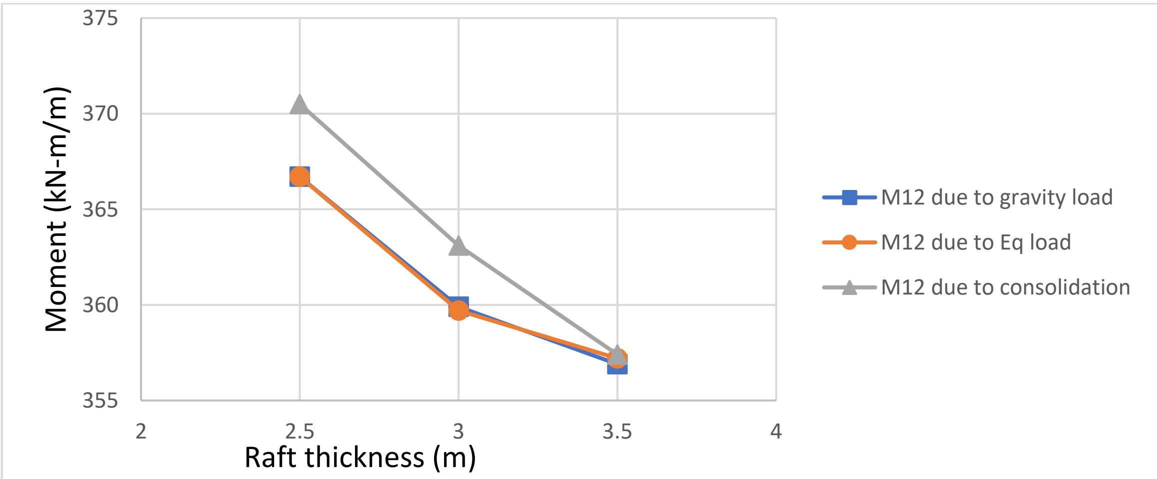

(c)

Figure 5.40: Effect of raft thickness on retaining wall maximum moments of piled rafts with 58 nos. 1m diameter piles. (a) M11, (b) M22, (c) M12

5.2.1.17 Maximum shear forces of retaining wall

For piled raft foundation system, the shear force values of retaining wall increase with the increase in raft thickness. Figure 5.41 shows the relation between raft thickness and retaining wall shear forces.

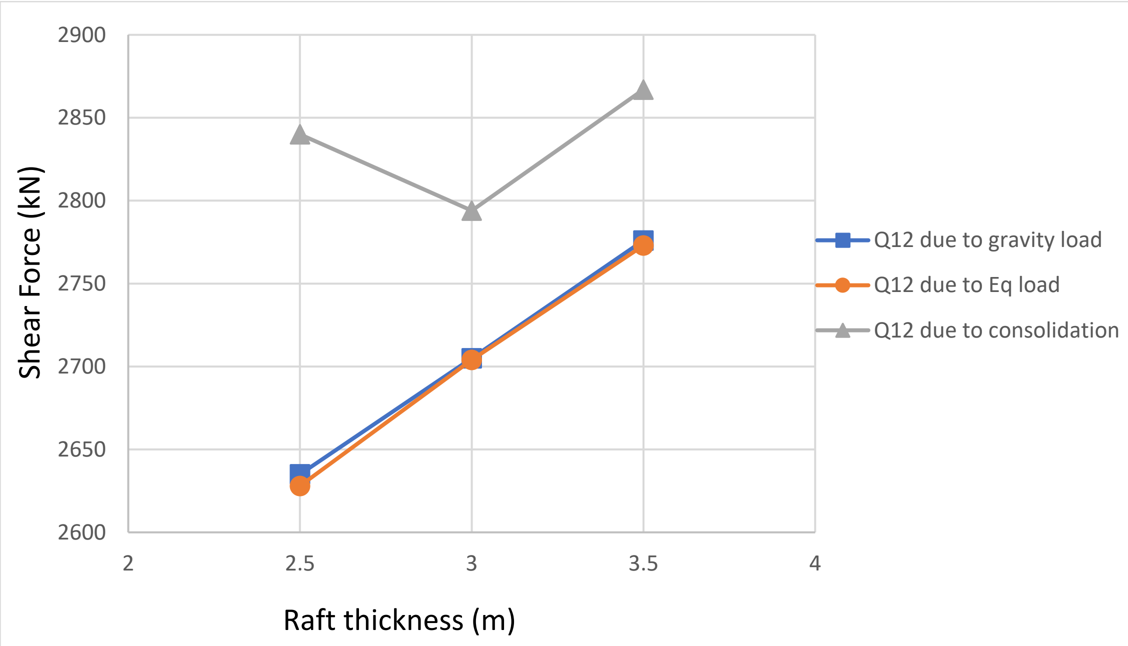

(a)

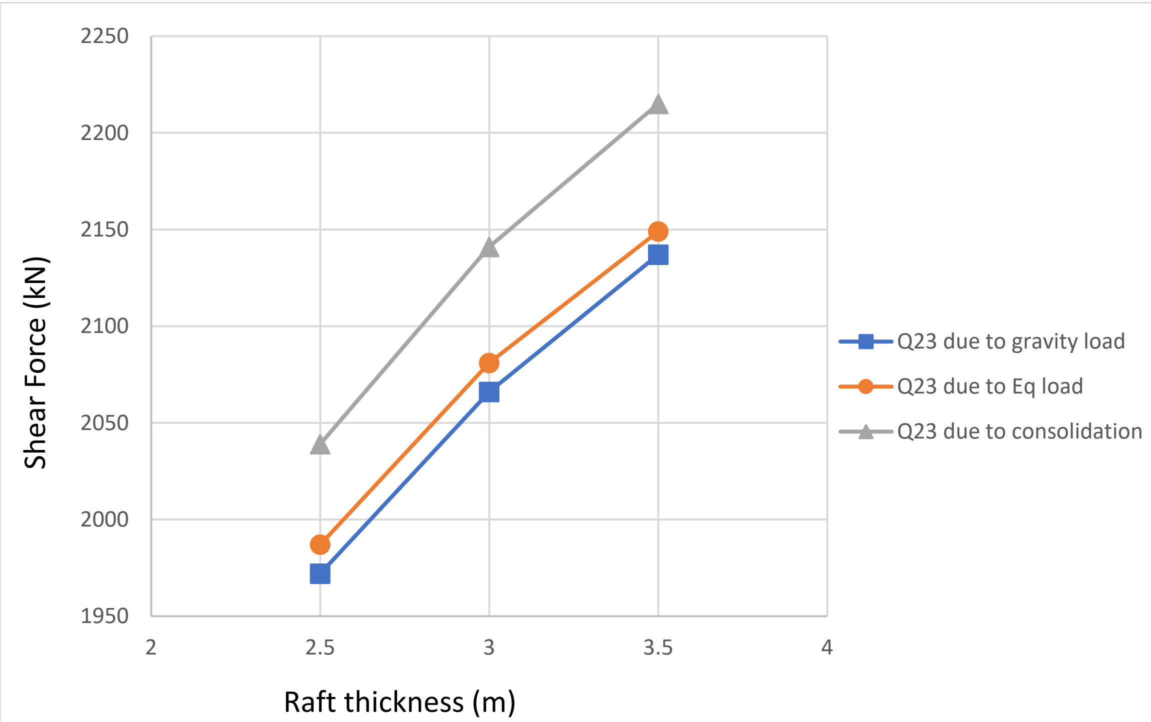

(b)

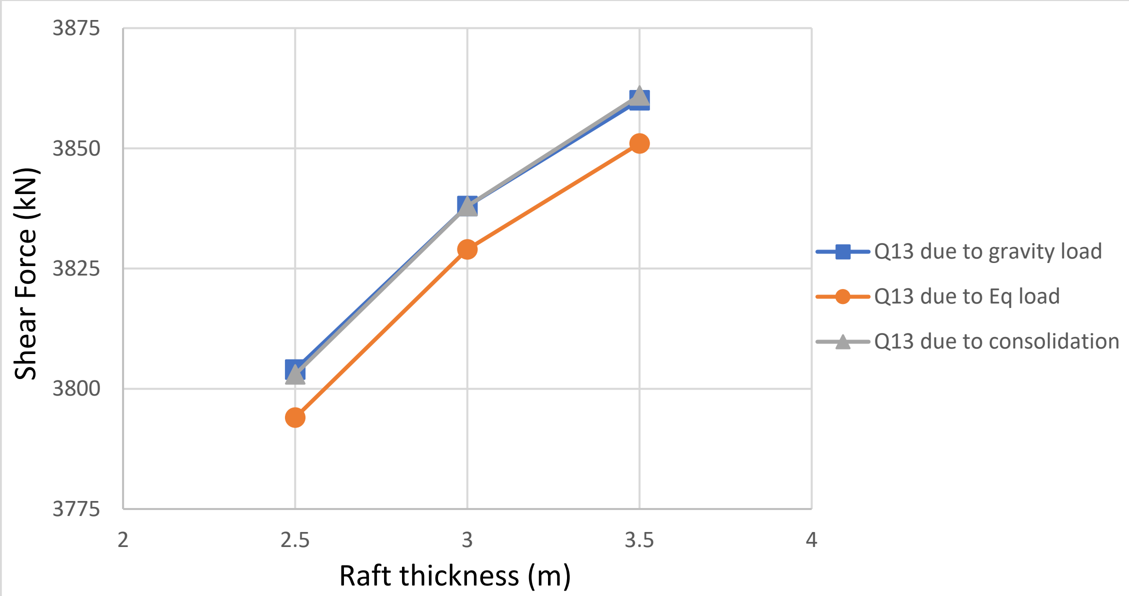

(c)

Figure 5.41: Effect of raft thickness on retaining wall maximum shear forces of piled rafts with 58 nos. 1m diameter piles. (a) Q12, (b) Q23, (c) Q13

5.2.1.18 Maximum normal forces of retaining wall

The normal force values N1 and N2 of retaining wall increase with the increase in raft thickness for piled raft foundation system. Figure 5.42 shows the relation between raft thickness and retaining wall normal forces.

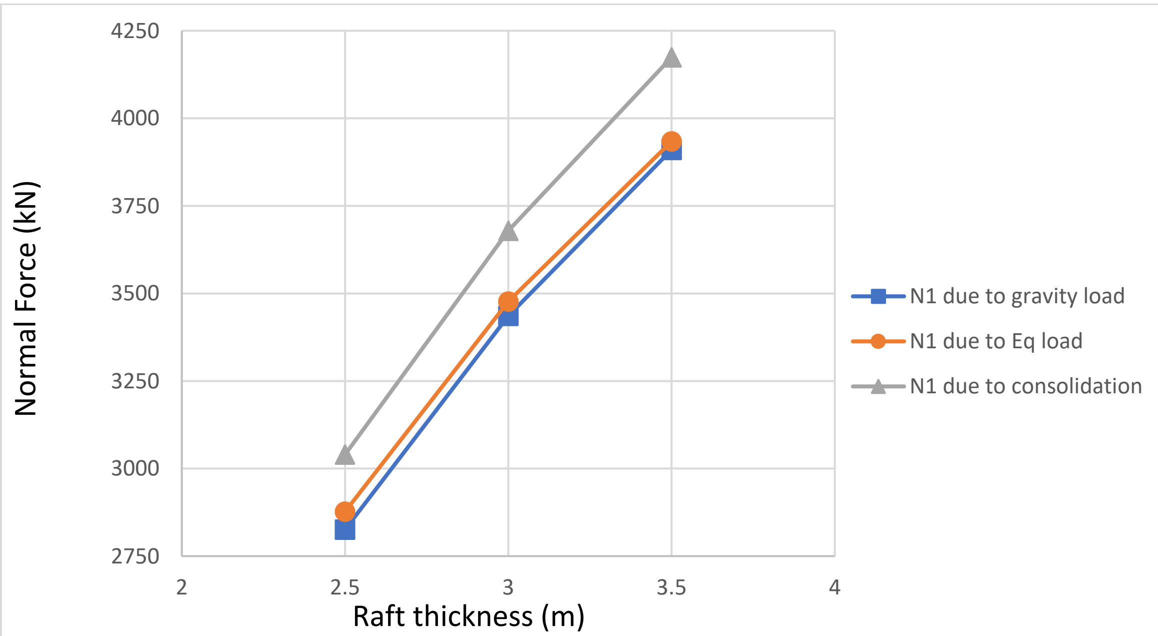

(a)

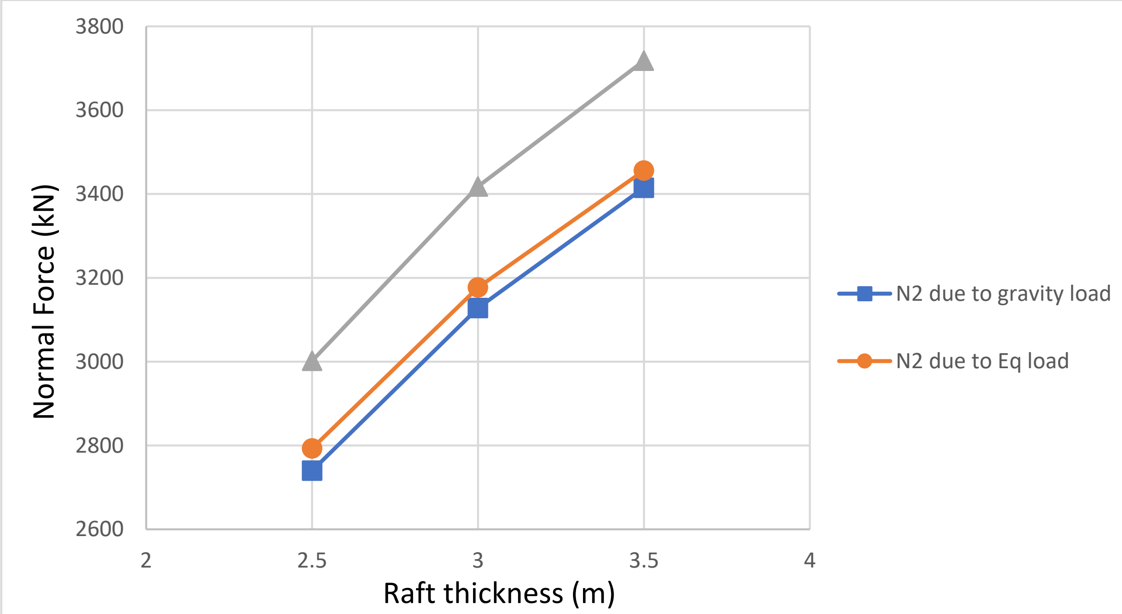

(b)

Figure 5.42: Effect of raft thickness on retaining wall maximum normal forces of piled rafts with 58 nos. 1m diameter piles. (a) N1, (b) N2

5.2.1.19 Lateral deflection of retaining wall

The effect of raft thickness on the retaining wall lateral deflection is very negligible. Figure 5.43 shows that the lateral defection along x-direction of retaining wall slightly increases as the raft thickness increases. However, the lateral defection along y-direction decreases to some extent with the increase in raft thickness.

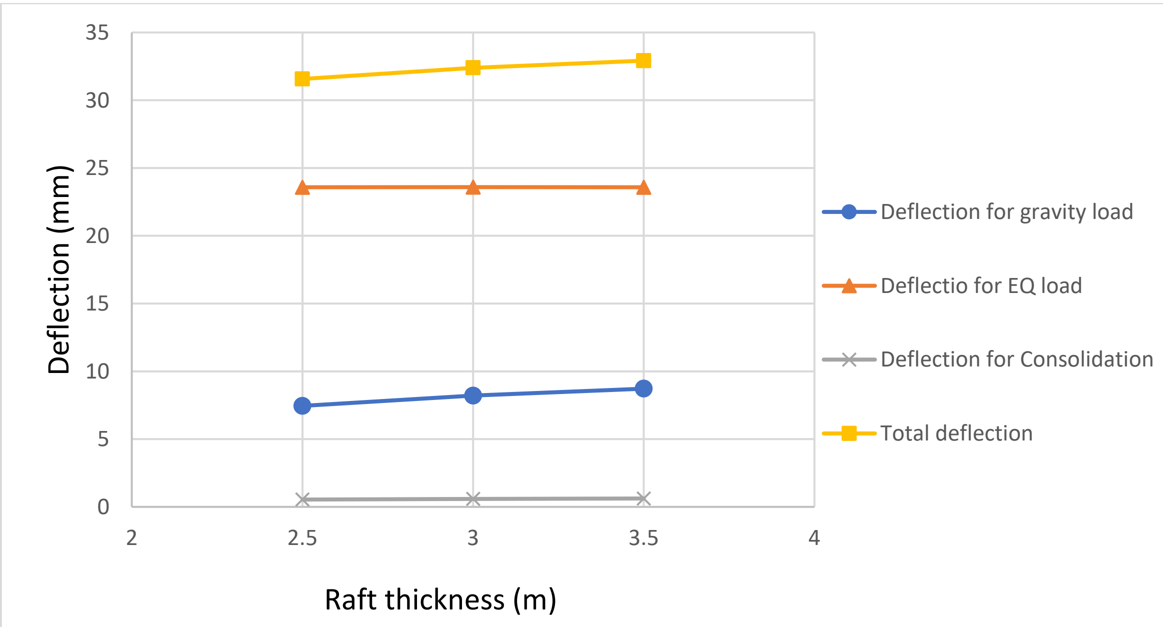

(a)

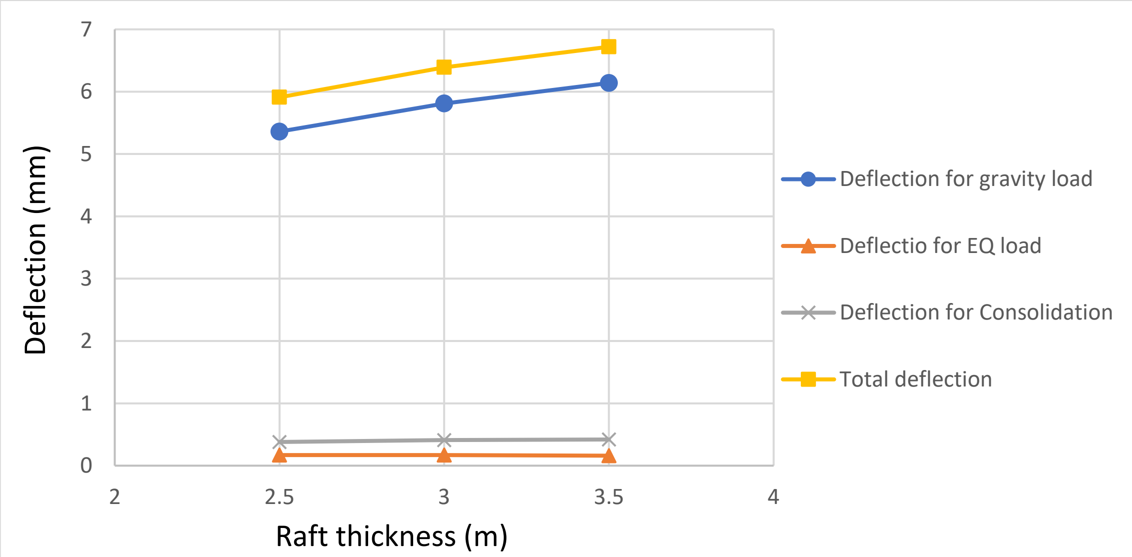

(b)

Figure 5.43: Effect of raft thickness on retaining wall lateral deflections of piled rafts with 58 nos. 1m diameter piles. (a) x-direction deflection, (b) y-direction deflection

5.2.1.20 Load distribution between raft and piles

The percent of load shared by the piles decreases with the increase in raft thickness. In other words, the percent of load shared by the raft increases with the increase in raft thickness. Increase in thickness increases the stiffness of the raft which allows the raft to attract more loads. Figure 5.44 shows the comparison of the load shared by the piles for different raft thickness.

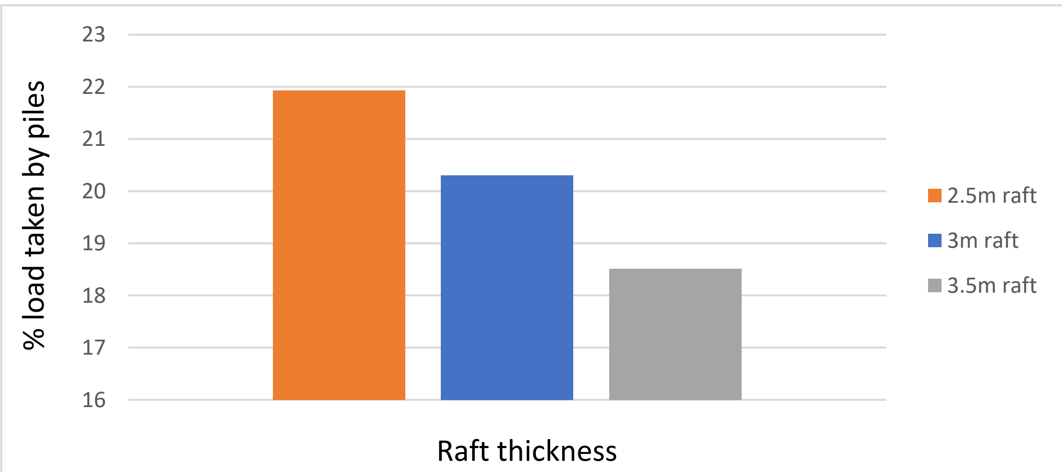

Figure 5.44: Effect of raft thickness on % of load sharing of piled rafts with 58 nos. 1m diameter piles

From the parametric study it is observed that, the raft alone takes more than 70% loads. The reason behind the raft taking this higher percentage of load is, the raft is rested at 18m below existing ground level where the soil is Medium dense to Dense Silty Sand. If the raft were rested on soft clay type soil, then the higher percentage of load would be transferred to piles.

The effects of raft thickness on different geotechnical and structural parameters have been discussed above for only the piled rafts of 58 piles with 1m diameter piles. Piled rafts having different pile numbers and pile diameters, show the same impacts of raft thickness and hence it is not mentioned here. Only exception is observed for the raft shear force Q23 value for 69 piles, where the raft Q23 value increases as the raft thickness increases. However, the effects of raft thickness on the other piled rafts are mentioned in Appendix-3.

5.2.2 Effect of Pile numbers

5.2.2.1 Settlement at raft center

Total settlement including immediate, consolidation and earthquake induced settlement occurred at the raft center is presented in figure 5.45 for different pile numbers.

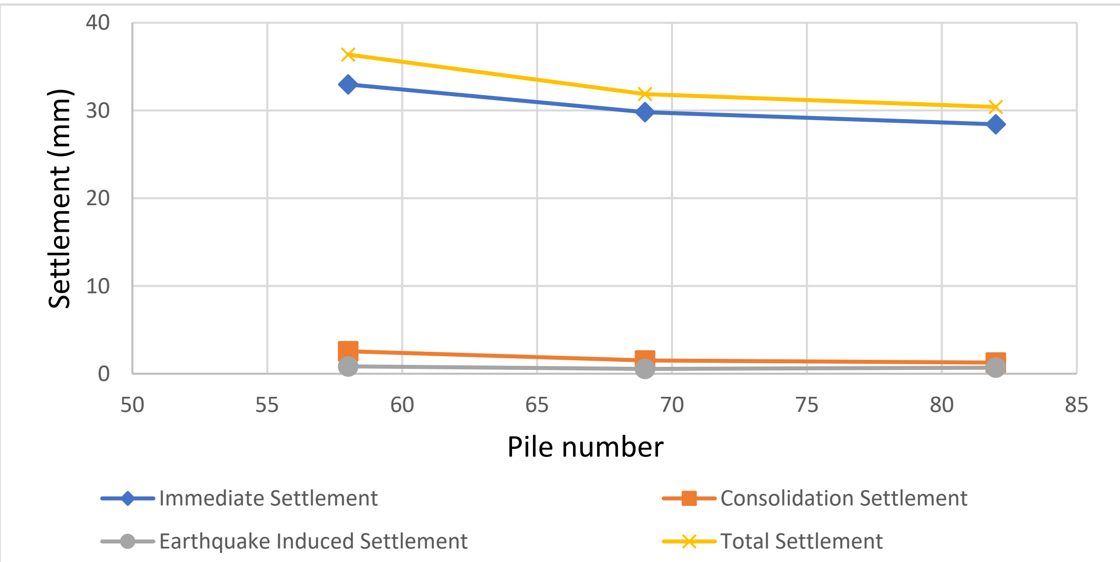

Figure 5.45: Effect of pile numbers on settlement values at raft center of Piled raft with 3m raft thickness and 1m diameter piles

From Figure 5.45 it is found that, with the increase of pile numbers, all the settlement (Immediate, consolidation, earthquake induced and total settlement) decreases. The higher number of piles helps the raft to transfer some percentages of the loads to the piles so the settlement below raft is reduced. Figure 5.45 also shows that the earthquake induced settlement and consolidation settlement is minor compared to the immediate settlement. The immediate settlement governs here as the soil beneath is raft is granular soil. The soil layer of 27m to 30m is responsible for consolidation settlement. The consolidation settlement is very minor compared to un-piled raft as a certain percentage of load is transferred through the piles to pile toe at 60m below existing ground level where the soil type is very dense sand.

5.2.2.2 Settlement at raft corner

A higher number of piles can reduce the settlement values at raft corner as well. Figure 5.46 shows the effect of pile numbers on the settlement values at raft corners. From Figure 5.46, it is observed that the immediate settlement is again the governing settlement at the raft corner.

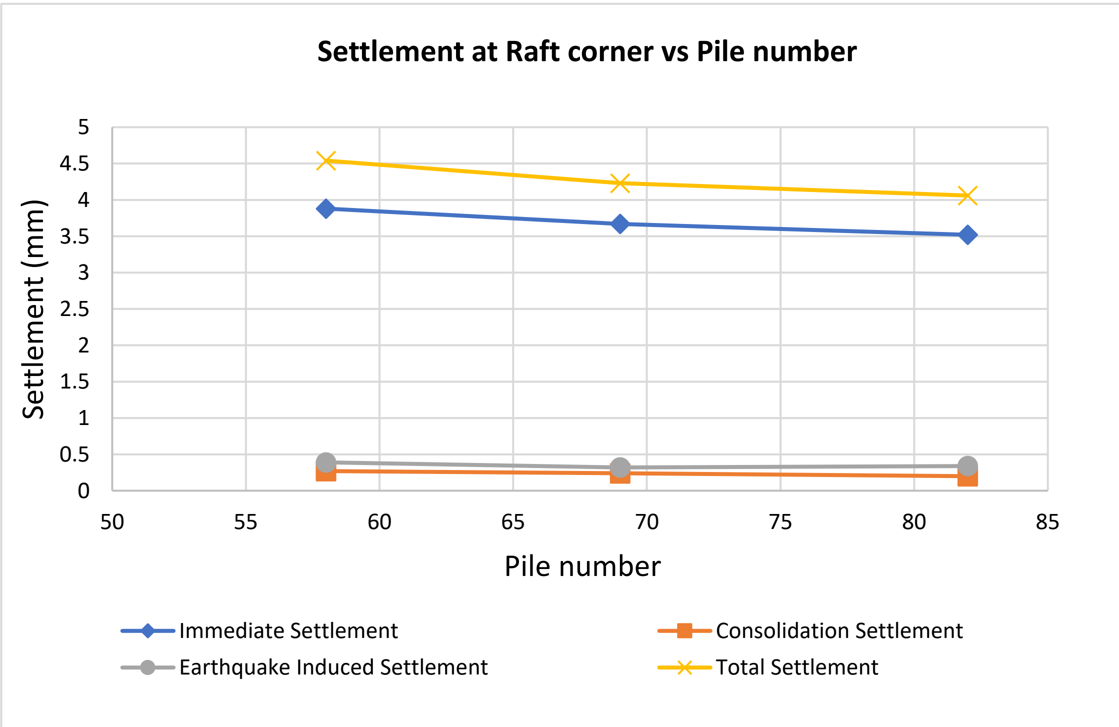

Figure 5.46: Effect of pile numbers on settlement values at raft corner of Piled raft with 3m raft thickness and 1m diameter piles

5.2.2.3 Differential settlement

Figure 5.47 indicates that the differential settlement of piled raft foundation decreases with the increase in pile numbers. A certain of load is transferred to piles which helps a piled raft foundation to reduce the differential settlement. In cases when un-piled raft is not sufficient to limit the differential settlement, raft with some piles could be the optimized solution instead of pile only foundation type. Figure 5.47 shows the relation between pile numbers and differential settlement.

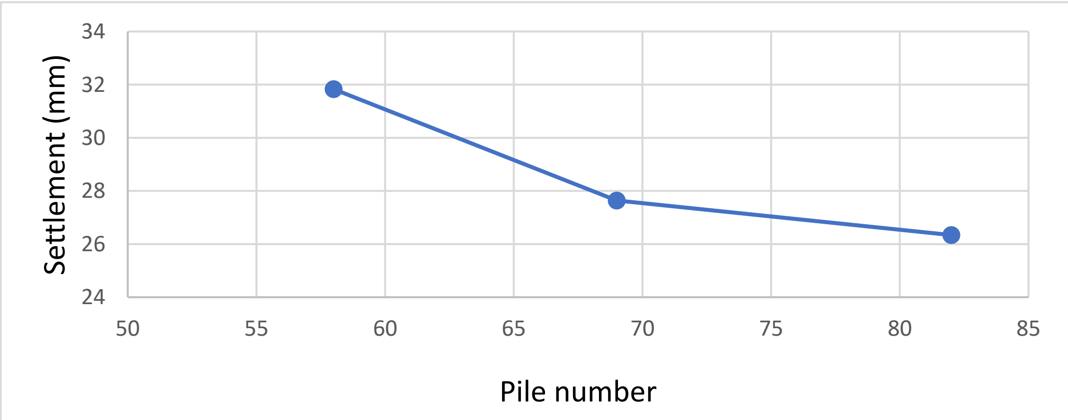

Figure 5.47: Effect of pile numbers on differential settlement values of Piled raft with 3m raft thickness and 1m diameter piles

5.2.2.4 Angular distortion

As Figure 5.48 shows, angular distortion of piled raft foundation decreases with the increase in pile numbers for the same reason that reduces the differential settlement.

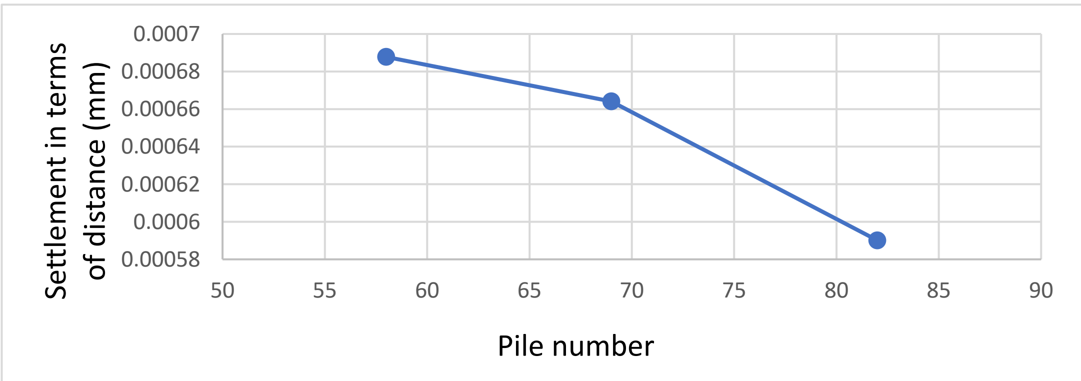

Figure 5.48: Effect of pile numbers on angular distortion values of Piled raft with 3m raft thickness and 1m diameter piles

5.2.2.5 Maximum developed stress at raft

The value of maximum stress developed at the raft decreases as the pile number increases. Due to increase in pile numbers, the percent of load shared by piles increases. For increasing the percentages of load shared by piles, the stress below raft is reduced to some extent preventing it from local stress concentration on the raft center.

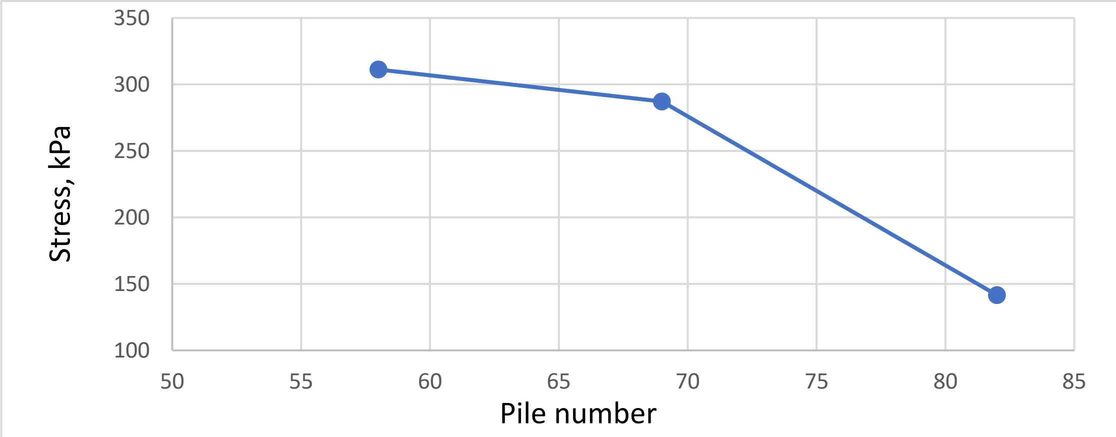

Figure 5.49: Effect of pile numbers on maximum developed stress values of Piled raft with 3m raft thickness and 1m diameter piles

5.2.2.6 Center pile reaction

The reaction of the center piles decreases with the increase in pile numbers for the same reason that reduces the maximum developed stress at raft center.

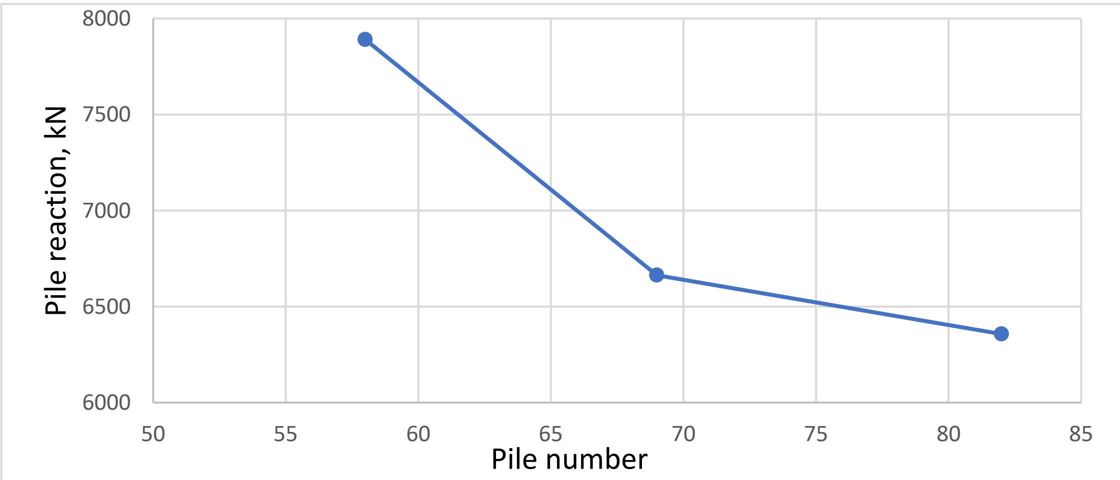

Figure 5.50: Effect of pile numbers on center pile reaction values of Piled raft with 3m raft thickness and 1m diameter piles

5.2.2.7 Corner pile reaction

Figure 5.51 shows that the reaction of corner piles also decreases with the increase in pile numbers.

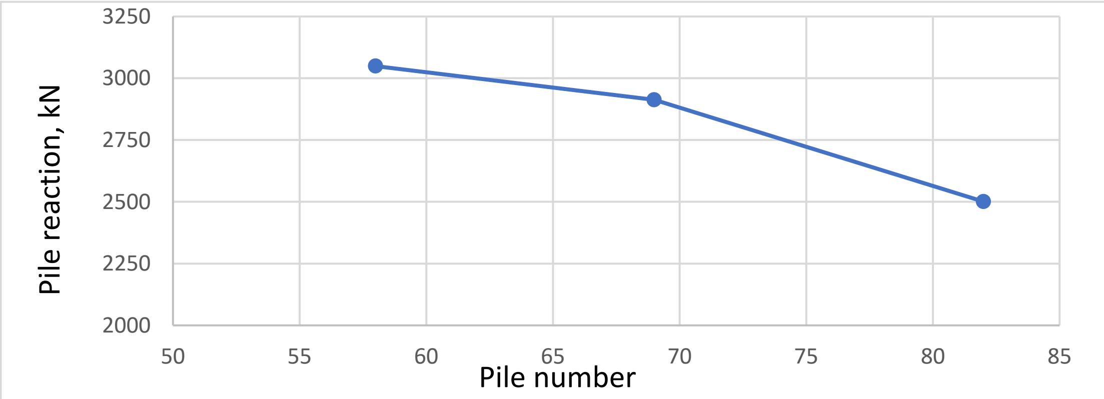

Figure 5.51: Effect of pile numbers on corner pile reaction values of Piled raft with 3m raft thickness and 1m diameter piles

5.2.2.8 Settlement of piles

Figure 5.52 shows that the pile number does not significantly affect the settlement value of the center pile. Center piles are not likely to settle much (total settlement ranges between 7-9mm) as pile tips are rested at 60m below existing ground level where the soil is very dense sandy layer. However, the settlement value of the corner piles is too little to analyze and hence it is ignored in this study.

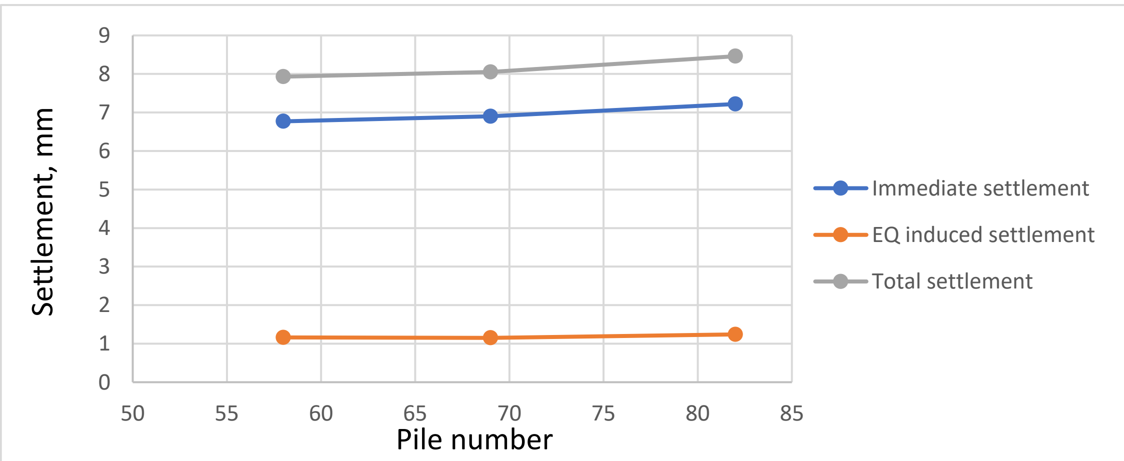

Figure 5.52: Effect of pile numbers on center pile settlement values of Piled raft with 3m raft thickness and 1m diameter piles

5.2.2.9 Maximum bending moment of center piles

The maximum bending moment of center piles increases as the pile number increases upto 69 piles. Beyond 69 piles, it starts to reduce. Figure 5.53 shows the effect of pile numbers on the maximum bending moment values of center piles.

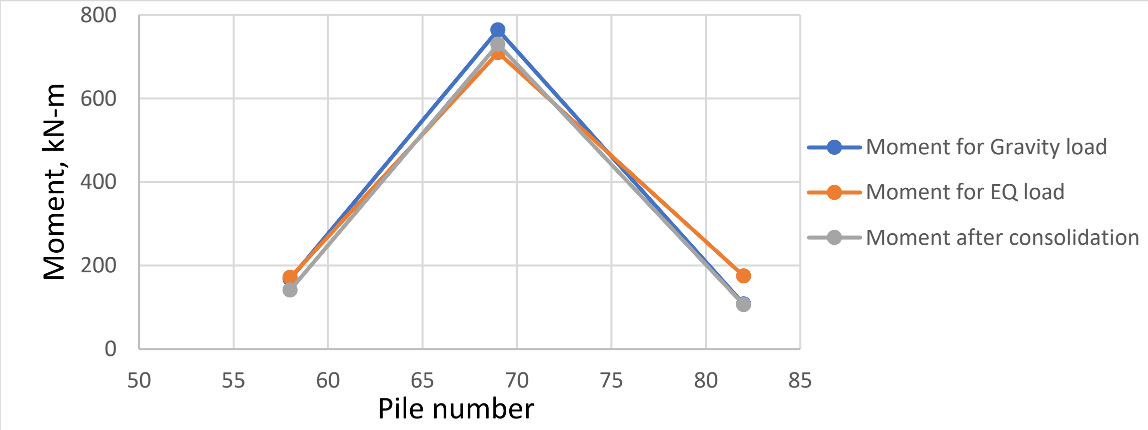

Figure 5.53: Effect of pile numbers on center pile maximum bending moment values of Piled raft with 3m raft thickness and 1m diameter piles

5.2.2.10 Maximum bending moment of corner piles

Figure 5.54 shows the effect of pile numbers on the maximum bending moment values of corner piles. Except for 69 nos. piles, maximum bending moment of corner piles decreases with the increase in pile numbers.

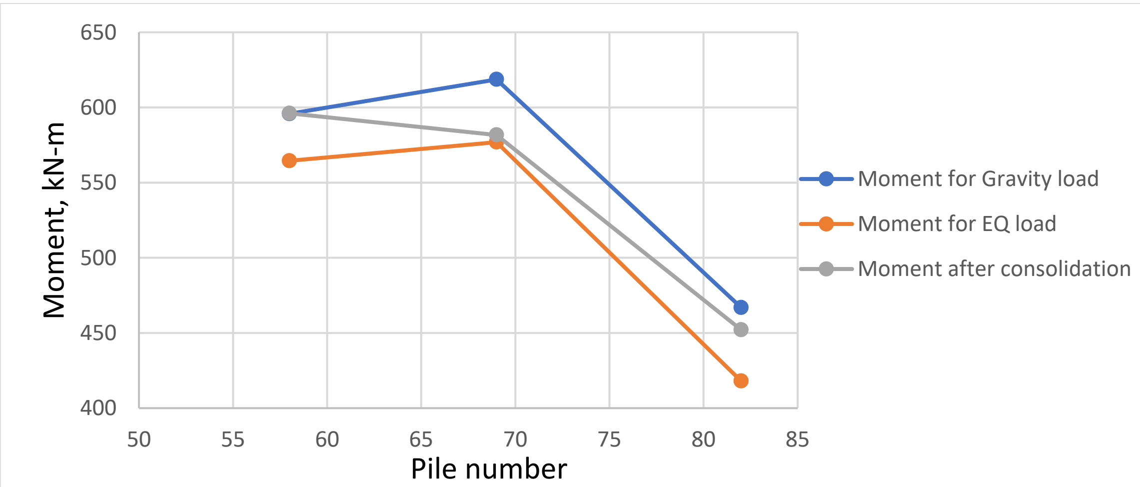

Figure 5.54: Effect of pile numbers on corner pile bending maximum moment values of Piled raft with 3m raft thickness and 1m diameter piles

5.2.2.11 Maximum shear force of center piles

The maximum shear force of center piles increases as the pile number increases upto 69 piles. Beyond 69 piles, it starts to reduce. Figure 5.55 shows the effect of pile numbers on the maximum shear force values of center piles.

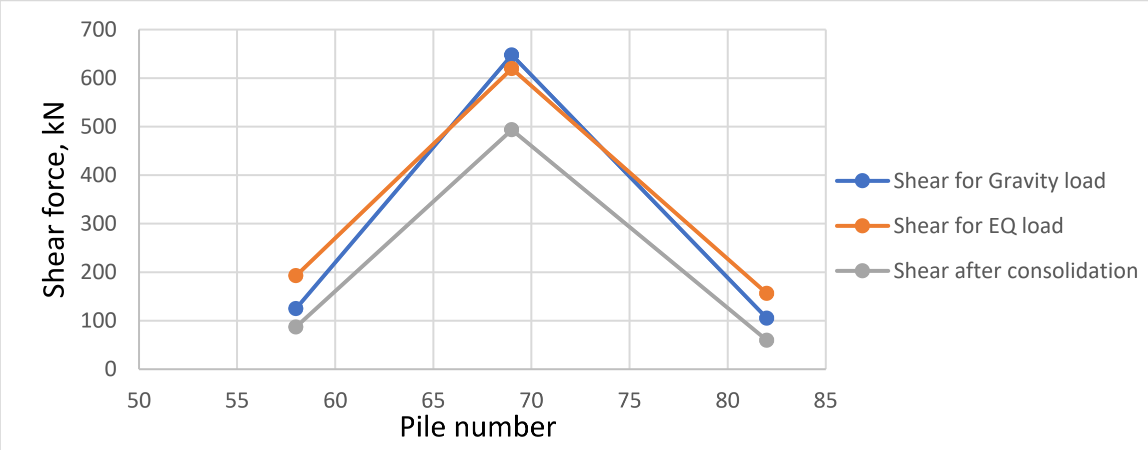

Figure 5.55: Effect of pile numbers on center pile maximum shear force values of Piled raft with 3m raft thickness and 1m diameter piles

5.2.2.12 Maximum shear force of center piles

Figure 5.56 shows the effect of pile numbers on the maximum bending moment values of corner piles. Maximum shear force of corner piles decreases with the increase in pile numbers.

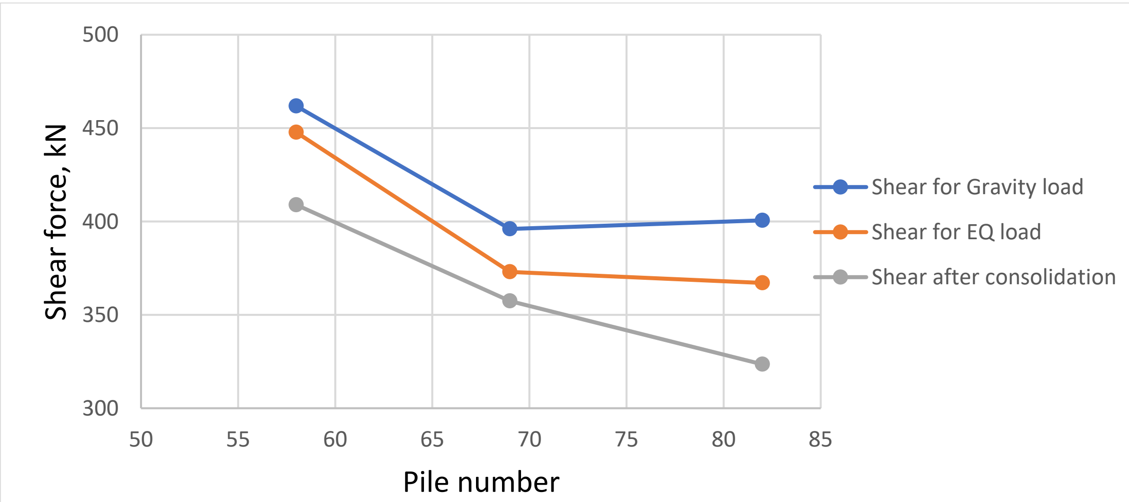

Figure 5.56: Effect of pile numbers on corner pile maximum shear force values of Piled raft with 3m raft thickness and 1m diameter piles

5.2.2.13 Lateral deflection of center and corner piles (along x-direction)

Pile number does not affect the lateral deflection value of the piles below the rafts along x-direction. The deflection along the x-direction of both the center and corner piles remains in between 23.2-23.7 mm for different pile numbers.

5.2.2.14 Maximum moments of raft

Maximum raft moment M11 and M12 decreases as the pile number increases. But M12 decreases upto 69 nos. piles. Beyond 69 piles, M22 value starts to increase.

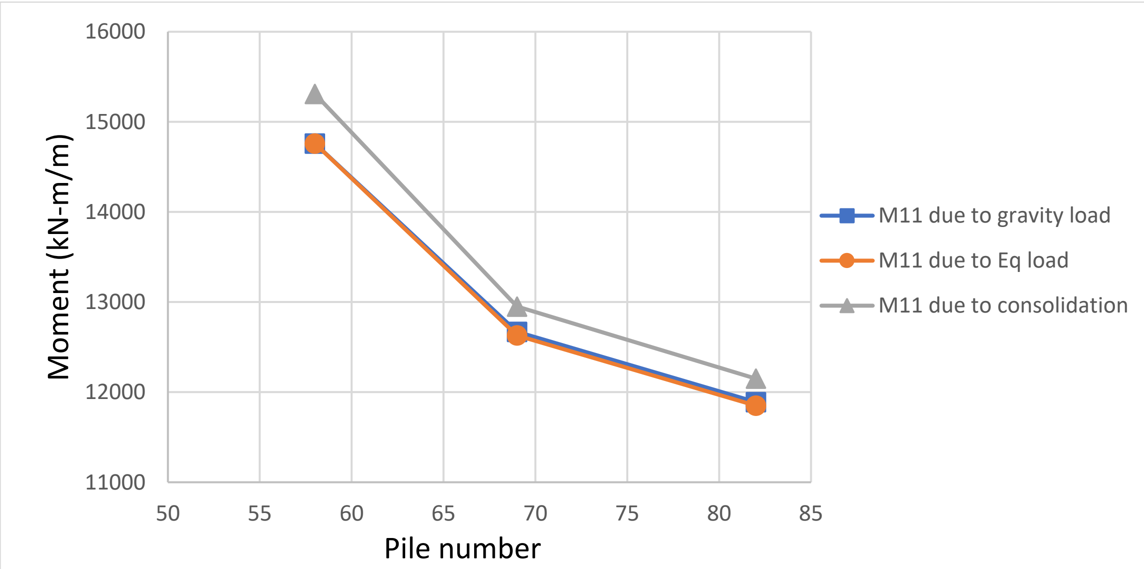

(a)

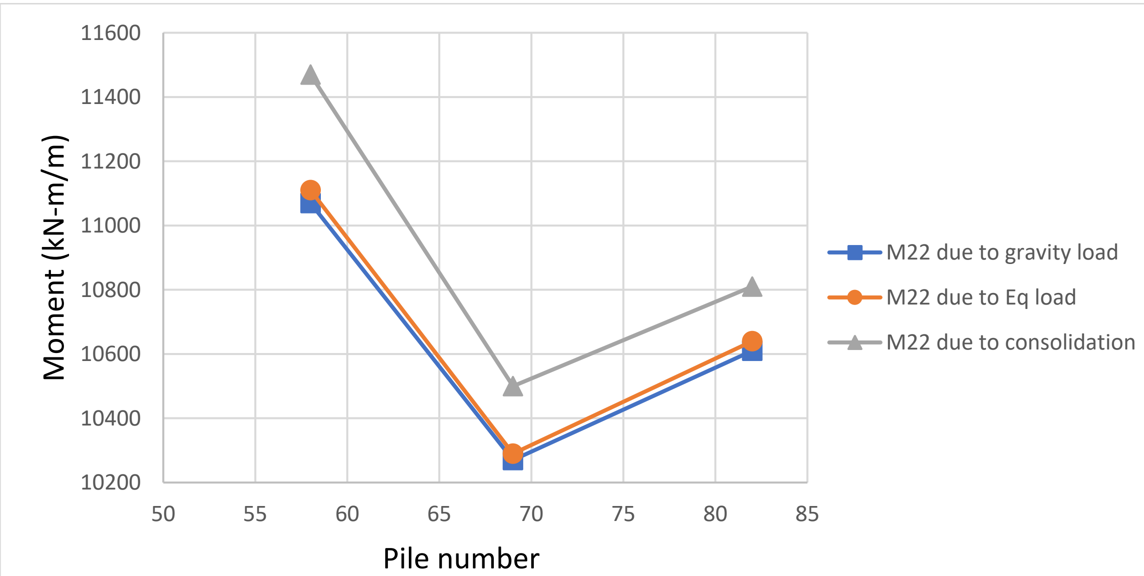

(b)

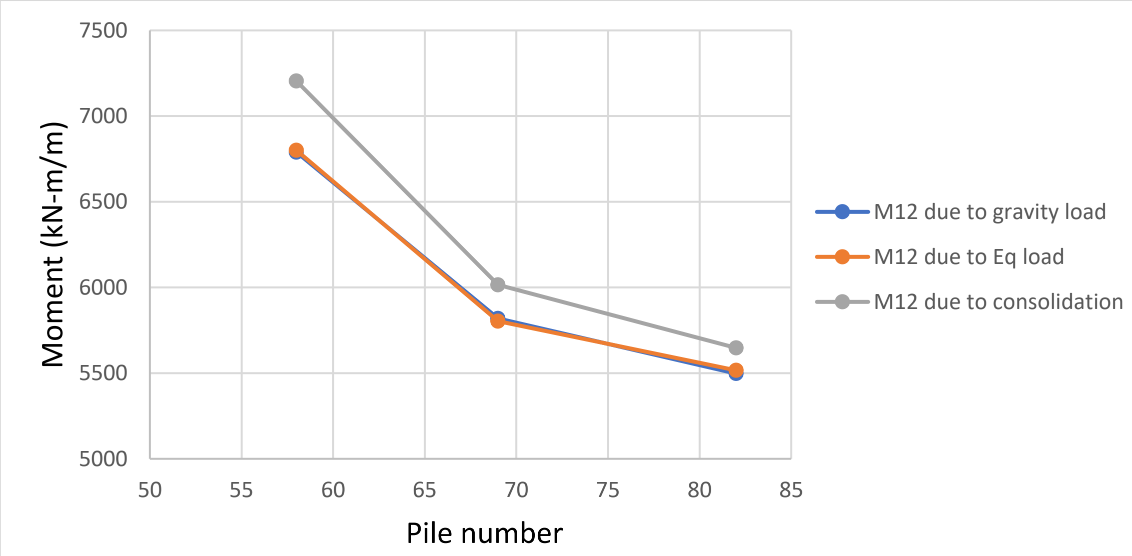

(c)

Figure 5.57: Effect of pile numbers on raft maximum moment values of Piled raft with 3m raft thickness and 1m diameter piles. (a) M11, (b) M22, (c) M12

5.2.2.15 Maximum shear forces of raft

The maximum shear force Q23 and Q13 of raft increases as the pile number increases upto 69 piles. Beyond 69 piles, it starts to reduce. The shear force Q12 shows the opposite behavior. Figure 5.58 shows the effect of pile numbers on the maximum shear force values of center piles.

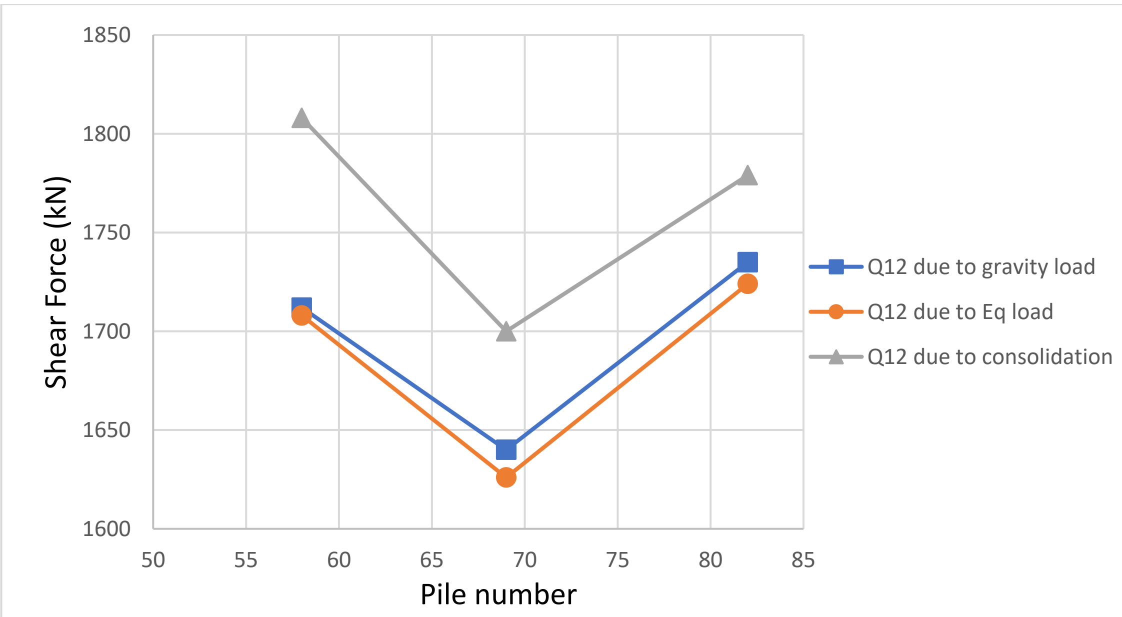

(a)

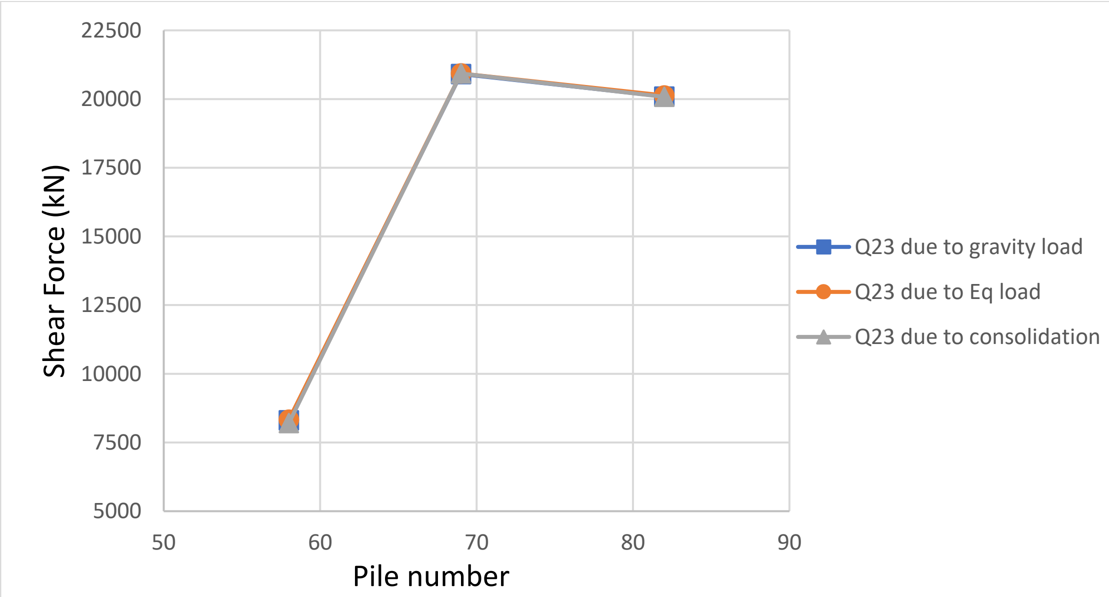

(b)

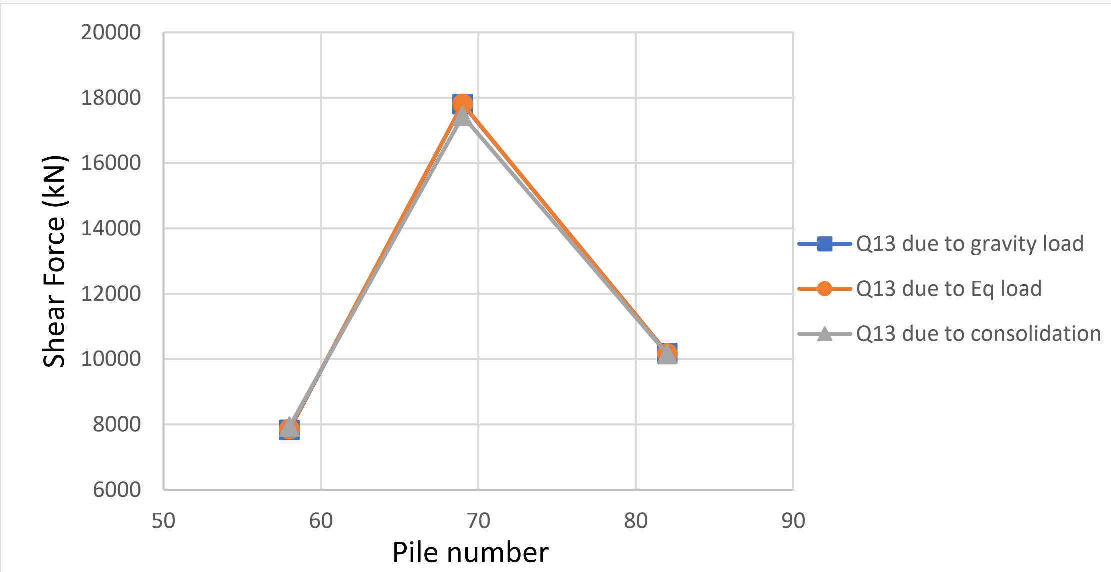

(c)

Figure 5.58: Effect of pile numbers on raft maximum shear force values of Piled raft with 3m raft thickness and 1m diameter piles. (a) Q12, (b) Q23, (c) Q123

5.2.2.16 Maximum moments of retaining wall

The effect of pile numbers on the retaining wall maximum moments is very minor. Figure 5.59 shows that the maximum moments of retaining wall slightly decreases as the pile number increases.

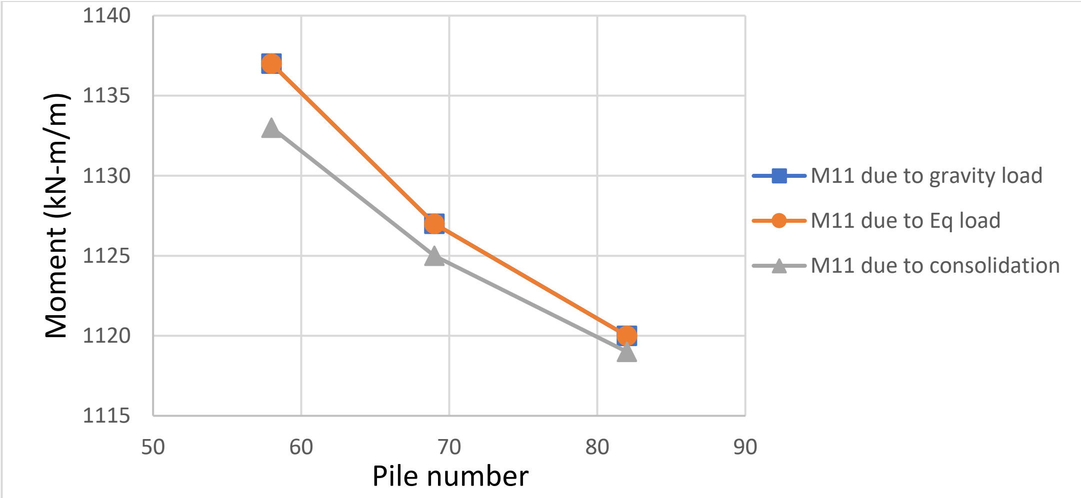

(a)

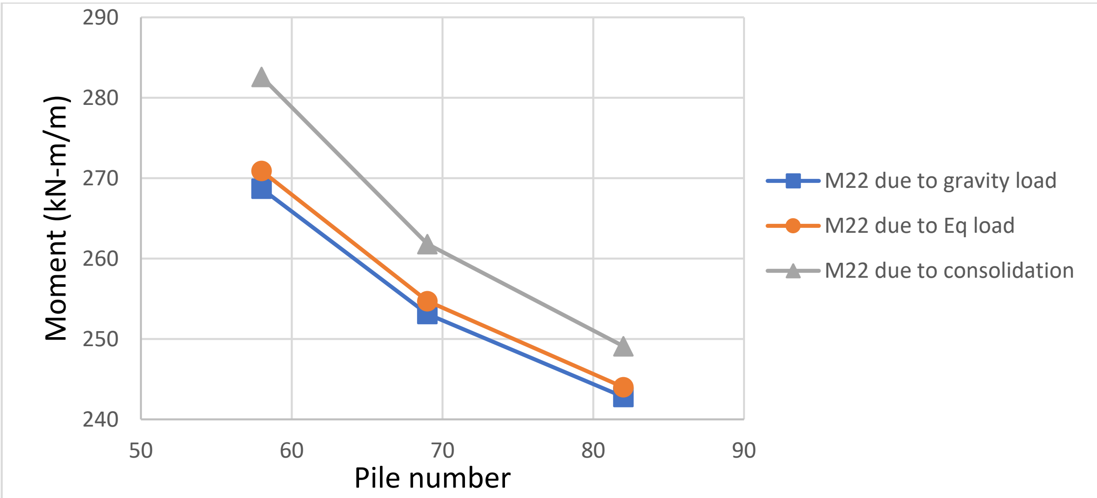

(b)

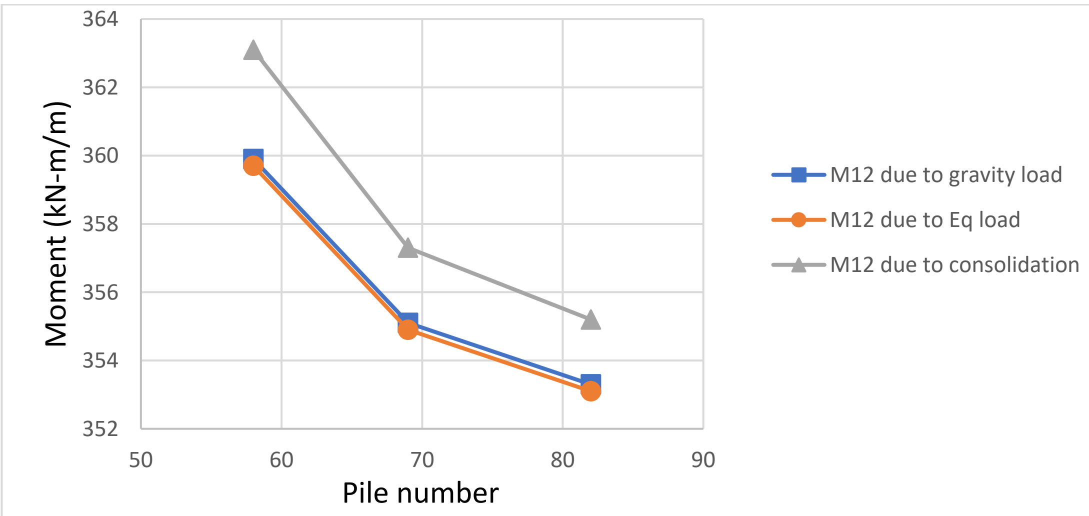

(c)

Figure 5.59: Effect of pile numbers on retaining wall maximum moment values of Piled raft with 3m raft thickness and 1m diameter piles. (a) M11, (b) M22, (c) M12

5.2.2.17 Maximum shear forces of retaining wall

The maximum shear force Q12 and Q13 of raft decreases as the pile number increases upto 69 piles. Beyond 69 piles, it starts to increase. The shear force Q23 decreases with the increase in pile numbers. Figure 5.60 shows the effect of pile numbers on the maximum shear force values of center piles.

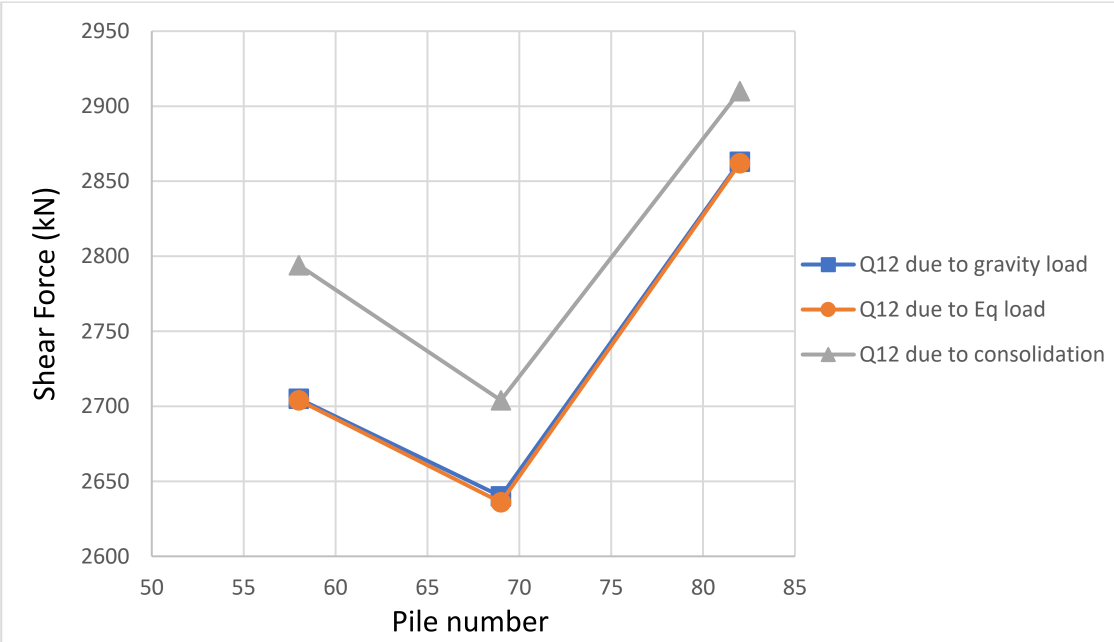

(a)

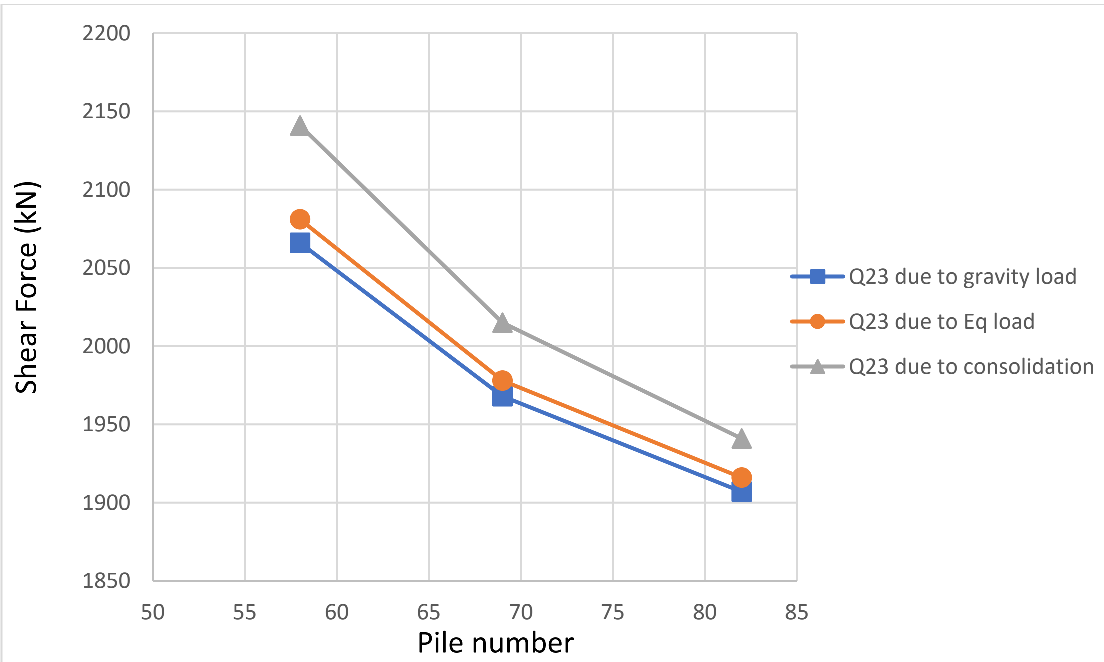

(b)

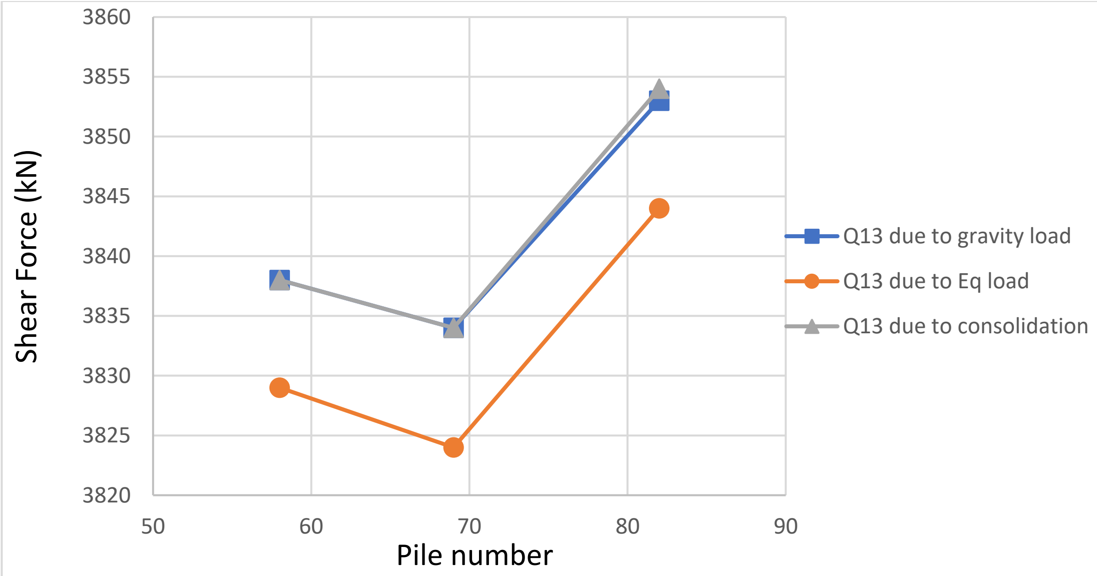

(c)

Figure 5.60: Effect of pile numbers on retaining wall maximum shear force values of Piled raft with 3m raft thickness and 1m diameter piles. (a) Q12, (b) Q23, (c) Q13

5.2.2.18 Maximum normal forces of retaining wall

The normal force values N1 and N2 of retaining wall decrease with the increase in pile numbers for piled raft foundation system. Figure 5.61 shows the relation between pile numbers and retaining wall normal forces.

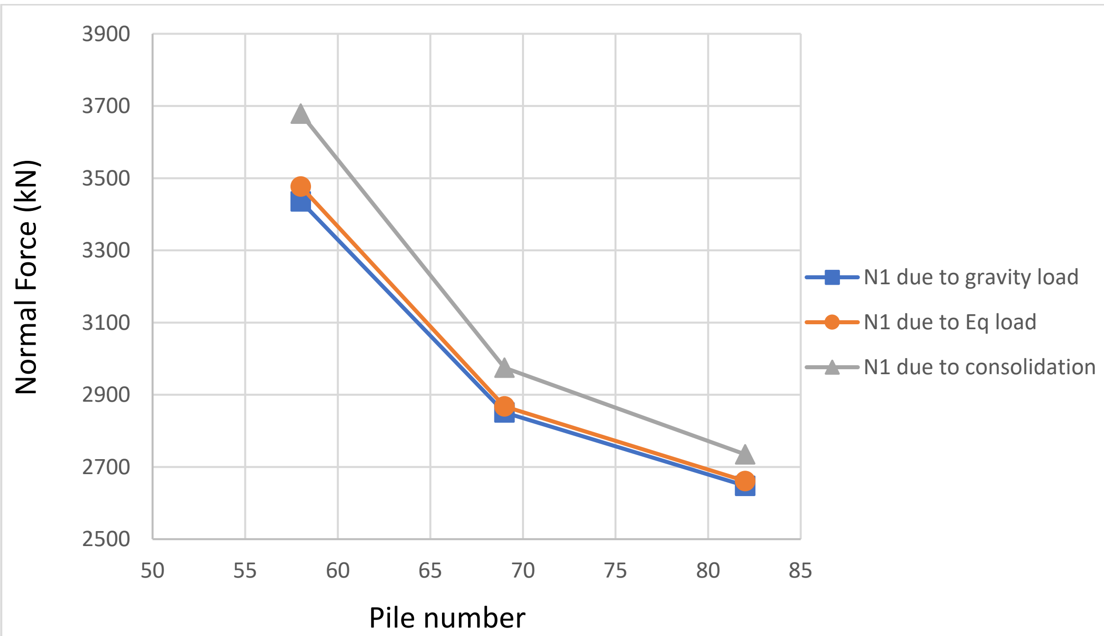

(a)

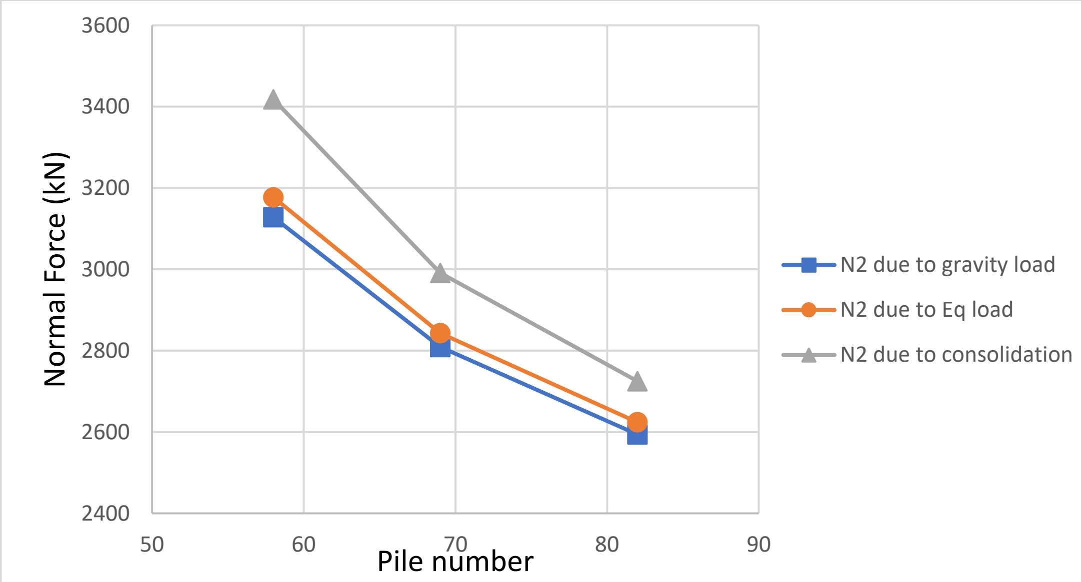

(b)

Figure 5.61: Effect of pile numbers on retaining wall maximum normal force values of Piled raft with 3m raft thickness and 1m diameter piles. (a) N1, (b) N2

5.2.2.19 Lateral deflection of retaining wall

The effect of pile numbers on the retaining wall lateral deflection is very negligible. Figure 5.62 shows that the lateral defection along x-direction of retaining wall slightly decreases as the pile numbers increases. However, the lateral defection along y-direction decreases to some extent with the increase in pile numbers.

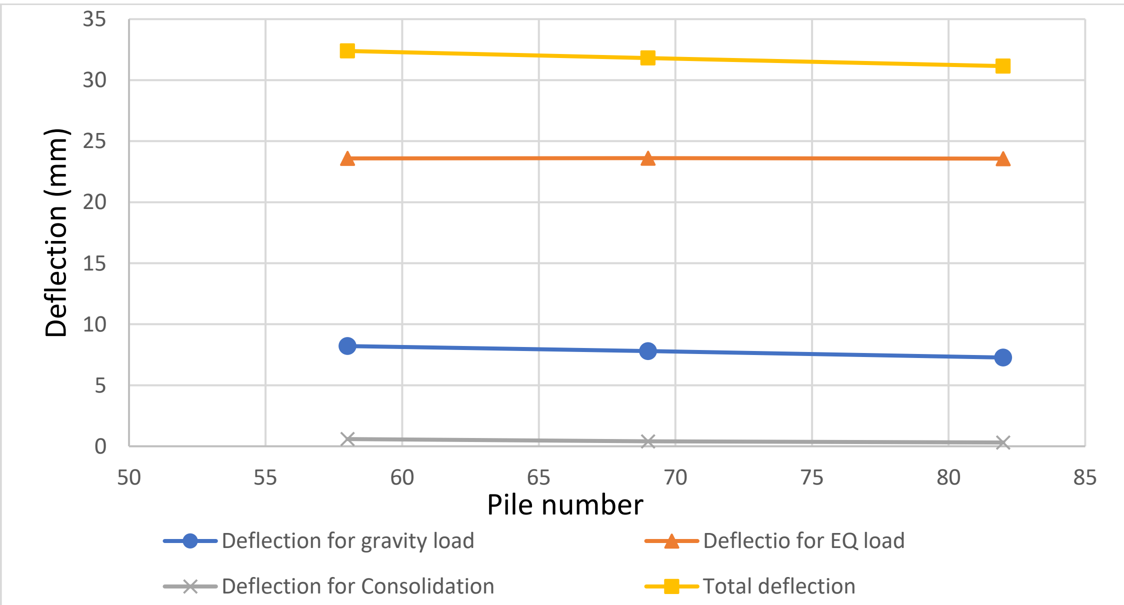

(a)

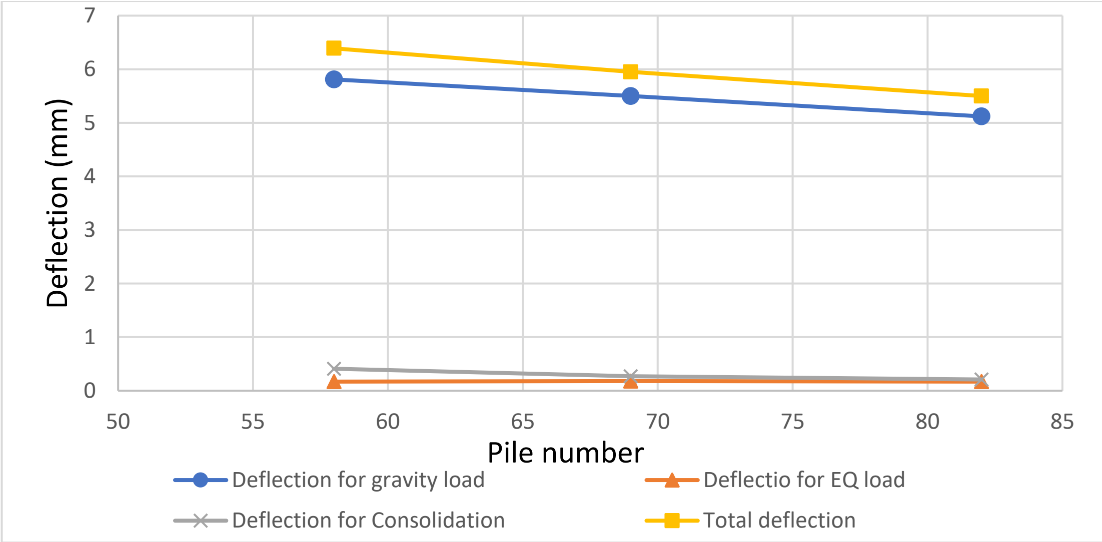

(b)

Figure 5.62: Effect of pile numbers on retaining wall lateral deflection of Piled raft with 3m raft thickness and 1m diameter piles. (a) x-dir deflection, (b) y-dir deflection

5.2.2.20 Load distribution between raft and piles

The percent of load shared by the piles increases with the increase in pile numbers. In other words, the percent of load shared by the raft decreases with the increase in pile numbers. Higher number of piles can carry additional load from the superstructure. However, from the parametric studies, it is found that increasing pile number does not mean that the reduction in settlement further increase, thus beyond some point the settlement curve tends to behave as a straight line.

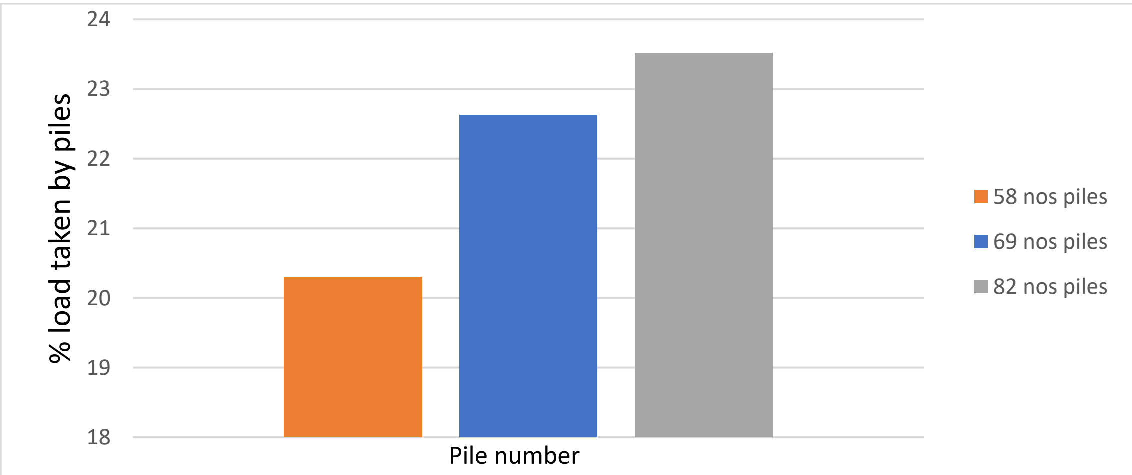

Figure 5.63: Effect of pile numbers on % of load sharing of piled rafts with 3m raft thickness and 1m diameter piles

The effects of pile numbers on different geotechnical and structural parameters have been discussed above for only the piled rafts with 3m raft thickness and 1m diameter piles. Piled rafts having different raft thickness and pile diameters, show the same impacts of pile numbers and hence it is not mentioned here. Only exceptions are observed as follows:

1. The maximum developed stress below raft for the piled raft of 69 nos. piles of 1.2m and 1.5m diameter is higher than the piled rafts of 58 nos. piles of 1.2m and 1.5m diameter and 82 nos. piles of 1.2m and 1.5m diameter.
2. Raft bending moment M22 value for the piled rafts of 2.5m thick raft increases with the increase in pile numbers.

However, the effects of pile numbers on the other piled raft foundations are mentioned in Appendix-3.

5.2.3 Effect of Pile diameter

5.2.3.1 Settlement at raft center

Total settlement including immediate, consolidation and earthquake induced settlement occurred at the raft center is presented in Figure 5.64 for different pile diameters.

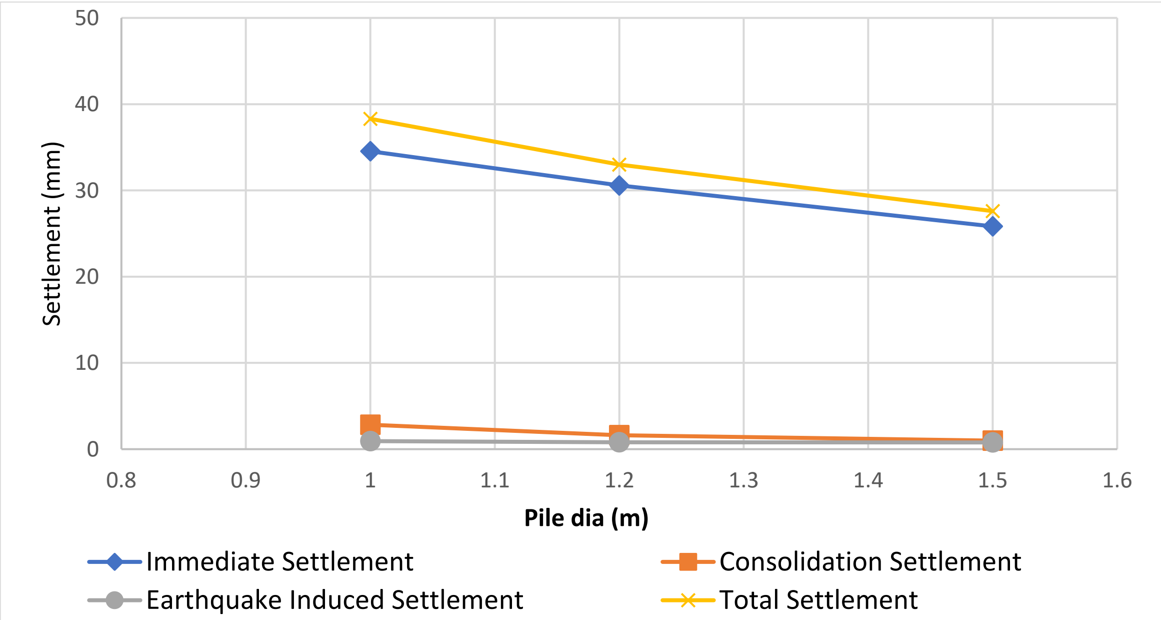

Figure 5.64: Effect of pile diameter on settlement values at raft center of Piled raft with 2.5m raft thickness and 58 nos. piles

From Figure 5.64 it is found that, with the increase of pile diameter, all the settlement (Immediate, consolidation, earthquake induced and total settlement) decreases. The large diameter piles help the raft to transfer some percentages of the loads to the piles so the settlement below raft is reduced. Figure 5.64 also shows that the earthquake induced settlement and consolidation settlement is minor compared to the immediate settlement. The immediate settlement governs here as the soil beneath is raft is granular soil. The soil layer of 27m to 30m is responsible for consolidation settlement. The consolidation settlement is very minor compared to un-piled raft as a certain percentage of load is transferred through the piles to pile toe at 60m below existing ground level where the soil type is very dense sand.

5.2.3.2 Settlement at raft corner

Larger diameter of piles can reduce the settlement values at raft corner as well. Figure 5.65 shows the effect of pile diameter on the settlement values at raft corners. From Figure 5.65, it is observed that the immediate settlement is again the governing settlement at the raft corner.

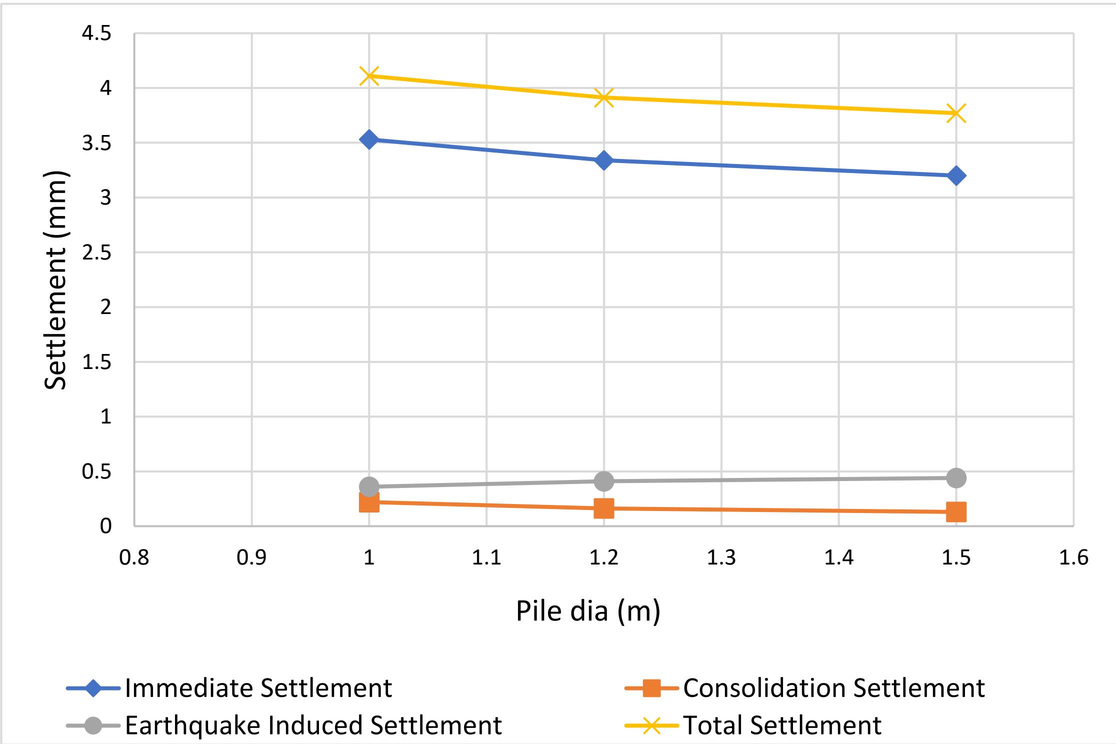

Figure 5.65: Effect of pile diameter on settlement values at raft corner of Piled raft with 2.5m raft thickness and 58 nos. piles

5.2.3.3 Differential settlement

Figure 5.66 indicates that the differential settlement of piled raft foundation decreases with the increase in pile diameters. A certain of load is transferred to piles which helps a piled raft foundation to reduce the differential settlement. In cases when un-piled raft and piled raft with small diameter pile is not sufficient to limit the differential settlement, raft with larger diameter piles could be the optimized solution instead of pile only foundation type. Figure 5.66 shows the relation between pile diameters and differential settlement.

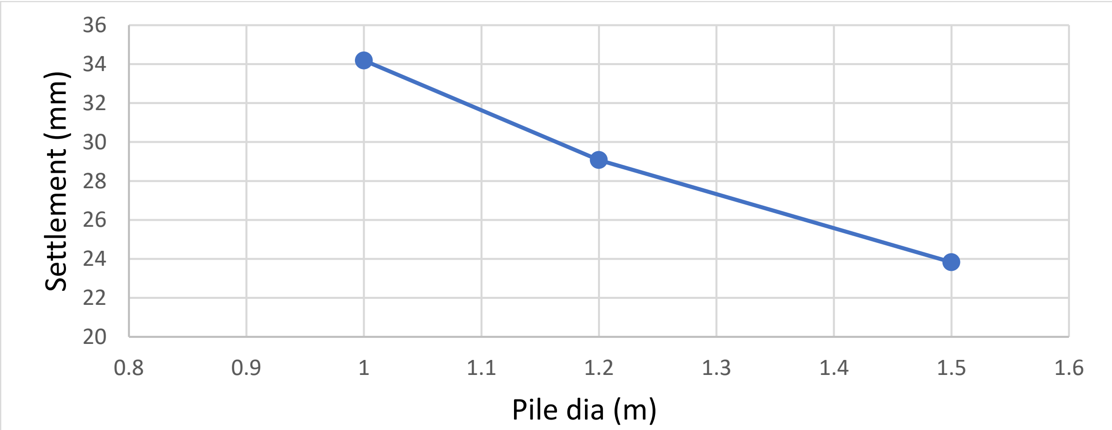

Figure 5.66: Effect of pile diameters on differential settlement values of Piled raft with 2.5m raft thickness and 58 nos. piles

5.2.3.4 Angular distortion

As Figure 5.67 shows, angular distortion of piled raft foundation decreases with the increase in pile diameters for the same reason that reduces the differential settlement.

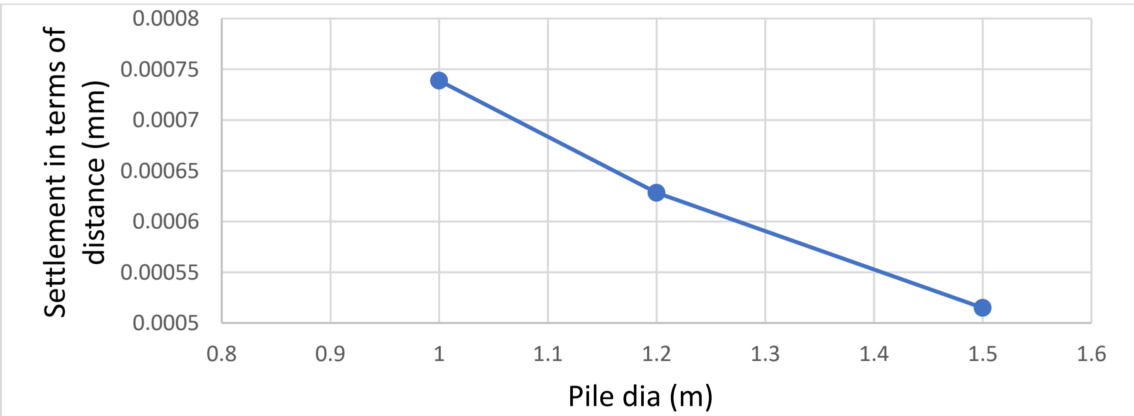

Figure 5.67: Effect of pile diameters on angular distortion values of Piled raft with 2.5m raft thickness and 58 nos. piles

5.2.3.5 Maximum developed stress at raft

The value of maximum stress developed at the raft decreases as the pile diameter increases. Due to increase in pile diameters, the percent of load shared by piles increases. For increasing the percentages of load shared by piles, the stress below raft is reduced to some extent preventing it from local stress concentration on the raft center.

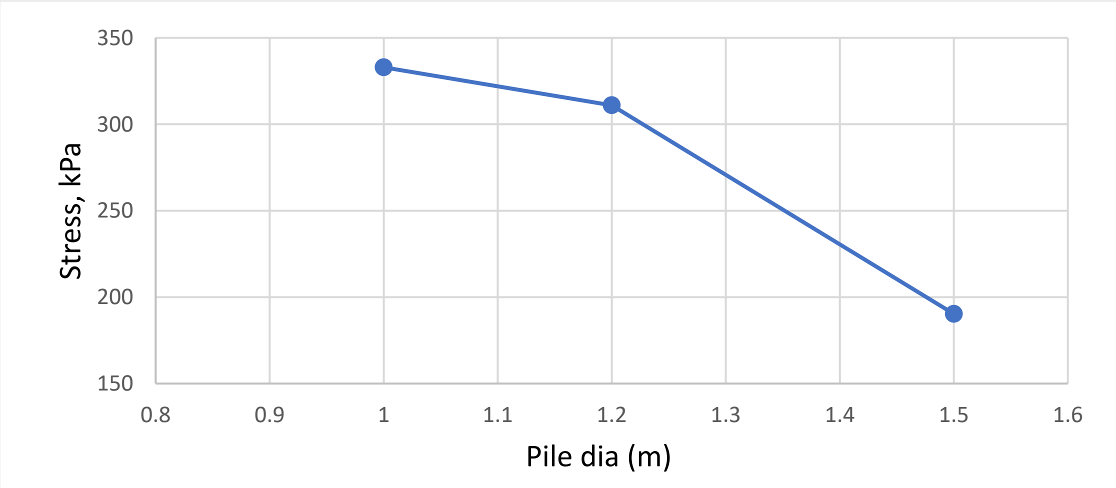

Figure 5.68: Effect of pile diameters on maximum developed stress values of Piled raft with 2.5m raft thickness and 58 nos. piles

5.2.3.6 Center pile reaction

Figure 5.69 shows that, the reaction of the center piles increases with the increase in pile diameters.

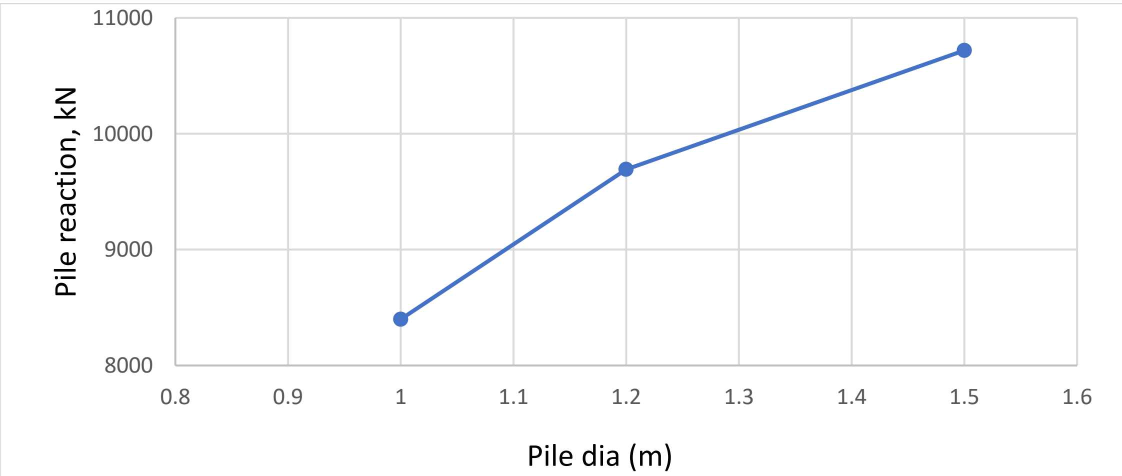

Figure 5.69: Effect of pile diameters on center pile reaction values of Piled raft with 2.5m raft thickness and 58 nos. piles

5.2.3.7 Corner pile reaction

Figure 5.70 shows, the reaction of corner piles also increases with the increase in pile diameters upto 1.2m diameter. Beyond 1.2m diameter, the reaction does not increase.

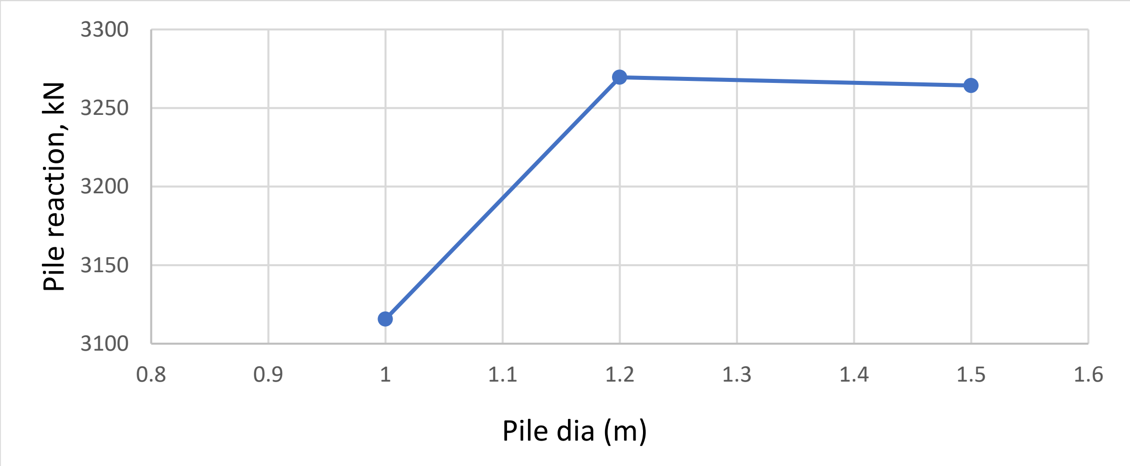

Figure 5.70: Effect of pile diameters on corner pile reaction values of Piled raft with 2.5m raft thickness and 58 nos. piles

5.2.3.8 Settlement of piles

Figure 5.71 shows that the pile diameter does not significantly affect the settlement value of the center pile. Center piles are not likely to settle much (total settlement ranges between 7-9mm) as pile tips are rested at 60m below existing ground level where the soil is very dense sandy layer. However, the settlement value of the corner piles is too little to analyze and hence it is ignored in this study.

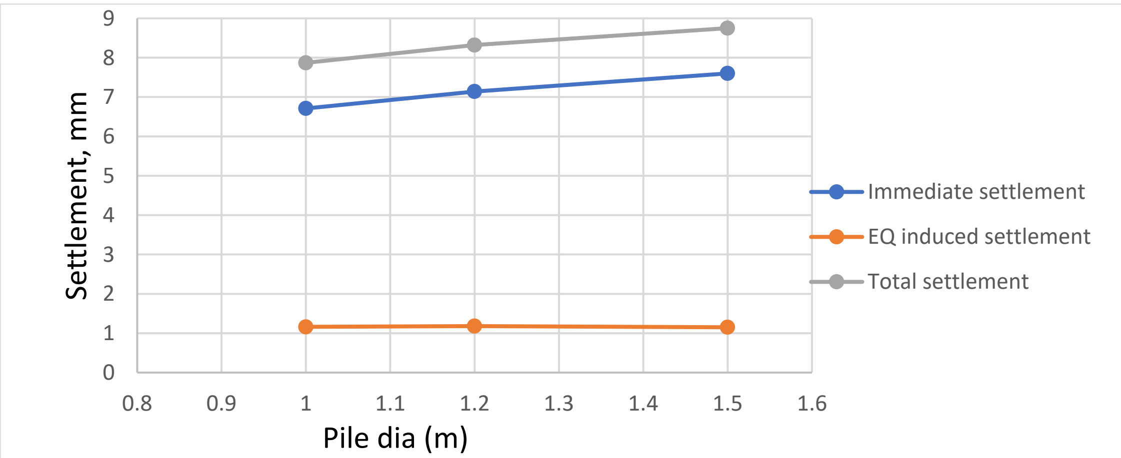

Figure 5.71: Effect of pile diameters on center pile settlement values of Piled raft with 2.5m raft thickness and 58 nos. piles

5.2.3.9 Maximum bending moment of center piles

The maximum bending moment of center piles increases as the pile diameter increases. Figure 5.72 shows the effect of pile diameters on the maximum bending moment values of center piles.

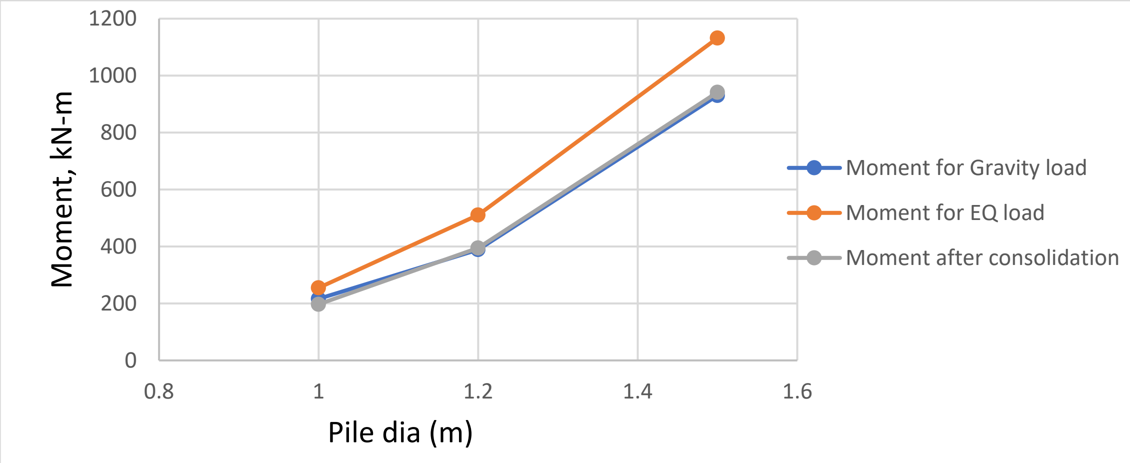

Figure 5.72: Effect of pile diameters on center pile maximum bending moment values of Piled raft with 2.5m raft thickness and 58 nos. piles

5.2.3.10 Maximum bending moment of corner piles

Figure 5.73 shows the effect of pile diameters on the maximum bending moment values of corner piles. Maximum bending moment of corner piles increases with the increase in pile diameters.

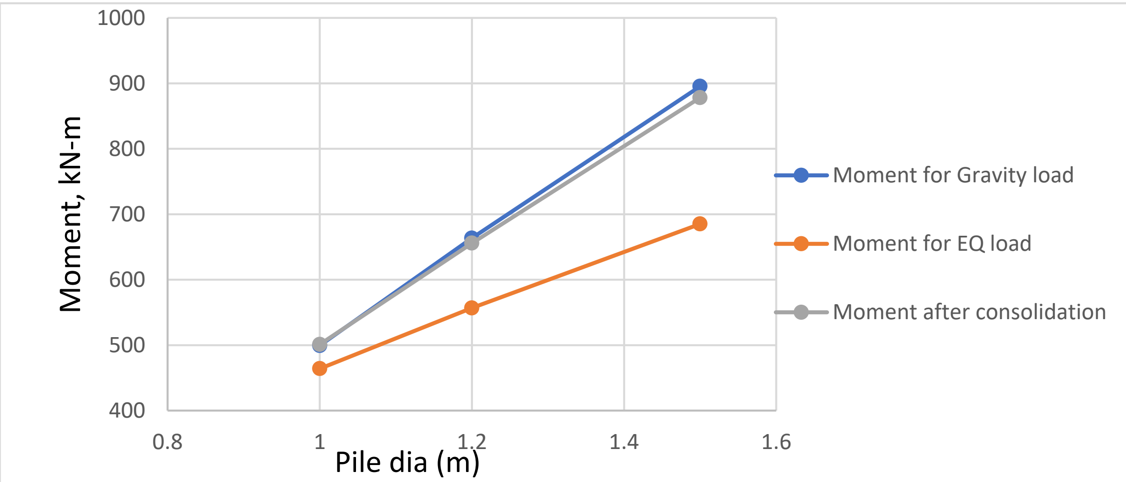

Figure 5.73: Effect of pile diameters on corner pile bending maximum moment values of Piled raft with 2.5m raft thickness and 58 nos. piles

5.2.3.11 Maximum shear force of center piles

The maximum shear force of center piles increases as the pile diameter. Figure 5.74 shows the effect of pile diameters on the maximum shear force values of center piles.

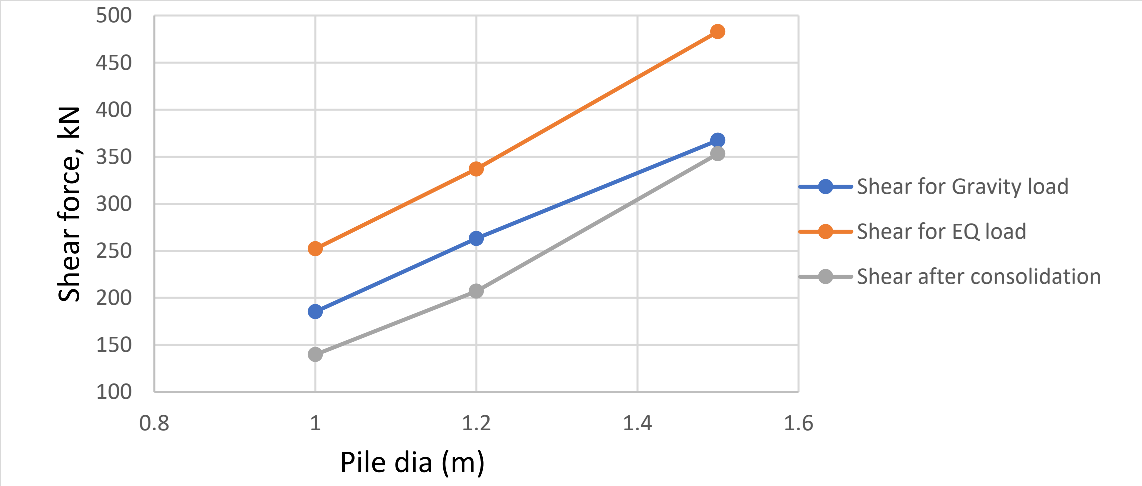

Figure 5.74: Effect of pile diameters on center pile maximum shear force values of Piled raft with 2.5m raft thickness and 58 nos. piles

5.2.3.12 Maximum shear force of center piles

Figure 5.75 shows the effect of pile diameters on the maximum bending moment values of corner piles. Maximum shear force of corner piles increases with the increase in pile diameters.

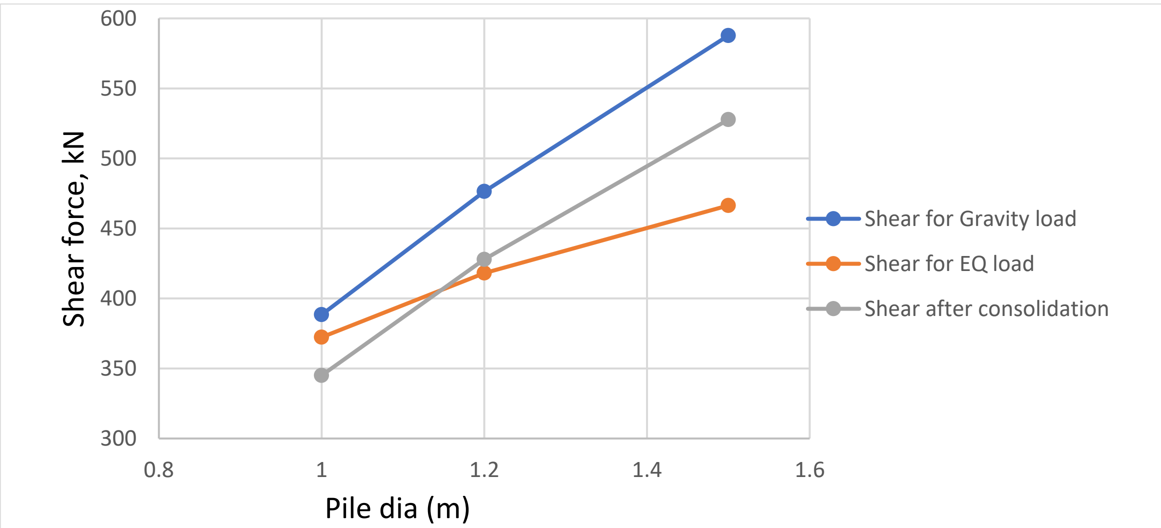

Figure 5.75: Effect of pile diameters on corner pile maximum shear force values of Piled raft with 2.5m raft thickness and 58 nos. piles

5.2.3.13 Lateral deflection of center and corner piles (along x-direction)

Pile diameter does not affect the lateral deflection value of the piles below the rafts along x-direction. The deflection along the x-direction of both the center and corner piles remains in between 23.2-23.6 mm for different pile diameters.

5.2.3.14 Maximum moments of raft

Figure 5.76 shows that maximum raft moments M11, M22 and M12 decreases as the pile diameter increases.

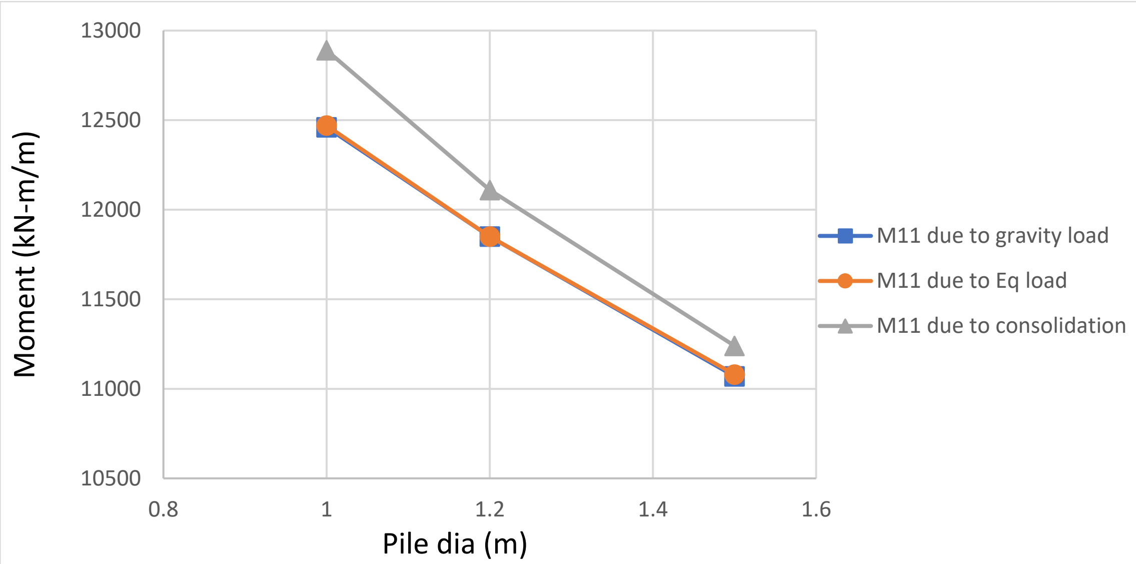

(a)

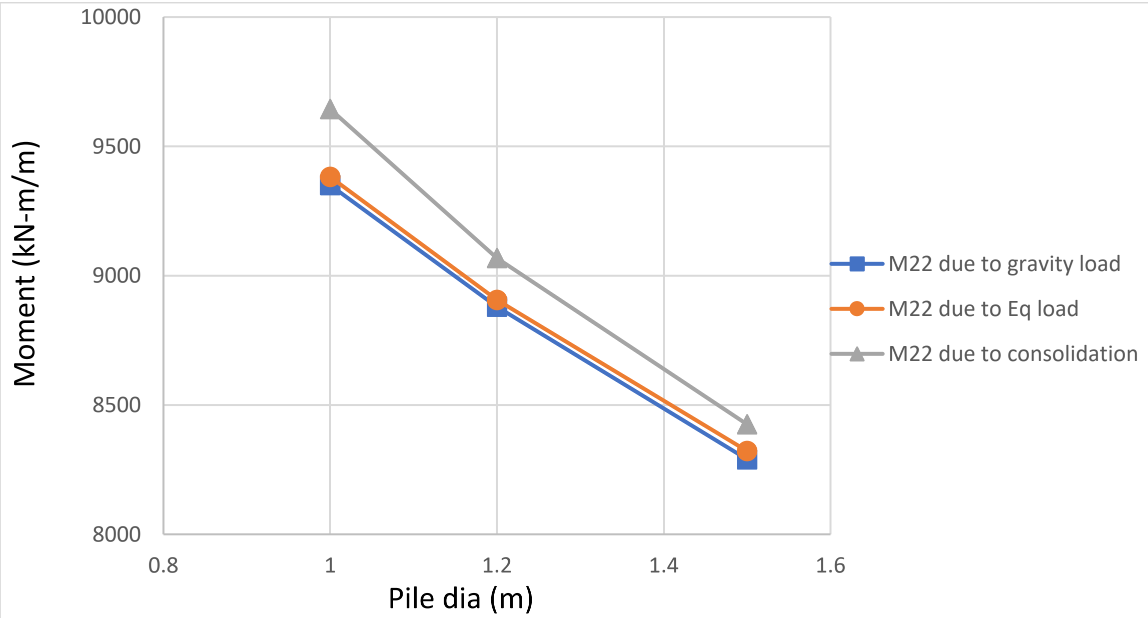

(b)

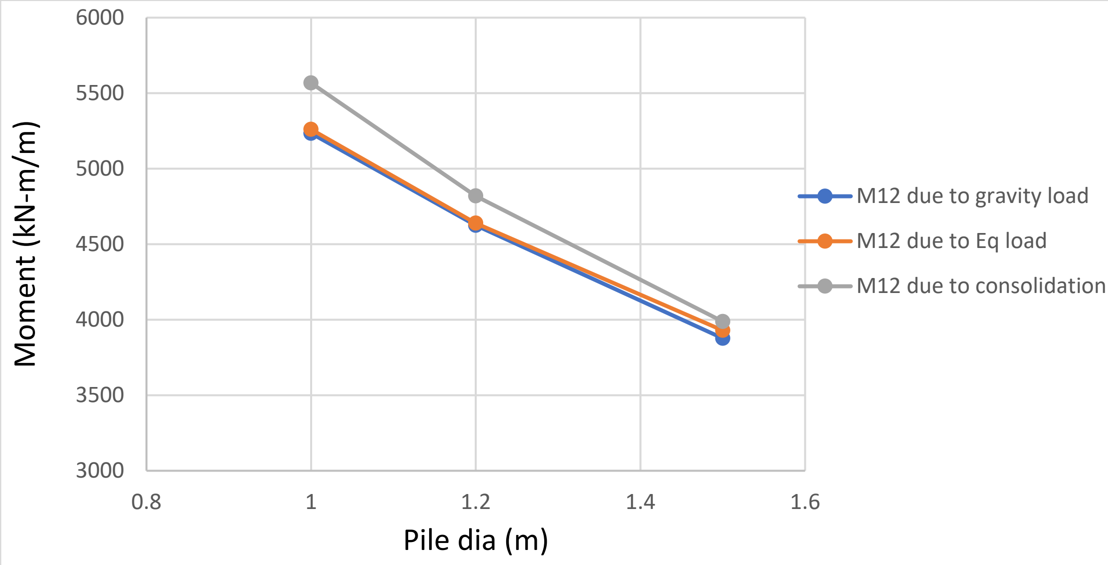

(c)

Figure 5.76: Effect of pile diameters on raft maximum moment values of Piled raft with 2.5m raft thickness and 58 nos. piles. (a) M11, (b) M22, (c) M12

5.2.3.15 Maximum shear forces of raft

The maximum shear force Q23 and Q13 of raft increases as the pile diameter increases. However, the shear force Q12 shows the opposite behavior. Figure 5.77 shows the effect of pile diameters on the maximum raft shear force values of center piles.

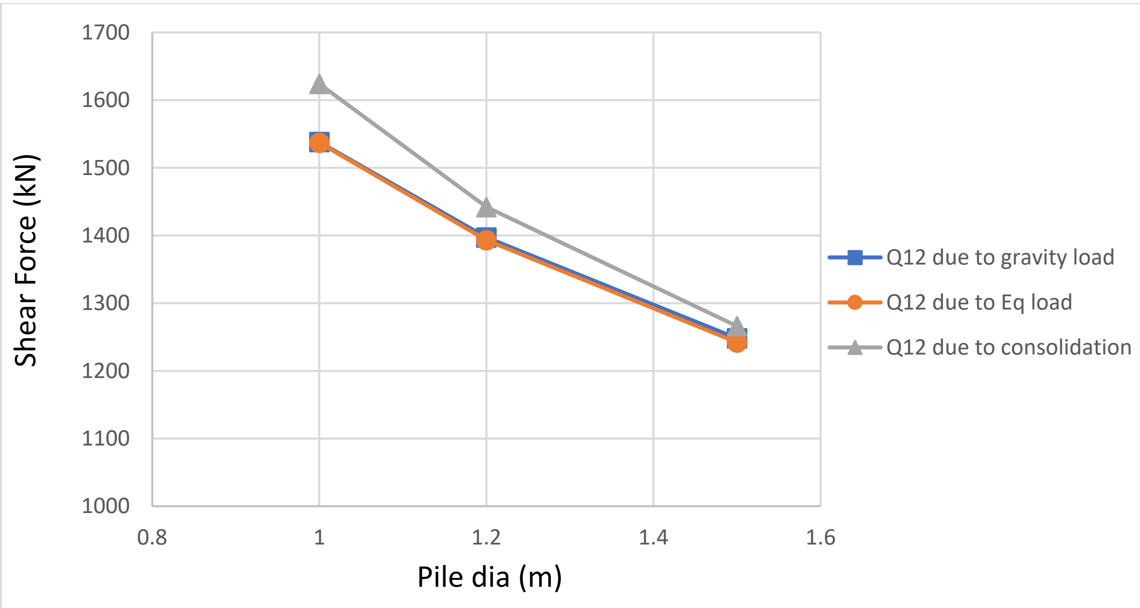

(a)

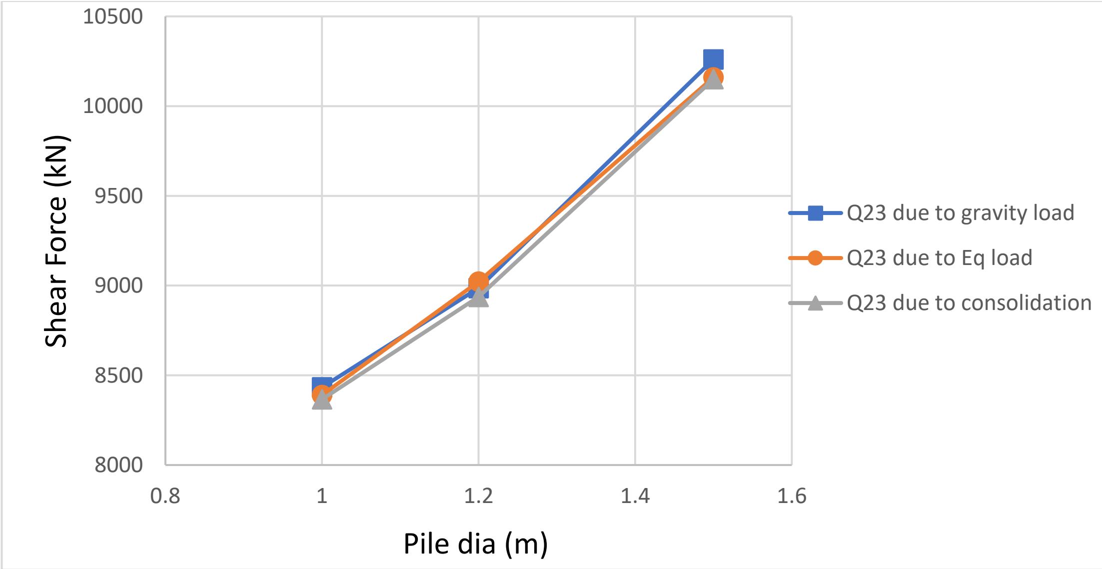

(b)

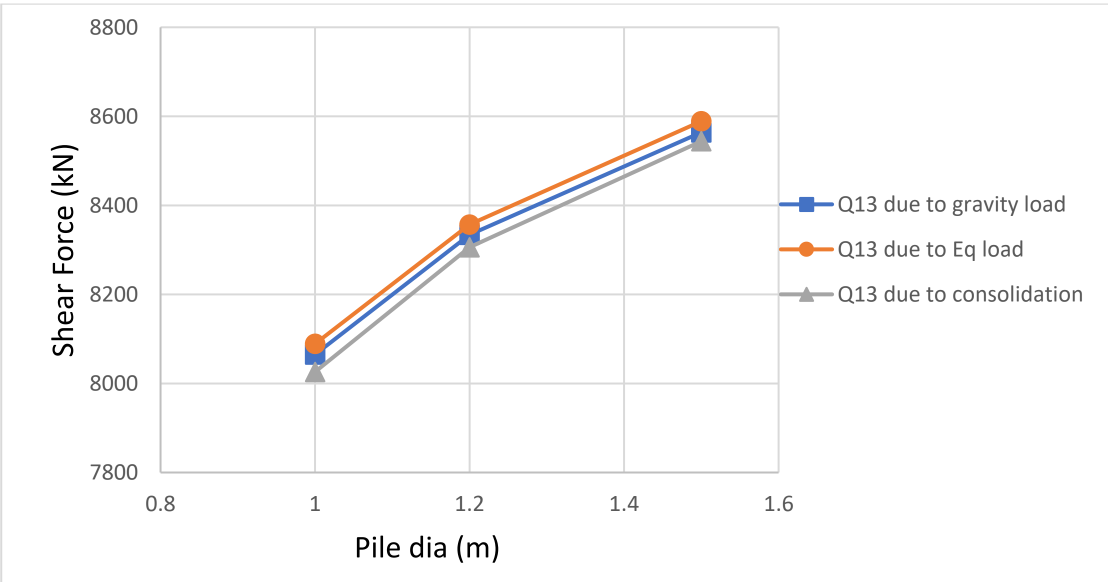

(c)

Figure 5.77: Effect of pile diameters on raft maximum shear force values of Piled raft with 2.5m raft thickness and 58 nos. piles. (a) Q12, (b) Q23, (c) Q13

5.2.3.16 Maximum moments of retaining wall

The effect of pile diameters on the retaining wall maximum moments is very minor. Figure 5.78 shows that the maximum moments M22 and M12 of retaining wall slightly decreases as the pile diameter increases. But moment M11 slightly increases with the increase in pile diameter.

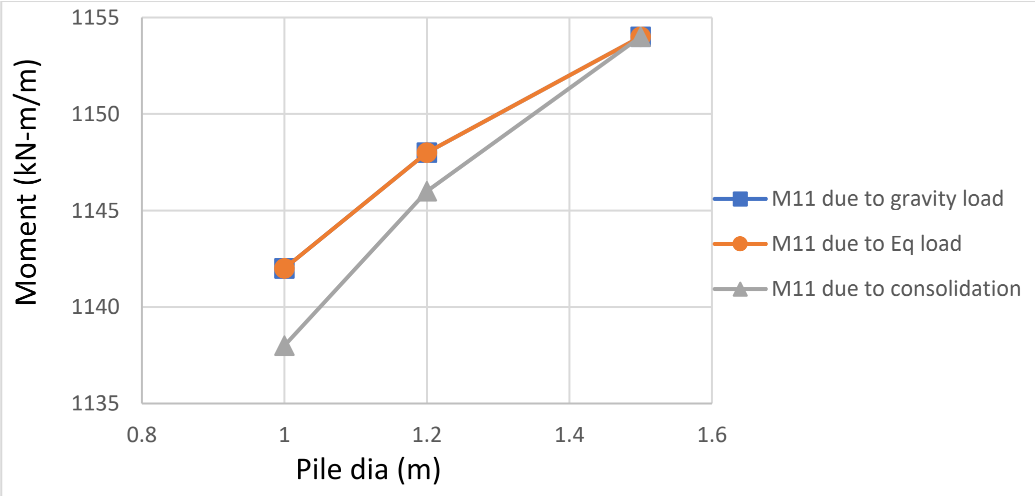

(a)

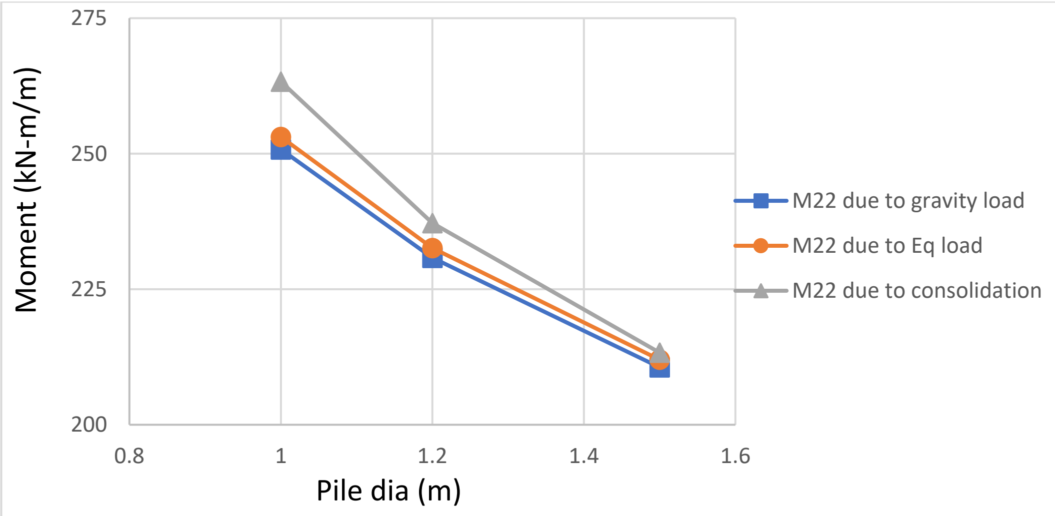

(b)

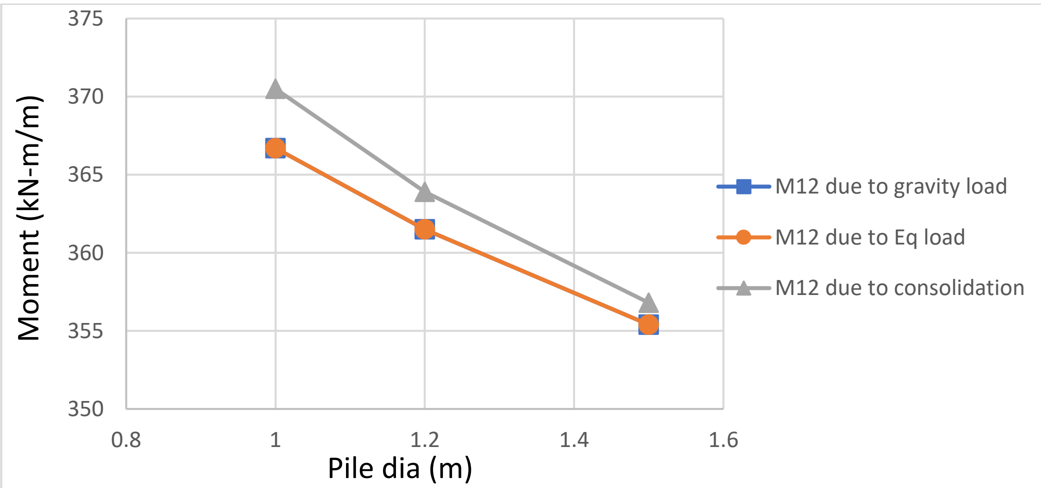

(c)

Figure 5.78: Effect of pile diameters on retaining wall maximum moment values of Piled raft with 2.5m raft thickness and 58 nos. piles. (a) M11, (b) M22, (c) M12

5.2.3.17 Maximum shear forces of retaining wall

The maximum shear force Q12 and Q23 of raft decreases as the pile diameter increases. However, the shear force Q13 increases with the increase in pile diameters. Figure 5.79 shows the effect of pile diameters on the maximum shear force values of center piles.

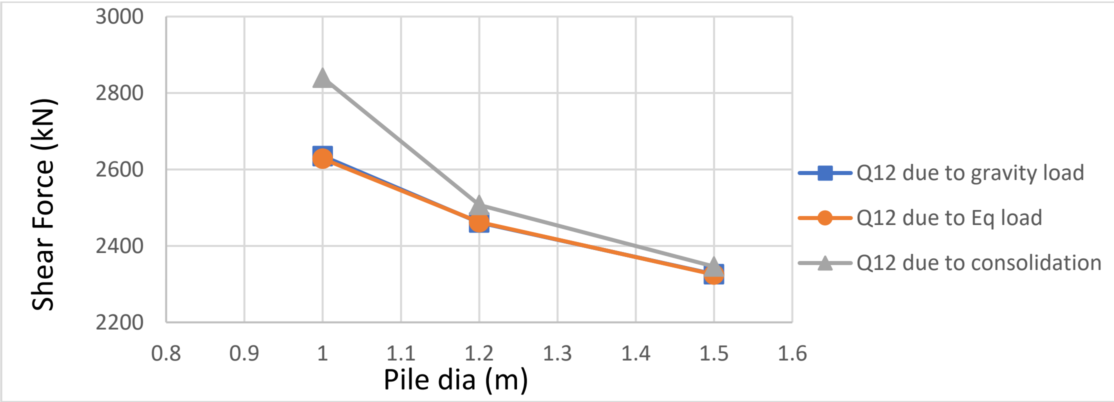

(a)

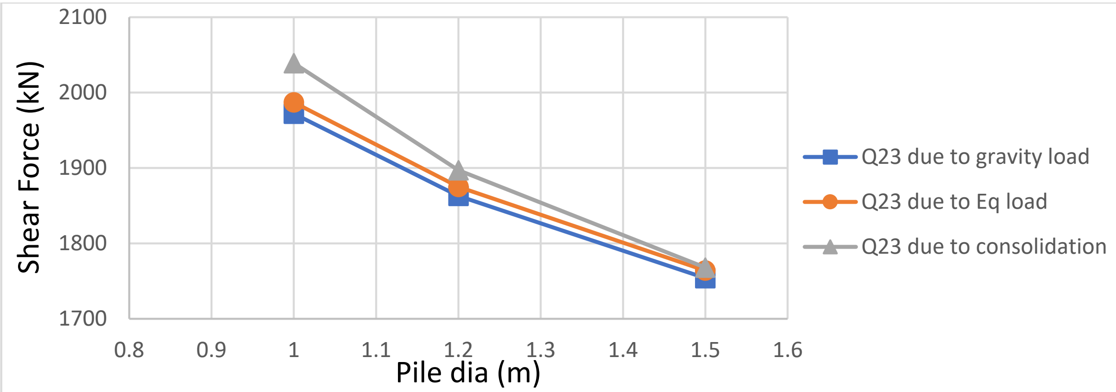

(b)

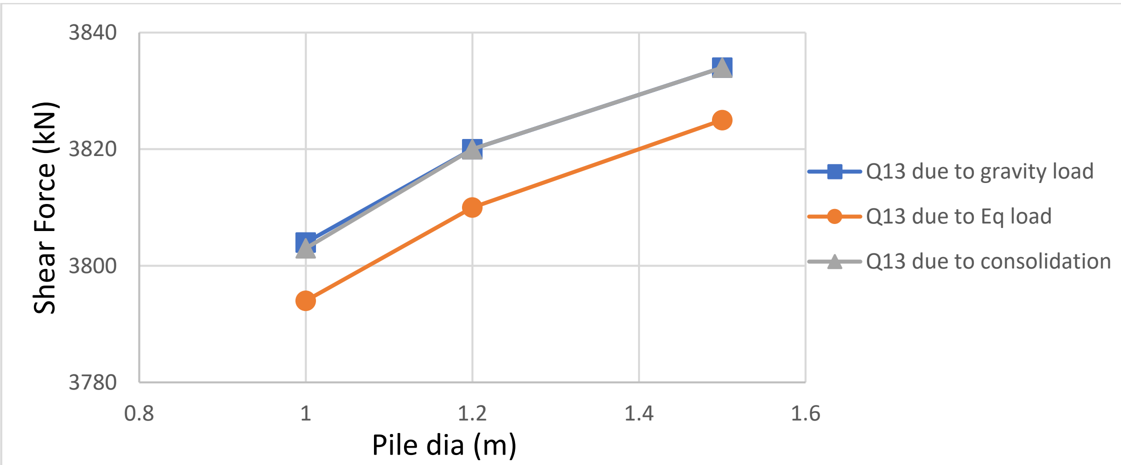

(c)

Figure 5.79: Effect of pile diameters on retaining wall maximum shear force values of Piled raft with 2.5m raft thickness and 58 nos. piles. (a) Q12, (b) Q23, (c) Q13

5.2.3.18 Maximum normal forces of retaining wall

The normal force values N1 and N2 of retaining wall decrease with the increase in pile diameters for piled raft foundation system. Figure 5.80 shows the relation between pile diameters and retaining wall normal forces.

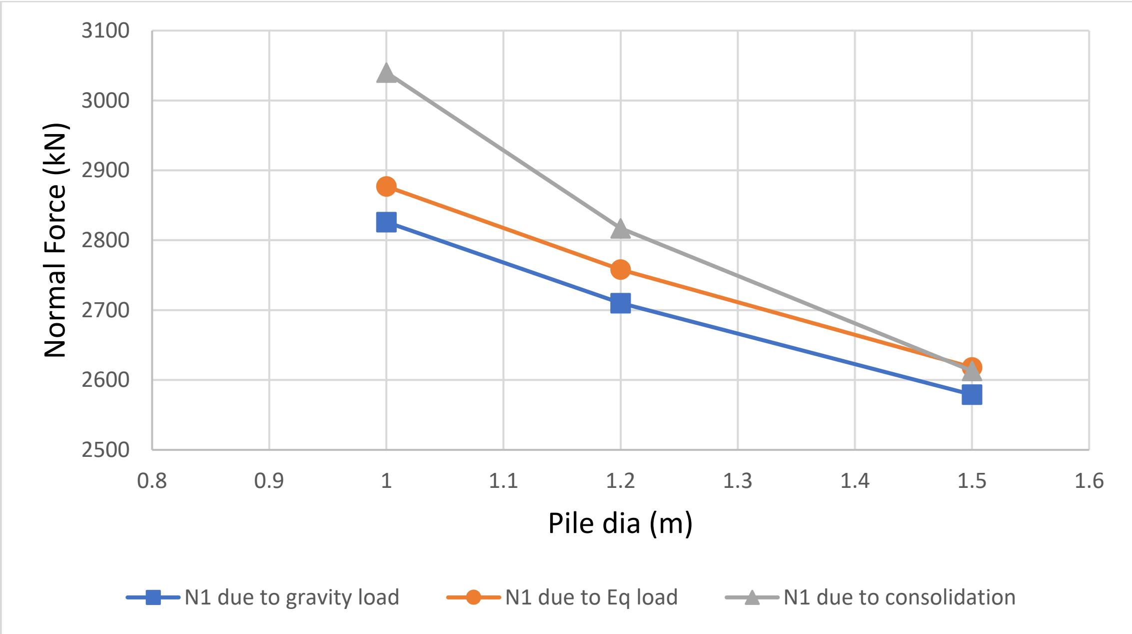

(a)

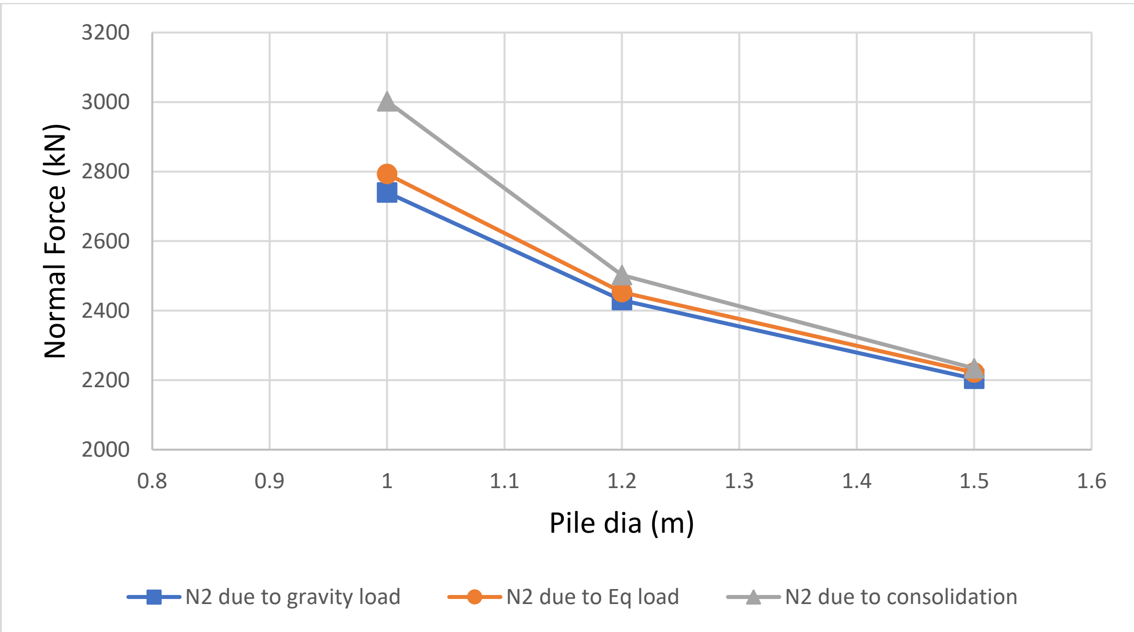

(b)

Figure 5.80: Effect of pile diameters on retaining wall maximum normal force values of Piled raft with 2.5m raft thickness and 58 nos. piles. (a) N1, (b) N2

5.2.3.19 Lateral deflection of retaining wall

The effect of pile diameters on the retaining wall lateral deflection is very negligible. Figure 5.81 shows that the lateral defection along x-direction of retaining wall slightly decreases as the pile diameter increases. The lateral defection along y-direction also decreases to some extent with the increase in pile diameters.

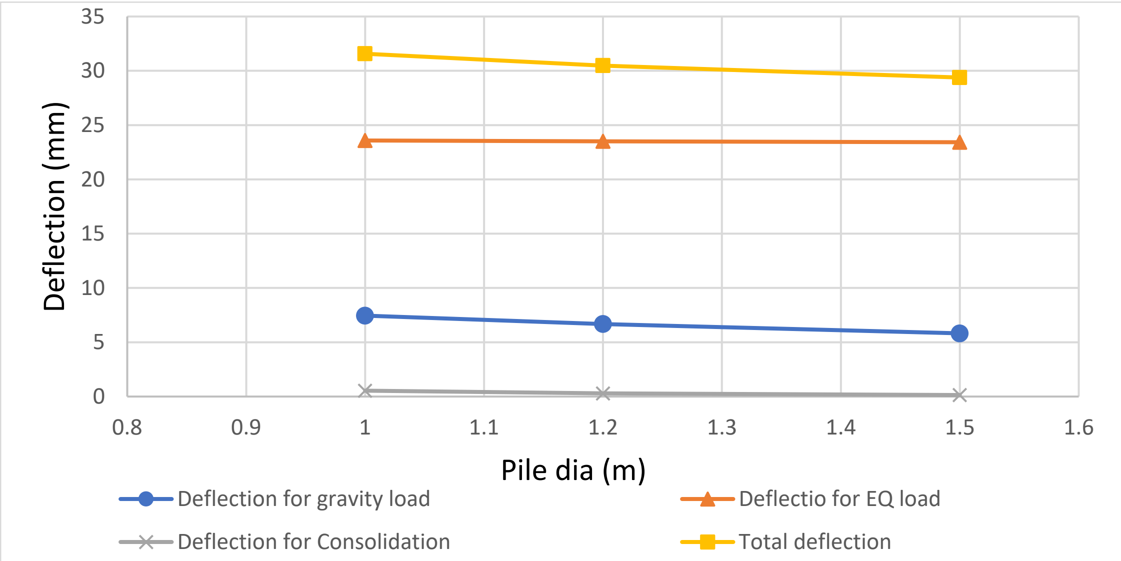

(a)

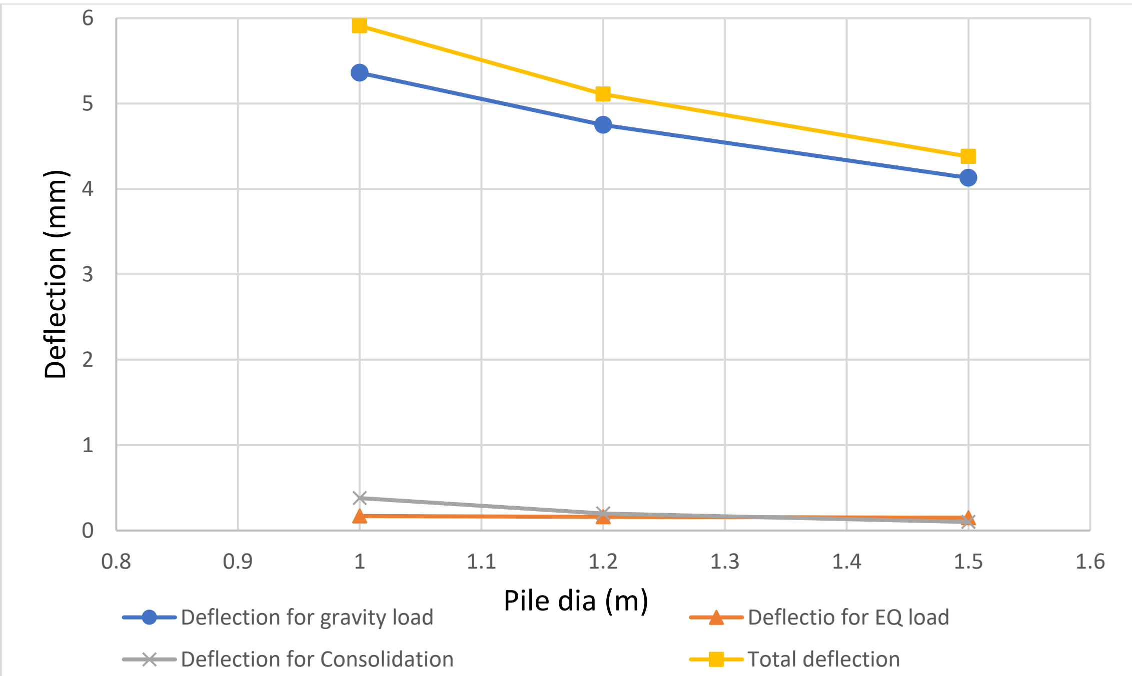

(b)

Figure 5.81: Effect of pile diameters on retaining wall lateral deflection of Piled raft with 2.5m raft thickness and 58 nos. piles. (a) x-dir deflection, (b) y-dir deflection

5.2.3.20 Load distribution between raft and piles

The percent of load shared by the piles increases with the increase in pile diameters. In other words, the percent of load shared by the raft decreases with the increase in pile diameters. Larger diameter of piles can carry additional load from the superstructure. However, from the parametric studies, it is found that increasing pile diameter does not always reduce total and differential settlement significantly. Even, the percentage of load shared by piles does not significantly change for increasing pile diameter for this selected structure.

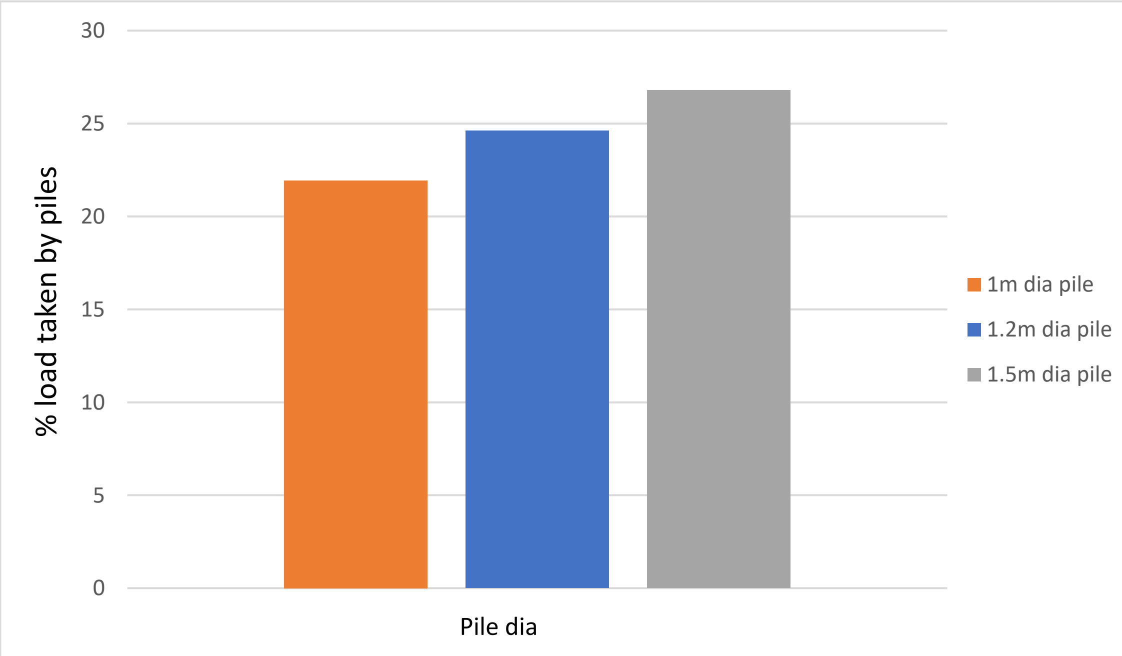

Figure 5.82: Effect of pile diameters on % of load sharing of piled rafts of Piled raft with 2.5m raft thickness and 58 nos. piles

The effects of pile diameters on different geotechnical and structural parameters have been discussed above for only the piled rafts with 3m raft thickness and 1m diameter piles. Piled rafts having different raft thickness and pile diameters, show the same impacts of pile diameters and hence it is not mentioned here. Only exception is found for normal force of retaining wall for the piled rafts with 69 piles. The N1 value changes with irregular with the increase in pile diameter. However, the impacts of pile diameters on the other piled raft foundations are mentioned in Appendix-3.

BANGLADESH NETWORK
OFFICE FOR URBAN SAFETY

PART-V

EVALUATION OF CONSOLIDATION CHARACTERISTICS FROM PIEZOCONE PENETRATION TEST

BANGLADESH NETWORK OFFICE FOR URBAN SAFETY (BNUS), BUET, DHAKA

Prepared By: Mohd Salman Mazhar
Mehedi Ahmed Ansary

Chapter 1

INTRODUCTION

1.1 General

Determining the compressibility characteristics of fine-grained soils, due to structural loadings or constructional activity, has always been an engineering discourse. It experiences large consolidation settlement over a long period of time and can be detrimental to both life and property. Therefore, it is imperative to appraise the magnitude and time rate of consolidation settlement accurately. Strength and compressibility characteristics are mostly interpreted from in-situ tests and laboratory tests. Even though Standard Penetration Test (SPT) is a widely used in-situ test in Bangladesh; efforts to standardize the SPT procedure has been a primary concern among engineers in the region—problems linked to consistency, repeatability, and reliability persists Saha (2015). Moreover, undisturbed samples required for the oedometer tests are small and are usually subjected to an unknown degree of disturbance. Consequently, laboratory determined consolidation parameters often underestimate the actual in-situ conditions Bishop and Al-Dhahir (1969).

Robertson (1986, 2012a) highlighted various geotechnical parameters, required for foundation design and analysis, that correlate with CPTu data. In addition, in-situ tests other than CPTu, for evaluating: soil pore pressure; compressibility characteristics; and the time rate of consolidation are listed according to their estimation degree by Robertson (2012a). This list also exhibits the reliability of CPTu in determining the essential geotechnical parameters. The perceived applicability for most of these parameters range from moderate to high. In contrast to laboratory testing, Mitchell et al. (1978) addressed the precision, speed, and feasibility of in-situ tests in assessing geotechnical parameters. CPTu provides rigorous subsurface profile due to its near continuous and uninterrupted data—tip resistance q_c, sleeve friction f_s, and pore water pressure (u_2) (Robertson, 2009). These measurements are correlated with several geotechnical parameters, hence making it valuable for numerous geotechnical applications on assorted soils [example:Krage et al. (2015), Robertson (2009), Shahri and Naderi (2016), Sully et al. (1999), and Yu and Abu-Farsakh (2011)]. As a result, expensive and time-consuming laboratory tests can be replaced with in-situ CPTu tests to characterize geotechnical parameters.

However, correlation models proposed in existing literature give equivocal results for different soil deposits, as outlined by Robertson (1986). Therefore, to attain an effective correlation, the model needs to be calibrated based on local experience. Given the inexorable pace of CPTu research, development, and popularity; it is imperative that Bangladesh continues developing its own set of statistical correlations, and establish the consolidation parameters from CPTu.

1.2 Objectives

A review of the literature reveals an absence of an experimental research program that quantifies consolidation parameters from CPTu in the context of Bangladesh. To quantify the consolidation characteristics of soils using piezocone penetrometers (also known as CPTu), the Committee for Advanced Studies and Research (CASR) of BUET has aided in initiating and funding a research program to fulfill this goal. The objectives are:

1. To evaluate the reliability of existing CPTu interpretation methods to estimate consolidation parameters, required for determining the magnitude and time rate of consolidation settlement, in the context of Bangladesh soil.

2. To develop and build a local correlation between CPTu and consolidation parameters of cohesive soils, and justify the reliability and interpretation of the correlations with laboratory determined consolidation parameters.

1.3 Thesis Organization and Background Information

The dissertation was written in a thesis format consisting of five chapters—the introduction, literature review, description of the experimental program, and finally the conclusion section.

Following Chapter 1, Chapter 2 presents the theoretical background behind the principles of CPTu. This chapter focuses on the contribution of several investigators in interpreting CPTu data to correlate it with key geotechnical engineering parameters. In this study, these parameters include the overconsolidation ratio, constrained modulus, compression index, small-strain shear modulus, rigidity index, and coefficient of consolidation. The different types of CPTu cones are also presented by outlining their advantages and limitations. The last section in this chapter examines the importance of statistical analysis in geotechnical engineering.

Chapter 3 focuses on the geotechnical investigations conducted in the Dhaka region study area. Also, the laboratory investigation program implemented in conjunction with the CPTu soundings to develop local correlations is detailed in this chapter.

Chapter 4 presents the analysis performed to develop local correlations for CPTu parameters with laboratory-derived constrained modulus, compression index, OCR, coefficient of consolidation, and undrained shear strength. The performance of existing correlations is quantified and graphically presented in this chapter.

Finally, Chapter 5 summarizes the main conclusion from the experimental analysis followed by recommendations from this research and suggestions for future work.

Chapter 3

GEOTECHNICAL INVESTIGATION

3.1 Introduction

This chapter summarizes the field investigations and the laboratory tests conducted in the Dhaka region. As seen in Figure 3.1, Rajdhani Unnayan Kartripakkha (RAJUK) supervised numerous in situ tests in Dhaka region as part of the Urban Resilience Project in 2019. Around 15% of the tests were validated in BUET. The author personally conducted the required laboratory tests for this research. Consequently, nineteen (19) points were selected for scrutiny. Additionally, from the 19 points, 10 points underwent the piezocone dissipation test. The location of these points is tabulated in Table 3.1.

The research objectives were met by conducting an experimental program comprising three phases. Figure 3.2 shows the different research phases, outlining the focus required at each phase to reach the objectives of this study. The first phase comprised collecting in situ data employing CPTu and SPT as a part of the Urban Resiliency Project in 2019, supervised by the RAJUK part. The second phase involved conducting several geotechnical tests in the laboratory. The collection and analysis of these data synthesized a data bank comprising of in situ and laboratory tests. The database was created using Microsoft Excel software. The third phase expanded on this database by updating it with the laboratory test results. This research focused on quantifying key geotechnical parameters such as undrained shear strength, constrained modulus, preconsolidation stress, coefficient of consolidation, and compression index. 19 points of in situ tests from this database were examined to fulfill the objectives of this thesis.

3.2 Geologic Formation of the Research Site

Dhaka is the capital city of Bangladesh in South Asia. The urban area spans at 305.47km^2, whereas the metro area spans around 2,161.17km^2. Geologically, it lies in the Bengal Basin block, near the southern tip of the Madhupur tract. Due to its location on the lowland plain of the Ganges Delta, the north is bounded by the Tongi Khal (Small River); the eastern portion bounded by the Balu River; the south and south east portion is bounded by the Buriganga River; and the Turag River in the west. Regionally, Dhaka is located in the central part of the Bengal basin. Since the topography of Dhaka is flat and close to sea level, it is susceptible to flooding during heavy rainfall and cyclones in the monsoon seasons. The greater Dhaka area is bounded by the districts of Manikganj, Tangail, Narsingdi, Gazipur, Rajbari, Munshiganj, and Narayanganj.

The subsurface geology of Dhaka city comprises of 6 to 12m thick formation of Madhupur

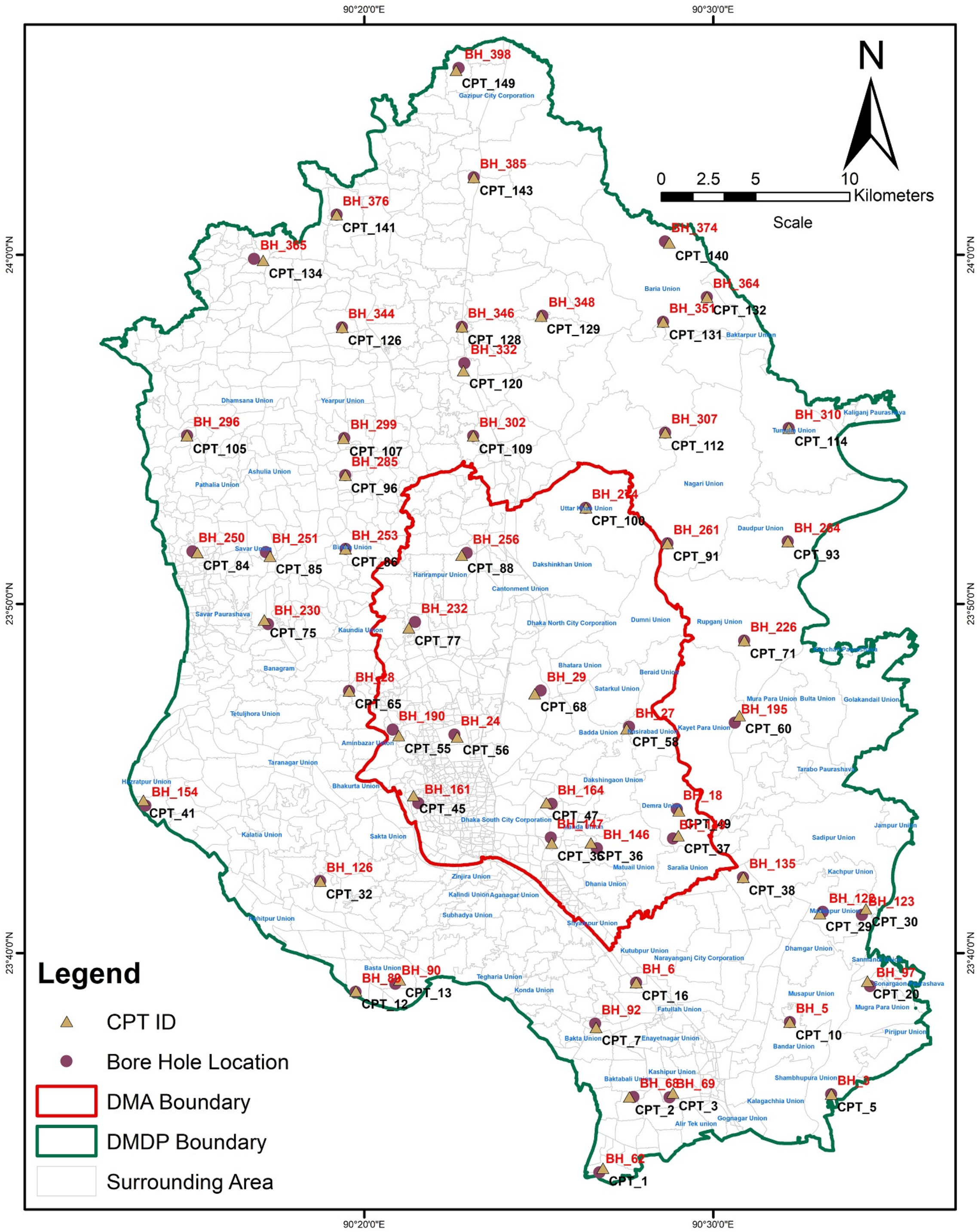

Figure 3.1: Study Site and locations of CPTu and SPT conducted.

Clay layer. The composition of Madhupur Clay is mainly Kaolinite (27% to 53%) and Illite (14% to 33%). Very small traces of Illite smectite (2%) is also found up to a depth of 5m. Course grained soil deposit underlies the Madhupur Clay layer. (Zahid et al., 2004)

Kamal and Midorikawa (2004) presented a detailed GIS-based geomorphological map of the Dhaka region by utilizing aerial photographs and the topographic map. The photos

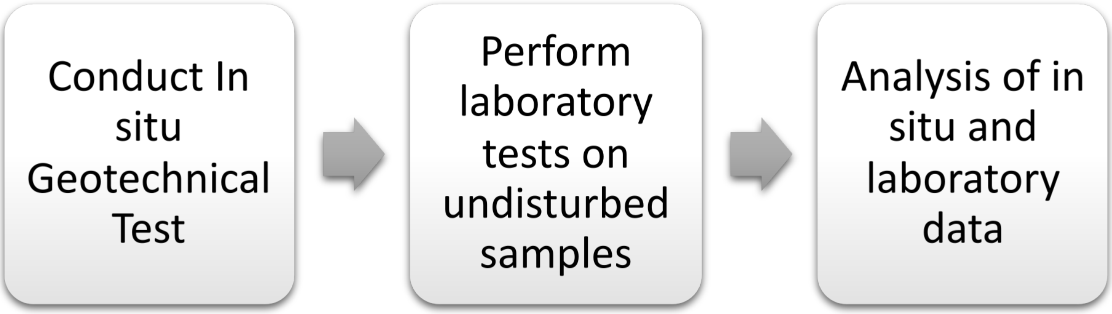

Figure 3.2: Research Phases for this Study.

BH-ID	**CPT-ID**	**Dissipation Test**	**Location**
BH-05	CPT-10	Yes	Tingao, Narayanganj
BH-06	CPT-16	Yes	Aligonj Madrasa, Fatullah
BH-18	CPT-149	Yes	Demra, Dhaka
BH-24	CPT-56	Yes	Shere Bangla Nagar Agricultural University, Dhaka
BH-27	CPT-58	No	Aftab Nagar, Dhaka
BH-68	CPT-2	No	Anondo Bazaar, Fatullah
BH-97	CPT-20	No	Anondo Bazaar, Fatullah
BH-123	CPT-30	No	Modonpur, Narayanganj
BH-146	CPT-36	Yes	Jatrabari, Dhaka
BH-250	CPT-84	Yes	Badda Government Primary School, Savar
BH-253	CPT-86	No	Kakabo Birulia, Savar
BH-264	CPT-93	Yes	Kuliyadi Government Primary School, Narayanganj
BH-274	CPT-100	Yes	Uttara, Dhaka
BH-285	CPT-107	No	Ashulia, Dhaka
BH-296	CPT-105	No	Annondo Bazaar Fatullah
BH-364	CPT-132	No	Anondo Bazaar, Fatullah
BH-365	CPT-134	No	Kashimpur, Gazipur
BH-374	CPT-140	Yes	Keshorita Government Primary School, Gazipur
BH-398	CPT-149	Yes	Bahadurpur Government Primary School, Gazipur

Table 3.1: Locations of the in situ points.

were interpreted by differentiating the ground of Dhaka region into 18 geomorphological units. Rapid expansion of the city is observed since 1960, even in the low-lying geomorphic units—by fill practices. Based on the thickness of the fills, the fill-sites were classified into four classes. This required data from the boreholes and an topographic map prepared in 1961. Figure 3.3 shows the geological map of Bangladesh. It is also seen that Alluvial Silt; Madhupur Clay residium; and Alluvial Silt and Clay, dominates the Dhaka region. The characteristics of these deposits are summarized:

1. **Madhupur Clay Residium:** The color of these deposits ranges from light yellowish-grey, orange, and light to brick red and grayish-white. Consists of micaceous silty clay to sandy clay. Plastic in nature and abundantly mottled in the upper 8m of the subsurface. It also contains small clusters of organic matter. Sand fraction is dominantly quartz; minor feldspar and mica; sand content increases with depth.

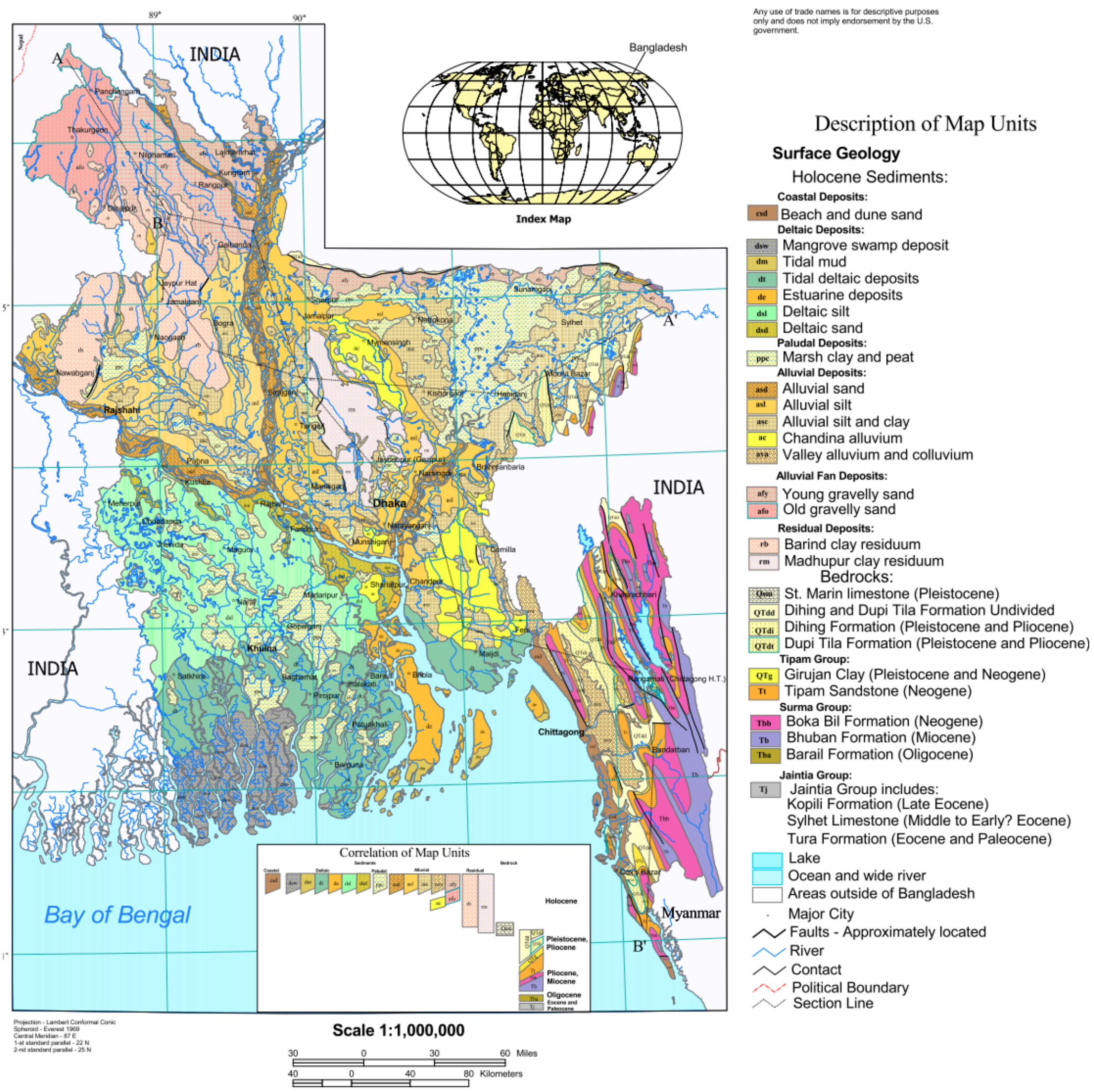

Figure 3.3: Geological Map of Bangladesh (after Persits et al., 2001)

Dominant clay minerals are kaolinite and Illite. Iron manganese oxide modules are rare.

2. **Alluvial Silt:** The color of these deposits ranges from light to medium grey and consists of fine sand to clayey silt. Illite is the primary clay mineral. Generally, it is poorly stratified. Also, the average grain size decreases away from the main channels. These deposits are predominantly present in the flood basins and the inter stream areas. Units include small back swamp deposits and varying episodic or unusually large floods. Most of these areas have been flooded annually. Included in this unit are thin veneers of sand spread by episodic large floods over flood plain silts. Historic pottery, artifact, and charcoal were found in the upper 4 m.

3. **Alluvial Sily and Clay:** The color of these deposits ranges from medium to dark grey and consists of Silt to Clay. The more the organic content, the darker the color

gets. The map unit in Figure 3.3 indicates that its unit is a combination of alluvial and paludal deposits, flood-basin silt, black swampy silty clay, and organic Clay found in sag ponds and large depressions. These depressions may have peat as well. Large areas underlain by this unit are dry for only a few months in a year. The deeper part of depressions and beels contains water throughout the year.

3.3 Field Investigations

A total of ninteen (19) pairs of CPT and SPT, performed up to a depth of at least 30m, were selected for this study. As seen in Figure 3.1, each pair of CPT and SPT were executed within 1m of each other.

3.3.1 Cone Penetration Test Equipment

Figure 3.4: The Gouda Geo-Equipment B.V. 350 kN CPT Penetrometer Pusher in Narayanganj, Dhaka

As shown in Figure 3.4, the CPT equipment consisted of a cone penetrometer, pushing equipment and data acquistion systems. The CPT soundings were advanced using a Gouda Geo-Equipment B.V piezocone penetrometer cone of 60°, having a cross-sectional area of 15cm^2. The position of the porus filter—to measure pore pressure—is behind the cone (u_2). This penetrometer is a subtraction-type cone penetrometer.

To perform the test, a hydraulic power pack—powered by an 18kW diesel engine—with a thrust capacity of 350kN pushes the cone at 2cm/s. During the advancement, it can simultaneously and continuously measure q_c, f_s, u_2 at 10mm depth increments. The typical penetration depth in this in situ program was 30m from the existing ground level.

The data acquisition system was suitable for both digital and analog piezocones. The CPT-logger was connected to a laptop computer for synchronizing CPT data with depth.

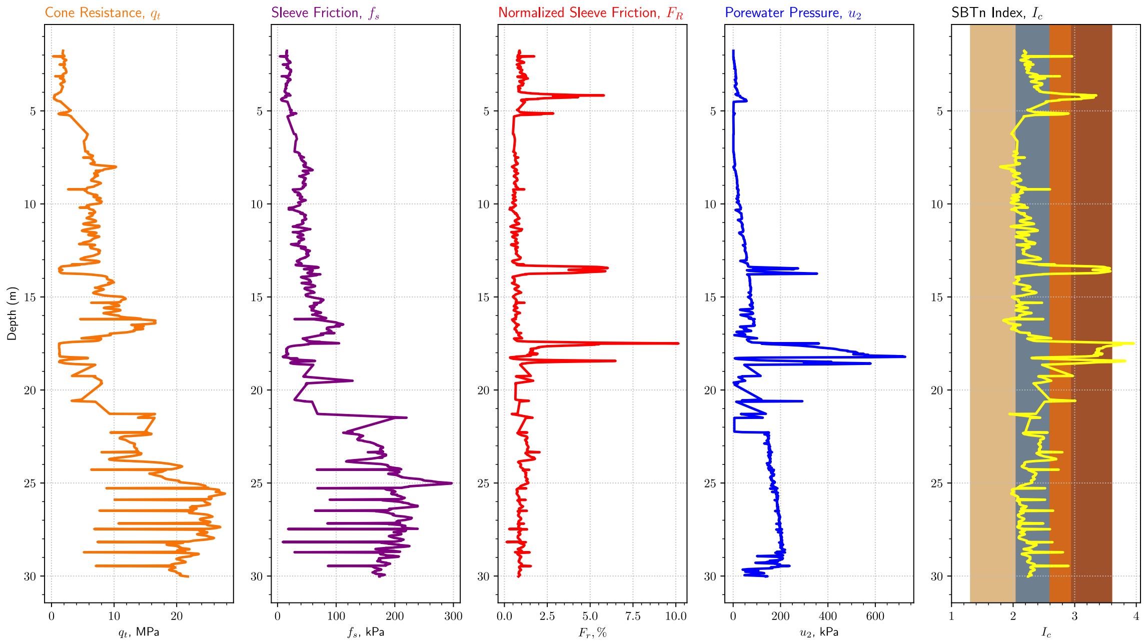

Figure 3.5: Typical CPT profile generated near BH-05 in Tingao, Narayanganj

A typical soil profile generated is shown in Figure 3.5. q_c was corrected to account for pore pressure effects as discussed in Section 2.3.4. SBT was generated using Equation 2.4. The corresponding methodology is described in Chapter 2.4. Using the parameters shown in Figure 3.5, the normalized Robertson (2010) chart was generated for the 19 points as shown in Figure 3.6.

Referring to Figure 2.17, Figure 3.6 reveals that the soil data is concentrated in region 5, which is the ”Sand mixtures—silty sand to sandy silt”. Regions 3 and 4 represent ”Clays—silty clay to clay” and ”Silt mixtures—clayey silt to silty clay”. Also, as seen in the bottom left of region 3, the Clays in this chart is mostly normally consolidated area with many data points concentrated in the region indicating ”increasing sensitivity”. For CPT profiles and charts synthesized for this study, the reader can refer to Appendix A.2.

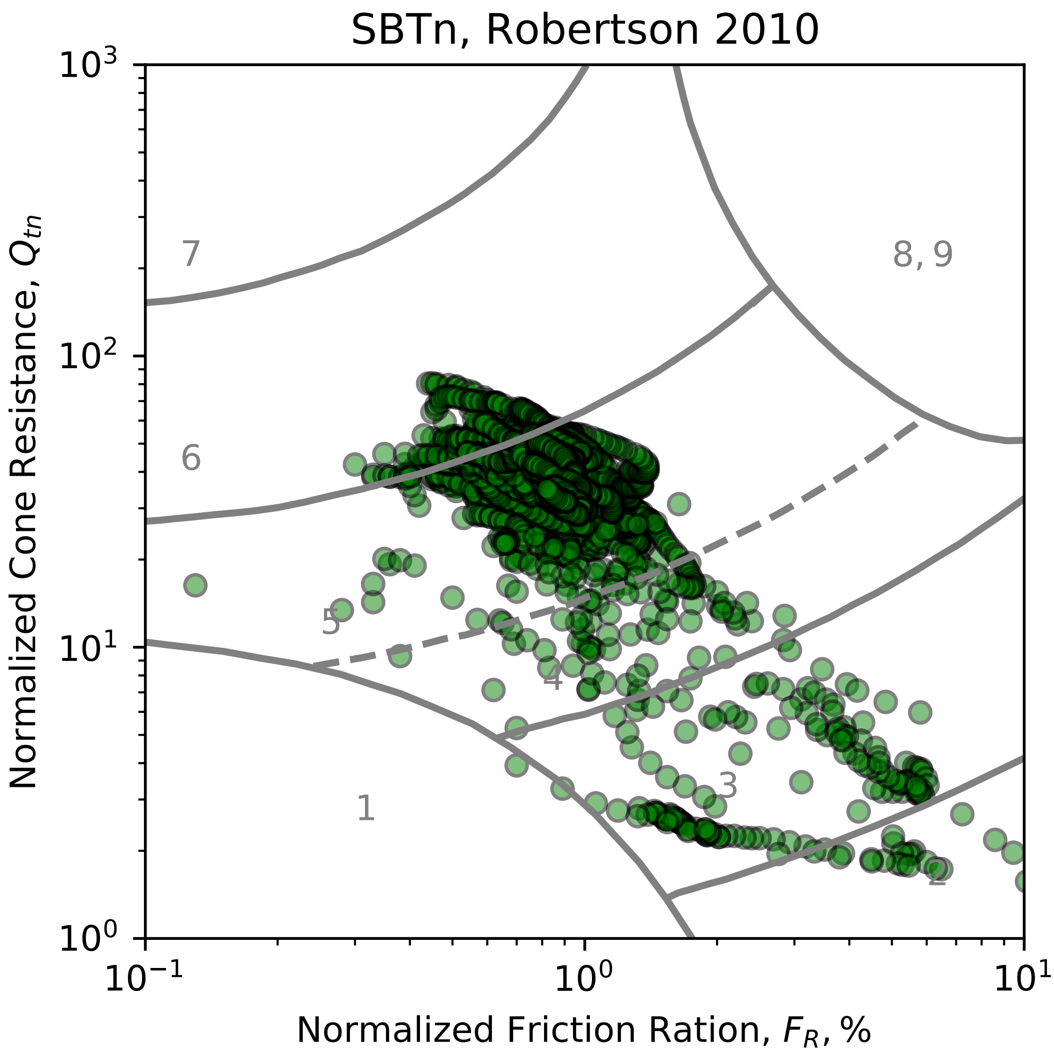

Figure 3.6: A typical normalized SBT chart generated near BH-05 in Tingao, Narayanganj.

3.3.2 Standard Penetration Tests

As shown in Figure 3.7, a rotary drill rig was employed for drilling the boreholes. The boring was advanced using the wash-boring method and a diamond cutter. A steel case is used to protect the topmost 1.0m depth of the borehole. The SPT was conducted as per ASTM D1586-18 (Standard Test Method for Standard Penetration Test and Split-Barrel Sampling of Soils). Field SPT N-values were recorded at 1.5m intervals using a donut auto-tripped hammer. The refusal criterion was set to at least 30m if the N-value is 50 with 230mm or less penetration in last consecutive three layers.

Figure 3.7: SPT by rotary drill rig conducted in Uttara, Dhaka.

Disturbed and undisturbed sampling were according to ASTM D1586. The samples were collected in a zipper plastic bag and stored in an airtight box. Shelby tube was used for undisturbed sampling—conforming to the specifications set out in ASTM D1587/D1587M-15 (Standard Practice for Thin-Walled Tube Sampling of Fine-Grained Soils for Geotechnical Purposes.)

A typical SPT profile is shown in Figure 3.8. Here, the exploration depth is up to 31.5m. The range of SPT is seen between 4 and 88. In the case of cohesive deposits, it implies that the consistency varied from being very soft to hard. SPT profiles used in this study are attached in Appendix A.1.

3.4 Laboratory Test Program

Laboratory tests were conducted on undisturbed samples collected from boreholes drilled close to the CPTu test points. Classification tests were performed to determine the soil type, while undrained shear strengths were evaluated using direct simple shear tests. Atterberg limit tests and oedometer consolidation tests were also conducted on the cohesive

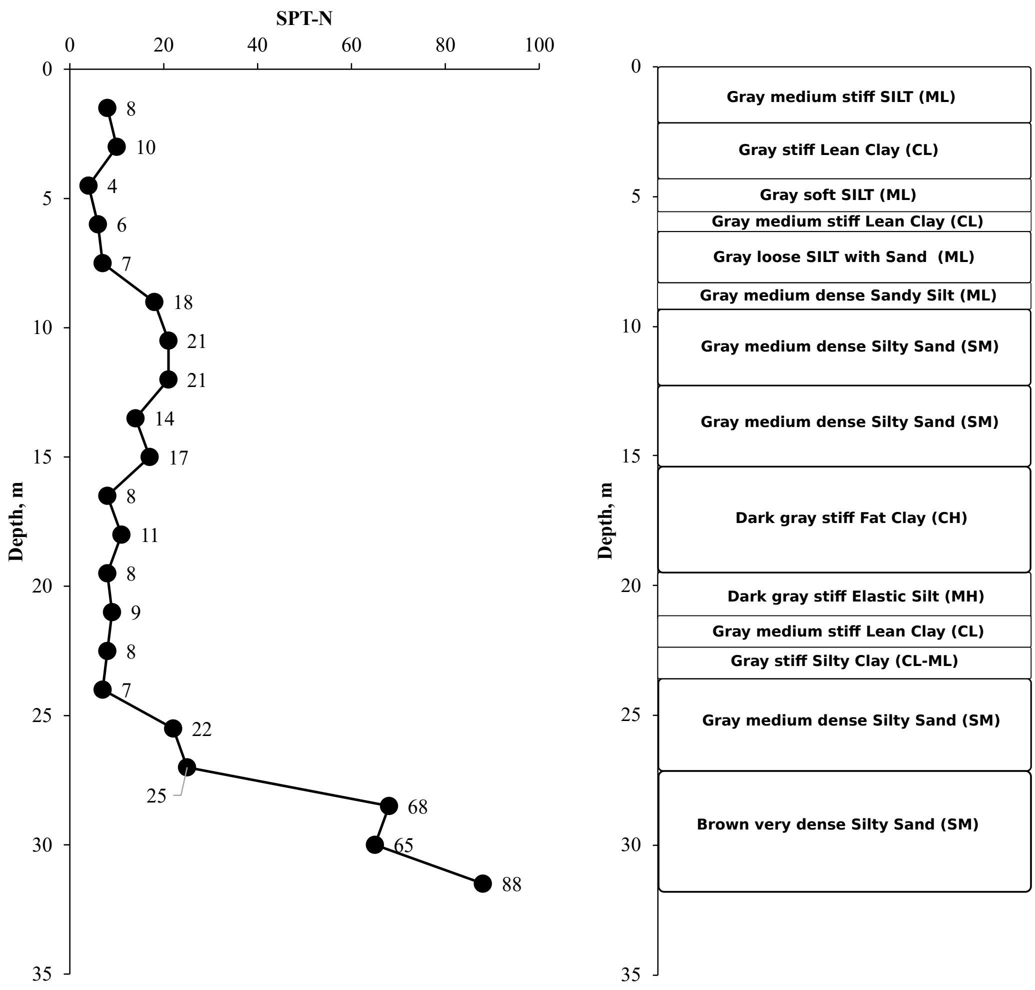

Figure 3.8: Typical SPT profile (Tingao, Narayanganj, BH-5)

deposits. The laboratory test results correspond to in situ test results of the same depth. The laboratory tests conformed to the standards set out by the American Society for Testing & Materials (ASTM). The subsequent sections summarizes the test results along with the corresponding ASTM code. The detailed results of the laboratory tests are enclosed in Appendix B.

3.4.1 Moisture Content

This test was conducted as per ASTM D2216-98. This test method covers the laboratory determination of the water (moisture) content by mass of soil particles where the reduction in mass by drying is due to water loss. The mass of soil solids is determined by drying the test specimen at a constant temperature of 110° ± 5°C. The loss of mass due to drying is the mass of water.

Results of the evaluation of the moisture content of the undisturbed samples and its corresponding borehole is summarized in Table 3.2. It is evident that the w% ranged from 20.1% to 44%.

Table 3.2: Summary of Moisture Content of different samples.

BH-ID	Sample Depth, m	w, %
BH-5	17.5	29.2
BH-6	10.5	25.6
BH-18	10	44
BH-18	4	32
BH-27	8	37.7
BH-123	2.5	29.3
BH-123	4	27.8
BH-146	8.5	23.2
BH-250	10	30.4
BH-253	4	23.6
BH-264	5.5	30.3
BH-264	16	30.5
BH-274	4	24.7
BH-285	4	24.3
BH-296	4	21.2
BH-365	5.5	20.1
BH-398	5.5	26.6
BH-24	4	26.7
BH-274	4	26.9
BH-364	4	26.3
BH-374	4	24.5
BH-398	2.5	22.3

3.4.2 Particle Size Distribution

Particle size distribution (PSD) of selected boreholes are presented in Table 3.3. The PSD curves are shown in Appendix B.1. According to the USCS, particle size less than 75μm are classified as clay and silt size fraction. Whereas, particle sizes over 75μm but less than 4.75mm are classified as sand size fraction. As seen in Table 3.3, the typical PSD for this investigation's course-grained or sand size fractions varied between 0 and 92%. Whereas, clay and silt size fraction varied between 8 to 99%. The subsequent sections describe the test procedure to determine the clay size fraction and sand size fraction.

Sieve Analysis

Conducted as per ASTM D422-63 and ASTM D6913-04. Sieve analysis quantifies particle size distribution of a soil, within a specified size range, in a granular material—by using sieves of different size openings. The distribution of particle sizes larger than 75μm (retained on #200 sieve) is determined by sieving, while the distribution of particle sizes smaller than 75μm is determined by a sedimentation process, using a hydrometer.

A typical PSD curve for particles larger than 75μm is illustrated in Figure 3.9, where 70% of the sample was determined to be of sand size fraction. For particle sizes smaller than 75μm, the sample that passes through #200 sieve is first washed and dried before conducting the hydrometer analysis. A typical curve generated from the hydrometer analysis is

Table 3.3: Particle Size Distribution of selected boreholes.

BH-ID	Fines Content (<0.075mm), %	Coarse-grained (0.075mm-4.75mm), %
BH-6	8 - 99	1 - 92
BH-18	29-100	0 - 71
BH-27	10-100	0 - 90
BH-123	28-100	0 - 75
BH-146	46-99	1 - 54
BH-250	28-99	1 - 71
BH-253	24-97	3 - 77
BH-264	31-99	0 - 69
BH-274	21-99	1 - 79
BH-285	22-92	8 - 78
BH-365	19-99	1 - 80
BH-24	24-92	6 - 72

illustrated in Figure 3.10.

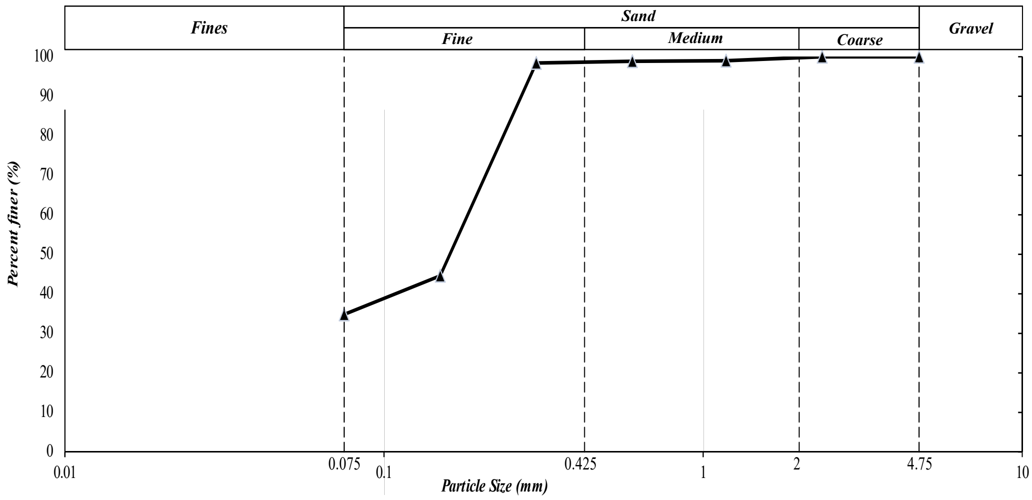

Figure 3.9: A typical PSD curve for BH-05, sample ID-20, sample depth 30.0m.

Wet Sieve Analysis

Conducted as per ASTM D1140-00. It is a procedure to quantify particles finer than a 75µm (#200) sieve by washing. The soil specimen undergoes washing, by water, over a 75µm (#200) sieve. Clay and impurities—removed from the soil specimen during the test—are dispersed by the water, including the water-soluble materials. The resulting loss in mass is calculated as the mass percent of the original sample and is reported as the percentage of material finer than a 75µm (#200) sieve. The resulting samples are then described conforming to the USCS.

3.4.3 Atterberg Limit Test

Following the ASTM D4318 convention, according to Das and Sivakugan (2018):

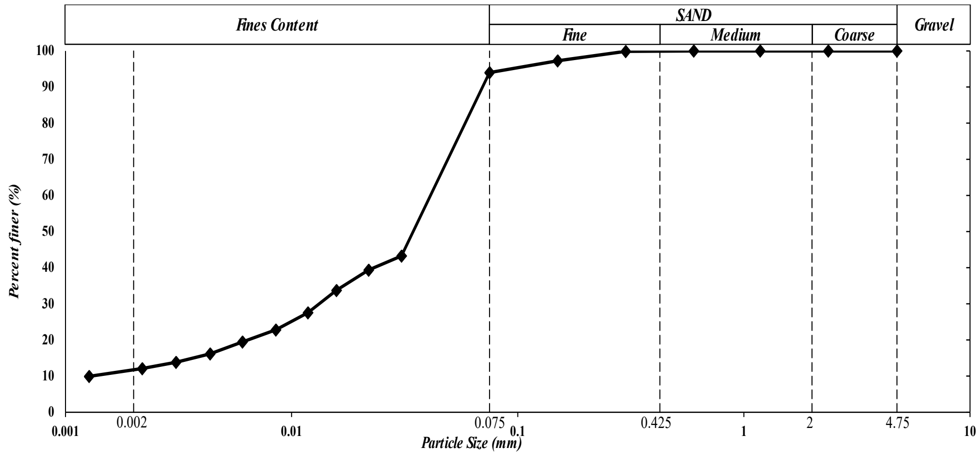

Figure 3.10: A typical curve obtained using hydrometer analysis for BH-05, sample ID-04, sample depth 6.0m.

A Casagrande device is employed to determine the liquid limit of soil. It is the moisture content at which a groove closure of 12.7 mm occurs at 25 blows. Whereas, the plastic limit is the moisture content at which the soil crumbles when rolled into a thread of 3.18 mm in diameter. Summary of the Atterberg limit tests of the 19 inorganic samples is presented in Table 3.4. The LL ranges between 20 an 90. Whereas the PI ranges between 12 and 65.

The index properties are used to classify the inroganic samples conforming to USCS as shown in Table 3.4 and Figure 3.11. It is evident that the characteristic LL for the majority of the samples is above 50%, and above the A-line—indicating a highly plastic clay (CH). Five samples have the characteristic LL below 50%, thus classified as clays with low plasticity (CL). Two of the samples are seen in Figure 3.11 to lie below the A-line, having LL below 50%—thus classified as silts (ML). Similar Atterberg limit charts for the 19 boreholes are attached in Appendix B.2.

3.4.4 Density (Unit Weight)

This test method—conducted as per ASTM D7263—describes two ways of determining the moist and dry densities (unit weights) of intact, disturbed, remolded, and reconstituted (compacted) soil specimens.

The values of the bulk and dry unit weight of the undisturbed samples are summarized in Table 3.5. The quantitative range of the bulk unit weight ranges from 16.9kN/m^3 to 20.9kN/m^3. Whereas, the dry unit weight ranges from 7.09kN/m^3 to 11.09kN/m^3. Laboratory data and its evaluation is attached in Appendix B.3.

3.4.5 Specific Gravity

This test was conducted as per ASTM D854-02. Specific gravity of soil solids is determined by using a water pycnometer. The soil solids are first sieved through a 4.75mm

Table 3.4: Summary of Atterberg Limit of different samples.

BH-ID	Sample Depth, m	LL	PL	PI	USCS Symbol
BH-5	17.5	60	27	33	CH
BH-6	10.5	66	23	43	CH
BH-18	4	40	26	14	ML
BH-123	2.5	40	26	14	ML
BH-123	4	35	23	12	CL
BH-146	8.5	53	26	27	CH
BH-250	10	48	24	24	CL
BH-253	4	90	25	65	CH
BH-264	5.5	74	27	47	CH
BH-264	16	46	20	26	CL
BH-274	4	47	22	25	CL
BH-285	4	59	29	30	CH
BH-296	4	85	21	64	CH
BH-365	5.5	75	22	53	CH
BH-398	5.5	59	23	36	CH
BH-24	4	76	20	56	CH
BH-274	4	57	23	34	CL
BH-374	4	80	25	55	CH
BH-398	2.5	49	20	29	CL

Table 3.5: Summary of unit weight of different samples.

BH-ID	Sample Depth, m	Bulk Unit Weight, KN/m^3	Dry Unit Weight, KN/m^3
BH-6	10.5	19.2	9.39
BH-5	17.5	17.1	7.29
BH-18	4	18.8	8.99
BH-18	10	16.9	7.09
BH-27	8	17.5	7.69
BH-123	2.5	18.9	9.09
BH-123	4	18.4	8.59
BH-253	4	19.7	9.89
BH-274	7	19.9	10.09
BH-285	4	19.5	9.69
BH-264	5.5	20.9	11.09
BH-264	16	20.7	10.89
BH-296	4	18.7	8.89
BH-398	5.5	19.4	9.59
BH-250	10	17.6	7.79
BH-365	5.5	19.1	9.29
BH-146	8.5	19.2	9.39
BH-68	47	20.1	10.29
BH-97	37	18.3	8.49

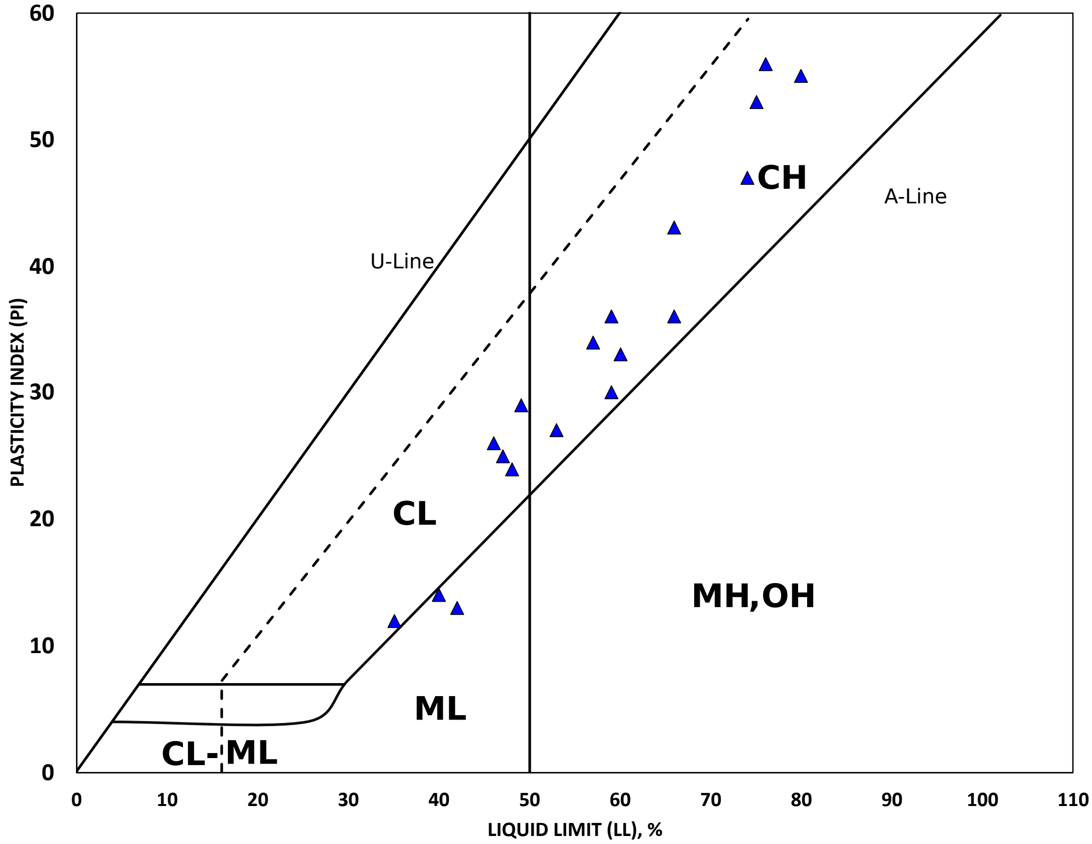

Figure 3.11: Plasticity chart developed for the investigated points developed using the Casagrande (1936) plasticity chart.

(Number-4) sieve. The ratio of the mass of a unit volume of a soil solids to the mass of the same volume of gas-free distilled water at 20°C is the specific gravity of soil solids (G_s) For this investigation, G_s is observed to vary between 2.65 to 2.80. Detailed calculations in evaluating G_s is attached in Appendix B.4).

3.4.6 Soil Classification

This test was conducted as per ASTM D2487-06. The USCS was employed to identify the soil. ASTM D 2487 standard covers the guidelines for USCS classification for engineering purposes.

3.4.7 One-Dimensional Consolidation Test

This test was conducted as per ASTM D2435-11. This test method covers the determination of consolidation properties of cohesive soils. Incremental loads are maintained until excess pore water pressures dissipate. The change in specimen height and the stress-strain graph are used to evaluate the time required for consolidation, coefficient of consolidation, compression index, and constrained modulus.

Table 3.6: Summary of one-dimensional consolidation test result.

BH-ID	Sample Depth, m	C_c	Initial Void Ratio	M, kPa	t_{50}, min	c_v, m^2/year
BH-5	17.5	0.38	0.79	1384.0	1.3	6.3
BH-6	10.5	0.23	0.60	1615.0	20	0.4
BH-18	10	0.58	1.15	611.0	0.5	16.1
BH-123	4	0.13	0.65	1028.1	1.5	5.6
BH-146	8	0.18	0.67	1696.0	4.5	1.9
BH-250	2.5	0.20	0.82	1657.4	0.4	20.8
BH-253	4	0.17	0.71	944.2	0.9	9.3
BH-264	8.5	0.35	1.62	1043.0	14	0.6
BH-274	10	0.17	0.81	1007.4	0.6	13.9
BH-285	4	0.18	0.59	802.0	3.3	2.6
BH-24	5.5	0.17	0.69	782.0	2	4.0
BH-364	16	0.24	0.89	589.2	0.4	19.9
BH-374	4	0.17	0.63	821.0	1	8.1
BH-398	4	0.14	0.66	690.0	4	2.0

In this research, compressibility characteristics of 14 samples were evlauated from incremental loading in one-dimensional oedometer consolidation test. The results are summarized in Table 3.6. Consolidation tests were carried out on samples of 61.1mm⌀ and an average height of 17.8mm. The incremental loads followed the sequence: 25kPa, 50kPa, 100kPa, 200kPa, 400kPa, 800kPa, and 1600kPa. Each loading step was held for at least twenty-four hours. Drainage of water took place from both the top and bottom of the sample through the porus stones. A mechanical dial-gauge was used to record the deformations at specified intervals of time.

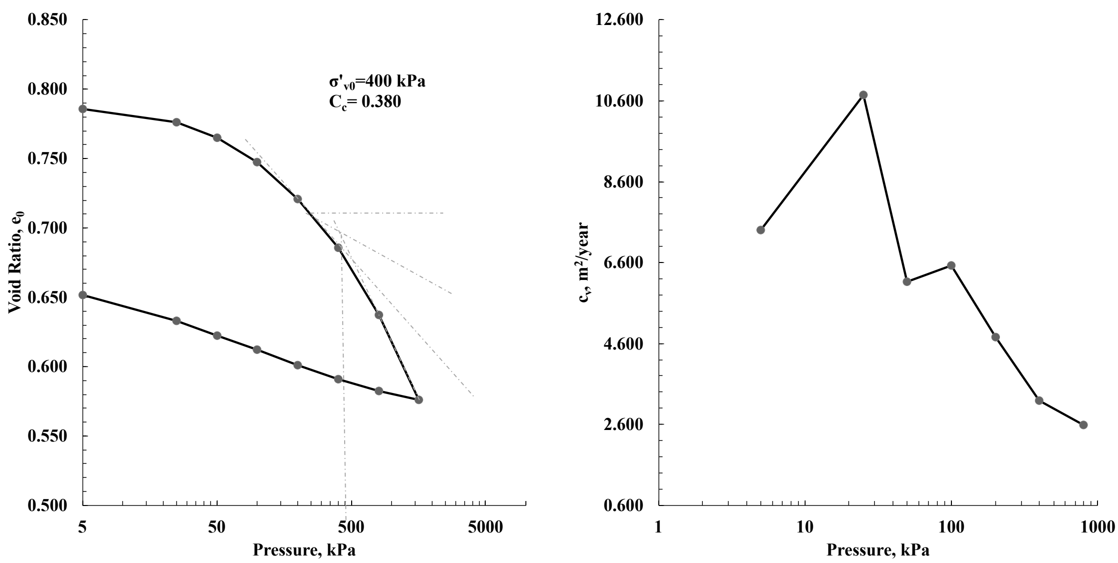

Figure 3.12: Graphical representation of one-dimensional oedometer test result for the sample in BH-05, depth at 17.5m. The graph of c_v is based on t_{50}.

A lined-scatter plot of void ratio versus log of effective pressure is shown in Figure 3.12 (refer Appendix B.6 for the plots generated in this investigation). The measured initial void ratio ranges from 0.59 to 1.62. Using deformation versus square root of time charts, t_{50} was estimated. This parameter aided in generating the charts of c_v as shown in Figure 3.12. t_{50} is seen to vary between 0.4min to a maximum of 14min. Also, using t_{50}, the values of c_v was observed to be 0.42m^2/year to 20.83m^2/year—depending on the stress load applied. Similarly, C_c of the samples were evaluated from the loading slope portion of the graph. C_c is observed to range from 0.13 to 0.58. Constrained modulus (M) was estimated using Equation 2.45. The values of M are seen to vary between 589.2kPa and 1615.0kPa.

3.4.8 Unconfined Compression Test

This test was conducted as per ASTM D2166-13. This test method covers the determination of the unconfined compressive strength (qu) of the soil specimen. It is experimentally conducted by measuring the maximum load required per unit area to attain 15% strain, or when the cylindrical soil specimen fails; whichever is attained first. q_u is calculated as the compressive stress at failure. s_u is half of q_u. As shown in Figure 3.13, q_u is evaluated to be 184.2kN/m^2. Thus, s_u was evaluated to be 92.1kN/m^2. The reader is referred to Appendix B.5 for the UCT plots used in this study.

Table 3.7: Summary of the UCT test results investigated in this study.

BH-ID	**Sample Depth, m**	q_u, kN/m^2
BH-5	17.5	223.1
BH-6	10.5	190.7
BH-18	10	112.6
BH-18	4	131.7
BH-27	8	70.3
BH-123	2.5	150.1
BH-123	4	104.4
BH-146	8.5	184.2
BH-250	10	42.3
BH-253	4	376.3
BH-264	5.5	278
BH-264	16	416.6
BH-274	4	284.1
BH-285	4	466.4
BH-296	4	170
BH-365	5.5	290.8
BH-398	5.5	465.2

3.5 Summary

The laboratory results are summarized as follows:

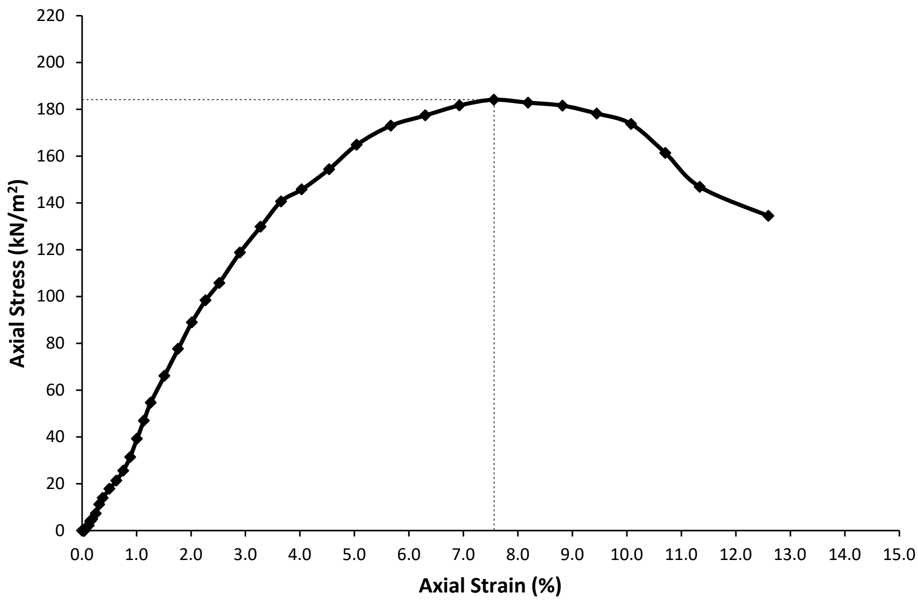

Figure 3.13: A typical UCT test result on an intact clay sample obtained from BH-146, depth at 8.5m.

1. Moisture content (w) varied between 20.1% to 44%.
2. For this investigation, sieve analysis reveals that sand size faction vary between 0 and 92%. Whereas, clay and silt size fraction is seen to range between 8 and 99%.
3. 19 inorganic samples were tested for evaluating Atterberg limit. The test unfolds that LL varied between 20 and 90, whereas the PI is seen to vary between 12 and 65.
4. Bulk unit weight of the soils in the study area varied between 16.9kN/m^3. Where as, the dry unit weight is seen to range from 7.1kN/m^3 to 11.1kN/m^3.
5. Specific gravity of the inorganic samples are observed to range in between 2.65 and 2.80.
6. Initial void ratio is observed to range in between 0.6 and 1.6. Compression index C_c varied between 0.1 and 0.6. Constrained modulus (M) is seen to vary between 589kPa and 1615kPa. Depending on the stress range, c_v is observed to vary between 0.4m^2/year to 20.8m^2/year.
7. Unconfined compression strength, obtained from UCT, is seen to be in the range of 70.3kN/m^2 to 466.4kN/m^2

Chapter 4

INTERPRETATION OF TEST RESULTS

4.1 Statistical Analysis for Constrained Modulus, M

One dimensional consolidation tests—adopting the procedures outlined in ASTM D2435—were conducted on undisturbed samples, obtained using Shelby tube from the field. Least-squares regression analyses were performed between the OCR and basic CPTu parameters—q_t, f_s, u_2—obtained from several points of the site. Also, basic soil parameters such the moisture content (ASTM D2216), and Atterberg limits (ASTM D4318) were determined from laboratory tests. Likewise, σ_{v0} and hydrostatic pore pressure (u_0) parameters were estimated from bore hole log information. 14 samples were utilized to conduct 1-D oedometer tests. The statistical measure of goodness of fit is reported in terms of the coefficient of determination R^2 and collinearity between the predictor and the independent data. The collinearity between the predictor and the independent data were graphically assessed. In this visual method, establishing the center of the quadrant required averaging the abscissa and the ordinate values. Thus, only correlations characterized by the highest visual collinearity and calculated R^2 are summarized in Table 4.1. Also, the perceived applicability for determining the parameter M from CPTu was rated as moderate by Robertson (2012a) (as shown in Figure 2.2).

Table 4.1: New proposed correlation for Constrained Modulus (M).

Correlation	Independent Function Type	n	R^2
$M = 3.61 * \sigma_{v0} + 607.67$	Field Based	14	0.43

Graphical assessment of the collinearity between M and σ_{v0} in Fig.4.1a demonstrates that the data points are mostly in the lower left and top right of the quadrant. Thus, an increasing linear trend between M and overburden pressure can be established with less scatter (R^2=0.87). Similarly, graphical analysis between M and moisture content (Fig.4.1b) reveals lot of scatter with no indication of a linear trend. A more scattered data was obtained between PI with M as shown in Fig.4.1c—thus no linear trend could be established with this dataset.

After evaluating 1-D oedometer constrained modulus, scatter plots with various CPTu parameters were plotted and presented in Figures 4.2 through 4.5. Scatter plot between M, q_c (as shown in Fig 4.2a) reveals no linear trend for this data set—the visual collinear assessment demonstrates that data points ($n = 14$) are concentrated at the center of the quadrant. Similarly, the plot between M and q_t as shown in Figure 4.2b demonstrates no

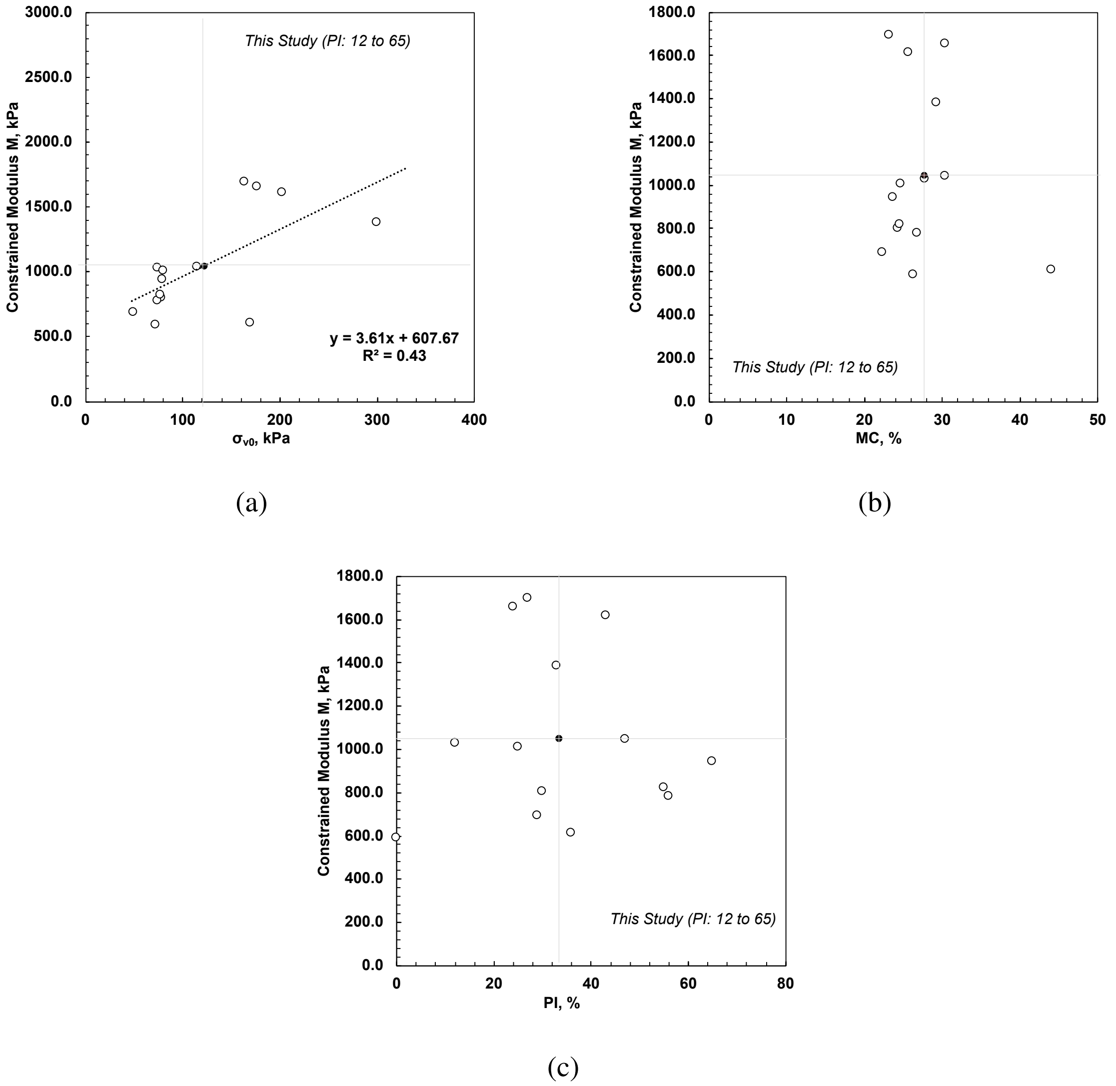

Figure 4.1: (a) Relationship between M and σ_{v0}. (b) Relationship between M and $w\%$. (c) Relationship between M and PI.

linear trend. In terms of cone penetration resistance, α_m obtained in this study is 0.28. This is a very low value relative to the α_m values seen in Table 2.3. Also, Kulhawy and Mayne (1990) observed that α_m magnitude ranges from 0.4 to 8, with majority being in the range between 1 and 3. The findings in this study are in stark contrast to the results reported in the literature. One possible explanation is that probes of different configurations and test methods were utilized in the reported literature. According to Kulhawy and Mayne (1990), non-standard cones (electrical and mechanical) and test procedures were utilized by these investigators. This observation also holds true for the CPTu probes used by Abu-Farsakh et al. (2007) as well.

Scatter plot between M and u_2 (as shown in Figure 4.3a) indicates no linear relationship between the data points ($n = 14$). Similarly, the trend between M and Δu (Figure 4.3b) exhibits a scattered data to establish any linear relationship for this data set.

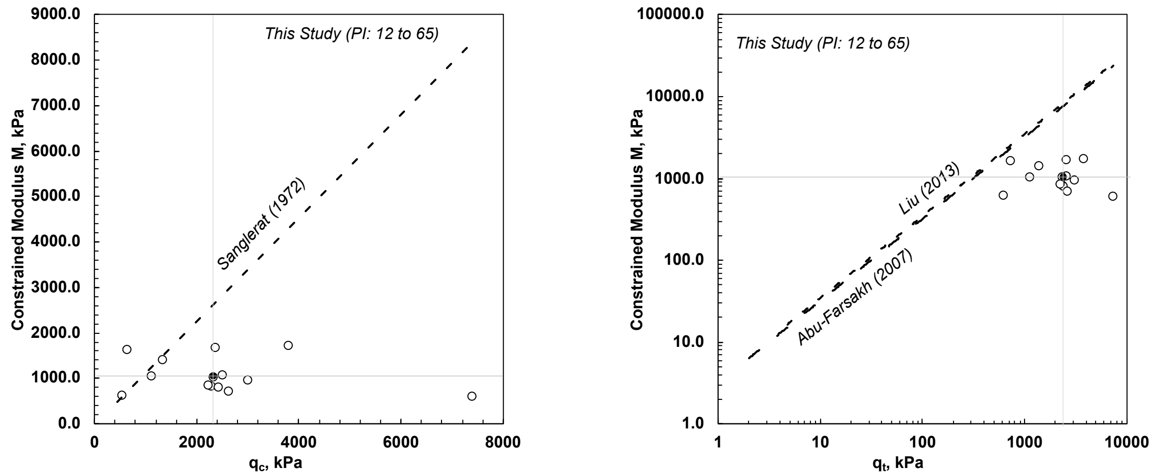

(a) (b)

Figure 4.2: (a) Relationship between M and cone penetration resistance (q_c). (b) Relationship between M and corrected cone penetration resistance (q_t).

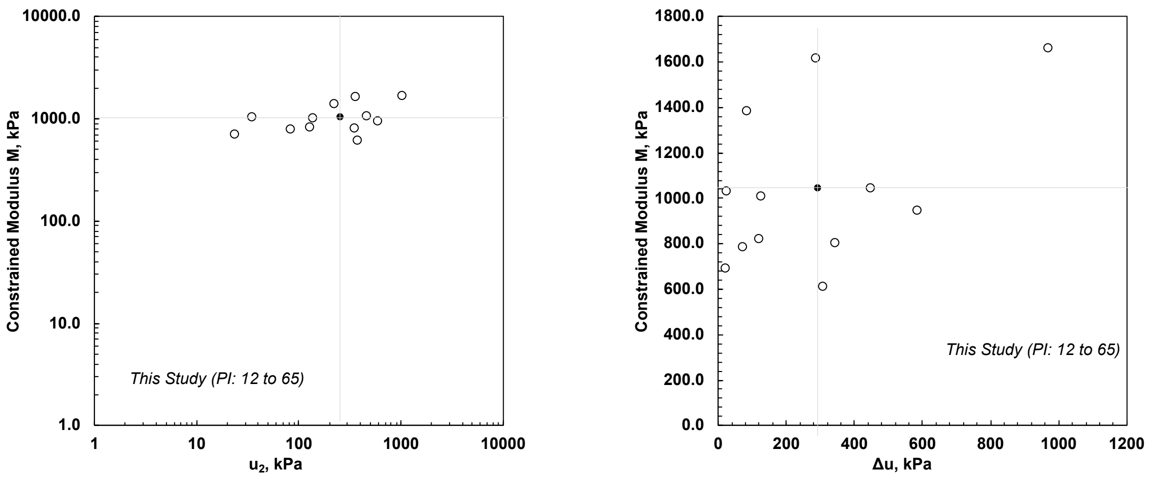

(a) (b)

Figure 4.3: (a) Relationship between M and pore pressure (u_2). (b) Relationship between M and excess pore pressure (Δu).

As seen in the scatter plot (Figure 4.4a), a visual assessment for collinearity reveals that the data is scattered between M and f_s to reach any conclusion. Similarly, scatter is also observed between M and F_r as seen in Figure 4.4b. In both the cases, most of the data points are located in the bottom right quadrant. This observation is more pronounced when the the CPTu parameters ($\sqrt{q_t}$ and $\sqrt{f_s}$) are taken as shown in Figure 4.5. Hence, no empirical correlation could be established with this data set (n = 14).

In terms of net cone resistance ($q_t - \sigma_{v0}$), the scatter plot (as shown in Figure 4.6a) suggests a similar result obtained using q_c, and q_t—accompanied by a lot of scatter exists for the

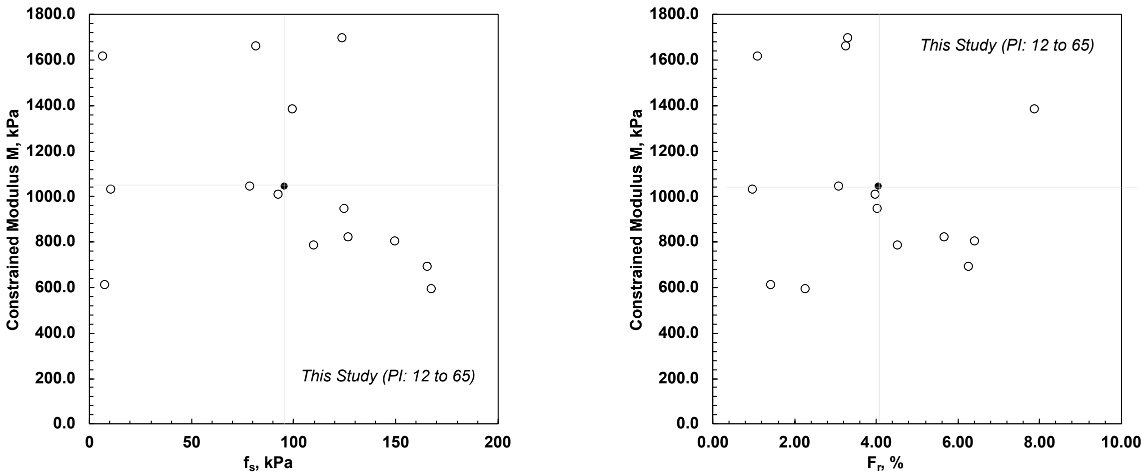

(a) (b)

Figure 4.4: (a) Relationship between M and sleeve friction (f_s). (b) Relationship between M and normalized sleeve friction (F_r).

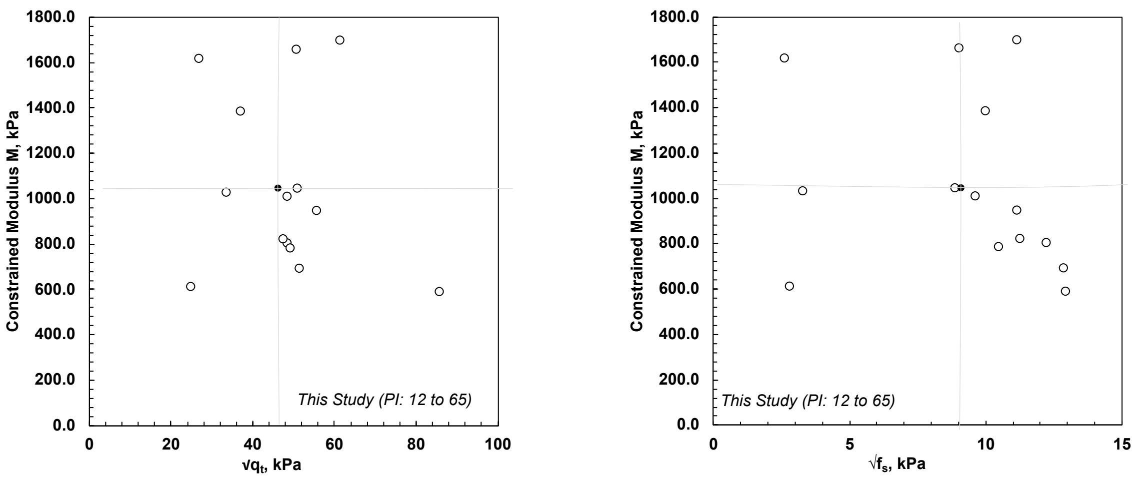

(a) (b)

Figure 4.5: (a) Relationship between M and square-root of corrected cone tip resistance ($\sqrt{q_t}$). (b) Relationship between M and square-root of sleeve friction ($\sqrt{f_s}$).

lower range of net cone resistance (less than 2400kPa). More data is required for the lower values of ($q_t - \sigma_{v0}$) to establish a correlation. Likewise, scatter plot between M and total cone resistance ($q_t + f_s + \sigma_{v0}$) also shows scatter with no linear trend (as seen in Figure 4.6b). This relation is not found in existing literature, however, since a linearly increasing trend was observed between M and σ_{v0} (as seen in Figure 4.1a), an attempt was made to explore its effect on q_t and f_s. In this study, no relationship could be established using the curated data set ($n = 14$).

Another set of relation not found in the literature are between M, Q_{tn}, and I_c. As seen in

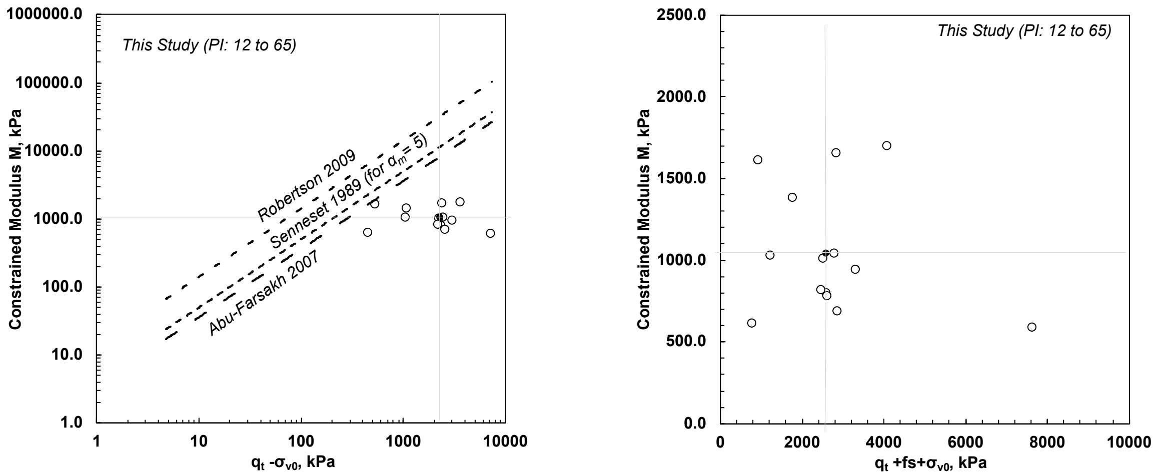

(a) (b)

Figure 4.6: (a) Relationship between M and net cone resistance ($q_t - \sigma_{v0}$). (b) Relationship between M and total cone resistance ($q_t + f_s + \sigma_{v0}$).

Figure 4.7a, unlike the CPTu parameters q_c, q_t and $q_t - \sigma_{v0}$ where the data points were concentrated in one point, a lot of scatter is observed between M and normalized cone tip resistance Q_{tn}. A negative trend is clearly visible. Howeever, it can be concluded that more data points are needed to reach a definite conclusion for cone tip resistance correlations for M. In terms of the dimensionless parameter I_c, the collinearity is clearly visible—the data points are located at the lower left and the rop right quadrants. Hence, an increasing linear trend is observed. In spite of obtaining a statistically significant correlation, Scattering is observed at the upper range (<2.5) of I_c as seen in Figure 4.7b. More data will be required in the upper range of I_c to reach a definite conclusion.

4.2 Statistical Analysis for Compression Index, C_c

As seen in Figure 4.8 through 4.10, the scatter plots between compression index (C_c) and cone tip resistance reveals a hyperbolic relationship. This finding is in agreement with the findings of Sanglerat (1972) (refer to Figure 2.23). It is observed that the most of the data points are within the upper limit defined by Sanglerat (1972). As seen in Figure 4.10, the scatter plot between q_t and q_t/C_c exhibits a distinct linear trend (R^2 = 0.95)—thus confirming the hyperbolic distribution of C_c with respect to q_t. Similar observation is also evident for the scatter plot between compression ratio (CR) and q_t as seen in Figure 4.9.

Figure 4.8 shows a positively linear trend between moisture content (w%) plotted against C_c. The statistical fit of goodness was measured in terms of coefficient of determination (R^2) of 0.78. The data points are consistently less scattered below 25%. The findings are also in agreement with Kulhawy and Mayne (1990) point that more consistent correlations

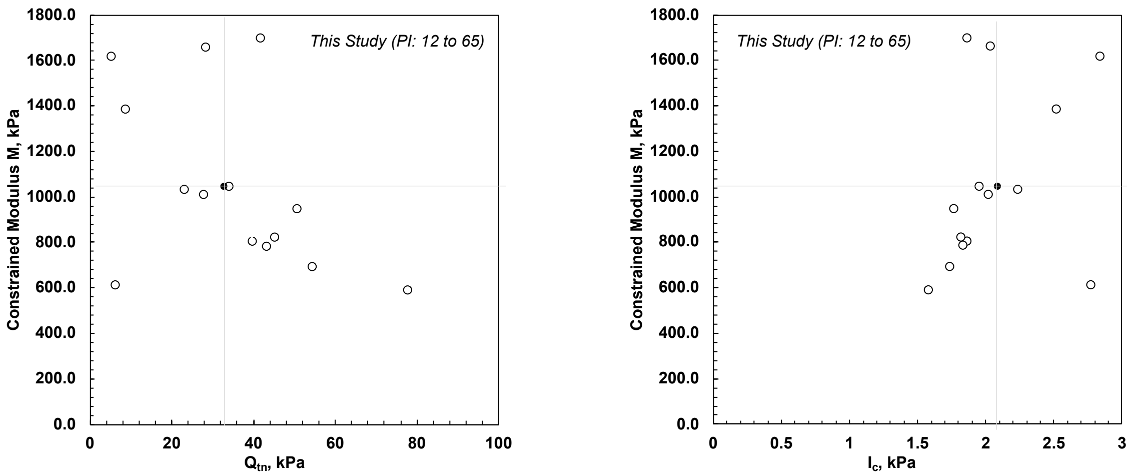

(a) (b)

Figure 4.7: (a) Relationship between M and normalized cone resistance resistance (Q_{tn}). (b) Relationship between M and Soil Behavior Type Index (I_c).

are obtained between $w\%$ and C_c.

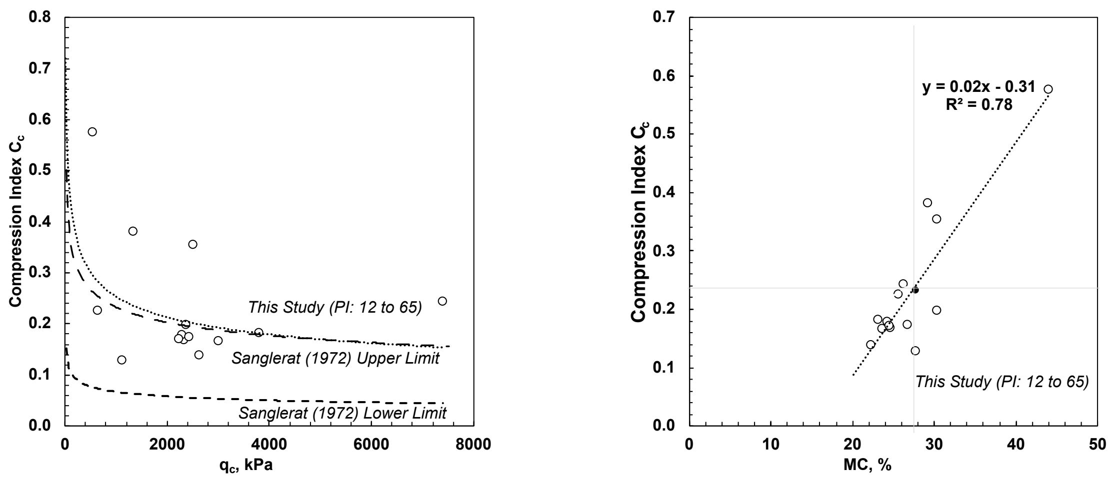

(a) (b)

Figure 4.8: (a) Relationship between C_c and cone resistance resistance (q_c). (b) Relationship between C_c and $w\%$.

4.3 Statistical Analysis for Overconsolidation Ratio, OCR

For profiling OCR in this work, $\sigma_p^{'}$ was determined using Casagrande (1936) graphical interpretation method. Also, $\sigma_{v0}^{'}$ was estimated using bore log information. Least-squares regression analyses were performed between the OCR and basic CPTu parameters—q_t, f_s, u_2. The statistical regression correlations models are divided into two independent function types—Field Based and Laboratory Based . In the field based models, measurements

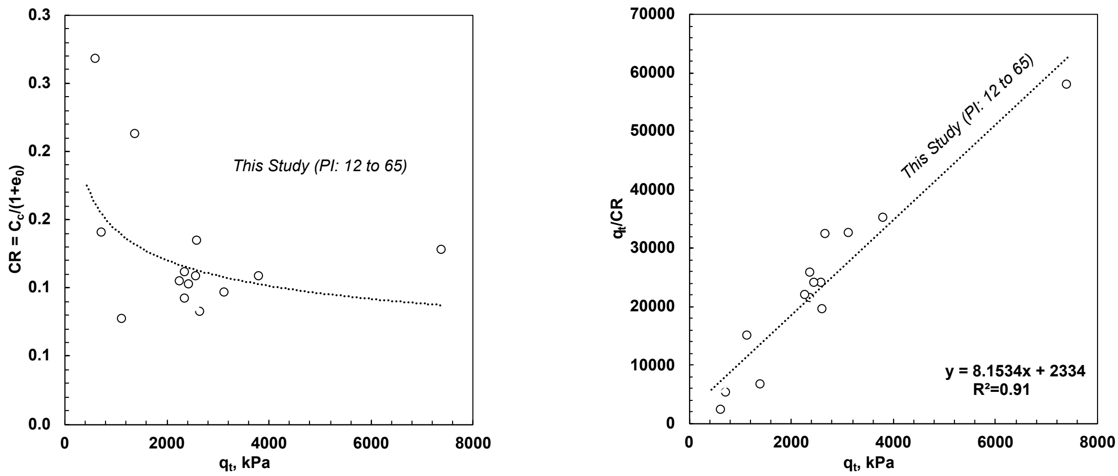

(a) (b)

Figure 4.9: (a) Relationship between CR and corrected cone resistance resistance (q_t). (b) Relationship between q_t/CR and corrected cone resistance resistance (q_t).

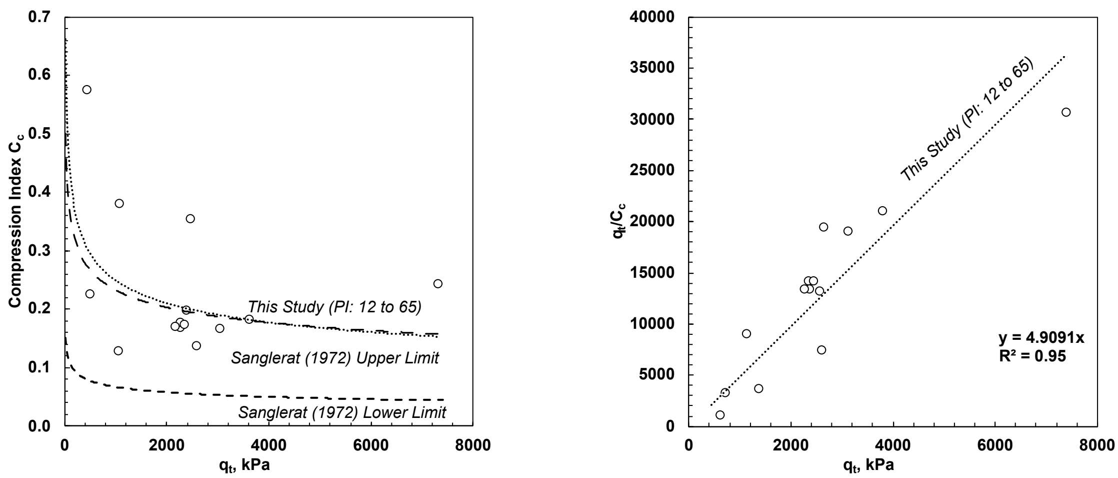

(a) (b)

Figure 4.10: (a) Relationship between C_c and corrected cone resistance resistance (q_t). (b) Relationship between q_t/C_c and corrected cone resistance resistance (q_t).

from the CPTu—q_c, q_t, f_s and u_2—are utilized to formulate the correlations. Whereas in the laboratory based models, laboratory data and or σ_{v0} are incorporated in addition to the CPTu data to explore the correlations. It should be noted that only 14 out of 17 samples were utilized to conduct 1-D oedometric tests on. This highlights the problems associated with recovering enough quality undisturbed samples for laboratory testing. Also, a certain degree of uncertainty involves in indexing σ_p' from a recovered undisturbed sample—since it requires judgment. However, statistical analysis reduces these uncertainties. The statistical measure of goodness of fit is reported in terms of the coefficient of determination R^2

and collinearity between the predictor and the independent data. The collinearity between the predictor and the independent data were graphically assessed. In this visual method, establishing the center of the quadrant required averaging the abscissa and the ordinate values. Thus, only correlations characterized by the highest visual collinearity and calculated R^2 are summarized in Table 4.3. It should be noted that Robertson (2012a) rated the perceived applicability for determining OCR from CPTu as moderate (see Figure 2.2). Also, as seen in Table 4.2, Chen and Mayne (1996) deemed R^2 less than 0.38 to be poor. Similarly, Chen and Mayne (1996) rated correlations in the range of $0.47<R^2<0.67$ to be fair.

Table 4.2: Degree of statistical goodness as per Chen and Mayne (1996) for OCR of clay deposits

Range of R^2	**Correlation Strength**
$0.01<R^2<0.38$	Poor
$0.47<R^2<0.67$	Fair

Correlation	**Independent Function Type**	**n**	**R^2**
$OCR = 0.0648 * Q_t$	Field Based	14	0.69
$OCR = 0.1412 * Q_{tn}$	Field Based	14	0.85
$OCR = 1.1467 * F_R$	Field Based	14	0.73
$OCR = 0.0645 * (q_t - u_2)/\sigma'_{v0}$	Field Based	14	0.67
$OCR = 0.0651 * (q_t - \sigma_{v0} - \Delta u)/\sigma'_{v0}$	Field Based	14	0.66
$OCR = 0.1346 * (q_t + f_s)/\sigma_{v0}$	Field Based	14	0.74
$OCR = 1.1978 * (f_s/\sigma'_{v0}) + 2.526$	Field Based	14	0.60

Table 4.3: New proposed correlations for OCR.

Scatter plot of q_c, q_t against OCR are plotted in Figure 4.11. The laboratory derived OCR is observed to increase with q_c—this is in agreement with the findings of Tavenas and Leroueil (1979) for destructured clay. Also, similar trends were obtained by Mayne and Holtz (1988). However, for this data set ($n = 14$), a graphical assessment of collinearity could not be established as seen in Figure 4.11a. Similarly, the collinearity between the laboratory derived OCR and q_t could not be established as seen in Figure 4.11b. More data is required to establish this relationship, as an increasing linear trend was demonstrated by Mayne and Holtz (1988) for a relatively larger clay database. Statistically, not much difference is observed between the parameters q_c, q_t, and $(q_t - \sigma_{v0})$ for evaluating OCR. Also, an upper and lower limit could not be established in this work using limited data points. However, assuming that Tavenas and Leroueil (1979) line is the upper limit, the results unfold that most of the data set points are well below it by at least a factor of 5. Heavily overconsolidated soils (OCR>5) were not omitted from these plots. In spite of statistically significant results reported in the literature, Wroth (1984) suggested that

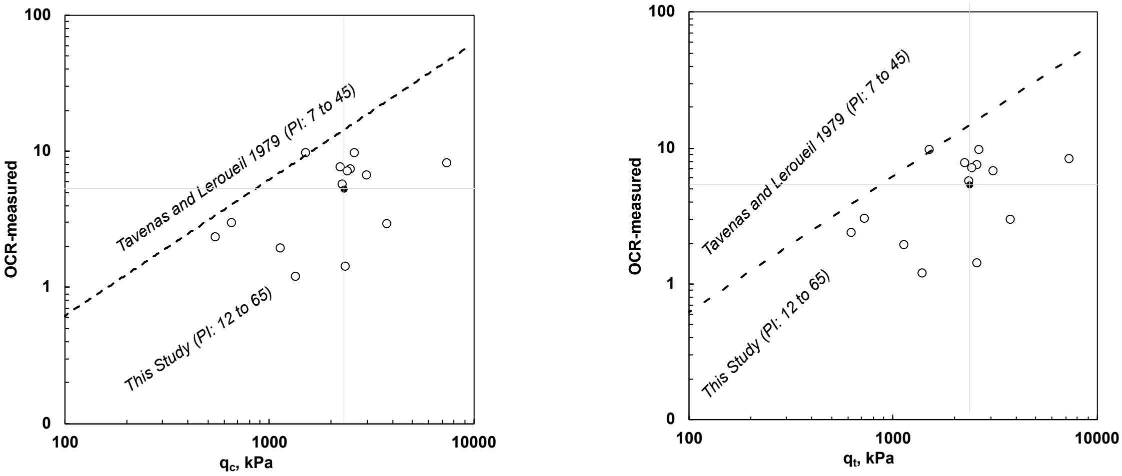

(a) (b)

Figure 4.11: (a) Relationship between OCR and cone penetration resistance (q_c). (b) Relationship between OCR and corrected cone penetration resistance (q_t).

the maximum shear stress attained in undrained conditions must be related to the difference between two total (or two effective) stresses. Hence, caution should be exercised in utilizing correlations involving cone tip resistance only.

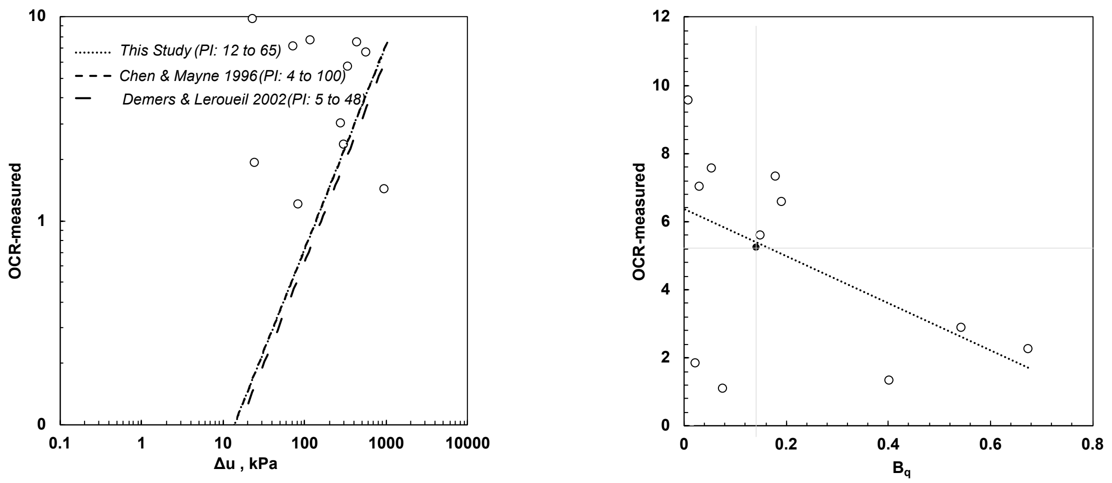

(a) (b)

Figure 4.12: (a) Relationship between OCR and B_q. (b) Relationship between OCR and excess pore pressure ($u_2 - u_0$).

No correlation between OCR and Δu was obtained as seen in Figure 4.12a. The data points—11 in total—are highly scattered even after removing data points with a negative value. Robertson et al. (1986a) recommended using pore pressure measurements over q_c for evaluating s_u (and in turn OCR). However, the results herein suggests otherwise. Demers and Leroueil (2002) also pointed out that the correlation of OCR using pore pressure data usually results in more scattered results than those using cone tip resistance. This observation is in agreement with the findings of this study (as shown in Figure 4.12a). Mayne and Holtz (1988) concluded that B_q generally decreases with increasing OCR. This is evident in Figure 4.12b, where a negative trend is observed (the highest values of OCR are characterized by the lower values of B_q). Similarly, Pant (2007) obtained linearly inverse relationship between excess pore pressure generated and OCR for Louisianna clay soils. Whereas Chen and Mayne (1996) observed marginal trend of OCR decreasing with increasing B_q for both intact and fissured clays. Likewise, Demers and Leroueil (2002) also obtained a linearly inverse relationship accompanied with a lot of scatter but concluded that B_q is not useful in determining OCR despite Wroth (1984) recommending on using B_q to index OCR. Similar conclusion was also reached by Chen and Mayne (1996). Chen and Mayne (1996) demonstrated that the assumption made by Wroth (1984) regarding B_q being akin to Skempton's triaxial pore pressure is misleading due to large octahedral normal stress component affecting the pore pressure readings from the piezocone, and thus B_q. In this research, due to negative pore pressure readings, the number of workable observed data points were reduced to only 11 in numbers—which is very few in quantity to even statistically reach any conclusion (see Figure 4.12). Hence, it is concluded that no correlation was obtained between B_q and OCR.

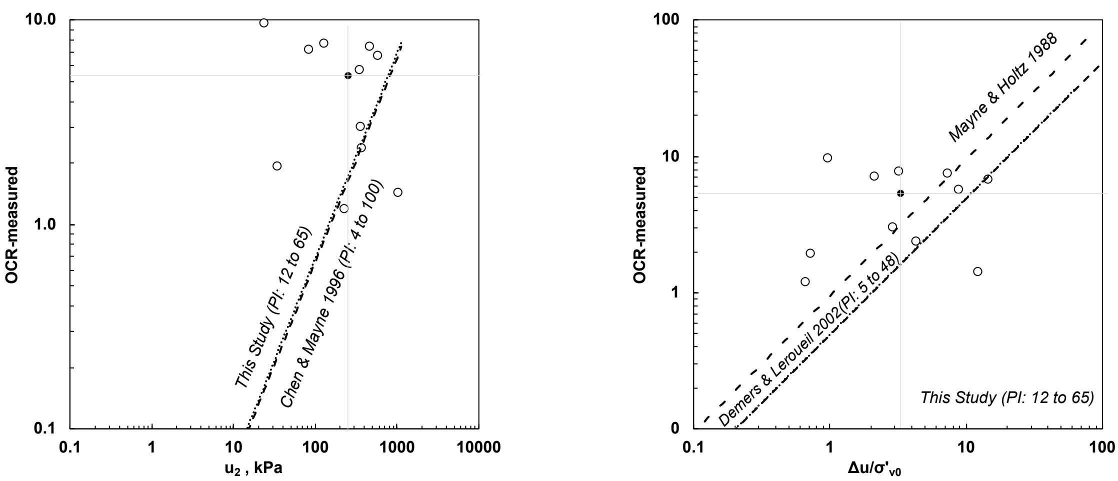

(a) (b)

Figure 4.13: (a) Relationship between OCR and pore pressure (u_2). (b) Relationship between OCR and Normalized pore pressure u_2/σ'_{v0}.

Similarly, no correlation between OCR and u_2 was obtained as seen in Figure 4.13a. The observed trend is slightly better than that seen in Figure 4.12, however, the data points remain limited and highly scattered. It can be concluded that pore pressure measurements are more scattered than that obtained with cone tip resistance. This observation is in line with Robertson (1990) that for interpreting OCR, pore pressure measurements are less reliable than cone resistance q_c. Pore pressure measurements are prone to error in the measurement—such as poor calibration, unstaurated filters, and dilatory response in high OCR soils (negative u_2) (Lunne et al., 1997). Despite u_2 and Δu being known to predict OCR of the soil deposit, a statistically significant relationship was not obtained in this study. Normalizing u_2 readings with respect to σ'_{v0} tend to smooth out the scatter slightly, however, no correlation could be established as seen in Figure 4.13b. However, using theory from CSSM and cavity expansion for driven piles in clay, Mayne and Holtz (1988) observed that $\Delta u/\sigma'_{v0}$ increases with OCR. Similarly, Robertson (2009) also pointed out the usefulness of normalizing to obtain better relationships.

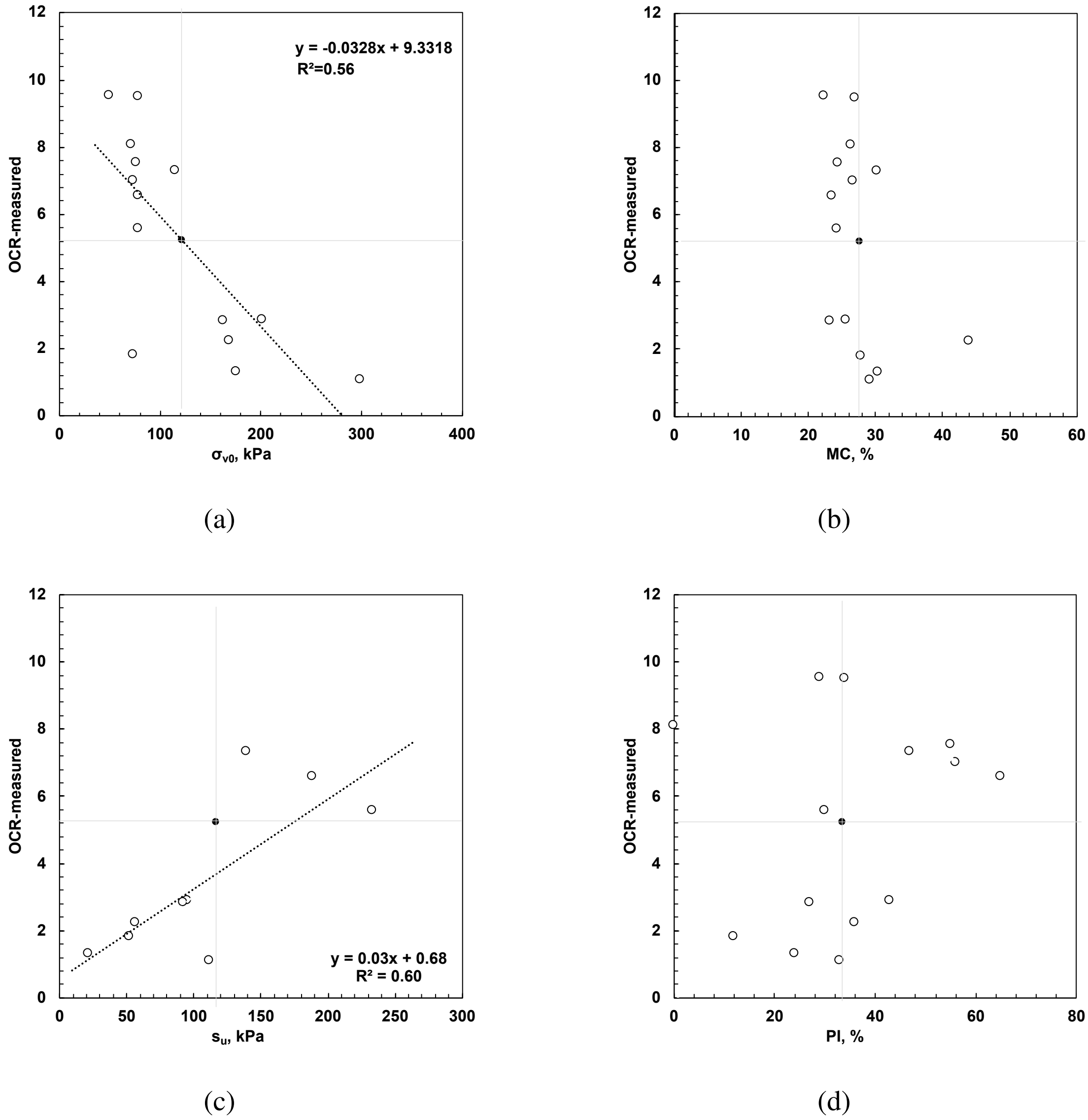

Figure 4.14: (a) Relationship between OCR and σ_{v0}. (b) Relationship between OCR and w%. (c) Relationship between OCR and s_u. (d) Relationship between OCR and PI.

Plot between OCR and in situ effective stress (Figure 4.14a) reveals a decreasing trend taking place. However, the data points are scattered (R^2= 0.56). OCR is also found to be influenced by s_u as shown in Figure 4.14c. However, no relationship could be established for plots between OCR, PI, and w% for the heavily consolidated soils (OCR>5) as seen in Figures 4.14b and 4.14d. A strong positively linear trend is observed in the plot between OCR and s_u (R^2= 0.88) for the 9 data points. Also, for low OCR values, the data points are less scattered than the data points for higher OCR. Likewise, the plot between OCR and PI, in linear scale, unfolds a positively increasing trend. However, more data is required to establish this relationship.

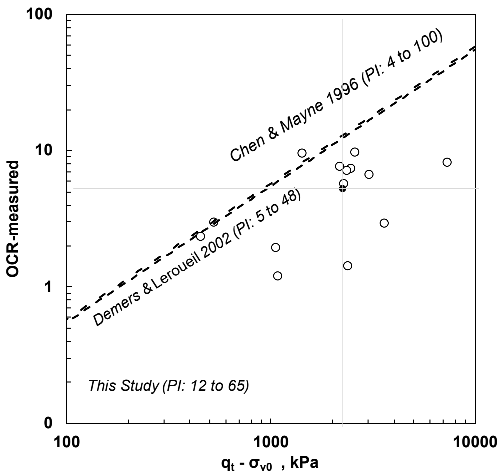

(a)

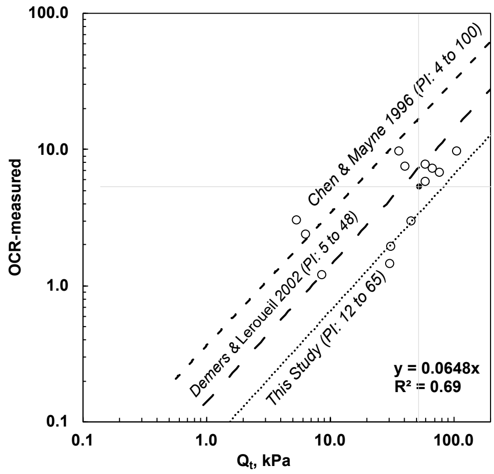

(b)

Figure 4.15: (a) Relationship between OCR and net cone resistance ($q_t - \sigma_{v0}$). (b) Relationship between OCR and Normalized cone tip resistance Q_t.

As seen in Figure 4.15b, the parameter Q_t demonstrates a linear trend (R^2=0.69). On the other hand, the CPTu parameter ($q_t - \sigma_{v0}$) does not produce any linear relationship visually as seen in Figure 4.15a—the data points are mostly concentrated near the center of the quadrant. Thus more data is required to confirm this relationship. However, normalizing the term ($q_t - \sigma_{v0}$)—resulting in Q_t—tend to smooth the scatter slightly. This is in line with reasoning of Wroth (1988). Several investigators also established good agreement between OCR and Q_t (e.g., Chen and Mayne, 1996; Demers and Leroueil, 2002; Pant, 2007 and others). Although Q_t does not utilize pore pressure measurements to evaluate OCR, it remains indispensable to obtain corrected cone resistance. Demers and Leroueil (2002) also recommended using Q_t for profiling OCR in sensitive clays due to it being independent of w%, PI and clay fraction.

Likewise, the term Q_{tn}, updated by Zhang et al. (2002), was used to profile OCR as seen in Figure 4.16a. The parameter Q_{tn} demonstrated a strong linear statistical trend with R^2=0.85. Also seen in Figure 4.16b is the normalized sleeve friction F_r plotted against OCR. The data points are relatively scattered, accompanied by R^2=0.73.

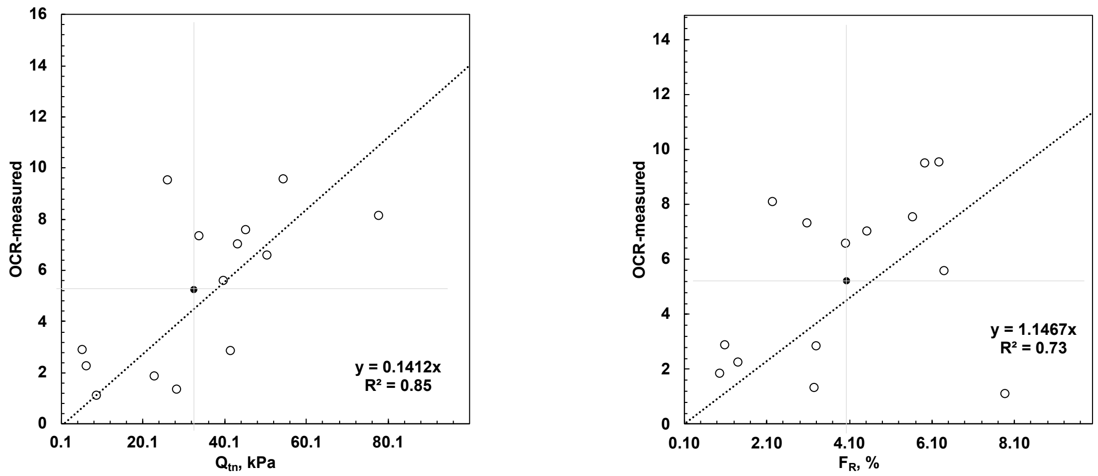

(a) (b)

Figure 4.16: (a) Relationship between OCR and Normalized cone resistance Q_{tn}. (b) Relationship between OCR and Normalized friction ratio F_R.

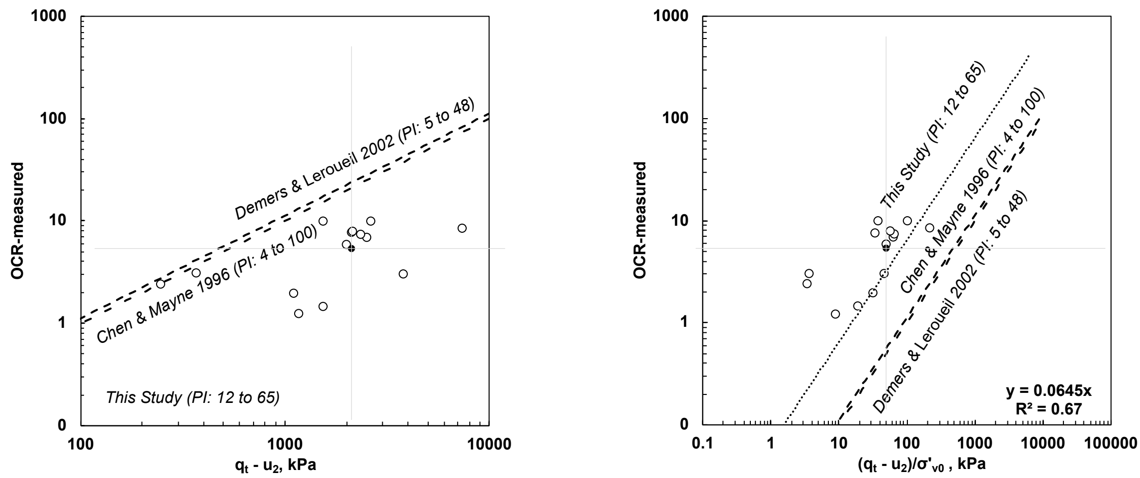

(a) (b)

Figure 4.17: (a) Relationship between OCR and effective cone resistance $(q_t - u_2)$. (b) Relationship between OCR and Normalized effective cone resistance $(q_t - u_2)/\sigma'_{v0}$.

Relationship between OCR and the parameter $(q_t - u_2)$ could not be established as seen in Figure 4.17a. Visual assessment reveals some scatter and thus failed to comprehensively produce a collinearity. It can be concluded that more data is required to establish this correlation. As seen in Figure 4.17b, utilizing σ'_{v0} as the normalization factor tend to smooth out this relationship significantly (R^2=0.88). This improved relationship is in agreement with the findings of other researchers [e.g., Chen and Mayne (1996) and Konrad and Law (1987a) and others]. Thus, the parameter $(q_t - u_2)/\sigma'_{v0}$ is found to be a good predictor of

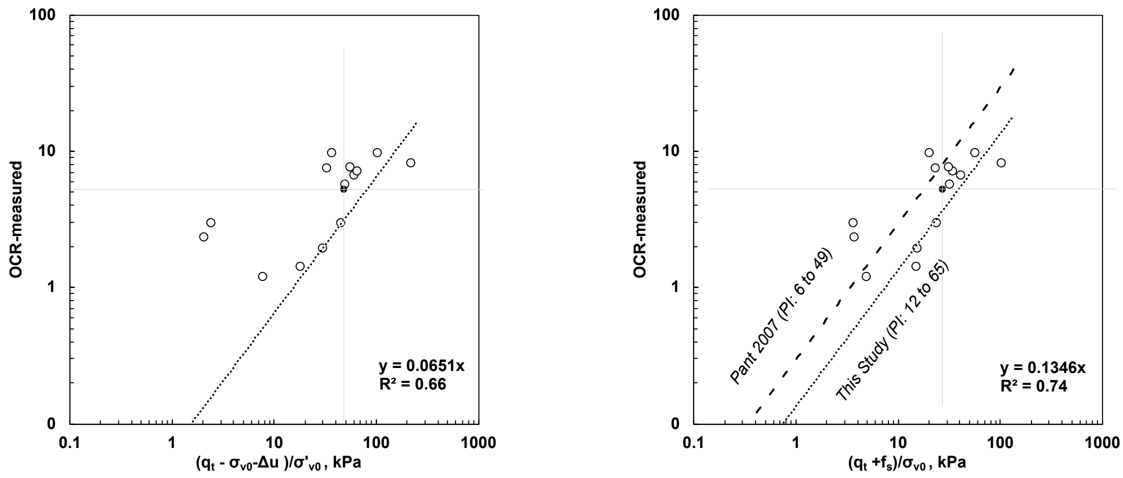

(a) (b)

Figure 4.18: (a) Relationship between OCR and Battaglio et al. (1986) referenced parameter $(q_t - \sigma_{v0} - \Delta u)/\sigma'_{v0}$). (b) Relationship between OCR and Normalized Total cone resistance $(q_t + f_s)/\sigma_{v0}$.

OCR. Also, a statistically significant correlation (R^2=0.66) was obtained using Battaglio et al. (1986) referenced parameter $(q_t - \sigma_{v0} - \Delta u)/\sigma'_{v0}$ (see Figure 4.18). A low scattering of data points is observed for OCR>5. Similarly, the normalized parameter $q_t + f_s$ with respect to σ'_{v0} slightly improves the relationship, and is thus strong indicator of OCR (R^2=0.89) as seen in Figure 4.18.

In terms of sleeve friction, a highly scattered relationship was obtained with the laboratory derived OCR as shown in Figure 4.19a. Many investigators, such as Chen and Mayne (1996), DeJong et al. (2001), and Lunne et al. (1997), did not explore OCR correlations with f_s as they deemed it unreliable and recommended minimizing its use. Normalizing f_s with respect to σ'_{v0} significantly improves the relationship (R^2=0.60) as shown in Figure 4.19b. Given the findings, it can be concluded that normalized sleeve friction can be a good indicator of OCR, despite what the literature suggests otherwise.

4.4 Dissipation Test Results

Method for obtaining t_{50} was obtained using the method outlined by Sully et al. (1999). Figures 4.20 through 4.24 indicates that most of the dissipation curve in this study were dialotry. Dilatory responses are associated with overconsolidated clays and silts (Burns and Mayne, 1998; Sully et al., 1999). t_{50} was evaluated using square root of time plot to find the initial u_i.

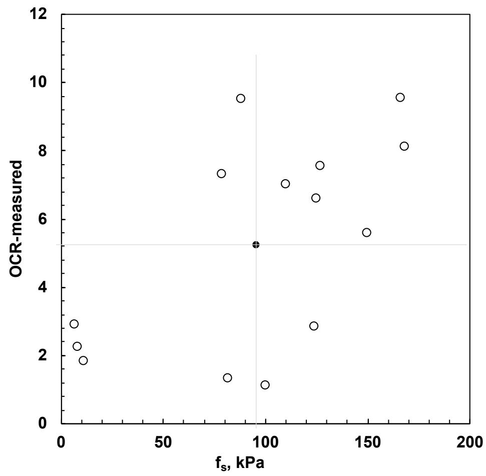

(a)

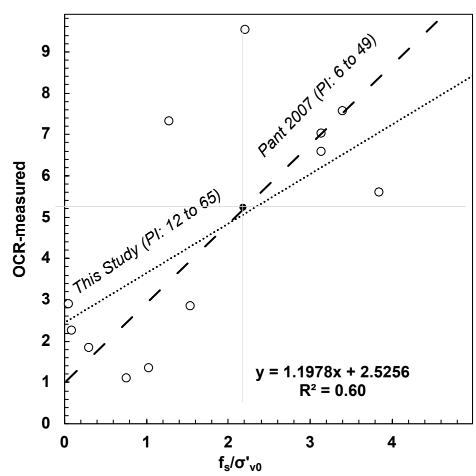

(b)

Figure 4.19: (a) Relationship between OCR and sleeve friction (f_s). (b) Relationship between OCR and Normalized sleeve friction (f_s/σ'_{v0}).

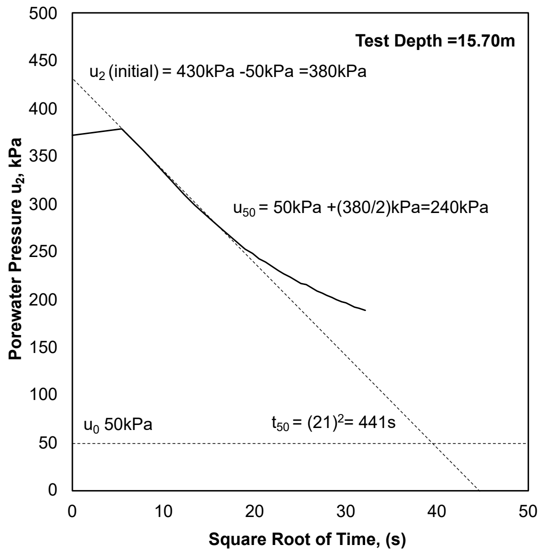

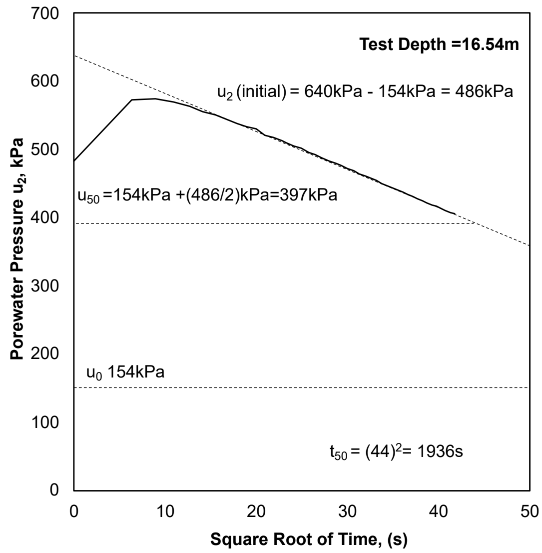

Figure 4.20: Dissipation test result interpretation for BH-05 and BH-06.

4.4.1 Statistical Analysis for Coefficient of Consolidation, c_v

Linear regression models were utilized to formulate correlations between laboratory derived c_v and CPTu parameters (q_t, Q_{tn}, $(q_t - \sigma_{v0})$, $(q_t - u_2)$, f_s, Δu_2, t_{50} and u_{50}). Parameters t_{50} and u_{50} were interpreted using dissipation curves shown in Figure 4.20 through Figure 4.24. Scatter plots of laboratory derived c_v versus CPTu parameters are shown in Figure 4.25 through Figure 4.29. Data from 10 samples could be utilized to formulate statistical correlations in terms of R^2. The statistical measure of goodness of fit is reported in terms of the coefficient of determination R^2 and collinearity between the predictor and the independent data. The collinearity between the predictor and the independent data

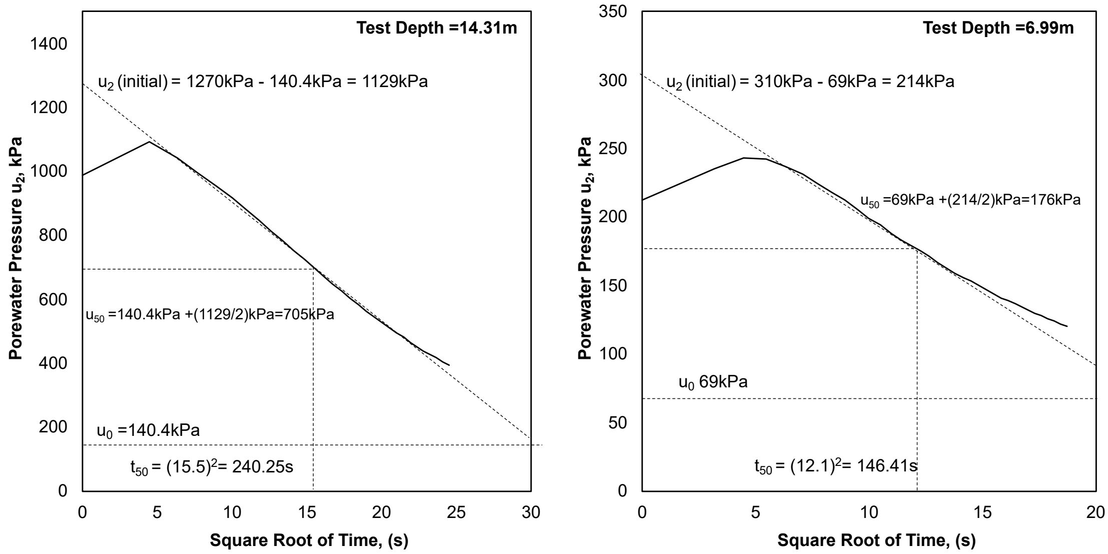

Figure 4.21: Dissipation test result interpretation for BH-18 and BH-24.

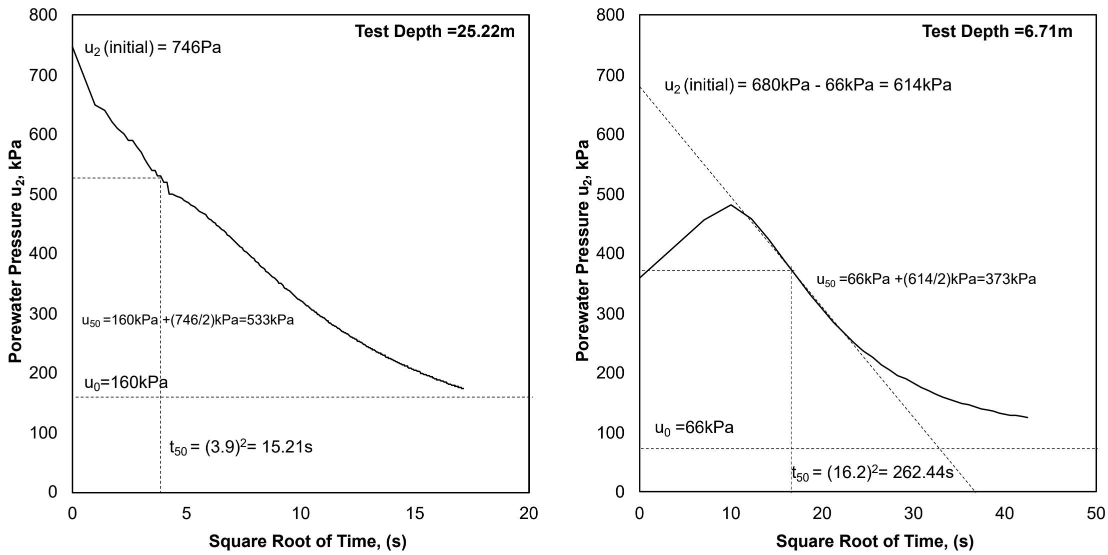

Figure 4.22: Dissipation test result interpretation for BH-146 and BH-250.

were graphically assessed. In this visual method, establishing the center of the quadrant required averaging the abscissa and the ordinate values.

Scatter plot between c_v and t_{50} in this study (Figure 4.20) did not follow the conventional inverse trend [e.g., Teh and Houlsby (1991)]. Also, no linear correlation exists with the calculated dissipation data set ($R^2 < 0$). Similarly, pore pressure corresponding to 50% dissipation (u_{50}) also reveals no correlation with c_v.

As seen in Figure 4.26, scatter plots between laboratory derived c_v and CPTu derived pore pressure (beginning of dissipation test, u_i) and Δu also demonstrates no correlation, accompanied by R^2 close to zero.

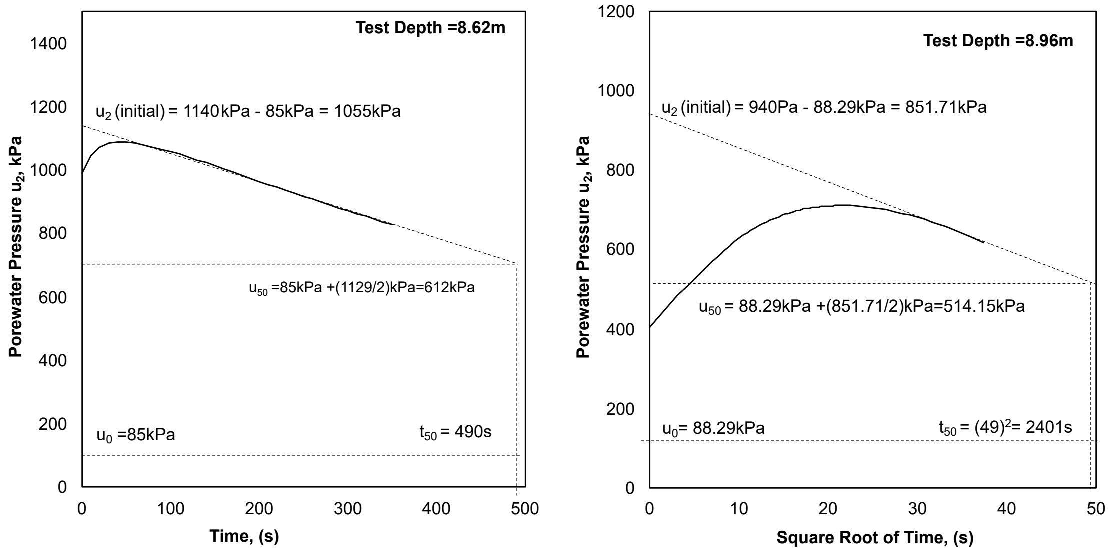

Figure 4.23: Dissipation test result interpretation for BH-264 and BH-274.

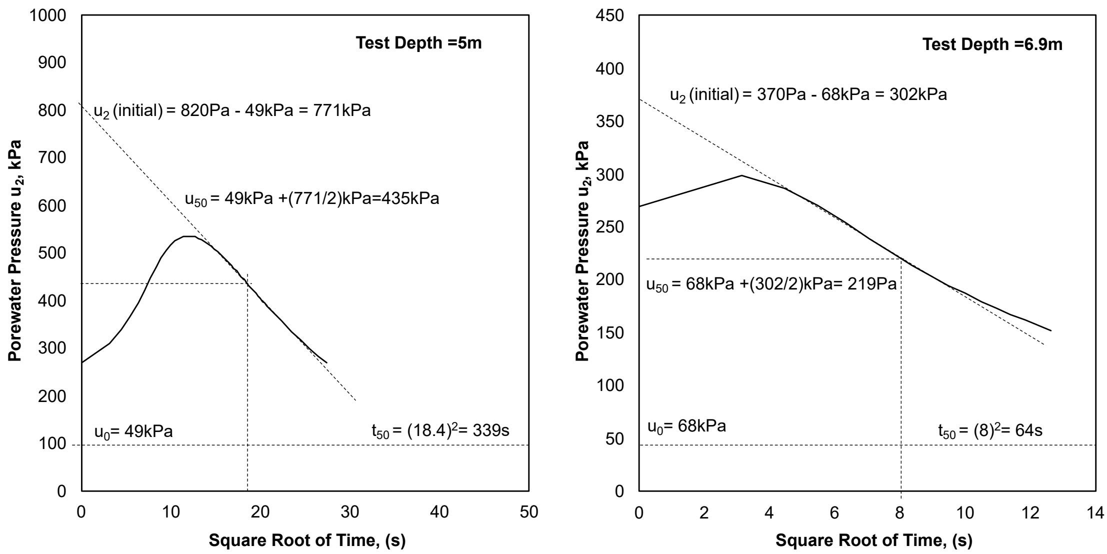

Figure 4.24: Dissipation test result interpretation for BH-374 and BH-398.

As seen in Figure 4.27, in this study, c_v is increasing linearly for an increasing $\sqrt{q_t}$ and f_s. However, more data is required to confirm the collinearity.

Figure 4.28 and Figure 4.29 shows that relationship remains scattered in terms of net cone resistance, effective cone resistance, and normalized cone tip resistance. Thus, more data points are required to reach a conclusion. Also, the laboratory derived c_v plotted against CPTu derived c_v is very scattered. A few reasons can be attributed to such observations:

1. The dissipation tests were not conducted for at least 4 hours. Consequently, the early fitting of the curve required a lot of judgement. Also, equilibrium pore pressure had to be assumed based on ground water level instead of observing the dissipation curve.

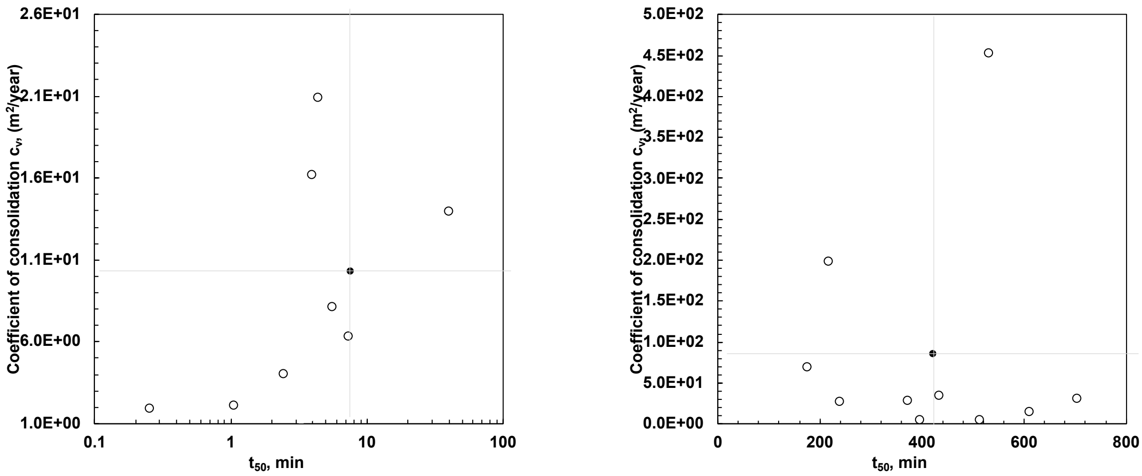

(a) (b)

Figure 4.25: (a) Relationship between c_v and t_{50} . (b) Relationship between c_v and u_{50}.

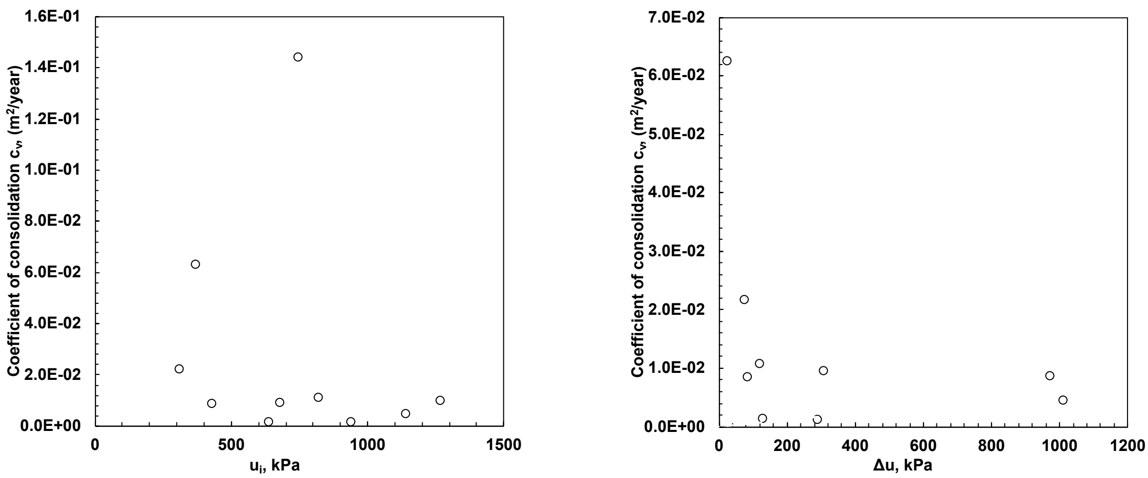

(a) (b)

Figure 4.26: (a) Relationship between c_v and u_i (estimated initial pore pressure in dissipation test). (b) Relationship between c_v and Δu.

2. In situ drainage condition may not match with the the two-way drainage condition of the sample in the consolidation cell.

4.5 Statistical Analysis for Undrained Shear Strength

Linear and non-linear regression models were explored to formulate correlations between s_u and basic CPTu parameters—q_t, f_s, u_2—for Dhaka soil. In this work, the reference $s_u(lab)$ is evaluated from unconfined consolidation test (UCT) by evaluating unconfined compressive strength. The undisturbed samples were collected from Shelby tubes in the laboratory. Also, the statistical regression correlations models are divided into two inde-

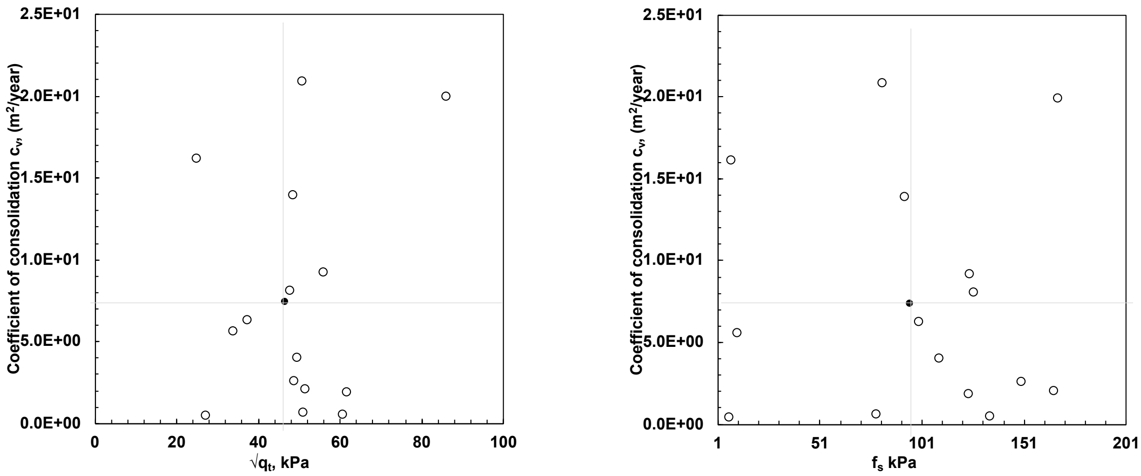

(a) (b)

Figure 4.27: (a) Relationship between c_v and $\sqrt{q_t}$. (b) Relationship between c_v and f_s.

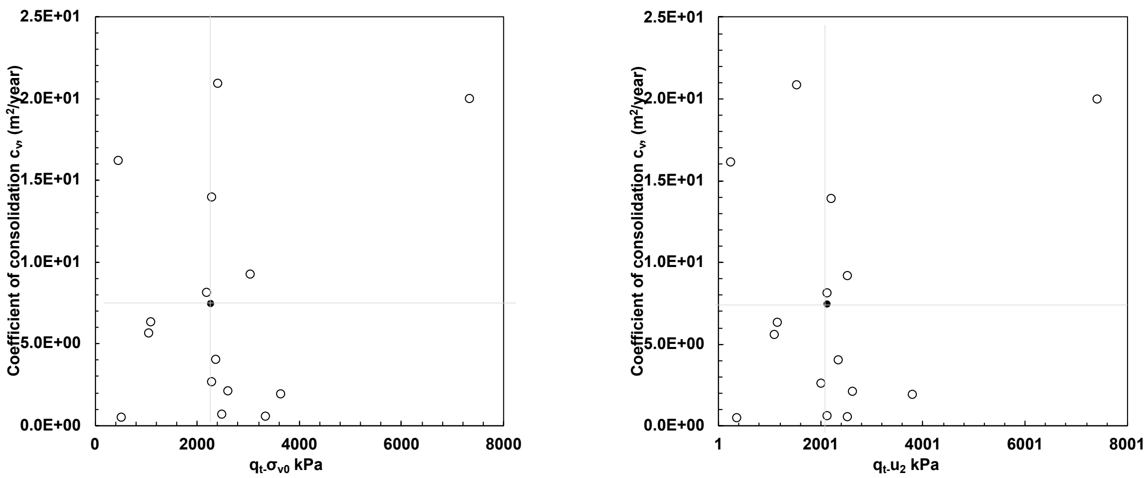

(a) (b)

Figure 4.28: (a) Relationship between c_v and net cone resistance. (b) Relationship between c_v and effective cone resistance.

pendent function types—Field Based and Laboratory Based . In the field based models, measurements from the CPTu—q_c, q_t, f_s and u_2—are utilized to formulate the correlations. Whereas in the laboratory based models, laboratory data and or σ_{v0} are incorporated in addition to the CPTu data to explore the correlations. The statistical measure of goodness of fit is reported in terms of the coefficient of determination R^2 and collinearity between the predictor and the independent data. The collinearity between the predictor and the independent data were graphically assessed. In this visual method, establishing the center of the quadrant required averaging the abscissa and the ordinate values. Thus, only correlations characterized by the highest visual collinearity and calculated R^2 are

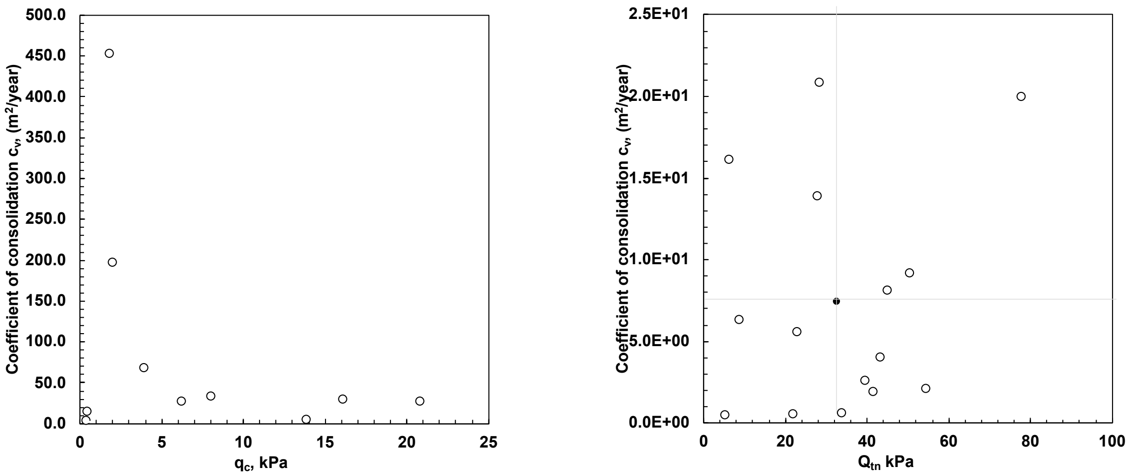

(a) (b)

Figure 4.29: (a) Relationship between Laboratory derived c_v versus CPTu derived c_v. (b) Relationship between c_v and Q_{tn}.

summarized in Table 4.4. It should be noted that Robertson (2012a) rated the perceived applicability for determining s_u from CPTu as high (see Figure 2.2).

Table 4.4: New proposed correlations for undrained shear strength.

Correlation	Independent Function Type	n	R^2
$s_u = 0.0680 * q_{net}$	Field Based	17	0.74
$s_u = 0.0641 * q_t$	Field Based	17	0.75
$s_u = 1.44 * f_s$	Field Based	17	0.82
$s_u = 0.0752 * (q_t - u_2)$	Field Based	17	0.71
$s_u = 34.36 * F_r$	Field and Laboratory Based	17	0.84
$s_u = 0.0650 * (q_t + f_s - \sigma_{v0})$	Field and Laboratory Based	17	0.75
$s_u = 0.0582 * (q_t + f_s + \sigma_{v0})$	Field and Laboratory Based	17	0.77

Based on Figure 4.30, the measured $s_u(lab)$ show lower scatter and better correlation with q_t instead of $(q_t - \sigma_{v0})$, i.e., $R^2 = 0.75$. It is observed that the evaluated empirical cone factor N_{kt} for clay deposits in Dhaka ranges from 14.7 to 15.6. Also, no correlation is observed between N_{kt} and PI data— which agrees with the findings of La Rochelle et al. (1988) report for CPTu tests on sensitive clay of eastern Canada. An attempt in defining the N_{kt} as a function of s_u (Figure 4.30c) revealed a weak power relationship (R^2=0.42)—a stark contrast to the findings of Lunne et al. (1997) and others where a very good correlation was obtained. As shown in Figure 4.30d, no relationship was obtained between N_{kt} and OCR. Another classic relationship in the literature indicates that N_{kt} decreases with B_q (e.g, Knappett (2012), Lunne et al. (1997), and Mayne et al. (2015) and others). In this study, no such correlation could be established between N_{kt} and B_q. The resulting data was highly scattered to establish any trend.

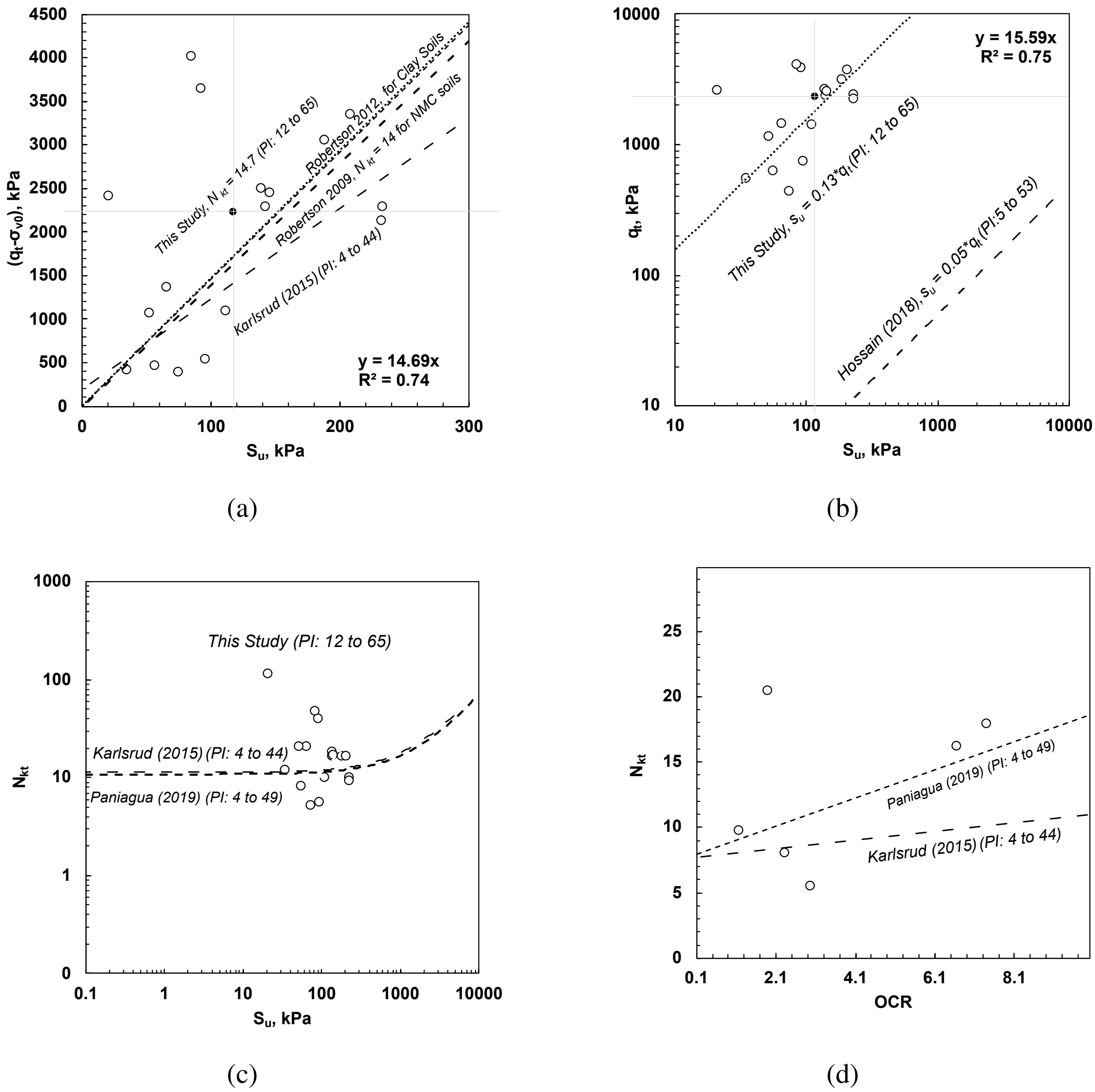

Figure 4.30: (a) Relationship between s_u and net cone resistance $(q_t - \sigma_{v0})$. (b) Relationship between s_u and corrected cone q_t. (c) Relationship between s_u and net cone resistance factor (N_{kt}). (d) Relationship between N_{kt} and OCR.

Plot of effective cone resistance $(q_t - u_2)$ against s_u (as shown in Figure 4.31a) is very similar to the plot of q_{net} in Figure 4.30. There is scatter at the lower range of q_t. This finding agrees with Lunne et al. (1997) observation for soft NMC (see section 2.3.1). Evaluation of the N_{ke}—obtained from q_{net} data—revealed no correlation between N_{ke} and B_q ($R^2 = 0.0163$). The result did not agree with the findings of Karlsrud et al. (2005) findings. Unlike $N_{\Delta u}$ and N_{kt}, N_{ke} correlated fairly linearly PI with increasing s_u and $R^2 = 0.45$(as shown in Figure 4.31). The plot is relatively scattered to be considered reliable. Similarly, a lot of scatter was observed between N_{ke} and s_u—a power trend with lot of scatter ($R^2 = 0.31$). Also, no relationship could be established between N_{ke} and OCR.

Using Δu only to correlate with laboratory-derived undrained shear strength yields a rela-

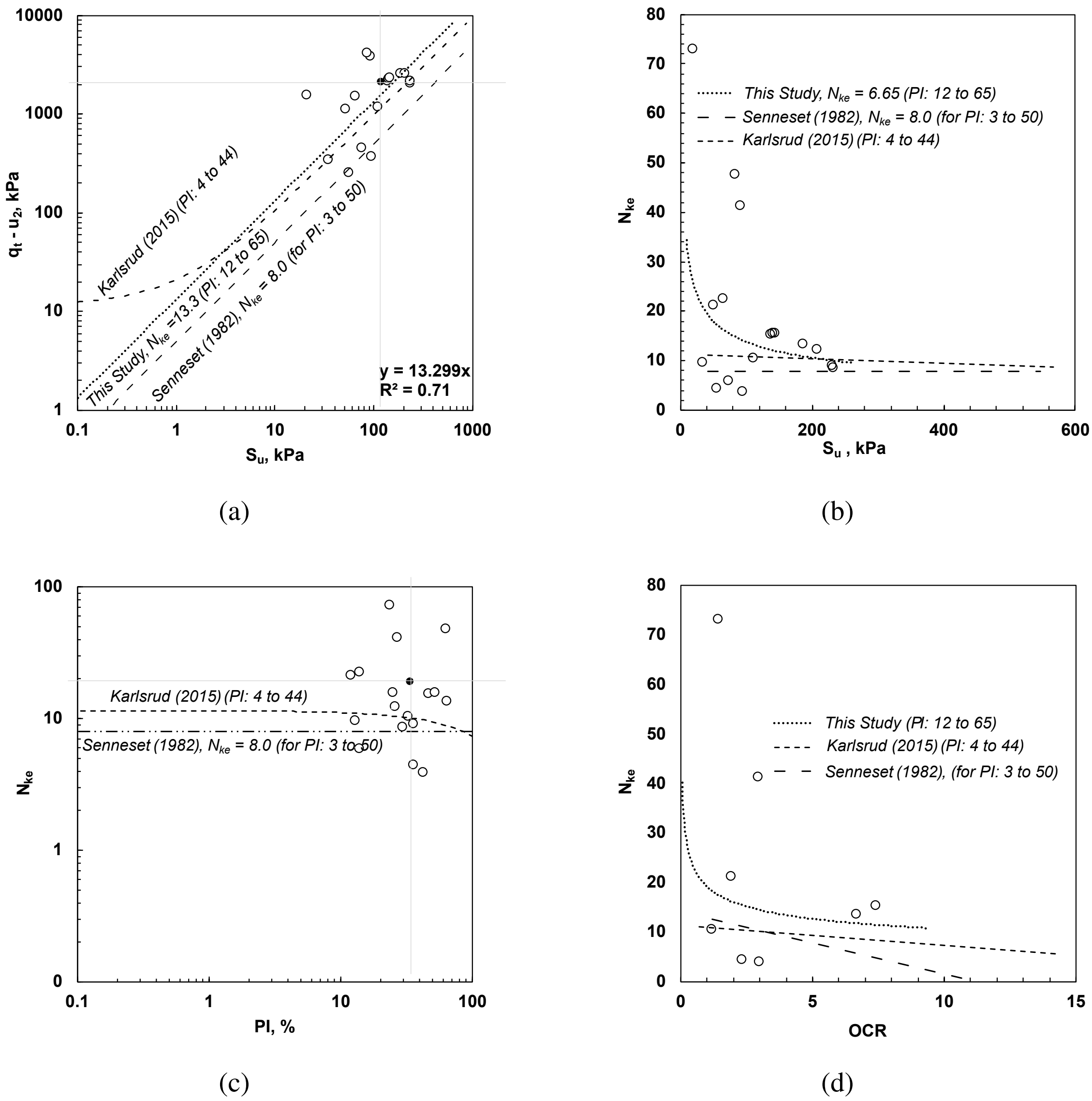

Figure 4.31: (a) Relationship between s_u and effective Cone Resistance $(q_t - u_2)$. (b) Relationship between s_u and cone resistance factor. (c) Relationship between net cone resistance factor (N_{kt} and PI). (d) Relationship between N_{ke} and OCR.

tively weaker correlation and scatter (as shown in Figure 4.32a). Also, attempts in defining $N_{\Delta u}$ as a function of OCR, PI and w (individually) was difficult since the data points show high scatte. Similarly, the relationship between $N_{\Delta u}$ and B_q demonstrated high scatter visually for the 17 data points (4.32b). This is in sharp contrast to the findings of the available literature [eg., Karlsrud et al. (2005), Lunne et al. (1997), Paniagua Lopez et al. (2019), and Robertson et al. (1986a)], where low scatter and strong correlations were obtained using Δu relationships. Relationship between normalized excess pore pressure $(\Delta u/\sigma_{v0})$ and s_u demonstrates a likely linear relationship which can be established with more data points. However, the relationship observed between $(\Delta u/\sigma_{v0})$ and PI is highly scattered

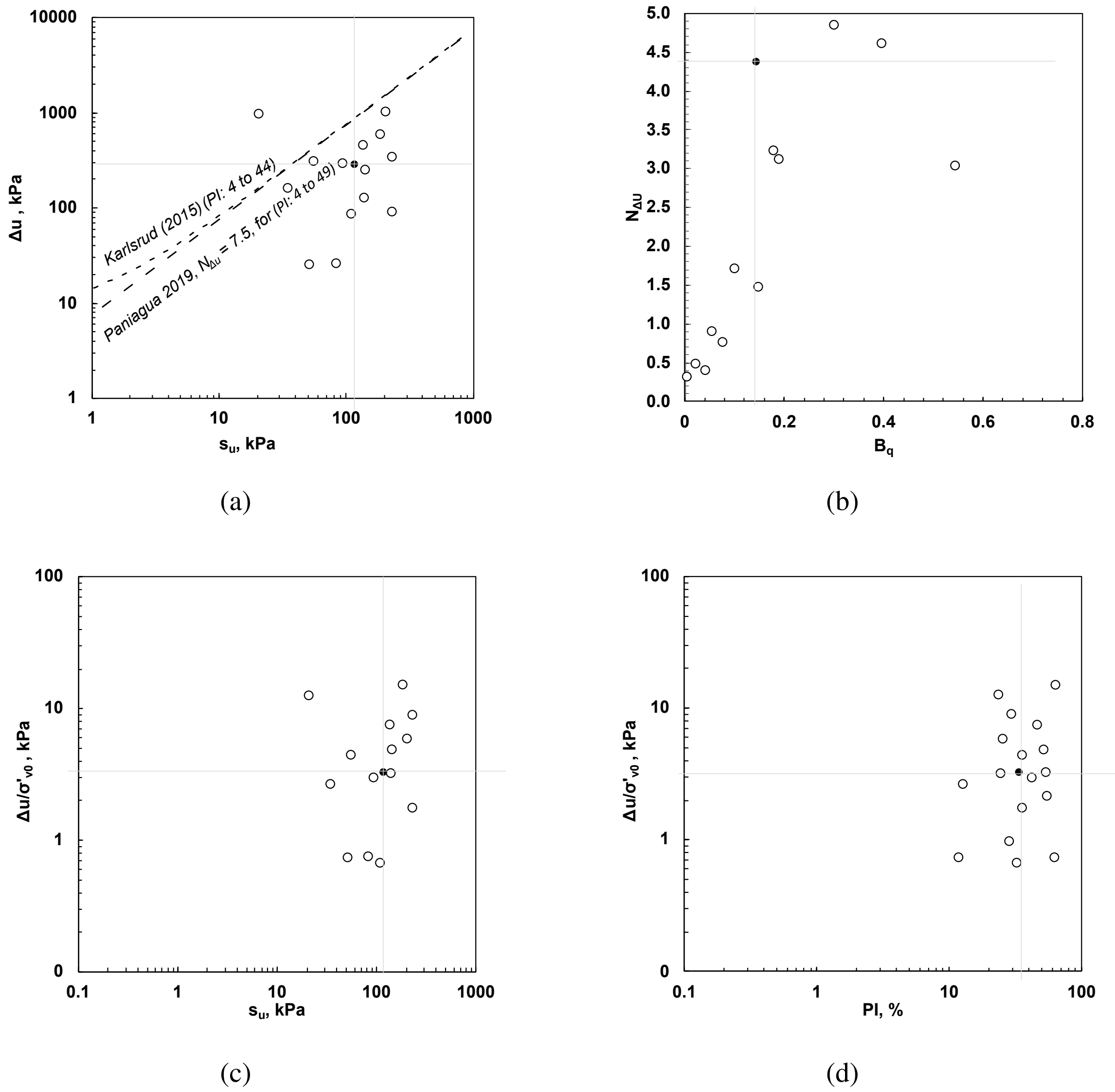

Figure 4.32: (a) Relationship between s_u and excess pore pressure (Δu). (b) Relationship between B_q and cone resistance factor $N_{\Delta U}$. (c) Relationship between normalized excess pore pressure and PI. (d) Relationship between normalized excess pore pressure and PI.

and would require more data to establish a correlation. Overall, the inconsistent results herein is mainly due to the negative pore pressure readings. This is mainly due to the location of the pore pressure element u_2—the readings are positive for intact clays. Whereas, for heavily overconsolidated fissured clays, the readings tend to be near zero or negative (Mayne et al. (1990)). The results herein confirms the findings of Demers and Leroueil (2002) and Mayne and Holtz (1988) and others that u_1 should be used instead of u_2 for superior data collection, especially for very stiff and heavily fissured clay. u_1 pore pressure readings are always positive, as indicated by Mayne and Holtz (1988).

An attempt was undertaken to explore correlations between s_u and normalized cone tip

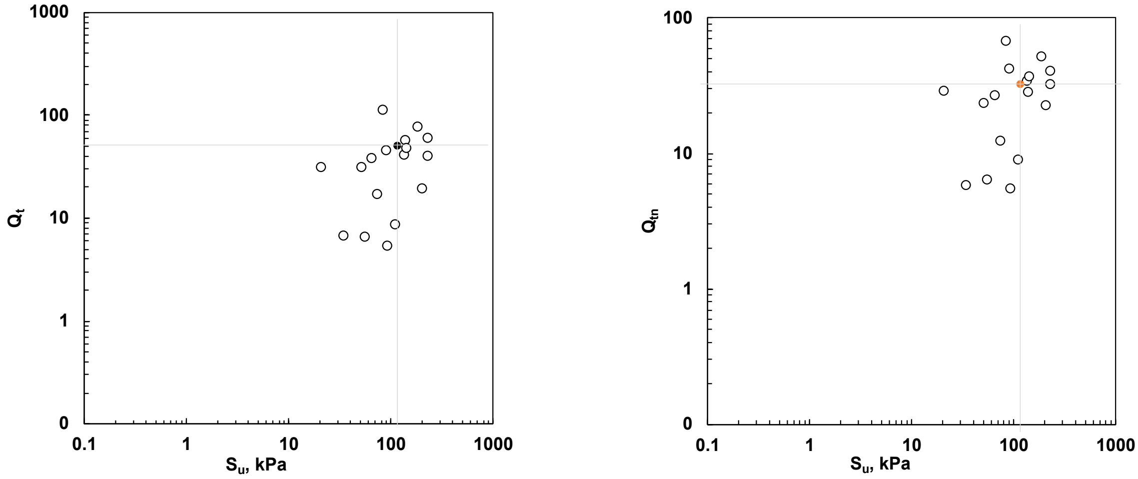

(a) (b)

Figure 4.33: (a) Relationship between s_u and Q_t. (b) Relationship between s_u and Q_{tn}.

measurements (Q_t, Q_{tn}). As seen in Figure 4.33, a good prediction is possible with more data. For both the plots, s_u data points are closely packed for higher values of laboratory-derived s_u. At the time of writing this research, the author did not find any similar correlations by other investigators.

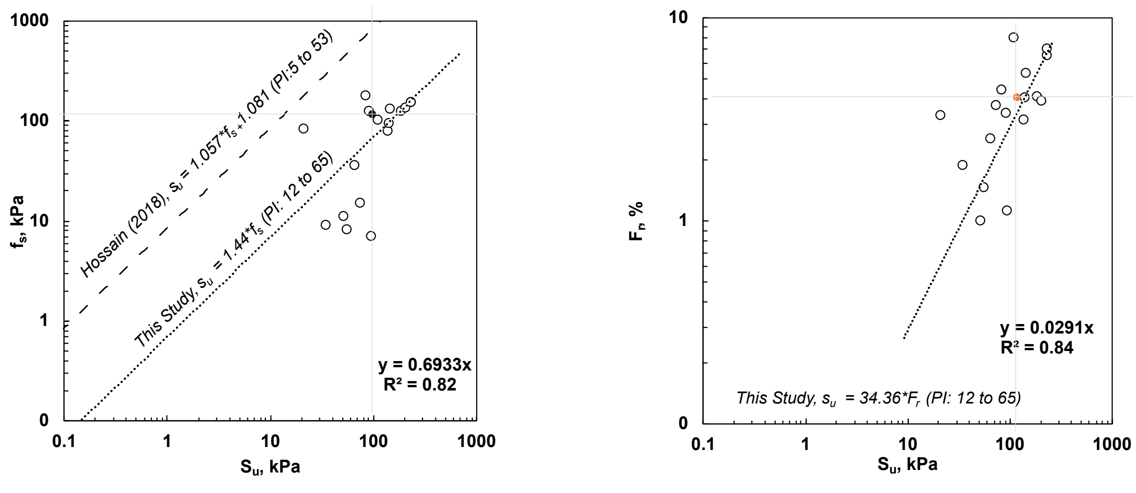

(a) (b)

Figure 4.34: (a) Relationship between s_u and f_s. (b) Relationship between s_u and F_R.

Plots of s_u and sleeve friction (f_s) and normalized fiction ratio (F_R) are presented in Figure 4.34. An increasing linear trend is evident from the scatter plots. In both the plots, the scatter is reduced with increasing s_u. This observation is profound in the F_R plot. Also, the scatter is relatively lower for the F_r plot (R^2 = 0.84). These observations are in agreement with the findings of the following:

1. Tomlinson (1957) findings of driven piles in clay, where its side friction was expressed as a percentage of the undisturbed cohesion of the clay. Implying that the sleeve friction of the cone represents a ”percentage” (0.35 in this study) of the s_u of clay soils.

2. Lunne et al. (1997) demonstrated good correlation between f_s and the remolded s_u of fine-grained soils. However, a reservation was suggested in the case of very soft sensitive clays, where very low remolded strength can result in very low f_s values and thereby reducing accuracy—as is observed for very low values of f_s in Figure 4.34, which shows a lot of scatter at the lower range of f_s.

Sleeve measurements are thought to be less reliable than the cone tip measurements [eg: Chen and Mayne (1996) and Lunne et al. (1997)]. However, in this work, the sleeve measurements have a significantly better correlation with the laboratory-derived s_u—unlike the correlations developed by the cone tip measurements and the pore pressure measurements.

Linear regression relations—for $(q_t+f_s-\sigma_{v0})$ and $(q_t+f_s+\sigma_{v0})$—unfolds good predictions accompanied by R^2= 0.75 and 0.77 respectively (as shown in Figures 4.35a and 4.35b). The correlation obtained is slightly better than correlations obtained using q_{net} and $(q_t - u_2)$. The data points are less scattered with increasing $(q_t + f_s - \sigma_{v0})$. Its corresponding cone factor shows fairly good agreement with s_u—the trend is that of a decreasing power function accompanied by R^2=0.50. However, no correlation was obtained when plotted against PI. Despite obtaining good correlations using q_t, f_s and σ_{v0}, the resulting N_{kt} ranges from 15.4 to 17.2—which is higher than the suggested value of 14 by Robertson (2009).

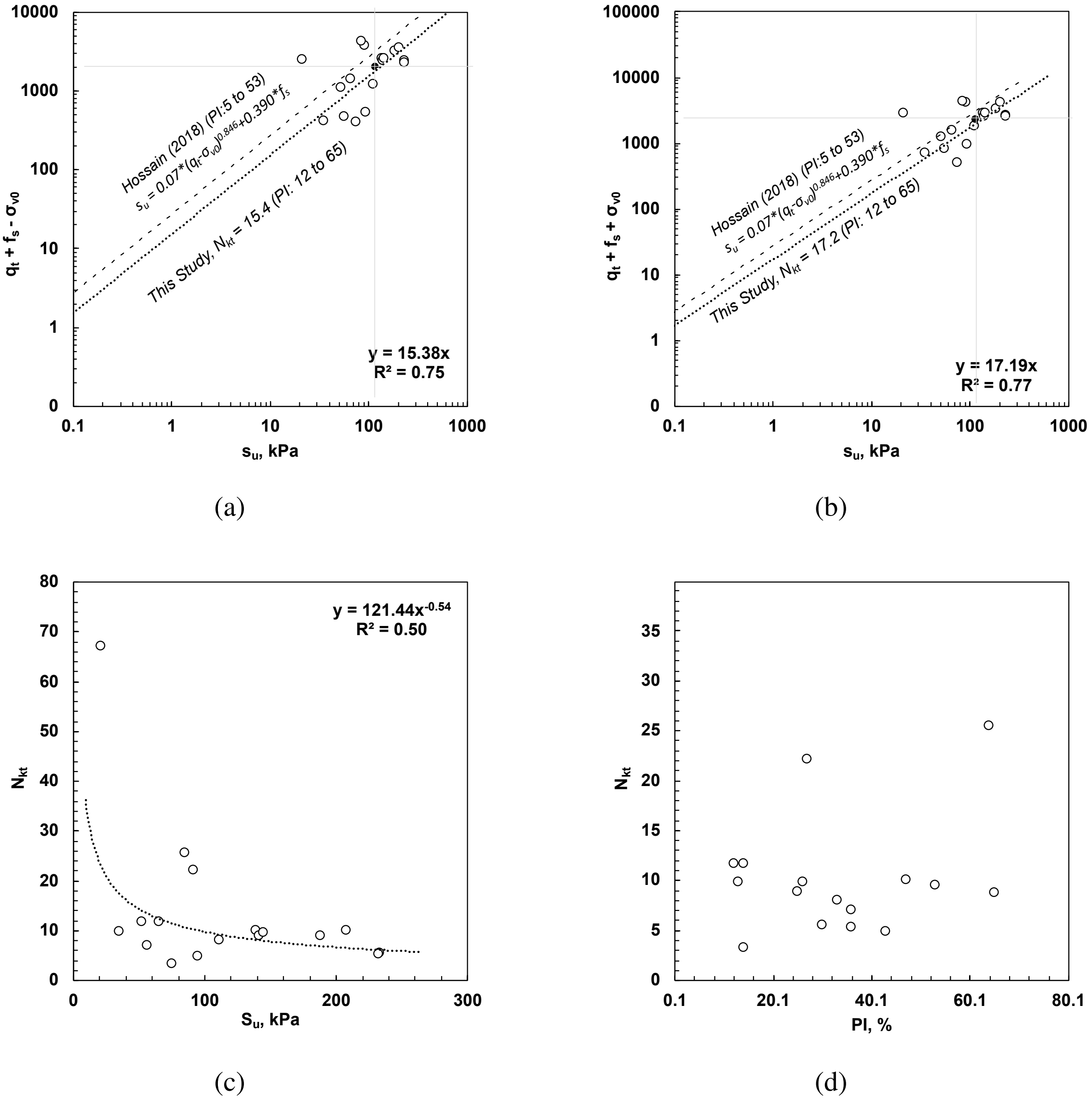

Figure 4.35: (a) Relationship between s_u and $(q_t + f_s - \sigma_{v0})$. (b) Relationship between s_u and $(q_t + f_s + \sigma_{v0})$. (c) Relationship between normalized excess pore pressure and PI. (d) Relationship between normalized excess pore pressure and PI.

4.6 Summary

This chapter compared the laboratory-derived geotechnical parameters with the CPTu-derived geotechnical parameters. In the process, several new correlations were developed. These correlations were then compared with the existing CPTu correlations graphically.

Constrained modulus M observations:

1. A strong linear trend is observed between overburden pressure, moisture content, plasticity index, and laboratory-derived constrained modulus. This is indicative that these parameters govern the constrained modulus.
2. f_s based correlations yielded more scattered results than q_c based data. However, taking the square-root of q_c and f_s also did not produce any relationship with the data set. Hence, more data is required to reach a conclusion.
3. u_2 based data could not be used to estimate laboratory-derived constrained modulus in this study.
4. σ_{v0} produced a positive linear correlation with M, accompanied by $R^2 = 0.43$.
5. Existing correlations in the literature seems to represent the upper bound of the results presented herein.

For the compression index C_c parameter, the following observations from this research can be summarized:

1. A hyperbolic relationship is observed beteen q_c and C_c, confirming the findings of Sanglerat (1972). The hyperbolic relationship was further confirmed as seen in Figure 4.9 and Figure 4.10.
2. The laboratory-derived C_c were most in the upper-limit of the boundary proposed by Sanglerat (1972).
3. Moisture content is seen to have a strong positive linear trend with C_c, accompanied by $R^2 = 0.78$.

For OCR, the following observations from this research can be summarized:

1. In this study, normalized cone tip resistances provided less scatter and better correlations:
   (a) Q_t: $R^2 = 0.69$
   (b) Q_{tn}: $R^2 = 0.85$
   (c) Normalized effective cone resistance, $(q_t - u_2)/\sigma'_{v0}$: $R^2 = 0.67$
   (d) Battaglio et al. (1986) referenced parameter, $(q_t - \sigma_{v0} - \Delta u)/\sigma'_{v0}$: $R^2 = 0.74$

(e) Normalized cone resistance, $(q_t + f_s)/\sigma_{v0}$: $R^2 = 0.74$

2. No relationship was found between CPTu derived pore pressure parameter and OCR.

The dissipation test results were conducted less than the required length of time. The following can be summarized for evaluating coefficient of consolidation c_v using CPTu:

1. With limited data set (10 in numbers), a relationship based on cone-tip resistance, f_s and u_2 could not be produced.
2. No correlation could be developed for CPTu derived u_{50} and t_{50}.
3. No relation could be established for the scatter plot between laboratory-derived c_v and CPTu-derived c_v. A few reasons attributed to this observation:
   (a) Dissipation tests were conducted less than 4 hours.
   (b) In situ drainage condition may not match with the two-way drainage condition of the sample in an odeometer consolidation cell.

For the undrained shear strength parameter s_u, the following observations from this research can be summarized:

1. In this study, the evaluated empirical cone factor N_{kt} for clay deposits in Dhaka ranges from 14.7 to 17.2.
2. Following the most popular approach, an attempt in defining the N_{kt} as a function of s_u was difficult $R^2 = 0.42$. Similarly, no correlation could be established between N_{kt} and B_q.
3. f_s based correlations ($R^2 = 0.82$) yielded better than q_t based correlations ($R^2 = 0.75$).
4. Multiple and non-linear regression resulted in between several parameters (as shown in Table 4.4) resulted in strong correlations.
5. For over-consolidated clay deposits, u_2 readings are not reliable.

BANGLADESH NETWORK
OFFICE FOR URBAN SAFETY

PART-VI

MICROZONATION OF RANGPUR CITY CORPORATION AREA BASED ON SITE AMPLIFICATION USING NONLINEAR TECHNIQUE AND LIQUEFACTION

BANGLADESH NETWORK OFFICE FOR URBAN SAFETY (BNUS), BUET, DHAKA

Prepared By: Nusrat Jahan
Mehedi Ahmed Ansary

Chapter 1
INTRODUCTION

1.1 General

Earthquakes are among the natural hazards that are most threatening due to their unpredictability and severity. The occurrence of earthquakes is caused by tectonic plate boundaries. Large earthquakes happen less often than major floods, but they have the potential to damage far greater regions and have long-lasting repercussions on society, the economy, and politics (Akhter, 2010). Bangladesh is vulnerable to earthquakes, according to historical seismic data for the country and surrounding areas. Bangladesh is the most highly populated place in the world. This means that if an earthquake happens there, it will affect too many persons per unit area than in other places where earthquakes occur often. Furthermore, due to the relatively low number of catastrophic quakes that have happened over the course of the past century, the majority of the people as well as those responsible for formulating policy do not consider seismic threats as being of significant concern. Recent seismic activity in Bangladesh reveals that the country is subject to a significant seismic threat. According to (Bilham et al., 2001), there is a significant disparity between the amount of energy that has accumulated in this area and the frequency with which earthquakes have occurred in the past, which suggests that the Territory is at an increased risk of experiencing a devastating earthquake in the near future.

The high pace of modernization, uncontrolled expansion, bad land utilization management, bad design tradition, insufficient framework and service supply, and ecological devastation have all contributed to an increase in the likelihood of earthquake disasters in cities during the past few decades (Erdik, 2006). Rapid urbanization and construction in hazardous areas increase the dangers already present in major cities. It is obvious from the histories of past earthquakes in various nations that they can’t be stopped from happening; nevertheless, appropriate risk minimization and management methods can lower the danger of this terrible event and the repercussions of its occurrence.

The assessment of ground response being one of the most significant challenges in earthquake engineering as well as a common challenge that engineers face. Predicting ground surface motions helps in developing design response spectra, determining earthquake-generated forces which can create instability of ground and earth retaining constructions, and assessing dynamic stress and strain helps in analysing seismic hazards. All of these are possible with the help of ground response analyses. Modelling the rupture framework at the earthquake's epicentre, simulating the travel of stress waves across the earth towards the top of strata underneath the specific site, and then figuring out how the soil above the bedrock affects ground surface motion: these are the components of a comprehensive ground response analysis. This strategy is not so feasible for typical engineering fields since the process of the fault rupture is convoluted, and the pattern of the transmission of energy between the origin and the location is so unclear. After then, the challenge of ground response analysis consists in figuring out how the soil deposit reacts to the movement of the bedrock directly beneath it. It has been known for a considerable amount of time that the local soil conditions can have a significant impact on the severity of earthquake damage. Ground response analysis has been done in many different ways over the years. Most of the time, the methods are categorized by the number of dimensions of the problems they can solve. However, many of the two-dimensional and three-dimensional methods are simple extensions of the respective one-dimensional methods.

A microzonation assessment of a city is an important stage in the process of reducing a city's exposure to the dangers posed by earthquakes and preparing for future seismic disasters. Seismic microzonation can be taken into account when thinking about the magnitude of earthquakes, the likelihood of liquefaction, and the potential for landslides. In all three scenarios, seismic microzonation relies heavily on geotechnical site classification and evaluation of site response at the time of earthquakes. When an earthquake impacts a human community, the local site circumstances and the effects of the local site are the most significant aspects to consider. Therefore, it is essential to evaluate the localized dynamic characteristics of soils and infrastructures before the occurrence of seismic occurrences.

Seismic hazard lets us describe the possible effects of earthquakes that should take into account while building new constructions or improving old ones. At a micro-scale, this assessment needs to look at the effects that seismological tremors could have on the stability of the soils, such as liquefaction and site amplification. It also needs to take into account the existence of active seismic faults near the locations, if their characteristics suggest that they could cause seismic deformations at the ground, and it needs to define reference seismic movements for each location, considering the different soil conditions.

The research that was done on several powerful earthquakes all over the world showed that the soil conditions, that include the unconsolidated sediments and geological characteristics of the rocks, the tectonic fabric, and the geomorphological features, have a significant impact on the amount of damage that is caused to structures when a powerful earthquake occurs.

The liquefaction problem has become significant when it began to disrupt both social and human activities by interfering with the operation of facilities. Additionally, the problem became significant following fast urbanization since it led to the expansion of cities into reclaimed land. In numerous ways, liquefaction impacts structures, bridges, subsurface pipes, and critical infrastructure. During previous earthquakes, such as the ones that occurred in 1964 in Niigata (Japan) and 1964 in Alaska (USA), 1971 in San Fernando, 1989 in Loma Prieta, 1995 in Kobe (Japan), and 2004 in Chuetsu (Japan), ground failures caused by liquefaction were a key contributor to the devastation that was caused. The majority of Bangladesh, including the city of Rangpur, is an alluvial plain that is composed of fine to medium sand and has a low percentage of fine deposits. Most locations in Bangladesh have ground water table that is shallow. In the event of a strong earthquake, the deposits can become liquid.

In this investigation, one dimensional (1-D) site response analysis has been carried out in Rangpur City Corporation Area. 16 borehole data up to a depth of 50 meters has been collected and used to assess site amplification, and 24 borehole data has been collected to assess (8 borehole data has been obtained from the test that was conducted previously by BUET) liquefaction potential in the area for microzonation purposes. For the purpose of generating the surface Peak Ground Acceleration (PGA) and Response Spectrum, Equivalent Linear (EL) and Nonlinear (NL) approaches have been used. To assess the liquefaction potential surface PGA values obtained from the NL method have been used along with different methods.

1.2 The Study Area

Rangpur is one of those places that has expanded in recent years despite the uncertain earthquake and liquefaction risk factors. Rangpur City Corporation is situated in the Rangpur Sadar Upazila of the Rangpur District and Rangpur district is located in

Bangladesh's north-western region. It is surrounded by Nilphamari and Lalmonirhat districts on the north, Gaibandha district on the south, Kurigram district on the east and Dinajpur district on the west shown in Figure 1.1 (Rangpur District - Banglapedia). The area of Rangpur is 2370.45 square km. It ranges in latitude from 25°43' to 25°48' and in longitude from 89°12' to 89°19'. The Teesta River is the largest river in the Rangpur district's north-eastern region. Rangpur has a tropical humid and dry climate. Monsoon months are characterized by the highest precipitation levels. The yearly precipitation in the region is approximately 1,448 millimetres (Qumruzzaman et al., 2008).

According to BNBC (2020), Rangpur City is located in the northwestern region of Bangladesh. On the seismic zonation map of Bangladesh, the area that includes Rangpur Town and its surrounds may be found in Zone III, which has a fundamental seismic coefficient (z) of 0.28 g. It has a severe seismic intensity. The design basis earthquake (DBE) ground motion is chosen at a level of ground shaking equal to 2/3 (two-thirds) of the maximum considered earthquake (MCE) ground motion (BNBC-2020). The design basis earthquake for this study is determined to be 0.19 g, and it is obtained by multiplying the maximum earthquake considered (0.28 g) by 2/3. The majority of Bangladesh, including the city of Rangpur, is an alluvial plain that is composed of fine to medium coarse sand and has a low percentage of fine deposits. Most locations in Bangladesh have a shallow groundwater table. In the event of a strong earthquake, the deposits can become liquid.

1.3 Objectives of the Study

The following are the main objectives of the research:

(1) To investigate the soil characteristics of the study site by conducting field and laboratory tests.

(2) To study site amplification for the study area.

(3) To develop site response spectra for some selected sites.

(4) To assess liquefaction for the study area.

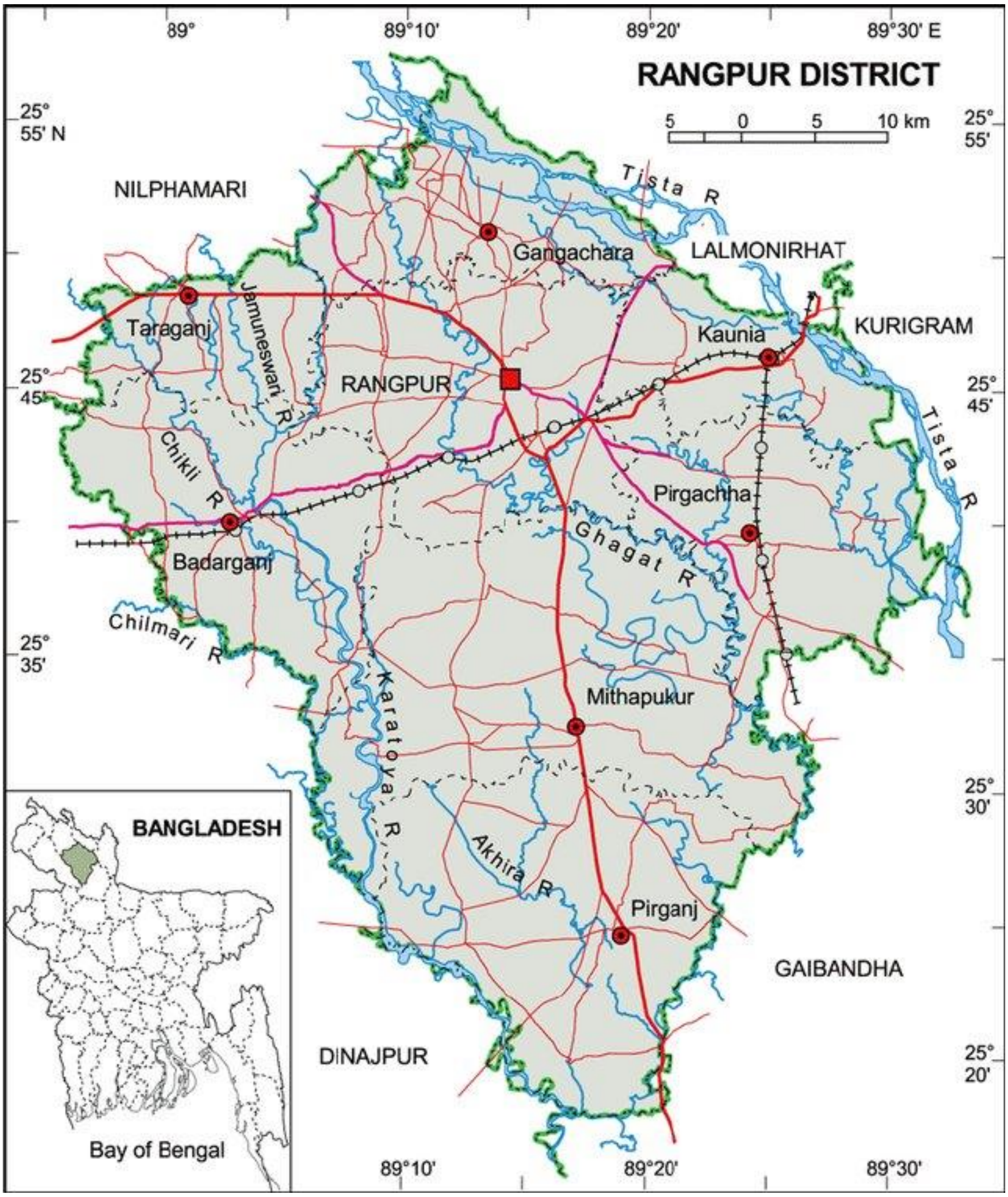

Figure 1.1: Rangpur District (after Banglapedia)

1.4 Organization of the Thesis

In order to accomplish the objectives that have been outlined, the thesis is separated into multiple chapters. The chapters are organized in the following manner:

In the first chapter, an overview of the background of the research, a statement of the problems, the aims, and outline of this research are given.

The findings of the prior study are presented in chapter two, which covers a wide range of themes including site response of soil, microzonation, site amplification and liquefaction, etc.

The third chapter describes the field SPT and laboratory tests undertaken to determine the subsoil condition of the Rangpur City Corporation area. Additionally, an overview of the DEEPSOIL software and the methodology as a whole is presented and addressed in this chapter.

Chapter four describes the analysis procedure of the DEEPSOIL software for a representative borehole. The location and SPT results of one borehole are presented to investigate the soil characteristics of the study location. A typical analysis is presented for one sample borehole using the DEEPSOIL software. Comparison graphs, target response spectra, a proposed design spectral acceleration curve, liquefaction susceptibility estimation, and a liquefaction hazard map are also presented in this chapter.

The results and discussion of the research program are presented in Chapter five. In addition to that, recommendations for the scope of future research are included in this chapter.

Chapter 3

DATA COLLECTION AND METHODOLOGY

3.1 Introduction

Data for a typical geotechnical investigation might originate from a wide number of sources, including field investigations, site inspections, model studies, and so on. The major goal of this study is to create a map of Rangpur City Corporation's sub-soil features (i.e., site amplification and site response spectra) and liquefaction potential. For collecting geotechnical data, both field and lab investigations were carried out. For the field investigation, boreholes were drilled, samples were collected and a Standard Penetration Test (SPT) was carried out. Some of the tests that were done in the lab were the specific gravity test, the grain size analysis test (using standard sieve), and the grain size analysis test using a hydrometer. This chapter provides a condensed summary of both the field and laboratory investigations that were carried out as part of the current research.

3.2 Geotechnical Data

An in-depth field survey of the Rangpur City Corporation jurisdiction was conducted. The locations to be tested using a standard penetration test are the focus of this investigation. Data that was necessary, such as reports on the subsurface and information on geology, geography, and other such topics, was gathered from a variety of relevant sources. In this particular research, a total of 16 (sixteen) subsoil investigations were carried out, and 8 (eight) additional subsurface reports were obtained from the test that was conducted previously by the Bangladesh University of Engineering and Technology (BUET).

3.3 Standard Penetration Test (SPT)

The Standard Penetration Test, often known as the SPT, is the most common type of subsurface investigation assessment used for foundation design not just in Bangladesh but all over the world. But SPT N-values can be misleading about the risk of liquefaction if the tests aren't done carefully due to their intrinsic variability, unpredictability and reactivity to the test procedure. For the purpose of investigating the site amplification and soil liquefaction potential characteristics of the Rangpur City Corporation region, the data from a total of 16 borehole standard penetration tests were utilized. The boreholes reached a depth of up to fifty meters (50 m) in certain places. The boreholes were dug in a vertical orientation utilizing the wash boring method and apparatus that was able to force tube samplers through the ground using hydraulic pressure. In each boring, a SPT was performed at intervals of nominally 1.5 meters, and the N values that is, the number of blows counted for each standard penetration, were recorded. Tests have been performed in accordance with ASTM D1586 to determine liquefaction potential using SPT data. This has been done in order to minimize or at the very least reduce some of the major sources of error. Even though granular soils are ideal for the Standard Penetration Test, it has been successfully applied to cohesive soils as well. The primary goals of the field investigations include boring and tracking of soil strata, sampling, implementation of Standard Penetration Test and recording the depth of ground water table.

The SPT value is affected by a wide variety of parameters, all of which are taken into consideration by ASTM. The length of the drill stem and its cross-section, the blow rate, the type of anvil, the method of operation, the type of hammer, the alignment of the hammer, the use of borehole fluid, and other factors are examples of some of these considerations.

3.4 Laboratory tests

During the SPT, both disturbed and undisturbed samples were collected for analysis. The collected samples were evaluated at the geotechnical laboratory of Bangladesh University of Engineering and Technology (BUET). The conducted experiments are listed in Table 3.1. These tests were carried out in accordance with the methodology outlined in the standard established by the American Society for Testing Material (ASTM). The specific gravity and grain size analysis test are examples of those that were carried out in the laboratory. The ASTM standards provide information regarding the specifications of the testing techniques.

Table 3.1: List of conducted tests

Name of the test	Standard Reference
Specific gravity test	ASTM D854-00
Grain size analysis (sieve analysis)	ASTM D422-63

3.5 Location of the Borehole

Within the Rangpur City Corporation, a total of sixteen boreholes were drilled. Saha (2005) provided the source for the collection of the data from eight boreholes, each of which were carried out by BUET in different part of Rangpur City. Borehole coordinates and locations can be found in Table 3.2. Figure 3.1 is a map of the Rangpur city corporation that shows where the locations of the boreholes are.

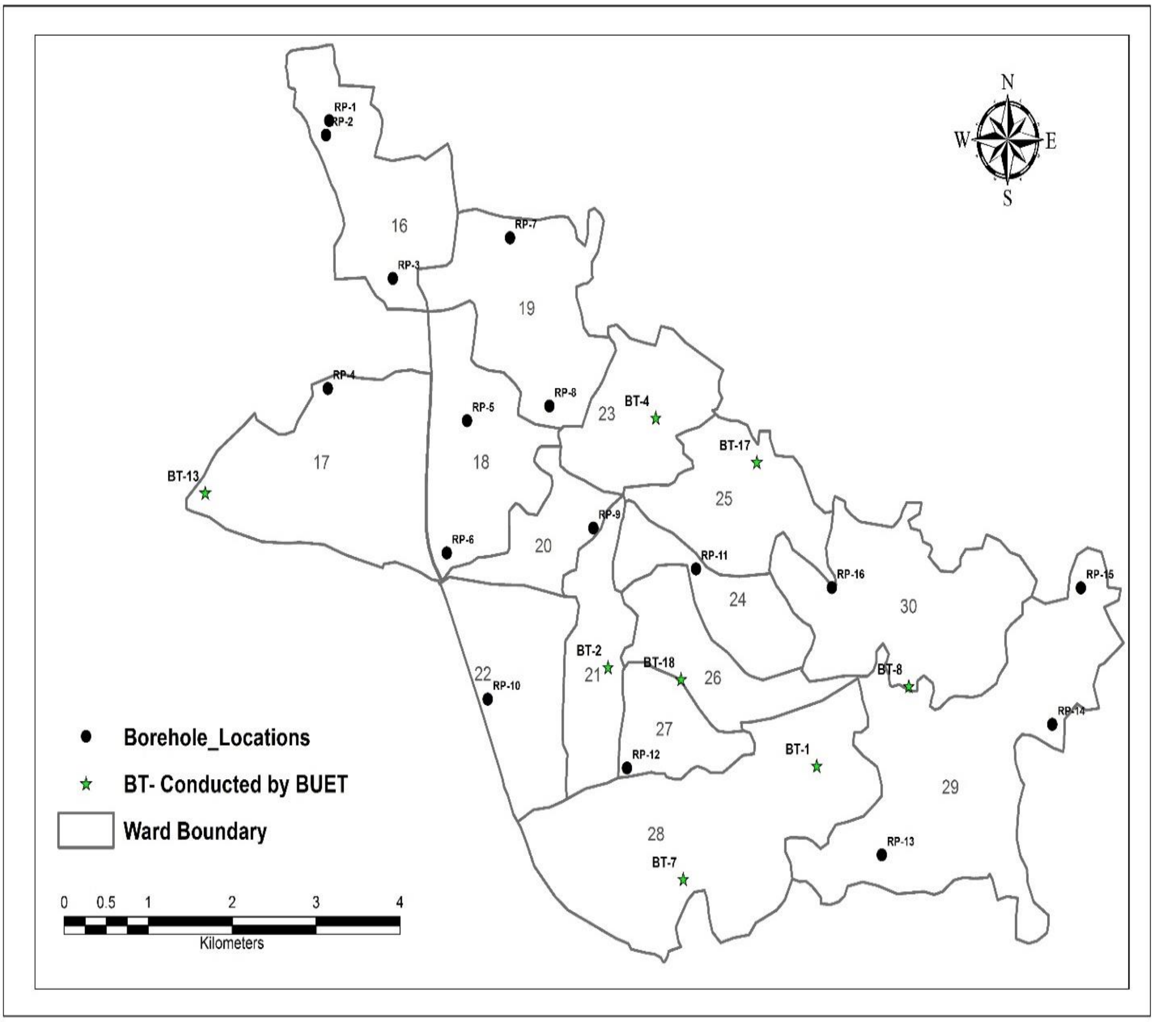

Figure 3.1: Borehole location in Rangpur City Corporation

Table 3.2: Location of the boreholes

Location Code	Ward	Borehole	N (Latitude)	E (Longitude)	Source
RP-1	Ward 16	BH1	25°46.855′	89°13.121′	This Study
RP-2	Ward 16	BH2	25°46.800′	89°13.140′	
RP-3	Ward 16	BH3	25°45.900′	89°13.800′	
RP-4	Ward 17	BH1	25°45.479′	89°13.155′	
RP-5	Ward 18	BH1	25°45.120′	89°14.100′	
RP-6	Ward 18	BH2	25°44.640′	89°14.040′	
RP-7	Ward 19	BH1	25°46.500′	89°14.400′	
RP-8	Ward 19	BH2	25°45.420′	89°14.700′	
RP-9	Ward 20	BH1	25°44.921′	89°15.066′	
RP-10	Ward 22	BH1	25°43.913′	89°14.342′	
RP-11	Ward 24	BH1	25°44.620′	89°15.802′	
RP-12	Ward 27	BH1	25°43.585′	89°15.344′	
RP-13	Ward 29	BH1	25°43.185′	89°17.169′	
RP-14	Ward 29	BH2	25°43.870′	89°18.361′	
RP-15	Ward 29	BH3	25°44.592′	89°18.543′	
RP-16	Ward 30	BH1	25°44.549′	89°16.771′	
BT-13	Ward 17	BH1	25°44.922′	89°12.300′	Study conducted by BUET (Saha, 2005)
BT-4	Ward 23	BH1	25°45.390′	89°15.492′	
BT-2	Ward 21	BH1	25°44.100′	89°15.192′	
BT-17	Ward 25	BH1	25°45.180′	89°16.218′	
BT-18	Ward 26	BH1	25°44.052′	89°15.714′	
BT-1	Ward 28	BH1	25°43.632′	89°16.692′	
BT-7	Ward 28	BH1	25°43.026′	89°15.762′	
BT-8	Ward 30	BH1	25°44.058′	89°17.334′	

3.6 Response Spectrum

An estimation of the peak linear structural response to dynamic motion can be obtained by analysing its response spectrum. This estimate can be presented in the form of displacement, velocity, as well as acceleration spectrum. In most cases, it is utilized in the process of response analysis to seismic events. It makes the assumption that the response system is linear in order for it to be examined in the frequency domain utilizing the system's natural modes, which have to be extracted in a step that comes before the eigenfrequency extraction stage (i.e., natural frequency extraction). For the purpose of generating the surface response spectrum, equivalent linear (EL) and nonlinear (NL) approaches will be utilized with the help of DEEPSOIL software.

3.7 Peak Ground Acceleration (PGA)

A measurement of the maximum acceleration of the surface during an earthquake is referred to as the Peak Ground Acceleration (PGA). For the sake of designing, it is the most significant parameter that can be considered. It is possible to calculate the PGA value at the bedrock level by conducting a Probabilistic Seismic Hazard Assessment at the location using the appropriate Ground Motion Prediction Equations. It is possible to express peak ground acceleration as a percent of g, which is the standard acceleration due to the gravity of the Earth and is comparable to g-force. With the aid of the DEEPSOIL program, EL and NL techniques will be used to generate the surface PGA.

3.8 Modulus Reduction and Material Damping Curves

Due to the lack of material-specific test findings for the area under investigation, modulus reduction and material damping curves were taken from the relevant body of published research. The normalized material damping and modulus reduction curves that were developed by Darendeli (2001), were employed in this study to estimate the Nonlinear (NL) behavior of the soft sedimentary layers of Rangpur City Corporation. These curves shown in Figure 3.2 were used to model the behavior of the soil deposits. It is necessary to have the following soil properties in order to use the relationships found in Darendeli (2001): the vertical stresses under the optimum condition in the starting state, the initial lateral earth pressure's coefficient, the loading cycle numbers, the loading frequency, the plasticity index and the OCR ratio (Ansary and Jahan, 2021).

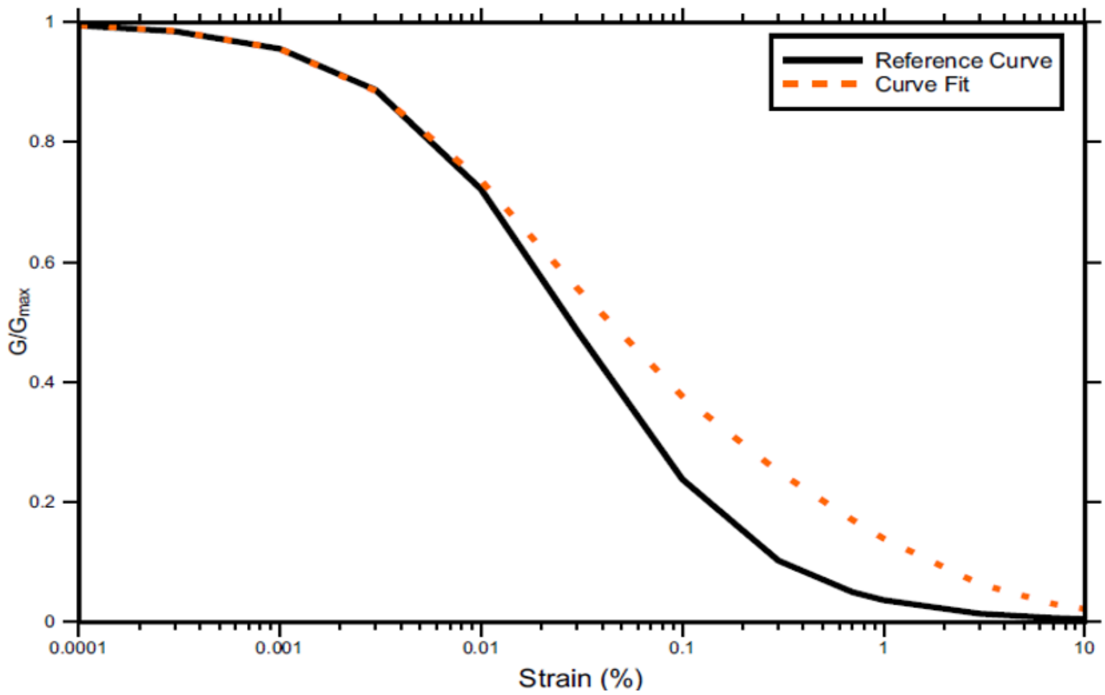

(a) Normalized shear modulus vs strain curve

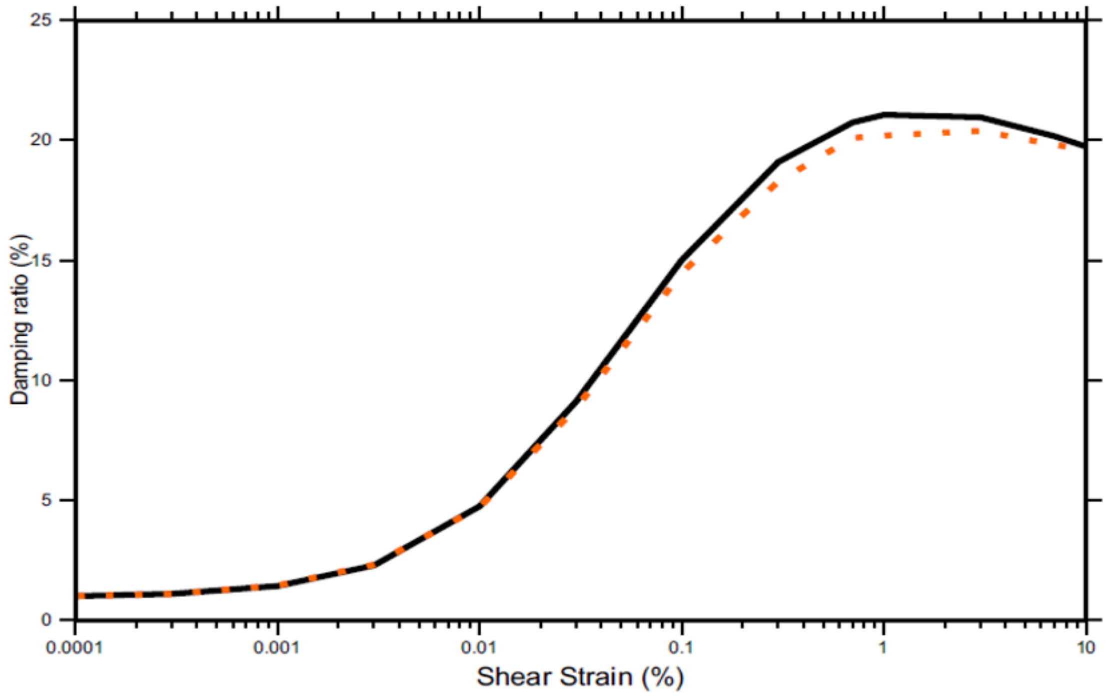

(b) Material damping vs shear strain curve

Figure 3.2: A representative example of Darendeli (2001) reference curves for the (a) normalized shear modulus reduction and (b) material damping (after Ansary et al., 2022).

3.9 Software for Site Response Analysis: DEEPSOIL

Hashash et al. (2020) created the DEEPSOIL software for the purpose of conducting a one-dimensional (1-D) site response study. This program may analyze the site response in a single dimension using linear, equivalent linear, or nonlinear methods. DEEPSOIL software provides options for time-domain linear and frequency-domain linear site response analysis, as well as frequency-domain equivalent-linear analysis and time-domain nonlinear analysis. DEEPSOIL is able to do the nonlinear site response analysis both with or without pore pressure generation. The software undergoes consistent updates that include the addition of new features as well as the correction of bugs in an effort to make the results more accurate.

3.9.1 Linear Analysis

There are two approaches to solving a model in Linear Analysis, one is the frequency domain and the other is the time domain. Both of the linear site response studies take into account the highest soil stiffness for the entirety of the time history, in addition to maintaining a constant damping ratio.

3.9.2 Equivalent Linear Analysis

An iterative process is utilized in the Equivalent Linear model for the purpose of selecting the shear modulus and damping ratio soil parameters. This methodology was initially developed by the program called SHAKE. Either discrete points or the soil parameters that constitute the core curve of one of the NL methods can be used to establish these features. Discrete points are the more common method. In order to observe the maximal amplification of seismic waves, a linear response analysis with equivalent parameters was carried out in this research.

3.9.3 Non-Linear Analysis

Non-linear analysis, often known as NL analysis, is used to solve equations of motion only in the time domain by employing either the Newmark β approach (implicit) or the Heun method (explicit). Users can choose from a number of different soil models such as the General Quadratic/ Hyperbolic Model (GQ/H), Pressure-Dependent Modified Kondner Zelasko (MKZ), User-Defined (UMAT), Discrete Points etc. It is possible to carry out the analysis either with or without the generation of porewater pressure. Whenever a nonlinear site response analysis is performed, the user has the option of automatically retrieving the results of the site response using the equivalent linear approach.

In this study General Quadratic/ Hyperbolic Model (GQ/H) was used as the soil model and a non-massing re/unloading formulation was used. As a reference curve, Darendeli's proposed curve was used. The time-domain was used to do the calculations for the nonlinear model. The ground motion at the soil column base was accounted for using the accelerogram of the matching bedrock spectral acceleration during the response analysis.

3.10 Summary of the Method of the Work

The approach that was used in this study is outlined in the form of a flow chart, which is shown in Figure 3.3. It is not possible to determine site amplification parameters using site response analysis without the properties for dynamic study of soils, such as shear wave velocities (Vs), accelerograms of earthquakes, shear modulus reduction curves and material damping.

In order to accomplish this goal, it is necessary to consider additional soil properties such as the over-consolidation ratio, the internal friction angle, the unit weight and the plasticity index. In order to conduct the site response analysis, the information required is acquired from 24 different borehole locations across the study site.

The liquefaction analysis employing various methods (such as Seed and Idriss simplified method, Chinese method and Japanese method) can be performed utilizing the surface PGA generated from the Nonlinear (NL) technique.

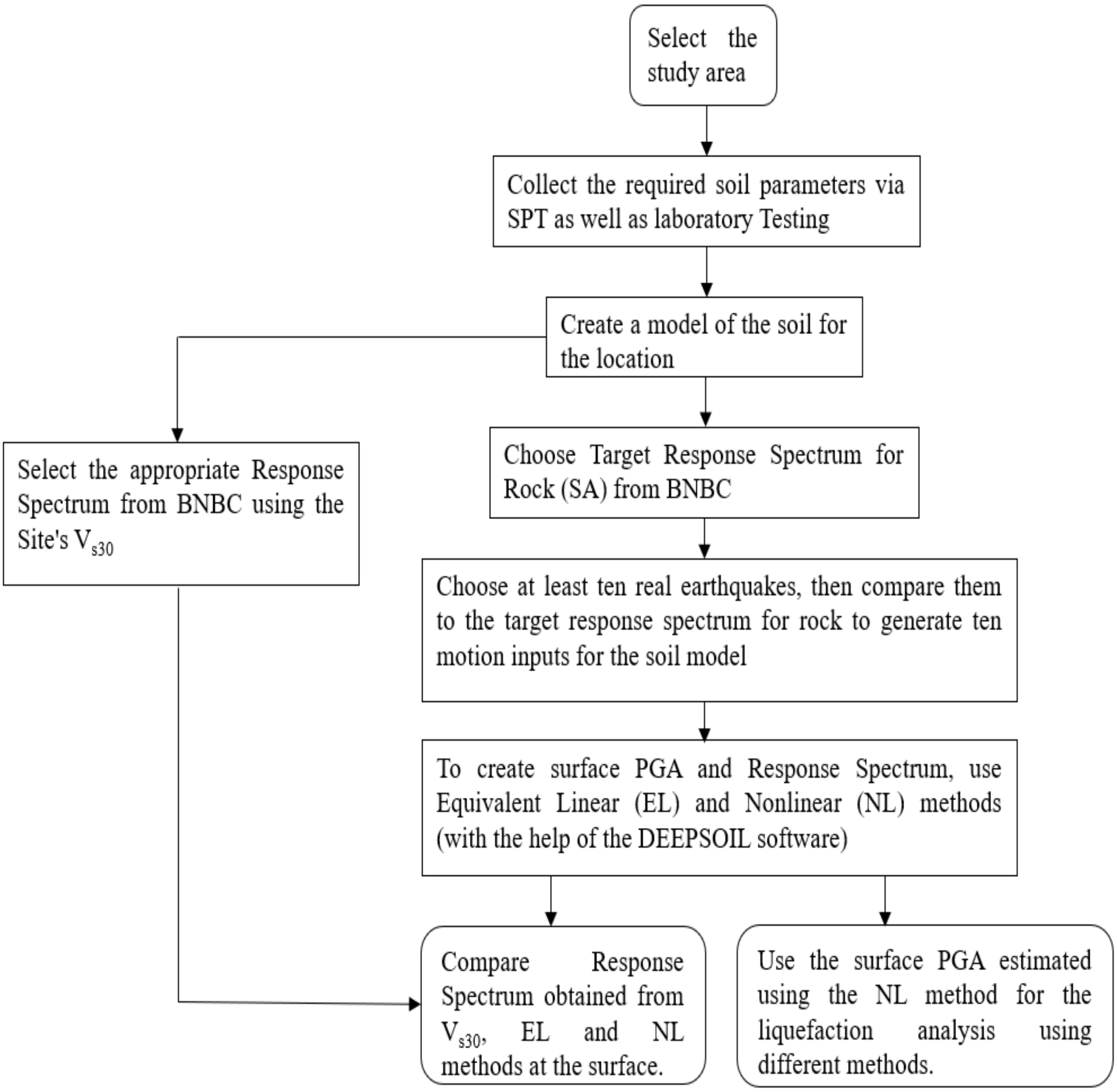

Figure 3.3: Flow chart of the methodology employed in this research

Chapter 4
RESULTS AND DISCUSSION

4.1 Introduction

The site amplification and response spectra of the city of Rangpur have been analysed with the aid of the DEEPSOIL program. To learn more about the soil at the site of the investigation, this chapter presents the location and SPT findings from a single borehole. For the purpose of demonstration, the DEEPSOIL software is used to perform an analysis on a single representative borehole. In this section, a number of comparison graphs (depth versus PGA, and PSA versus time) are illustrated. This chapter also includes the target response spectrum, a proposed design spectral acceleration curve, an estimate of the likelihood of liquefaction, and a map depicting the potential danger caused by such an event.

In the Rangpur city corporation, the borehole 1 (BH1) of ward 16 named as RP-1 in this study is located at the side of the Agricultural tools-making factory, the right side of the main road. It has a latitude of 25°46.855′ and a longitude of 89°13.121′. It has a groundwater level of 4.42 meter from the existing ground level (EGL). The location of the borehole is presented in Figure 4.1 and the standard penetration test result of RP-1 are shown in Table 4.1. During each boring, a standard penetration test (SPT) was carried out at intervals of nominally 1.5 meters, and the N values (the number of blows recorded for each standard penetration) were noted down. The standard penetration test result of all 24 boreholes used in this study is presented in Appendix A.

4.2 DEEPSOIL Analysis

The analysis has been carried out using DEEPSOIL Software. In this Analysis the Nonlinear method has been chosen as Analysis Method, the time domain is selected as the solution type, General Quadratic/Hyperbolic Model (GQ/H) is selected as the default soil model, the Non-Masing Re/Unloading is selected as Default Hysteretic Re/Unloading Formulation, the Metric unit is selected as Unit System, and Equivalent Linear – frequency domain is selected as Complementary Analysis as shown in Figure 4.3.

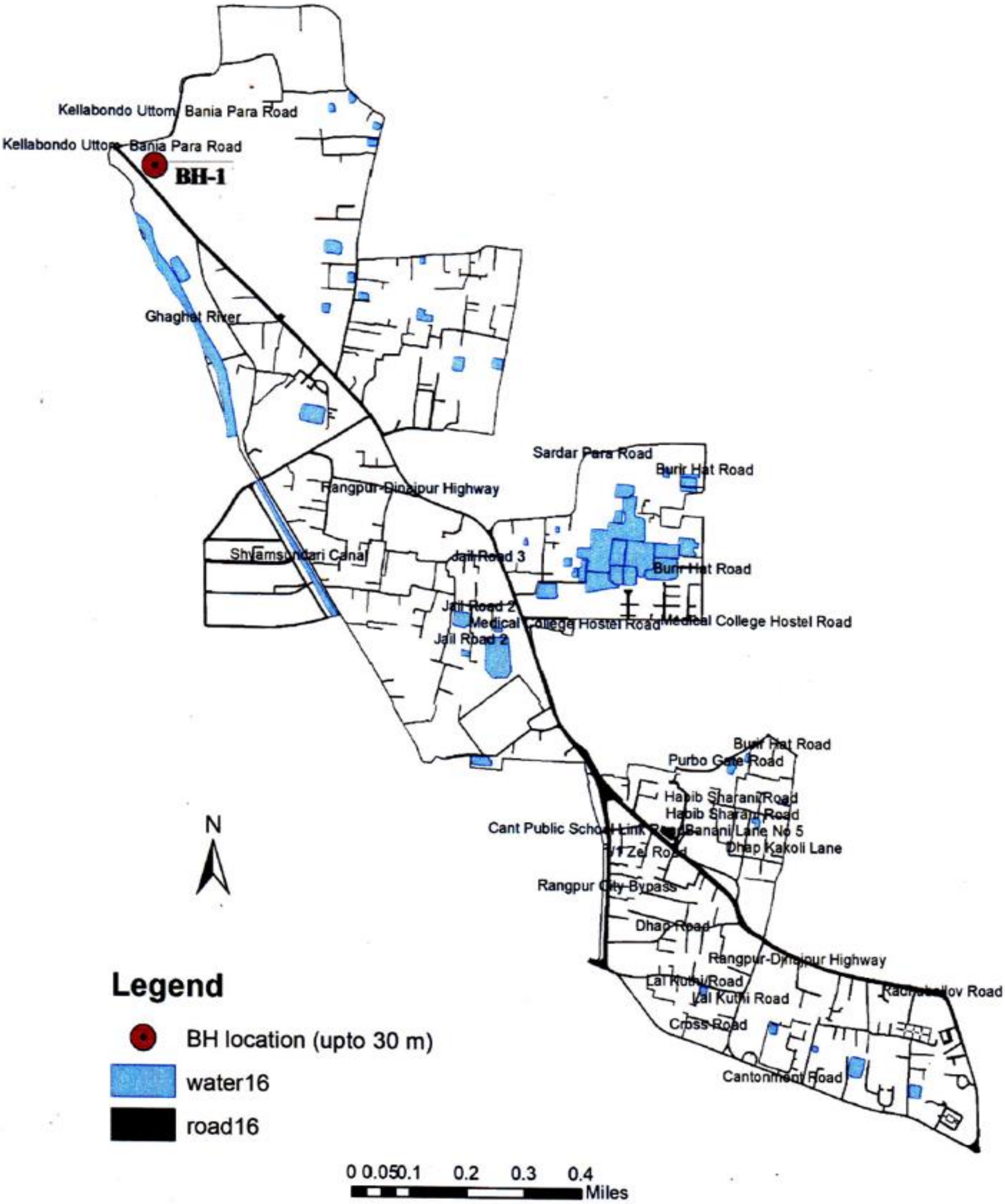

Figure 4.1: Location of RP-1 (Ward 16_BH1)

Table 4.1: Standard Penetration Test (SPT) result of RP-1 (Ward 16_BH1)

Depth (m)	Thickness (m)	Soil Description	SPT-N
1.5	9.0	Grey, loose to medium dense, silty FINE SAND, trace mica	6
3.0			5
4.5			10
6.0			14
7.5			15
9.0			17
10.5	1.5	Light grey, FINE SAND and SILT, trace mica	5
12.0	1.5	Light grey, loose, silty FINE SAND, trace mica	7
13.5	12.0	Grey to light brown, medium dense to dense, silty FINE SAND, trace mica	19
15.0			28
16.5			29
18.0			33
19.5			40
21.0			34
22.5			43
24.0			47
25.5	6.0	Light brown, very dense, silty FINE SAND, trace mica	50
27.0			50
28.5			50
30.0			50

4.3 Basic Soil Properties Used in DEEPSOIL Software

The basic soil properties used in this research are the thickness of soil layer, unit weight, shear wave velocity, effective vertical stress, shear strength etc. The unit weight is taken from the soil test report and effective vertical stress is calculated using the following equation 4.1.

$$\text{Effective vertical stress} = \gamma * h \tag{4.1}$$

Here, γ = unit weight of soil and h = height of the soil layer.

4.3.1 The Thickness of the Soil Layer

The thickness of the layer has been chosen in such a way that, the maximum frequency should not be less than 30 Hz (i.e., the minimum value of the frequency should be 30 Hz) and this is only applicable for time domain analysis. The formula for determining the maximum frequency, which is the highest frequency of the layer that is capable of propagating, is shown in the following equation 4.2. The maximum frequency (f_{max}) can be increased by lowering the layer's thickness (Hashash et al., 2020). If the maximum frequency of any layer is less than 30 Hz, then the layer should be divided to sublayers with smaller thickness with some properties to increase the frequency (f_{max}) value.

$$f_{max} = \frac{V_s}{4H} \qquad (4.2)$$

4.3.2 Determination of Shear Wave Velocity (V_s)

In this research, the shear wave velocity is determined from the standard penetration test (SPT) value. The empirical relation that has been shown here will be utilized to convert the SPT value into shear wave velocity. This is necessary since the program DEEPSOIL requires the shear wave velocity as one of the input parameters. The relation is adopted from Tasmiah and Ansary (2022). The relation is shown in the following equation 4.3. The shear wave velocity profile of RP-1 located in the Rangpur City Corporation Area is shown in Figure 4.2. From the shear wave velocity profile, it is clear that up to a depth of 55 meters, there is a significant amount of fluctuation. The reduction in the thickness of the soil layer, which was done in order to keep the minimum frequency of 30 Hz as described in section 4.3.1, causes this variation to take place. The shear wave velocity is around 800 m/sec at a depth of 160 m. So, it can be assumed that the bedrock is located 160 m below the ground level in the study location.

$$V_s = 63.068 * D^{0.3597551} * N^{0.1194517} \qquad (4.3)$$

Where, V_s = Shear Wave Velocity (m/sec); D = Soil Depth (m); and N = SPT blow count.

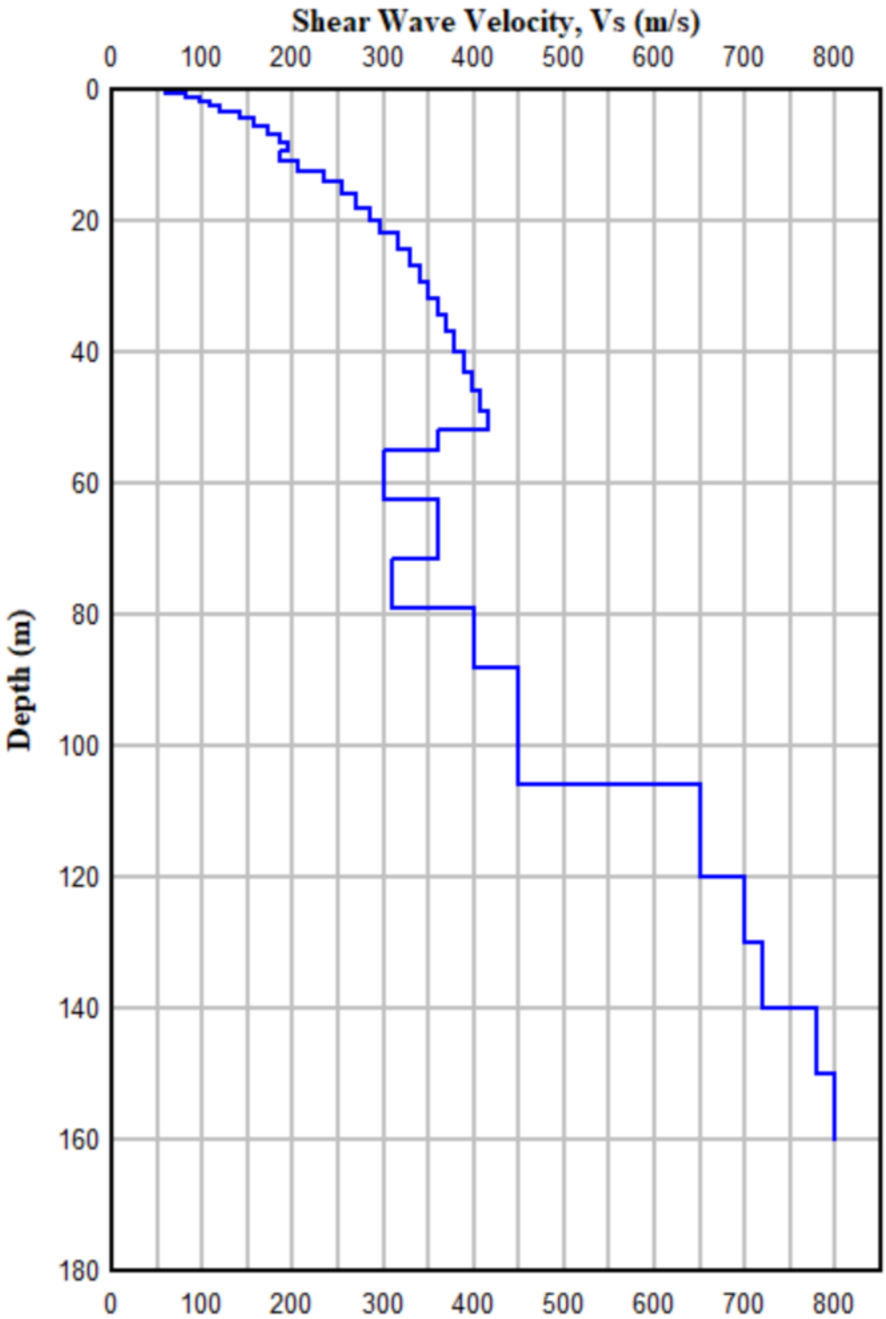

Figure 4.2: Shear wave velocity profile for RP-1 located in Rangpur city Corporation

4.3.3 Determination of Shear Strength (τ)

When attempting to characterize the large-strain characteristics of the soil with the GQ/H model, it is necessary to enter the shear strength of the soil stratum. The Mohr-Coulomb equation is used to determine the desired shear strength for a given nonlinear shear modulus reduction.

$$\tau_{target,\ implied} = c_{v_s} + \sigma'_v * \tan(\varphi) \tag{4.4}$$

Where, σ'_v = effective vertical stress, φ = angle of internal friction, c_{v_s} = shear strength that a linear elastic material with 80% of its maximum shear modulus is assessed to have at 0.1% shear strain (Hashash et al., 2020).

4.3.4 Reference Curve

The Darendeli (2001) curve is selected as a reference curve with some parameters like Plasticity Index (PI) = 0, Over Consolidation Ratio (OCR) = 1, and the coefficient of earth pressure at rest (K_0) which is calculated using the following equation 4.5.

$$K_0 = [1 - \sin(\varphi)] * OCR^{\sin(\varphi)} \tag{4.5}$$

Here, φ = Angle of internal friction and $\varphi = \sqrt{(20*SPT)} + 15$ (Hatanaka et al., 1998). φ can be found using the SPT N value.

The Modulus Reduction and Damping Curve Fitting (MRDF) with UIUC reduction factor are used as the fitting procedure in curve fitting. GQ/H Model is set up for a shear strain range of up to 0.05%, based on the Modulus Reduction Curve, as long as the shear stresses reach 95% of the target shear strength. All the soil profile definitions, shear strength inputs, and reference curve inputs are shown in Figure 4.4. GQ/H model fitting is shown in Figure 4.5. Soil profile plot such as depth wise shear wave velocity, maximum frequency, small strain damping ratio, implied shear strength, normalised implied shear strength, implied friction angle is shown in Figure 4.6.

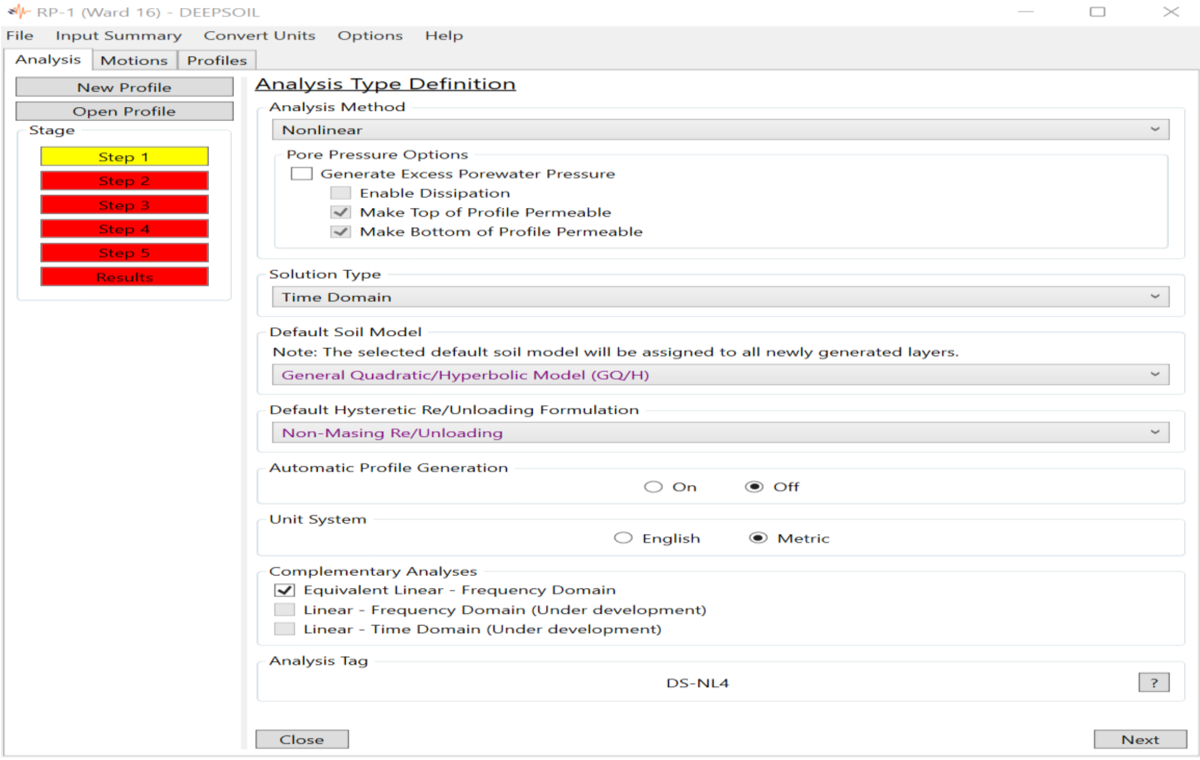

Figure 4.3: Analysis type definition for RP-1

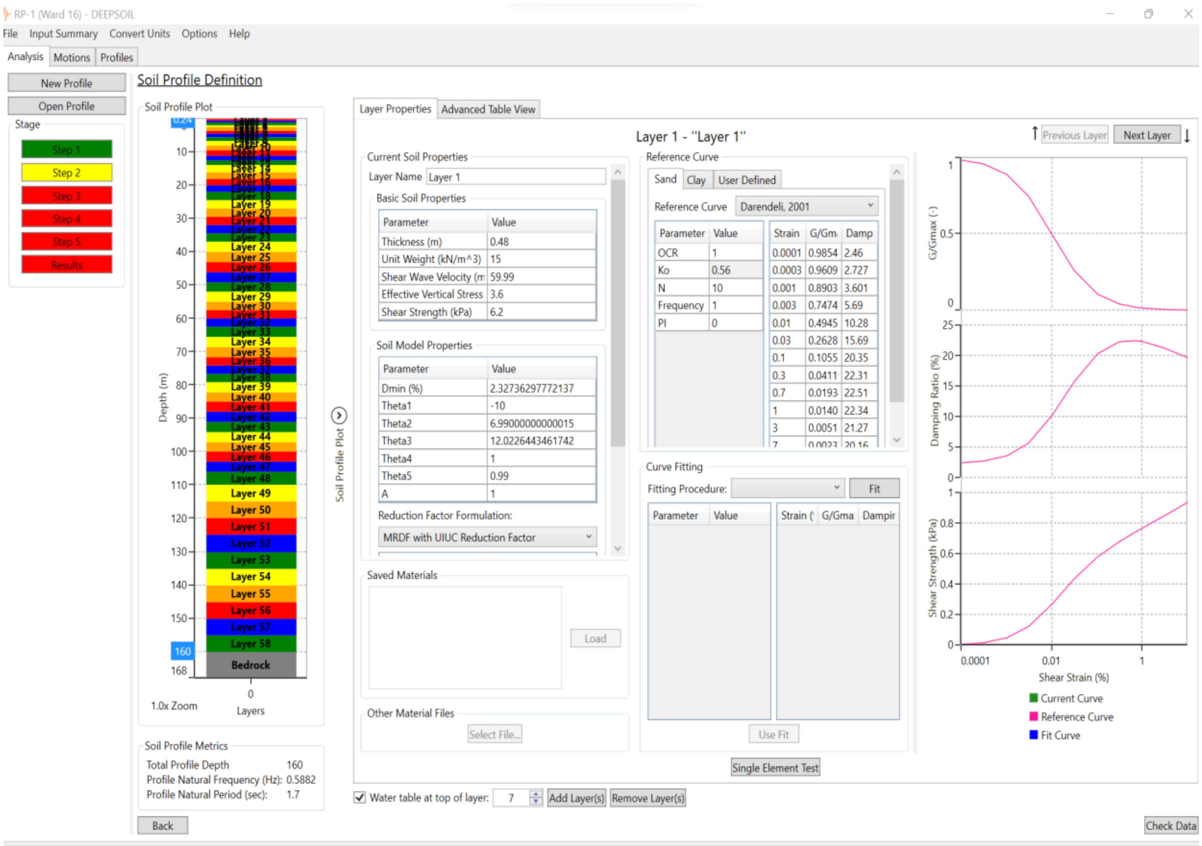

Figure 4.4: Soil Profile Definition and Dareldeli’s Reference Curve Input for RP-1

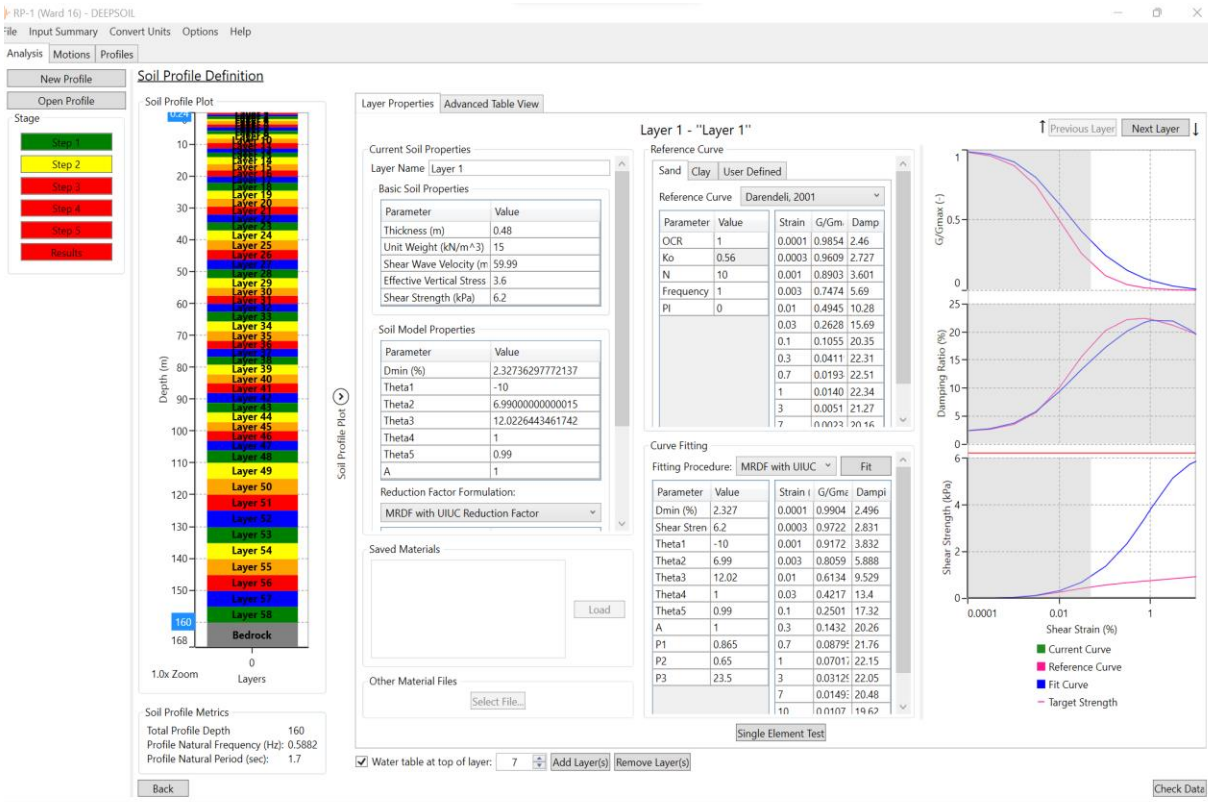

Figure 4.5 :GQ/H model fitting and soil model properties

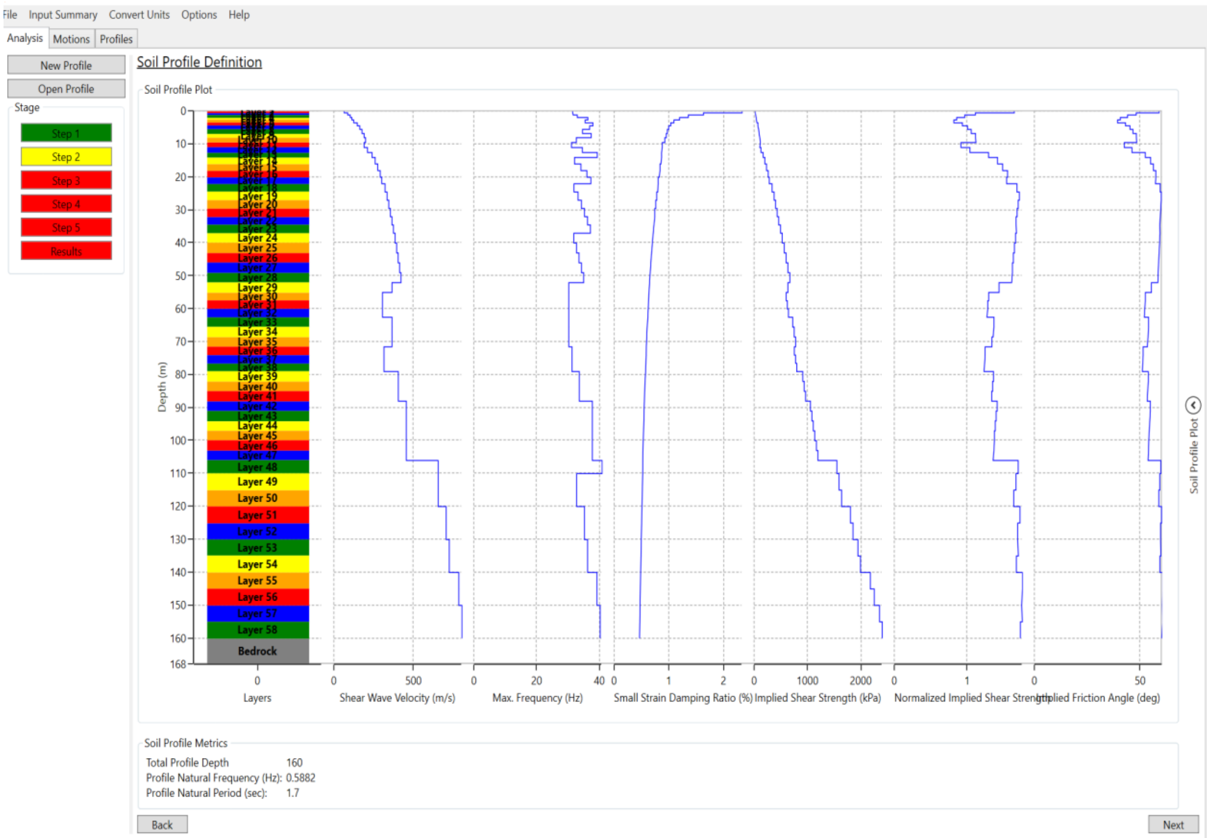

Figure 4.6: Soil Profile Plot

4.3.5 Input Motion Selection

RSN3976_SANSIMEO_CMR090_0.19g has been selected from Pacific Earthquake Engineering Research Centre (PEER) as input motion for the purpose of analysis (PEER-Ground-Motion-Data-Base-Reader). The design basis earthquake (DBE) ground motion is chosen at a level of ground shaking equal to 2/3 (two-thirds) of the maximum considered earthquake (MCE) ground motion (BNBC-2020). The design basis earthquake for this study is determined to be 0.19 g, and it is obtained by multiplying the maximum earthquake considered (0.28 g) by 2/3. So, the input's PGA value has been scaled as 0.19 g in the single motion view. The peak ground acceleration (PGA) at the surface is calculated by multiplying the bedrock peak ground acceleration (PGA) by a calculated site coefficient (which is 0.19 g for Rangpur). Previous researchers did not evaluate the surface PGA value for this site and instead relied on BNBC

4.3.6 Analysis Control Definition

The number of iterations on the frequency domain is 15, the effective shear strain ratio (SSR) is 0.65, and the frequency independent is selected as a complex shear modulus formulation. In the case of time domain analysis, the step control is flexible, the maximum strain increment is 0.005%, the Newmark Beta method is selected as the integration scheme, and the time history interpolation method is zero-padded in the frequency domain.

4.3.7 Results

The time history plots showing the EL (Blue line) and NL (Gray line) are shown in Figure 4.7, and the response spectra summary is shown in Figure 4.8.

4.4 Earthquake Input Motions

For the purpose of DEEPSOIL analysis in this study, data for ten (10) earthquakes has been collected from the PEER-Ground-Motion-Data-Base-Reader. All their record sequence, earthquake name, year, station name, magnitude, mechanism, the closest distance to the rupture surface (R_{RUP}), the Joyner - Boore distance (R_{JB}), shear wave velocity value, horizontal-1 filename and horizontal-2 filename, etc. are shown in the following Table 4.2. These ten earthquakes input motion data have been selected for the nonlinear and equivalent linear analysis of each borehole. The average of 10 earthquakes' data has been taken for the comparison of depth vs. PGA, and PSA vs. period.

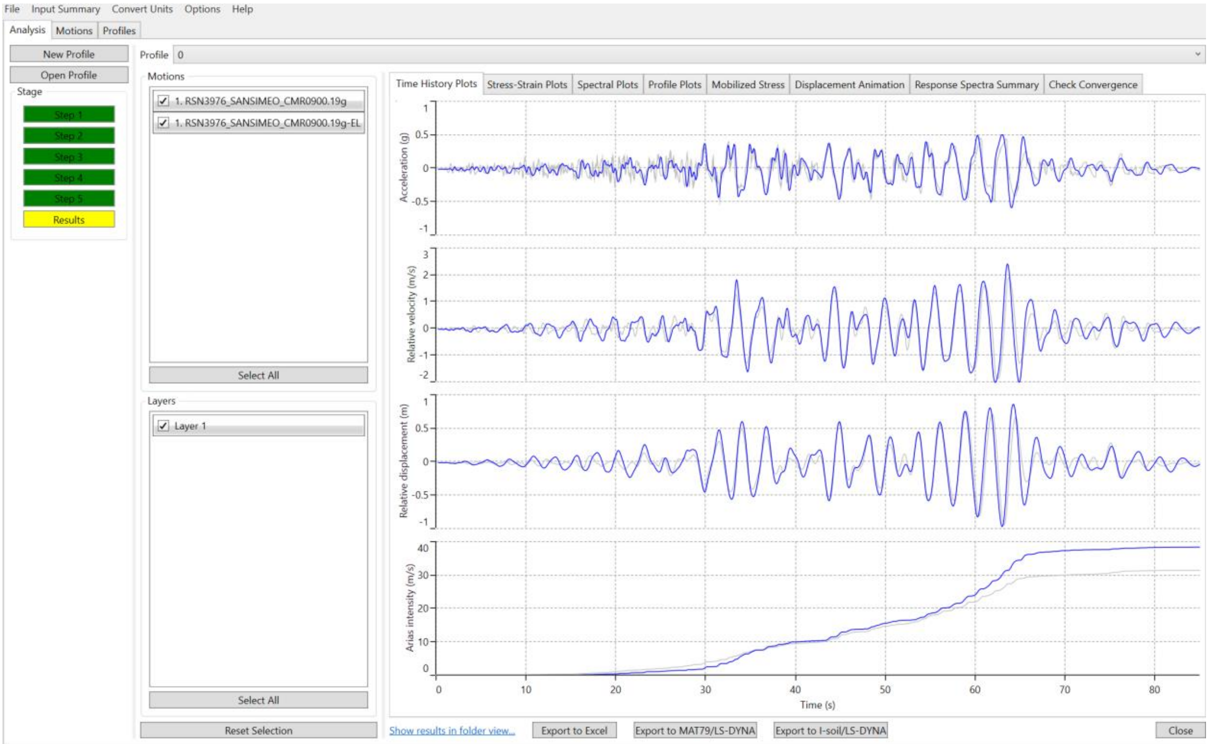

Figure 4.7: Time History Plots (for both NL and EL)

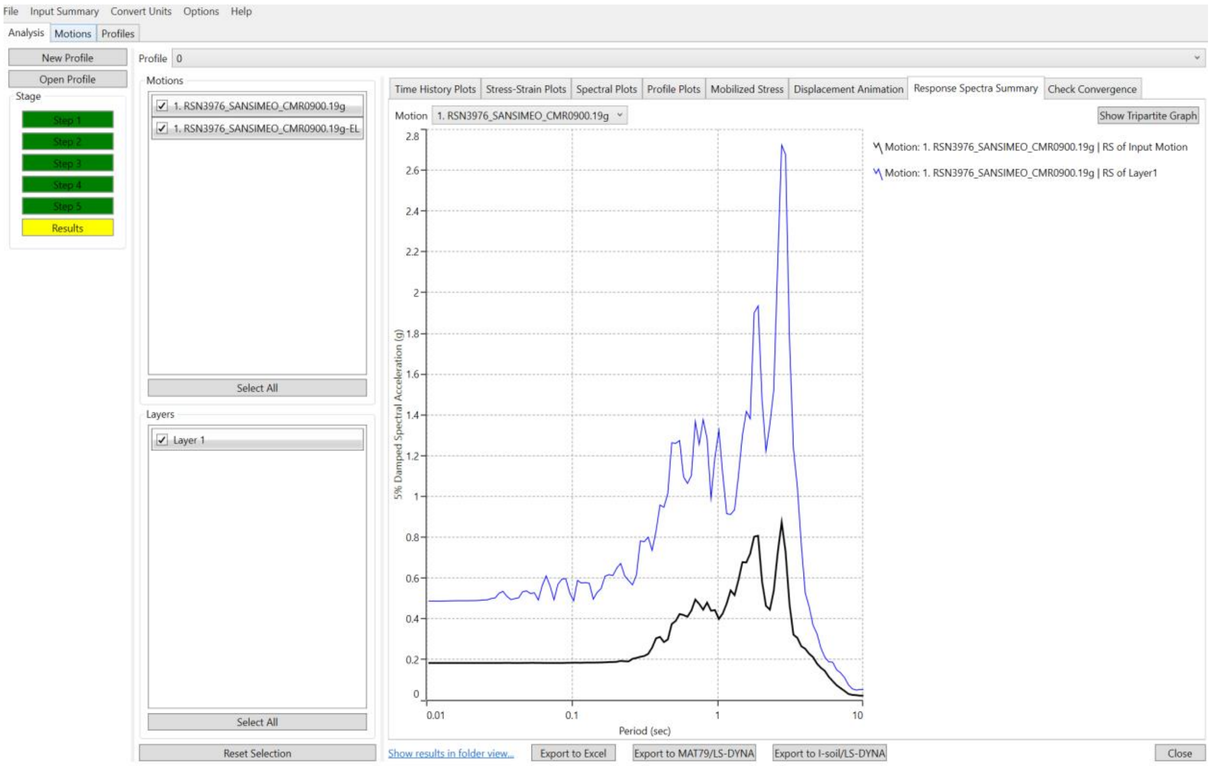

Figure 4.8: Spectral Acceleration for 5% damping (for both NL and EL)

Table 4.2: Time histories Input Motion (PEER-Ground-Motion-Data-Base-Reader)

Record Sequence Number	Earthquake Name	Year	Station Name	Earthquake Magnitude	Mechanism	R_{JB} (km)	R_{RUP} (km)	V_s^{30} (m/s)	Horizontal-1 Acc. Filename	Horizontal-2 Acc. Filename
51	"San Fernando"	1971	"2516 Via Tejon PV"	6.61	Reverse	55.2	55.2	280.6	RSN51_SFERN_PVE065.AT2	RSN51_SFERN_PVE155.AT2
52	"San Fernando"	1971	"Anza Post Office"	6.61	Reverse	173	173.2	360.5	RSN52_SFERN_AZP045.AT2	RSN52_SFERN_AZP315.AT2
58	"San Fernando"	1971	"Cedar Springs Pumphouse"	6.61	Reverse	92.3	92.59	477.2	RSN58_SFERN_CSP126.AT2	RSN58_SFERN_CSP216.AT2
68	"San Fernando"	1971	"LA - Hollywood Stor FF"	6.61	Reverse	22.8	22.77	316.5	RSN68_SFERN_PEL090.AT2	RSN68_SFERN_PEL180.AT2
123	"Friuli_ Italy-01"	1976	"Conegliano"	6.5	Reverse	80.4	80.41	352.1	RSN123_FRIULI.A_A-CLV000.AT2	RSN123_FRIULI.A_A-CLV270.AT2
124	"Friuli_ Italy-01"	1976	"Feltre"	6.5	Reverse	102	102.2	356.4	RSN124_FRIULI.A_A-FLT000.AT2	RSN124_FRIULI.A_A-FLT270.AT2
141	"Tabas_ Iran"	1978	"Kashmar"	7.35	Reverse	194	194.6	280.3	RSN141_TABAS_KSH-L1.AT2	RSN141_TABAS_KSH-T1.AT2
425	"Taiwan SMART1(25)"	1983	"SMART1 C00"	6.5	Reverse	95.6	96.06	309.4	RSN425_SMART1.25_25C00EW.AT2	RSN425_SMART1.25_25C00NS.AT2
435	"Borah Peak_ ID-01"	1983	"ANL-768 Power Plant (Bsmt)"	6.88	Normal	100	100.2	445.7	RSN435_BORAH.MS_ANLCSOU.AT2	RSN435_BORAH.MS_ANLCEAS.AT2
3976	"San Simeon_ CA"	2003	"Camarillo"	6.52	Reverse	216	215.6	351.4	RSN3976_SANSIMEO_CMR090.AT2	RSN3976_SANSIMEO_CMR360.AT2

4.5 Comparison of Depth and Average PGA

The data analysis is carried out using equivalent linear and nonlinear methods. Individual analysis has been performed for 10 (ten) time histories for Nonlinear (NL) and Equivalent Linear (EL) analysis shown in Figure 4.9 (a and b). The values of the PGA for the NL analysis range from 0.185 g to 0.494 g, and the values of the PGA for the EL analysis range from 0.241 g to 0.653 g. Following that step, the data from ten earthquakes were averaged for both the NL and EL analyses. The depth against peak ground acceleration (PGA) (for the average of ten earthquakes) is shown in Figure 4.9 (c). For RP-1 the value of the PGA measured at the surface is 0.50 g as a result of the equivalent linear analysis, while the value is 0.35 g as a result of the nonlinear analysis.

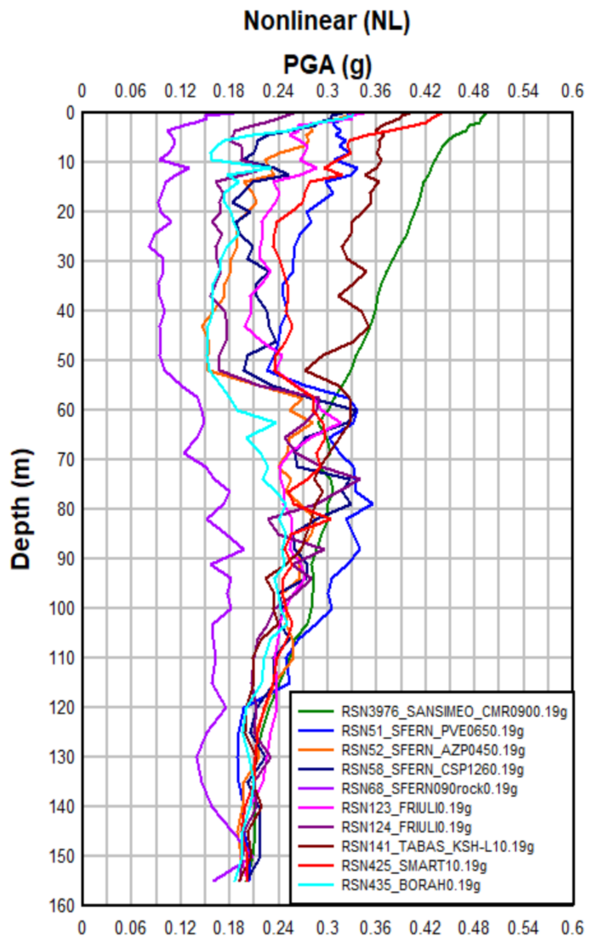

(a) Depth (m) vs PGA (g) plots for NL analysis

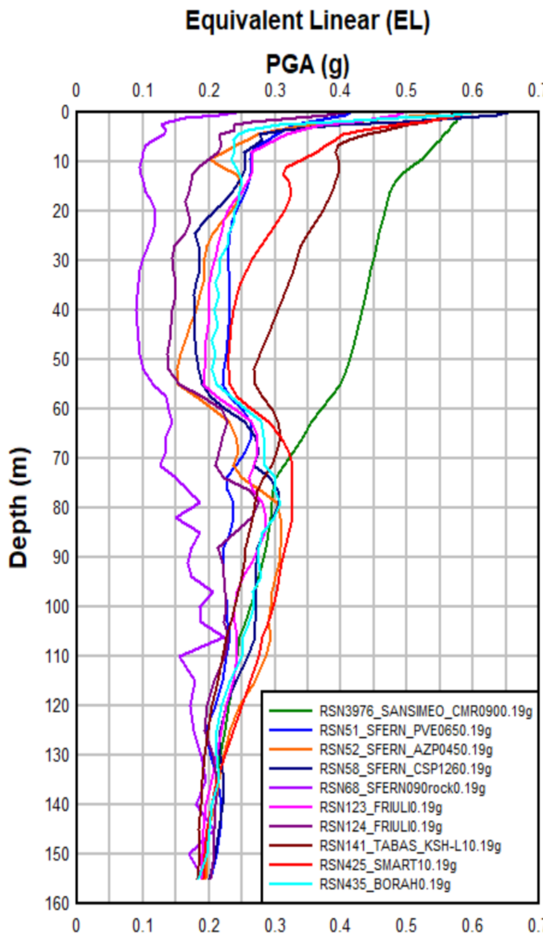

(b) Depth (m) vs PGA (g) plots for EL analysis

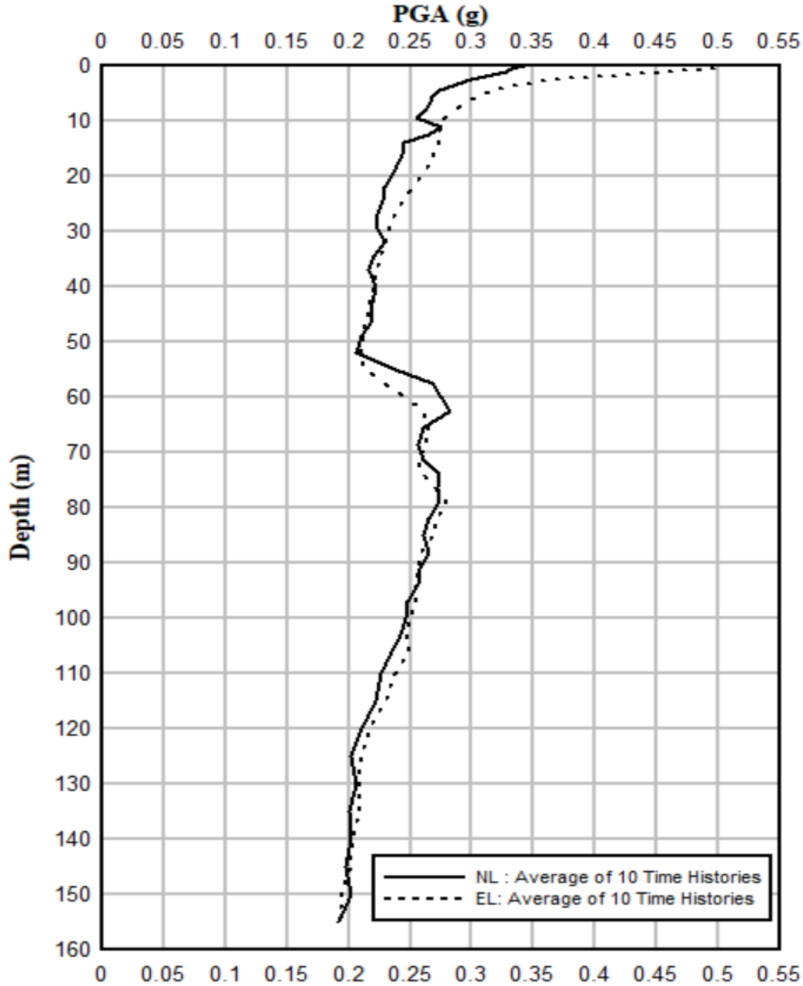

(c) Depth (m) vs PGA (g) plots (Average of 10 (ten) time histories for both NL and EL)

Figure 4.9: Depth against Peak Ground Acceleration plots. (a) for NL analysis, (b) for EL analysis and (c) Average of 10 (ten) time histories for both EL and NL analysis

4.6 Comparison of PSA and Time

Figure 4.10 (a) and (b) depict nonlinear (NL) and equivalent linear (EL) assessments performed separately for each of the 10 (ten) time histories. The comparison between pseudo spectral acceleration (PSA) and period by averaging 10 (ten) time histories for nonlinear and equivalent linear analysis is shown in 4.10 (c). It is shown that the plot of PSA for equivalent linear analysis is greater than the nonlinear PSA. The value of spectral acceleration is maximum at the period of 0.38 seconds for equivalent linear analysis, and the value of spectral acceleration is maximum at the period of 0.61 seconds for nonlinear analysis. In addition to this, it has been demonstrated that the value of the spectral acceleration is decreasing as time goes on, and the PSA value is very close to being zero at the time period of 10 seconds.

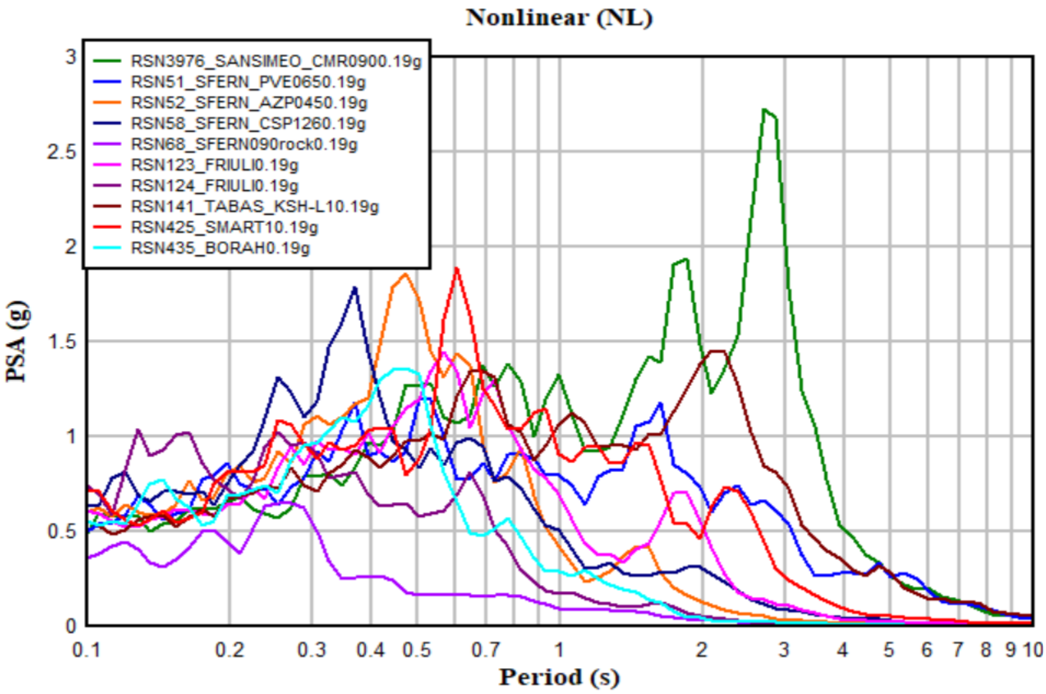

(a) PSA (g) vs Period (sec) plots for NL analysis

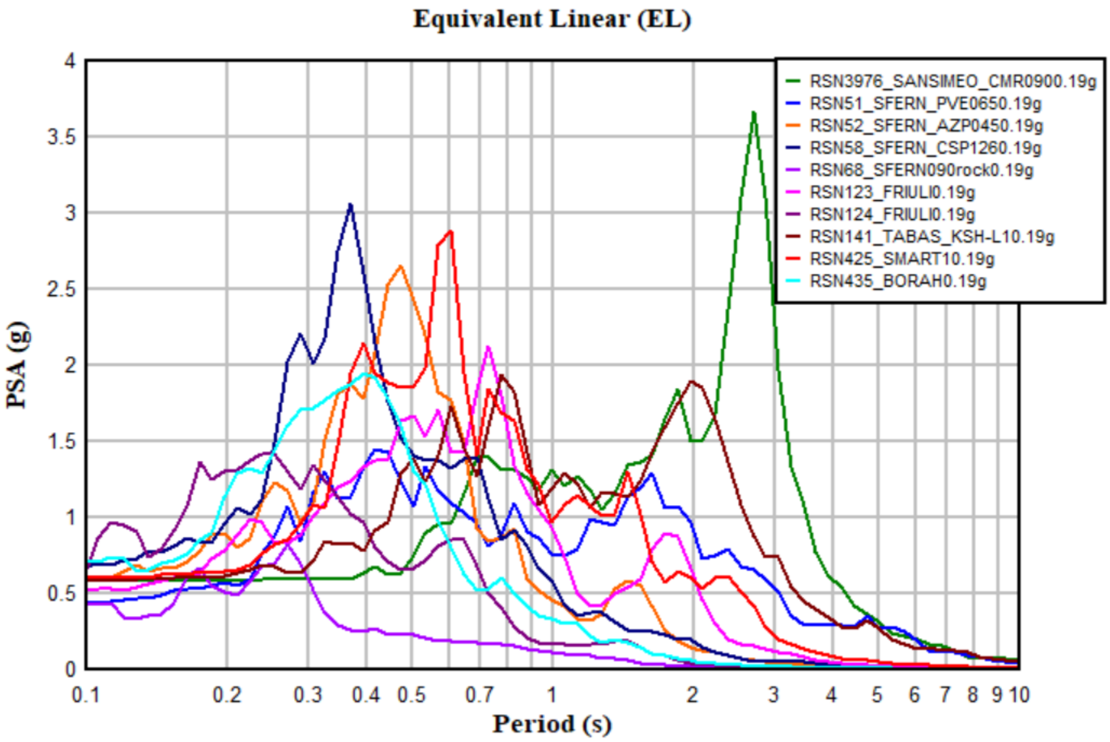

(b) PSA (g) vs Period (sec) plots for EL analysis

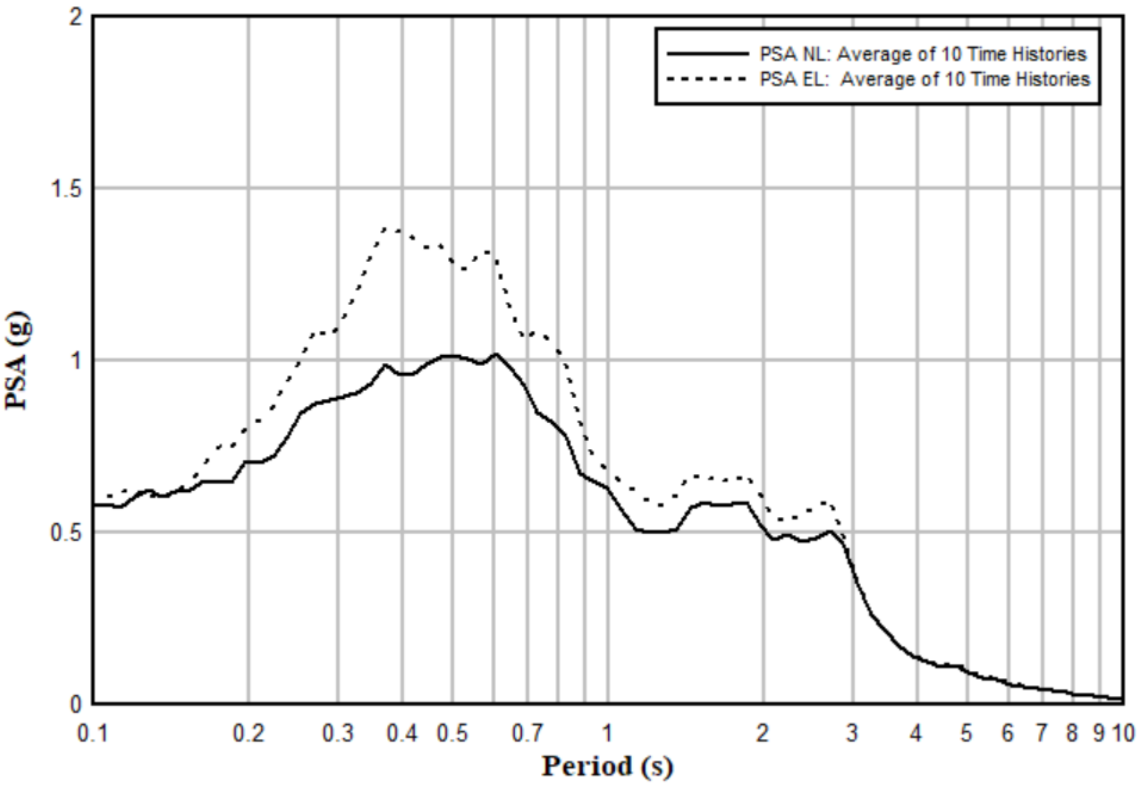

(c) PSA (g) vs Period (sec) plots (Average of 10 time histories for both NL and EL)

Figure 4.10: Variation of Peak Spectral Acceleration against Period plots (a) for NL analysis, (b) for EL analysis and (c) Average of 10 time histories for both EL and NL analyses.

The comparison curves between NL and EL for other 15 boreholes used in this study are presented in Appendix-C, and the comparison of the variation of spectral acceleration with BNBC are shown in Appendix-D.

4.7 Site Classification

The standard penetration values are obtained from the SPT test and are gathered for this investigation. After doing the necessary calculations for the top 30 m of soil equation 2.4 was used (details calculation shown in Table 4.3) to determine the $\overline{\mathrm{N}}$ (blows/30 cm) values and the depth of the RP-1 borehole, it has been discovered that the N value is 14.94, which places it in the site class SD according to BNBC (discussed in Table 2.5 in chapter 2).

Table 4.3: Calculation for determining site class

Depth (m)	d (m)	SPT N	d/SPT-N	SPT value, $\overline{N}$ (blows/30 cm)
0	0	0	-	
1.5	1.5	6	0.25	
3	1.5	5	0.30	
4.5	1.5	10	0.15	
6	1.5	14	0.11	
7.5	1.5	15	0.10	
9	1.5	17	0.09	
10.5	1.5	5	0.30	
12	1.5	7	0.21	
13.5	1.5	19	0.08	$\overline{N} = \frac{\sum d}{\sum \frac{d}{SPT-N}}$
15	1.5	28	0.05	
16.5	1.5	29	0.05	= 14.94
18	1.5	33	0.05	Site Class = SD
19.5	1.5	40	0.04	
21	1.5	34	0.04	
22.5	1.5	43	0.03	
24	1.5	47	0.03	
25.5	1.5	50	0.03	
27	1.5	50	0.03	
28.5	1.5	50	0.03	
30	1.5	50	0.03	
	∑d=30		∑ d/SPT-N =2.01	

4.8 Target Response Spectrum

The normalized design acceleration response spectrum for different site classes according to BNBC (2020) is shown in Figure 2.4 (Chapter 2). The surface hazard spectrum was calculated by multiplying the normalized design acceleration response spectrum (for soil type SD) by 0.19 g as recommended by BNBC (2020). After that, the spectral acceleration for the SD site class has been plotted in the PSA vs. period curve. Figure 4.11 shows the Comparison of the variation of spectral acceleration with BNBC for the site class SD (0.19g). The graph shows that the site class SD (0.19 g) is much lower than the PSA obtained from the analysis.

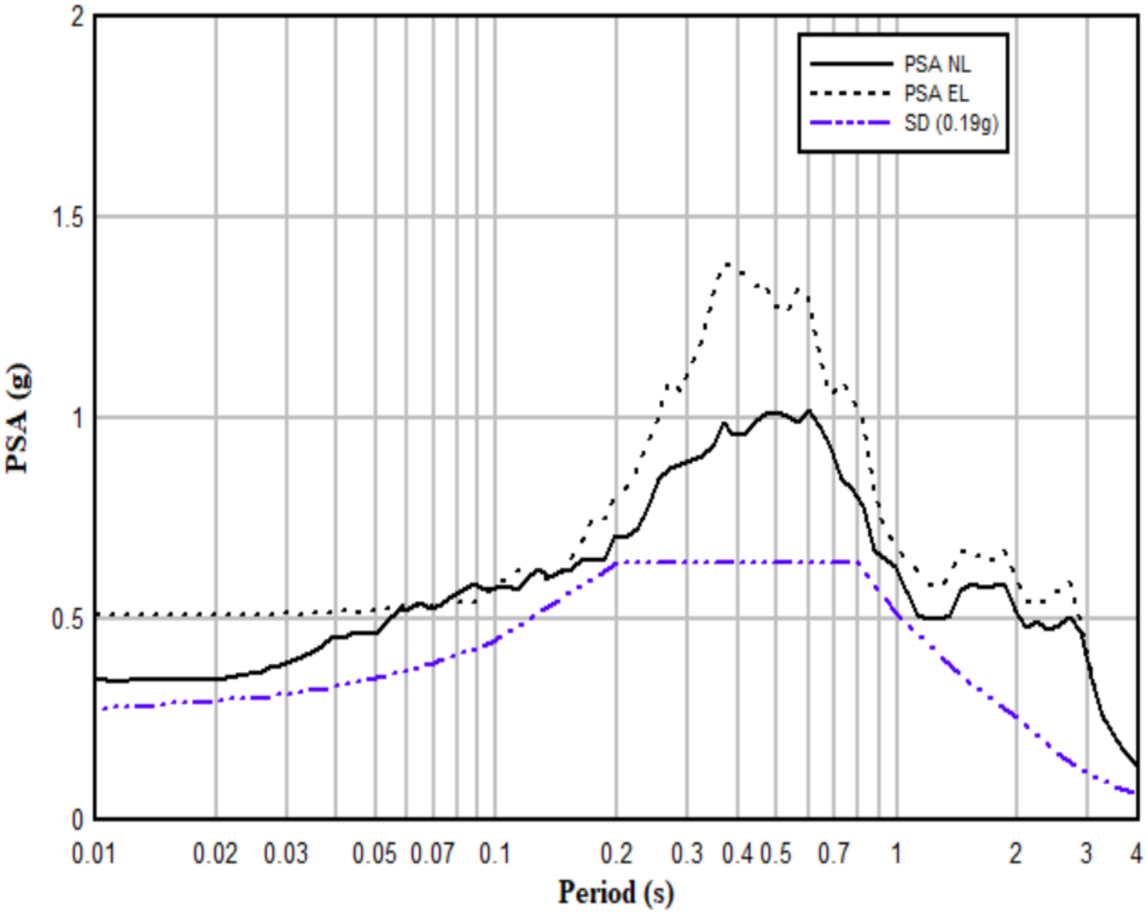

Figure 4.11: Comparison of the variation of spectral acceleration with BNBC (SD 0.19g)

4.9 Proposed Design Acceleration Response Spectrum for Rangpur

Based on the SPT $\overline{N}$ values, and the site class has been determined in accordance with BNBC (2020). A significant majority of the SPT $\overline{N}$ values for Rangpur City Corporation are less than 15 (following Table 2.5). The site class of 12 of the 16 boreholes is determined to be SD, whereas the site class of 4 of the boreholes is determined to be SC, as shown in Table 4.4. When considering the total number of boreholes in the Rangpur area, the site class is determined to be an SD site class by taking the average of all boreholes' $\overline{N}$ values. One conclusion that might be drawn from this is that the site class of the soil in the Rangpur area is classified as SD.

Table 4.4: Site class for all the boreholes

Borehole No.	SPT value, $\overline{N}$	Site Class (According to BNBC-2020)
RP-1	14.94	SD
RP-2	11.08	SD
RP-3	17.7	SC
RP-4	12.69	SD
RP-5	16.97	SC
RP-6	10.08	SD
RP-7	11.62	SD
RP-8	16.55	SC
RP-9	10.83	SD
RP-10	11.88	SD
RP-11	11.95	SD
RP-12	12.83	SD
RP-13	16.17	SC
RP-14	9.43	SD
RP-15	7.79	SD
RP-16	6.58	SD

Figure 4.12 demonstrates that the average spectral acceleration plot of all sixteen boreholes is significantly greater than the BNBC site class SD (0.19 g). Even though the spectral acceleration for SD soil is low in BNBC (2020), the computation shows that SD soil is significantly higher for Rangpur City. A design acceleration response spectrum has been presented for site class SD (0.19 g), which may be seen in Figure 4.12. The solid black line illustrates the average nonlinear spectral acceleration for all boreholes, the dashed-dotted blue line depicts the BNBC site class SD (0.19 g), and the solid red line illustrates the recommended PSA for the SD site class in Rangpur City.

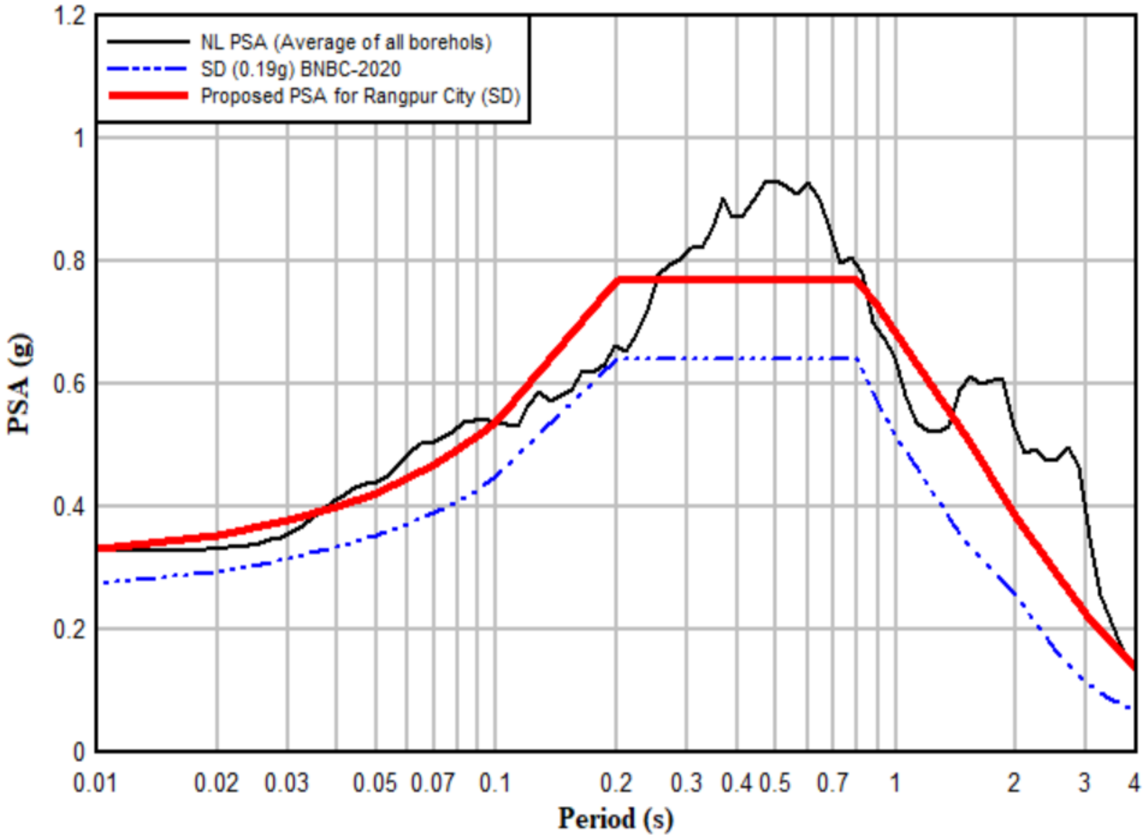

Figure 4.12: Proposed design Spectral Acceleration Response Spectrum for Rangpur City

4.10 Soil Profiles for the Study Area

The borehole location and cross-sectional direction of Rangpur City Corporation are shown in Figure 4.13, and two cross-sections showing the soil profile of the study site are shown in Figure 4.14. According to the cross-sectional profile (section 1-1), it is clearly visible that the soil of the study site is mostly composed of silty fine sand on the top few meters, and dense silty fine sand with trace mica is present in the soil up to a depth of 30 meters. Based on the cross-sectional profile (section 2-2), it can be said that the top soils of the study site consist of loose to medium dense fine sand, and up to a depth of 36 meters, the soil is medium dense to very dense fine sand with trace mica. It may be possible to draw the conclusion, based on the cross sections 1-1 and 2-2, that the soil has a liquefaction susceptibility when an earthquake occurs.

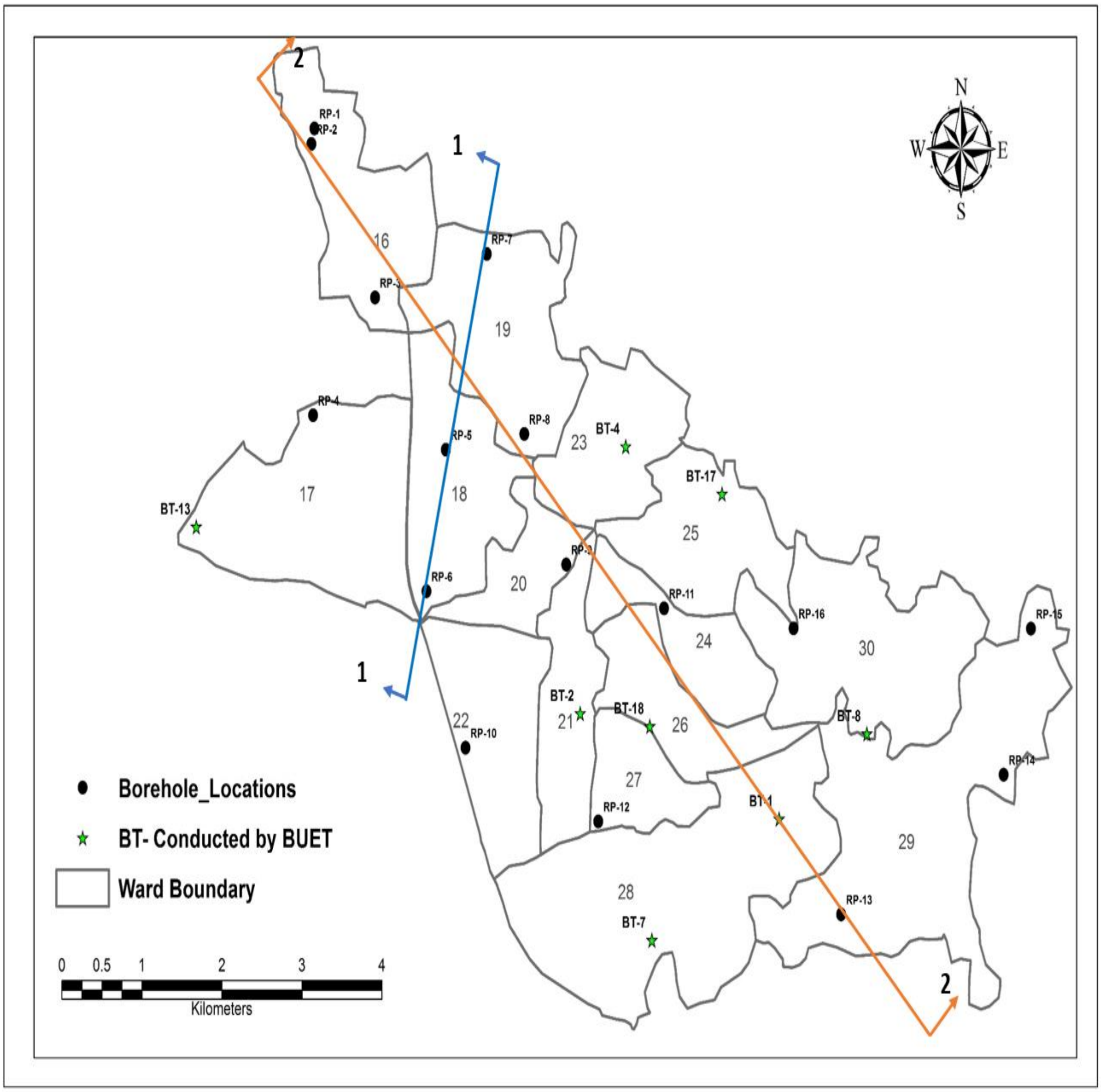

Figure 4.13: Rangpur City Corporation Area showing the borehole location and cross-sectional direction.

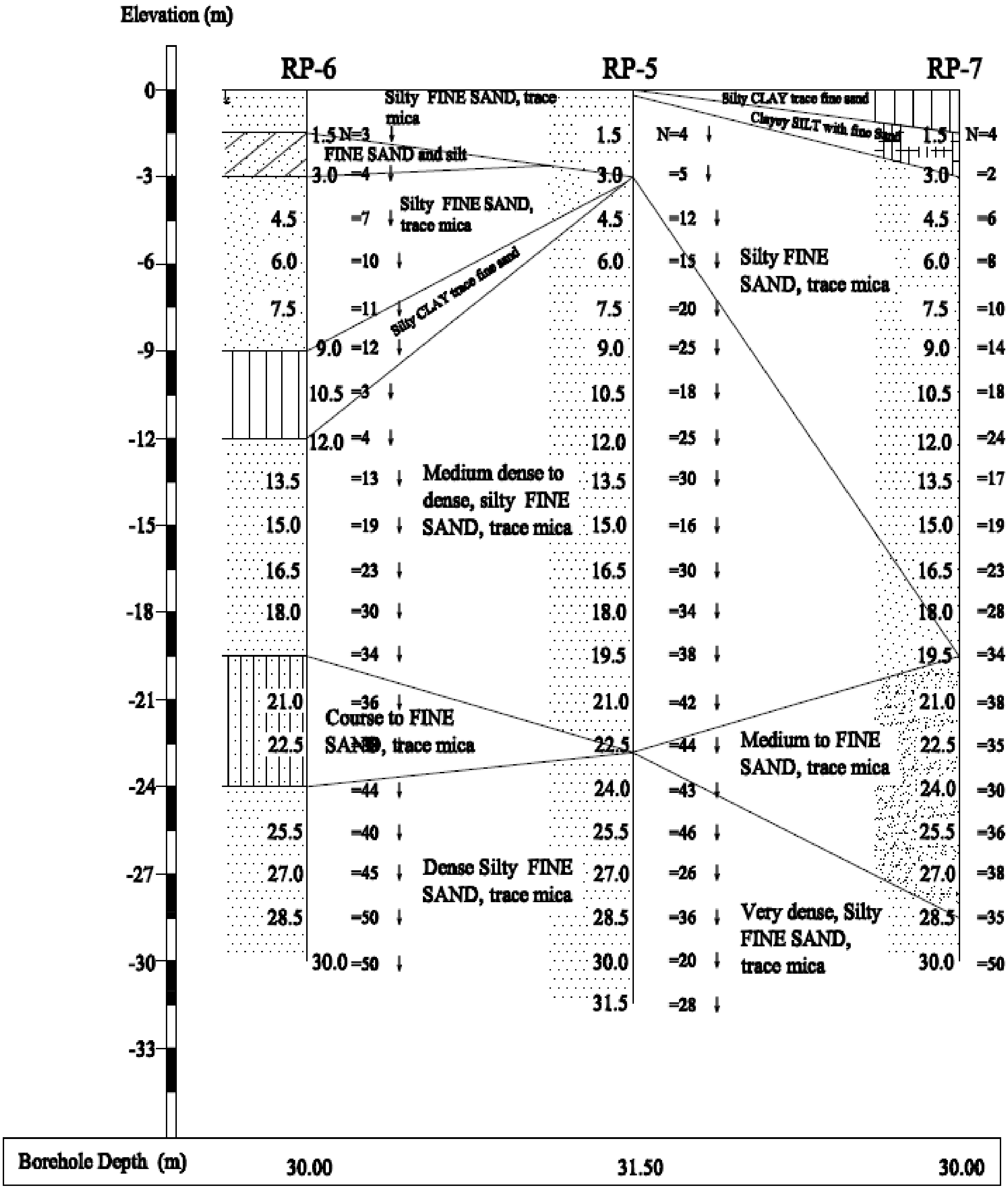

(a) Typical Cross Section 1-1 for the study site (with SPT N value)

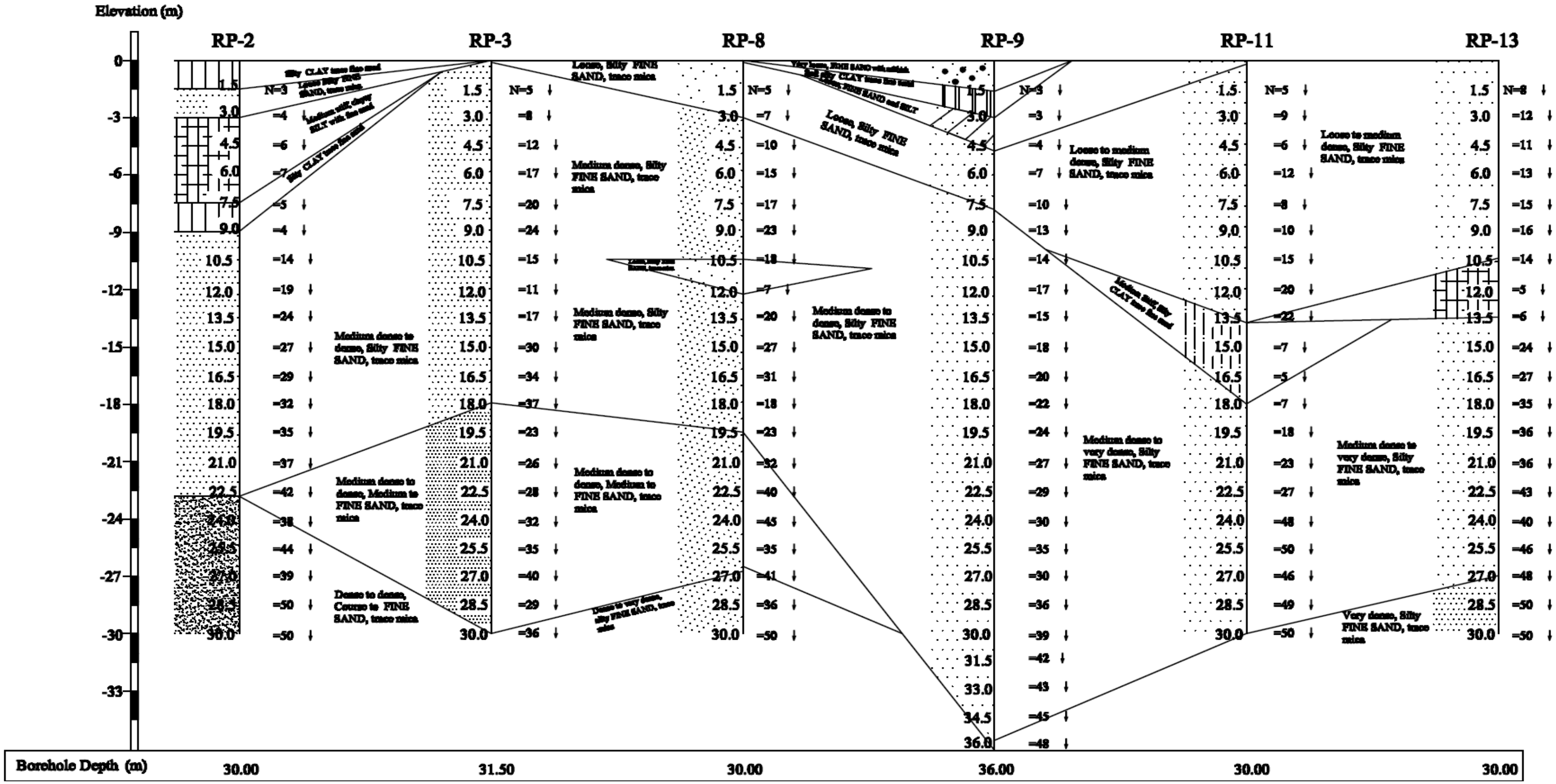

(b) Typical Cross Section 2-2 for the study site (with SPT N values)

Figure 4.14: Typical cross section of the soil profile with SPT values of Rangpur a) section 1-1, b) section 2-2

4.11 Estimation of Liquefaction Susceptibility

In this study, the liquefaction susceptibility has been carried out by using the Seed and Idriss simplified method, the Japanese method, and the Chinese method. For the assessment of the liquefaction susceptibility SPT N values, and Fineness Content (FC) are required. N values have been found from the standard penetration test (attached in Appendix A), and FC has been taken from the grain size distribution curve (attached in Appendix B). As discussed in the literature review (Article 2.11), the liquefaction tendency of an underlying soil may be evaluated using geological data and the soil's current features.

The factor of safety for all boreholes is less than 1, based on the three liquefaction methods that have been carried out in this study (Using the equation 2.5 to 2.23 that have been discussed in Chapter 2). $F_L<1.0$ implies that the shear stress induced by the earthquake exceeds the liquefaction resistance of the soil, and hence liquefaction will occur. For $F_L>1.0$, liquefaction will not occur. So, it can be said that liquefaction will occur at the study site at the time of an earthquake. Figure 4.15 depicts the depth versus factor of safety plot at RP-11 for the three different approaches when the PGA value is 0.3238 g and the magnitude (M_w) value is 7.5.

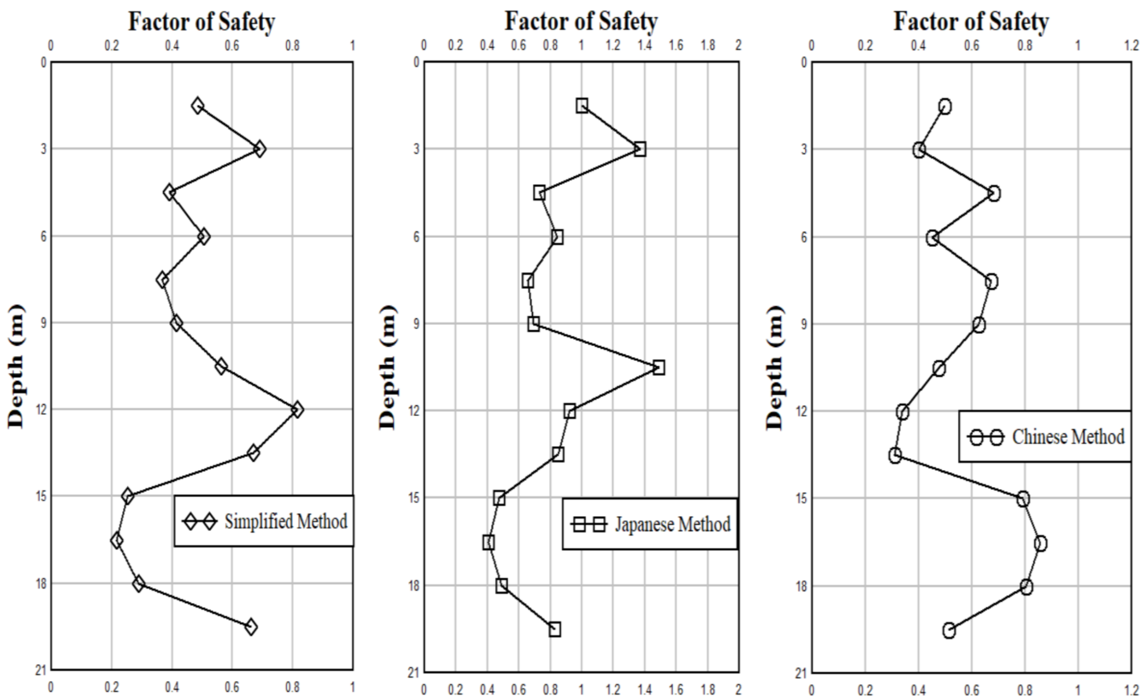

Figure 4.15: Variation of factor of safety with depth (for the three different approaches)

From the DEEPSOIL analysis, it is found that the surface PGA value for the Rangpur City Corporation area is 0.3238 g (for NL) by averaging all the borehole data. Equation 2.24 was utilized in the calculation of LPI values for the simplified method and the Japanese method, while equation 2.29 was utilized for the Chinese method. The LPI values for the three approaches as well as the different scenarios of earthquakes with varying levels of GWT are presented in Table 4.5, Table 4.6, Table 4.7, Table 4.8, Table 4.9, and Table 4.10. From the tables it can be noticed that the LPI value is increasing with the increase in magnitude.

Table 4.5: Scenario of Earthquake (PGA = 0.3238 g and Magnitude, M_w = 6.5) for different groundwater table depth

Borehole No.	GWT Depth (m)	Liquefaction Potential Index (LPI)		
		Japanese Method	Chinese Method	Seed & Idriss Method
RP-1	4.42	3.49	19.15	10.26
RP-2	2.74	1.41	32.25	17.84
RP-3	2.13	6.57	13.88	15
RP-4	4.12	4.74	37.62	20.61
RP-5	2.59	1.18	19.88	12.3
RP-6	0.76	21.96	56.98	36.27
RP-7	1.52	8.77	38.9	19.9
RP-8	2.29	2.59	13.43	7.47
RP-9	3.66	6.1	46.27	15.38
RP-10	3.13	9.38	35.9	17.6
RP-11	2.44	10.75	37.69	17.7
RP-12	2.44	12.23	35.03	17.83
RP-13	3.35	3.84	16.54	7.48
RP-14	2.74	12.42	47.61	22.75
RP-15	2.44	16.1	60.8	26.42
RP-16	3.51	8.46	49.77	16.93
BT-13	1.5	9.98	30.18	29.01
BT-4	1.5	10.75	35.58	24.39
BT-2	1.5	14.27	55.05	29.06
BT-17	1.5	9.23	29.97	19.59
BT-18	1.5	5.57	33.31	14.63
BT-1	1.5	8.09	30.42	26.75
BT-7	1.5	7.74	31.4	20.13
BT-8	1.5	8.12	33.12	18.71

Table 4.6: Scenario of Earthquake (PGA = 0.3238 g and Magnitude, M_w = 6.5) for same groundwater table depth

Borehole No.	GWT Depth (m)	Liquefaction Potential Index (LPI)		
		Japanese Method	Chinese Method	Seed & Idriss Method
RP-1	1.5	32.41	30.57	20.88
RP-2	1.5	5.14	38.03	23.82
RP-3	1.5	11.32	15.73	18.25
RP-4	1.5	16.77	50.43	31.12
RP-5	1.5	7.28	24.22	17.69
RP-6	1.5	13.31	54.77	30.76
RP-7	1.5	8.77	38.98	19.9
RP-8	1.5	5.98	15.95	10.59
RP-9	1.5	16.7	54.49	25.39
RP-10	1.5	15.49	44.21	25.48
RP-11	1.5	14.23	42.29	22.46
RP-12	1.5	15.56	38.32	21.63
RP-13	1.5	11.53	23.42	16.17
RP-14	1.5	16.88	52.72	28.85
RP-15	1.5	20	63.52	30.03
RP-16	1.5	19.76	55.77	26.03
BT-13	1.5	9.98	30.18	29.01
BT-4	1.5	10.75	35.58	24.39
BT-2	1.5	14.27	55.05	29.06
BT-17	1.5	9.23	29.97	19.59
BT-18	1.5	5.57	33.31	14.63
BT-1	1.5	8.09	30.42	26.75
BT-7	1.5	7.74	31.4	20.13
BT-8	1.5	8.12	33.12	18.71

Table 4.7: Scenario of Earthquake (PGA = 0.3238 g and Magnitude, M_w = 7.5) for different groundwater table depth

Borehole No.	GWT Depth (m)	Liquefaction Potential Index (LPI)		
		Japanese Method	Chinese Method	Seed and Idriss Method
RP-1	4.42	3.49	34.05	21.82
RP-2	2.74	1.41	48.29	29.11
RP-3	2.13	6.57	30.29	25.68
RP-4	4.12	4.74	53.27	32.85
RP-5	2.59	1.18	35.42	24.71
RP-6	0.76	21.96	67.64	44.08
RP-7	1.52	8.77	54.12	32.05
RP-8	2.29	2.59	29.09	18.99
RP-9	3.66	6.1	59.75	28.9
RP-10	3.13	9.38	51.27	29.69
RP-11	2.44	10.75	53.34	30.7
RP-12	2.44	12.23	47.55	27.6
RP-13	3.35	3.84	31.87	20.47
RP-14	2.74	12.42	60.46	33.97
RP-15	2.44	16.1	70.51	36.86
RP-16	3.51	8.46	62.06	28.3
BT-13	1.5	9.98	42.63	38.92
BT-4	1.5	10.75	51.08	34.99
BT-2	1.5	14.27	65.07	38.51
BT-17	1.5	9.23	46.84	32.14
BT-18	1.5	5.57	45.22	27.52
BT-1	1.5	8.09	43.73	36.81
BT-7	1.5	7.74	48.03	31.25
BT-8	1.5	8.12	48.39	30.09

Table 4.8: Scenario of Earthquake (PGA = 0.3238 g and Magnitude, M_w = 7.5) for same groundwater table depth

Borehole No.	GWT Depth (m)	Liquefaction Potential Index (LPI)		
		Japanese Method	Chinese Method	Seed and Idriss Method
RP-1	1.5	32.41	44.16	32.55
RP-2	1.5	5.14	53.09	33.59
RP-3	1.5	11.32	33.69	28.04
RP-4	1.5	16.77	62.85	40.31
RP-5	1.5	7.28	40.28	29.46
RP-6	1.5	13.31	65.95	40.2
RP-7	1.5	8.77	54.19	32.05
RP-8	1.5	5.98	33.31	22.93
RP-9	1.5	16.7	65.88	36.4
RP-10	1.5	15.49	58.2	36.21
RP-11	1.5	14.23	56.78	34.3
RP-12	1.5	15.56	50.01	31.13
RP-13	1.5	11.53	42.32	29.57
RP-14	1.5	16.88	64.56	38.75
RP-15	1.5	20	72.54	39.44
RP-16	1.5	19.76	66.82	35.7
BT-13	1.5	9.98	42.63	38.92
BT-4	1.5	10.75	51.08	34.99
BT-2	1.5	14.27	65.07	38.51
BT-17	1.5	9.23	46.84	32.14
BT-18	1.5	5.57	45.22	27.52
BT-1	1.5	8.09	43.73	36.81
BT-7	1.5	7.74	48.03	31.25
BT-8	1.5	8.12	48.39	30.09

Table 4.9: Scenario of Earthquake (PGA = 0.3238 g and Magnitude, M_w = 8.5) for different groundwater table depth

Borehole No.	GWT Depth (m)	Liquefaction Potential Index (LPI)		
		Japanese Method	Chinese Method	Seed and Idriss Method
RP-1	4.42	3.49	44.17	32
RP-2	2.74	1.41	58.63	36.77
RP-3	2.13	6.57	44.25	33.6
RP-4	4.12	4.74	62.61	40.71
RP-5	2.59	1.18	48.36	33.54
RP-6	0.76	21.96	74.07	48.91
RP-7	1.52	8.77	63.28	40.11
RP-8	2.29	2.59	43.32	28.47
RP-9	3.66	6.1	67.77	37.88
RP-10	3.13	9.38	61.01	38.23
RP-11	2.44	10.75	62.66	39.2
RP-12	2.44	12.23	55.01	36.94
RP-13	3.35	3.84	45.51	31.55
RP-14	2.74	12.42	68.34	41.56
RP-15	2.44	16.1	76.35	43.6
RP-16	3.51	8.46	69.61	36.7
BT-13	1.5	9.98	52.78	45.17
BT-4	1.5	10.75	60.85	41.56
BT-2	1.5	14.27	71.63	44.87
BT-17	1.5	9.23	57.1	40.21
BT-18	1.5	5.57	52.51	36.82
BT-1	1.5	8.09	52.94	43.63
BT-7	1.5	7.74	58.43	38.39
BT-8	1.5	8.12	58.04	38.63

Table 4.10: Scenario of Earthquake (PGA = 0.3238 g and Magnitude, M_w = 8.5) for same groundwater table depth

Borehole No.	GWT Depth (m)	Liquefaction Potential Index (LPI)		
		Japanese Method	Chinese Method	Seed and Idriss Method
RP-1	1.5	32.41	55.32	39.79
RP-2	1.5	5.14	62.46	40.27
RP-3	1.5	11.32	46.99	35.76
RP-4	1.5	16.77	70.24	46.17
RP-5	1.5	7.28	52.24	37.35
RP-6	1.5	13.31	72.71	46.1
RP-7	1.5	8.77	63.33	40.11
RP-8	1.5	5.98	46.68	31.34
RP-9	1.5	16.7	72.66	43.34
RP-10	1.5	15.49	66.53	43.06
RP-11	1.5	14.23	65.4	41.82
RP-12	1.5	15.56	56.97	39.51
RP-13	1.5	11.53	53.87	38.37
RP-14	1.5	16.88	71.61	45.05
RP-15	1.5	20	77.98	45.52
RP-16	1.5	19.76	73.41	42.62
BT-13	1.5	9.98	52.78	45.17
BT-4	1.5	10.75	60.85	41.56
BT-2	1.5	14.27	71.63	44.87
BT-17	1.5	9.23	57.1	40.21
BT-18	1.5	5.57	52.51	36.82
BT-1	1.5	8.09	52.94	43.63
BT-7	1.5	7.74	58.43	38.39
BT-8	1.5	8.12	58.04	38.63

From the above six tables, it is clearly visible that a variation may occur when the magnitude is changed. It can be observed that the liquefaction potential index value increases as the earthquake magnitude increases from 6.5 to 8.5. So, it can be seen that the higher the magnitude, the greater the liquefaction potential index value. The groundwater table (GWT) is another important factor that affects the LPI value. If the GWT depth is low from the existing ground level (EGL), the LPI value increases. So, it can be observed that the lower the GWT from EGL, the higher the liquefaction susceptibility.

4.11.1 Liquefaction Contour Map

As described in Chapter 2, when the LPI value is greater than 15, the risk of liquefaction is very high; when the LPI value is between 15 and more than 5, the risk of liquefaction is high; when the LPI value is between 5 and more than 0, the risk of liquefaction is low; and when the LPI value is equal to 0, the risk of liquefaction is very low. Due to the fact that the LPI values for both the simplified method developed by Seed and Idriss and the Chinese method are greater than 15, the potential for liquefaction is extremely high in accordance with the limit, as shown in the above four tables of different scenarios that were presented earlier in this article. As all the LPI values are greater than 15 for the simplified and Chinese methods, the liquefaction contour maps for all the scenarios (different moments and GWT variations) will be the same as shown in Figure 4.16. The Japanese method is less conservative than the other two methods that's why the LPI values for Japanese method vary with different scenarios as illustrated in Figure 4.17. It has been demonstrated that when the magnitude increased, there was also an increase in the LPI values. As the simplified and Chinese methods are more conservative than the Japanese method, the entire liquefaction contour map for Rangpur city can be represented by Figure 4.16. The predicted LPI contours reveal that nearly 100 percent of the overall area is vulnerable to liquefaction.

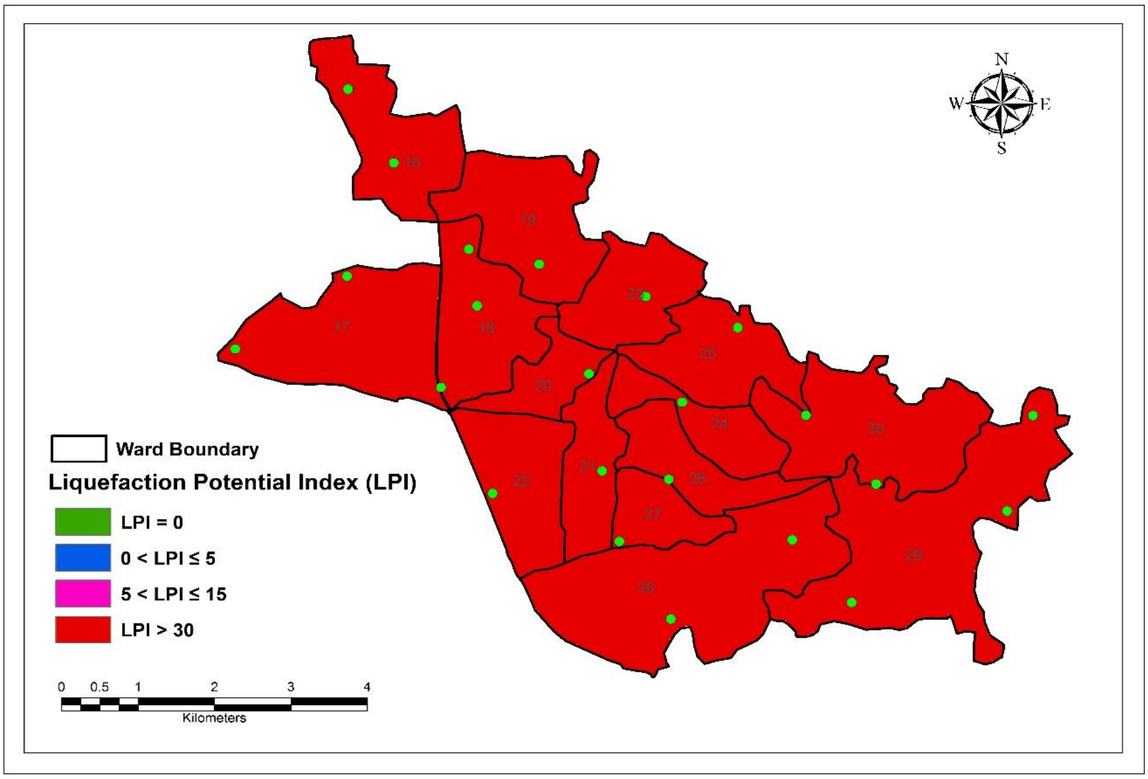

Figure 4.16: LPI based microzonation map for the Rangpur city corporation area for a PGA value of 0.3238 g (for both Chinese and Seed & Idriss methods).

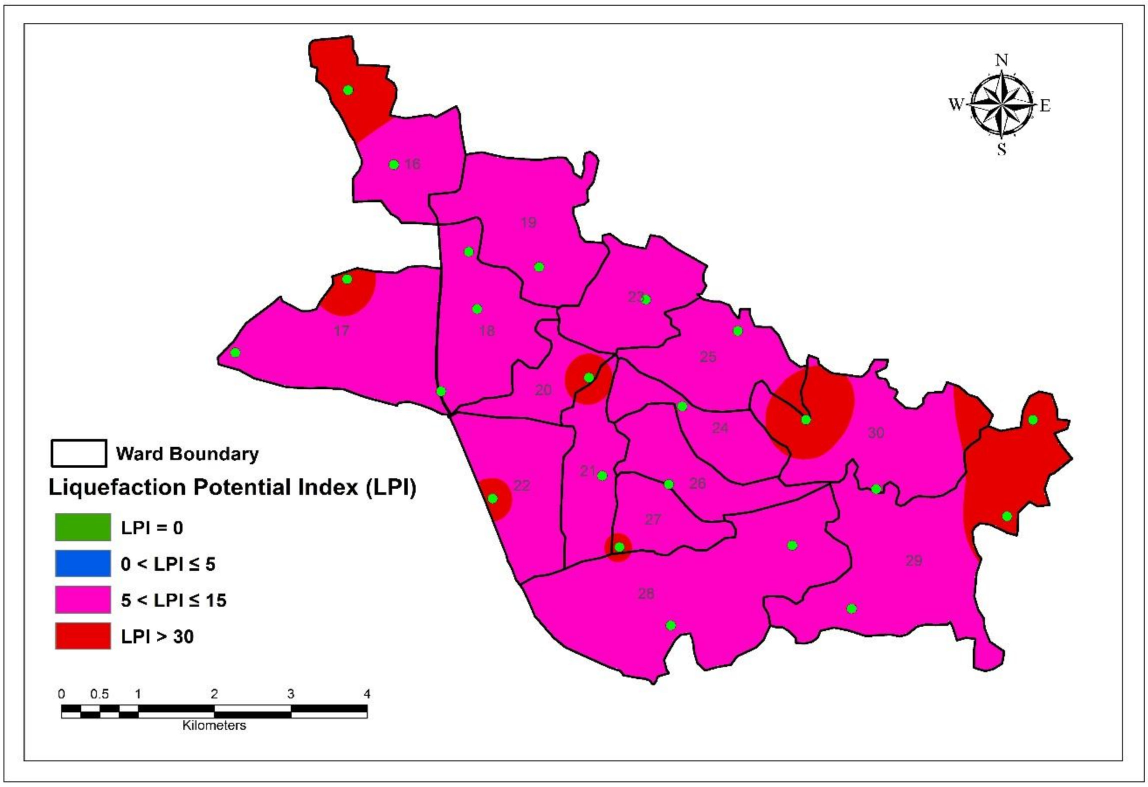

(a) Magnitude = 6.5 and different GWT depth (Japanese)

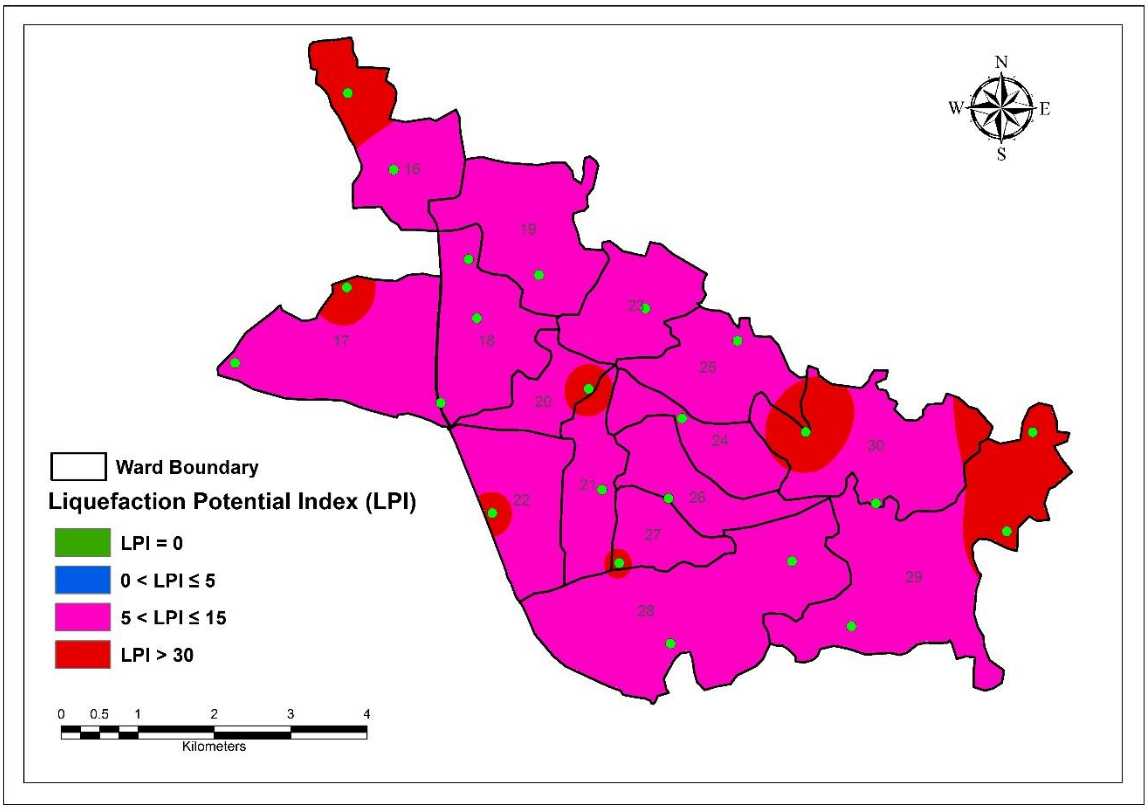

(b) Magnitude = 6.5, and GWT depth = 1.5 m (Japanese)

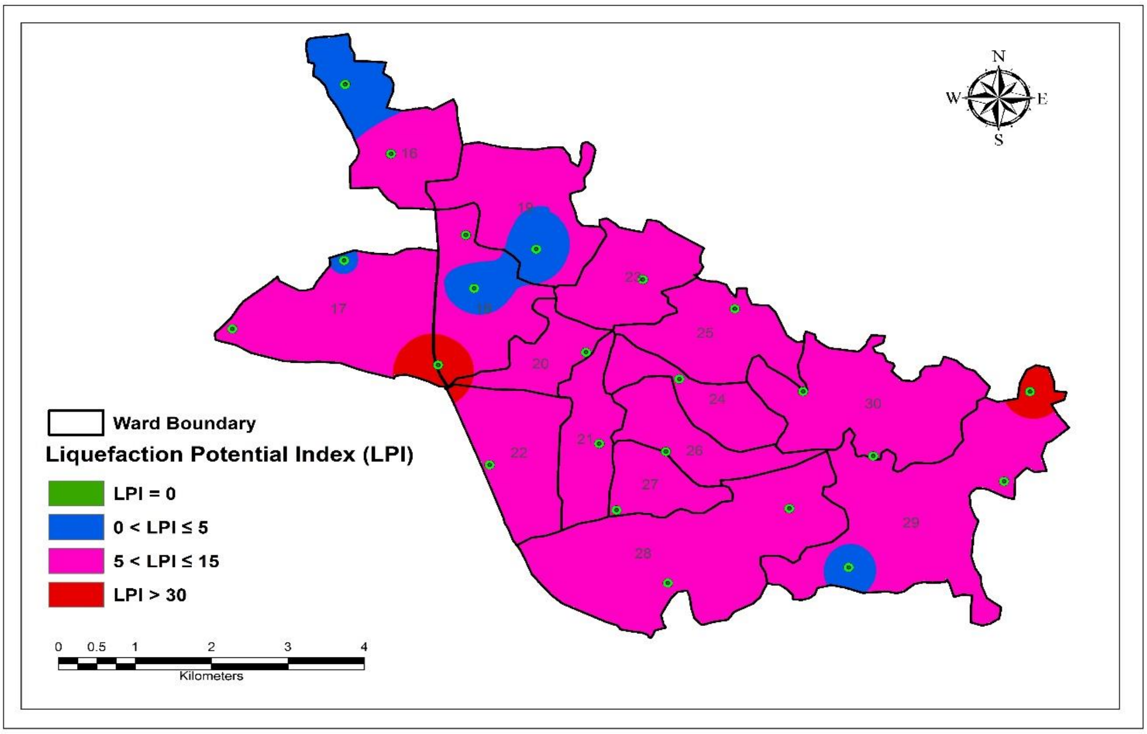

(c) Magnitude = 7.5 and different GWT depth (Japanese)

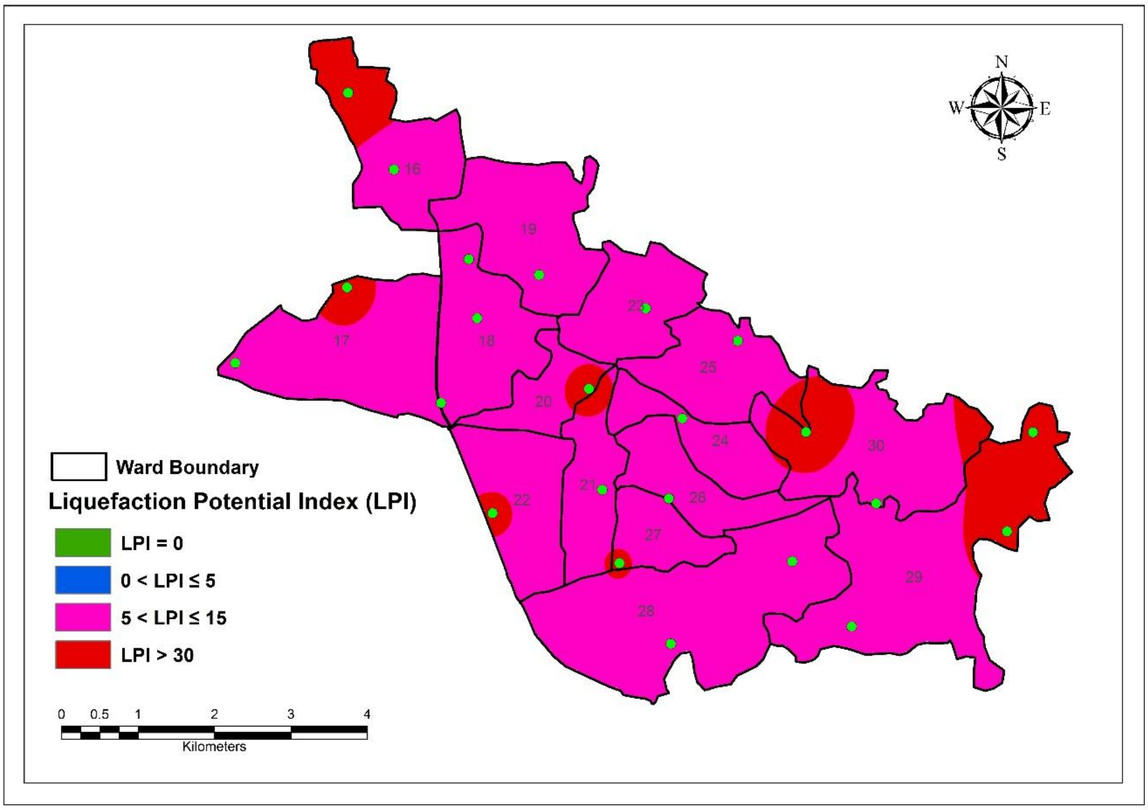

(d) Magnitude = 7.5, and GWT depth = 1.5 m (Japanese)

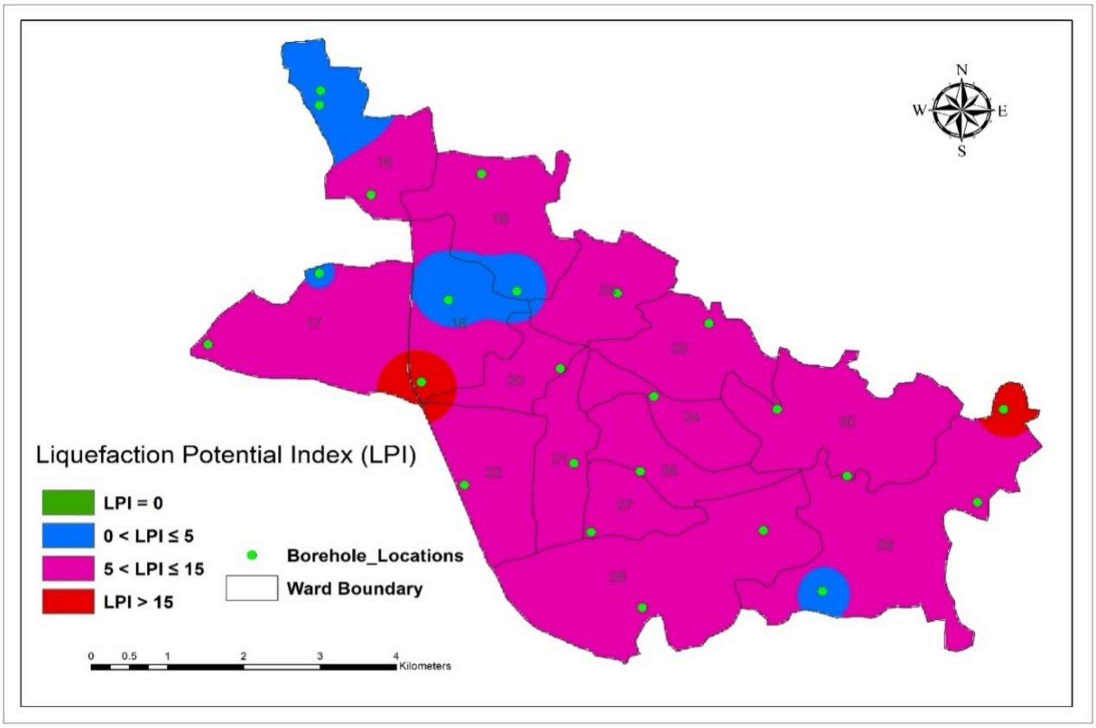

(e) Magnitude = 8.5 and different GWT depth (Japanese)

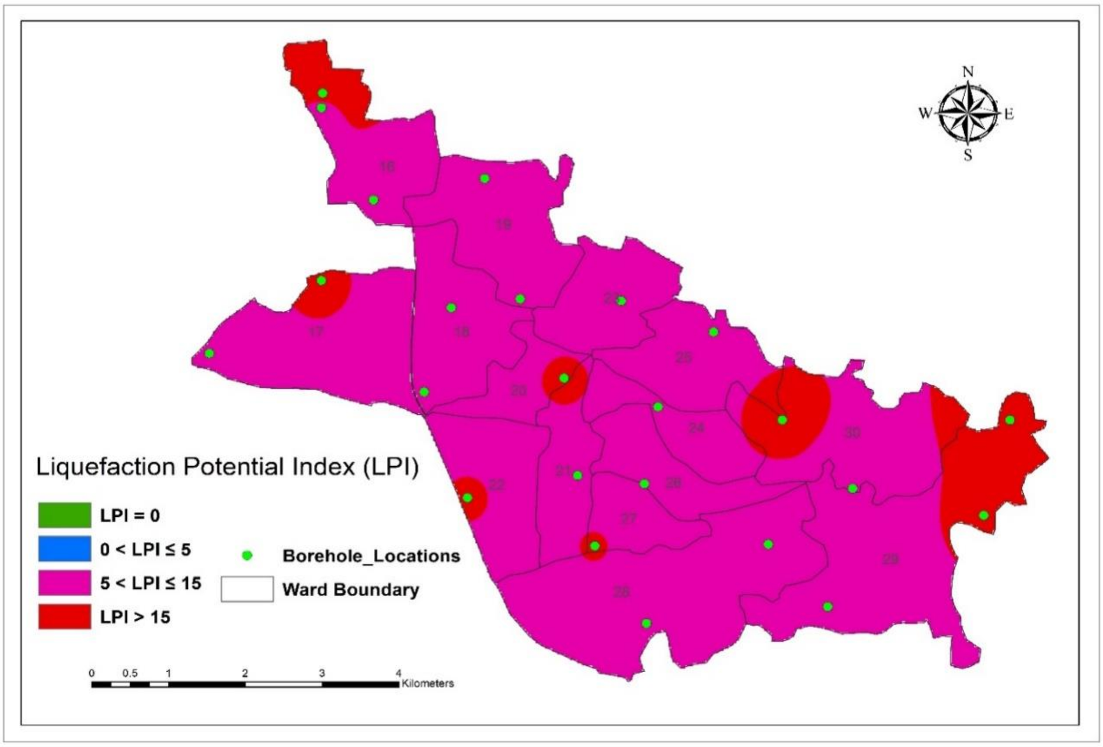

(f) Magnitude = 8.5, and GWT depth = 1.5 m (Japanese)

Figure 4.17: LPI based microzonation map for the Rangpur city corporation area for a PGA value of 0.3238 g (for the Japanese method). (a) Magnitude = 6.5 and different GWT depth, (b) Magnitude = 6.5, and GWT depth = 1.5 m (c) Magnitude = 7.5 and different GWT depth, (d) Magnitude = 7.5, and GWT depth = 1.5 m, (e) Magnitude = 8.5 and different GWT depth, and (f) Magnitude = 8.5, and GWT depth = 1.5 m

BANGLADESH NETWORK
OFFICE FOR URBAN SAFETY

PART-VII

ESTIMATION OF LIQUEFACTION SUSCEPTIBILITY OF A NEW INTERNATIONAL AIRPORT SITE IN SYLHET, BANGLADESH

BANGLADESH NETWORK OFFICE FOR URBAN SAFETY (BNUS), BUET, DHAKA

Prepared By: Mehedi Ahmed Ansary

INTRODUCTION

For important sites like airports, power plants etc. estimation of liquefaction potential is important owing to the existence of several important infrastructures. Resistance of soil to liquefaction has turned into an essential condition to be estimated before any major construction during recent time. Liquefaction is the alteration of previously secure coarse aggregate of soils becoming a liquid mass owing to the enhancement of pore water pressure. According to Marcuson (1978), liquefaction is mainly observed in areas where the soil mainly consists of sandy type and water table is situated near the ground level. The cyclic random loading of a seismic event is the source for water pressure inside the soil pores to enhance, which causes the soil mass to perform as a fluid. The 1964 Alaska, USA and Niigata, Japan earthquakes are the major examples where liquefaction played a main role in increasing the damage level of those two events (Kramer, 1996; Youd, 2014). After these two events, liquefaction becomes an important factor to be assessed prior to any new important construction takes place. Also, wide-ranging investigation has been done in this field to avoid any such catastrophic damages in the future. The findings of many researchers (Ansary, 2003; Ansary and Sharfuddin, 2002; Ansary and Arefin, 2020; Rahman et al., 2021) advocate that important cities of Bangladesh have been struck by numerous historical large earthquakes, that is why the current study is important.

The simplified procedure for the determination of the liquefaction susceptibility based on SPT-N value provided by Seed and Idriss (1971) has been authenticated and amended by various researchers (Youd and Idriss, 2001; Idriss and Boulanger, 2006; Juang et al., 2000; Lee et al., 2007) over the years. Iwasaki et al. (1984) has suggested a technique to estimate the liquefaction potential index for the entire depth of a 20m deep borehole, which is popular for seismic microzonation of an area.

In this research, the under-construction new international airport site at a neighborhood in Sylhet City, Bangladesh has been considered. The soil of the eastern part of the project site mainly composed of loose to medium dense silty fine sand within the top few meters which is underlain mainly by hard clay soil up to a depth of 45m (sometimes medium to dense sand can be found there) and the western part of the project site mainly composed of medium stiff to hard clay up to a depth of around 30m which is underlain by very dense sand up to a depth of 45m.

EXISTING FAULTS AROUND BANGLADESH

Raoof et al. (2017) has developed 3-D seismic velocity structures for the adjoining areas of Bangladesh to gain knowledge about the geodynamic processes of this region. This study gives useful information about the site condition. The Indian plate is under-thrusting the Himalayas at low angles at the Main Boundary Thrust (MBT) along the entire ~2500 km long Himalayan belt (Molnar et al., 1973; Baranowski et al., 1984). It is subducting at dip angles ~30°–50° at the Indo-Burmese arc with the Benioff zone down to depths ~150–200 km, as observed from the intermediate-depth seismicity (Satyabala, 1998 , 2003; Li et al., 2008). Several researchers suggested that subduction along the Indo-Burmese arc has slowed down or may have stopped, and the Indian plate is dragged to the north, which is partly accommodated by the long Sagaing fault in central Burma (Le Dain et al., 1984; Chen and Molnar, 1990). The Sagaing is a fault in the plate boundary. Its sinistral movement shows a part of the junction of Burma and India plates.

The major faults that have an impact on the study area are: The Indus-Tsangpo Suture (ITS), the Main Boundary Thrust (MBT), the Main Central Thrust (MCT), and the Main Frontal Thrust (MFT) (see Figure 1). These are the major Himalayan crustal discontinuities spanning the length of the northern border of the northeast Indian region (Yin and Harrison, 2000; Yin, 2006).

SEISMIC HAZARD ASSESSMENT

Seismic Data Processing

A homogeneous seismic database is a vital instrument in any assessment of earthquake hazard. An earthquake database that involves pre-1900 (all historical), and post-1900 (that occurred after 1900) events need to be compiled. Organizing lists of seismic events in a database that covers the studied region; requires collecting data from the various published catalogs, literature, and those provided by national and international agencies.

The earthquake catalog has been assembled from the International Seismological Centre (ISC) UK and the United States Geological Survey (USGS) event data. The maximum seismic magnitude for this study has been estimated from this catalog. The developed catalog has been homogenized to obtain a unified magnitude value M_W. This has been carried out applying conversion relations for magnitude provided by Scordilis (2006) and Kolathayar and

Thallak (2012). The past earthquakes from the period 1760 to 2020 have been selected using the cut-off value of magnitude $M_W \geq 3$, the events are presented in Figure 2.

In probabilistic seismic hazard analysis, it is generally considered that the seismic occurrences follow a Poisson distribution (Kadirioğlu et al., 2018). For this purpose, a declustering algorithm to remove aftershock and foreshock from the original catalog is used. Numerous declustering processes have been suggested over the years such as Gardner and Knopoff (1974), and Reasenberg (1985) algorithms with different space time windows. These methods are implemented in the software ZMAP (Wiemer, 2001). In the present study, the Gardener and Knopoff (1974) algorithm has been applied for declustering. After declustering, 2565 seismic events have been compiled for the above mentioned period. This study assumed equal weightage to all faults considered. Linear as well as smoothed point source models have been considered to estimate the PGA values (Kolathayar et al., 2012). Figure 3 presents the study location together with the in-situ test locations.

Ground Motion Prediction Equations

Ground motion prediction equation (GMPE) is a relation among ground motion, magnitude, distance and other relevant parameters. Through these equations ground motion at any locations can be estimated if magnitude, distance and other parameters are known. GMPEs pertinent to the current tectonic region with shallow earthquakes such as Abrahamson and Silva (1997), Iyengar and Raghukanth (2004), Amiri et al. (2007) and Tabassum and Ansary, (2020) have been used in this study to determine PGA at the bedrock. Finally for the assessment of liquefaction at the study site, PGA value needs to be determined at the surface. For this purpose, DEEPSOIL software has been used here to obtain that PGA.

METHODOLOGY FOR SITE RESPONSE AND LIQUEFACTION ASSESSMENT

Figure 4 shows the flow chart of the total methodology employed in this study. The properties for dynamic analysis of soils, such as accelerogram of earthquakes, shear wave velocity (Vs), material damping, and shear modulus reduction curves are necessary to estimate site amplification parameters through site response analysis. Other soil parameters, for example internal friction angle, over-consolidation ratio, plasticity index, and unit weight are also required for this purpose. This information is gathered from 61 borehole locations and seven PS-Log locations of the study site as shown in Figure 3 to carry out the site response analysis.

SPT and Shear-wave Velocity Profile

Figure 5 presents two cross-sectional profiles (section 2-2 and 9-9 according to Figure 3) of the study site. The soil of the eastern part of the project site (based on section 2-2) mainly composed of loose to medium dense silty fine sand within the top few meters which is underlain mainly by hard clay soil up to a depth of 45m (sometimes medium to dense sand can be found there) and the western part of the project site mainly composed of medium stiff to hard clay up to a depth of around 30m which is underlain by very dense sand up to a depth of 45m. Similarly, the soil of the southern part of the project site (based on section 9-9) mainly composed of loose sand within the top few meters which is underlain by soft to medium stiff clay, dense sand and hard clay up to a depth of 45m and the northern part of the project site mainly composed of loose to medium dense sand up to a depth of around 8m which is underlain by soft to medium stiff clay, dense sand and hard clay up to a depth of around 45m.

The shear wave velocity (Vs) information from the study location has been compiled from the ground level up to a depth of maximum 55 m from the seven PS-logs carried out at the airport site (Figure 6). The data has been determined utilizing a suspension PS-log system. The Vs data from 55 m to 200 m depth have been gathered using array microtremor measurements (AMT) from CDMP (2009) in nearby Sylhet city as shown in Figure 7. The bedrock (when the shear-wave velocity is larger than 760 m/s) is located at 150 m below the ground level. So, the bedrock for this site is also assumed to be at 150m depth. Figure 8 shows the shear-wave velocity model used for the airport site.

Material damping and shear modulus reduction relations

For the site response analysis, the dynamic parameters of shallow ground layers are significant. These are illustrated by the damping ratio and shear modulus reduction curves to assess the soil condition under cyclic loading. Due to the unavailability of these curves for the study site, the suggestion of many researchers (Kumar et al., 2014; Chandran and Anbazhagan, 2020) to utilize the existing standard curves may be followed. Several damping ratio and shear modulus reduction relations can be found in different available literature (such as Seed and Idriss, 1970; Sun et al., 1988; Darendeli, 2001) to estimate the dynamic parameters of numerous soil patterns. According to different researchers (Darendeli, 2001; Bajaj and Anbazhagan, 2019), effective confining pressure, loading frequency, plasticity index, loading cycle numbers, strain and soil type are the main essential properties that affect the damping ratio and shear modulus reduction. In the study site, the soil layer from the ground level up to 55 m deep is mostly consisting of sandy soils in the eastern part of the site and mixture of clay and sandy soil in the western part of the site (Figure 5). According to Hashash et al. (2010) for sandy deposits, the damping ratio and shear modulus reduction relations recommended by Darendeli (2001) are preferred to analyze the site assessment by nonlinear means. Hence, the material damping and normalized shear modulus reduction relations suggested by Darendeli (2001) are applied to estimate the sandy deposits nonlinear characteristics of the study site (Figure 9).

Bedrock and surface hazard spectra

The normalized design acceleration response spectrum proposed in BNBC (2020) for ground condition (Vs > 760 m/s) [soil type SA] has been considered in this study as shown in Figure 10a. This spectrum for soil type SA has been multiplied by PGA for a return period of 475 years (in this case, it is 0.30g) to obtain the target spectrum, which is here referred as the hazard spectra at the bedrock (UHS). In this particular site, the mean shear-wave velocity for the initial 30m of a soil column is 188 m/s (using Figure 8), which falls in soil type C (SC) category. The normalized design acceleration response spectrum for soil type SC as per BNBC (2020) has been multiplied by 0.30g to obtain the surface UHS. Both these UHSs are shown in Figure 10b.

Earthquake acceleration time history and spectral matching

Recently, Bangladesh has set up a seismic network all over the country (Ansary and Arefin, 2020). Although this network has recorded several weak ground motions, so far no strong ground motion has been recorded by this system. Strong ground motions having the time history data expressed in terms of acceleration are needed for site assessment. For this purpose, freely available ten worldwide data are used: the 1961 Hollister (USA) earthquake (USGS station 1028), the 1976 Friuli (Italy) earthquake [Tolmezzo (000)], the 1979 Imperial Valley USA (USGS station 5115), the 1983 Trinidad (USA) earthquake (090 CDMG station 1498), the 1989 Loma Prieta USA (090 CDMG station 47381), the 1992 Landers (USA) earthquake (000 SCE station 24), the 1994 Northridge USA (090 CDMG station 24278), the

1995 Kobe Japan (Kakogawa CUE90), the 1999 Kocaeli Turkey (Yarimca, Koeri330) and the 1999 Chi-chi Taiwan (TCU045) earthquakes.

The spectral acceleration of the earthquake accelerograms is fitted to the target bedrock response spectra to generate time history data compatible with the target spectra (Figure 11). The matching of spectra has been done by using the SEISMOSOFT software to adapt the time history data by fitting its spectral acceleration with the target response spectrum (Figures 12). The spectral response of 10 earthquake acceleration time histories is fitted with the target spectra for a return period of 475 years (Figures 13 and 14). The time versus acceleration data of the fitted spectral acceleration curve have been applied for the site assessment (see Figure 12).

One-dimensional site assessment

DEEPSOIL software resulted from the research of Hashash et al. (2010) has been used to carry out one-dimensional nonlinear and equivalent-linear site assessment analysis. The soil model for response analysis requires material damping and shear modulus reduction relation in normalized form. The relations suggested by Darendeli (2001) have been utilized in this research. To utilize the relationships of Darendeli (2001), the following soil parameters are needed: vertical stress under effective condition in initial state, initial coefficient of lateral earth pressure, loading frequency, loading cycle numbers, OCR ratio, and plasticity index (Figure 9).

DEEPSOIL has numerous soil models to carry out the site assessment analysis. In the current study, the model suggested by Groholski et al. (2016) has been applied to match material damping and modulus reduction relations of the materials of the soil column with the benchmark relations of Darendeli (2001) for certain shear strength. This model consists of non-Masing reloading-unloading hysteretic set up based on the general quadratic/hyperbolic model (GQ/H). The effective shear strength condition has been applied for all calculations by considering the water table at the top of the surface. According to Groholski et al. (2016), the GQ/H form has the capability to depict the relatively big shear stress strain characteristics of the materials to precisely approximate the motion of the ground at the surface for relatively big strains. Viscous damping term which has been frequency-independent has been utilized for nonlinear response assessment in time domain. During response analysis, the accelerogram of the matched bedrock spectral acceleration have been applied for motion of the ground at the bottom of the soil column. Figure 15 shows the depth versus average PGA plots using equivalent-linear and nonlinear ground response analysis. The PGA value at the surface due to the nonlinear analysis is 0.39g and due to the equivalent-linear analysis is 0.65g.

Liquefaction assessment techniques

Several methods have been built up to evaluate the liquefaction susceptibility of soils. This paper focuses on the following methods to estimate liquefaction potential: Seed-Idriss simplified procedure (Seed and Idriss, 1971), Japanese Code of Bridge Design (Tatsuoka et al., 1980), Japanese Code of Bridge Design based on the Chinese criterion (Ishihara, 1993), and Chinese Code for Seismic Design of Buildings method (GB50011-2010) (as outlined in Sun et al., 2015). These methods are Standard Penetration Test (SPT) based liquefaction assessment methods where empirically determined curves—utilizing Cyclic Stress Ratio (CSR) and Cyclic Resistance Ratio (CRR)—are employed to predict liquefaction and no-liquefaction occurrence. After the detailed assessment, liquefaction severity is evaluated based on liquefaction potential index (LPI), similar to that suggested by (Iwasaki et al., 1978; Iwasaki et al., 1981, 1984). Iwasaki et al. (1984) has classified the LPI in three levels: (a) LPI < 5, implies 'Low liquefaction potential; b) $5 \leq$ LPI ≤ 15, implies 'High' liquefaction potential and c) LPI > 15, implies 'Very High' liquefaction potential.

RESULTS AND DISCUSSIONS

Development of surface hazard spectra

The hazard spectra at the surface (UHS) of the study site have been developed utilizing the three site assessment methods: site coefficients based on Vs30, equivalent-linear, and nonlinear (Figure 16). The spectral acceleration of the hazard spectra at the surface at different periods are at all times bigger than that of the hazard spectra at the bedrock for Vs30-based site coefficients, whereas the spectral acceleration of hazard spectra at the surface are slightly larger to relatively larger at relatively low periods (less than 0.20 s) and bigger at large periods (more than 0.20 s) in comparison with the spectral accelerations of the hazard spectra at the bedrock during equivalent-linear response assessment. The spectral acceleration of the hazard spectra at the surface are smaller at low periods (from 0.03 s to 0.30 s) and larger at large periods (0.30 s and 4 s) in comparison with the spectral accelerations of the hazard spectra at the bedrock during nonlinear response assessment. The period of the highest acceleration has moved towards the larger periods during the equivalent-linear, and nonlinear models with respect to the Vs30 dependent assessment.

The equivalent-linear model based hazard spectrum (UHS) is in general larger than the nonlinear based model. The period of the highest acceleration is almost equal for both the cases. The Vs30 dependent UHS is not suitable to represent the characteristics of the alluvial deposits of sufficient thickness of the site well since the bedrock is located at a depth of around 150m. Kaklamanos et al. (2015) have commented that the equivalent-linear model happens to be erroneous at shear strain of around 0.1 to 0.4%. Also they mentioned that the nonlinear model can better predict the motion at the ground surface at large shear strain. The obtained biggest shear strain is larger than 0.1% in the majority of the layers throughout site response analysis. Hence, for thick sedimentary deposits the nonlinear site assessment is suitable for the determination of UHS at the surface. The average obtained PGA value at the surface for a return period of 475 years is around 0.39g using nonlinear assessment technique.

Liquefaction susceptibility estimation

In this study, the liquefaction susceptibility at each layer of 1.5m interval where SPT-N value exist and liquefaction potential index (LPI) values have been estimated for 61 boreholes located all over the site up to a depth of 20m. The locations where borehole data are not present, LPI have been estimated by Kriging method. LPI estimation have been made for the three methods Seed and Idriss (1971) method, Japanese method (Tatsuoka et al., 1980) and Chinese method (Sun et al., 2015) for two cases: (a) A lower bound value of PGA=0.29g (for 23% probability of exceedance in 50 years or for a return period of 200 years) and M_w = 7.5 and (b) a upper bound value of PGA=0.39g (estimated through nonlinear site assessment for a return period of 475 years) and M_w = 8.15 which has been estimated with the help of past seismic data. Figure 17 shows the factor of safety versus depth plot at BH-168 for the three methods for PGA=0.29g and M_w=7.5 (lower bound case). Tables 1 and 2 have presented LPI values for the three methods and for lower and upper bound cases. To show LPI contours, the three levels of hazard as described by Iwasaki et al. (1984), have been utilized as shown in Figure 18 for both the lower bound and the upper bound cases. The estimated LPI contours show that 80% to 90% of the total area will be highly susceptible to liquefaction and the rest of the area will be lowly susceptible.

It is apparent from the results of the LPI values that the site is mainly composed of inferior quality soil. There is a high probability that sand boils and lateral spreading may occur at the site during a seismic event. This may become decisive for essential structures within the power plant site. From the findings of the current study, it may be concluded that structures with shallow foundation for this site may be recommended only if the entire soil up to a depth of 20m is fully improved by suitable ground improvement techniques. Alternatively, length of pile greater than 20m below EGL may be recommended along with ground improvement of the top 5m of the loose sand soil zone. In this research, borehole data of 61 locations with SPT have been utilized for a relatively small area. The large number of borehole for a relatively small area of the site would generally produce dependable results in the assessment of LPI.

CONCLUSIONS

During the whole design lifecycle, the assessment of Liquefaction Potential Index (LPI) is important for the development of a new international airport site in inferior quality soils for proper working condition of the facility. The PGA value at bedrock level has been evaluated utilizing past seismic data, seismo-tectonical details and suitable GMPE relations. To approximate the time history at the surface in a site where the relatively loose or soft soil deposits of larger than 30 m thick is located on top of the bedrock, 1D nonlinear site assessment is needed. For these sites, the ground motion depending on Vs 30 based site amplification at low periods is relatively higher and the ground motion at large periods is relatively lower. The nonlinear site assessment determines the motion at the ground surface better than the linear or equivalent-linear analyses, since the soils properties are nonlinear too. A nonlinear site assessment using DEEPSOIL has been performed to estimate the site amplification and consequently to obtain the surface level PGA at the site. The LPI of the site under study has been assessed utilizing the SPT-N value data at 61 locations of the site applying three methods and two sets of PGA values and magnitudes up to a depth of 20m. Approximately 80% to 90% of the total area of the site has been found to be highly vulnerable to liquefaction up to a depth of about 20 m. For this reason, two alternative foundation solutions are recommended for this site. The first one is providing shallow foundation above an improved ground up to a depth of 20m or alternatively providing 20m deep piles. Also, the LPI contours will be helpful for future development in the vicinity of the current site.

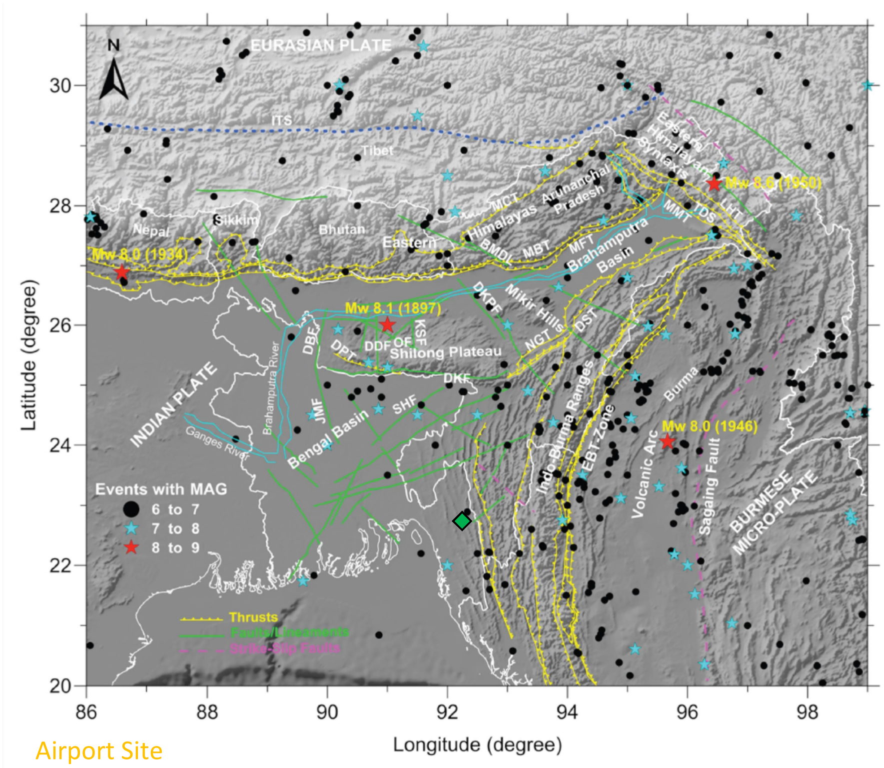

Figure 1 Tectonic map of the area.

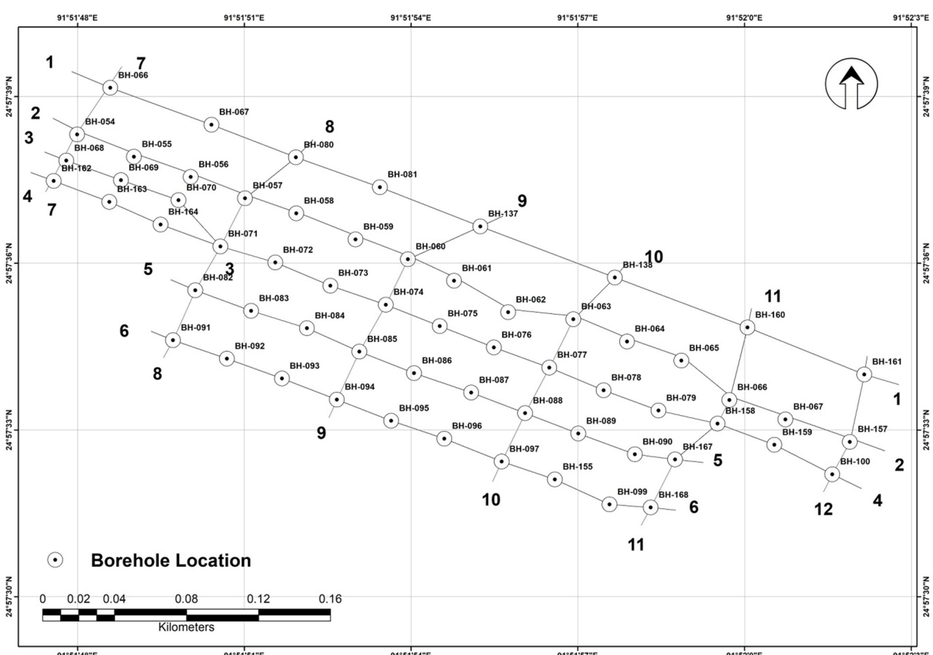

Figure 3 Proposed airport area showing borehole locations

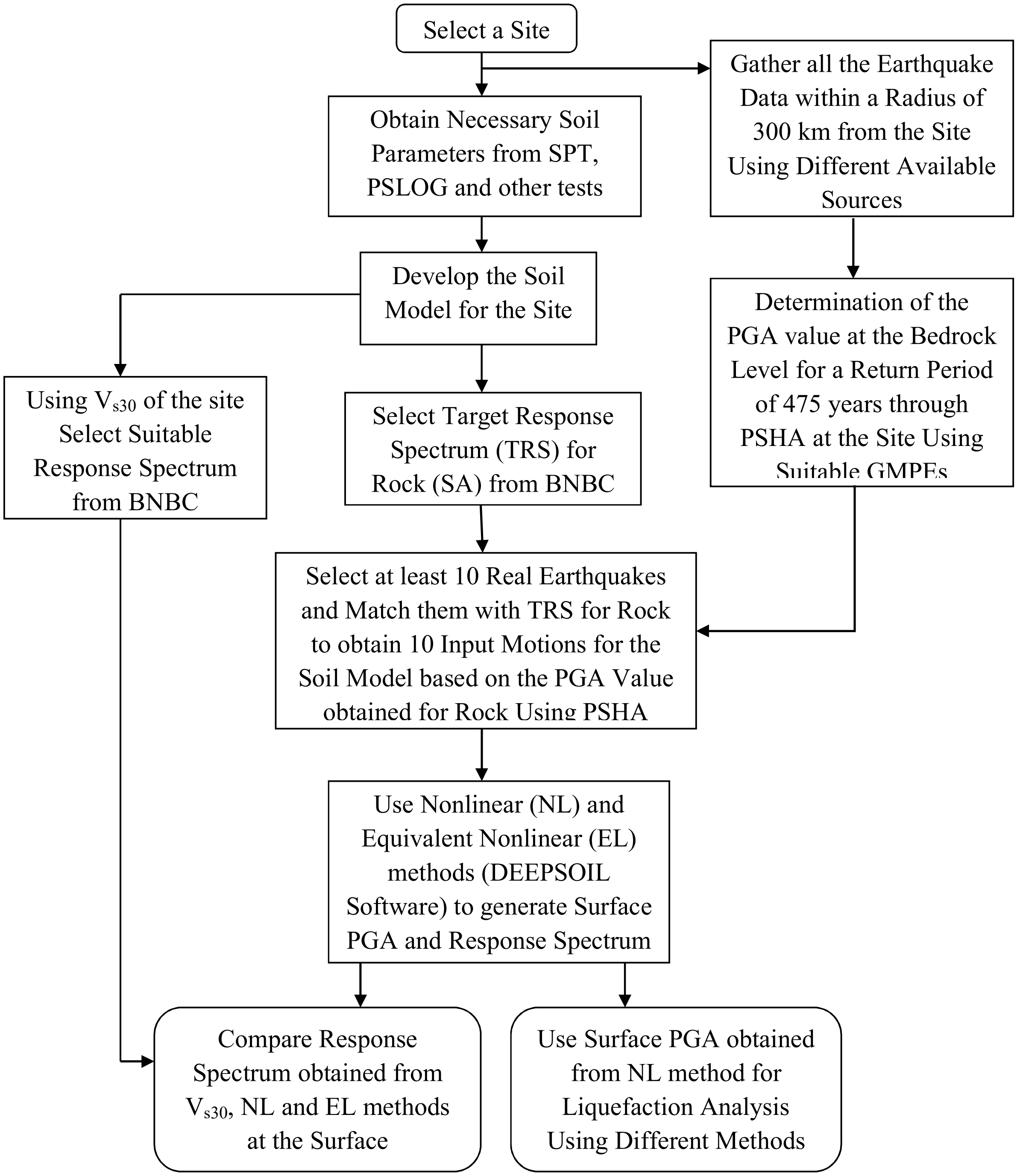

Figure 4 Flow chart of the methodology used in this study

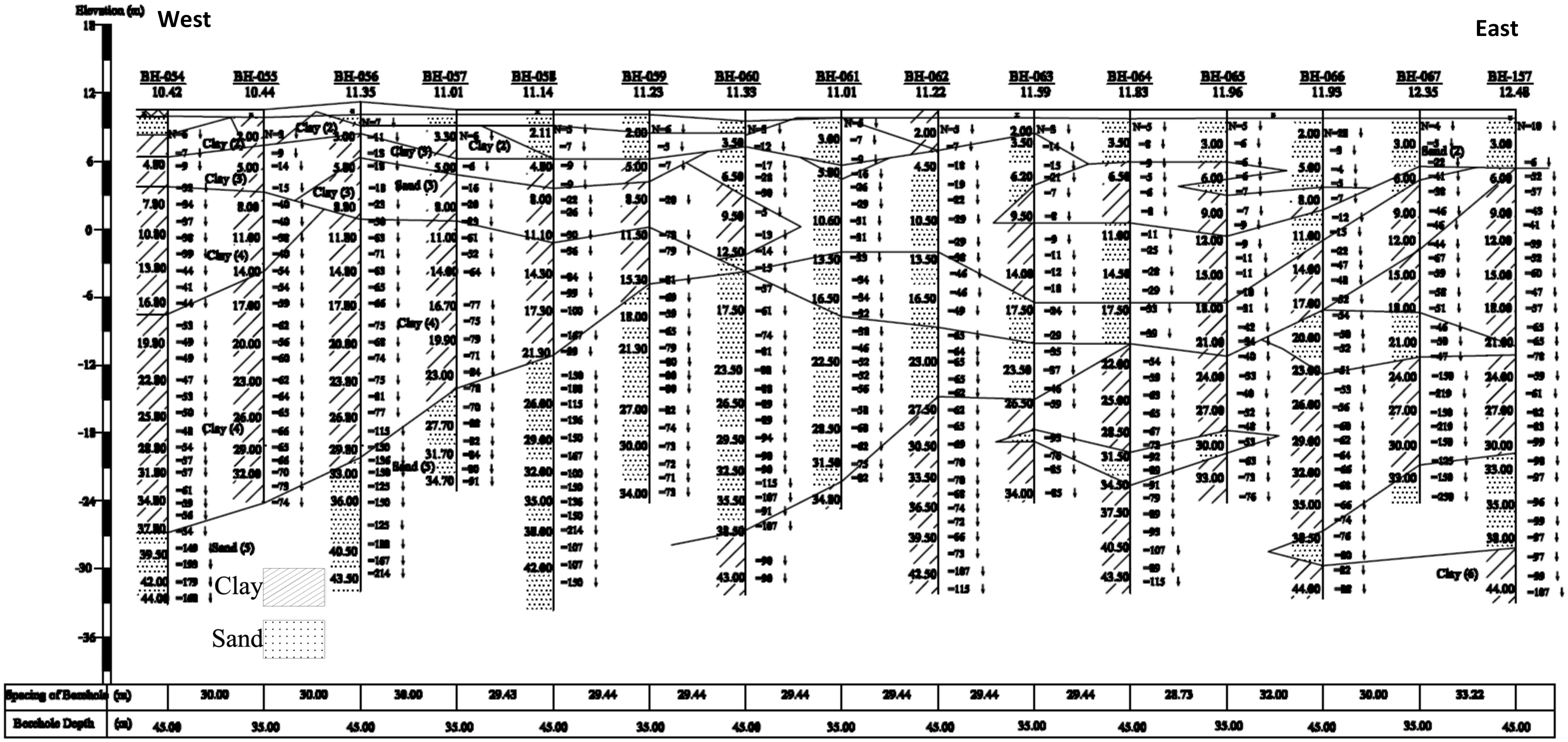

Figure 5 (a) Typical cross-sectional profile (2-2) of the study site with SPT-N values

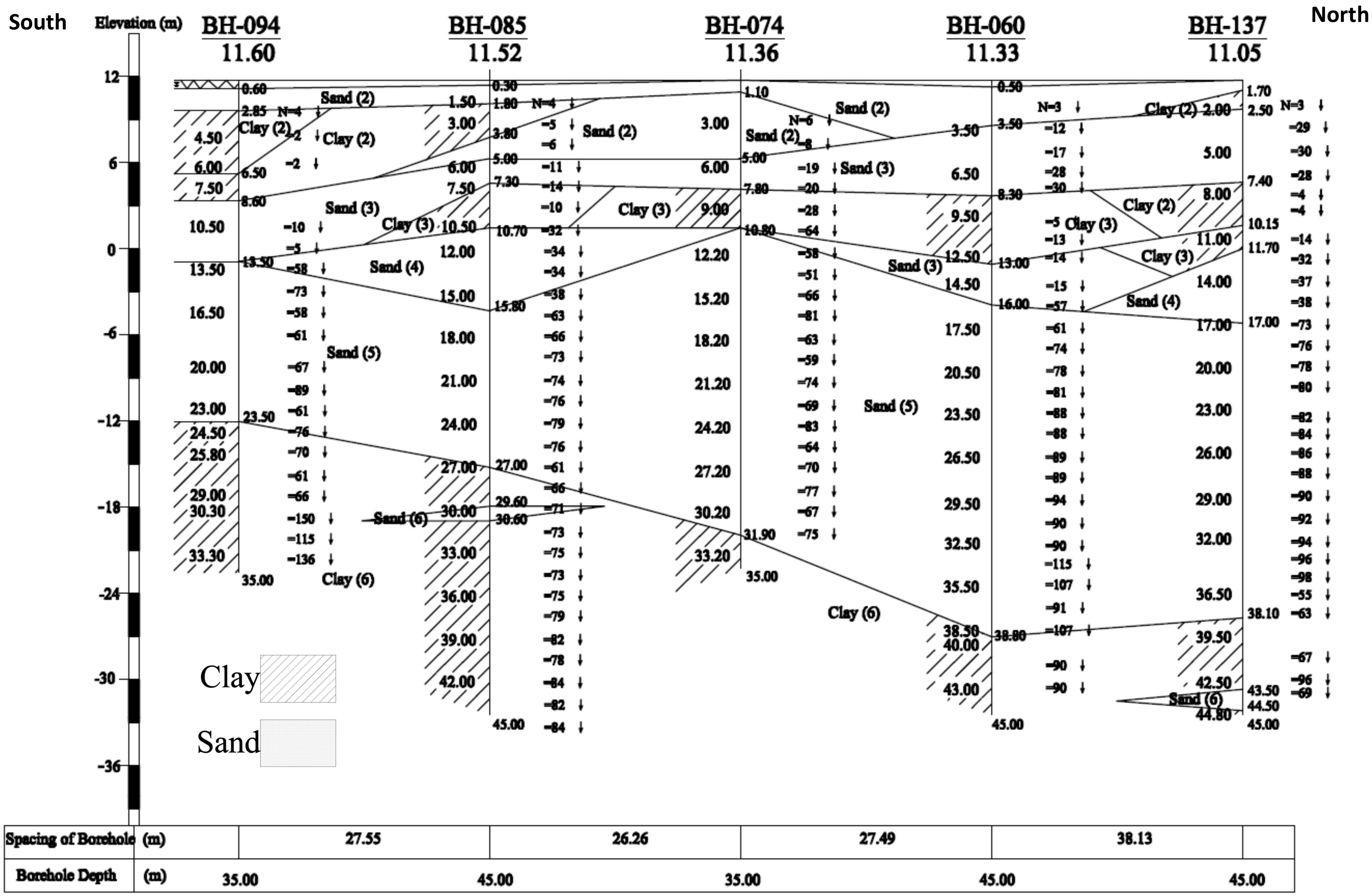

Figure 5 (b) Typical cross-sectional profile (9-9) of the study site with SPT-N values

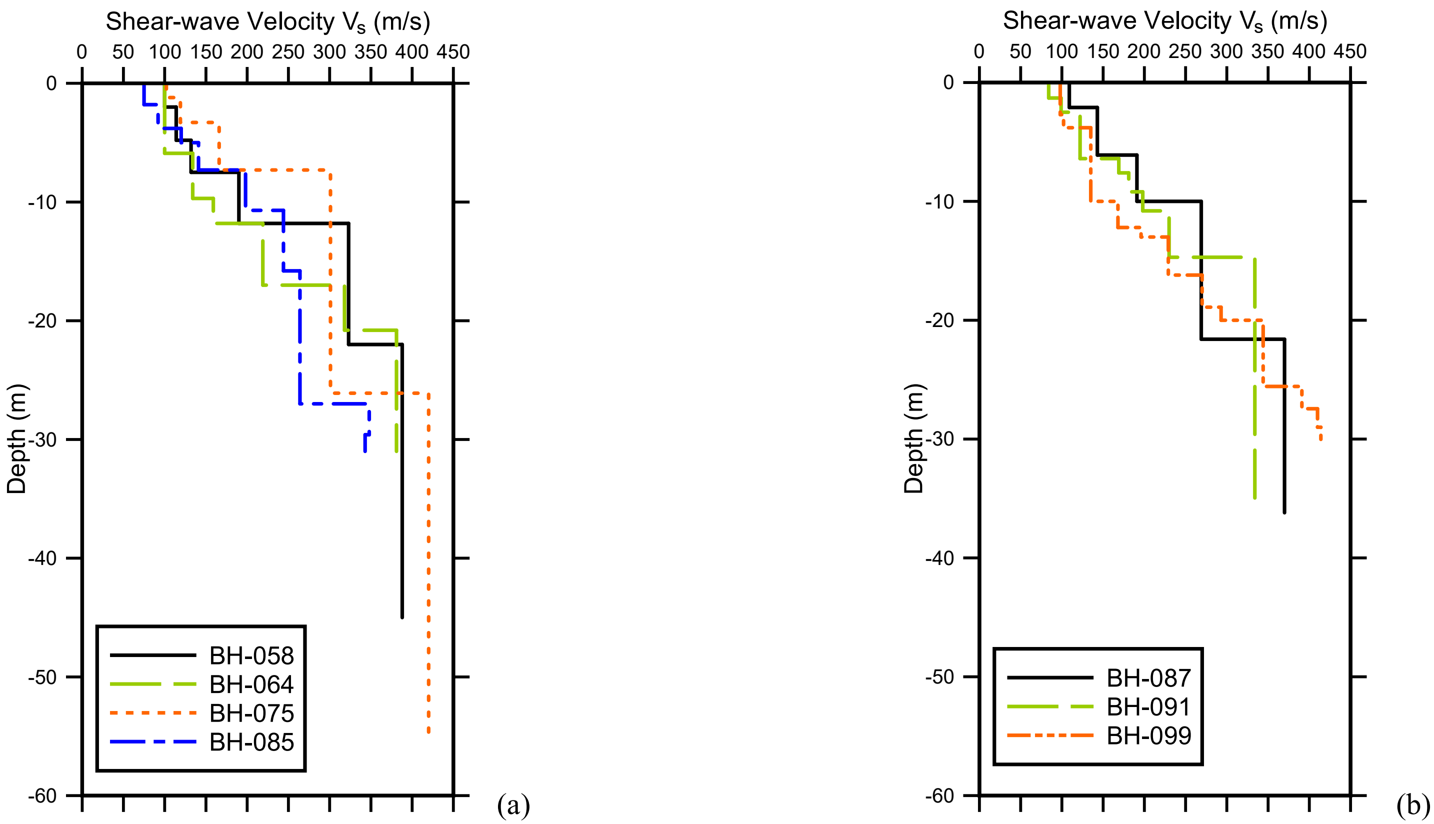

Figure 6 Shear-wave velocity profiles at seven borehole location at the airport site

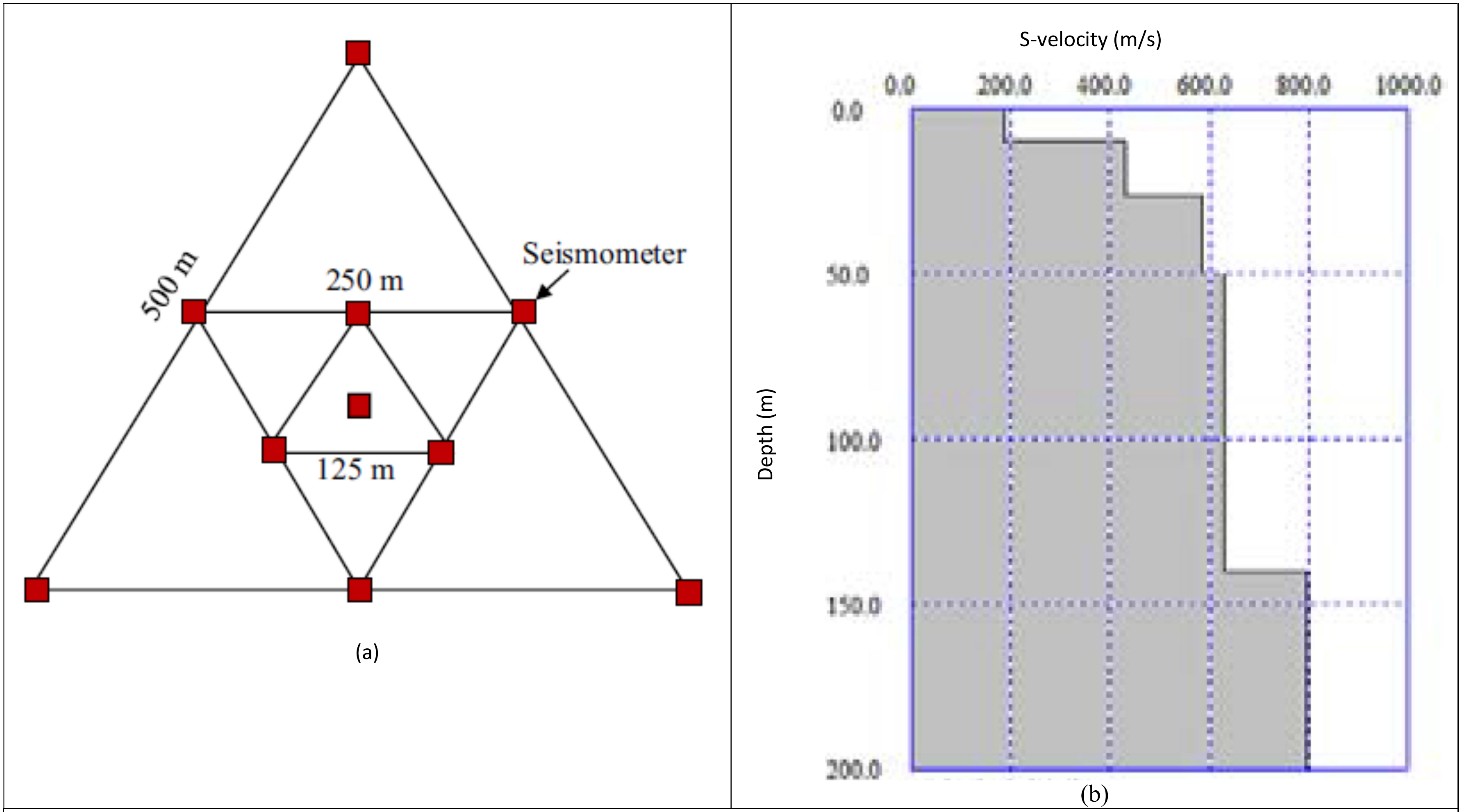

Figure 7 (a) Array microtremor measurements (AMT) configuration: array sizes: 125 m, 250 m, and 500 m; seismometers used: 10 with natural frequency of 0.5 Hz, sampling rate of 10 ms and sampling duration 60 min and (b) an example of shear wave velocity structure up to the depth of 200 m obtained from array microtremor measurements (AMT) data at borehole site SMT-1, Sylhet (CDMP 2009)

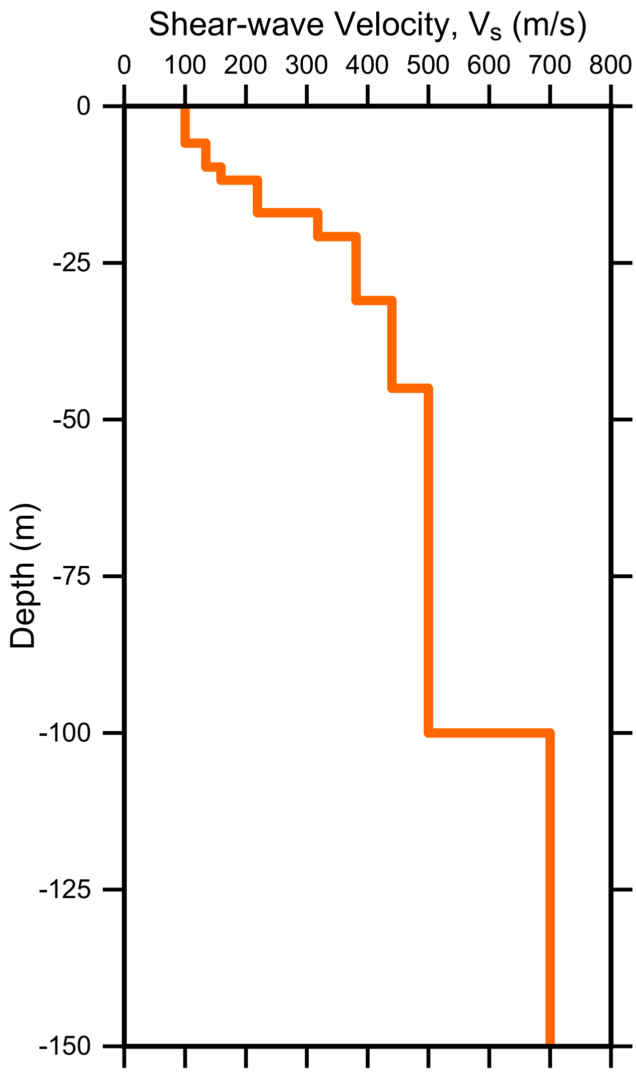

Figure 8 Shear wave velocity (Vs) model for the airport site

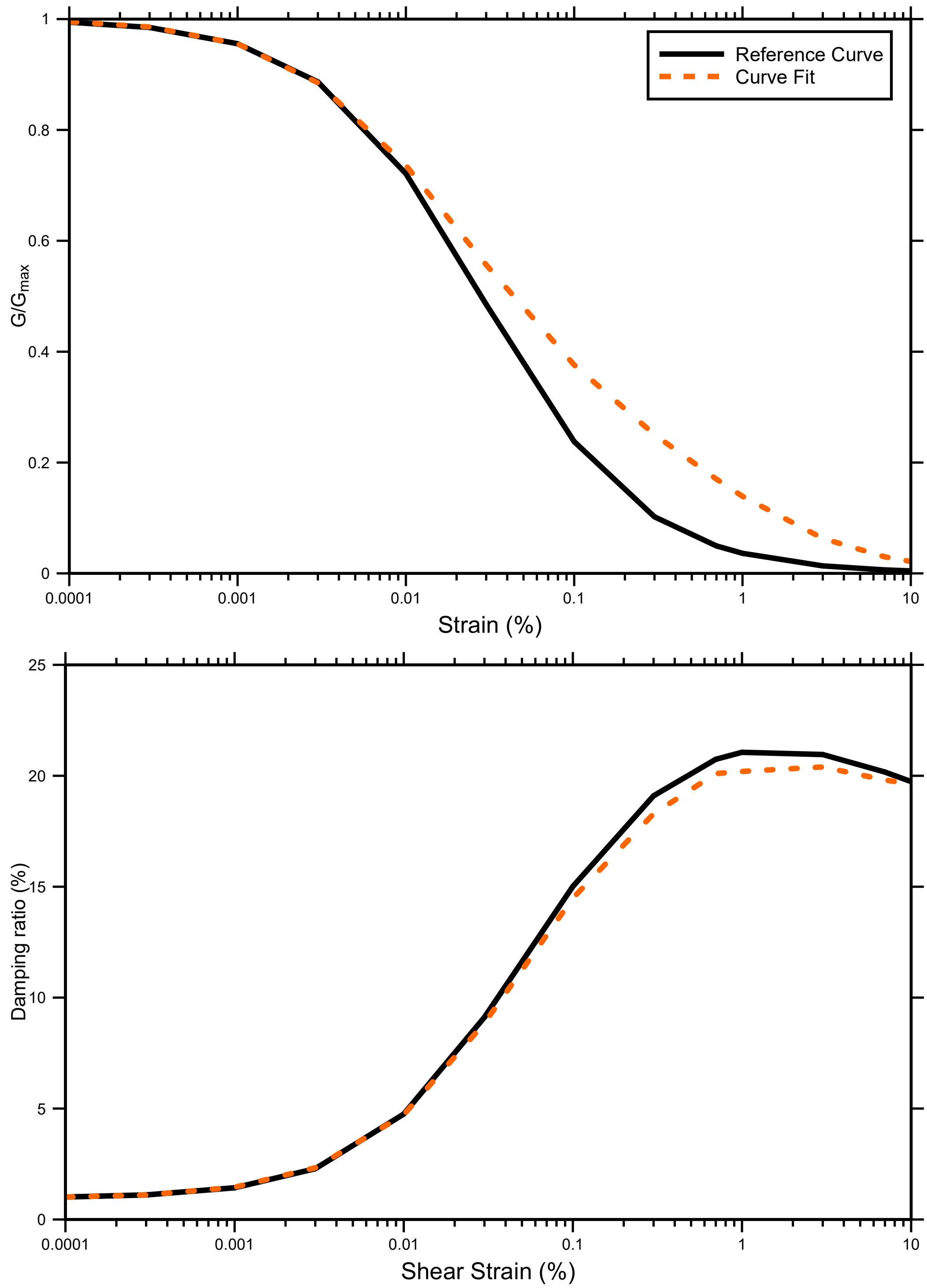

Figure 9 Sample of normalized shear modulus reduction and material damping curves where the reference curves are taken from Darendeli (2001)

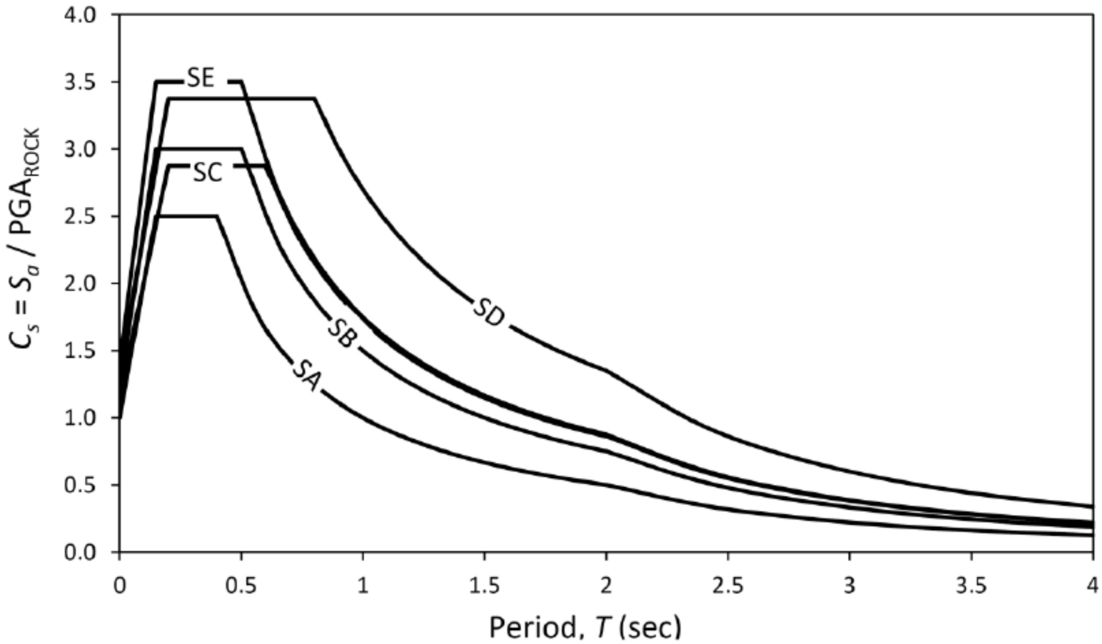

(a)

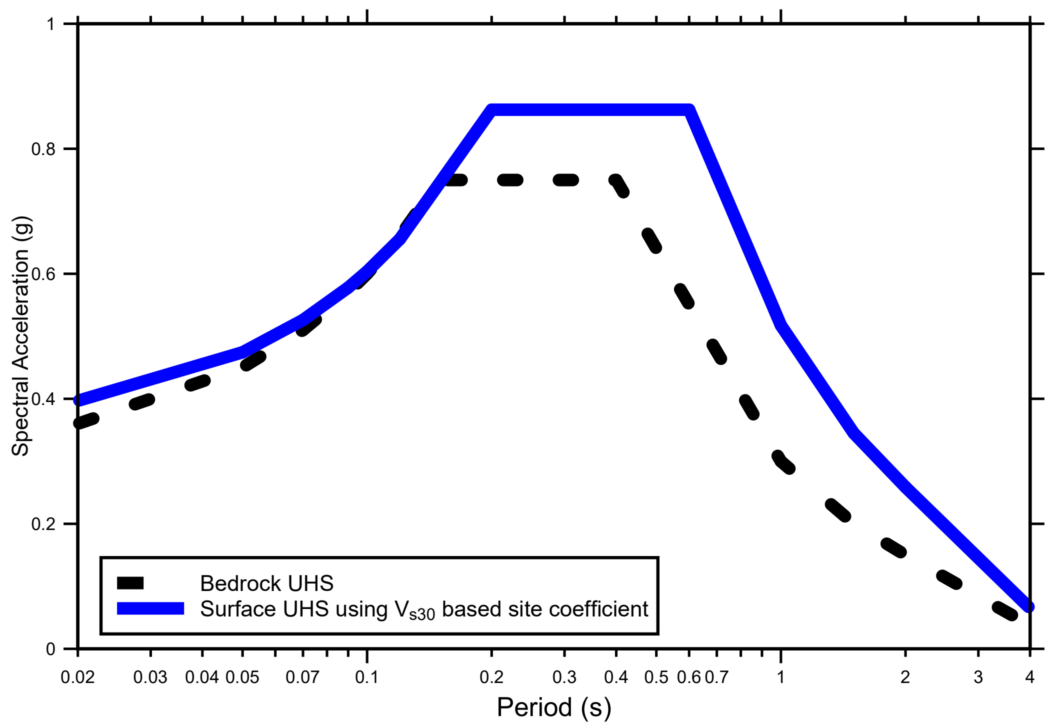

(b)

Figure 10 (a) Normalized design acceleration response spectrum for different site classes (after BNBC, 2020) and (b) UHS for a return period 475 years for soil class SA and SC

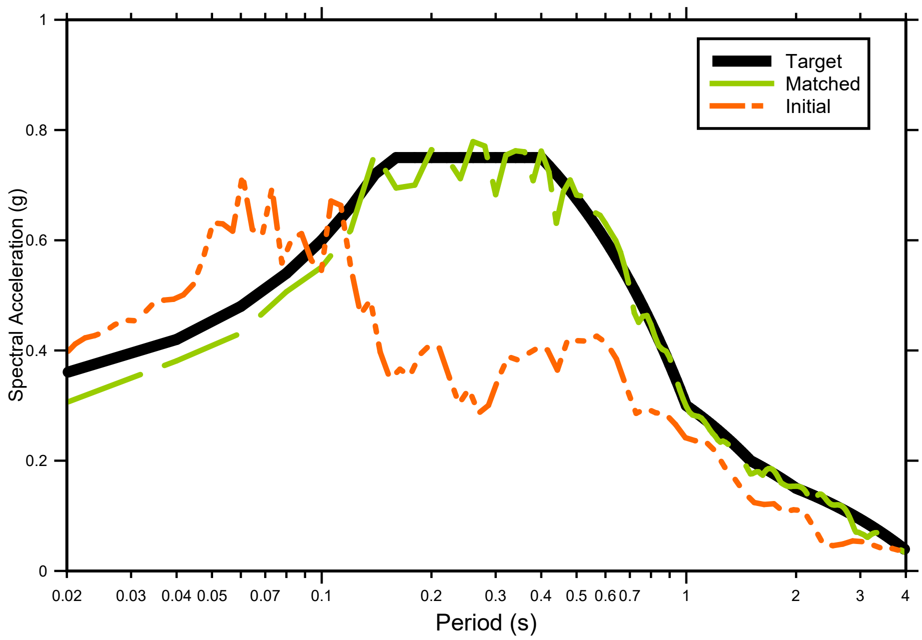

Figure 11 Spectral matching of the response spectrum of the earthquake time history with target response spectra for a return period 475 years. Initial is the response spectrum of the earthquake time history (orange), and green is the matched response spectra with target response spectra (black) of bedrock ground condition

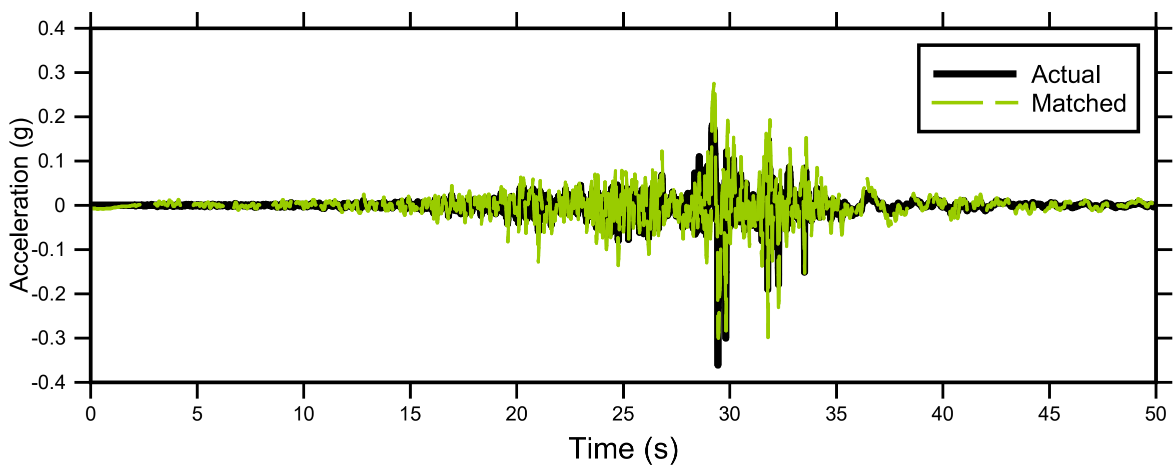

Figure 12 Initial earthquake time history (solid black line) from the database and matched time history (dashed green line) for a return period 475 years at bedrock ground condition

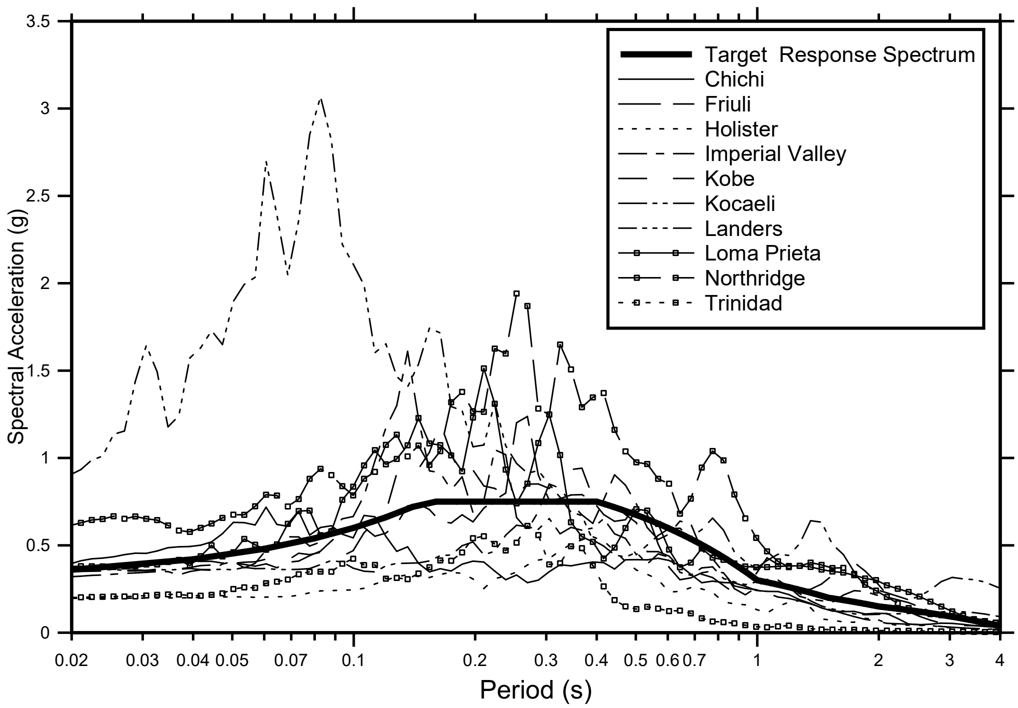

Figure 13 Response spectra of 10-time histories from real earthquakes with target response spectrum for a return period 475 years at the site

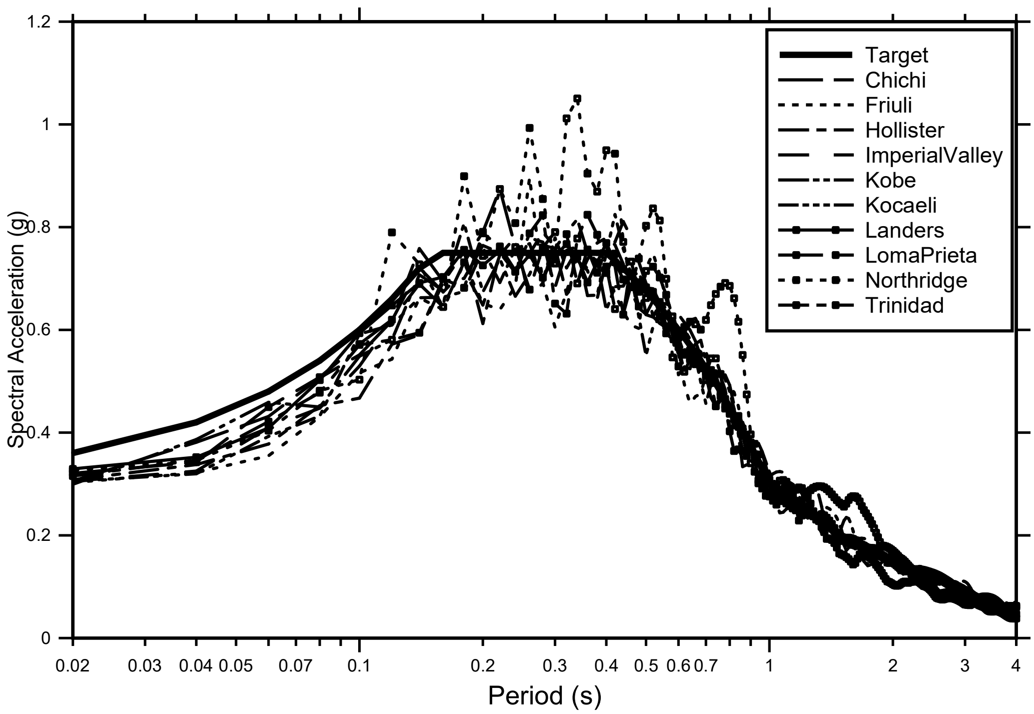

Figure 14 Matched response spectra of 10-time histories with target response spectrum for a return period 475 years at the site

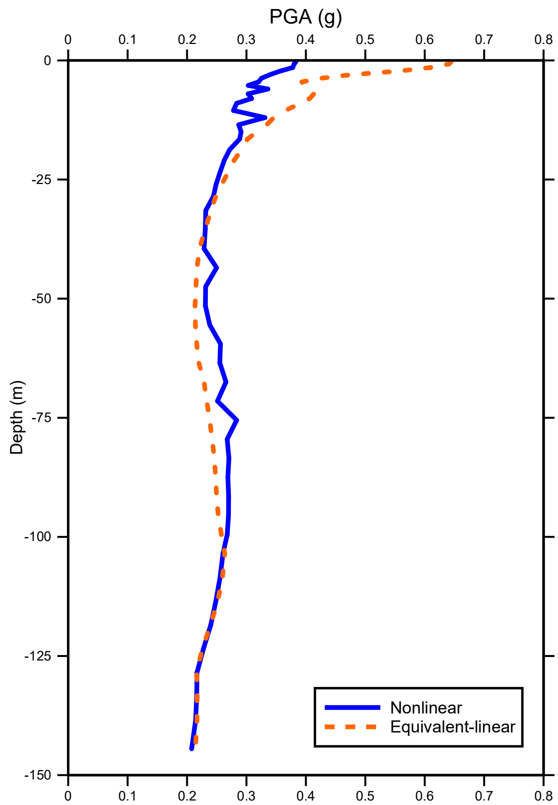

Figure 15 Depth versus average PGA plots using equivalent-linear and nonlinear ground response analysis

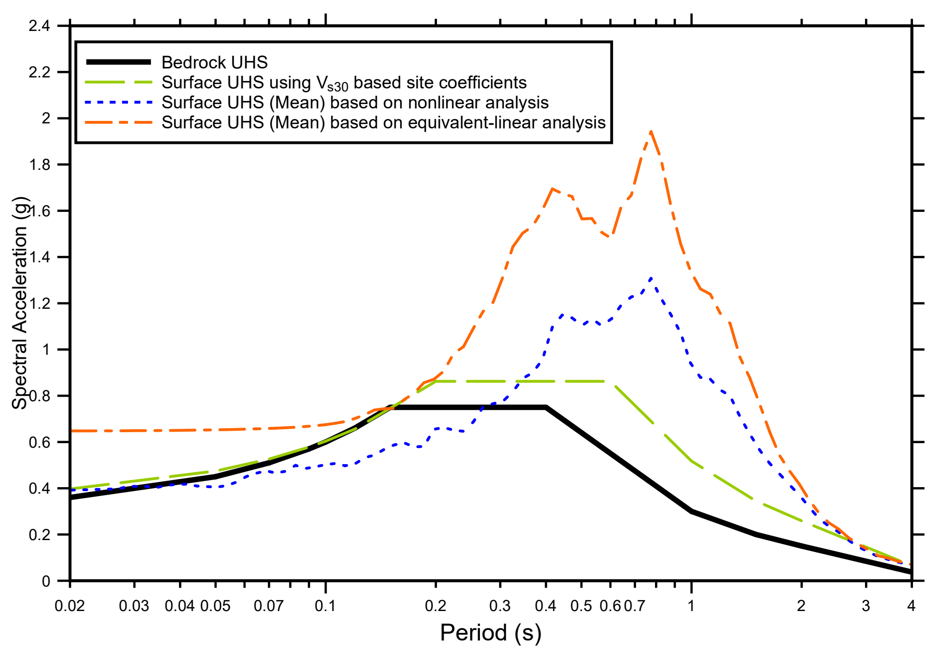

Figure 16 Uniform hazard spectra (UHS) at ground surface using Vs30-based site coefficients and UHS at ground surface using equivalent-linear, and nonlinear ground response analysis at the site for a return period 475 years

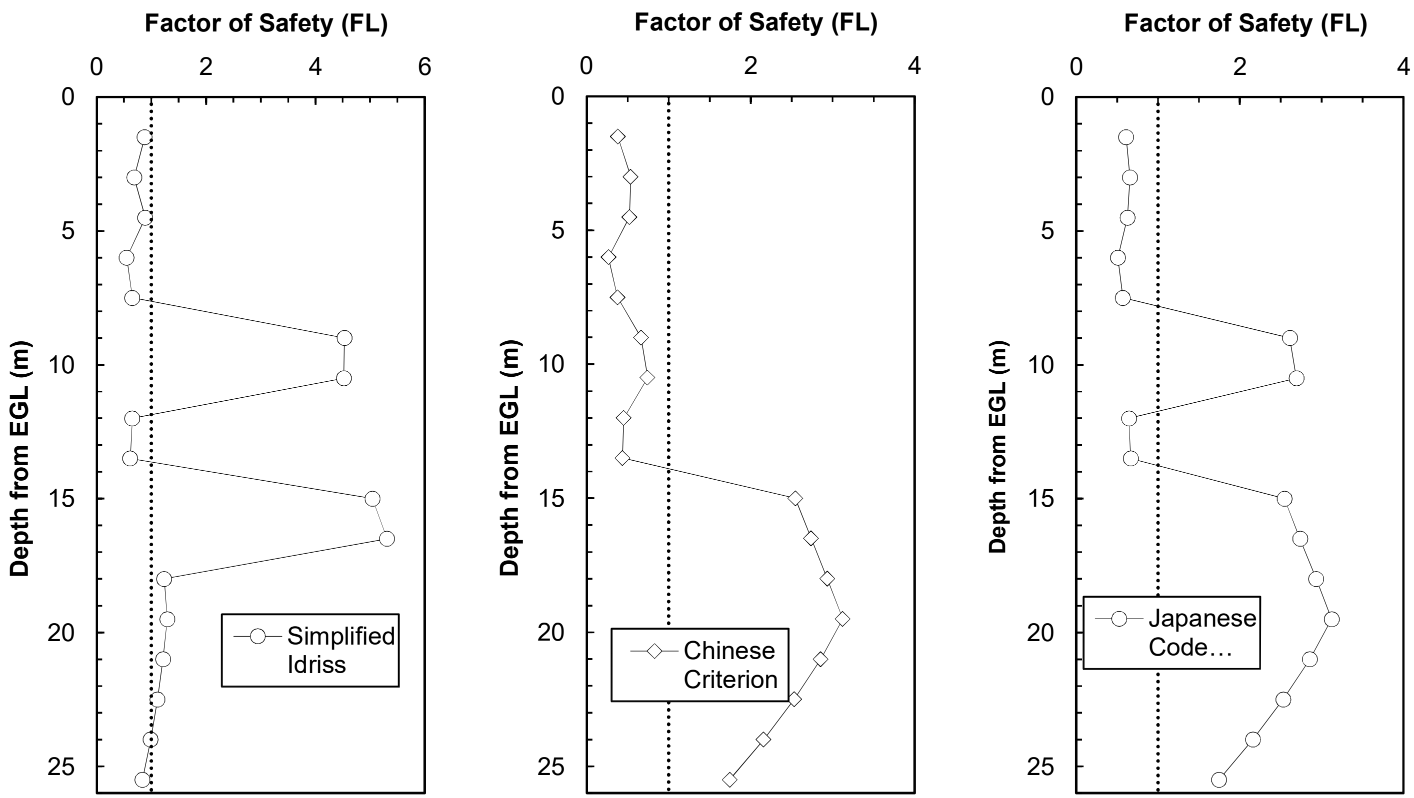

Figure 17 Factor of safety versus depth plot at BH-138 of the three methods for PGA=0.29g and M_w=7.5

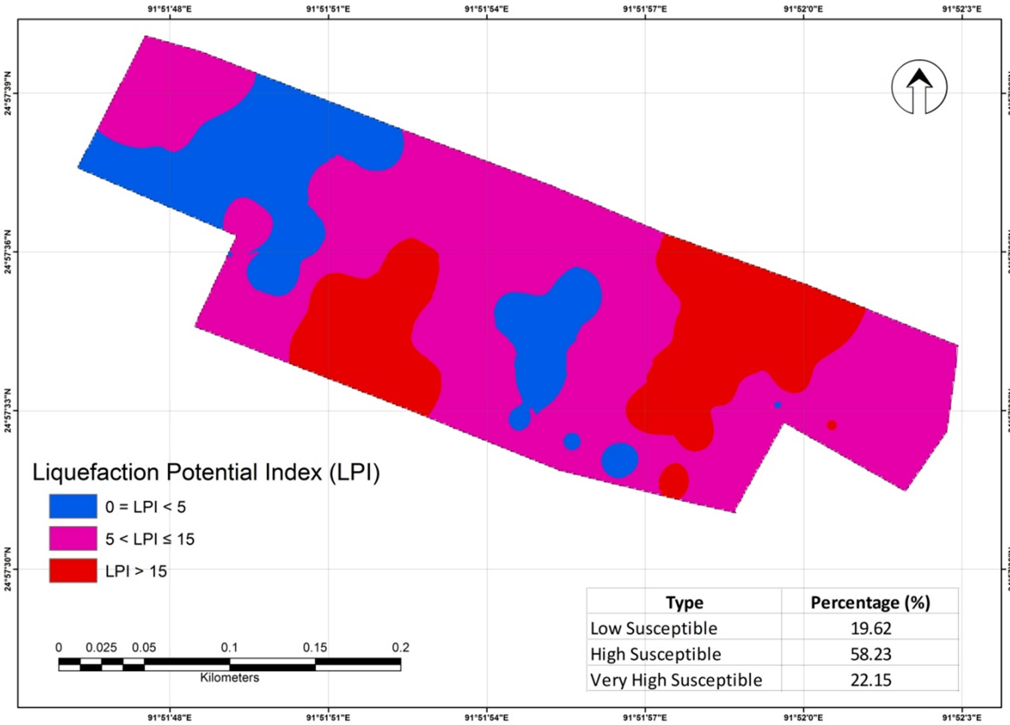

Type	Percentage (%)
Low Susceptible	19.62
High Susceptible	58.23
Very High Susceptible	22.15

(a)

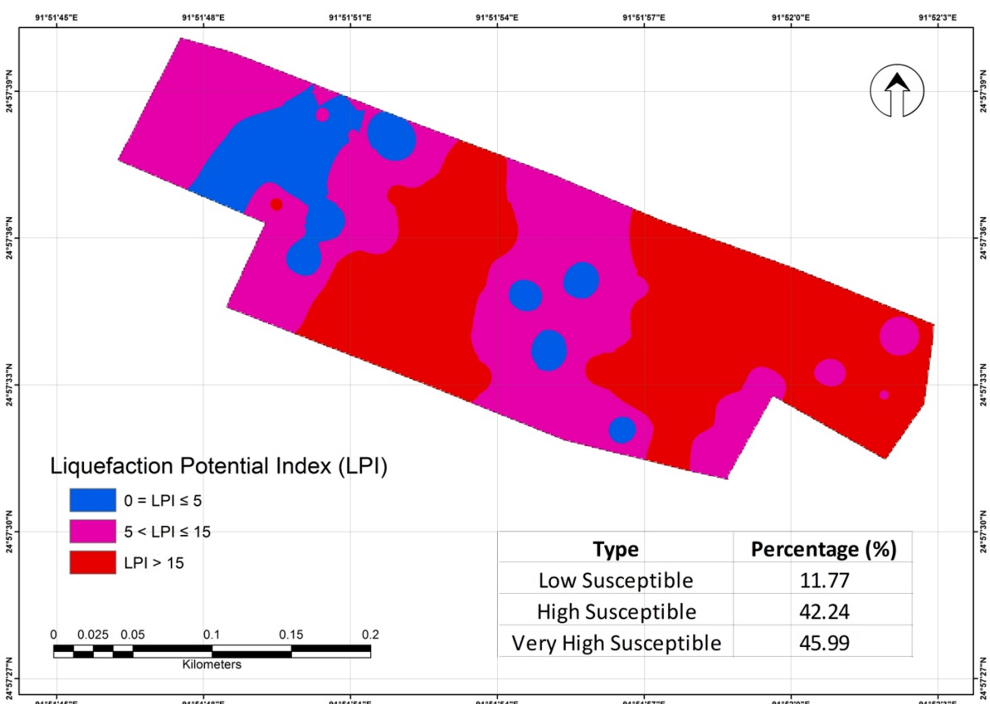

Type	Percentage (%)
Low Susceptible	11.77
High Susceptible	42.24
Very High Susceptible	45.99

(b)

Figure 18 LPI contour of the site for (a) PGA=0.29g and M_w=7.5 and (b) (a) PGA=0.39g and M_w=8.15

BANGLADESH NETWORK
OFFICE FOR URBAN SAFETY

PART-VIII

ASSESSMENT OF SOIL-BUILDING RESONANT EFFECT FOR DMDP AREA IN BANGLADESH

BANGLADESH NETWORK OFFICE FOR URBAN SAFETY (BNUS), BUET, DHAKA

Prepared By: Mehedi Ahmed Ansary

1 Introduction

Bangladesh is located in a significantly active seismic region, most of the people and policymakers do not consider the seismic risk to be important. Bangladesh has not faced any damaging major earthquakes in the recent years; although, during the last few centuries, numerous major seismic events have taken place in this region. Most of the seismic events have taken place far away from the key settlements, and have caused distress to relatively small population. Several researchers (Ansary et al. 2013; Morino et al. 2014; Steckler et al. 2016; Rahman et al. 2020) have shown that a future major seismic event may happen in the Himalayan or Burmese front at any moment and source of significant distress to all type of structures in Bangladesh, especially in Dhaka.

Earthquakes are one of such disasters that are associated with ongoing tectonic processes. It unexpectedly happens for a few seconds and can be the basis of enormous loss to life and assets. Therefore, earthquake disaster prevention and mitigation strategy are of global concern today. According to Gallipoli et al. (2020), earthquake hazard alleviation comprises of a set of plans targeted at decreasing the harmful consequences of seismic events on all susceptible components. Distress due a seismic event is generally managed by three interdependent issues - local geological and geotechnical conditions, source and path characteristics, and type of structures (Mucciarelli et al. 2001). According to Gullu and Pala (2014), major distress at great distances may happen owing to the effects of local site condition and double resonance (it is the resonance of the frequency of the body wave of the ground and also resonance with the predominant frequency of a building). Apparently, all of this would involve the study and arrangement of a huge quantity of geological, geotechnical, and seismological information.

Experimental and numerical are the two techniques for studying the effect of ground due to earthquakes. The key goal of investigational techniques is to estimate the predominant frequency of the ground through observations of earthquakes or microtremor, or noise data (Pinzon et al. 2019). The microtremor Horizontal-to-vertical spectral ratio (HVR) method is primarily applied to understand the effect of local sites and for microzonation studies. The findings of those studies are afterward expanded to recognize the predominant periods of structures (Nakamura et al. 2000; Gallipoli et al. 2004; Bindi et al. 2015; Petrovic and Parolai 2016). Gosar (2010) and Gallipoli et al. (2004) have studied soil and structure interaction as well as their distress observing microtremors. Also resonance between structure and soil has been identified using the microtremor method. The soil-building relations for URM buildings and various kinds of surface soil have been numerically assessed by Piro et al. (2019). Additionally, every time the predominant vibration period of a structure is relatively near to that of the surface soil, the soil-structure resonance issue is activated. According to Bard et al., (1996) and other researchers (Tsogka and Wirgin, 2003; Mucciarelli et al., 2011) this issue can initiate the distress of the structure in case of a seismic event.

Mucciarelli et al. (2004) has studied the reasons behind high damage to two RC buildings in the town of Bonefro during the 2002 seismic sequence in Molise (Italy). One of them is a four-storied building with a damage grade of 4 in European Macroseismic Scale (EMS) and the other is a three-storied building with a damage grade of 2 in EMS scale. These buildings are located on soft sediments, close to each other and very similar in design and construction. The recorded data has been analyzed by four different techniques: short-time fourier transform (STFT), wavelet transform (WT), horizontal-to vertical spectral ratio (HVSR), and horizontal-to-vertical moving window ratio (HVMWR). To test if the soil–building resonance effect could have increased the damage, they also evaluated the soil fundamental frequency by three different techniques: noise HVSR, strong motion HVSR of seven aftershocks, and 1D modeling based on a velocity profile derived from noise analysis of surface waves (NASW) measurements. The results are in good agreement, showing that resonance frequencies of the soil and of the more damaged building are very close. Navarro et al. (2004) has assessed the dynamic behavior of RC building structures in Granada city. The map of probable resonance phenomena in Granada city, comparing predominant period of soil and natural period of RC buildings, shows that a significant number of buildings be able to have dominant periods close to the ground motion ones and consequently resonant phenomena would be able to appear if an earthquake occur in the zone. Gallipoli et al. (2020) has undertaken a study aiming to recognize the interaction effect between near surface geology and all overlying buildings in the urban area of the city of Matera, Italy. Microtremor measurements have been performed on the main lythologies and on the principal building typologies. Soil and building measurements allowed estimating the main frequencies and relative amplitudes of the soil fundamental peaks as well as the first vibrational frequency of buildings. Matera presents an important case study because the first vibration frequency for most of the buildings is quite close to those of the foundation soils. Tallini et al. (2020) has studied the soil-building resonance effect in the downtown of L'Aquila city, Italy. A very heterogeneous building stock is present in this area: mainly consisting of two to four-storied stone masonry, some brick and a few reinforced concrete buildings. They have showed that the buildings with possible seismic coupling due to the shallow geological setting and the fundamental building period, which is further supported by the areal distribution of seismic building damages caused by the 2009 L'Aquila earthquake. As can be seen from the above studies that for a few cities in the world soil-building resonance effect have been studied. The Government of Bangladesh has recently initiated a project to retrofit some old school buildings in the capital city Dhaka, where this study has been carried out. This kind of study is a pre-requisite for taking decision to retrofit or demolish vulnerable buildings in a city. This is essential since retrofitting is expensive. If we know beforehand that there is a chance of soil-building resonance to take place, either we need to take additional measure to avoid that or take decision to demolish the building.

In order to learn the consequence of resonance between the nearby ground and structures in the Dhaka Metropolitan Development Plan (DMDP) area, microtrremor measurement has been done to assess the site effect and characteristics of the buildings. In this study, 114 educational institutions site has been selected considering the availability of free field and the existence of past SPT and PS logging data as compared to other facilities. Microtremor measurements have been performed in each of those selected 114 buildings and free-field locations.

In this research, the consequence of resonance between the nearby ground and structures in the DMDP area has been experimentally evaluated. An effort has been made to identify the potential areas of resonance between structure and soil within the study area by putting the principal vibrational frequencies of the structures on the frequency contour map based on the predominant frequencies of the soil.

2 Geological background

Dhaka Municipal Corporation and the surrounding Thanas (the lowest administrative unit among four administrative tiers of Bangladesh), is combinedly known as Dhaka Metropolitan Area (DMA), having an area of 300 km^2 with a population density of 23,234 people/ km^2 (World Population Review 2021). Dhaka marked by the Dhaka Metropolitan Development Plan (DMDP) area is a megacity that spreads over 4 other districts covering an area of over 1500 km^2 with a population of around 15 million. DMDP area is situated in a central location of Bangladesh as shown in **Figure 1**.

According to Jain et al. (2020), within Indian subcontinent Bangladesh, which is located in the northeastern side, shares the geology of the Bengal Basin with some part of India. The entire country has been cramped within the Brahmaputra–Ganga–Meghna Delta, is underlain by the alluvial recent deposits of those rivers. The sediments of Bangladesh Geology can be divided into six principal groups (Jain et al. 2020). These are Coastal deposits, Deltaic deposits, Paludal deposits, Alluvial deposits, Alluvial Fan deposits, and Residual deposits (Persits et al., 2001). **Figure 2** shows the geological map of Bangladesh and the study area. **Figure 3** presents the Standard Penetration Test (SPT) and Seismic Downhole Test (SDHT) locations within the DMDP area. **Figures 4 and 5** show the lithology of the horizontal and vertical cross-sections of the study area based on the SPT profile. The Madhupur Clay Residuum is the main soil deposit in the top (which is part of Pleistocene terrace deposit: very stiff soil shown by red color in **Figures 4 and 5**) and then Alluvial Sand, Silt and Clay, and their various combinations. According to the SDHT data, the engineering bedrock of Dhaka city (Shear-wave velocity $\geq$ 400 m/s) is situated around 70 m below the existing ground level. Dhaka is located between the Meghna and Brahmaputra Flood Plains. Two characteristic geological units cover the DMDP area and the surroundings: Madhupur clay deposit (MCD) of the Pleistocene age and alluvial Flood plain deposits (FPD) of the recent age can be seen from **Figure 2b**.

3 Materials and methods

3.1 The built environment

To estimate the vulnerability and risk of Dhaka's critical facilities and develop a prioritized investment plan through an analytical approach, 3252 individual facilities have been assessed recently using Rapid Visual Assessment (RVA) technique combining FEMA P-154 (2015) and ASCE 41 (2017). **Figure 6** presents the spatio-temporal divisions of 3252 structures divided based on their types, construction years, and floor numbers. The RVA methodology applied to the buildings has two major components: structural and nonstructural vulnerability. In the seismic risk prioritization approach, seismic hazard and other vulnerability indicators such as building importance, urban context and economic impact have been included in addition to RVA results. The principal level seismic prioritization methodology is summarized in **Figure 7**. The total number of the prioritized buildings for Preliminary Engineering Assessment (PEA) is 611.

3.2 Microtremor Measurements on Soils and Buildings

To develop a Risk-Sensitive Land Use Planning (RSLUP) map for the DMDP area, 500 single station microtremor measurements have been carried out by dividing the study area into 2km by 2km grids and the fundamental frequency, amplification and seismic vulnerability index variation of the study area have been mapped (Ansary et al. 2019). A total number of 400 locations have also been selected to perform Standard penetration test (SPT) and Seismic downhole test (SDHT) based on the homogeneity and non-homogeneity of the study area based on the microtremor measurements. Those SPT and SDHT locations are shown in **Figure 3**. In this study, during the selection of the educational institutions out of the prioritized 611 buildings, the institutions close to the SPT and SDHT are given priority. This way, 114 buildings are selected for this study. **Figure 8** shows the number of study sites located on MCD and FPD geological units. **Figure 9** presents those buildings according to their construction years and floor numbers.

In this study, microtremor measurements have been carried out on ground and structures in the DMDP area at 114 locations. Site selection and microtremor observations have been executed according to the guideline of SESAME (2004). The microtremor observation on nearby ground and structures have been made by utilizing the digital seismograph manufactured by "OYO International" (McSEIS-MT-NEO-1134) and have been analyzed following the procedures suggested by SESAME (2004). The system has an internal 12V rechargeable battery having the ability to record 5 hour continuously. Surveys have been carried out at 100 samples per second for about 30 minutes.

Measurements have been performed at 114 selected buildings of different height (1 to 10 storied, but most of the buildings are less than 5-storied). Microtremor has been observed on the top floor of the buildings. Two horizontal directions of the sensor have been positioned along the two main axes of the buildings. The sensor has been located as near as possible to the mass center of the structure. Microtremor observations on the soils have been made at least 5m away from the buildings to avoid its influence. The measurements on the soils and buildings, both lasted for 30 minutes with a sampling frequency of 100 Hz. **Figure 10** shows microtremor observations at a free field and at a rooftop of a building.

HVR technique for the free field has been executed according to the criteria of SESAME (2004). The data processing to obtain the HVR at each location has been carried out using the following steps using the GEOPSY software: traced data have been visually observed for probable errors; after that the total data has been divided into 41s wide windows petered out with a 5% cosine function. A Fast Fourier Transform (FFT) has been performed for each split data for each component. Konno and Ohmachi's (1998) technique with a smoothing constant of 40 has been applied to smooth the data.

4 Data Analysis and results

4.1 Soil frequencies

The main resonant peak obtained from the data acquired at 114 sites using HVR technique mainly ranges between 0.5 to 2 Hz (**Figure 11**). The average predominant frequency for MCD and FPD deposit types do not vary significantly as can be seen from **Figure 3**.

Although surfacial geology varies for the MCD and FPD deposits but the average shear-wave velocities for top 30 m of those sites vary between 160m/s and 320m/s (Ansary and Saidur 2013; Zillur et al. 2021). Most of the estimated HVRs show clear resonance peaks for both types of soil deposits as can be seen from **Figure 12 (ii)a** for FPD deposits and **Figure 12(ii)b** for MCD deposits.

The soil frequency and soil amplitude maps (**Figure 13**) show that the soils for most of the DMDP area are characterized by similar predominant frequencies with moderate amplification values for both types of soil deposits. These iso maps are based on 614 microtremor data collected by Ansary et al. (2019) and the current study. The predominant frequencies which have been found for most of the locations of the area under study clearly indicate that the soil which exists below the DMDP area are not suitable for midrise to highrise buildings of the city, in general.

4.2. Building frequencies

The elevation of the 114 observed buildings vary from 3 and 30 m (most of the buildings are lower than 5-storied) and their principal vibrational frequency vary from 1.6 to 8.5 Hz (**Figure 14**). For the reinforced concrete buildings (RCC), the principal vibrational frequencies are considerably smaller and significantly inconsistent than the masonry buildings (URM) with 3.5 Hz as the median values for both types of buildings (**Figure 14a**). The average fundamental frequency values of buildings generally decrease with the increase of the floor numbers of the building (**Figure 14b**). This relation can be taken as an indication of superior statistics as it is an expected relation.

For the observed 107 RCC structures, linear regression with zero intercept in the shape **$T=\alpha N$** (**Figure 15a**) has been used to develop the relation between the principal vibrational period **$T(s)$** and the corresponding floor numbers (**N**). This developed relationship has been estimated in period versus the number of floors to compare our results with those of other researchers (**Figure 15b**). The estimated α value is 0.0747, which is in accord with those found by Guler et al. (2008) for six buildings in Turkey; Michel et al. (2010) for sixty buildings in France, and Gallipoli et al. (2020) for ninety-six buildings in Italy. Also, a similar relation proposed in the BNBC (2020) [**$T=0.0466(3N)^{0.9}$**] has been drawn in the same figure, showing a similar trend.

Due to the availability of the number of floors (**Figure 6c**) for the assessed 3252 institutional buildings within the DMDP area, it has been feasible to estimate the principal vibrational periods (**$T=0.0747N$**) for those structures. The projected principal vibrational frequencies for most of the structures varied from 0.55 to 13.2 Hz. In this database, there are 40 buildings having the number of floors greater than 10, 791 buildings are 2-storied and 514 buildings are single-storied. Out of those 40 buildings, five buildings are more than 15-storied. Most of the buildings having more than 10-storied are located within the city center.

4.3. Development of soil-building resonance map

Figure 16 presents the univariate allotments of principal frequencies of the 3252 surveyed structures and 614 soil locations for which microtremor data are available. The numbers of the two allotments significantly overlap in the lower frequency range (<2 Hz) indicating that relatively taller building stocks will be susceptible to resonance within the DMDP area. In order to assess the probable resonance phenomena in the DMDP area, the predominant frequency of the ground near the structures is compared with the principal vibrational frequency of the 3252 buildings. **Figure 17** presents the average Fourier amplitude spectrum, which has been computed for a 6-storied RCC-building and average HVR of the nearby soil (FPD) showing that their predominant frequencies are relatively close. When both the frequencies are close to one another, in this case, the ratio of the predominant frequency of soil and the principal vibrational frequency of buildings vary from 0.85 and 1.15; it has been assumed that a strong soil-building resonance effect is likely to occur; these buildings are marked in the soil-building resonance map (**Figure 18**) with red color. On the other hand, if the ratio varies from 0.75 and less than 0.85 or greater than 1.15 and less than or equal to 1.25; it has been assumed that a moderate soil-building resonance effect is likely to occur; these buildings are marked with violet color on the map (**Figure 18**). For other ratios, the resonance effect is considered to be low or none and is marked with yellow color on the map. The analysis shows that for 73 buildings, the resonance is relatively high and for 48 buildings, it is moderate. One of the reasons why the effect of resonance is low is due to the fact that out of the 3252 buildings assessed, 80% are less than 5-storied having a principal predominant frequency greater than 3 Hz, whereas the soil predominant frequency for most of the DMDP area is less than 2 Hz. This finding is important since out of the total building stock of 2.2 Million within the DMDP area, 5000 buildings are taller than 10-storied.

Soil frequency has been taken from the microtremor study of 614 free-field points scattered within DMDP area (**Figure 13**). For a single building, all microtremor points around that building have been found using the GIS software as shown in **Figure 19**. For resonance purpose, the microtremor point with the least distance has been considered. For more than 80% of buildings assessed, the least distance is less than 700m.

5 Conclusions

The resonance effect which may lead a building to vulnerable condition within the DMDP area have been assessed and discussed in this paper. Results clearly indicate the importance of site effects in the study area. It is found that the measured predominant soil frequencies using HVR method within the DMDP area for 614 locations are in general below 2 Hz which is expected for the geological conditions underlain by the study area. Also for 114 buildings, the principal vibrational frequencies have been estimated from microtremor observations. This investigation on structures permitted the estimation of the principal vibrational periods; these data allowed developing a relation between the observed period (T) and number of floors (N). Applying this newly developed relation for the building of the DMDP area and ascertaining the floor numbers of each building, the principal vibrational period or frequency of the 3252 buildings has been obtained. The principal vibrational frequency range for the assessed buildings varies from 0.6 to 13.5 Hz with a median value of 4.4 Hz.

A building-soil resonance plot has been developed by matching up the variations of frequencies for the buildings with that of the underlying ground. A moderate to severe resonance level has been obtained for 121 buildings (3.7%); the rest 94.3% of buildings (3131), there is almost no overlap, which implies that no resonance may occur between a building and the nearby ground. The DMDP area has around 2.2 Million building stocks, around 0.5 Million are located within the city center. Out of these 0.5 Million, around 5000 are more than 10-storied high and vulnerable to the resonance effect since most of the areas of DMDP area has soil predominant frequency of less than 2 Hz.

This method allowed evaluating the effect of resonance between buildings and the underlying ground. The finding of this study is a significant ingredient as it makes us to identify those areas of a metropolis where the building-soil resonance is more prone to occur causing relatively more distress during a seismic event.

References

Ansary M.A., Rahman M.S. (2013). Site amplification investigation in Dhaka, Bangladesh, using H/V ratio of microtremor. Environmental Earth Sciences, ISSN 1866-6280, 70:559–574.

Ansary M.A., Helaly A.L., Hassan M., Khair A., Bhuiya M.M.R., Saha S., Helaly SM (2019). Assessment of Seismic Vulnerability Index of RAJUK Area in Bangladesh Using Microtremor Measurements. The 18th International Symposium on New Technologies for Urban Safety of Mega Cities in Asia, USMCA 2019, December 9-10, 2019 Yangon, Myanmar.

Petrovic, B., Parolai, S., 2016. Joint deconvolution of building and downhole strong- motion recordings: evidence for the seismic wavefield being radiated back into the shallow geological layers. Bull. Seismol. Soc. Am. 106, 1720–1732. https://doi.org/ 10.1785/0120150326.

Pinzóna, LA, L. G. Pujadesa, A. Macaub, S. Figuerasb (2019); Increased seismic hazard in Barcelona (Spain) due to soil-building resonance effects, Soil Dynamics and Earthquake Engineering 117 (2019) 245–250

Piro, A., de Silva, F., Parisi, F., Scotto di Santolo, A., Silvestri, F., 2019. Efects of soil-foundation-structure interaction on fundamental frequency and radiation damping ratio of historical masonry building sub-structures. Bull. Earthq. Eng. 18 (4), 1187–1212.

Rahman MZ, Siddiqua S, Kamal ASMM (2020) Probabilistic Seismic Hazard Analysis for Bangladesh. Nat Hazards 103: 2489-2532

Rahman MZ, Siddiqua S, Kamal ASMM (2021) Site Response Analysis for Deep and Soft Sedimentary Deposits of Dhaka City, Bangladesh. Nat Hazards DOI: 10.1007/s11069-021-04543-w

SESAME European research project, (2004). Guidelines for the implementation of the h/v spectral ratio technique on ambient vibrations, measurements, processing and interpretation. European commission-research general directorate project no. CT2000--00026 SESAME.

Steckler MS, Mondal DR, Akhter SH, Howe M (2016) Locked and loading megathrust linked to active subduction beneath the Indo-Burman Ranges. Nat Geosci 9: 615-618.

Tallini, M., Sardo, LL, Spadi, M (2020). Seismic site characterisation of Red Soil and soil-building resonance effects in L'Aquila downtown (Central Italy). Bulletin of Engineering Geology and the Environment. 79:4021–4034. https://doi.org/10.1007/s10064-020-01795-x.

Tsogka, C., Wirgin, A. (2003). Simulation of seismic response in an idealized city. Soil Dyn. Earthq. Eng. 23, 391–402. https://doi.org/10.1016/S0267-7261(03)00017-4.

World Population Review (2021). https://worldpopulationreview.com/world-cities/dhaka-population ((last accessed 26 February 2021)

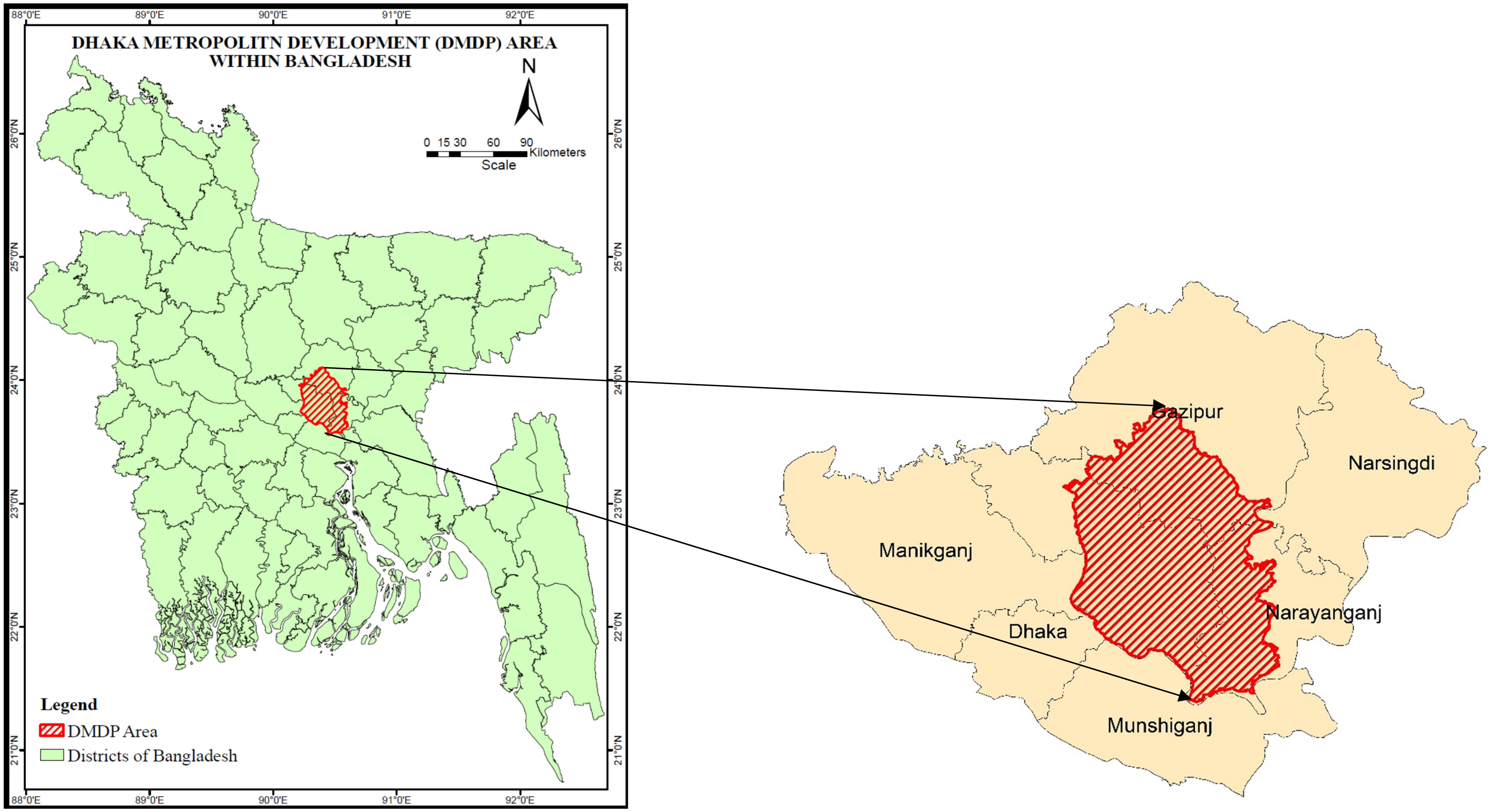

Figure 1: DMDP area with and its surrounding region

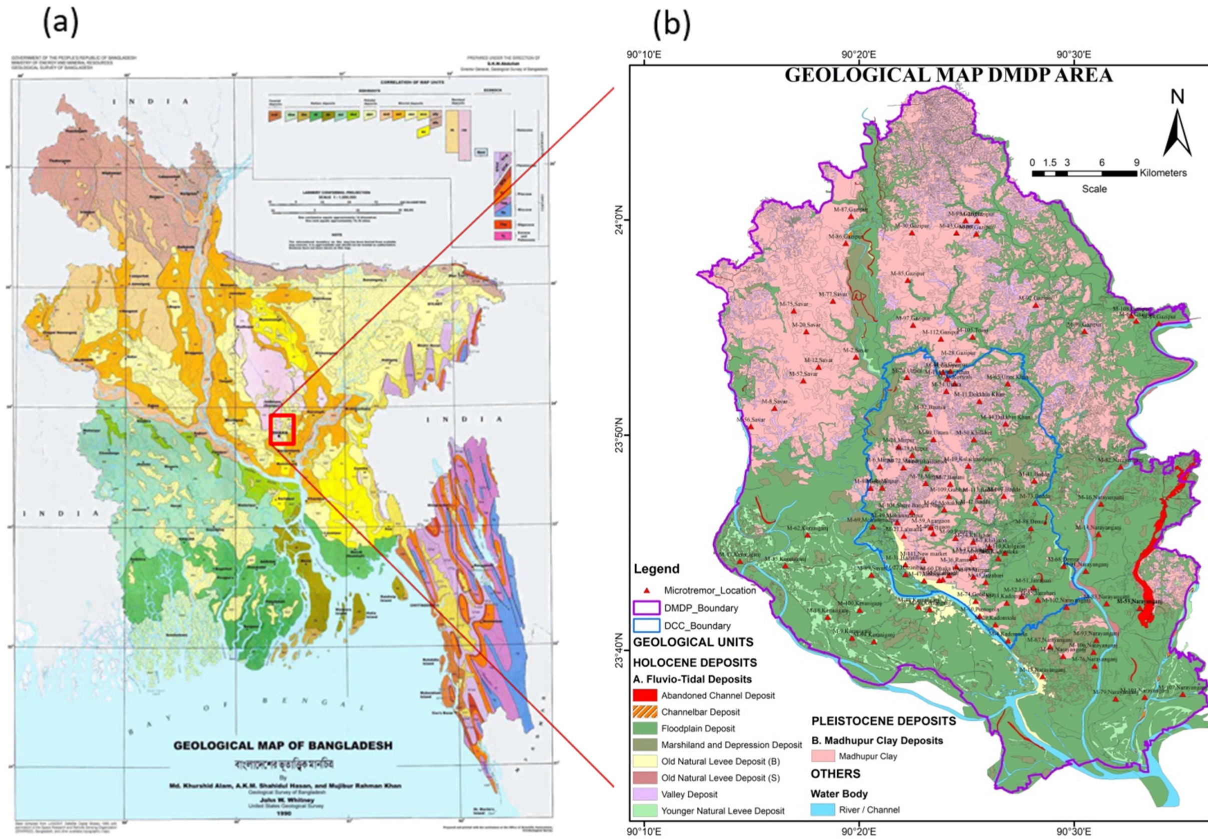

Figure 2: (a) Geological Map of Bangladesh (Alam et. al. 1990) (b) Geological map of the study area showing sites where data have been acquired in this study

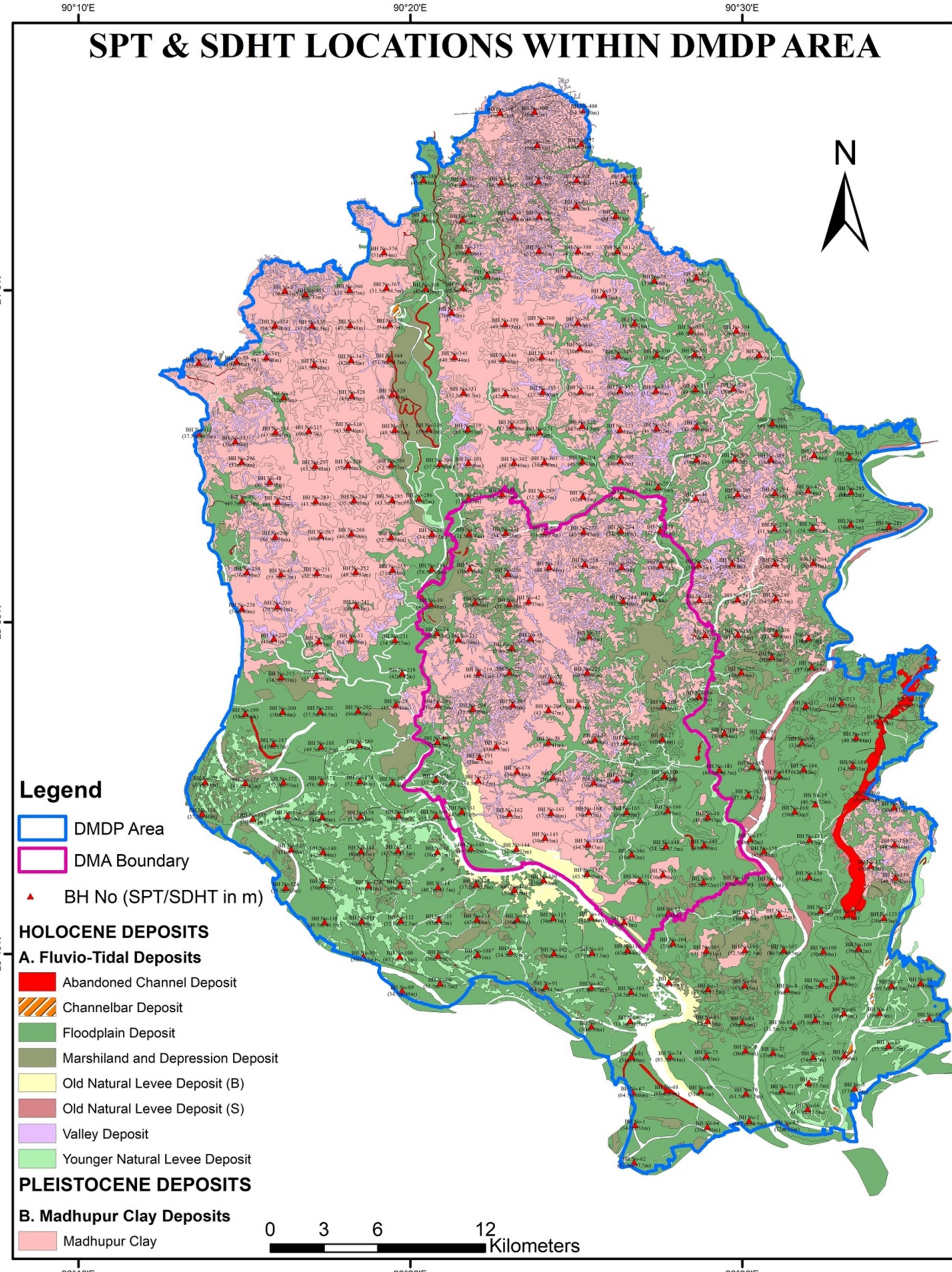

Figure 3: SPT and SDHT locations within the DMDP area

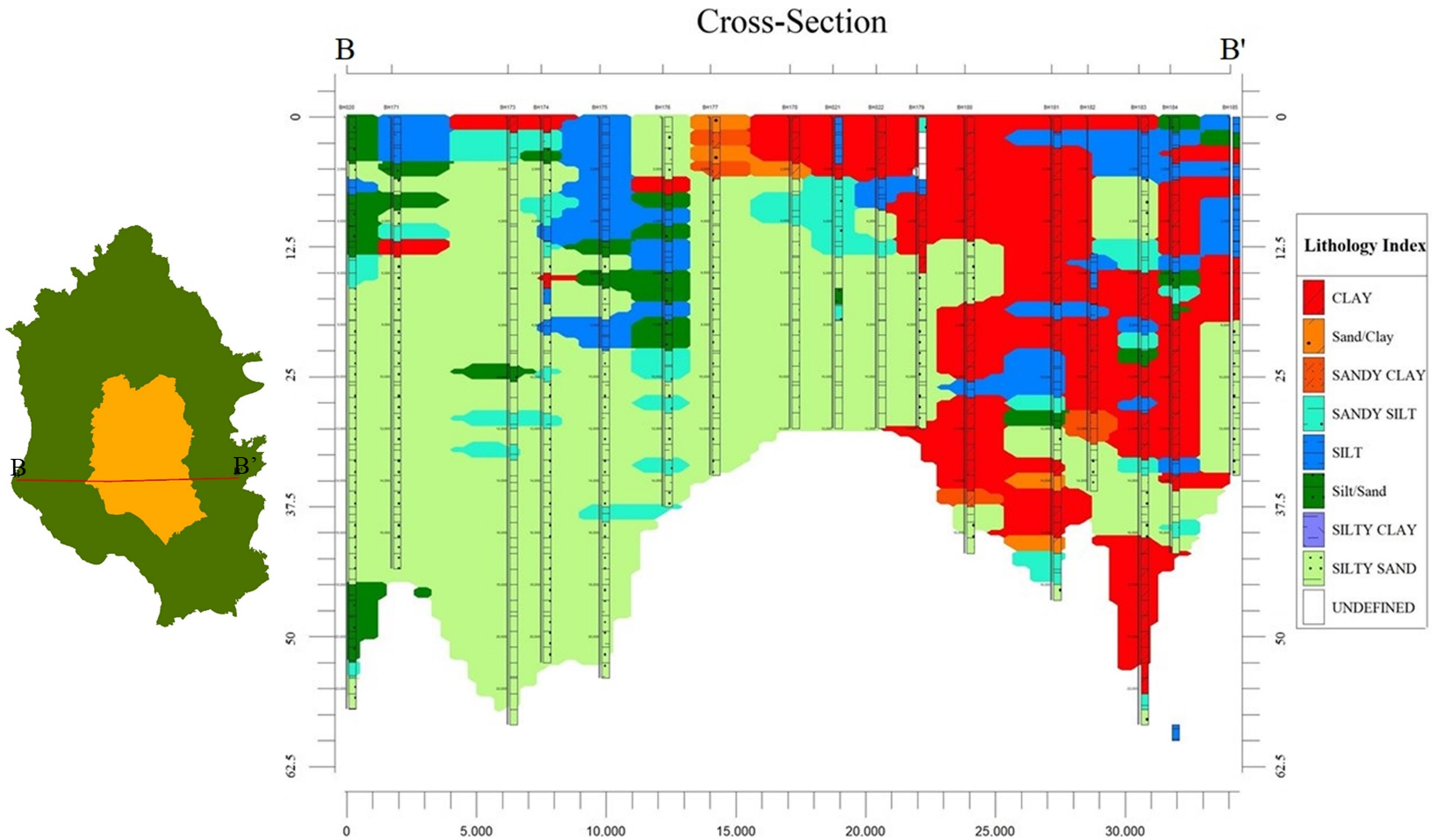

Figure 4: The lithology of the horizontal cross-section

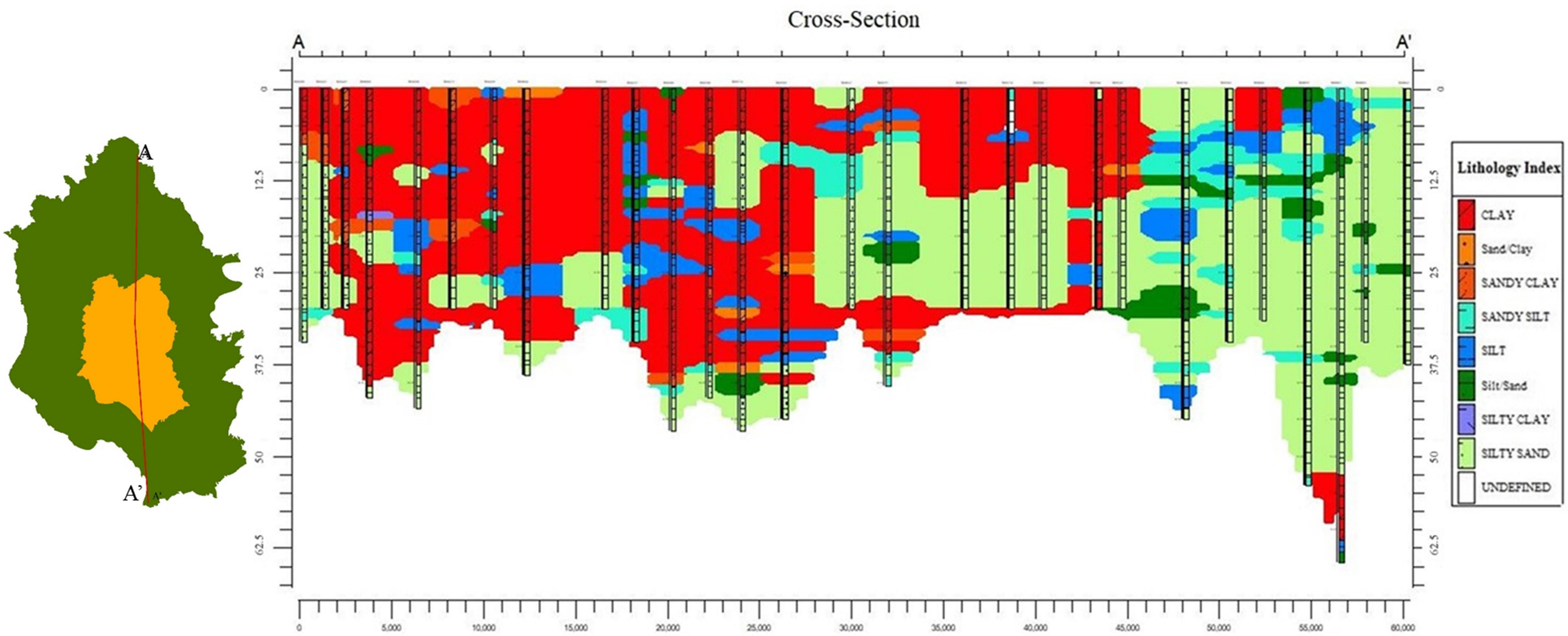

Figure 5: The lithology of the vertical cross-section

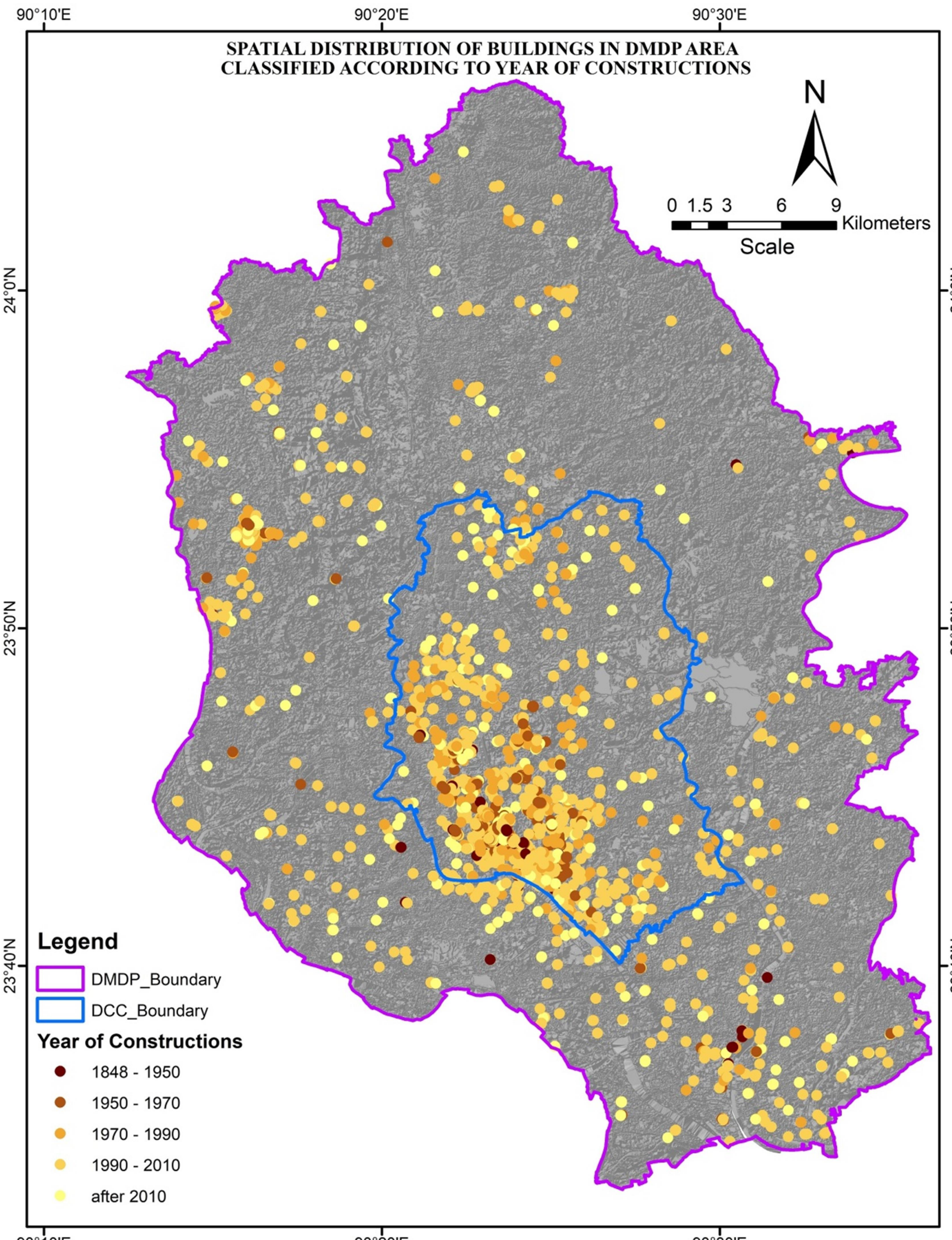

(a)

Figure 6: Spatial distributions of buildings classified according to (a) year of construction; (b) built typology; (c) number of floors of total 3252 buildings

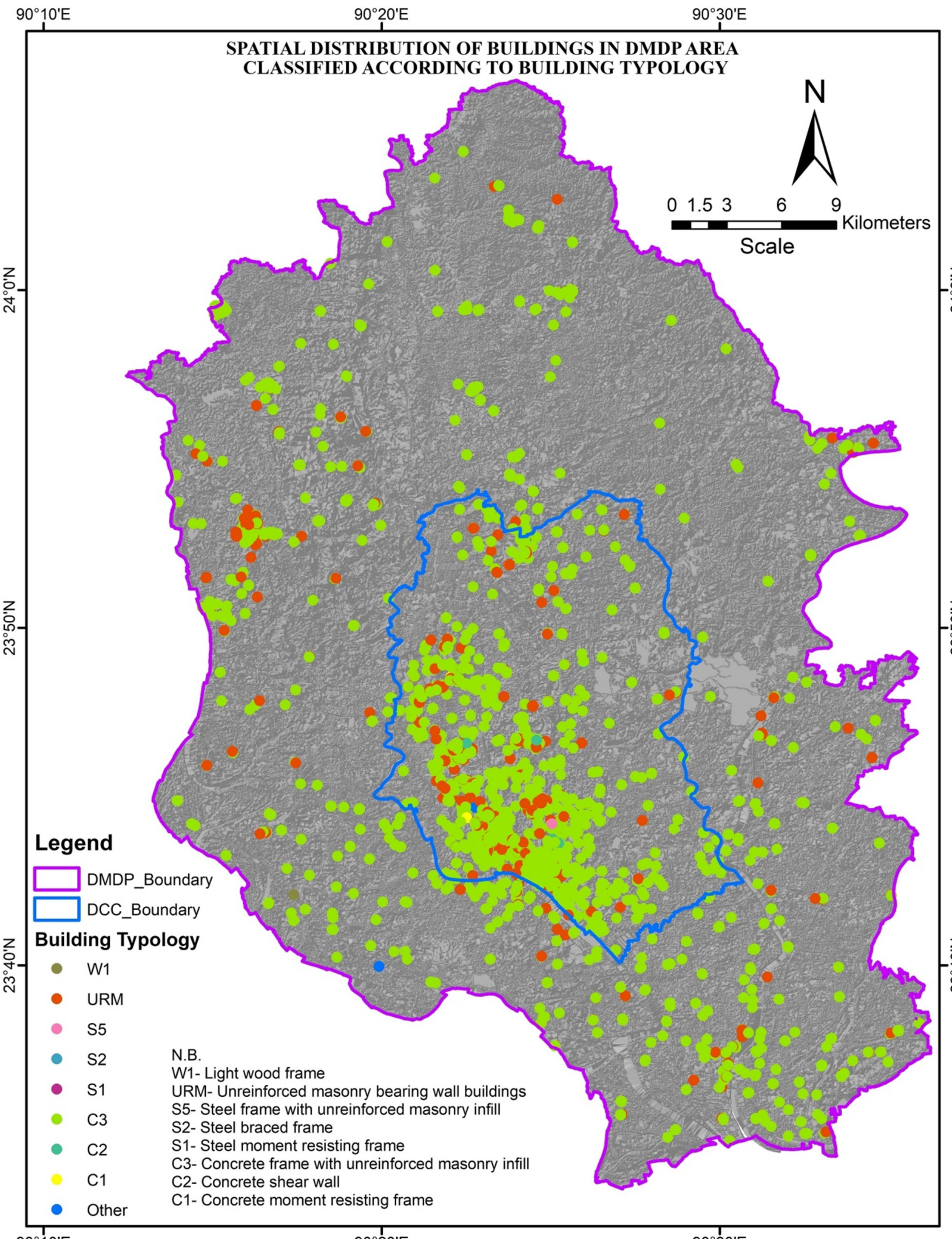

(b)

Figure 6 (contd.): Spatial distributions of buildings classified according to (a) year of construction; (b) built typology; (c) number of floors of total 3252 buildings.

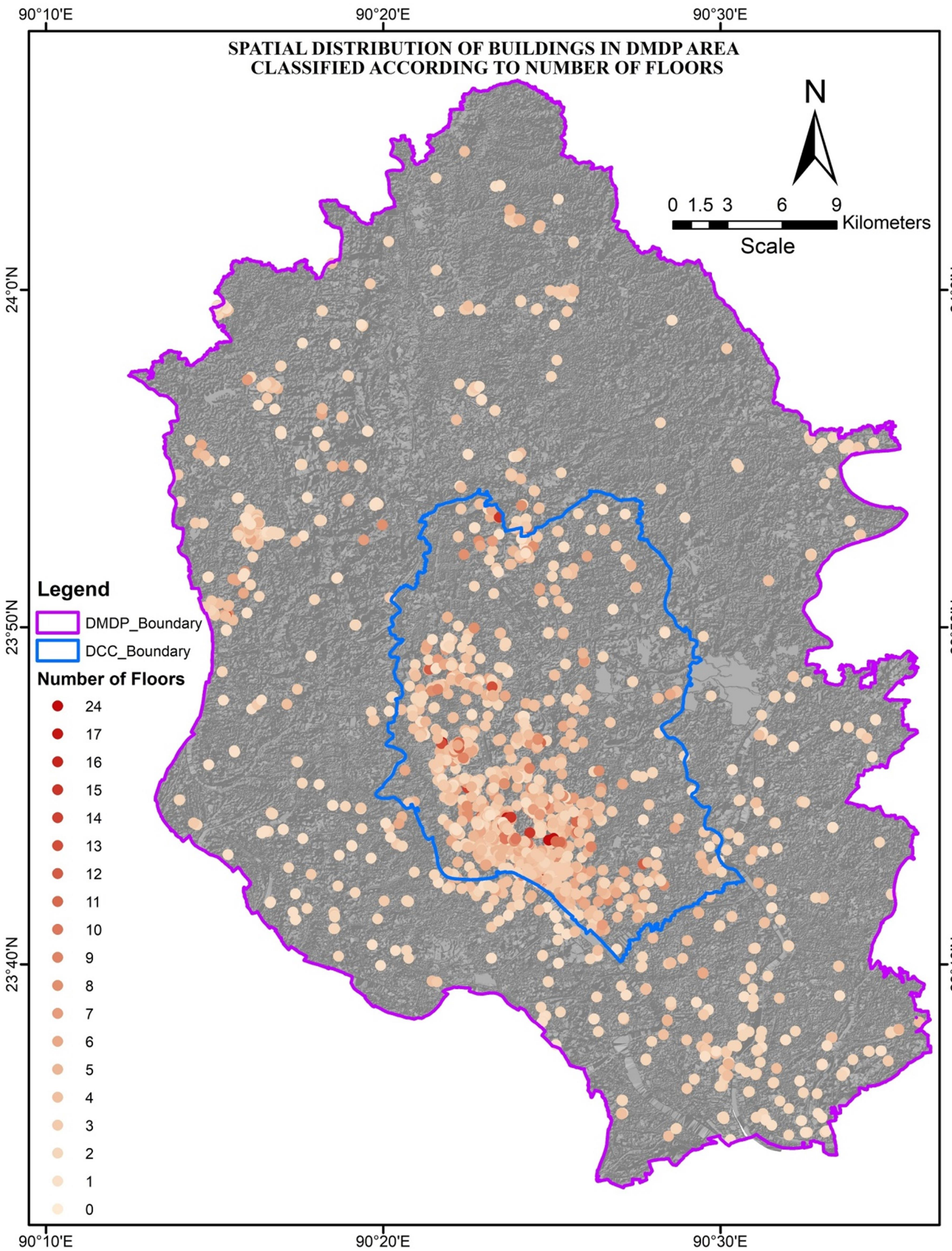

(c)

Figure 6 (contd.): Spatial distributions of buildings classified according to (a) year of construction; (b) built typology; (c) number of floors of total 3252 buildings.

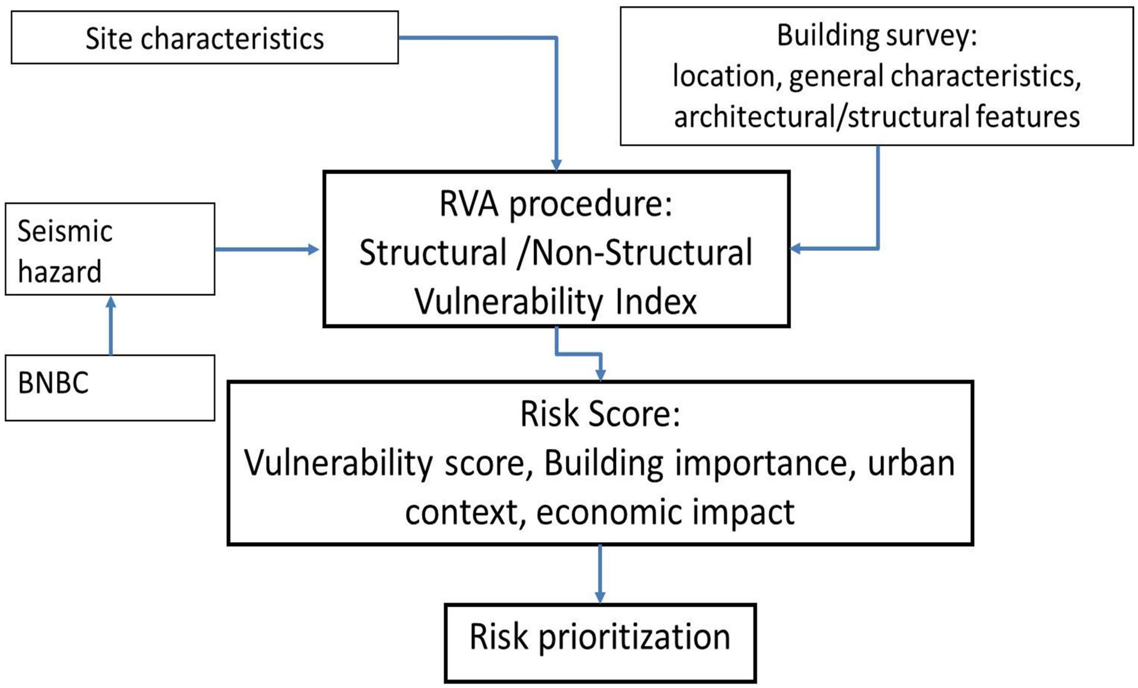

Figure 7: Flowchart of Level 1 risk prioritization procedure

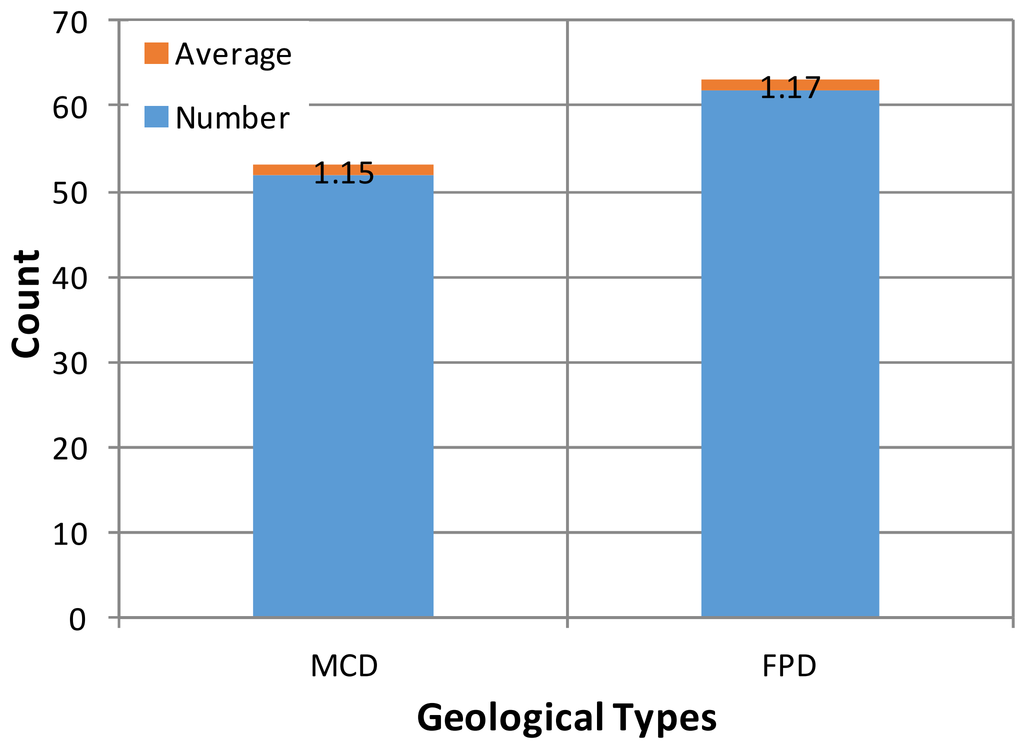

Figure 8: Number study sites on Madhupur Clay Deposit (MCD) and flood plain deposit (FPD) with average predominant frequency

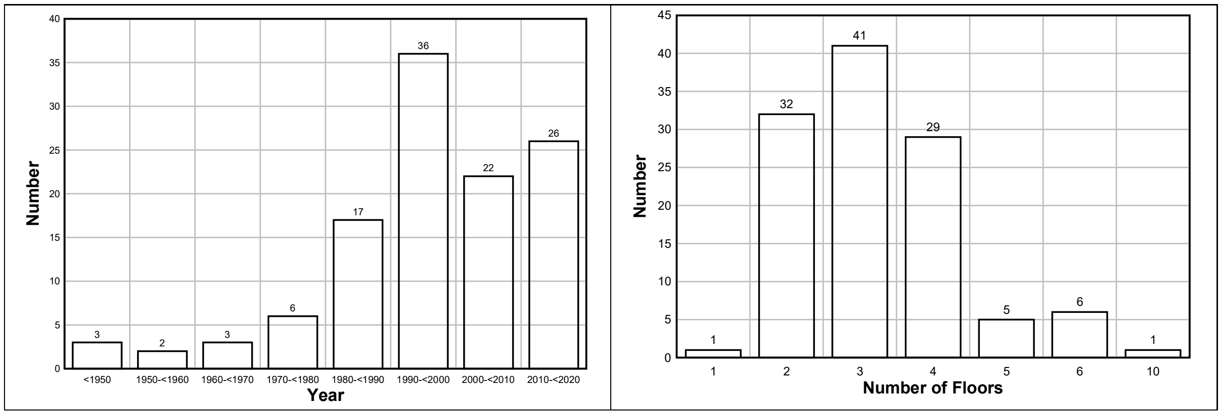

Figure 9: Year of construction and number of floors of the selected 114 buildings

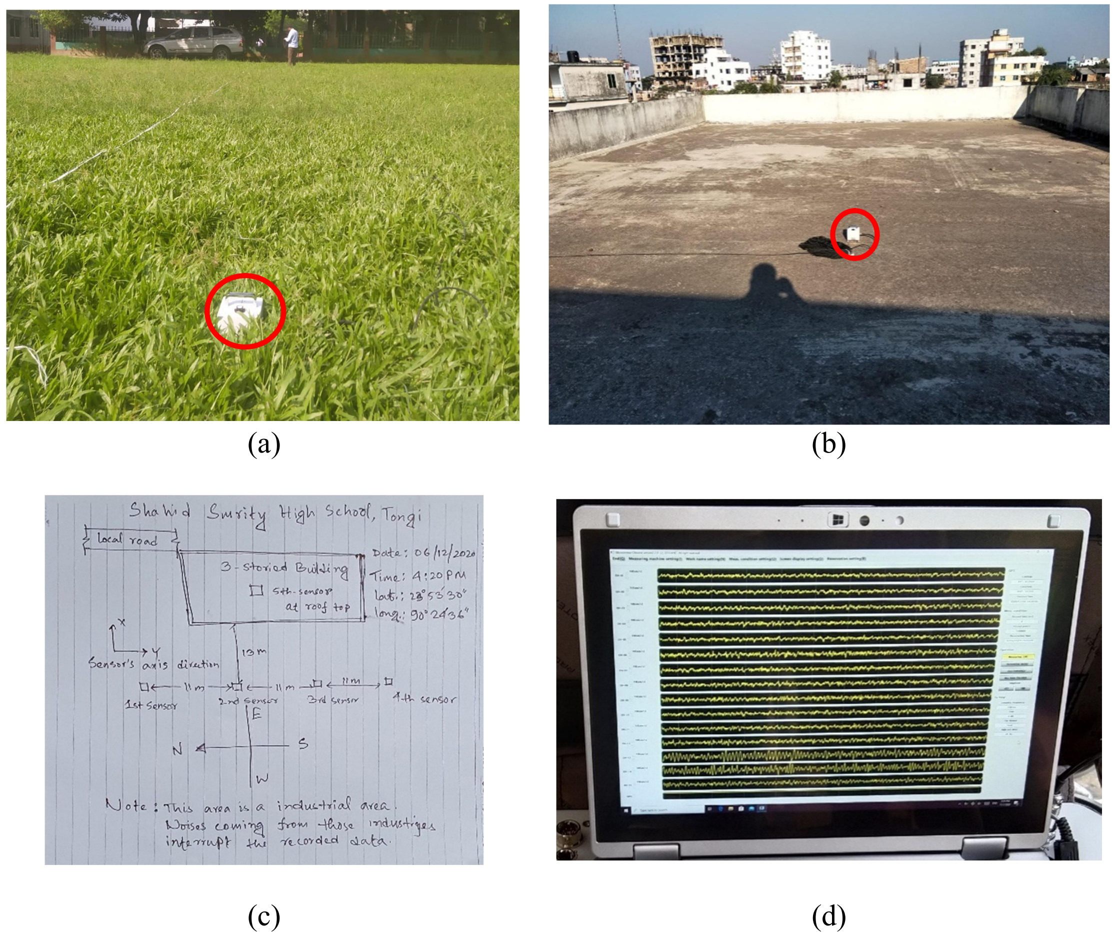

Figure 10: Microtremor recording (a) at a free-field, (b) at roof top of a building, (c) sketch of sensor's map for one location and (d) channels showing time history data

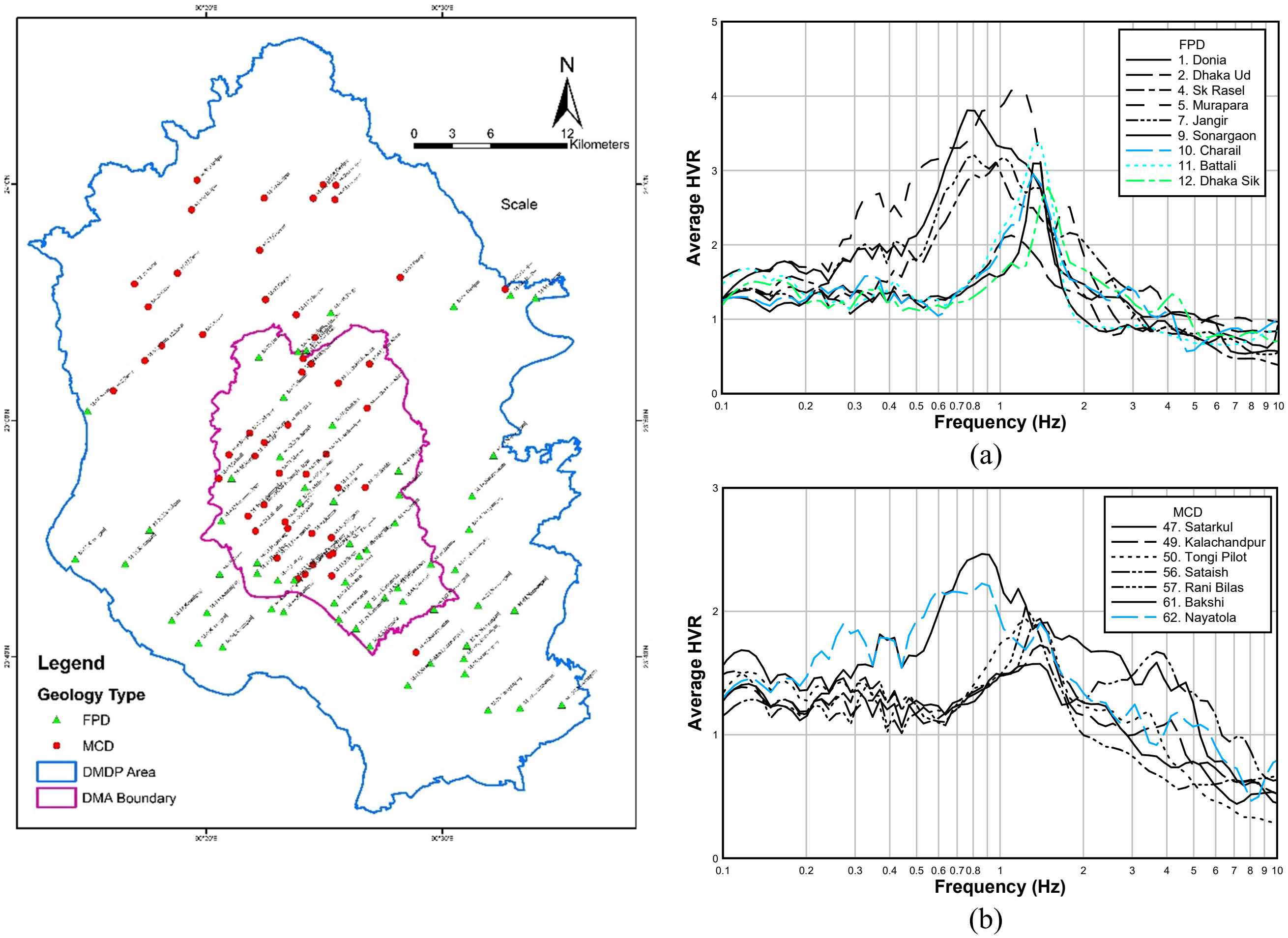

(i) (ii)

Figure 12: (i) Spatial Distribution of test sites as per MCD and FPD deposit type and (ii) comparison between HVSRs obtained on (a) FPD and (b) MCD deposits

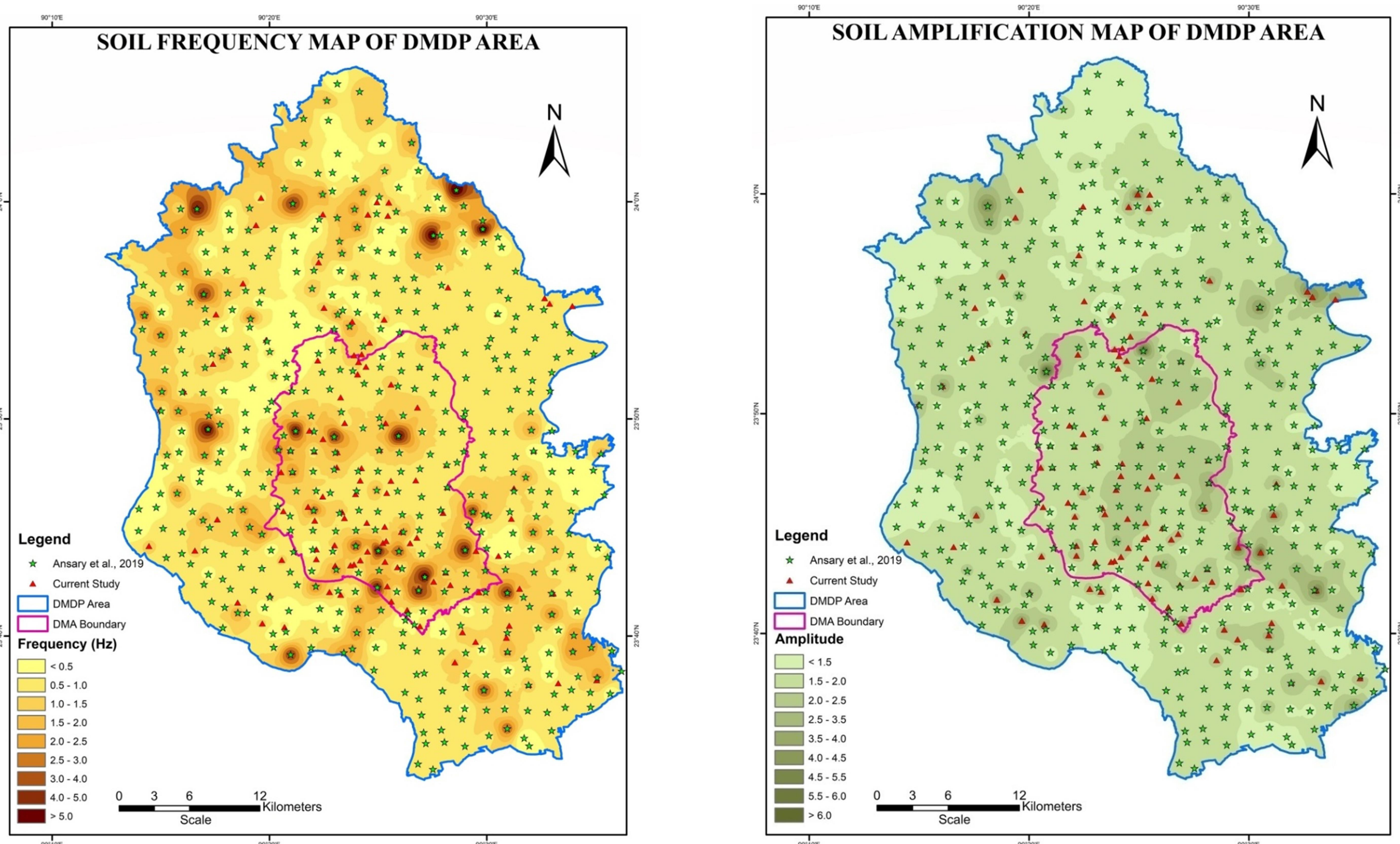

(a) (b)

Figure 13: (a) Soil frequency contour and (b) soil amplification contour maps of DMDP area

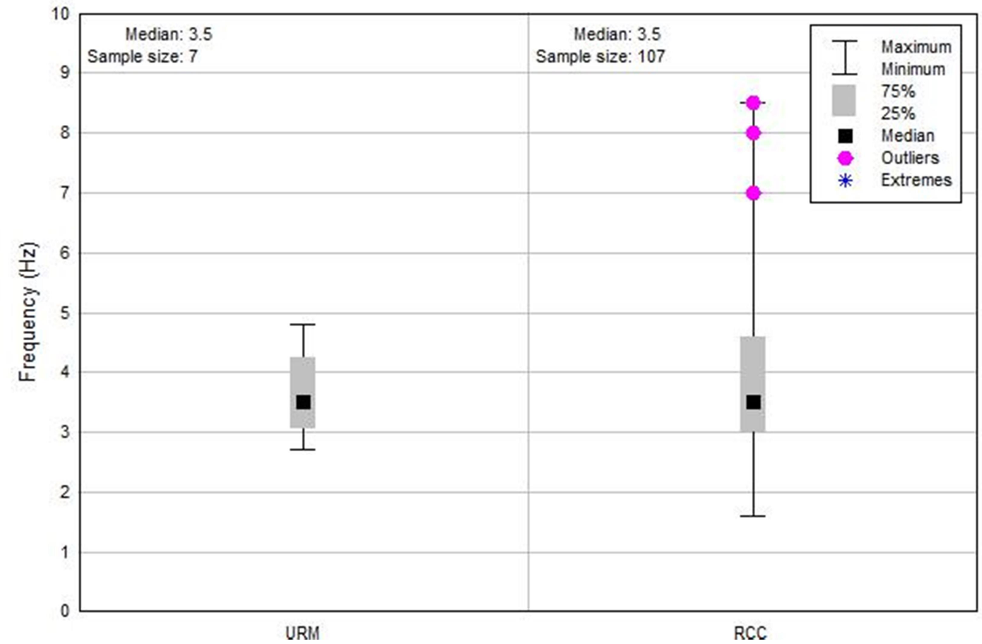

(a)

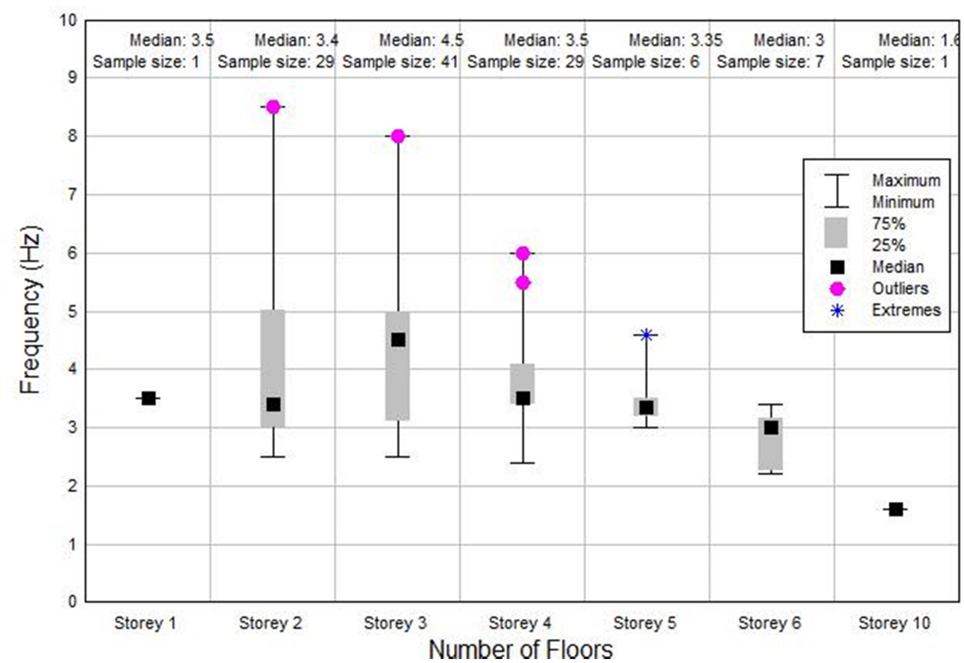

(b)

Figure 14: Empirical distributions of the principal vibrational frequency of the 114 buildings versus (a) construction typology and (b) number of floors

The lower and upper part of the grey rectangular box correspond to the first and third quartiles (the 25th and 75th percentiles); the black square box is the median (50^{th} percentile)

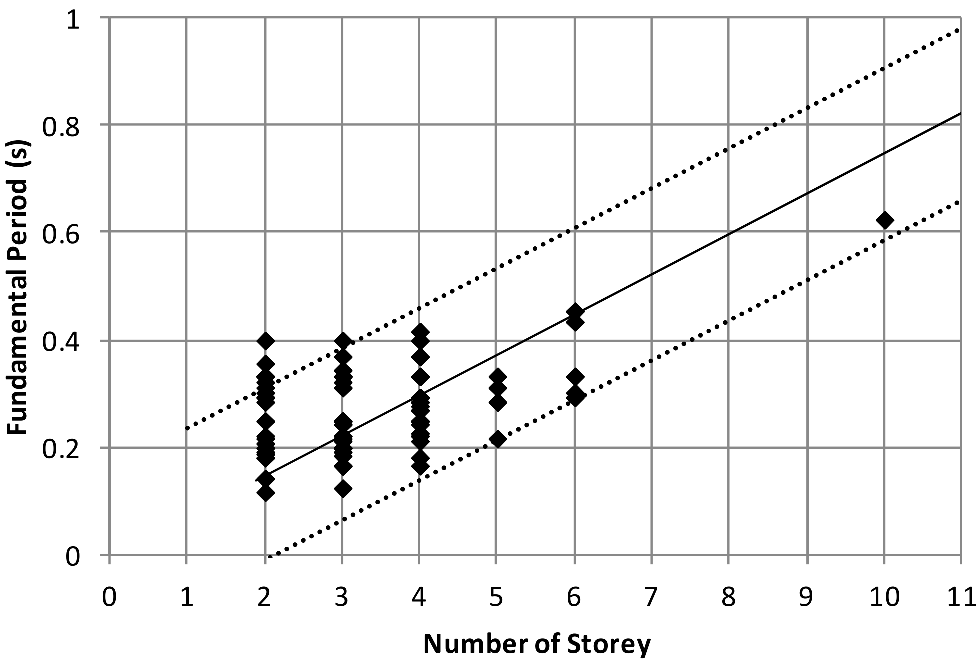

(a)

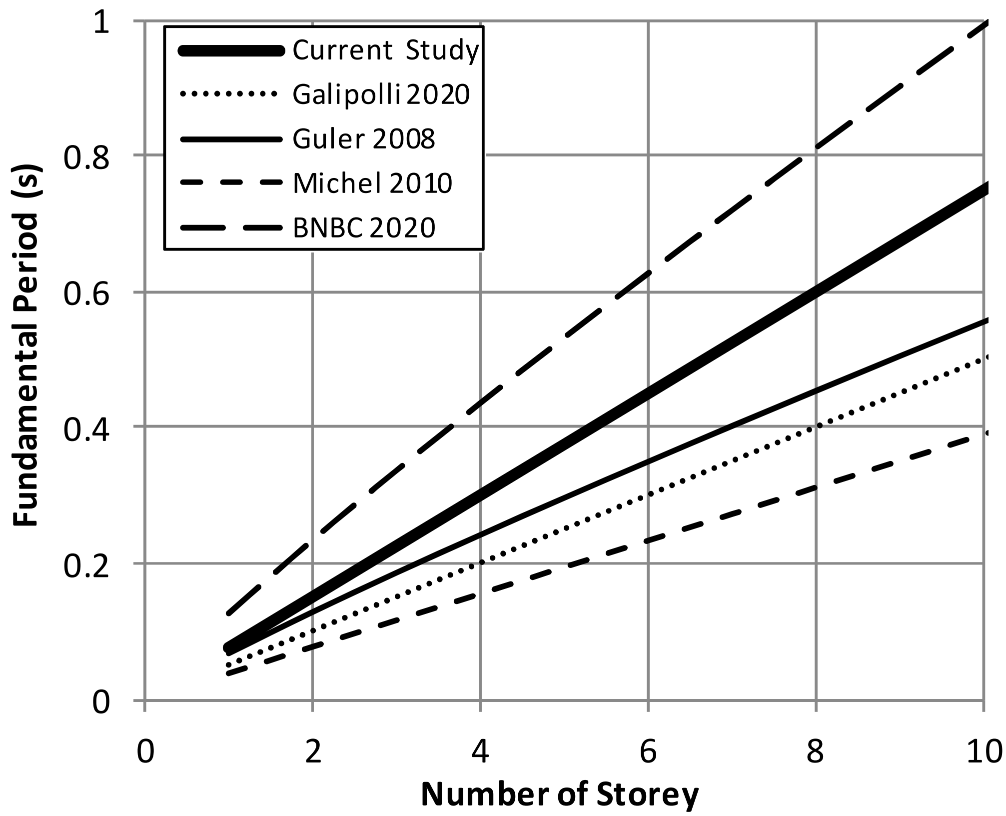

(b)

Figure 15: Experimental relation between building period and the number of floors for (a) the 107 sampled buildings and (b) other studies. In (a), the thin black line represents the predicted values (T = 0.0747N), and in (b) the thick black line represents the prediction interval of the regression

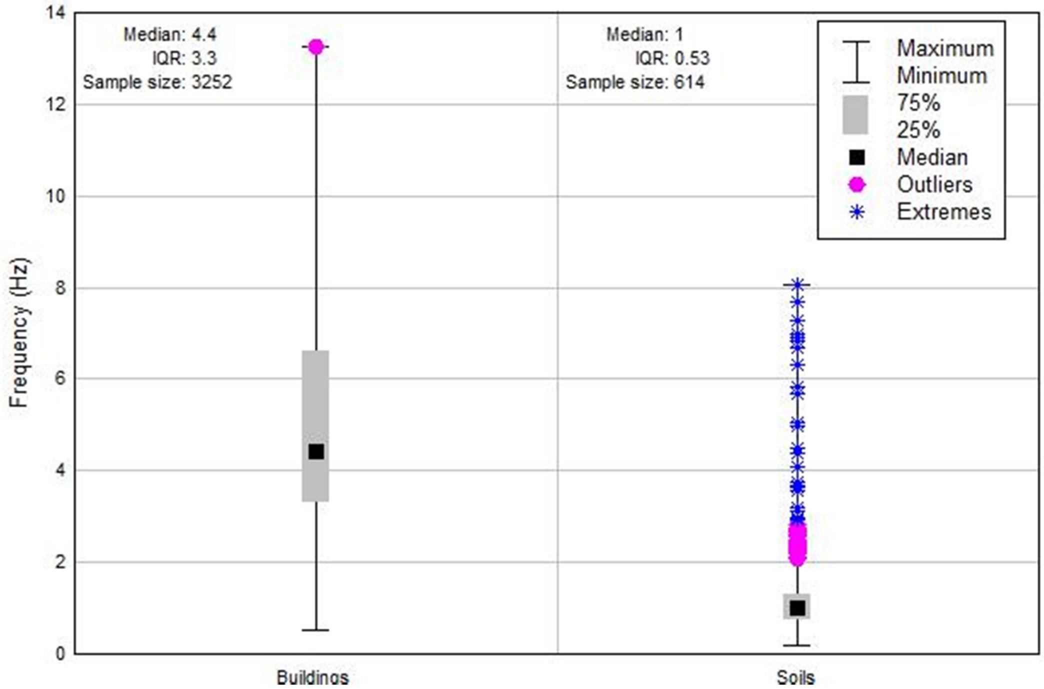

Figure 16: Distributions of the fundamental frequency for soils and buildings

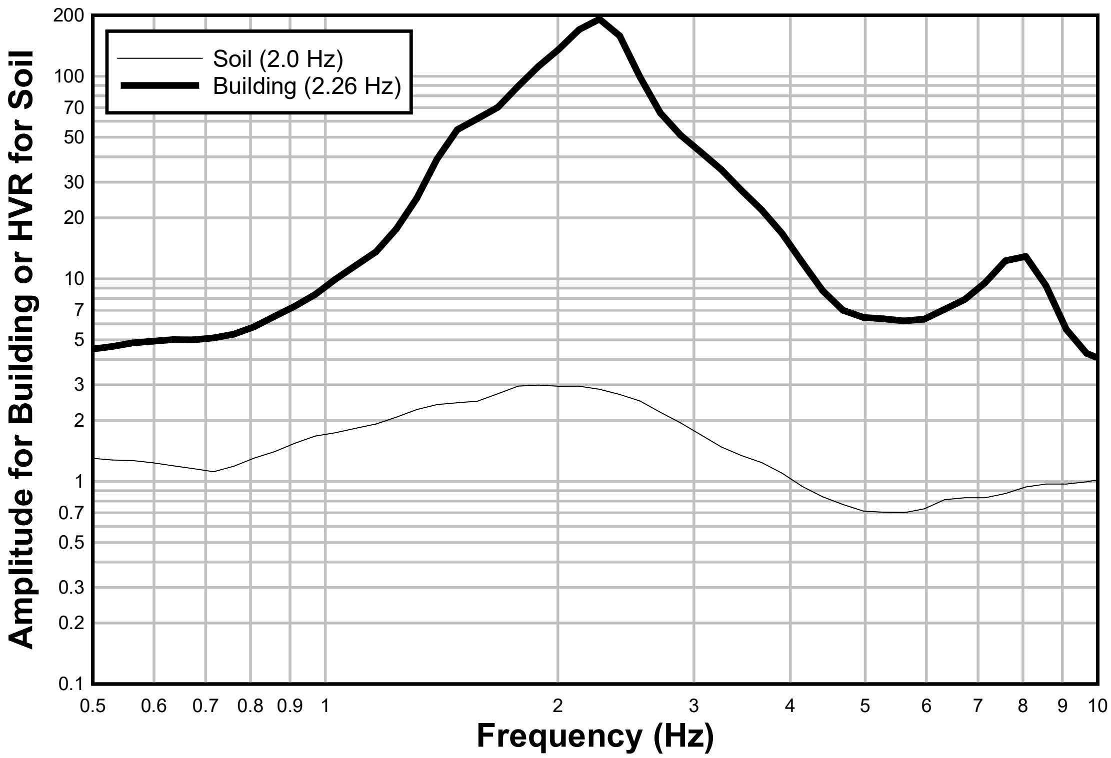

(a)


(b)

◆ Microtremor Sensor (c)

Figure 17: (a) Fourier amplitude functions estimated on the top-floor of the 6-storied reinforced concrete building and HVR on the nearby soil; (b) microtremor observation of the building resting on FPD; (c) location of building on the googlemap

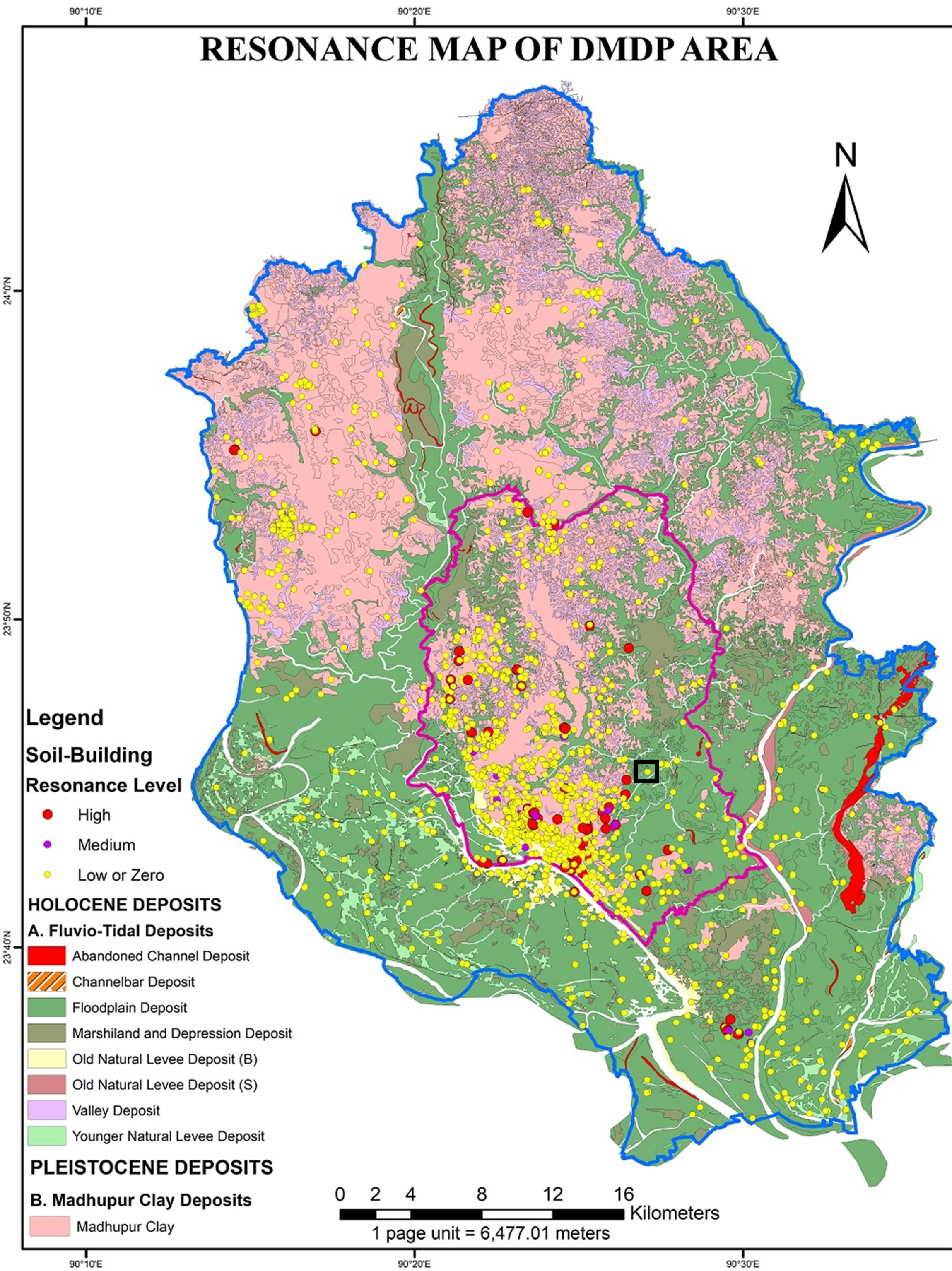

Figure 18: Soil-building resonance map of 3252 buildings

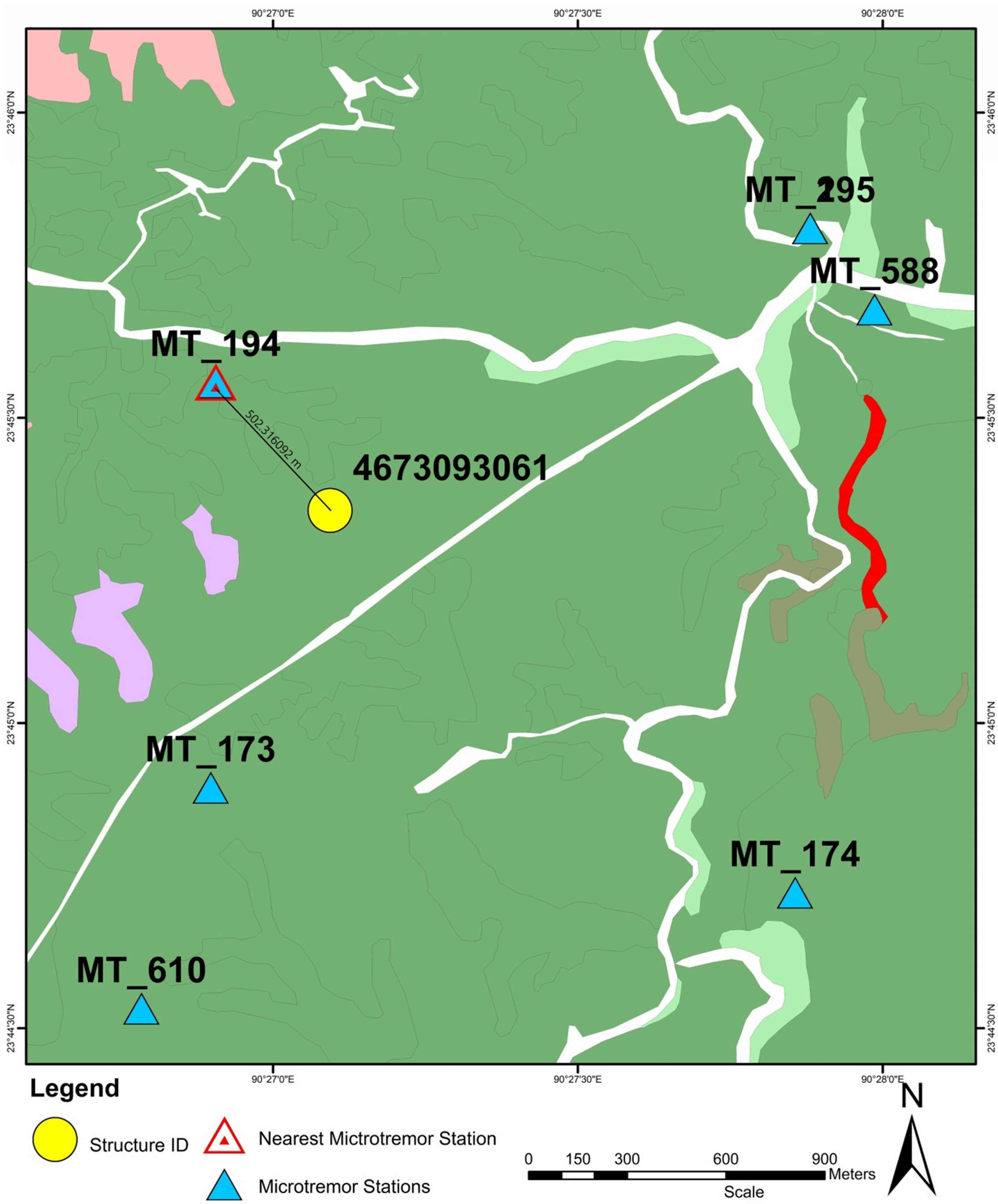

Figure 19: Nearest microtremor stations for an individual building

BANGLADESH NETWORK
OFFICE FOR URBAN SAFETY

PART-IX

DEVELOPMENT OF CORRELATION EQUATIONS BETWEEN SHEAR WAVE VELOCITY AND STANDARD PENETRATION TEST VALUES FOR DIFFERENT SOIL TYPES FOR DMDP AREA OF BANGLADESH USING MULTIVARIATE ANALYSIS

BANGLADESH NETWORK OFFICE FOR URBAN SAFETY (BNUS), BUET, DHAKA

Prepared By: Anikah Tasmiah

Mehedi Ahmed Ansary

Introduction

Shear wave velocity V_s is an essential metric when assessing the dynamic properties of shallow subsurface soil [1, 2]. Design seismic movements, wave amplification, and soil structure interaction are all major issues in earthquake engineering and these necessitate understanding of shear wave velocities in soil deposits in order to be solved[3]. The usage of Vs became widespread and is now widely employed in practice due to the fact that it is a quantitative index that can be quantified using geophysical techniques [4].

Correlation equation of Vs with various soil indexes has been established by numerous researchers over the years in various geographical locations because direct determination of shear-wave-velocity is expensive [1, 5] and requires leading-edge instrument and appropriate industrial and traffic noise free environment [6]

Numerous studies have established correlations between V_s and soil indexes such as depth, SPT-N (or N), geological epoch and soil type [3, 7, 8]. The geologic influence could be attributed to geologic age or the sedimentary environment[7] .Adopting a similar technique to the one described above may be advantageous for previously bored boreholes, as they often have just data on N and the accompanying depths, but no measured V_s [8].

Hamilton[9], Boore and Joyner[10] , Klimis et al. [11] , Wang and Wang [12] established depth based regression equations in the past. Empirical correlation equation between shear wave velocity and penetration resistance or N value from SPT has been established by lots of researchers over the years in different geographical locations. For example in Japan research was conducted by, Imai et al.[13], Imai and Yoshimura [14], Imai [15] and Imai and Tonouchi [16] & Dikmen [17] in Turkey, Fauzi [18] in Indonesia, Sun et al.[19] in Korea, Maheswari [20] , Thokchom et al. [1] and Bandyopadhyay et al. [5] in India. However the shear wave velocity cannot be well characterized by the N-value alone. Several approaches have been proposed to improve such empirical equations by incorporating other elements such as type of soil and depth estimated from the ground surface [3].

The study of Ohta and Goto [3] first proposed multivariable analysis technique in V_s empirical equations. Multiple studies considered depth and N based correlation equations in their studies [3, 7, 21] and resorted to multiple regression analysis. Both Ohta and Goto [3]and Lee [22] discovered that the essential parameter in a regression equation is “depth” rather than the N-value, assuming the type of soil and effect of geology are initially studied. The equation of Chapman et al. [21] incorporated effective overburden pressure (σ_v). However, Kuo et al. [8] advised in their study that the model for regression should be chosen based on the highest coefficient of correlation R^2 between Vs and N or depth.

The purpose of this paper is to create multivariate regression equations of Vs based on depth and SPT-N for various soil types in the 1530-square-kilometer Dhaka Metropolitan Development Plan (DMDP) Area. A total of 400 boreholes were drilled throughout the research area. N levels were assessed using SPT at 1.5m depth intervals and PS logging was performed in all 400 boreholes, resulting in a total of 9334 data pairs for all soils (6159 for sand; 3175 for clay).

Existing Shear Wave Velocity Equations

Ohta and Goto [3] adopted four soil indexes namely the soil depth, the Standard Penetration Test N-value, soil type(grain size) & geological period and established 15 sets of empirical equation in order to approximate low-strain level shear wave velocity by use of about 300 data. Since the indexes can be both quantitative and qualitative type they resorted to scale classification where above mentioned indexes were categorized into few clusters by their features. Since the N-value and depth were matric variables derivation was done by means of multivariate analysis. The depth and SPT-N based equation of shear wave velocity had correlation coefficient larger than 0.8.

Lee [7] used 491 sets of data from the Taipei basin, including SPT N-value, shear wave velocity, and "depth." To identify the most rational model of the shear wave velocity, aside from simple linear model, the multiple regression models & the intrinsically linear models are also investigated. In addition, a method for examining the problem of multicollinearity in a multiple regression equation was proposed. When type of soil and geological influence are taken into account in the regression model ($V_s = aN^bD^c$), he concludes that the multiple regression model yields the highest coefficient of determination (R^2). However, because "depth" and "N" are not mutually exclusive, a multicollinearity problem may develop. The "rule of thumb" test, which states that the correlation coefficient R between any two variables ought not to be greater than 0.70, is one way for avoiding the problem suggested by Lee [7] from Anderson et al., [23]. Additionally, he found that the multiple regression model, $V_s = aN^bD^c$ overcome the disadvantages of the single variable regression equation, $V_s = aD^b$ or $V_s = a(D+1)^b$, by presenting the variations amongst soils at the same depth in the same area. According to his analysis, one disadvantage of intrinsically linear regression model where depth (D) is the principal parameter is that the shear wave velocities will be all the same in depth throughout the investigated area. Thus, the equations cannot reflect the weaker strata, and multiple regression equations without the multicollinearity problem would prevail in this case.

In his previous study, Lee [22] pointed that the fundamentally linear form of equation with the depth factor was appropriate when the indigenous soils were originally categorized according to type of soil and the effect of geology; its value of R-square was comparable to the value of R-square of the multiple regression equation. In this paper, 88 data sets of SPT N value, shear wave velocity, and depth were examined in the Taipei basin from fifteen borelogs. To select the finest model for the shear wave velocity, the linear, the intrinsically linear, the multiple regression and the second-order polynomial models are evaluated.

In the study of Kuo et al. [8] empirical regression equations were assessed utilizing over 641 sets of data from Ilan area as well as 719 sets of data from Taipei Basin area based on the correlation between V_s and soil indicators. In this study, multivariable analysis was employed to improve the precision of regression models. To analyze the regression equations, specimens with N less than 50 and depth less than or equal to 50 m were chosen. Due to this reason, 56 and 38 locations in Taipei and Ilan, respectively, were used. For boreholes that had only N values and had not been drilled to a depth of 30 meters, empirical equations for V_s were performed, and extrapolations for V_s^{30} were utilized.

Table 1 Regression Equations established in previous studies

Author(s)	No of Data Point	Soil Type	Equation	R^2
Ohta and Goto(1978) [3]	300	All	$V_s = 61.62N^{0.254}H^{0.222}$	0.820
Lee (1989) [22]	88	CL/All	$V_s = 74.44N^{0.16}D^{0.25}$	0.78
		CL /Keelung	$V_s = 71.52N^{0.08}D^{0.29}$	0.83
		CL /Tanshuei	$V_s = 58.56N^{0.13}D^{0.37}$	0.92
		ML/All	$V_s = 73.70N^{0.14}D^{0.26}$	0.88
		SM/All	$V_s = 57.97N^{-0.01}D^{0.46}$	0.86
Lee (1992) [7]	126	SM	$V_s = 76.16N^{0.076}D^{0.313}$	0.776
			$V_s = 68.77N^{0.075}(D+1)^{0.340}$	0.779
	265	CL	$V_s = 95.72N^{0.124}D^{0.210}$	0.785
			$V_s = 86.10N^{0.116}(D+1)^{0.244}$	0.788
	100	ML	$V_s = 90.57N^{0.140}D^{0.205}$	0.829
			$V_s = 82.79N^{0.134}(D+1)^{0.233}$	0.830
	365	CL/ML	$V_s = 93.54N^{0.125}D^{0.213}$	0.798
			$V_s = 84.53N^{0.118}(D+1)^{0.246}$	0.801
Kuo et al. (2011) [8]	719	Sand	$V_s = 93.11N^{0.242}D^{0.136}$	0.671
		Clay/Silt	$V_s = 114.55N^{0.168}D^{0.143}$	0.685

Database Used for Conducting Study

SPT was used to conduct borehole drilling at 400 places throughout the DMDP area. A downhole seismic test was carried out at each location. The borehole log displays the N-values derived from SPT with depth and the Vs profiles established from seismic downhole testing. Fig. 1 presents an illustration of test results at a site in Hemayatpur, Savar of DMDP area.

For all soil types, downhole tests provided 9334 pairs of data points. In the past, N values produced from SPT tests were corrected for rod length, overburden stress, and equipment type, as well as borehole diameter. [19]. Correlations are calculated in the current study using uncorrected N values.

In-situ test is a widely used means for site characterization in geotechnical engineering [14, 20]. In present study SPT is used for in-situ geotechnical test. The SPT process is described in ASTM D 1586 [24]. Both seismic and electromagnetic techniques are used for in-situ geophysical tests to estimate subsurface properties[19]. V_s can be estimated both in laboratory tests as well as in-situ tests [6, 19]. In this study seismic downhole test is done in the same borehole where SPT has been performed to determine the shear-wave-velocity of soil. This test procedure is described in ASTM D 7400 [25].

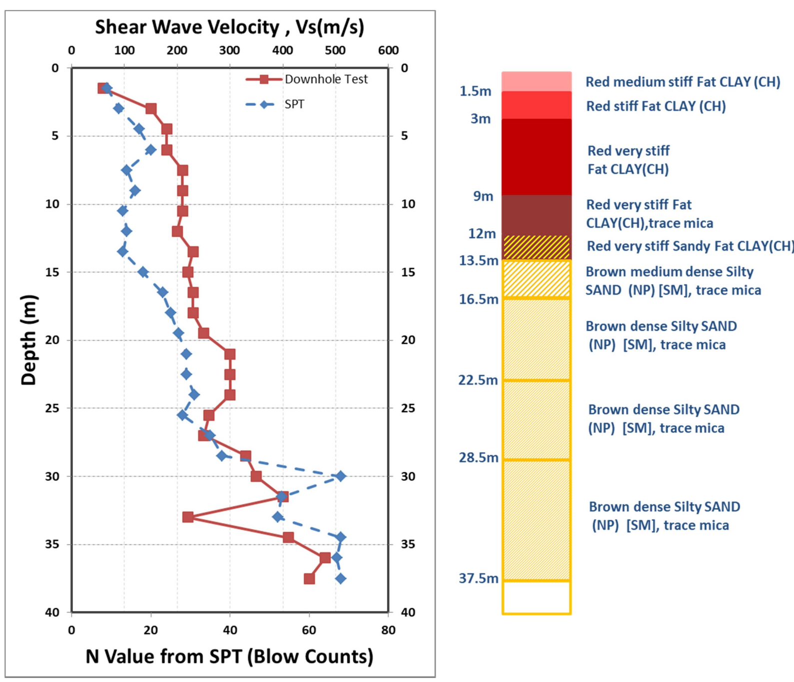

Fig. 1 . A sample set of SPT and downhole test results along with soil description in DMDP Area

Fig. 2 shows the data statistics for sand, clay, and all soils. Considering all soil type data, it is found that 75% of the values of N fall below 40, maximum data point is around 400 and minimum data point is 1. The median in the mid-point of the box implies symmetric or normal distribution. The interquartile range is 15-40. For clay, data is left skewed or negatively skewed but for sand, data is symmetric for SPT-N values. In case of clay interquartile range is around 8-20 whereas in case of sand it is 20-50 which indicates for sand layers higher SPT-N value was found. Also, N for sand is more dispersed than clay.

In case of all type of soils shear wave velocity data, it is observed to be negatively skewed and 75% of the data falls below 300. Maximum value found is around 750 and minimum value found is around 15. For clay, V_s data is observed to be symmetric and interquartile range is 150-300 whereas for sand it is 200-350 and data is negatively skewed. So, we can state that dispersion of V_s data is almost similar for clay and sand soil.

Geological Review of the Study Area

Our research focus is the DMDP area, which comprises Dhaka, Gazipur, Narayanganj, and Narshingdi districts. It covers approximately 1530 square kilometers in total, and it is evident that the greater the number of data points, the more accurate and dependable the output. The geomorphologic map of the DMDP area is depicted in Fig. 3.

The area is level topographically, with elevations ranging from 1 to 14 meters. The majority of metropolitan areas are located anywhere between 6 and 8 meters above sea level[26]. Dhaka is at high risk when it comes to earthquake sensitivity. The city is located between the Eurasian and the Indian Plates, next to the seismically active convergent plate boundary [27, 28]. The city and its environs were covered by two distinct geologic units, namely current alluvial deposits and Pleistocene Madhupur Clay. The principal geomorphic units are floodplains, abandoned canals, depressions, and the Dhaka terrace, or high land. Other significant topographic characteristics are low-lying swamps and marshes found throughout the DMDP area.

For describing the reliance of a response variable on a number of independent factors, regression analysis is one of the most popular methods [29, 30]. Every time we want to model the link between one response variable and more than one regressor variable, we employ multiple linear regression analysis[31].

According to [32] mathematically Multiple Linear Regression can be defined as a regression analysis where independent variable Y linearly depends on many independent variables $X_1, X_2, \ldots, X_k$

The form of a multiple linear regression can be as below:

$$Y = f(X_1, X_2, \dots \dots, X_k)$$

Here $f(X_1, X_2, \dots \dots, X_k)$ is a linear function of $X_1, X_2, \dots \dots, X_k$.

According to [33] the model formulation, assumption and least square estimation can be known

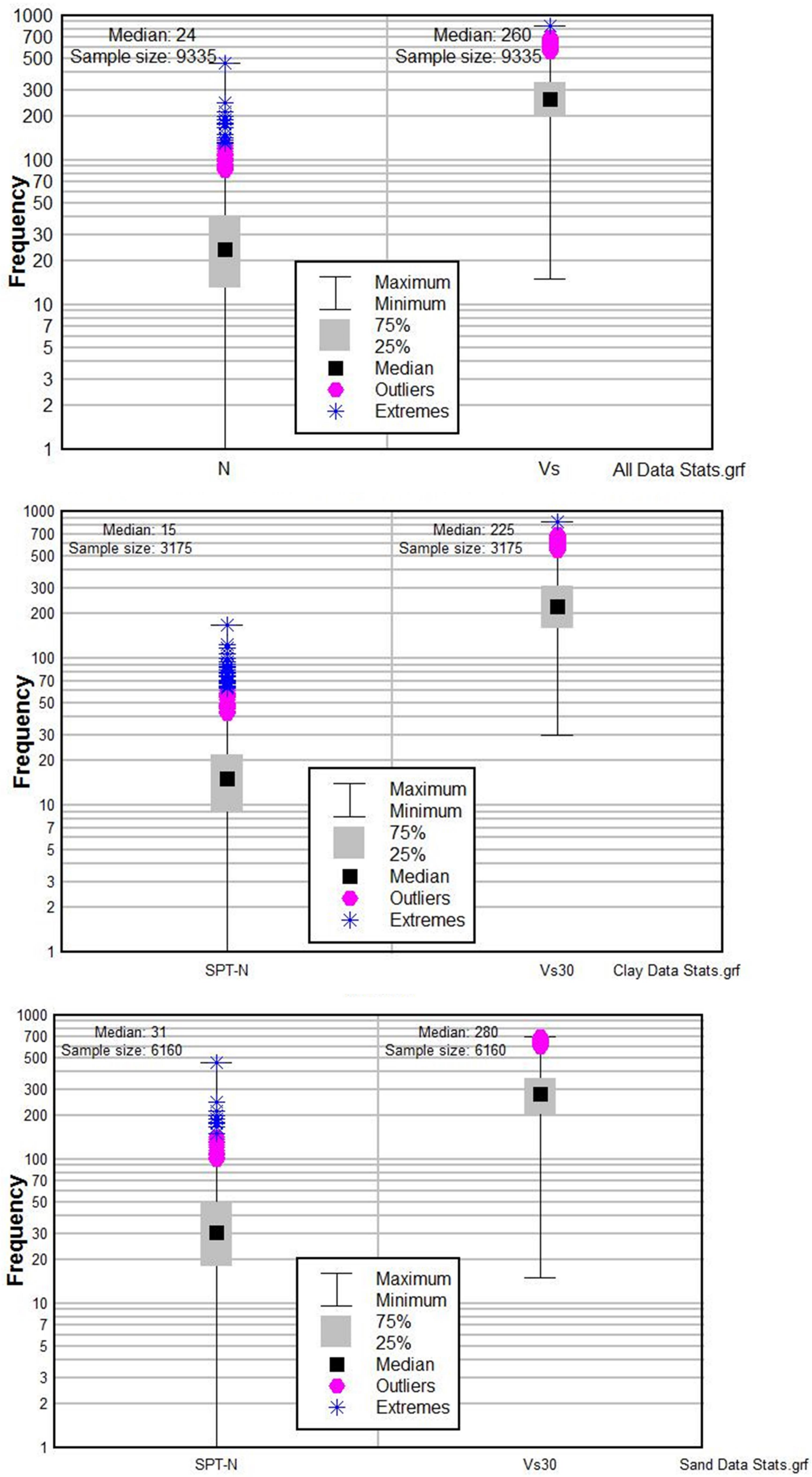

Fig. 2: Data statistics, showing minimum, maximum, and mean for sand, clay and all data

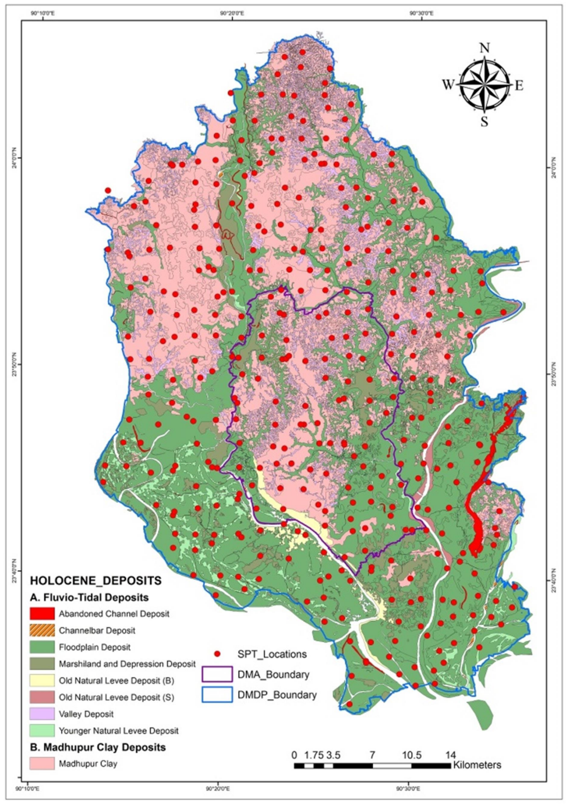

Fig. 3 Locations of downhole/SPT tests performed in the DMDP area

Mathematical Theory: Multiple Regression Analysis and Non-linear Regression Analysis

Assuming *p explanatory variables* $X_1, X_2, \dots \dots, X_p$ that will be related to a dependent variable Y. Assuming the data matrix derived from sample of n observations$(x_{i1}, x_{i2}, \dots \dots, x_{ip}, y_i)$, $i = 1,2, \dots \dots, n$, or equivalent to an $n \times (p+1)$ data matrix.

It is assumed that the (p+1) random variables will satisfy the following linear model

$$y_i = \beta_0 + \beta_1 x_{i1} + \beta_2 x_{i2} + \cdots + \beta_p x_{ip} + u_i \qquad i = 1,2, \dots, n$$

Here

1. The $u_{1,}$ $i = 1,2, \dots, n$ are the values of unobserved error term U and are identically distributed and mutually independent
2. The unknown parameters namely $\beta_0, \beta_1, \beta_2, \dots\dots, \beta_p$ are constants

Now a sample of n no. of observations on Y and $X_1, X_2, \dots \dots, X_p$ forms a $[n \times (p+1)]$ data matrix. The n equations provide equations linking the n observations.

$$y_1 = \beta_0 + \beta_1 x_{11} + \beta_2 x_{12} + \cdots + \beta_p x_{1p} + u_1$$

$$y_2 = \beta_0 + \beta_1 x_{21} + \beta_2 x_{22} + \cdots + \beta_p x_{2p} + u_2$$

.

$$y_n = \beta_0 + \beta_1 x_{n1} + \beta_2 x_{n2} + \cdots + \beta_p x_{np} + u_n$$

This set of n equations can be expressed as follows using matrix notation:

$$\boldsymbol{y} = \boldsymbol{X\beta} + \boldsymbol{u},$$

Where:

$$y = \begin{bmatrix} y_1 \\ y_2 \\ \vdots \\ y_n \end{bmatrix}_{(n\times 1)} ; \begin{bmatrix} 1 & x_{11} & x_{12} \cdots x_{1p} \\ 1 & x_{21} & x_{22} \cdots x_{2p} \\ \vdots & & \\ 1 & x_{n1} & x_{n1} \cdots x_{np} \end{bmatrix}_{n\times(p+1)} ;$$

$$\beta = \begin{bmatrix} \beta_0 \\ \beta_1 \\ \beta_2 \\ \vdots \\ \beta_p \end{bmatrix}_{(p+1)\times 1} \text{; and}$$

$$u = \begin{bmatrix} u_1 \\ u_2 \\ \vdots \\ u_n \end{bmatrix}_{(n\times 1)}$$

Starting from the model we can obtain the estimation of $\hat{\beta}$ of the β vector by means of the least-square technique [32]

[33] has explained the method of obtaining $\hat{\beta}$ by using least square procedure, that minimizes the sum of squares given by

$$\zeta^2 = \sum_{i=1}^{n} \left(y_i - \beta_0 - \beta_1 x_{i1} - \beta_2 x_{i2} - \cdots - \beta_p x_{ip}\right)^2 = (y - X\beta)'(y - X\beta)$$

After utilizing calculus the resulting equation for β can be given by the following normal equation written in matrix notation

$$X'y = X'X\beta$$

Where:

$$X'y = \begin{bmatrix} \sum_{i=1}^{n} y_i \\ \sum_{i=1}^{n} x_{i1} y_i \\ \sum_{i=1}^{n} x_{i2} y_i \\ \vdots \\ \sum_{i=1}^{n} x_{ip} y_i \end{bmatrix}_{(p+1)\times 1}$$

$$X'X = \begin{bmatrix} n & \sum_{i=1}^{n} x_{i1} & \sum_{i=1}^{n} x_{i2} & \cdots & \sum_{i=1}^{n} x_{ip} \\ \sum_{i=1}^{n} x_{i1} & \sum_{i=1}^{n} x_{i1}^2 & \sum_{i=1}^{n} x_{i1}x_{i2} & & \sum_{i=1}^{n} x_{i1}x_{ip} \\ \sum_{i=1}^{n} x_{i2} & \sum_{i=1}^{n} x_{i1}x_{i2} & \sum_{i=1}^{n} x_{i2}^2 & & \sum_{i=1}^{n} x_{i2}x_{ip} \\ \vdots & \vdots & \vdots & & \vdots \\ \sum_{i=1}^{n} x_{ip} & \sum_{i=1}^{n} x_{i1}x_{ip} & \sum_{i=1}^{n} x_{i2}x_{ip} & \cdots & \sum_{i=1}^{n} x_{ip}^2 \end{bmatrix}_{(p+1)\times(p+1)}$$

Where the solution vector for the abovementioned normal equations is

$$\hat{\beta} = (X'X)^{-1}X'y$$

The fitted model after obtaining $\hat{\beta}$ can be written as

$$\hat{y} = X.\hat{\beta}$$

And residuals denoted by vector e can be written as

$$e = y - \hat{y}$$

The error sum of squares or SSE is

$$\sum_{i=1}^{n}(y_i - \hat{y}_i)^2 = (y - X\hat{\beta})'(y - X\hat{\beta})$$

And the total sum of squares SST is

$$\sum_{i=1}^{n}(y_i - \bar{y})^2$$

This value defines the total variation in y based on one or multiple x variables.The ration of the SSR and SST value is coefficient of multiple determination and is denoted by R^2 [33]We can also derive the adjusted R^2 value.

The regression sum of squares SSR can be defined as follows

$$\sum_{i=1}^{n}(\hat{y}_i - \bar{y})^2$$

An F-test in an analysis of variance (ANOVA) format can be used to evaluate the model's overall goodness of fit[33]. It assists in testing the null hypothesis thatH_0: $\beta_1 = \beta_2 = \cdots = \beta_p = 0$. Under this hypothesis, the statistic MSR/MSE has an F distribution having p and n-p-1 degrees of freedom[32, 33]

Table 2 Analysis of Variancs or ANOVA table for Multiple Regression[33]

Source	d.f	Sum of Squares	Mean Square	F
Regression	p	SSR	MSR=SSR/ p	MSR/MSE
Error	n-p-1	SSE	MSE=SSE/ n-p-1	
Total	n-1	SST		

In nonlinear regression, observational data are represented by a function that depends on one or more independent variables and is a nonlinear combination of the model parameters[29].Nonlinear regression may estimate models with arbitrary relationships between independent and dependent variables, in contrast to classic linear regression, which can only estimate linear models[29].

The general form of a nonlinear regression given by Yaser et al. [29] is as followed

$$Y = \alpha_0(X_1^{\alpha_1})(X_2^{\alpha_2}) \ldots (X_n^{\alpha_n})$$

Here, $\alpha_0 - \alpha_n$ are the equation parameters for the relation.

Yaser et al. [29] has incorporated a method of moving nonlinear regression problems to a linear domain utilizing an appropriate transformation of the model formulation which is as followed

Taking the log of the aforementioned equation we get a linear relationship

$$\log(Y) = \log(\alpha_0) + \alpha_1\log(X_1) + \alpha_2\log(X_2) + \cdots + \alpha_n\log(X_n)$$

And thus regression of $\log(Y)$ on $\log(X_1), \log(X_2),\ldots, \log(X_n)$ can be used to assess the α_0, $\alpha_{1\ldots}$ α_n [29, 34]

Regression of the empirical equation/Data Analysis Process

The majority of researchers predicted that V_s had a power-law relationship with either the depth or the in situ penetration test result N[8]. According to Kuo et al.[8], the most accurate regression model can be determined by the greatest value of correlation coefficient or R between V_s and depth or N. To minimize the problem of multicollinearity, some statisticians advocated for a "rule of thumb" method where the correlation coefficient R between any two variables ought not to exceed 0. 70 [7, 8].

When all of the variables are metric, or can be expressed as numbers, a simple multivariate analysis can be used easily [3]. Initially, SPT N-value, the shear wave velocity, and depth value have been plotted on a logarithmic graph (Fig. 4) in order to understand the nature of the data and to obtain a useful link between shear wave velocity and individual index.

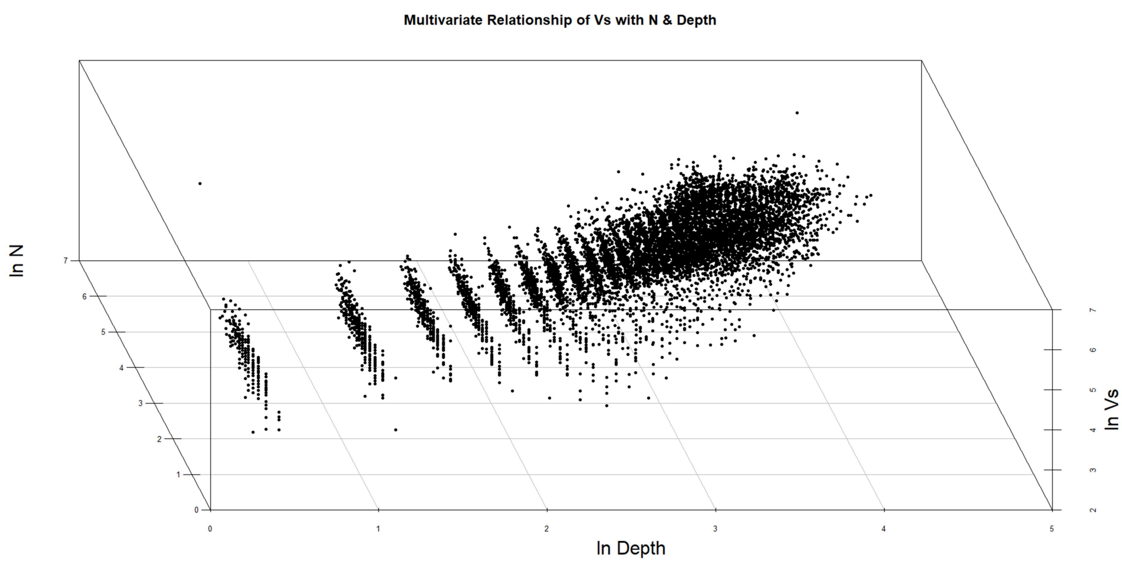

Fig. 4 Visualizing relation of SPT N-value, shear wave velocity (V_s) and depth

We have hypothesized a nonlinear regression relationship between response variable shear wave velocity (V_s) and two regressor variables Depth (D) and SPT blow counts (N) . We adopted the methodology mentioned in [29] and brought the logarithms of the variable to a linear domain to establish a multiple linear regression relationship among the response and regressor variable and by means of inverse calculation established the nonlinear regression equation correlating V_s with D & N.

By inspection of the graph and regression analysis, the we have hypothesized a linear relation between log V_s and log N using 9334 data points for all types of soil, and the least squares curve obtained this way is as follows:

$$ln\, V_s = 4.1442093 + 0.3597551\, ln\, D + 0.1194517\, ln\, N \qquad (1)$$

This is equivalent to $V_s = 63.068 * D^{0.3597551} * N^{0.1194517}$ (m/s). In Equation (1), the R^2 value is 0.7171. In the same process the multiple regression equations for the soil of DMDP area based on soil type are as follows

For sand $$V_s = 59.61 * D^{0.320568344} * N^{0.165197956} \qquad (2)$$

For clay $$V_s = 63.29 * D^{0.382881786} * N^{0.111205452} \qquad (3)$$

Fig. **5** demonstrates the summary of the regression analysis performed on the dataset for all types of soil, sand and clay respectively including the value of equation parameters, R square value and ANOVA table mentioned in **Table 2**

SUMMARY OUTPUT

Regression Statistics	
Multiple R	0.8467889
R Square	0.7170515
Adjusted R Square	0.7169908
Standard Error	0.2452383
Observations	9335

ANOVA

	df	*SS*	*MS*	*F*	*Significance F*
Regression	2	1422.3092	711.155	11824.6	0
Residual	9332	561.2433	0.06014		
Total	9334	1983.5525			

	Coefficients	*Standard Error*	*t Stat*	*P-value*	*Lower 95%*	*Upper 95%*	*Lower 95.0%*	*Upper 95.0%*
Intercept	4.1442093	0.0095613	433.434	0	4.125466992	4.16295159	4.12546699	4.16295159
ln Depth	0.3597551	0.0045281	79.4496	0	0.350879014	0.36863111	0.35087901	0.368631107
ln N	0.1194517	0.0043425	27.5073	3E-160	0.110939413	0.12796408	0.11093941	0.127964082

SUMMARY OUTPUT

Regression Statistics	
Multiple R	0.827288088
R Square	0.68440558
Adjusted R Square	0.684303065
Standard Error	0.239394176
Observations	6160

ANOVA

	df	*SS*	*MS*	*F*	*Significance F*
Regression	2	765.2098	382.6049	6676.108	0
Residual	6157	352.855	0.05731		
Total	6159	1118.065			

	Coefficients	*Standard Error*	*t Stat*	*P-value*	*Lower 95%*	*Upper 95%*	*Lower 95.0%*	*Upper 95.0%*
Intercept	4.087906583	0.013371	305.729	0	4.061694729	4.114118	4.061695	4.114118
ln Depth	0.320568344	0.007216	44.42429	0	0.306422344	0.334714	0.306422	0.334714
ln N	0.165197956	0.006391	25.84715	6.1E-140	0.152668696	0.177727	0.152669	0.177727

SUMMARY OUTPUT

Regression Statistics	
Multiple R	0.86184082
R Square	0.742769599
Adjusted R Square	0.74260741
Standard Error	0.249327695
Observations	3175

ANOVA

	df	*SS*	*MS*	*F*	*Significance F*
Regression	2	569.385	284.6925	4579.679	0
Residual	3172	197.1852	0.062164		
Total	3174	766.5702			

	Coefficients	*Standard Error*	*t Stat*	*P-value*	*Lower 95%*	*Upper 95%*	*Lower 95.0%*	*Upper 95.0%*
Intercept	4.147738112	0.015476	268.0024	0	4.117393163	4.178083	4.117393	4.178083
ln Depth	0.382881786	0.005824	65.73924	0	0.371462107	0.394301	0.371462	0.394301
ln N	0.111205452	0.006967	15.96284	3.11E-55	0.097546114	0.124865	0.097546	0.124865

Fig. 5 Summary of Regression analysis of all type of soil, sandy soil and clayey soil respectively performed in Excel's Data Analysis Toolpack

In Equations (2) and (3), the R^2 values are 0.6844 and 0.7428 as well as the standard errors are 0.239394176 and 0.249327695, respectively. The three dimensional plots of the above three equations are presented in Fig. 6.

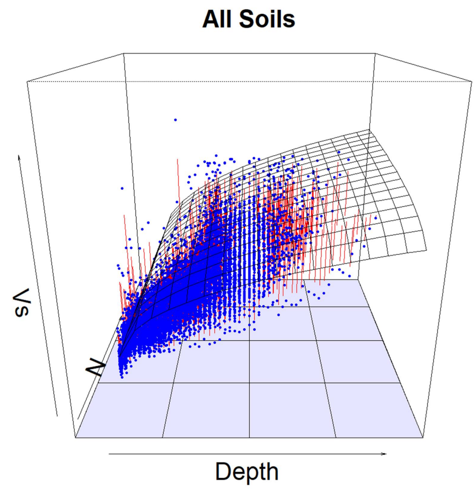

(a)

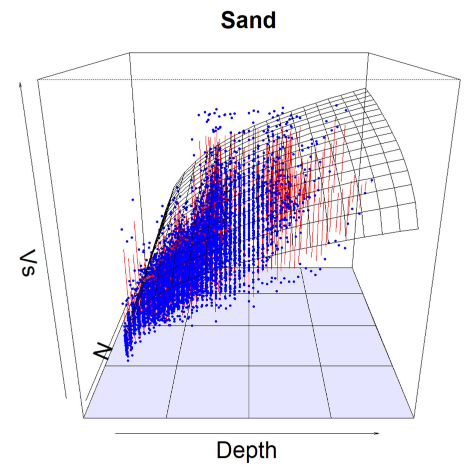

(b)

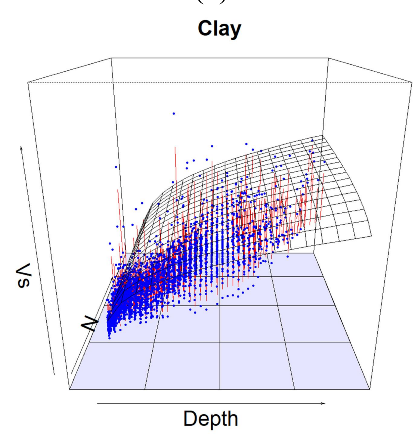

(c)

Fig. 6 Three-dimensional illustrations of regression equations and data sets for DMDP area

Validation of the Proposed Equation

The regression outcomes in this investigation are within the range suggested by previous researches. The R^2 value obtained in multi-regression equation is the largest among other combinations. This complies with the conclusion of Lee [7] that according to the theoretical basis of shear wave velocity, $V_s = aN^bD^c$ has a specific physical meaning and also has the highest R^2 value. All the correlation models developed in this study with R^2 are presented in Table 3.

Table 3 Regression Equations established in the current study

Soil Type	Equation Type	R^2
All soils	$V_s = aN^b$	0.5257
Sand		0.5832
Clay		0.3923
All soils	$V_s = aD^b$	0.6941
Sand		0.6502
Clay		0.7221
All soils	$V_s = aN^bD^c$	0.7171
Sand		0.6844
Clay		0.7428

Besides it has been discovered by Ohta and Goto [3] and by Lee [22] that instead of "N-value", "depth" is the most important parameter in a regression equation if the geologic effect and soil types are taken into account first in the regression equation. It also overcomes one disadvantage of using intrinsically linear regression with depth (D). In this case, a multiple regression equation without the multi-collinearity problem will be advantageous [7]. The above table clearly shows that the hypothesis of Ohta and Goto and Lee is correct.

From statistical point of view we can further validate our equation by means of *F-test* in the ANOVA table presented in Fig. **5** .As mentioned before F-test is used to evaluate the goodness of fit of a model[33].As per [32] it allows us to test the null hypothesis which is

$$H_0 = \beta_1 = \beta_2 = \cdots = \beta_p = 0$$

against the alternative hypothesis:

$$H_1\colon at\ least\ one\ of\ the\ parameters\ \beta_1, \beta_2, \ldots, \beta_p\ is\ different\ from\ zero$$

In a regression model, significance F represents the probability that the null hypothesis cannot be rejected.

In the ANOVA table the *Significance F* represents the p-value for the F-test that determines whether our model's ability to explain the variability of the dependent variable is better than that of a model with no independent variables when all of our model's independent variables are taken into account. Since our p-value is smaller than any possible value of significance level we can say that we obtained a statistically significant regression model.

Conclusions

This paper has attempted to establish a depth and SPT-N based empirical equation of shear wave velocity in the DMDP area of Bangladesh by means of multiple regression analysis. It has been found that multiple regression model yields higher value of R^2 than one variable regression equation and overcomes the disadvantage of one variable regression equations. This paper has also produced a three dimensional diagram of regression equation including a regression plane.

BANGLADESH NETWORK
OFFICE FOR URBAN SAFETY

PART-X

EFFECT OF SURCHARGE PRESSURE ON MODEL GEOTEXTILE WRAPPED-FACE WALL UNDER SEISMIC CONDITION

BANGLADESH NETWORK OFFICE FOR URBAN SAFETY (BNUS), BUET, DHAKA

Prepared By: Ripon Hore

Mehedi Ahmed Ansary

1. Introduction

It is about four decades since the construction of first geosynthetic reinforced soil (GRS) wall and it is now established as an adaptable soil retention technique (Latha & Manju 2016). The GRS walls have several beneficial effects such as-saving in cost ease of construction, better performance under seismic loads (Tafreshi et al., 2015; Hegde & Sitharam 2015), design flexibility, capacity to sustain large deformations without structural distress and aesthetics made them suitable for a variety of geotechnical engineering applications (Latha & Manju 2016). Over the year's extensive research were carried out on stability and performance of GRS and reinforce soil (RS) walls under different seismic events, for which a summary review is provided in this section.

Seismic effect on soil structures assumed a significant part in the area of earthquake geotechnical engineering and was discovered impressive turn of events in the recent past. In this exploration, a wrap reinforced soil wall was fabricated on clay soil enclosed by a laminar box and subjected to sinusoidal input motions through the shake table. In view of shaking table tests, this study aims to explore the impact of surcharge on wrap faced geotextile reinforced sand wall. The outcomes from this examination give helpful rules with respect to the relative performance of reinforced soil under different test conditions with clear ramifications for plan. Hatami et al. (2005) carried out parametric studies on model reinforced soil retaining walls with a wide range of geometrical and material properties. Ling et al. (2005) reported full-scale shaking table tests and observed that reinforcement spacing and the length of the top reinforcement layer each had a significant influence on measured facing deformation. Chakraborty et al. (2021) and Hore et al. (2020) conducted small scale shaking table tests to evaluate the response GRS walls under sinusoidal loading. Ehrlich et al. (2012) conducted full-scale model tests on two walls and evaluated the influence of backfill compaction on the measured reinforcement load. They showed that increased compaction effort could help reduce the reinforcement connection loads and facing deformations resulting from surcharge loads following construction. Ertugrul & Trandafir (2013) proved lightweight deformable geofoam can reduce the earth pressure on the retaining wall. Bilgin & Mansour (2014) observed that reinforcement type (e.g., geogrids, geotextiles, metal strips, and metal bar mats) can affect both the required reinforcement length and governing design criteria.

Latha & Santhanakumar (2015) observed that denser backfill and reinforcement layers improved the seismic performance of walls with modular facing significantly more than those with the full-height panel facing. Panah et al. (2015) conducted shaking table tests on reinforced soil retaining walls with polymeric strips and investigated the effect of the length of reinforcement, the number of steps and shape of the reinforcement arrangement on the failure mode, the wall displacement, and the acceleration amplification factor, respectively. Wang et al. (2015) performed a large-scale shaking table tests of geogrid reinforced rigid retaining walls and observed that geogrid layers can decrease the development of excess pore water pressures and accelerate the dissipation of excess pore water pressures. Chaudhary et al. (2016) performed a numerical analysis of reinforced soil retaining walls using FLAC and observed that the reinforcement affects the earth pressure as well as lateral displacement of the retaining wall significantly.

Yazdandoust (2017; 2018) carried out a series of 1-g shaking table tests was to investigate the influence of the peak acceleration, the loading duration, and the strip length on the dynamic behaviour of steel-strip reinforced soil walls (SSWs). Huang (2019) performed shaking table tests on geosynthetic-reinforced walls with a height of H=0.6 m and described that maximum tensile forces induced by shaking increase as the depth of reinforcement increases, generating a trapezoidal shape rather than the inverted trapezoidal shape.

Goktepe et al. (2019) studied numerical and experimental research on scaled soil-structure model for small shaking table tests and the structural behaviour is significantly affected by the frequency content of the earthquakes considered in the soil-structure interaction (SSI) problem. Gidday & Mittal (2020) and Hore et al. (2021a, b) conducted shaking table tests on geotextile wrap faced reinforced soil walls and compared with the numerical results done by PLAXIS software. They observed that, vertical crest settlement and horizontal displacement of reinforced soil wall decrease with an increase in reinforcing layers. Xu et al. (2020) conducted two shaking table tests on a full-height panel and modular block reinforced soil retaining wall models in order to examine the influence of facing type on the connected loads in the two models.

This paper describes, the results from twenty-four shaking table tests on geotextile wrap faced reinforced soil retaining wall models, where the soil wall is resting on soft clayey soil foundations. Sinusoidal harmonic motions were applied to the model; with different surcharge pressure, frequency of shaking, and base acceleration, respectively. This research paper mainly highlights the surcharge pressure effect on model walls for evaluating the reinforced wall response and foundation soil at higher depths (higher vertical stress) under cyclic loadings. Varied surcharge pressure was used on the model wall to evaluate the cyclic behaviour of reinforced wall and foundation at same wall height. Different surcharge pressure conditions were used in the tests not as a procedure to simulate different wall heights but to evaluate the response of each slice of reinforced sand wall. Moreover, the impact of surcharge was evaluated for different conditions of frequency and acceleration, face displacements and pore water pressures were also discussed.

2. Equipment and materials

A computer-controlled servo-hydraulic single degree of freedom shaking table facility was used to simulate the horizontal shaking action, associated with seismic and other vibration conditions. The testing platform is a square type, having 2 m×2 m dimension and approximate payload capacity of 1000 kg, which was made from steel plates. The shaking table can be operated over an acceleration range of 0.05g to 2g and frequency range 0.05 to 50 Hz with a maximum amplitude of ±200 mm. Maximum velocities are 0.3 m/s.

The ideal container is one that gives a seismic response of the soil model identical to that obtained in the prototype. The laminar shear box developed at Bangladesh University of Engineering Technology (BUET) has consisted of 24 hollow aluminium layers of frames as shown in Figure 1. Each layer consists of an inner frame with inside dimensions of 915 mm × 1220 mm × 1220 mm. The aluminium alloy is adopted for its sufficient strength and rigidity, and it's lightweight to minimize the effect of the inertia of the frame on the soil movements. The gap between the successive layers is 2 mm. The layers are separated by linear roller bearings arranged to permit relative movement between the layers in the longitudinal direction with minimum friction.

In this study, Dhaka clay has been reconstituted by thoroughly mixing the oven dried clay powder with an initial water content equal to the LL—a procedure described by Burland (1990). The thorough mixing of the slurry has been attained with the aid of a 'Hobart' rotary mixer. With this slurry, a 300 mm thick reconstituted clay layer has been constructed within the laminar shear box; and then one-dimensional consolidation were carried out under the drained condition at loads: 15kPa, 20kPa, 25kPa, 30kPa, 40kPa, 60kPa, 80kPa, and 100kPa. The consolidation process has been observed through the settlement versus time graph, plotted with the aid of calibrated mechanical dial gauges, instrumented on either side of the laminar shear box. A model soil with appropriately scaled stiffness and strength properties was developed for the project and consisted of 75% kaolinite, 25% Illite (by weight). The model soil has a unit weight of 14.8 kN/m3, a specific gravity of 2.64, undrained shear strength of 28 kPa, and ultimate bearing capacity of 17.20 kPa. Undrained shear strength was determined by Unconsolidated Undrain (UU) test. The ultimate bearing capacity was determined from CPT test result by following (Meyerhof 1956) method. The water content (*w %*) of the collected reconstituted Clay samples have been determined to be 27%. Average liquid limit (LL) and plastic limit (PL) were established to be 41% and 16%, respectively. It was observed that the

PL points located above the A-line defined by PI = 0.73(LL-20), where PI is the plasticity index. The soil was defined as Lean Clay (CL), as per as USCS. Locally available dry sand (called as Sylhet) was used as the backfill material. Figure 2 shows the particle size distribution of the sands. The sand is classified as poorly graded sand (*SP*) according to the Unified Soil Classification System. General Geotechnical properties of the sands are presented in Table 1.

A woven polypropylene multifilament geotextile (*DF50*) was used for reinforcing the sand in the tests. Here in *DF50*, *DF* stands for Dart Felt. The individual multifilament is woven together so as to provide dimensional stability relative to each other. The ideal container is one that gives a seismic response of the soil model identical to that obtained in the prototype. The boundary conditions created by the model container walls have to be considered carefully, otherwise the field conditions cannot be simulated properly. In this study, embankment with soft Clay soil models was constructed in a laminar box to reduce boundary effects as far as practicable. The boundary conditions for physical modelling in problems of earthquake geotechnical engineering have a significant influence on the test results. In order to reduce the undesirable effects of boundaries on the model responses, the laminar shear boxes are used. In laminar shear boxes, the stiffness of the walls is proportional to the stiffness of soil. For increasing the flexibility of the box walls, depending on soil type, model dimensions and the studied phenomena, setting each layer on the other, within the frame made of rigid light material which can easily move on each other. The tensile strength of the geotextile was determined by the wide-width strip method (ASTM D4595) as 15.5 kN/m.

Table 1. Geotechnical properties of Sylhet Sand

Physical properties	Sylhet sand
Coefficient of uniformity (C_u)	2.00
Coefficient of curvature (C_c)	0.95
Effective size, D_{10} (mm)	0.400
Average size, D_{50} (mm)	0.7
Specific gravity (G_s)	2.65
Maximum dry density (kN/m^3)	16.4
Minimum dry density (kN/m^3)	13.494
Relative density (*Dr%*)	48
Friction angle (°)	31
Void ratio	0.524
Fineness modulus (*FM*)	2.63
USCS soil classification	SP

Figure 1. Laminar box mounted on the shake table.

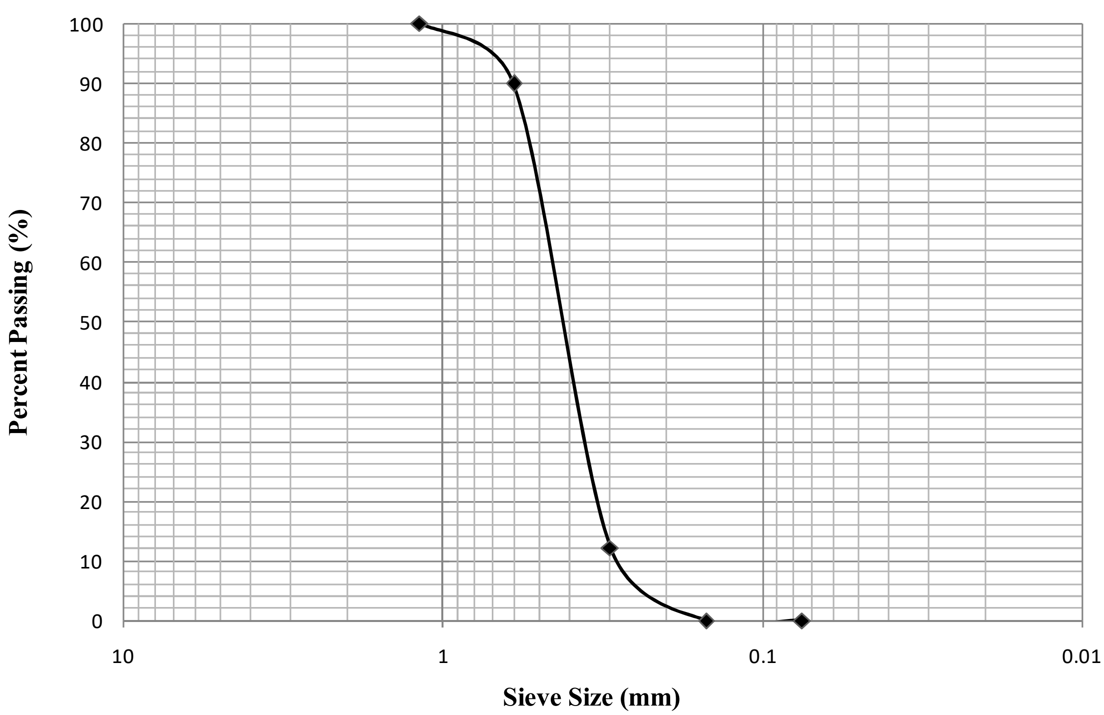

Figure 2. Particle size distribution curve of the Sylhet sand.

3. Testing process

One of the complications with laboratory tests, especially dynamic laboratory tests, is scale modelling. Several approaches were considered to size the model walls by different researchers over the years. One such scaling law was proposed by Kokusho (1980) and Yu & Richart (1984) wherein a reinforcement ratio is calculated based on the properties of the geotextile and the stresses and strains in the soil were considered for this study. Table 2 presents the scaling factors for this study, assuming $\alpha = 0.5$ (Kokusho 1980 and Yu & Richart 1984) for sand and considering the prototype to model scale being $N = 10$.

Table 2. Prototype-Model Similitude (Sabermahani et al., 2009)

Description	Parameter	Scale factor	Scale factor *M/P*	Scale factor *P/M*
Acceleration	*A*	1	1	1
Density	*P*	1	1	1
Length	*L*	$1/N$	0.10	10
Stress	*Σ*	$1/N$	0.10	10
Strain	*G*	$1/N^{1-\alpha}$	0.32	3.125
Stiffness	*G*	$1/N^{\alpha}$	0.32	3.125
Displacement	*D*	$1/N^{2-\alpha}$	0.031	32.25
Frequency	*F*	$N^{1-\alpha/2}$	5.62	0.18
Force	*F*	$1/N^{3}$	0.001	1000
Force/L	*F/L*	$1/N^{2}$	0.01	100
Shear Wave velocity	V_s	$1/N^{\alpha/2}$	0.56	1.785
Time	*T*	$1/N^{1-\alpha/2}$	0.178	5.62

***P*-Prototype; *M*-Model**

This paper describes, the results from twenty-four shaking table tests on geotextile wrap faced reinforced soil retaining wall models, where the soil wall is resting on soft clayey soil foundations. Sinusoidal harmonic motions were applied to the model; with different surcharge pressure, frequency of shaking, and base acceleration, respectively. The model embankment was constructed in a laminar box and each geotextile wrapped sand slice had the equal height of 100 mm. In this study, a portable traveling pluviator developed and calibrated by Hossain & Ansary (2018) at BUET, was operated to maintain the corresponding relative density of sand layer at 48%, 64% and 80% for Sylhet sand and 27%, 41% and 55% for Local sand depending on height of fall of the soil. We have compared Sylhet Sand (48%) and Local Sand (41%). In this research, used 60% relative density as sample based. To achieve uniform relative density (*Dr*), sand was placed in the laminar box using the pluviation (raining) technique. In this study

60% relative density was maintained for construction of the all models. As indicated in Figure 3, the surcharge load was also applied to the backfill material. Surcharge pressure values were taken as close to the study of Krishna & Latha (2007) for comparing the result. Surcharge pressure height in prototype to mode scale was not considered. In this study a concrete block was used as surcharge pressure. The height of the concrete block was constant in all three different conditions but the length and width of the concrete block was varied. Accelerometers (A1, A2, A3, A4, A5 and A6) were used to monitor the accelerations of the shaking table and the soil along with a vertical array. The LVDT transducers were employed to monitor the displacements of the sand model wall in the horizontal direction. Two Pore water pressure sensors were placed in the clayey soil layer to determine the excess pore pressure response. 11 data channels were used in total. In details, sensors arrangement and model configuration are presented in Fig.3 and Fig.4.

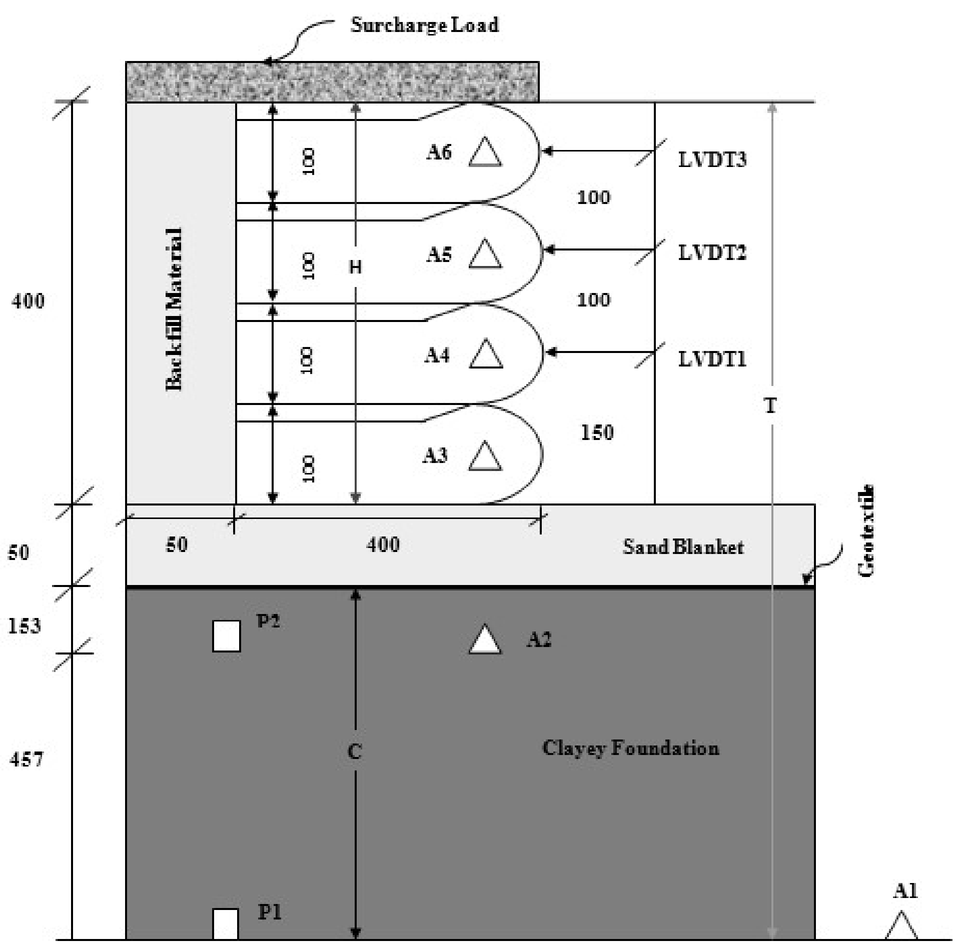

Figure 3. Schematic diagram of typical test wall configuration and instrumentation. (All the dimensions are in mm)

Figure 4. Completed test set-up.

4. Results and discussions

For each test, the horizontal accelerations were applied with acceleration amplitudes of 0.1g, 0.2g, 0.3g, 0.4g and 0.5g for approximately 20 cycles. Effect of surcharge on the displacements, acceleration amplifications and pore pressure of geotextile wrap faced sand walls (*WFSW*) was studied through a series of tests on model walls as shown in Table 3. The frequency has been varied from 1 Hz, 3 Hz, 5 Hz, 10 Hz, 12 Hz, and 15 Hz, respectively. Reinforced-soil wall was constructed using sand upon the clayey soil layer in equal lifts (*Sv*) of 100 mm to achieve a total wall height (*H*) of 400 mm. The height of clayey soil and reinforced sand wall together (*T*) had been taken as the full model height is 1060 mm. Each shake was applied to the newly constructed individual model walls.

Table 3. Shaking table model test matrix.

Test Set	Test Code	Base Acceleration (g)	Frequency (Hz)	Surcharge Load (kPa)	Pore pressure ratio (*Pr*%)
Set-1	ST1	0.1	1	0.71	34.86
	ST31	0.1	1	1.12	22.09
	ST61	0.1	1	1.72	15.13
Set-2	ST2	0.1	3	0.71	33.08
	ST32	0.1	3	1.12	24.16

	ST62	0.1	3	1.72	17.19
Set-3	ST4	0.1	10	0.71	30.77
	ST34	0.1	10	1.12	20.11
	ST64	0.1	10	1.72	18.92
Set-4	ST-8	0.2	3	0.71	49.38
	ST-38	0.2	3	1.12	35.16
	ST-68	0.2	3	1.72	14.55
Set-5	ST-15	0.3	5	0.71	97.23
	ST-45	0.3	5	1.12	69.80
	ST-75	0.3	5	1.72	36.96
Set-6	ST-22	0.4	10	0.71	78.58
	ST-52	0.4	10	1.12	50.14
	ST-82	0.4	10	1.72	23.22
Set-7	ST-29	0.5	12	0.71	92.20
	ST-59	0.5	12	1.12	56.70
	ST89	0.5	12	1.72	29.68
Set-8	ST30	0.5	15	0.71	87.56
	ST60	0.5	15	1.12	59.78
	ST90	0.5	15	1.72	34.47

4.1 Acceleration response

Effect of surcharge on acceleration amplification was studied by subjecting the model to a horizontal shaking for each of the eight set. Results from set 1 are presented in Fig. 5 and 6. Results of reinforced sand wall from set 1 to 8 are presented in Fig 7.

Figure 5 represents the surcharge pressure effect both for sand and clayey layer altogether. In Figure 5 it is observed that in clayey soil layer at elevation z/T=0.43, for 0.7 kPa, 1.12 kPa and 1.72 kPa surcharge pressures (from ST1, ST31, and ST61 tests), the acceleration amplitude was 1.05, 1.02, and 1, respectively. Whereas, at elevation z/T=0.95 in the sand layer, amplitudes increased to 1.7, 1.55, and 1.42, for the same surcharge pressures respectively. In clayey soil layer acceleration amplified much less than reinforced sand layer. This has been constant in all the test result. The range of acceleration amplitude of clayey layer was in between 0.9 to 1.05 whereas the range of acceleration amplitude of reinforced sand wall was in between 1 to 1.92.

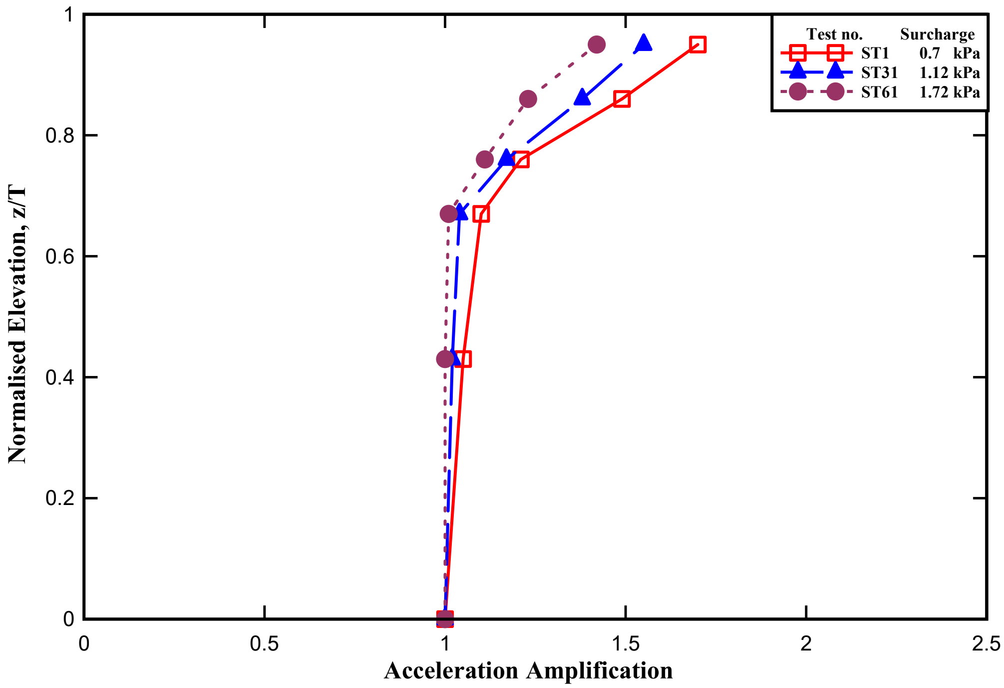

Figure 5. Effect of Surcharge on acceleration amplification for Set-4 configuration (both for *WFSW* and clayey layer).

Figure 6 represents a comparison between the present studies with the study of Krishna & Latha (2007) for the reinforced sand wall only. Acceleration response against different surcharge pressures in the model wall was presented from tests ST1, ST31 and ST61 of set-4. It is observed from the figure that, the acceleration amplification values at elevation *z/H*=0.875 were 1.7, 1.55 and 1.42 for 0.7 kPa, 1.12 kPa and, 1.72 kPa surcharge pressures respectively. Accelerations at the top of the wall were inversely proportional to the surcharge pressures for all the tests. This observation is in concurrence with the results of Krishna & Latha (2007).

From Figure 7(a) to 7(h) it can be seen that, at the top of the wall acceleration amplification is greater than any other elevation in all the test sets and also inversely proportional to the surcharge pressures only for the top of the wall at all the test sets.

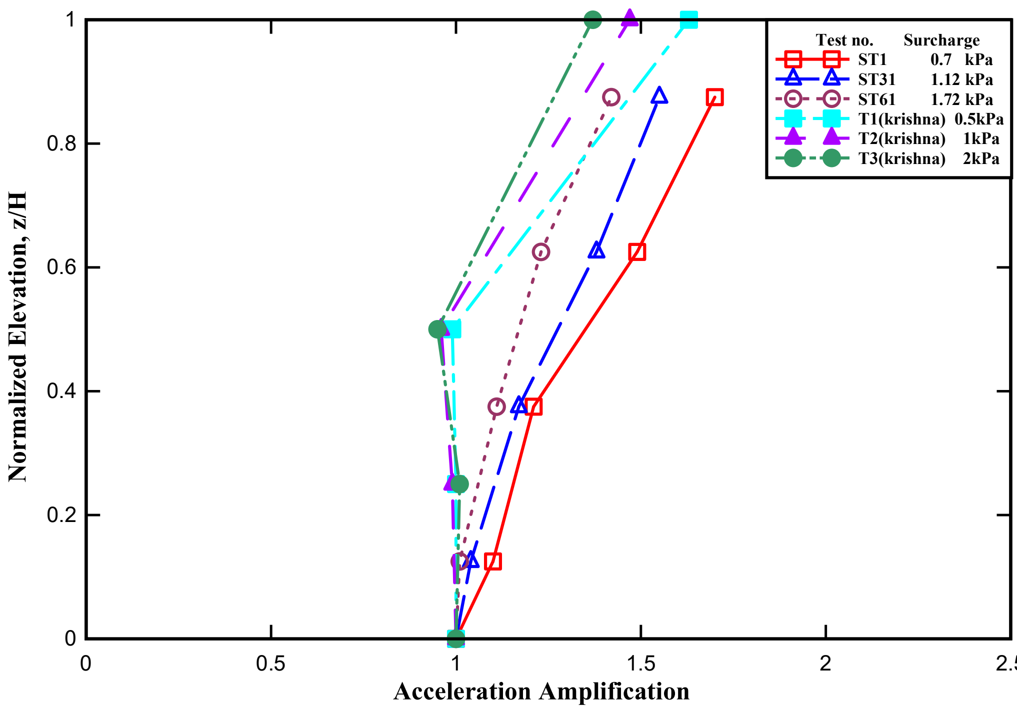

Figure 6. Effect of Surcharge on acceleration amplification for Set-4 configuration (only for *WFSW*)

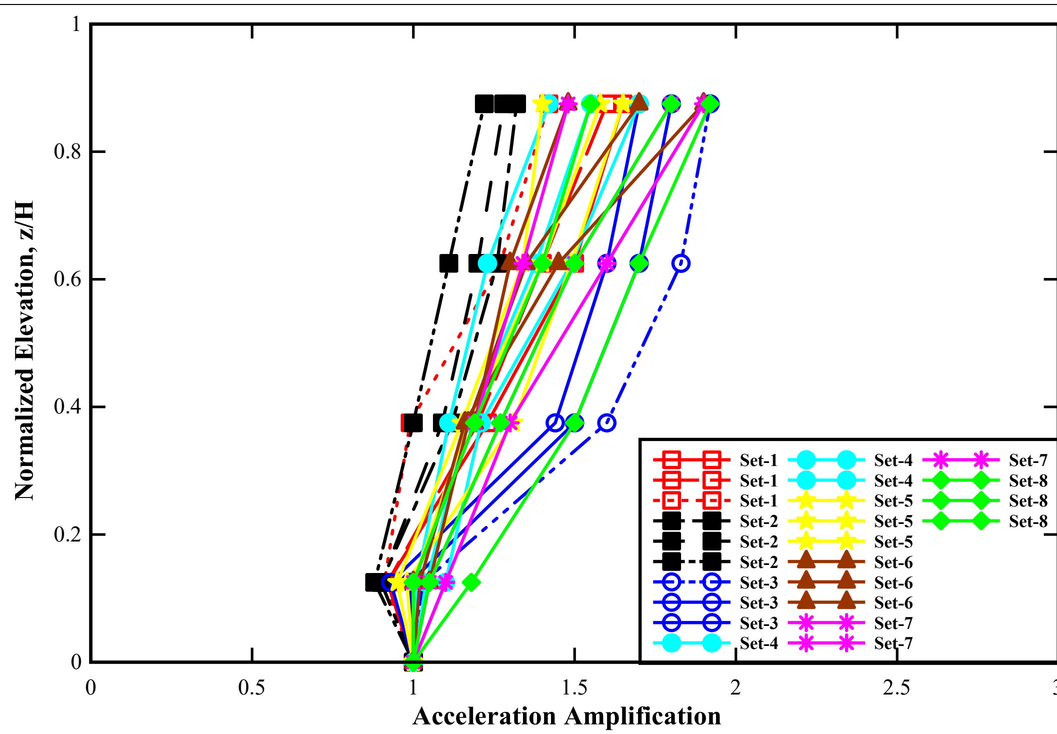

Figure 7. Effect of Surcharge on acceleration amplification (a) Set-1; (b) Set-2; (c) Set-3; (d) Set-4; (e) Set-5; (f) Set-6; (g) Set-7 and (h) Set-8 (only for *WFSW*)

4.2 Face displacement response

When the retaining walls are subjected to horizontal seismic shaking, they tend to slide or overturn. Since the thickness of facing, in this case, is sufficient to overcome the sliding movement at the base, deformations are seen only in terms of wall movement frontward. However, overall forward movement of the backfill and the active thrust of the backfill on the geotextile facing cause the wall to deform more at higher elevations. The results of face displacement response of all 8 sets are presented in figure 8. Displacements at all elevations of the *WFSW* are decreased with an increase in surcharge pressure. It is also observed that for figure 8 (set 'h') the maximum displacement of the wall was occurred. The maximum displacement of the wall is 8 mm ($\delta h/H = 2\%$) at a surcharge pressure of 0.71 kPa, whereas it is decreased to 0.2 mm ($\delta h/H$ = 0.05%) at a surcharge pressure of 1.72 kPa. Since the base acceleration and frequency of set 8 is 0.5g and 15 Hz respectively. Also, it is noticeable that displacement occurred more at the top elevation of the wall in all the sets. There is no clear pattern for frequency response was observed except at low frequencies as it can be seen from figure 8 (set 'a' to set 'c') where displacement values were close for all the surcharge pressures respectively.

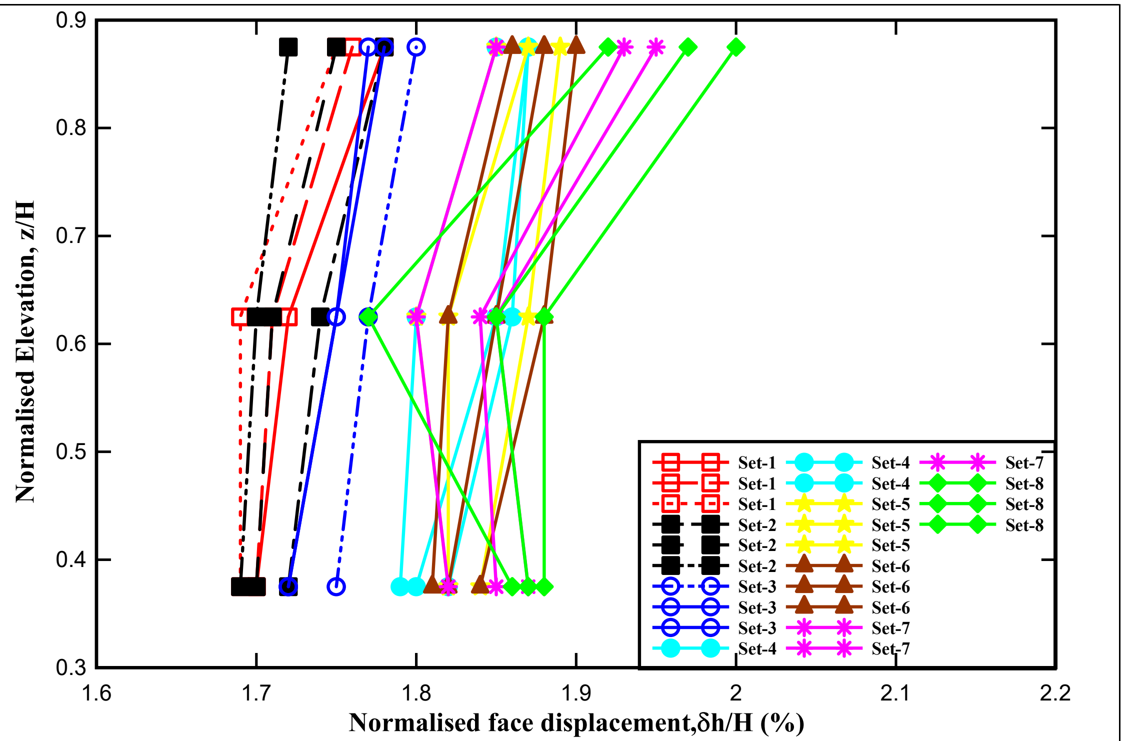

Figure 8. Effect of Surcharge on displacement profile (a) Set-1; (b) Set-2; (c) Set-3; (d) Set-4; (e) Set-5; (f) Set-6; (g) Set-7 and (h) Set-8.

Deformation in the like of overturning of the facing was observed as shown in figure 9. The overturning mode of failure was highly noticeable after 10 Hz, 12 Hz and 15 Hz. Although the deformation was visible enough to notice after 1 Hz, 3 Hz and 5 Hz. The maximum visible lateral displacement had occurred at the top of the wall and the reinforced zone moved outwards of those layers.

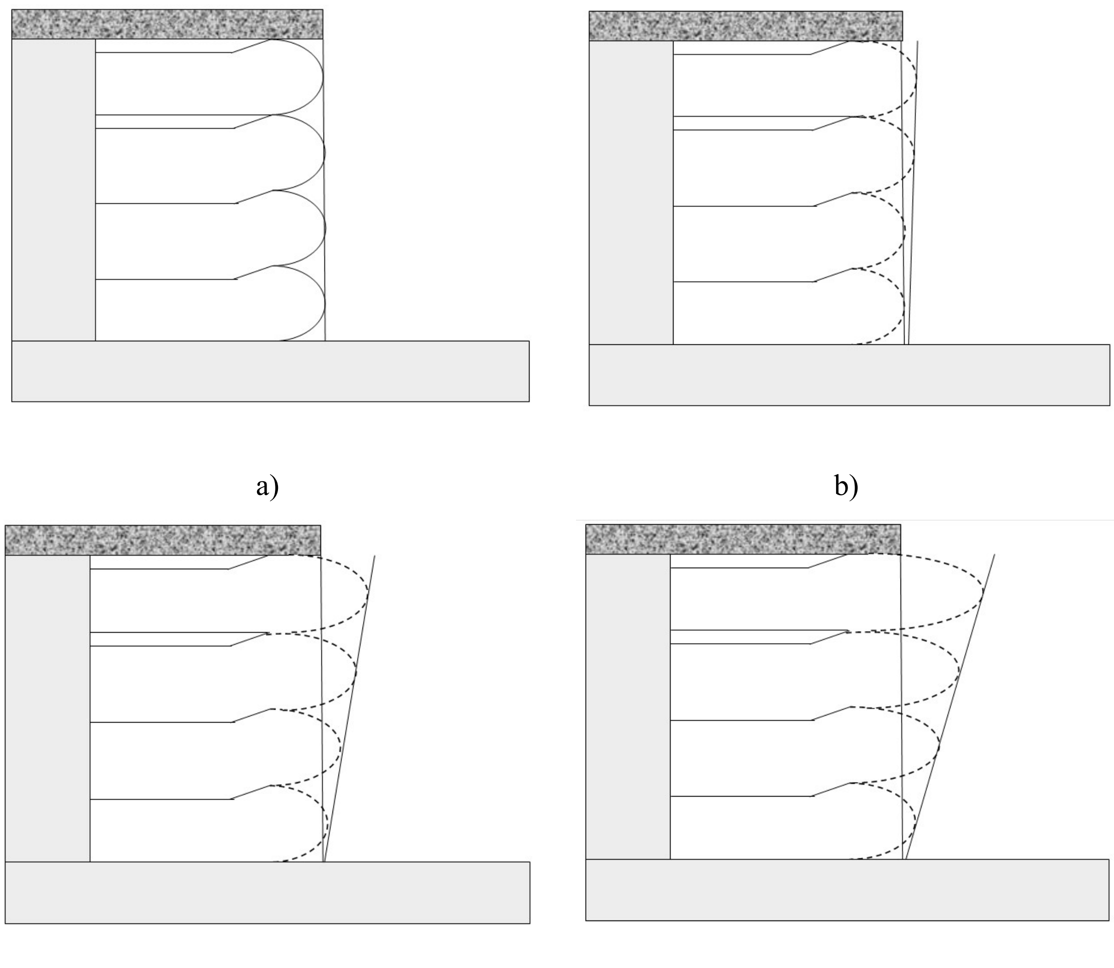

a) b) c) d)

Figure 9. Formation of overturning mode during shaking: (a) before shaking; (b) after shaking by 1, 3 and 5 Hz; (c) after shaking by 12 Hz; (d) after shaking by 15 Hz.

4.3 Pore pressure response

Pore pressure responses were evaluated by considering the Set-8 configuration. The height of the clayey soil layer (*C*) was 610 mm and used to normalize the elevations. Fig. 10 depicts the effect of surcharge on pore pressure in clayey soil layer. The maximum pore water pressure 0.30 kPa was determined at z/C=0.75 for surcharge load of 0.7 kPa. At z/C=0, the minimum pore pressure (0.06 kPa) was found. The maximum pore water pressure for model tests ST30, ST60 and ST90 were 0.30 kPa, 0.21 kPa, and 0.09 kPa, respectively at *z/C*=0.75.

Excess pore pressure ratio and acceleration time histories are presented in the Fig. 11 by considering Set-1, 4, 5, 6, and 8, respectively. Moreover, Table 3 depicts the maximum values of *Pr*% (of each one of the 24 tested cases) to show the effects of the parameters evaluated on the pore water pressure. To more clearly depict the change of pore pressures with surcharge and elevation, the excess pore pressure ratio (*Pr*%) was normalized and obtained by dividing the measured excess pore pressure by the initial vertical effective stress at each pore pressure cell depth. Peak to peak values of horizontal pressures is also high at higher base accelerations. The 100% pore pressure ratio indicates complete liquefaction. It can be seen from Fig. 11 that, with increasing the surcharge load, the pore pressure is decreasing, though it was increasing elevations wise. Moreover, the elevation wise change of pore pressure is very limited, or it can be said that very negligible. According to Bishop and Morgenstern (1960) pore pressure ratio is defined as $Ru = u/\gamma z$, where e u is the pore-water pressure, γ is the unit weight of the soil and z is the depth below ground. The excess pore pressure ratio (*Pr*%) is increasing with the increase of the accelerations and the maximum pore pressure ratio (about 90%) was developed for 0.5g acceleration. The average excess pore pressure ratio (*Pr*%) was within the range of 40-70%.

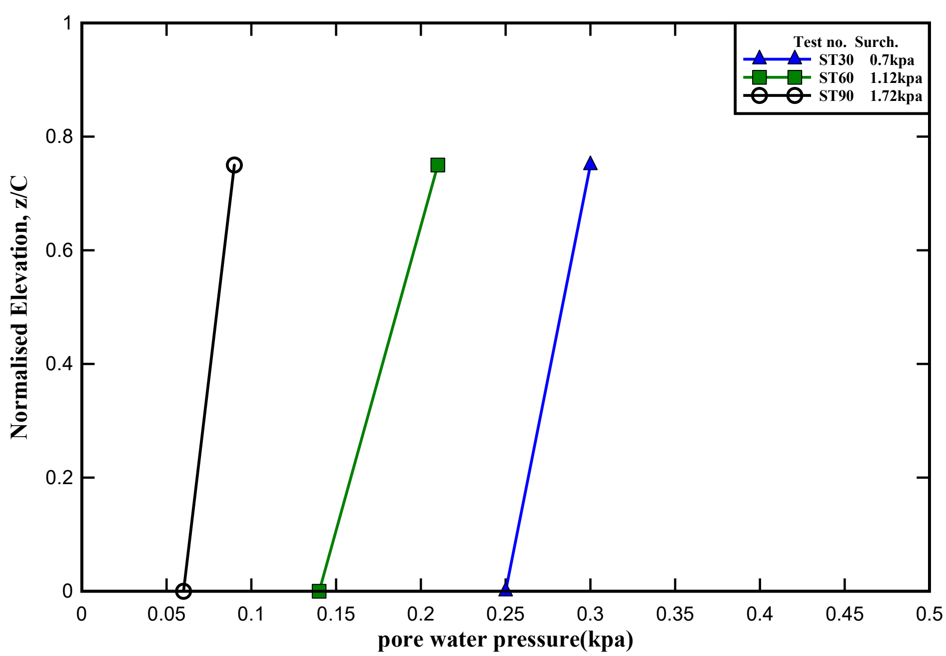

Figure 10. Variations of pore water pressure with respect to Elevation for set-8 (Effect of

Surcharge).

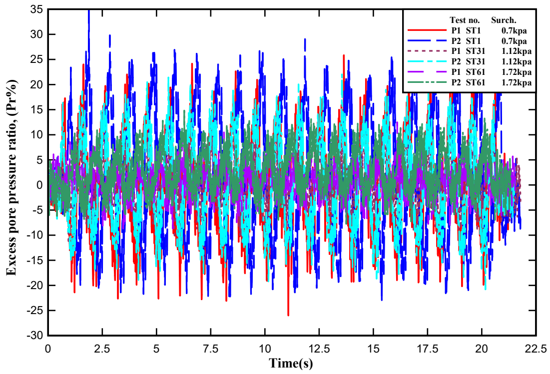

a)

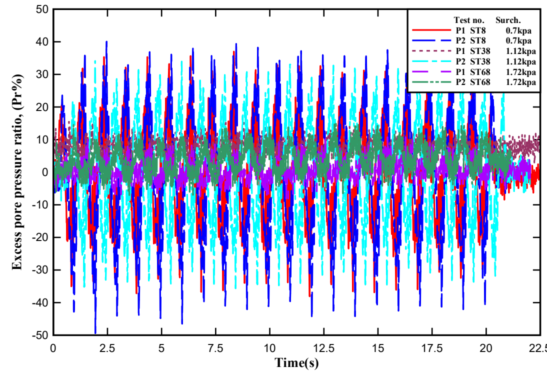

b)

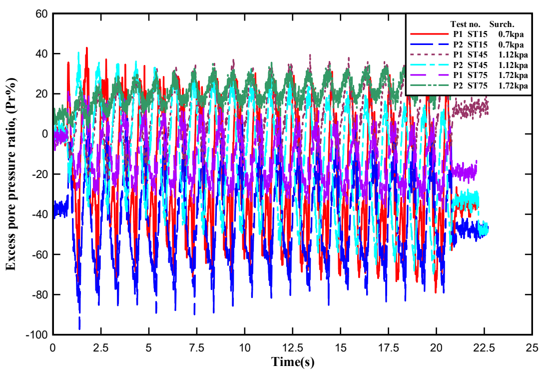

c)

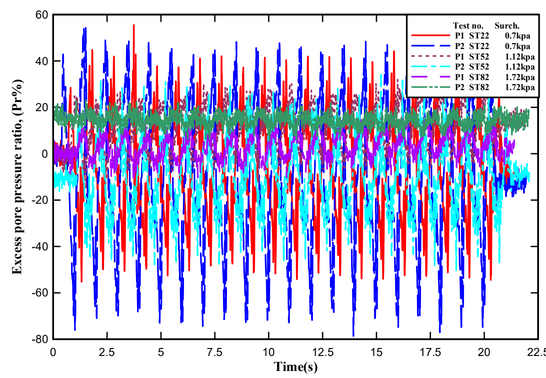

d)

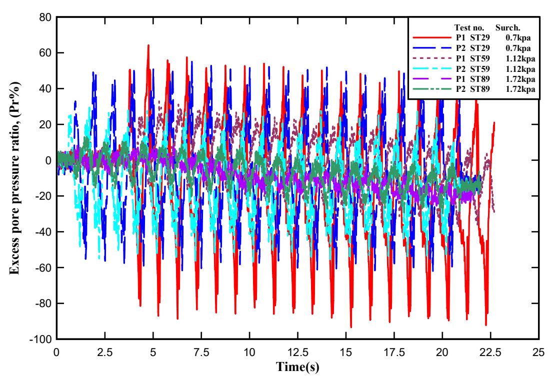

e)

Figure 11. Excess pore pressure ratio at two depths versus time curves(a) Set-1; (b) Set-4; (c) Set-5, (d) Set-6 and (e) Set-8.

5. Conclusions

The main conclusions from reduced scale shaking table model tests on wrap faced geotextile retaining walls can be summarized as follows:

- Acceleration amplifications at the top of the geotextile wall were inversely proportional to the surcharge pressures for all the tests. Acceleration amplifications are not much affected by the change in surcharge loads, especially at lower elevations of the wall. In clayey soil layer acceleration amplified less than geotextile sand wall in all the tests.
- Displacements along the facing were reduced due to an increase in the surcharge pressure. This phenomenon was observed at all the elevations. Maximum 2% displacements were observed for 0.7 kpa pressure. Because of overturning mode of failure maximum displacement occurred at the top of the wall. In the overturning mode, the reinforced zone of facing moved outwards like a rigid block. In general, face displacements are high for low surcharge pressures.
- Pore water pressure gets intensified with decreased surcharge pressure. Peak to peak values of horizontal pressures is also high at higher base accelerations. Moreover, the variation is not significantly shown in the higher elevations. As the excess pore pressure ratio was found below the 100%, means no complete liquefaction occurred. The outcomes from this examination give helpful rules with respect to the relative performance of reinforced soil under different test conditions with clear ramifications for plan.

PART-XI

RECENT MAJOR FIRE/OTHER INCIDENCES IN BANGLADESH

BANGLADESH NETWORK OFFICE FOR URBAN SAFETY (BNUS), BUET, DHAKA

Prepared By: Mehedi Ahmed Ansary

49 KILLED, OVER 450 INJURED IN CHITTAGONG CONTAINER DEPOT FIRE (05.06.2022)

Large explosion have killed at least 49 people and injured hundreds more at a storage depot near the city of Chittagong, Bangladesh. Hundreds of people had arrived to tackle the fire when a number of shipping containers exploded at the site in Sitakunda. It is thought that chemicals were stored in some of the containers. Industrial fires are common in Bangladesh, and are often blamed on poor safety regulations.

Many of the injured are said to be in a critical condition and the number of people killed is expected to rise. Hospitals in the area are overwhelmed, with crowds of people waiting in hallways for treatment. Medics have appealed for blood donations and military clinics are helping to treat the injured.

IMAGE SOURCE,GETTY IMAGES

Image caption,

Parts of the depot were still on fire on Sunday

The fire broke out at around 21:00 local time (15:00 GMT) on Saturday and hundreds of firefighters, police and volunteers quickly arrived on the scene. As they tried to extinguish the blaze a huge explosion rocked the site, engulfing many of the rescuers in flames and throwing debris and people into the air.

"The explosion just threw me some 10 metres from where I was standing. My hands and legs are burnt," lorry driver Tofael Ahmed told AFP news agency. Volunteers, some wearing only sandals on their feet, continued to bring bodies from the smouldering wreckage on Sunday morning. Pictures of the aftermath show the twisted remains of metal shipping containers and the collapsed roof of a warehouse. A local journalist told the BBC that there was a pungent odour in the air. At least five firefighters were killed in the blast and several more were injured. Many people are still missing, including journalists who were reporting on the fire before the explosion.

The blast was so large it was heard several kilometres away and shattered the windows of nearby buildings. One local shopkeeper told reporters that a piece of debris had flown half a kilometre and landed in his pond. He described seeing "fireballs falling like rain" after the explosion.

IMAGE SOURCE,GETTY IMAGES

Image caption,

Bodies were still being taken from the scene on Sunday

Many people in Bangladesh are comparing the explosion to the huge blast that hit Beirut in 2020, says the BBC's Akbar Hossain in the capital, Dhaka. He says people have reported hearing the blast from 30-40km (19-25 miles) away.

Firefighters were still struggling to put out the fire on Sunday, with continued explosions making it more difficult, according to fire officials. The army has deployed sandbags to prevent chemicals flowing into the Indian Ocean.

Around 4,000 containers were stored at the depot in Sitakunda, which is around 40km (25 miles) from Chittagong - Bangladesh's main sea port and second-largest city. Sitakunda acts as a transit point for goods travelling through the port.

IMAGE SOURCE,REUTERS

Image caption,

The storage site held around 4,000 containers

A regional government official said the depot contained millions of dollars of garments waiting to be exported to Western retailers.

Bangladesh is a major supplier of clothing to the West and has prospered over the past decade to become the world's second largest exporter of garments.

But safety regulations are often ignored or poorly enforced, and there have been several large fires and other incidents at factories in recent years.

GULSHAN BUILDING FIRE: DEATH TOLL 2 (FEB 2023)

At least two people were killed trying to save themselves by jumping from a high-rise building on **fire** in Dhaka's **Gulshan** on Feb 23. A couple on Feb 2 was killed in an explosion inside their kitchen. The explosion and subsequent **fire** were caused by gas leaking from an LPG cylinder.

The modern apartment building in Gulshan that caught fire on Sunday lacked a "fire safety plan", a fire service probe has found.

"This is a modern building but during our primary investigation, we found that it has different types of problems. We are not disclosing the details for the sake of investigation," said Lt Col Mohammad Tajul Islam Chowdhury, head of a five-member probe committee, after visiting the fire-ravaged building.

The building authorities had a no-objection certificate from the fire service during construction, but they failed to get the fire safety plan which is required under the Fire Prevention and Extinction Act, he added.

Fire service-approved Fire Safety Plan indicates that a building has been inspected and working fire safety measures are in place as per the norms and regulations.

Replying to a query, he said the two died as they jumped off the building. "We repeatedly told them not to jump. After some time, our firefighters with breathing gear entered the building and rescued trapped victims alive," he said. Meanwhile, another person who jumped off the building to avoid the blaze died yesterday, raising the death toll to two.

Mohammad Raju, 30, who was a cook in an apartment on the 12th floor, died around 3:30am yesterday at a hospital in Gulshan. On Sunday night, Anwar Hossain, 32, died.

Three people are under treatment at the Sheikh Hasina National Institute of Burn and Plastic Surgery.

The fire began around 7:00pm on the sixth floor and spread up to the 12th floor. It could be brought under control around 11:00pm with the efforts of firefighters who were joined at one point by the air force and army personnel. Firefighters rescued 22 people, including 11 women and a child, from the building on Road-104 of Gulshan-2.

CAUSE OF FIRE?

The fire could have originated from a short circuit inside the building's lift which then spread quickly due to the wooden décor inside the lift, Brig Gen Md Main Uddin, director general of Fire Service and Civil Defence, told The Daily Star. He said wood had been used a lot for interior decoration in the building and that could be a reason for the fire spreading this quickly.

Two firefighters who conducted the search operation told this newspaper that ducts from the third to the 11th floors were badly burnt and those had various electrical lines. The gas line was close by too. The ducts were next to the lift. Engineer Mahfuzul Hasan, who worked at the building during construction, claimed that the building had a central air conditioning system which helped the fire spread.

He also claimed that the 10th floor was damaged the most and that floors 10 and 11 belonged to a garment factory owner.

Mohammad Sajal, a caretaker of a flat, told The Daily Star that he and his colleagues first heard the fire alarm at 6:35pm and then they called the reception. "When the smoke was rushing in, we went downstairs [from the sixth floor] with a fire extinguisher. We first saw the fire near one of the two staircases … . We somehow managed to get down from the building. The fire spread to the whole building through the central air conditioning system," he suspected. Visiting the spot yesterday, Dhaka North City Corporation Mayor Atiqul Islam claimed that the building was compliant and that it followed every code stipulated by Rajuk. But unfortunately, the residents of the building did not have training on how to respond to fires.

The mayor said the extinguishing of the fire and the rescue efforts were hampered due to the huge crowd blocking surrounding roads.

NO FIRE STATION IN GULSHAN, BANANI

There is no fire station in Gulshan and Banani areas which sometimes causes delays in firefighters reaching those areas, fire service officials said.

However, firefighters managed to reach the spot within 10 minutes of receiving the call. The neighbourhoods need a fire station close by as unfavourable conditions in future could delay fire service response, they said.

Brig Gen Main Uddin said they wrote to the DNCC for space to establish fire stations in Gulshan and Banani but did not get any response.

Mayor Atiqul said the city corporation does not have any piece of land to allocate and it was Rajuk that allocates plots. "The fire department should write to Rajuk, not the city corporation," he said.

Fire service officials said there are 20 fire stations in Dhaka north and south city corporation areas. As there is no fire station in Gulshan and Banani, fire engines from Bhatara respond to incidents in those areas.

During a spot visit yesterday afternoon, police were seen guarding the building. Not even caretakers and guards were allowed in.

6 DEAD, SEVERAL INJURED IN BLAST AT OXYGEN PLANT IN BANGLADESH'S CHITTAGONG (5TH MARCH 2023)

The explosion shook the buildings in the nearby area within a range of two square kilometres. Several objects were seen flying from the oxygen plant in the Chittagong area after the massive explosion.

Chittagong Oxygen Plant Blast: At least six people were killed while 30 others were injured in an explosion at an oxygen plant in Kadam Rasul (Keshabpur) area of Chittagong's Sitakunda upazila in Bangladesh on Saturday afternoon. The explosion shook the buildings in the nearby area within a range of two square kilometres. Several objects were seen flying from the oxygen plant in the Chittagong area after the massive explosion.

Those killed included, 5 people who were inside the plant at the time explosion occurred while a 65-year-old Shamshul Alam, who was sitting at his shop Kadam Rasul Bazar – about a kilometre away from the oxygen plant – died after a metal object fell on him following the massive explosion.

According to Alam's brother Mowlana Obaidul Mostafa, a metal object, weighing around 250-300kg, fell on top of him after the explosion and he was killed on the spot.

According to the fire officials, the explosion took place around 4:30 pm. On receiving information, nine fire tenders from Sitakunda and Kumira Fire Service were collectively rushed to the spot. It took the personnel more than an hour to bring the fire under control. The cause of the explosion is yet to be ascertained.

CHATTOGRAM, March 6, 2023 (BSS) - The Investigators believe that the blast at Sema oxygen plant in Sitakunda might have originated in its air separation unit. Directorate of Explosives believes that the deadly blast occurred in air separation column at Sema Oxygen Plant under Sitkakunda upazila. The investigation team of the district administration also feels that the explosion may have occurred from the air separation column. The fire service says that the fire did not cause the explosion, the explosion caused by the fire. Earlier, members of district administration investigation committee visited the site and collected evidence on Sunday. “The inquiry committee suspected the blast originated in the air separation column of the oxygen plant,” said Rakib Hossain, Additional Deputy Commissioner, also head of the investigation committee.

Rakib Hossain said they need to carry out more investigation to find out the actual cause of the accident. Another investigation committee member Dr Suman Barua, chairman of applied chemistry of Chattogram University, said the blast was caused by pressure fluctuation in the air separation plant. They apprehended that the pressure was not released properly. Rakib Hossain said the factory engineer could not provide proper answers to questions from the committee as he did not have a clear idea about the technical matters related to the plant. The committee would ask the owner Mamun Uddin for the information, he said. Six people were killed and 25 others injured as a fire broke out at a private oxygen plant following an explosion in Kadam Rasul (Keshabpur) area of Sitakunda upazila of the district on Saturday.

BLAST IN SCIENCE LAB AREA: BUILDING HAD NO FIRE SAFETY SYSTEM (TUE MAR 7, 2023 04:11 AM)

Shirin Mansion, the three-storey commercial building in the capital's Science Lab area, where a deadly explosion took place on Sunday, lacked any fire safety features or other means of preventing a fire, said a top fire service official. The walls and roof of the building caved in and projectiles and glass shards shot across the area after the blast on the second floor around 10:50am, killing three people and injuring at. There were offices of an insurance company and a stationery product supplier on the second floor.

"There was no fire safety equipment or anything that could stop a fire in the building…The second floor has been so damaged that it needs to be reconstructed," said Hafizur Rahman, deputy assistant director at Bangladesh Fire Service and Civil Defence, who led the rescue operation at the scene on Sunday.

Fire service officials said they were yet to form a probe body over the incident.

"We primarily suspect gas accumulation to be the reason behind the blast. We are investigating it further and looking into other possible reasons," Brig Gen Md Main Uddin, director general of the fire service, said, while talking to reporters after attending an event in Mirpur yesterday.

The bomb disposal unit of Counter Terrorism and Transnational Crime found no sign of explosive substances but found the presence of gas at the scene.

The CTTC suspect the explosion might have originated from the office of the insurance company.

Meanwhile, Dhaka South City Corporation (DSCC) declared the Shirin Mansion as "risky" and put up a banner, restricting entry to the building.

FIGHTING FOR THEIR LIVES

Six injured employees of the insurance company were admitted to the Sheikh Hasina National Institute of Burn and Plastic Surgery.

Three of them -- Zahur Ali, with 44 percent burns, Ayesha Akter Asha, with 38 percent burns, and Akbar Ali, with 37 percent burns, -- are in critical condition, said Dr Samanta Lal Sen, coordinator of the hospital.

A Dhaka University student Nur Nabi, 23, on whom parts of the wall collapsed, is fighting for his life at the Dhaka Medical College Hospital.

"His condition is critical. We are doing our best," Dr Asit Chandra Sarkar, chief of DMCH's neurosurgery department, told The Daily Star, after conducting surgery on his head yesterday.

Meanwhile, shop owners of the building are worried.

"There were goods worth Tk 50 lakh inside my two shops. Ramadan and Eid are coming up fast. The frequent college student clashes on top of the Covid pandemic have already done enough damage to our business. Now, this is another massive blow," said Mahabub Mollick, proprietor of two shops in the market.

Shafiqul Gani Shabu, officer-in-charge of New Market Police Station, said, "As far as we've come to know, the owner of the building -- Shirin Chowdhury lives abroad. We have yet to contact her."

DHAKA BLAST: 19 KILLED, OVER 100 INJURED AS EXPLOSION ROCKS SEVEN-STOREY BUILDING (TUE MAR 7)

A t least 14 people were killed and over 100 others injured on Tuesday in a powerful explosion at a seven-storey building in Bangladesh's capital Dhaka, police said. Eleven firefighting units have been mobilised at the spot after the blast, which occurred around 4:50 pm (local time) at Old Dhaka's crowded Gulistan area, the fire service control room said. "Fourteen bodies have been found (so far) but the toll could rise as the rescue operation is underway," a fire service official told reporters.

The cause of the explosion could not be known immediately, but local residents suspected chemicals illegally stored inside the building, mostly used as an office and business complex, might have sparked the blast. "At first, I thought it was an earthquake. The entire Siddik Bazar area was shaken by the blast," eyewitness Safayet Hossain, a local shopkeeper, told The Daily Star newspaper.

"I saw 20-25 people lying in the road in front of a damaged building. They were seriously injured and bleeding. They were crying out for help. Some people were running around in panic," he said.

He added that the locals were carrying the injured in vans and rickshaws to the hospital.

Alamgir, who was close to the blast site, said, "After the loud noise, people quickly came out of the building. There was panic on everyone's faces. The glass of the building's windows shattered and fell onto the street. Many pedestrians on the street were injured."

The Rapid Action Battalion's bomb disposal unit was rushed to the spot to inspect the buildings. Dozens of injured were taken to Dhaka Medical College Hospital, said DMCH police outpost j+spector Bacchu Miah. He added that all of them were receiving treatment at the hospital's emergency unit. The building has several stores for sanitary products on the bottom floor and a branch of BRAC Bank was located in the building adjacent to it. The blast shattered the glass walls of the bank and also damaged a bus standing on the opposite side of the road, reports said.

Firefighters and rescue workers search for survivors and bodies at the site of an explosion in Dhaka, Bangladesh, on March 7, 2023.

An explosion ripped through a building in a crowded area of Bangladesh's capital on Tuesday, killing at least 19 people and injuring more than 50 others, according to authorities in the South Asian country.

Mahid Uddin Khondekar, additional commissioner of the Dhaka Metropolitan Police, said the cause of the blast was unknown but it may have been a gas explosion.

"We are not sure, but it seems accidental," he said, adding that the number of casualties and scale of the damage would become clearer after firefighters and rescue workers had completed their operations. Not many people were inside the building at the time of the blast, but its location on a busy road near a market meant pedestrians were impacted, Dhaka Metropolitan Police said.

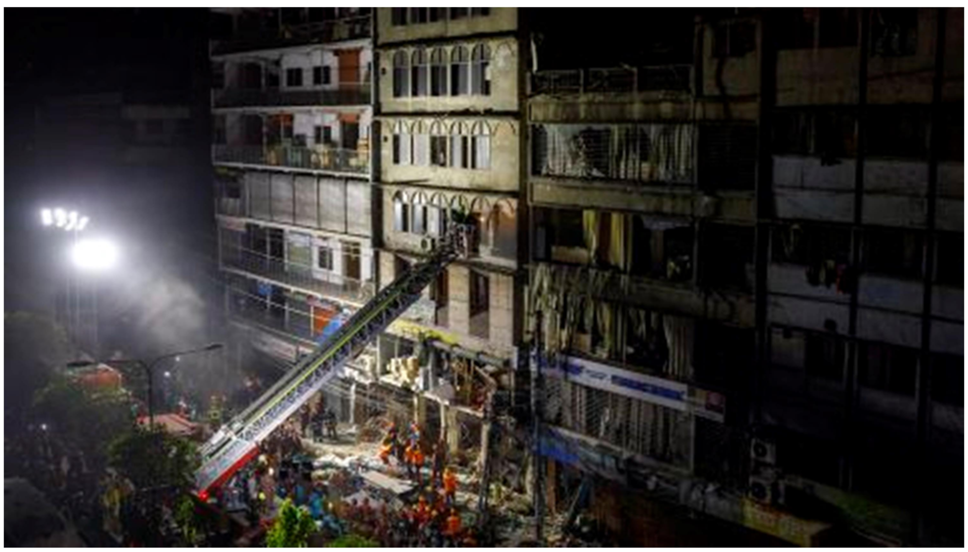

Firefighters and rescue workers at the site of an explosion in Dhaka, Bangladesh, on March 7.

Photos show firefighters and emergency responders carrying out search and rescue operations after dark. The damaged building has crumbling and missing walls; some units appear to have collapsed completely and debris covers the ground outside. Relatives of the victims are seen mourning outside. As of Wednesday morning, 22 people remain in hospital, according to fire service official Dinomoni Sharma.